

ABSTRACT

DHAWAN, ANUJ. Development of Robust Fiber Optic Sensors Suitable for Incorporation into Textiles, and a Mechanical Analysis of Electronic Textile Circuits. (Under the guidance of Dr. John F. Muth, Dr. Tushar K. Ghosh, and Dr. Abdelfattah M. Seyam.)

Electronic and optoelectronic textiles are an emerging area with many potential applications including the distribution of sensors within fabrics. One of the principle challenges of textile based electronics is to understand how the conductors and fiber optics behave under the mechanical forces of construction and use. Thus, first part of this thesis focuses on the development of fiber optic sensors that are sensitive, yet robust enough to be incorporated into textiles. The second part of the thesis focuses on the problem of understanding the bending stiffness of fabric-based electrical circuits and presents a model to quantify the effect of incorporating rigid elements, such as conducting threads into woven fabrics.

Several novel fiber optic sensors are developed in this thesis, with the main focus on optical affinity sensors that employ surface plasmon resonance effects that are sensitive to local changes in the surrounding refractive index. These sensors can be employed to monitor the change of concentration of a chemical or adsorption of chemical or biological molecules on the surface of the sensor. A variety of techniques to control the surface plasmon are investigated, including annealing of gold thin films to form discontinuous and islanded thin films with nanoscale size dimensions, colloidal nanoparticles of gold, and surface plasmon engineered thin films where the extraordinary transmission of arrays of sub wavelength apertures can be exploited. In general these sensors are tested by changing the surrounding refractive index medium and monitoring the optical transmission. To demonstrate the detection of molecules, the detection of Streptavidin binding to Biotin is demonstrated. A variety of novel in-line temperature sensors are also developed, by incorporating temperature sensitive nanoparticles within the core of the optical fiber, or by constructing an inline Fabry-Perot cavity within the structure of the fiber. The first major result is the development of in-line fiber optical systems that are constructed by fusing different fiber optic elements together into a continuous fiber with uniform diameter. Using this approach, the light can be transmitted to the sensor efficiently by a single mode optical fiber, a coreless optical fiber can be used as a beam expansion region or as a sensor region, and short segments of graded index fibers can be used as lenses to collimate or focus the light as appropriate. In addition to being substantially more robust than tapered fiber optic

sensors or fiber optic sensors where the cladding is removed by etching, the interaction region of the sensor with the environment can be substantially increased.

The second major result is the incorporation of metallic and semiconducting nanoparticles into the core of fiber optic in-line sensors. These sensors are fabricated by coating the tip of the optical fiber with the desired metal or material such as vanadium oxide, and over coating the tip with a protective layer of silicon dioxide. The fiber can then be annealed, and fused to another optical fiber to form the in-line sensor. Since the size of the metallic nanoparticles can be determined by the annealing and fusion process, the optical properties of the sensor can be optimized. This approach is used to fabricate temperature sensors, where for gold nanoparticles, the shift and broadening of the plasmon resonance is used, and for vanadium oxide compounds where shifts in the absorption edge are monitored. Using thicker metallic films, partial mirrors can also be constructed using this assembly method to form a Fabry-Perot cavity where positions of the resonances can be monitored to track changes in temperature. In addition to in-line sensors, fiber tip sensors are constructed, where nanoparticles or engineered nanostructures of gold are placed on the fiber tips and used to monitor the refractive index changes of a solution. The use of arrays of subwavelength apertures constructed on the ends of etched and tapered fiber tip using focused ion beam milling are shown to be especially promising for future optical affinity sensors.

In the second part of the thesis, the problem of bending stiffness of fabric-based electrical circuits is addressed. This is approached by assessing the effect of incorporating rigid elements such as conducting threads into woven fabrics. Although the models described in this thesis are employed to understand the bending behavior of fabric circuits, these models can also be applied for determining the bending rigidity of other fabrics with rigid metallic threads woven into the fabric structure. The key elements of a model employed to determine fabric bending rigidity are described and a procedure to determine fabric bending rigidity, based on an energy method that incorporates fabric structural parameters is developed. A theoretical model that explains the effect of incorporating finite number of rigid threads in a fabric, in the warp and weft directions, along with flexible threads on the bending rigidity of the fabric is presented. The theoretical models are then compared with experimental measurements. An elastica-based theoretical model is developed and applied to fabrics containing multiple welded, fused, or soldered interconnects at the crossover point.

**DEVELOPMENT OF ROBUST FIBER OPTIC SENSORS SUITABLE
FOR INCORPORATION INTO TEXTILES, AND A MECHANICAL
ANALYSIS OF ELECTRONIC TEXTILE CIRCUITS**

by

ANUJ DHAWAN

Thesis submitted to the Graduate Faculty of
North Carolina State University
in partial fulfillment of the requirements for the
Degree of Doctor of Philosophy in

**ELECTRICAL AND COMPUTER ENGINEERING
&
FIBER AND POLYMER SCIENCE**

Raleigh

2007

APPROVED BY:

Dr. John F. Muth
(Co-Chair)

Dr. Gianluca Lazzi

Dr. Doug W. Barlage

Electrical and Computer Engineering

Dr. Tushar K. Ghosh
(Co-Chair)

Dr. Abdelfattah M. Seyam
(Co-Chair)

Dr. Perry L. Grady

Fiber and Polymer Science

BIOGRAPHY

Anuj Dhawan was born on July 24, 1976 in New-Delhi, India as a son of Shashi Dhawan and Sushil Dhawan. He joined the Indian Institute of Technology-Delhi in the fall of 1995 and received a Bachelor of Technology degree in Textile Technology, with a minor in Polymer science and engineering, in August of 1999 from that institute. He joined the College of Textiles, North Carolina State University in the fall semester of 1999 to pursue graduate studies. At NC State, he received a co-major Master's degree in Computer Engineering and Textile Technology in December 2001. As a part of his master's work, he worked on a Defense Advanced Research Project Agency (DARPA) project dealing with computational textiles. Upon graduation from his masters, he joined the doctoral program at North Carolina State University co-majoring in Electrical Engineering and Fiber and Polymer Science. As a doctoral student, he was involved in projects funded by the US Naval Research Laboratory, the US Army Research Office, and DARPA. As part of his Ph. D. research work, Anuj has focused on the development of robust fiber optic environment sensors and the integration of these sensors into textile substrates. Another part of his thesis involves the evaluation of the bending behavior of woven fabric based electronic textiles.

ACKNOWLEDGMENT

I would like to express the deepest appreciation to my advisors, Dr. John Muth, Dr. Tushar Ghosh, and Dr. Abdelfattah Seyam, for their guidance, patience and encouragement throughout my study as a Ph.D. student. Their mentoring, dedication and enthusiasm enabled me to learn a lot and to develop my skills as a researcher. Moreover, I would like to thank Dr. Doug Barlage, Dr. Gianluca Lazzi, and Dr. Perry Grady for their guidance and encouragement during my study.

Financial support for my research work was provided by the Army Research Office, the Office of Naval Research, and the Defense Advanced Research Project Agency (DARPA). I would like to thank their staff for the financial support and for providing me with an opportunity to work on their projects. Special thanks go to Dr. Michael Gerhold at the Army Research Office and Dr. Elana Ethridge at DARPA for their guidance and support. I would also like to thank Dr. Leda Lunardi, Dr. Veena Misra, Dr. Bhupinder Gupta, Dr. Subhash Batra, Dr. Rebecca Rufty, Dr. Tom Stafford, and Dr. William Oxenham for their support and guidance throughout my stay at NC State. I would also like to thank Peggy Olive, Carolyn Krystoff, Tara Britt, Brenda Beatty, Tywana Johnson, Robert Cooper, and Dawn Hartley for their support. Special thanks go to my co-worker and friend Xiyao Zhang for his encouragement and support. I would also like to thank my co-workers and friends Arun Suresh, Praveen Golakotta, Hugh Porter, John Mcglade, Andrew Shelton, Jason Kekas, and Patrick Wellenius for being supportive. I would also like to thank our lab manager, Mr. Joe Matthews for his assistance in the clean room and for his timely advice on different research problems.

Special thanks are given to my parents Shashi and Sushil Dhawan, who have always supported me and guided me towards the achievement of my goals in life. Special thanks are also given to my brother-in-law Praveen Duggal and my sister Charu Duggal for all their support and help. I would also like to thank my friends Anuj Jaggi, Vijay Patel, Chirag Lakhani, Jackson Brown, and the Jaggi family for being supportive and helpful throughout my stay at NC State. I would also like to express my thanks to all my friends and relatives in India and in the United States for all their help and encouragement.

TABLE OF CONTENTS

List of Tables	xi
List of Figures.....	xii

PART I. DEVELOPMENT OF ROBUST FIBER OPTIC SENSORS SUITABLE FOR INCORPORATION INTO TEXTILES.....1

CHAPTER 1. INTRODUCTION.....2

1.1 Reasons for using optical fibers for sensing.....	4
1.2 Incorporation of sensors into textiles.....	7
1.2.1 Integration into woven and knitted fabrics.....	7
1.2.2 Integration into non-woven fabrics.....	8
1.3 Outline of the Thesis.....	10
1.4 References.....	11

CHAPTER 2. LITERATURE REVIEW12

2.1 Sensing fundamentals.....	13
2.1.1 Metrics for chemical and biochemical Sensing.....	14
2.1.2 Different kinds of chemical sensing.....	19
2.2 Optical fiber based sensing.....	20
2.2.1 Optical fiber sensing mechanisms.....	22
2.2.1.1 Intensity modulated fiber optic sensors.....	23
2.2.1.2 Spectrally based fiber optic sensors.....	24
2.2.1.3 Phase modulated fiber optic sensors.....	24
2.2.2. Applications of fiber optic sensors.....	25
2.2.2.1 Optical fiber sensors for sensing chemicals and biological molecules.....	27
2.2.2.2 Optical fibers for temperature sensing.....	28
2.3 References.....	32

CHAPTER 3. REVIEW OF SENSORS BASED ON SURFACE PLASMONS.....	36
3.1 Definition of surface plasmons.....	37
3.2 Description of evanescent waves.....	39
3.3 Excitation of surface plasmon waves.....	41
3.3.1 Excitation of surface plasmons by Attenuated Total Reflection (ATR).....	41
3.3.2 Generation of surface plasmons by using diffraction gratings.....	42
3.3.3 Generation of surface plasmons in optical waveguides.....	43
3.4 Field enhancement due to surface plasmon excitation.....	44
3.5 Derivation of the surface plasmon resonance condition.....	46
3.5.1 Definition of surface plasmon resonance.....	46
3.5.2 Interrogation of surface plasmon resonance.....	51
3.6 Resonance in scattering and absorption properties of metallic particles.....	52
3.6.1 Mie resonance theory.....	54
3.6.2 Absorbance spectra of oblate spheroid particles (Quasi-static approximation).....	56
3.7 Non fiber-based SPR Chemical and biological sensors.....	58
3.7.1 Fundamentals of chemical sensing employing SPR.....	58
3.7.2 Chemical and biological sensors based on attenuated total reflection (Kretschmann or Otto configurations).....	60
3.7.3 Chemical and biological sensors based on planar optical waveguides.....	62
3.7.4 Chemical and biological sensors based on gratings.....	63
3.8 Surface plasmon resonance-based optical fiber sensors.....	64
3.8.1 SPR sensors based on side-polished single-mode optical fiber.....	64
3.8.2 SPR Sensors based on metal-coated unclad fibers.....	67
3.8.3 SPR sensors based on tapered optical fibers.....	70
3.8.4 Surface plasmon resonance sensors having a sensing section at the tip of the optical fiber.....	72
3.9 Optical fiber sensors based on plasmon resonances of metallic particles.....	76
3.10 References.....	78

CHAPTER 4. IN-LINE OPTICAL FIBER STRUCTURES FOR EXPANSION

AND RE-FOCUSING OF GAUSSIAN BEAMS	81
4.1 Chapter Summary.....	82
4.2 Background.....	82
4.3 Principle and Analysis.....	84
4.4 Derivation of Gaussian beam intensity considering multiple beam reflections.....	96
4.5 Results and Discussion.....	98
4.6 Beam Propagation Method simulations on the In-line fiber optic structures.....	101
4.6.1 Results and Discussion.....	102
4.7 Conclusions.....	106
4.8 References.....	107

CHAPTER 5. FIBER-OPTIC CHEMICAL SENSORS: END-FACE AND IN-LINE

SENSORS	108
5.0 Fiber-optic chemical sensors: End-face and in-line sensors.....	109
5.1 Different optical fiber structures for sensing applications.....	109
5.2 Experimental.....	114
5.2.1 Development of nanoparticles.....	114
5.2.1.1 Nanoparticle development by annealing of very thin metallic films.....	114
5.2.1.2 Formation of nanoparticles using citrate reduction.....	120
5.2.1.3 Development of metallic nanoparticles using Focused Ion Beam (FIB) Milling	123
5.2.2 Development and evaluation of the sensor structures.....	130
5.3 Results and Discussion.....	131
5.4 Optical fiber sensors for sensing of biomolecules.....	137
5.5 Development of a sensor system to sense chemicals/biomolecules.....	142
5.6 Conclusions.....	145

5.7 References.....	145
---------------------	-----

CHAPTER 6. IN-LINE DEVICES BASED ON THE INCORPORATION OF METALLIC NANOPARTICLES INSIDE OPTICAL FIBERS.....147

6.1 Introduction.....	148
6.2 Analytical calculations.....	155
6.2.1 Determination of absorption and scattering cross-sections based on Mie theory.....	155
6.2.2 Absorption and scattering cross-sections based on Quasi-static theory.....	157
6.2.3 Temperature dependence of absorption and scattering cross-sections of metallic nanoparticles in an optical fiber matrix.....	157
6.2.4 Design of a distributed temperature sensor.....	167
6.3 Experimental Results and Discussion.....	170
6.4 Conclusions.....	171
6.5 References.....	174

CHAPTER 7. INCORPORATION OF FABRY-PEROT CAVITIES AND VANADIUM OXIDE FILMS INSIDE OPTICAL FIBERS FOR TEMPERATURE SENSING AND OPTICAL SWITCHING APPLICATIONS.....175

7.1 Introduction.....	176
7.1.1 Vanadium oxide based inline fiber optic sensors.....	178
7.1.2 Fabry-Perot cavity based inline fiber optic sensors	181
7.2 Experimental.....	182
7.2.1 Development of vanadium oxide based fiber optic sensors.....	182
7.2.2 Development of Fabry-Perot cavity based fiber optic sensors.....	186
7.3 Results and Discussion.....	186
7.3.1 Vanadium oxide based inline fiber optic sensors.....	186
7.3.2 Fabry-Perot cavity based inline fiber optic sensors.....	193
7.4 Conclusions.....	199
7.5 References.....	200

**CHAPTER 8. FABRICATION OF SURFACE PLASMON ENGINEERED FIBER-
OPTIC PROBES USING AN ARRAY OF SUB WAVELENGTH**

APERTURES.....203
8.1 Introduction..... 204
8.2 Experimental.....208
8.3 Results and Discussion.....215
8.4 Conclusions..... 222
8.5 References.....222

CHAPTER 9. CONCLUSIONS.....224

PART II. MECHANICAL ANALYSIS OF ELECTRONIC TEXTILE CIRCUITS.....228

CHAPTER 1. INTRODUCTION AND OVERVIEW.....229

1.1 Introduction of fabric based electrical circuits.....230
1.2 Importance of studying the bending behavior of woven fabric based electrical
circuits..... 232
1.3 Thesis overview.....233
1.4 References..... 234

CHAPTER 2. BACKGROUND AND LITERATURE REVIEW.....236

Abstract.....237
2.1 Introduction.....238
2.2 Research in the development of fabric based circuits and devices.....239
2.2.1 Fabric-based circuits and circuit boards.....239
2.2.2 Device attachment.....261
2.2.3 Transistors on thin films/threads.....263
2.2.4 Fabric-based antennas.....266
2.3 Sensors and Actuators.....271
2.3.1 Pressure/tactile sensing systems.....273

2.3.2 Environment sensing systems.....	277
2.3.2.1 Chemical sensing.....	277
2.3.2.2 Sensing of biomedical information.....	280
2.3.2.3 Context awareness.....	282
2.3.3 Strain sensors.....	285
2.3.4 Actuators.....	287
2.4 Fibers/Fabrics in energy storage & generation.....	294
2.5 Heating systems.....	298
2.6 References.....	302

CHAPTER 3. THEORETICAL MODEL TO DETERMINE EQUILIBRIUM

STRUCTURE AND BENDING RIGIDITY OF A WOVEN FABRIC.....	316
Abstract.....	317
3.1 Introduction.....	318
3.2 List of Symbols.....	319
3.3 Determination of equilibrium fabric structure.....	320
3.3.1 Assumptions made in the model.....	320
3.3.2 Equations defining equilibrium yarn shape in a fabric.....	322
3.3.3 Boundary conditions required for determining the equilibrium fabric structure	327
3.3.4 Solution of the boundary value problem.....	338
3.4 Determination of fabric bending rigidity.....	339
3.5 References.....	344

CHAPTER 4. BENDING RIGIDITY OF WOVEN FABRIC-BASED ELECTRICAL

STRUCTURES. PART I: EFFECT OF CROSSOVER POINTS AND RIGID CONDUCTIVE YARNS IN THE WARP & WEFT DIRECTIONS.....	346
Abstract.....	347
4.1 Introduction.....	347
4.2 Description of the theoretical models.....	349
4.2.1 Parallel Beam model of conductive fabrics	349

4.2.2 Elastica Model of conductive fabrics.....	351
4.2.2.1 Equilibrium fabric structure.....	351
4.2.2.2 Determination of fabric bending rigidity.....	353
4.2.2.3 Determination of bending rigidity of a conductive fabric.....	356
4.3 Experimental.....	358
4.4 Results and Discussion.....	363
4.4.1 Parallel Beam model	363
4.4.2 Elastica Model.....	364
4.5 References.....	374

**CHAPTER 5. BENDING RIGIDITY OF WOVEN FABRIC-BASED ELECTRICAL
STRUCTURES. PART II: EFFECT OF WELDING/SOLDERING**

CROSSOVER POINTS OF CONDUCTIVE THREADS WOVEN IN THE FABRIC STRUCTURE.....	376
Abstract.....	377
5.1 Introduction.....	377
5.2 Theoretical model to determine bending rigidity of a woven fabric circuit...	379
5.3 Experimental.....	388
5.4 Results and Discussion.....	390
5.5 References.....	399

LIST OF TABLES

PART I

CHAPTER 2

Table 1. Different kinds of stimuli that could be sensed.....	14
Table 2. Classification of sensors on the basis of principle of sensing.....	14
Table 3. Properties of different types of chemical sensors.....	19
Table 4. Classification of fiber optic sensors.....	23

CHAPTER 3

Table 1. Sensitivities and resolutions of different interrogation procedures and different kinds of coupling systems.....	62
---	----

CHAPTER 4

Table 1. Calculation of lengths of coreless and Graded-Index fiber segments in the In-Line Fiber optic structures.....	95
--	----

LIST OF FIGURES

PART I

CHAPTER 1

- Figure 1. Sensors that are (a) Wavelength Multiplexed, (b) Time Multiplexed, and (c) Time Multiplexed.....5
- Figure 2. A schematic showing a means of incorporating an optical fiber, containing one or more environment sensors on it, into flexible substrates such as textile fabrics.....7
- Figure 3. Optical fiber integrated into woven fabrics along with conventional threads....8
- Figure 4. (a) Optical fibers embedded into a non-woven fabric and (b) SEM micrograph of electrospun nonwoven fibers used to sandwich an optical fiber sensor in between a spun-bonded nonwoven fabric and the electrospun fibers.....9

CHAPTER 2

- Figure 1. An example of a ROC curve which shows two curves for two hypothetical diagnostic tests.....16
- Figure 2. Temporal response of a resistance sensor used to detect an odorant in an electronic nose. The plot of resistance vs. time highlights the response time and the recovery times involved in the sensing process.....17
- Figure 3. Single-mode and multimode step-index and graded-index optical fibers.....21
- Figure 4. Cross-sectional views of the transverse electrical field vectors for the four lowest-order modes in a step-index fiber.....21
- Figure 5. (a) Mach Zender Interferometer (b) Intrinsic Fabry-Perot Interferometer (c) Extrinsic Fabry-Perot Interferometer (d) Michelson's Interferometer.....26
- Figure 6. In-line fiber optic structure employed for temperature sensing applications based on the fusion of a single mode fiber to a multimode fiber which is further fused to a single mode fiber in order to form a Fabry-Perot Cavity.....29
- Figure 7. (a) Optical fiber temperature sensor based on temperature dependent shift in the absorption edge of the semiconductor material and (b) A semiconductor material inserted between two optical fibers to form a temperature sensor based on shift in the absorption edge of the semiconductor.....31

CHAPTER 3

Figure 1. (a) Figure showing the phenomenon of total internal reflection. Light incident from medium 1 having refractive index n_1 is totally internally reflected for $\theta > \theta_c$. In medium 2, k_z is imaginary and k_x is real (b) Evanescent fields decaying away from a boundary with and without a thin gold layer present.....	37
Figure 2. Otto configuration employed for surface plasmon generation.....	41
Figure 3. Kretschmann configuration (a) and Kretschmann-Raether configuration (b) to generate evanescent waves to excite surface plasmon waves at the metal air interface employing attenuated total internal reflection (ATR).....	42
Figure 4. A grating coupler employed to excite surface plasmon modes by the process of diffraction.....	43
Figure 5. A planar waveguide structure used for sensing employing surface plasmon resonance.....	44
Figure 6. Excitation of a surface plasmon wave with a plane-wave coupler (prism, a grating, or random roughness) which is shown by dashed lines.....	48
Figure 7. Geometry depicting excitation of surface plasmon waves at the Metal-Air interface through attenuated total reflection (ATR). Electric and magnetic fields of the reflected and transmitted radiation in the three media are shown. Thickness of the metal film (d) is $\sim 10\text{-}50$ nm for excitation of surface plasmons.....	48
Figure 8. Surface plasmon resonance curve indicating minima in reflectance from a metallic thin film on varying the angle (for a fixed wavelength) of incident radiation.....	50
Figure 9. Raether configuration (a) by changing θ_1 (angle of incidence) for a fixed λ (wavelength) or (b) by changing λ for a fixed θ_1	53
Figure 10. A sphere on a substrate, with an electric field incident at an angle to the surface of the substrate. Mediums 1, 2, and 3 are the surrounding medium, substrate, and the sphere respectively.....	57
Figure 11. Theoretical model by Meriaudeau et al. was used to calculate the (a) Effect of varying the refractive index, of the medium surrounding a gold-coated fiber optic sensor, on the value of absorbance and (b) Effect of varying the thickness of the MgF_2 over layer on a gold-coated fiber optic sensor, on the value of absorbance.....	58

Figure 12. Schematic of a planar waveguide used for SPR sensing.....	61
Figure 13. Shift is the SPR resonance wavelength on changing the thickness of the gold layer and the Ta ₂ O ₅ over layer.....	63
Figure 14. Surface plasmon resonance sensing structure based on a side-polished single mode fiber.....	65
Figure 15. Surface plasmon resonance sensing system consisting of the light source, the depolarized, the flow cell, polarization mixer, and the spectrograph.....	65
Figure 16. Sensing element, based on Surface Plasmon Resonance, consisting of a silver film deposited on the core of an optical fiber in a region where cladding has been removed.....	66
Figure 17. Spectra of a fiber optic surface plasmon resonance based sensor indicating (a) Shift in resonance point of the normalized intensity curves to higher wavelengths on increasing the refractive index of the surrounding medium and (b) Increase in depth of the surface plasmon resonance spectra on increasing length of the SPR sensing area.....	67
Figure 18. Theoretical and experimental values of the surface plasmon resonance coupling wavelength as a function of the refractive index of the fructose sample solutions surrounding the exposed core SPR-based fiber optic sensor.....	68
Figure 19. (a) Sensing segment of an SPR-based optical fiber sensor having a gold layer deposited on the exposed core and (b) Experimental setup to interrogate the SPR-based fiber optic chemical sensor.....	69
Figure 20. (a) Gold coated tapered optical fiber with length of the taper waist being L_w and the diameter of the waist being d_w ; (b) Asymmetric sensor device; (c) Quasi-circular sensor device with a uniform coating of gold on the waist of the optical fiber taper.....	70
Figure 21. (a) Micrograph of a metal-coated tapered optical fiber probe developed by chemical etching of the fiber tip; (b) Schematic of a metal-coated tapered optical fiber probe used for SPR sensing; (c) Experimental setup employing polarization spectroscopy to interrogate the surface plasmon resonance based sensor.....	73
Figure 22. Temporal response of the SPR-based fiber optic sensor showing change in intensity of light detected by the photodiode when the medium surrounding the fiber tip was changed from air (A) to Methanol (M), Water (W), and Ethanol (E) repetitively.....	73

Figure 23. (a) A surface plasmon resonance-based optical fiber sensor with a silver film deposited on the unclad core of the fiber; (b) Interrogation mechanism of the sensor employing a 2 by 1 coupler to input light into the sensor from a polychromatic light source and carry the output radiation, reflected from the chromium mirror at the end of the fiber tip, to the spectrometer.....	74
Figure 24. Optical fiber sensor consisting of a section where the cladding is removed and a 4 nm annealed gold film is deposited. An over coating of MgF ₂ is provided to prevent light from coupling out when the refractive index of the medium being sensed is higher than that of the fiber core.....	76
Figure 25. Experimental absorbance curves for a fiber optic sensor with a 4-nm gold film annealed 4 min at 600 °C (a) Peak resonance shifts to higher wavelength when the refractive index of the medium surrounding the fiber optic sensor is changed from 1 to 1.36. (b) The absorbance curves for a 350 nm cover layer deposited on top of the gold layer and varying the refractive index of the surrounding medium from 1 to 1.7.....	77

CHAPTER 4

Figure 1. (a) Schematic of Structure A, i.e. an in-line optical fiber structure to expand a Gaussian light beam in the coreless optical fiber and to couple maximum amount of light back into the SMF (single mode optical fiber) using GIF (graded index fiber) lenses and (b) Slight variation of structure A with a multimode fiber (MMF) replacing the combination of graded index fiber and the single mode fiber.....	86
Figure 2. Plot of the half beam waist i.e. $w(z)$, in meters, vs. the length ‘a’, in meters, of the first graded index fiber GIF1 in structure A.....	87
Figure 3. Plot of the half beam waist i.e. $w(z)$, in meters, vs. the length ‘c’, in meters, of the second graded index fiber GIF2 in structure A.....	87
Figure 4. Schematic of Structure B, i.e. an in-line optical fiber structure to expand a Gaussian light beam in the second coreless optical fiber and to couple light back into the single mode optical fiber.....	91
Figure 5. (a) Ray tracing analogue of structure A, which uses graded index optical fibers as lenses to expand and collect a Gaussian beam and a coreless fiber as an environmental interaction volume with a corresponding (b) Ray tracing schematic of structure B, which uses multiple graded index and coreless fiber elements. The angles of incidence are exaggerated in the figure, and remain greater than the critical angle of the glass/air interface.....	93
Figure 6. Plot of tangential component of the electric field (E_{ϕ}) for LP ₀₁ mode plotted against the radius r	94

Figure 7. Schematic of Structure C, i.e. in-line optical fiber structure to expand a Gaussian light beam in the second coreless optical fiber and to couple light back into the single mode optical fiber.....	94
Figure 8. Plot of the normalized Gaussian beam intensity profiles for different values of Z , MMM0 is at $Z=0$, MMM1 at $Z = z_0$, MMM2 at $Z = 2z_0$, MMM3 at $Z = 3z_0$, MMM4 at $Z = 4z_0$, MMM5 at $Z = 5z_0$, MMM6 at $Z = 6z_0$, MMM7 at $Z = 7z_0$, MMM8 at $Z = 8z_0$, where z_0 is the Rayleigh length.....	98
Figure 9. Plot of the normalized Gaussian beam intensity profiles for different values of Z , M0 is at $Z=0$, M1.4 at $Z = 1.4z_0$, M1.6 at $Z = 1.6z_0$, M1.8 at $Z = 1.8z_0$, M2 at $Z = 2z_0$, where z_0 is the Rayleigh length. As Z is increased from $Z=0$ to $Z=2$, at $Z = 1.6z_0$, we observe a start of divergence from the Gaussian profile indicating the start of the interaction region.....	99
Figure 10. Plot of the normalized Gaussian beam intensity profiles for different values of Z , M0 is at $Z=0$, M2 at $Z = 2z_0$, M3 at $Z = 3z_0$, M4 at $Z = 4z_0$, M4.2 at $Z = 4.2z_0$, M4.4 at $Z = 4.2z_0$, where z_0 is the Rayleigh length. Estimation of the distance after which the interaction region ends in the coreless fiber is carried out.....	100
Figure 11. Field profile in a single mode fiber, a graded index fiber cut at a length of 1700 μm , and input into a coreless fiber.....	104
Figure 12. Field profile in a coreless fiber section 5000 μm in length showing the expansion of a Gaussian beam to the fiber-air boundary and the superposition of beams being reflected at the boundary.....	105

CHAPTER 5

Figure 1. (a) Deposition or formation of gold nanoparticles on the fiber tip, and (b) Tapered optical fiber employed for evanescent and surface plasmon sensing.....	111
Figure 2. A schematic of the silicon piece, having a V-groove, employed to hold the optical fiber for sensing a change of refractive index of the medium around the sensor.....	111
Figure 3. Gold nanoparticles are formed on the surface of (a) A fused MMF-CF-MMF structure and (b) A fused SMF-GIF- CF-MMF structure.....	113
Figure 4. Ray Tracing schematic of Structure B, which is an in-line fiber structure consisting of single mode, graded index, coreless, and multimode fibers to expand the Gaussian beam to the surface of the coreless fiber.....	113

Figure 5. (a) Absorbance vs. wavelength plot for annealed and unannealed, 4-10 nm thick gold films on a glass substrate, (b) Plasmon resonance related peak shifts when placed in media having different refractive indices, (c) AFM picture of an annealed gold film deposited on a glass substrate after annealing at 400 Deg C, and (d) Change of color of the gold films upon annealing at different temperatures.....	116
Figure 6. Micro-heater used for annealing gold films on fiber tips to form nanoparticles.....	117
Figure 7. Effect of annealing on transmission spectra of thin gold film on fiber tips before (red) and after (blue) annealing.....	117
Figure 8. Plasma arc annealing of 4-10 nm gold film on the optical fiber tip using a fusion splicer.....	118
Figure 9. (a) Appearance of a plasmon resonance related dip in the transmission spectra upon application of plasma arcs to a gold coated (8 nm) fiber tip, (b) Plasmon resonance related dip becomes sharper when both thermal annealing and plasma arc are applied to the fiber tip.....	118
Figure 10. (a) Appearance of a plasmon resonance related dip in the transmission spectra upon application of plasma arcs to a gold coated (8 nm) fiber tip as shown by the blue curve, (b) Plasmon resonance related dip becomes sharper when both thermal annealing and plasma arc are applied to the fiber tip, as shown by the red curve.....	119
Figure 11. Citrate reduction process to form gold nanoparticles (~ 20-120 nm) on the tip of the optical fiber.....	121
Figure 12. Transmission spectrum of an optical fiber having gold nanoparticles (~ 20 – 120 nm), formed by citrate reduction, deposited on its tip.....	122
Figure 13. Development of circular gold nanoparticles on a glass substrate by employing Focused Ion Beam lithography (FIBL). FIBL was applied to a 50 nm gold film on a glass substrate to pattern the array of these nanostructures. The diameter of the nanostructures was measured as (a) ~ 80 nm and (b) ~ 100 nm.....	125
Figure 14. Development of triangular gold nanoparticles on a glass substrate by employing Focused Ion Beam lithography (FIBL). FIBL was applied to a 50 nm gold film on a glass substrate to pattern the array of these nanostructures.....	126
Figure 15. Development of elliptical gold nanoparticles on the tip of a multimode optical	

fiber by employing Focused Ion Beam lithography (FIBL). FIBL was applied to a 50 nm gold film deposited on the tip of the optical fiber. The long axis of the nanostructures was measured to be ~ 250 nm while the short axis was ~ 150 nm.....	127
Figure 16. (a) Development of gold nanoislands on the tip of a multimode optical fiber by employing Focused Ion Beam lithography (FIBL). FIBL was applied to a 100 nm gold film deposited on the tip of the optical fiber, and (b) Relative transmission spectrum of a multimode fiber with gold nanoislands on the tip.....	128
Figure 17. Development of gold nanoislands on the tip of a multimode optical fiber by employing Focused Ion Beam lithography (FIBL). FIBL was applied to a 100 nm gold film deposited on the tip of the optical fiber.....	129
Figure 18. Schematic showing a measurement set-up for an in-line fiber optic sensor, where the sensor region consists of a nanoparticle-coated coreless fiber.....	132
Figure 19. Shift in absorbance spectra when a fiber tip containing gold nanoparticles, formed by thermal annealing, is placed in water.....	133
Figure 20. Shift in transmission spectrum when a fiber tip containing gold nanoparticles, formed by plasma arc annealing annealing, is placed in air with refractive index ~ 1 (x), in methanol with refractive index ~ 1.33 (y), and acetone with refractive index ~ 1.36 (z).....	134
Figure 21. Shift in transmission spectrum when a fiber tip containing gold nanoparticles, formed by a combination of thermal annealing and plasma arcing, is placed in water.....	135
Figure 22. Shift in plasmon-resonance related dip when (a) fused MMF-CF-MMF structure and (b) fused SMF-GIF-CF-GIF-MMF fibers with gold nanoparticles formed on the coreless section of the fibers, were placed in water (Plot Q) as compared with when it was in air (Plot P).....	136
Figure 23. (a) Prism configuration for detecting refractive index change due to protein binding and (B) Shift in plasmon resonance angle at a given wavelength is employed to sense presence or concentration of chemical and biological molecules; Refractive index of the medium above the gold film changes when biomolecules, e.g. proteins, bind to the binding sites (curve N) as compared to the case with no binding.....	139
Figure 24. A schematic of employing Biotin-Streptavidin Chemistry (High affinity interaction: $K_a = 10^{15} \text{ M}^{-1}$) for detection and sensing of biological agents (anti-IgG for example) and contaminants.....	140

Figure 25. (a) Shift in plasmon resonance peak wavelength upon addition of Biotin, (b) Response of Streptavidin addition to a Biotin coated fiber; The value of the wavelength at which plasmon resonance-related dip occurs was plotted vs. time for an in-line fiber optic biosensor based on structure A.....141

Figure 26. (a) Incorporation of optical fiber into nonwoven-textile filter that can be placed in an in-line water monitoring system, and (b) SEM micrograph of electrospun nonwoven fibers used to sandwich an optical fiber sensor in between a spun-bonded nonwoven fabric and the electrospun fibers.....143

Figure 27. (a) Schematic of fiber optic fiber sensor system consisting of multiple sensors placed on the same optical fiber, which is integrated into a textile fabric. Sensor X is an in-line fiber optic sensor with a structure similar to structure B that has the coreless fiber region coated with silver nanoparticles and sensor Y is an in-line fiber optic sensor with a structure similar to structure B that has the coreless fiber region coated with gold nanoparticles. Change of refractive index in the localized environment around sensor X, i.e. at position 1, is sensed by sensor X, while sensor Y is spatially separated from the region in which the refractive index change occurs and (b) Shift in plasmon resonance related peak associated with sensor X material (silver) upon exposure to a fluid of refractive index n_2 , when the original refractive index of the medium surrounding sensor is n_1 . Refractive index of the medium around sensor Y is assumed to be always at n_1 144

CHAPTER 6

Figure 1. (a) Relative Transmission vs. wavelength plot for unannealed and annealed gold films, (b) AFM picture of an annealed (400 °C) gold film, and (c) Change of color of the thin gold films on glass slides upon annealing. The relative transmission is taken with respect to an uncoated substrate.....150

Figure 2. Effect of annealing on the transmission spectra of thin silver film on fiber tips (a) before and (b) after annealing.....151

Figure 3. Plasma arc annealing of gold film on the optical fiber tip using a fusion splicer152

Figure 4. Appearance of a plasmon resonance related dip in the transmission spectra upon application of plasma arcs to a gold coated (8 nm) fiber tip.....152

Figure 5. Plasmon resonance related dip becomes sharper when both thermal annealing (330° C) and plasma arc are applied to the fiber tip.....153

Figure 6. Schematic of a pulsed electron deposition system employed for depositing silicon dioxide on tip of an optical fiber.....153

Figure 7. (a) Image of a fiber tip with a layer of nanoparticles and coated with fused silica and (b) Plasmon resonance related dip in the transmission spectrum is preserved when nanoparticles on the fiber tip are covered by a fused silica protective layer before fusion to another optical fiber.....154

Figure 8. Analytical calculations results for extinction cross-section for gold nanoparticles. Calculations based on Mie theory showing the effect of particle size on the normalized plasmon peak shape and position – The normalization here was done to make the peaks to have a value 1 so as to effectively compare the plots.....160

Figure 9. Analytical calculations results for extinction cross-section for silver nanoparticles. Calculations based on Mie theory showing the effect of particle size on the normalized plasmon peak shape and position – The normalization here was done to make the peaks to have a value 1 so as to effectively compare the plots.....161

Figure 10. Analytical calculations results for extinction cross-section. (a) Quasi-static model for spherical gold nanoparticles with radius of 34 nm in a silica matrix and (b) Quasi-static model for ellipsoidal gold nanoparticles with $a_1 = 39$ nm, $a_2 = 34$ nm, and $a_3 = 34$ nm, showing the effect of increasing temperature on position of the plasmon resonance-related peak and on peak broadening.....162

Figure 11. Analytical calculations results for extinction cross-section. (a) Quasi-static model for spherical silver nanoparticles with radius of 34 nm in a silica matrix and (b) Quasi-static model for ellipsoidal silver nanoparticles with $a_1 = 39$ nm, $a_2 = 34$ nm, and $a_3 = 34$ nm, showing the effect of increasing temperature on position of the plasmon resonance-related peak and on peak broadening.....163

Figure 12. Analytical calculations results for extinction cross-section. Quasi-static model for ellipsoidal silver nanoparticles with $a_1 = 22$ nm, $a_2 = 20$ nm, and $a_3 = 20$ nm, showing the effect of increasing temperature on position of the plasmon resonance-related peak and on peak broadening.....164

Figure 13. Analytical calculations for extinction cross-section showing the effect of increasing temperature on position of the plasmon resonance-related peak and on peak broadening (a) Quasi-static model for spherical gold and silver nanoparticles, with radii of 34 nm, at different locations in a silica matrix and (b) Quasi-static model for ellipsoidal gold and silver nanoparticles, with $a_1 = 39$ nm, $a_2 = 34$ nm, and $a_3 = 34$ nm, at different locations in a silica matrix.....165

Figure 14. Analytical calculations for extinction cross-section showing the effect of increasing temperature on position of the plasmon resonance-related peak and on peak broadening using the Quasi-static model for ellipsoidal gold and silver nanoparticles, with $a_1 = 22$ nm, $a_2 = 20$ nm, and $a_3 = 20$ nm, at different locations in a silica matrix.....166

Figure 15. Schematic of fiber optic fiber sensor system consisting of multiple sensors placed on the same optical fiber, which is integrated into a textile fabric. Sensor X is an in-line fiber optic sensor with silver nanoparticles inside the fiber and sensor Y is an in-line fiber optic sensor with gold nanoparticles inside the fiber. Change of temperature in the localized environment around sensor X, i.e. at position 1, is sensed by sensor X, while sensor Y is spatially separated from the region in which the refractive index change occurs.....168

Figure 16. Schematic showing a shift in plasmon resonance dip or peak in the (a) transmission spectra and (b) Extinction Cross-section associated with sensor X material (silver nanoparticles inside the optical fiber) upon change of temperature from T1 to T2 at position 1 while the temperature at position 2 is kept constant at T1.....169

Figure 17. (a) Schematic of the arrangement employed for measurement of the effect of temperature on the plasmon resonances of metallic nanoparticles incorporated inside an optical fiber, (b) Measured shift in the plasmon resonance related dip upon heating, (c) Shift in plasmon peak to lower wavelengths upon cooling using ice-water and liquid nitrogen, and (d) Effect of increasing the temperature on the position of the plasmon resonance-related peak.....173

CHAPTER 7

Figure 1. Phase diagram for vanadium oxide (VO_x) showing multiple phases of VO_x , with x varying between 1 and 2.5.....180

Figure 2. Structures and lattice constants for the monoclinic (low temperature, semi conducting) and tetragonal (high temperature, metallic) phases of vanadium dioxide.....180

Figure 3. (a) Pulsed laser deposition to deposit Vanadium oxide on the tip of an optical fiber, and (b) Pulsed electron deposition of fused silica on top of an annealed Vanadium oxide film so as to protect the film before fusion to another fiber..184

Figure 4. (a) Application of plasma arcs to the Vanadium Oxide film deposited on the tip of an optical fiber, and (b) Effect of application of plasma arcs to the Vanadium Oxide film deposited on the tip of an optical fiber; An increase in the absorption

edge was observed upon application of subsequent plasma arcs indicating the increase in crystallinity of the film.....	184
Figure 5. (a) Schematic showing the formation of a tip based fiber sensor with vanadium oxide deposited on the tip of the fiber by using pulsed laser deposition, (b) A fiber with vanadium oxide on its tip after annealing of the film by the application of controlled plasma arcs, and (c) Schematic of the setup employed for evaluation of temperature dependence of the spectrum of the optical fiber containing the Vanadium oxide film on the tip of the optical fiber.....	185
Figure 6. (a) Schematic showing the formation of an inline fiber sensor with vanadium oxide incorporated inside the optical fiber matrix, (b) A fiber with an annealed vanadium oxide film incorporated inside an optical fiber matrix to form a continuous in-line fiber optic temperature sensor, and (c) Schematic of the setup employed for evaluation of temperature dependence of the spectrum of the optical fiber containing the vanadium oxide film inside the fiber matrix.....	187
Figure 7. Figure 7. A schematic showing electric and magnetic fields of the reflected and transmitted radiation, when a light wave is incident from a dielectric medium such as silica on a thick metallic film, thickness of the metal film 'd' is ~50 - 75 nm.....	188
Figure 8. Schematic of the setup employed for evaluation of temperature dependence of the spectrum of the optical fiber containing the Fabry-Perot cavity on the tip or inside the optical fiber.....	189
Figure 9. (a) Effect of temperature on Spectrum of an optical fiber containing an annealed Vanadium oxide film on the fiber tip, and (b) Effect of temperature on the optical transmission of an optical fiber, containing an annealed vanadium oxide film on its tip, evaluated at 561 nm wavelength of input radiation.....	191
Figure 10. Effect of temperature on the normalized spectrum of the optical fiber, containing vanadium oxide film on the tip of the optical fiber, indicating a shift in the band edge upon increase in temperature around the optical fiber. The band edge comes back to nearly the original position upon cooling back to room temperature. The spectrum was normalized to the intensity of the room temperature spectrum at ~ 700 nm wavelength.....	192
Figure 11. Effect of temperature on the spectrum of the optical fiber containing a vanadium oxide film inside the optical fiber matrix, indicating a shift in band edge upon increase in temperature around the optical fiber.....	194
Figure 12. Effect of temperature on the transmission spectrum of the Fabry-Perot cavity.....	195

Figure 13. Decrease in temperature on the transmission spectrum of the Fabry-Perot cavity evaluated at a wavelength of 633 nm.....	198
--	-----

CHAPTER 8

Figure 1. SEM micrograph showing a 180 nm gold film having a periodic square array of nanoholes on the tip of an optical fiber tip: (a) A cleaved end-face of a single mode optical fiber etched with HF and having a 180 nm of gold on it, (b) Close up of the single mode optical fiber, coated with 180 nm gold, showing that the ~ 4 μm core region can be identified due to the HF etching. The inset shows the whole fiber (c) A 24 by 24 array of nanoholes on the core region of the optical fiber tip, and (d) An array of nanoholes on the tip of a four mode optical fiber having a 8 μm core region.....	210
Figure 2. SEM micrograph showing a 180 nm gold film having a periodic square array of nanoholes on the tip of an optical fiber tip: (a) A cleaved end-face of a step-index multimode fiber with a thick layer of gold and a periodic array of nanoholes, (b) A 24 by 24 array of nanoholes on the optical fiber tip, (c) and (d) close-up view of nanoholes on the fiber optic tip.....	212
Figure 3. SEM micrograph showing a 180 nm gold film having a periodic square array (24 by 24) of nanoholes on the tip of an optical fiber tip: (a) and (b) Nanohole array on the tip of a tapered multimode fiber, (c) close-up view of nanoholes on the tapered fiber optic tip and (d) tapered multimode fiber (top fiber view) having the nanohole array.....	213
Figure 4. Schematic showing the setup used to evaluate the spectrum of the array of nanoholes in transmission mode. The sensor holder chamber can be filled with a medium of different refractive indices in order to study the effect of medium refractive index on the optical transmission of the gold-coated fiber having nano-sized holes.....	214
Figure 5. Transmission spectrum of a 24 by 24 square nanohole array in a 180 nm gold film on the tip of a multimode optical fiber, having a 100 μm core. The spacing between the holes was (a) 612 nm and (b) 420 nm. The transmission spectra was evaluated using a white light source and a Spectra©500 spectrophotometer.....	216
Figure 6. Transmission spectra of a 180 nm gold film having a 24 by 24 square nanohole array on the tip of a multimode fiber. The transmission spectrum was evaluated in the wavelength range 440 -760. One can observe a change in the spectrum and a substantial decrease in normalized transmission at 600 nm wavelength upon changing the medium surrounding the fiber tip from air to water; The transmission spectra was evaluated using a white light source and a Spectra©500 spectrophotometer. The spacing between the holes was 600 nm.....	218

Figure 7. Transmission spectra of a 180 nm gold film having a 24 by 24 square nanohole array on the tip of a multimode fiber. The transmission spectrum was evaluated in the wavelength range 440 -760 nm. One can observe a change in spectrum and a substantial decrease in the normalized transmission at 580 nm wavelength, upon changing the medium surrounding the fiber tip from air to water; The transmission spectra was evaluated using a white light source and a Spectra©500 spectrophotometer. The spacing between the holes was 420 nm.....219

Figure 8. Transmission spectrum, normalized to the D-band absorption related peak, of a 24 by 24 square nanohole array in a 180 nm gold film on the tip of a 4 mode optical fiber, having a 8 μm core diameter. The spacing between the holes was 612 nm. The transmission spectra was evaluated using a white light source and a Spectra©500 spectrophotometer.....220

Figure 9. Transmission spectra of a 24 by 24 square nanohole array on the tip of a 4-mode optical fiber, having a 8 μm core, that is coated with a 180 nm gold film as the localized environment around the fiber tip is varied. The spacing between the holes was 612 nm. The transmission spectra was evaluated using a white light source and a Spectra©500 spectrophotometer.....221

PART II

CHAPTER 2

Figure 1. (a) 3-D sectional view of a multilayered printed circuit board showing interconnections between different layers that are achieved by using vias. Separation between the different interconnect, ground, and power planes is achieved by using insulating mediums between the different layers; (b) Interconnection between a driver chip and several receiver chips using through vias in a multilayered circuit board.....241

Figure 2. Cross-section of a holographic fiber showing the different layers with different cross-sections.....241

Figure 3. SEM micrographs of copper (light) and polyester (dark) threads: Plan view of a welded interconnect using (a) top-bottom probe resistance welding, (b) parallel gap resistive welding.....244

Figure 4. Crosstalk noise between woven interconnect lines for a 1 Volt signal (1 MHz frequency) sent into an aggressor line: Crosstalk noise vs. spacing between the twisted pair and bare copper lines.....244

Figure 5. Portable, woven fabric-based acoustic sensor array with 20 microphones

attached to twisted pair wires woven into the fabric.....	247
Figure 6. Woven, fabric-based coplanar waveguide-like transmission line with signal (S) lines surrounded by ground (G) lines.....	247
Figure 7. A Sensate Liner – a woven garment with intelligence capability.....	248
Figure 8. Signal transmission in a sensate liner.....	248
Figure 9. Conductive and Non-conductive fibers woven orthogonally to construct a smart strap.....	251
Figure 10. A communicative wrist watch.....	251
Figure 11. Woven transmission cable.....	252
Figure 12. The input signal is split at the input of signal yarns 12a and 12 b separated by the ground yarn 10b.....	252
Figure 13. Schematic view of a planar conductive piece with electrical anisotropy	255
Figure 14. a) A woven fabric treated with a chemical etching agent to remove the conductive polymer coating from unprotected areas, b) Cross-section of the fabric shown in figure 16 (a) cut along line AA.....	255
Figure 15. Electrically conductive fabric with conductivity gradient.....	258
Figure 16. Electrically conductive fabric with conductivity gradient by varying the number of conductive filaments in the yarn cross-section.....	258
Figure 17. Schematic view of a textile fabric coated with a conductive polymeric film, which is removed selectively from the cross-shaped region shown.....	259
Figure 18. Formation of electrically conductive fabrics having a conductivity gradient.....	259
Figure 19. Musical jacket which has the embroidered fabric keypad (shown on the right), a sequencer/synthesizer, amplifying speakers, and batteries.....	260
Figure 20. Top view of the fabric webbing developed by Gorlick.....	260
Figure 21. Square and round PTCC (Plastic Threaded Chip Carrier).....	262

Figure 22. Plastic threaded chip carrier package prototype attached to a fabric substrate.....	262
Figure 23. Wire bonding of narrow fabric strips containing conducting threads to an integrated circuit.....	264
Figure 24. Flexible circuit board used to form interconnects between an integrated circuit and the conducting threads woven into narrow fabric strips.....	264
Figure 25. Strips of thin film transistors woven into a fabric and interconnected to form a desired logic circuitry.....	264
Figure 26. Source, Gate, and Drain gold contacts for a thin film transistor (TFT) developed on a Kapton thin film.....	267
Figure 27. Structure of an organic thin film transistor developed on a flexible plastic substrate.....	267
Figure 28. Planar Inverted F Antenna consisting of an inverted L section of a conducting patch, a ground plane, and a coaxial cable feed.....	267
Figure 29. Fabric-based Planar Inverted F Antenna consisting of a conducting fabric patch made from an electroless copper plated fabric.....	269
Figure 30. A model of a crossed loop (Merenda) antenna.....	269
Figure 31. Radiation pattern of loop antennas (unidirectional pattern) as compared to that of a crossed-loop antenna (omnidirectional pattern).....	270
Figure 32. Fabric implementation of a crossed-loop antenna, consisting of conducting elements woven into narrow fabrics that are integrated into a vest.....	270
Figure 33. Structure of a tactile sensor made of an electrically conductive fabric.....	272
Figure 34. Softswitch Technology used for the formation of interactive fabrics: Metal particles present in the elastomeric binder are brought close to each other on application of pressure thereby allowing conduction through the elastomeric binder by the process of quantum tunneling.....	272
Figure 35. Capacitive weight sensor formed by placing a foam layer between two conducting fabric layers.....	275
Figure 36. Weight sensor formed by creating apertures in a foam layer between two conducting fabric layers.....	275

Figure 37. Optical fiber sensor developed for the detection of toxic gases by removing a part of the optical fiber cladding and replacing it with a chemochromic material.....	278
Figure 38. Optical fiber-based sensor system for the detection of DMMP as environmental stimulant.....	278
Figure 39. Decrease in the measured resistance of the NDSA-doped polypyrrole coated polyester fabric on exposure to DMMP. The resistance increases on removal of DMMP showing a reversible process.....	281
Figure 40. Woven textile fabric with integrated sensing elements like a temperature sensing unit.....	281
Figure 41. (a) Sensor jacket with integrated stretch sensors to determine the movement of limbs of the wearer of the jacket (b) A strip of the knitted stretch sensor used to form the sensor jacket.....	284
Figure 42. Increase in resistance of the knitted fabric-based stretch sensor on application of stretch.....	284
Figure 43. Force changes observed for free-standing films of PPy (polypyrrole) with two different counterions: pTS (para-toluene sulfonic acid) and PVS (polyvinylsulfonate). Applied potential was varied between -0.8 V to 0.4 V.....	289
Figure 44. Polypyrrole coated (below) and uncoated (above) Pt/PET fiber bundle.....	289
Figure 45. Evaluation of doped-polyaniline fiber/solid polymer electrolyte/copper fiber based actuator: Isometric stress and Isotonic strain vs. time during short wave pulse (period 200 s) stimulation between the electrodes.....	289
Figure 46. A dry fiber actuator based on polyaniline fiber, a solid polymer electrolyte, and copper wire.....	290
Figure 47. (a) Polyaniline hollow fiber containing a polyaniline conducting fiber at its core and filled with gel electrolyte between the two conducting surfaces and (b) Electrical connections to the outer (hollow polyaniline fiber) and inner conducting (solid polyaniline fiber) fibers to form an electrochemical actuator.....	290
Figure 48. SEM micrograph showing a woven wool fabric with polypyrrole chemically deposited on it.....	290

Figure 49. Schematic of an all textile-based battery comprising of a conducting fabric cathode and anode. The middle layer of the fabric holds an electrolyte to form an all-fabric battery system.....	293
Figure 50. Dye sensitized solar cell consisting of dye molecules and titanium oxide enclosed between two electrodes.....	293
Figure 51. (a) Dye Sensitized Solar Cell developed on (b) a flexible substrate or a fabric that could be rolled up.....	296
Figure 52. Schematic of a microstructured current collector leading to an increased surface area.....	296
Figure 53. A metal-coated fabric used to form a microstructured electrode.....	299
Figure 54. Weaving of conducting yarns in warp and weft direction to form an electric heating sheet for heating blankets, carpets etc.....	299
Figure 55. Polartec heating blanket developed by malden mills.....	299

CHAPTER 3

Figure 1. Free body diagram of a yarn section.....	323
Figure 2. (a) Plan view of a plain woven fabric highlighting a unit cell, i. e. U, and (b) Sectional view of the fabric unit cell for a planar fabric, i. e. fabric with bending angle $\psi = 0$. The schematic shows a warp yarn I, going over and under two weft yarns, in the X, Y plane.....	325
Figure 3. Schematic of equilibrium fabric configurations for planar fabrics showing the normal and tangential forces acting on the axial yarns at the crossover points (a) Equilibrium yarn configuration in the X, Y plane of bending and (b) Equilibrium yarn configuration in the Y, Z plane of bending.....	326
Figure 4. Schematic of equilibrium fabric configuration for a bent fabric, bent by an angle ψ . The schematic shows bending of a warp yarn, going over and under two weft yarns, in the X, Y plane.....	323
Figure 5. Schematic showing forces acting on a warp or a weft yarn going over a crossover yarn. In case the axial yarn makes a line contact with the crossover yarn the angle of wrap β_{1j} ($j = 1$ for yarn I being a warp yarn and $j = 2$ for yarn I being a weft yarn) is greater than zero; and if it makes a point contact with the cross yarns β_{1j}	330

CHAPTER 4

- Figure 1. (a) Schematic of a yarn cross-section assuming hexagonal close packing of the fibers in the yarn, with each fiber having a diameter d and (b) A simplified view of a woven fabric considers it to be a parallel arrangement of yarns placed next to each other, ignoring the effect of crossover yarns.....350
- Figure 2. Schematic demonstrating the procedure employed to determine bending rigidity of fabric circuits. Bending rigidity of a fabric circuit is modeled as a series and parallel combination of the bending rigidities associated with different unit cells, each unit cell consisting of a crossover point, as shown in this figure.....360
- Figure 3. Part of a fabric sample that was evaluated for determining the effect, of increasing the number of copper threads in the weft direction, on the fabric bending rigidity. The number of copper threads in the warp direction was taken as 8, while the number of copper weft threads was varied in the different samples from 4 to 64. The length of the evaluated samples was 6 inches while the width was taken as either 1 inch or 3 inches. The warp density in these evaluations was taken as 32 ends per inch, while the weft density was taken as 30 picks per inch.....361
- Figure 4. (a) Samples that were evaluated for the effect of increasing number of copper threads in the warp directions, with all the threads in the weft direction being polyester, and (b) Fabric sample woven on a rapier loom with a Jacquard head, having copper threads in the warp and weft directions.....362
- Figure 5. Schematic of the Cantilever test for bending rigidity evaluations.....362
- Figure 6. Experimental and calculated bending rigidity, values plotted as a function of fraction of copper threads in the direction of bending.....364
- Figure 7. Equilibrium fabric configuration evaluated by solving the elastica equations described in section 4.2 for a unit cell with copper yarns in both warp and weft directions, (a) Warp yarn configuration for normalized fabric curvatures $K_F = 0.0000, 0.0232, 0.0464, \text{ and } 0.0696$ and (b) Close up view of the warp and weft yarn configurations for normalized fabric curvatures $K_F = 0.0000$ and 0.0696366
- Figure 8. A plot showing values of normal force at the boundary of a fabric unit cell, i. e. $F_n(0)$, as a function of fabric bending angle. The plot shows the comparison of values evaluated for different values of A_r , i. e. ratio of bending rigidities of warp and weft threads.....367
- Figure 9. Plot showing normalized values of A_F/A_1 , i. e. ratio of fabric bending rigidity to yarn bending rigidity evaluated for each bending step by employing the energy

method described in section 4.2, as a function of the normalized fabric curvature. The plot shows the comparison of values of A_F/A_1 evaluated for different values of A_r , i. e. ratio of bending rigidities of warp and weft threads
 1.....368

Figure 10. Plots showing the values of bending rigidities of plain woven conductive fabrics as a function of the number of copper weft threads for (a) 0 Copper warp threads and (b) 4 Copper warp threads, with the remaining threads in the warp and weft directions being polyester yarns. The ratio of the bending rigidity of the copper yarns to that of polyester yarns was taken to be 2 in these evaluations. In the fabric sample evaluated, the total number of warp threads was 96 and the total number of weft threads was 180. The normalization was carried out by dividing the value of the fabric bending rigidity by that of a fabric with no copper threads.....369

Figure 11. Plots showing the values of bending rigidities of plain woven conductive fabrics as a function of the number of copper weft threads for (a) 0 Copper warp threads and (b) 4 Copper warp threads, with the remaining threads in the warp and weft directions being polyester yarns. The ratio of the bending rigidity of the copper yarns to that of polyester yarns was taken to be 5 in these evaluations. In the fabric sample evaluated, the total number of warp threads was 96 and the total number of weft threads was 180. The normalization was carried out by dividing the value of the fabric bending rigidity by that of a fabric with no copper threads.....370

Figure 12. Plot showing the values of bending rigidities of plain woven conductive fabrics as a function of the number of copper weft threads with the fabric containing. The four fabrics evaluated had 0, 8, 16, and 32 copper threads in the warp direction. The ratio of the bending rigidity of the copper yarns to that of polyester yarns was taken to be 5 in these evaluations. In the fabric sample evaluated, the total number of warp threads was 96 and the total number of weft threads was 180.....371

Figure 13. Comparison of fabric bending rigidity values that are evaluated experimentally and those that are determined theoretically by employing the elastica model.....373

CHAPTER 5

Figure 1. (a) Schematic of a part of a plain woven fabric highlighting a unit cell, and (b) Schematic of equilibrium fabric configuration for a fabric bent by an angle ψ . The schematic shows a warp yarn I, going over and under two weft yarns, in the X, Y plane.....382

Figure 2. Schematic demonstrating the procedure employed to determine bending rigidity of fabric circuits. Bending rigidity of a fabric circuit is modeled as series and parallel combination of the bending rigidities associated with different sections, each section consisting of a crossover point, as shown in this figure.....386

Figure 3. Fabric samples evaluated for determining the effect of increasing the number of constrained crossover points of orthogonal conductive threads. The lines shown in grey color depict weft copper threads and the lines in the brown color depict copper threads in the warp direction. The region having yellow color depicts polyester warp and weft threads. Different samples, 6 inches long and 3 inches wide, were prepared containing 7, 8, 16, 32, 64 or 96 copper warp threads out of a total of 96 warp threads and 11, 13, 22, 45, 90, or 180 copper weft threads out of a total of 180 Weft threads. The red dots in the figure depict constrained (welded, fused, or bonded) crossover points of orthogonal copper threads. The warp and weft directions are in the Y and X directions respectively and the fabric was bent in the Z direction.....387

Figure 4. Fabric sample woven on a rapier loom with a Jacquard head, having copper threads in the warp and weft directions such that some of the crossover points of orthogonal copper threads were constrained by localized application of conductive adhesive.....389

Figure 5. Schematic of the Cantilever test for bending rigidity evaluations.....389

Figure 6. Theoretical values of normalized bending rigidity as the number of bonded crossover points, of orthogonal copper threads in a woven fabric circuit, is increased. All fabric samples that were evaluated had 8 copper yarns in the warp direction, the total number of warp threads in the fabric samples being 96. The normalization was carried out by dividing the theoretical value of bending rigidity of fabric samples containing bonded crossover point interconnects by the theoretical bending rigidity value of fabric circuit samples with no bonded crossover points.....391

Figure 7. Theoretical values of normalized bending rigidity as the number of bonded crossover points, of orthogonal copper threads in a woven fabric circuit, is increased. All fabric samples that were evaluated had 16 copper yarns in the warp direction, the total number of warp threads in the fabric samples being 96. The normalization was carried out by dividing the theoretical value of bending rigidity of fabric samples containing bonded crossover point interconnects by the theoretical bending rigidity value of fabric circuit samples with no bonded crossover points.....392

Figure 8. Theoretical values of normalized bending rigidity as the number of bonded crossover points, of orthogonal copper threads in a woven fabric circuit, is increased. All fabric samples that were evaluated had 32 copper yarns in the warp direction, the total number of warp threads in the fabric samples being

96. The normalization was carried out by dividing the theoretical value of bending rigidity of fabric samples containing bonded crossover point interconnects by the theoretical bending rigidity value of fabric circuit samples with no bonded crossover points.....394

Figure 9. Theoretical values of normalized bending rigidity as a function of the number of constrained (welded, bonded, or fused) crossover points. All fabric samples that were evaluated had 96 copper yarns in the warp direction, the total number of warp threads in the fabric samples being 96.....395

Figure 10. (a) Experimental value the normalized bending rigidity as the proportion of the number of bonded crossover points, of orthogonal copper threads in a woven fabric circuit developed from copper and polyester threads is increased. The normalization was carried out by dividing bending rigidity of fabric samples containing bonded crossover point interconnects by the bending rigidity value of fabric circuit samples with no bonded crossover points. (b) The effect of weight in the bending rigidity values is divided to obtain the effect of only constraining the crossover points on the bending rigidity of the fabric.....397

Figure 11. Comparison of experimental and theoretical values of increase in the normalized bending rigidity as the proportion of the number of bonded crossover points, of orthogonal copper threads in a woven fabric circuit developed from copper and polyester threads, is increased. The normalization was carried out by dividing all bending rigidity values, experimental and theoretical, by the experimental value of bending rigidity of fabric circuit samples with no bonded crossover points.....398

PART I.

**DEVELOPMENT OF ROBUST FIBER OPTIC SENSORS SUITABLE
FOR INCORPORATION INTO TEXTILES**

CHAPTER 1. INTRODUCTION

1.0 Introduction

There is substantial interest in the development of distributed sensor systems for numerous applications ranging from chemical and biological sensing, monitoring of process control and environmental parameters such as temperature, and to perform structural monitoring of buildings [1-3]. The incorporation of fiber optic environment sensors, such as chemical, biological, and temperature sensors, in textiles is proposed in this thesis. The main focus in this thesis was on making sensitive, yet mechanically robust sensors that can be incorporated into nonwoven and woven fabrics. Roll to roll fabrication of textile fabrics potentially enables large area conformable sensor systems that can be implemented in a reasonable straight forward manner.

Optical fiber based evanescent wave and surface plasmon optical sensors require the evanescent field of the electromagnetic wave to extend beyond the glass-air interface and interact with the environment. A variety of strategies have been employed in the past to force the guided modes normally confined to the core of the optical fiber to interact with the external environment including: tapering of the optical fiber to small dimensions on the order of 25 microns, chemical etching of the optical fiber cladding, and mechanical polishing the cladding to provide environmental access to the core of the optical fibers. Although sensors based on these techniques are sensitive they become mechanically fragile and difficult to fabricate. Hence, it is difficult to deploy the optical fibers for remote environmental sensing or to incorporate them into flexible substrates such and textile fabrics.

In this work, development of robust optical fiber environment sensors was carried out by developing inline structures via fusing different optical fiber elements to precisely control the propagation of light such that it interacts effectively with the environment; or by incorporating metallic and semi conducting nanoparticles or Fabry-Perot cavities inside the optical fibers. By forming sensors on continuous in-line optical fiber structures, the optical fiber diameter is not reduced, thereby making these sensors mechanically robust.

Improved chemical and biological sensors can find a wide array of applications like sensing of harmful chemical and biological agents released by industrial plants, and for monitoring of water quality [4-5]. The fiber optic sensors developed in this work are environment sensors and sense temperature and the change in refractive index of the medium surrounding the sensor. The change of refractive index could be the result of a change of type or concentration of a chemical

or adsorption of chemical or biological molecules on the surface of the sensor. The chemical and biological sensors described in our work are surface affinity sensors that employ a variety of surface plasmon resonance phenomena to transduce a local change in refractive index to an optical signal. These sensors require the fabrication of a variety of metallic nanostructures including: continuous and discontinuous metallic thin films, metallic nanoparticles, and surface plasmon engineered arrays of sub wavelength apertures.

In addition to optical affinity sensors, a variety of temperature sensitive sensors are achieved by incorporating metallic and semi conducting nanoparticles into the core of fiber optic in-line sensors. These sensors are fabricated by coating the tip of the optical fiber with the desired metal or semi conductor, and over coating the tip with a protective layer of silicon dioxide. The fiber can then be annealed, and fused to another optical fiber to form the in-line sensor. Since the size of the metallic nanoparticles can be determined by the annealing and fusion process, the optical properties of the sensor can be optimized. This approach is used to fabricate temperature sensors, where for gold nanoparticles, the shift and broadening of the plasmon resonance is used, and for vanadium oxide compounds where shifts in the absorption edge are monitored. Using thicker metallic films, partial mirrors can also be constructed using this assembly method to form a Fabry-Perot cavity where positions of the resonances can be monitored to track changes in temperature.

In the course of developing in-line fiber optic sensors, fiber tip based optical affinity sensors were also developed and investigated. The use of arrays of sub wavelength apertures constructed on the ends of etched and tapered fiber tip using focused ion beam milling are shown to be especially promising. In this chapter, a justification for employing optical fibers for environmental sensing is provided. Different processes of incorporating the fiber optic sensors in textile fabrics, to form conformable sensor systems, are also described.

1.1 Reasons for using optical fibers for sensing

Chemical and biological sensor technologies like mass spectroscopy, infrared spectroscopy, and gas chromatography have a disadvantage of having large size, long analysis times, complicated electronics support, lack of specificity and high cost [3-4]. Similarly electronic sensors such as Chem-Fets, IS-Fets, and resistive sensors typically have small dynamic range

and slow response and recovery times. Some of the other advantages that are unique to optical fiber sensors are listed below:

- **Multiple sensors on a fiber:** A single optical fiber may have multiple chemical or temperature sensors fabricated on it [5]. As a specific example, different sections of an optical fiber can have different fluorescence indicators to sense multiple analytes. Different analytes and fluorescence indicators respond to different excitation wavelengths and have different emission spectra. Hence, one could apply time division multiplexing or wavelength division multiplexing techniques to distinguish between the signals coming from the different chemical sensors on the same optical fiber, as shown in Figure 1.

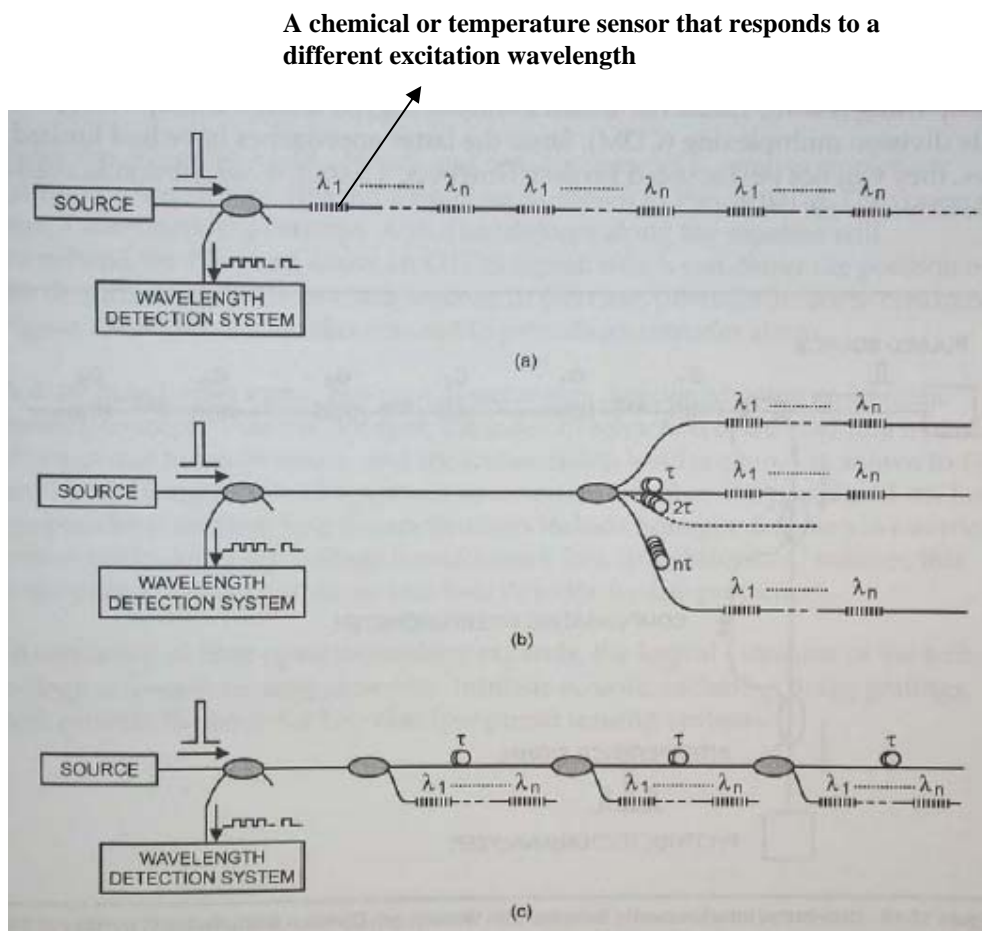


Figure 1. Sensors that are (a) Wavelength Multiplexed, (b) Time Multiplexed, and (c) Time Multiplexed [5]

- **Transmission medium:** Another advantage is that the optical fiber could serve both as a sensor and as a medium of propagation of electromagnetic energy (light).

- **Electrical Interference:** Optical fiber sensors have a high resistance to electromagnetic interference and do not have problems that are associated with electrical sensors, such as crosstalk of the different electrical signals detected from the different sensors [3, 4, 5].
- **More information transfer:** As an optical fiber can transmit much more information than an electrical interconnect, one can achieve very high levels of information density using optical fiber sensing. Moreover, time division, wavelength division, and code division multiplexing techniques could be used to distinguish between different signals if more than one signal being carried by the optical fiber.
- **Remote sensing:** Optical fiber sensors could be employed for remote sensing applications and for sensing in locations that are not easily accessible.
- **High operation temperatures:** As optical fibers are generally made up of silica, they can be used in high temperature conditions. Plastic optical fibers can't withstand temperatures as high as the silica optical fibers but, like silica fibers, they are generally resistant to harsh chemical environments.
- **Distributed sensing by incorporation into flexible substrates:** Sensors developed on the surface or the tip of optical fibers can be embedded into flexible and conformable substrates such as polymeric films and textile fabrics. The textile substrates could be woven, non-woven, or knitted fabrics and embedding optical fiber sensors in them can allow the formation of large area flexible and conformable distributed sensing systems [1]. As textile fabrics can be easily rolled and transported, embedding optical fiber sensors into them can allow easy deployment and redeployment of these sensors over a large area. Figure 2 shows one possible way of incorporating inline optical fiber sensors, formed on the same optical fiber, into flexible substrates. One or more of such fibers, with each fiber containing one or more sensors, could be integrated into a flexible platform such as a polymeric film or a textile fabric by either weaving the optical fibers into the fabric or by sandwiching the sensor optical fiber between two layers of fabrics or polymeric films and applying heat or chemical means to hold the structure together [1-2]. Other means of incorporation of optical fiber sensors into textile structures are described in section 1.2.

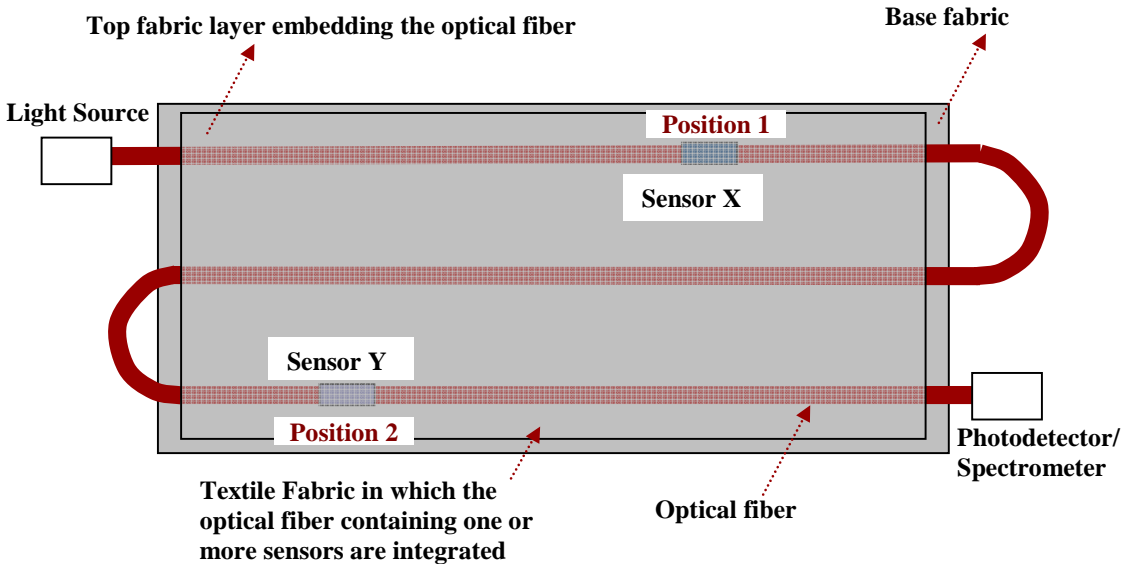


Figure 2. A schematic showing a means of incorporating an optical fiber, containing one or more environment sensors on it, into flexible substrates such as textile fabrics

1.2 Incorporation of sensors into textiles

1.2.1 Integration into woven and knitted fabrics

Multiple optical fibers, having one or more sensors on them, could be integrated into textiles by weaving the optical fibers along with conventional threads. Optical fibers can be treated as monofilament yarns while weaving them into the fabric. They can be inserted into the fabric along the weft direction (See Figure 3) on a single or double rapier weaving machine or on a shuttle weaving machine. If the reed dent spacing of the looms is made larger they could also be inserted in the warp direction. This limitation arises due to the optical fiber dimensions being generally larger than the reed dent spacing. During the weaving process, silica-based optical fibers may break due to several sharp edges guides, tensions etc or breaks during unwinding. One needs to modify the conventional looms or weaving machines to provide smooth, and frictionless tensioners and guides and a special unwinding process for weaving optical fibers into fabrics on an automated scale. One could also use plastic optical fibers made from polymers like polymethylmethacrylate (PMMA) to circumvent these problems, but some of the optical advantages of silica fibers may be lost. Weaving of optical fibers into fabrics also causes micro bending of the fibers introduced into the fiber by the orthogonal warp threads at the crossover point thereby leading to loss of optical power at the points of bending. If a shuttle loom

or a weaving machine is used to weave an optical fiber then macro bending occurs at the end of every pick of the inserted optical fiber thereby leading to bending losses at those points.

Optical fibers sensors could also potentially be knitted into fabrics using weft knitting or warp knitting processes. As the process of knitting involves formation of loops, this structure is not ideal for incorporation of optical fibers sensors into textiles. The loops in a knitted fabric that could lead to a considerable loss of optical power from the optical fibers, and are also points of high strain that can lead to breakages.

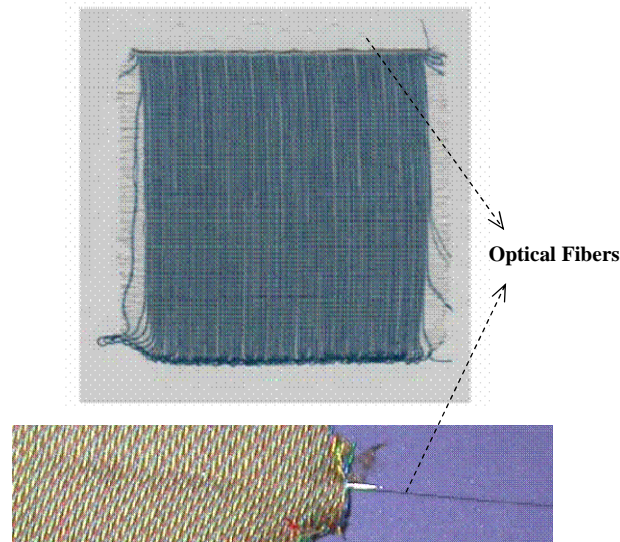


Figure 3. Optical fiber integrated into woven fabrics along with conventional threads

1.2.2 Integration into non-woven fabrics

Optical fibers and optical fiber sensors could be embedded into a non-woven fabric by taking a non-woven web or fabric layer, placing the optical fiber sensors on the first layer at the desired locations, and placing or depositing another layer of non-woven fabric on top of the first layer and the optical fiber.

In one such structure, one can take a spun bonded, electrospun, meltblown or hydro entangled fabrics as the first layer, place the optical fibers or optical fiber sensors at the desired locations, put another layer of spun bonded, electrospun, meltblown or hydro entangled fabrics on top of the optical fibers and the first layer, and heat set the entire composite structure. One can also design a process in which one could form melt or wet spun fibers directly on top of the

optical fibers placed on top of the first layer of non-woven fabric i.e. form a spun bond fabric on top of the optical fibers and the first layer.

Moreover, one could also design a process involving electrospinning of nano fibers directly on top of optical fiber sensors, which are placed and arranged on a layer of a substrate non-woven fabric. This non-woven layer could be a spun bonded, electrospun, meltblown or a hydro entangled fabric. Thus a composite structure, consisting of optical fibers sandwiched between two layers of nonwoven fibers is formed, as shown in Figure 4. Electrospinning of fibers, such as polyethylene terephthalate, polyethylene oxide, or polyurethane fibers, could be done by dissolving the polymers in appropriate solvents to prepare solutions and connecting the high voltage electrode of a high voltage supply (20-25 kV) to the solution while connecting the ground electrode of the high voltage supply to a fiber collection surface. One could also employ

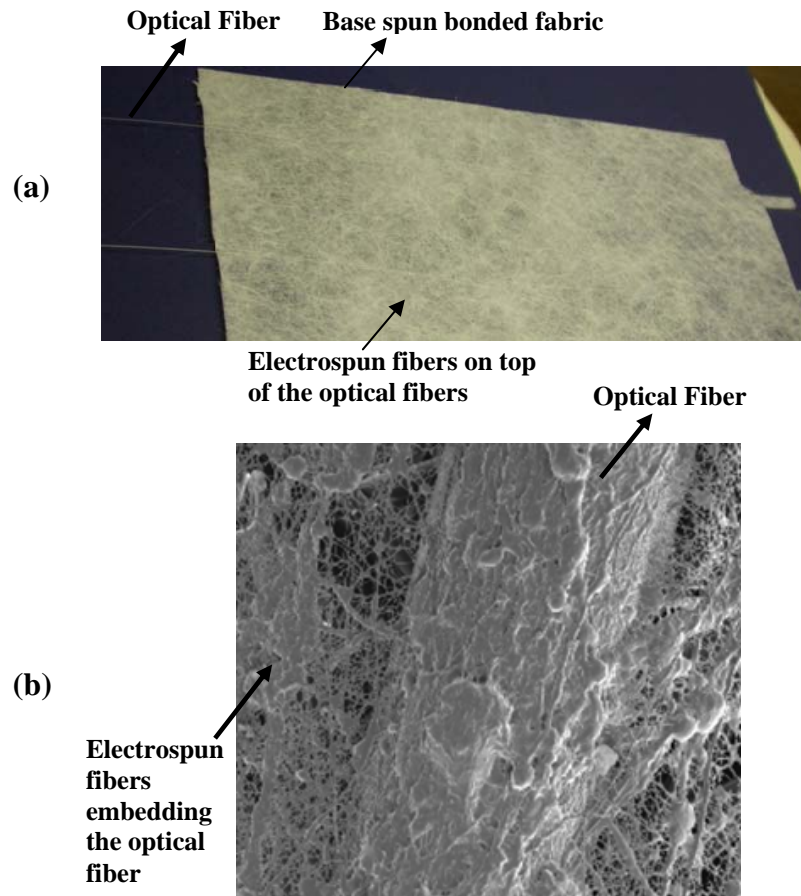


**Figure 4. (a) Optical fibers embedded into a non-woven fabric
(b) SEM micrograph of electrospun nonwoven fibers used to sandwich an optical fiber sensor in between a spun-bonded nonwoven fabric and the electrospun fibers**

the meltblowing process for deposition of polymeric fibers, such as polyethylene terephthalate or polypropylene fibers, on top of optical fibers that are placed on top of a non-woven web.

The advantage of using non-woven fabrics for incorporating the optical fiber sensors is that these fabrics have a very large surface area due to the presence of small sized fibers, especially in the case of nanofibers formed by electrospinning, and hence could adsorb gases that could then be sensed by the optical fibers embedded in the non-woven composite structure. A web or a non-woven fabric, containing very fine fibers having diameters in the nanometer range, is porous thereby leading a large surface area for fluid adsorption. Moreover, the levels of mechanical stresses involved in the incorporation of optical fiber sensors in non-woven fabrics are much lower than those in the case of woven or knitted fabrics thereby leading to less fiber breakages, especially when silica optical fibers are used.

1.3 Outline of the Thesis

Chapter 2 provides an overview of chemical and temperature sensors and their metrics along with a literature review of optical fiber sensors and sensing mechanisms. This is followed by a summary of the different applications of optical fiber sensors.

Chapter 3 explains the fundamentals of plasmon resonance and provides a literature review of the different kinds of fiber-optic plasmon resonance based sensors.

In chapter 4 of the thesis, novel in-line optical fiber structures - based on fused single-mode or multimode, coreless, and graded index optical fibers - are proposed and modeled.

In chapter 5, the experimental resulted in development of chemical sensors based on the structures described in chapter 4 and some other optical fiber structures. Chapter 5 also describes the development of biosensors based on optical fibers and their evaluations along with possible ways of integrating the sensors to form sensor systems.

In chapter 6 of the thesis, incorporation of metallic nanoparticles into the core of standard telecommunications grade optical fibers, is described. This creates a simple, yet robust, platform which can be used to investigate the properties of nanoparticles, for sensing, spectroscopy, and optical switching applications. The optical response of gold nanoparticles embedded in the optical fiber matrix, was evaluated as a function of temperature and the use of the structure as an inline fiber-optic temperature sensor is described. This chapter also provides analytical calculations that describe the effect of increasing temperature of the optical fiber, containing the

metallic nanoparticles, on the position of plasmon resonance related dip in the transmission spectrum or a peak in the extinction cross-section spectrum of the fiber containing the nanoparticles.

Chapter 7 describes the development of novel in-line fiber-optic temperature sensors based on Fabry-Perot cavities formed on the tips or inside optical fibers. This chapter also describes the development of temperature sensors based on the incorporation of semiconducting films, such as vanadium oxide films, inside the optical fibers or on their tips.

Chapter 8 describes the development of highly sensitive fiber-optic sensors that are based on extraordinary light transmission, due to a periodic array of nanoholes in metallic films on the tips of the optical fibers. The nano-hole fiber tip sensors can be employed for sensing of chemical and biological molecules.

Finally, Chapter 9 provides a summary of the research work described in this thesis and provides a direction for future work.

1.4 References

1. Muth J., Grant E., Dhawan A., Seyam A., and Ghosh T., "Signal Propagation and Multiplexing Challenges in Electronic Textiles," Proceedings of the Materials Research Society Conference Symposium D, Boston, Ma, December 2-3, 2002.
2. Dhawan A., Muth J., Kekas D., and Ghosh T., "Optical nano-textile sensors based on the incorporation of semiconducting and metallic nanoparticles into optical fibers," Proceedings, Materials Research Society Conference Symposium S, March, 2006.
3. Fraden J., Handbook of modern sensors: physics, designs, and applications, Springer-Verlag, New York, 1996.
4. Gopel W., Hesse J., and Zemel J. N. Eds., Cumulative index, in: Sensors, A Comprehensive Survey, Vol. 9, Wiley-VCH, Weinheim, 1995.
5. Jin, Z., Su, Y. and Duan, Y., "Development of a polyaniline-based optical ammonia sensor", Sensors and Actuators B: Chemical, 72(1), 75-9, 2001.
6. Krohn, D. A., Fiber Optic Sensors: Fundamentals and Applications, Instrument Society of America, NC, 2000.
7. Walt, D. R., Dickinson, T., White, J., Kauer, J., Johnson, S., Engelhardt, H., Sutter, J. and Jurs, P., "Optical sensor arrays for odor recognition", Biosensors and Bioelectronics, 13 (6), 697-699, 1998.

CHAPTER 2. LITERATURE REVIEW

2. Literature Review

The first part of this chapter explains the fundamentals of sensing along with describing important metrics that are considered for sensing of chemical and biological agents. This is followed by an overview of sensors and sensing mechanisms. Finally, a summary of different applications of optical fiber sensors is provided.

2.1 Sensing Fundamentals

A sensor is defined as a “device that receives and responds to a signal or stimulus” [1]. The objective of a sensor is to respond to some form of an input physical property and convert it into an output in the form of an electrical or optical signal. The input physical property is called a stimulus or a measurand. Different kinds of stimuli that can be sensed are enlisted in Table 1 and are sensor types are often grouped into categories as shown in Table 2. A sensor is distinguished from a transducer, which is defined by the Instrument society of America’s ANSI MC6.1 1975 standard as a “device, which provides a usable output in response to a specified measurand”. A transducer converts signals received in the form of mechanical, thermal, electrical, magnetic, radiation, or chemical energy (i.e. primary signals) into output signals in one of the different forms of energy (i.e. secondary signals). A sensor is specific class of transducer since a sensor converts different forms of energy into electrical or optical energy only.

A sensor or a number of sensors are usually a part of a large data acquisition system consisting of interface electronic circuitry, multiplexers, analog to digital converters, and memory elements. A sensor system is often part of a control system having feedback mechanisms. Thus sensing is fundamental to technology as it helps to precisely detect and monitor different measurands so that a feedback control can be used to attain certain desirable values of the measurands. The sensing system can also be attached to actuators so that different actions can be taken in response to the sensed information [2]. As a lot of chapters in this thesis are devoted to the development of chemical sensors, the following subsection describes the metrics that are relevant to chemical sensing.

Table 1. Different kinds of stimuli that could be sensed [5]

Chemical	Acoustic	Biological	Electric	Magnetic	Optical	Mechanical	Radiation	Thermal
- Composition - Concentration - pH - Reaction Rate - Oxidation or Reduction Potential	- Wave Amplitude - Phase - Wave Velocity	- Type - Concentration	- Voltage - Current - Resistance - Inductance - Capacitance - Polarization - Electric Field - Frequency - Dipole Moment - Dielectric Constant	- Field Intensity - Flux Density - Magnetic Moment - Permeability	- Wave Amplitude - Phase - Wave Velocity - Refractive Index - Reflectivity - Emissivity	- Force - Torque - Pressure - Mass Flow - Length - Area - Volume - Linear and angular velocity and acceleration	- Type - Energy - Intensity	- Temperature - Specific Heat - Entropy - Heat Flow - State of Matter

Table 2. Classification of sensors on the basis of principle of sensing [5]

	Inductive Sensors	Piezoelectric sensors	Capacitive sensors	Microwave sensors	Resistive sensors	Optical sensors	Electro magnetic wave sensors	Thermal sensors
Measurand or Stimulus	Motion, Pressure	Pressure, Force	Position, Motion, and Displacement	Motion, Humidity	Chemical, Temperature	Chemical, Strain, Motion, Biological Reactions, Temperature	Flow, Velocity and Acceleration	Chemical sensing, Humidity

2.1.1 Metrics for Chemical and Biochemical Sensing

Important metrics to be considered for sensing of chemical and biological molecules are:

Sensitivity: The change in output of a sensor for a change in the input. In the case of chemical sensors, sensitivity of a sensor (S) to a chemical is the change in the sensor output parameter (y) for a change in the input parameter (x), i.e. concentration, amount, or partial pressure of the chemical. Mathematically,

$$S = \Delta y / \Delta x$$

assuming the y-x relationship is linear. In case the relationship between the output parameter (y) and the input parameter (x) is not linear, the sensitivity (S) is not constant and has different values for different values of x. Mathematically, it is calculated by calculating the slope of the y-x curve i.e.

$$S = \frac{dy}{dx}$$

evaluated at a particular x. In case ‘n’ number of chemicals are present in the system around the sensor, then the partial sensitivity of a sensor (S_i) to the ith chemical is given by the following relationship:

$$S_i = \frac{\partial y}{\partial x_i} \quad (1)$$

where x_i is the concentration of the i^{th} chemical and $1 \leq i \leq n$.

Specificity: Ability of a sensor to respond to one chemical or biological molecule in the presence of other molecules is called specificity. Levels of interference effects from constituents other than those being measured are considered while evaluating specificity. If the partial sensitivity of a sensor (S_i) to the i^{th} chemical is very large as compared to the partial sensitivities of the sensor to chemicals other than i , then the sensor has high specificity for the i^{th} chemical. If a sensor does not have a high value of specificity, it implies that it has a high cross-sensitivity i.e. high sensitivity for more than one specific chemical.

Selectivity: The ratio of partial sensitivity of a species being monitored to that of the interfering components. The value of this ratio and thereby of the selectivity is high if the partial sensitivity, of the species being monitored, is high.

Detection Limit or Resolution: The minimum change in the concentration, amount, or partial pressure of a chemical or biological molecule that could be detected by a sensor. The detection limit of a sensor is usually given in parts per million or parts per billion.

Failure rate: The frequency of malfunctioning of a sensor under test. It is associated with inability of a sensor to properly sense the right molecules, which can occur if a specific molecule, being monitored by a sensor, goes undetected. Failure may even occur if a wrong molecule is detected and a false alarm is raised. ROC curves could be used to analyze the failure rates of the sensors.

Receiver-operating characteristic (ROC) curves: One of the ways of characterizing the sensitivity and specificity of chemical and biological sensors is by using receiver-operating characteristic curves. Any point along a ROC curve represents the trade-off in sensitivity and specificity, depending on the threshold for a test. An example of a ROC curve is shown in Figure 1 [3] which shows two curves for two hypothetical diagnostic tests. The ROC curve with

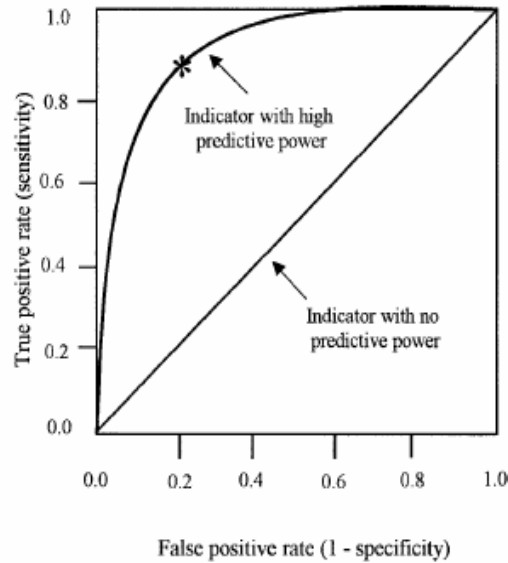


Figure 1. An example of a ROC curve which shows two curves for two hypothetical diagnostic tests [3]

the line on the top represents a better diagnostic test than the ROC curve at the bottom as it has a greater sensitivity for any given specificity. In the case of the top curve, the sensor has high sensitivity even when the rate of false positives is low, i. e. when the sensor has a high specificity.

Response time: The rate at which the analyte detection is visibly indicated by the transducer system used to sense the analyte. In gas measurement, the response time is generally defined as the time required to attain 90% of the final value of the transduced signal. The response time and the recovery time of an electronic nose, employing a resistance sensor, is shown in Figure 2 [4]. E-nose systems utilize an array of sensors to give a fingerprint response to a given odour, and pattern recognition software then performs odour identification and discrimination [4]. Different kinds of sensors employed in e-nose sensor systems are conductivity sensors, piezoelectric sensors, optical sensors, and MOSFET sensors. It is desirable to have a low response time.

Recovery Rate: The rate at which the sensor goes back to its original state after the analyte being sensed is removed. It is desirable to have a low value of recovery time, which implies a high recovery rate.

Maximum measurement frequency: It is the maximum frequency at which different measurements can be made by a sensor and depends on the response time and the recovery time associated with the sensor.

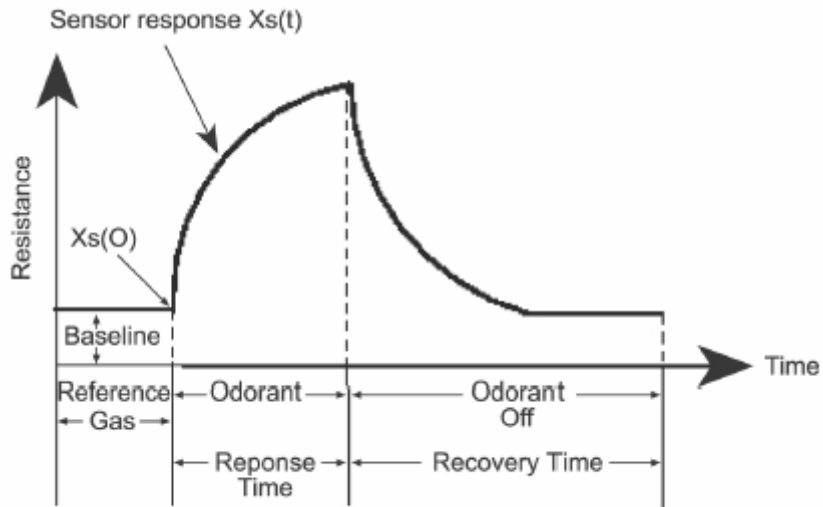


Figure 2. Temporal response of a resistance sensor used to detect an odorant in an electronic nose. The plot of resistance vs. time highlights the response time and the recovery times involved in the sensing process [4]

Sensor Drifts: The deviations from the expected values of the sensor output signal. Non-cumulative drifts are caused due to statistical variations of the sensor signal, whereas the cumulative drifts occur due to contamination of the active sensing area of the sensor, which leads to irreversible changes in the calibration curves [5]. Environmental factors such as humidity and temperature changes can often cause the sensor to drift.

Saturation Level: The maximum concentration of analyte that can be sensed by a sensor. It becomes important if large amounts of analyte are present around the sensor.

Dynamic range: The range of values of concentration, amount, or partial pressure of a chemical being sensed, that could be detected by a chemical sensor. It is characterized by the range between the lowest detectable amount of a chemical component being sensed and maximum detectable amount in dB. The dynamic range is limited by saturation effects for high concentrations of measurand. For low concentrations of the measurand, the dynamic range is typically limited by the quantization error if an analog to digital converter is used or by thermal or shot noise for analog systems. Often compromises are made between the sensor sensitivity and dynamic range.

Linearity of the sensor response: A sensor response is considered to be linear if slope, of the output response (y) vs. the input parameter (x) curve, is constant. The input parameter could be concentration of chemical or biological agents or temperature. In some sensors, the response of a sensor may be linear only for certain ranges of the chemical concentration.

Operation Conditions: Maximum and minimum values for the following sensor operating conditions are important:

- Temperature
- Relative Humidity
- Volume of chemical (in gaseous or solution form) around the chemical sensor.

Power consumption: Ideally the sensors should have low power consumption.

2.1.2 Different kinds of chemical sensors

A variety of sensors have been used for sensing of chemical and biological molecules including: resistive sensors and gravimetric sensors, thermal sensors, enzyme sensors, catalytic sensors, electrochemical, MOSFET sensors, and optical sensors [6]. To provide a context in which to understand the advantages and disadvantages of optical sensors, Table 3 lists the typical performance parameters of different classes of chemical sensors.

Table 3. Properties of different types of chemical sensors [5, 6]

Sensor Type	Response time	Detection Limit/Sensitivity	Sensing Range
Resistive Sensors	2-200 s	5-500 pm	0.1-1000 ppm
Mass Spectrometry		Low ppb	0.1 ppb-10 ppm
Quartz Micro-balance	< 10 s	1.0-ng mass change	0.01-100 ppm
Electrochemical sensors (ChemFETs)		~ 1 ppm	
Surface Acoustic Wave	< 5 s	1.0-pg mass change	0.6-100 ppm
MOSFET	0.1-300 s	1 ppm	
Optical Sensors	< 10 s	1 ppb	0.001-180 ppm

2.2 Optical fiber based sensing

Optical fiber-based sensors have been used for a large number of applications including the measurement of electric and magnetic fields, vibration, acceleration, rotation, humidity, and presence of chemical and biological agents. The inherent advantages of the fiber optic sensors are their small size, lightweight, low-power consumption, resistance to electromagnetic interference, high sensitivity, and their high bandwidth. Moreover, development of sensors on optical fibers allows the development of distributed sensing systems and embedding these fiber-optic sensors in a wide array of substrates.

The properties of sensors developed on optical fibers depend on the type, material, and other properties of the fibers themselves. An optical fiber conventionally consists of three different layers – the core, the cladding, and a protective coating or jacket [7-8]. The core, with a refractive index n_1 is surrounded by a cladding layer which has a refractive index n_2 that is less than n_1 . The cladding serves several purposes. It reduces scattering losses occurring due to discontinuities at the surface of the core. It also provides mechanical strength to the optical fiber. A plastic jacket encapsulates the cladding layer, protecting it from scratches and moisture that can significantly weaken the glass and also provides mechanical strength to the fiber. Overall diameter of a typical optical fiber varies between 80 and 1000 μm [7], with standard communication cladding diameter sizes of 80 μm , 125 μm , and 140 μm .

The refractive index of the fiber core can be varied as a function of radius of the fiber and this distribution is called the refractive index profile. Different refractive index profiles of the core of an optical fiber are the step index profile, graded index profile, multi-step index profile, W-profile, etc. [7-9]. In a step index optical fiber, refractive index of the core does not vary with the radius and is greater than that of the cladding for confinement of the light wave in the optical fiber core. In a graded-index fiber, the core refractive index varies as a continuous function of the radial distance from the center of the fiber. The principle reason for having different refractive index profiles is to control the dispersion in the fiber. Single mode and multimode optical fibers with different profiles are shown in Figure 3.

Different modes propagating in an optical fiber (with 2 or more layers) can be found mathematically by calculating eigenvalue solutions of the Maxwell's equations in cylindrical coordinates and applying boundary conditions of continuity of tangential E and H fields at the

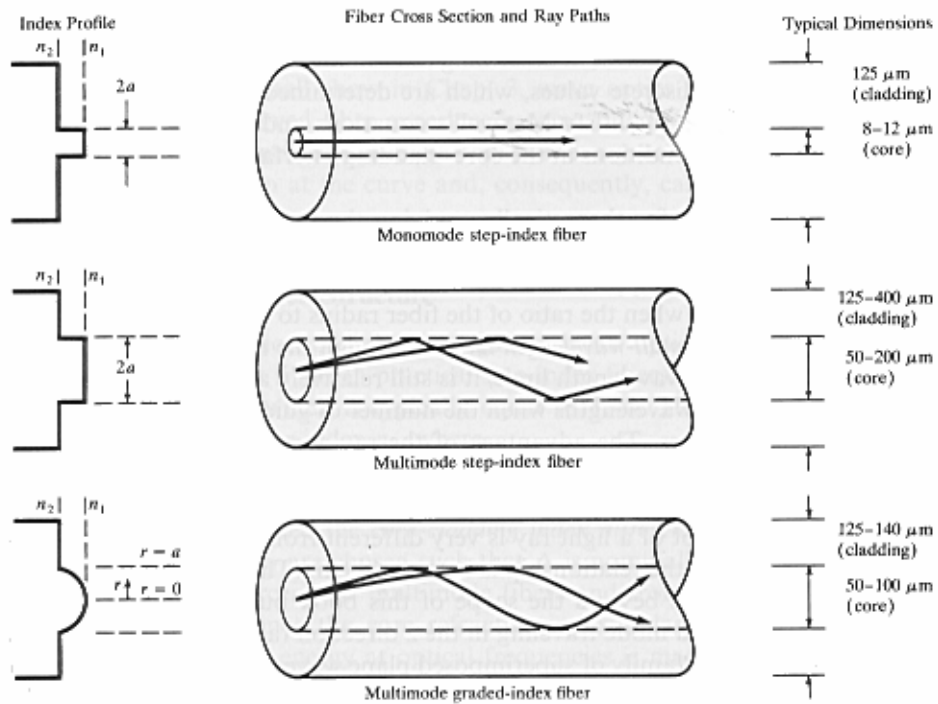


Figure 3. Single-mode and multimode step-index and graded-index optical fibers [8]

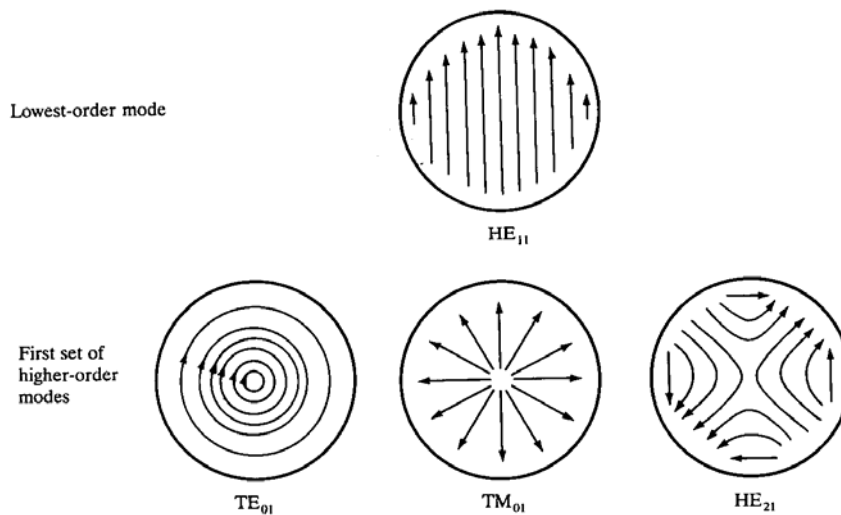


Figure 4. Cross-sectional views of the transverse electrical field vectors for the four lowest-order modes in a step-index fiber [8]

boundaries. A boundary here is defined as an interface across which there is a change of refractive index. Thus one can calculate the propagation constant β and the value of electric (E) and magnetic (H) field distributions for each mode, i.e. for each eigen value solution. The four lowest order modes in a step index fiber are the HE_{11} , TE_{01} , TM_{01} , and HE_{21} modes and are shown in Figure 4.

The TM modes are mathematically obtained by solving the cylindrical coordinate scalar wave equation (derived from Maxwell's equation) for an optical fiber waveguide boundary value problem with the condition that the direction of the magnetic field has to be perpendicular to the direction of propagation of the electromagnetic wave. TE modes are mathematically obtained by solving the optical fiber waveguide boundary value problem with the condition that the direction of the electric field has to be perpendicular to the direction of propagation of the electromagnetic wave. Coupling between E and H fields results in HE or EH hybrid modes, which can be mathematically obtained by solving the cylindrical-coordinate optical fiber waveguide boundary-value problem without applying any transverse condition for electric or magnetic fields.

In a step index optical fiber, a mode is guided as long as the propagation constant β satisfies the condition:

$$n_2k < \beta < n_1k \quad (2)$$

where n_1 and n_2 are the refractive indices of the core and cladding, respectively, and $k = 2\pi/\lambda$.

When the value of the propagation constant is less than n_2k , power leaks out of the core into the cladding region through the tunneling effect. The modes that satisfy the condition $\beta < n_2k$ are called leaky modes. The leaky modes are only partially confined to the core region, and attenuate by continuously radiating their power out of the core as they propagate along the fiber.

2.2.1 Optical fiber sensing mechanisms

Optical fiber based sensors are typically classified as shown in Table 4 as either extrinsic, or intrinsic. In extrinsic fiber optic sensors, light exits the optical fiber in the sensing region, where the light intensity, phase, or spectral content are modulated by the environmental effects. The light then gets coupled back to the same or another optical fiber and carries information about the environmental effects. In case of intrinsic fiber optic sensors, the lightwave propagates in the optical fiber as it senses the environment around the fiber sensor. Within these categories, sensors can be classified as either intensity modulated, spectrally or wavelength modulated, or

phase modulated, where the optical phase is usually converted to an intensity by an interferometric technique.

Table 4. Classification of Fiber Optic Sensors

Sensor	Intensity Modulated	Wavelength or Spectrally Modulated	Phase Modulated (Interferometers)
Intrinsic	<ul style="list-style-type: none"> a. Microbend sensors b. Tapered fiber sensors c. Surface plasmon resonance sensors 	<ul style="list-style-type: none"> a. Bragg grating sensor b. Tapered fiber sensor c. Surface plasmon resonance sensors 	<ul style="list-style-type: none"> a. Intrinsic Fabry-Perot interferometers b. Mach Zender interferometers c. Michelson's interferometers
Extrinsic	<ul style="list-style-type: none"> a. Fluorescence b. Proximity c. Mode Coupling 		<ul style="list-style-type: none"> a. Extrinsic Fabry-Perot interferometers

2.2.1.1 Intensity modulated fiber optic sensors

Intensity modulated fiber optic sensing [10] involves observing the variation in intensity or power of the light wave at the output of the fiber optic sensor in response to the environmental effects. These sensors could be used for displacement sensing [11], position sensing [10], sensing liquid levels, vibration, acoustics, pressure, strain, temperature, humidity, and other environmental effects. Intensity-modulated fiber optic sensors employ different techniques to sense changes in environmental effects such as microbends and macrobends, evanescent fields [12-13], or extrinsic coupling between optical fibers [7]. In microbend fiber sensors,

environmental effects result in increase or decrease in the output light wave intensity due to light loss resulting from small bends in the fiber. Evanescent field-based sensors rely on the interaction of the electro-magnetic field that extends beyond the core of the fiber into the environment. Extrinsic coupling-based sensors rely on light exiting an optical fiber waveguide and getting coupled to same or another optical waveguide, to sense environmental effects.

2.2.1.2 Spectrally based fiber optic sensors

Spectrally based fiber optic sensors [10] employ modulation of wavelength of light to sense an environmental effect. Light wave is input into an optical fiber and its output spectrum is observed. When there is a change in environmental conditions like pH, temperature, humidity, or presence of chemical gases, etc., these changes can be sensed by a change observed in the output spectrum of the light wave. Different kinds of spectrally based sensors are absorption sensors [10], fluorescent-based sensors [7], and dispersive grating-based sensors [7]. In the absorption-based sensors, the absorption profile of the sensor probe changes with a change in environmental conditions. In the case of fluorescent-based fiber sensors [7, 10], fluorescence induced by an evanescent field couples back into the optical fiber and can also be used to sense environmental changes. A fiber Bragg grating (FBG) sensor [7, 14-15] is based on an optical fiber, generally a single mode fiber, with a set of intermittent reflective Bragg gratings along the length of the fiber. The Bragg gratings are written into the core by exposing the side of the fiber to an interference pattern. In fiber optic Bragg grating sensors, the core of the optical fiber has periodic variations of refractive index. The grating reflects light at a wavelength $\lambda_B = 2n\Lambda$ according to Bragg's law, where Λ is the period of the grating and n is the effective index of the propagating mode in the optical fiber. Any perturbation, caused due to strain, temperature or pressure changes, can modify the n , i. e. the effective index of the propagating mode, or Λ , which can be detected by a shift in the Bragg wavelength. When an embedded fiber Bragg grating sensor is subjected to changes in environmental conditions, induced changes in the spectral response of the grating can be related to these environmental effects. Fiber Bragg grating sensors are used to sense strain, temperature, pressure, acceleration, ultrasound, mechanical load, electromagnetic fields, and as gas detection sensors [7].

2.2.1.3 Phase modulated fiber optic sensors

Phase modulated or interferometric sensors are used to sense strain, temperature, chemicals, vibrations, and as an acoustic sensor [7, 16-17]. These sensors measure phase changes either

within an optical fiber or between two optical fibers due to interference between two light beams generated from the same source. These sensors have high levels of sensitivity. Three types of interferometric sensors are commonly used, namely Mach-Zehnder, Michelson and Fabry-Perot. The different kinds of interferometers are shown in Figure 5. A Mach-Zehnder interferometric sensor requires two optical fibers one for sensing and the other as a reference. The sensing fiber is exposed to changing environmental effects, which creates a change in the optical path length, and thereby a change in the phase, as compared to that in a reference fiber. In a Michelson fiber optic interferometric sensor, the sensing region is formed by the differential optical path length between mirrored ends of two parallel fibers. The two paths differ by virtue of the transduction in one of the fiber legs, and the phase shift between the two light signals provides the measurement.

Fabry-Perot sensors consist of two mirrors separated by a cavity and are used to sense environmental effects that change the optical path length between the mirrors [7, 10]. A Fabry-Perot interferometric sensor can be constructed from a single optical fiber, called the intrinsic Fabry-Perot sensor. In an intrinsic Fabry-Perot interferometric sensor, two fusion-spliced reflective mirrors form the sensing region. These sensors are extremely sensitive to perturbations that affect the optical path length between the mirrors. An extrinsic Fabry-Perot interferometric sensor has two optical fibers housed within a hollow glass tube by either fusion splicing or adhesive bonding. The mirrored ends of the two optical fibers are perpendicular to the fiber axes, and are separated by an air gap. These sensors measure environmental effects through a change in the optical path length, which leads to a phase change between the input-output and the reflection fibers.

2.2.2. Applications of fiber optic sensors

Optical fiber-based sensors and sensor systems have been used for sensing strain, vibration, chemicals and environment, acceleration, rotation, pressure, position, and humidity, temperature, acoustic waves [7], as Biosensors [18-20], and as Biomedical sensors [7]. Optical fibers have also been used to obtain real-time information on processing, mainly melting and solidification processes, of thermoplastic polymers and fiber-reinforced composites [21]. This subsection discusses the application of optical fibers for chemical, biomedical, and temperature sensing.

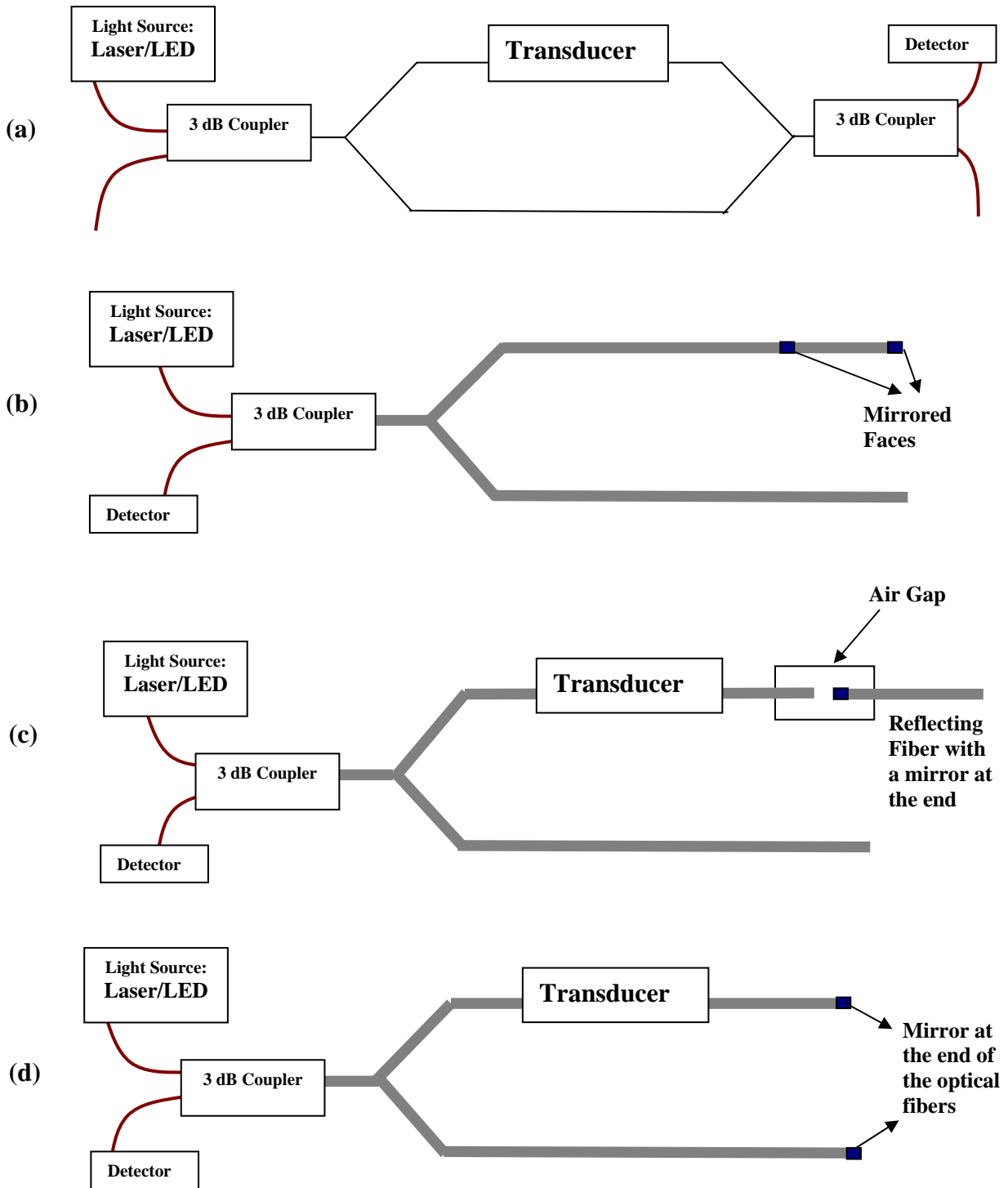


Figure 5. (a) Mach Zender Interferometer (b) Intrinsic Fabry-Perot Interferometer (c) Extrinsic Fabry-Perot Interferometer (d) Michelson's Interferometer

2.2.2.1 Optical fiber sensors for sensing chemicals and biological molecules

Development of optical fiber-based environment, chemical and vapor sensors have been reported by many researchers [7, 22-28]. The active sensing region of these sensors may be located at the end of the optical fiber, on the side of the optical fiber or in porous sections in the fiber. In side-fiber configuration, the cladding of the optical fiber is removed in the active region and the sensing is carried out based on evanescent field emanating from core of the optical fiber.

Sensing of oxygen, carbon dioxide, and ammonia, in gaseous form or dissolved in a liquid, has been carried out using fiber optic sensors [7]. The most commonly used optical sensing methodology for sensing gaseous and dissolved oxygen is dynamic quenching of luminescence by oxygen. Sensing of organic compounds like chlorinated hydrocarbons and volatile organic compounds has also been reported. Sensing of organic compounds is based changes of refractive indices of polymer coatings on optical fibers on exposure to the analytes [7].

Development of optical fiber-based chemical and vapor sensors has lead to the development of fiber-based electronic noses [22]. Electronic and optical noses comprising of optical fiber-based arrays of conductive polymer sensors have been developed in the past [4, 7] to sense and identify individual gases and vapors from a mixture. These electronic noses consist of arrays of cross-reactive sensors, in which each sensor responds to several analytes. The analytes are discriminated from each other based on the unique temporal response patterns from the sensors. Barnard et al. [23] have described the development of a polymer-based optical fiber vapor sensor. This sensor was developed by entrapping a dye Nile red in a dimethylsilicone polymer attached to the distal tip of a single mode optical fiber. The fluorescence changes of the optical fiber sensors on exposure to various vapors such as benzene, toluene, ethyl benzene, xylene, and gasoline were monitored. An optical fiber-based nose was developed [24] by taking a bundle of nineteen optical fibers with a different polymer sensing layer, i. e. polymer with an entrapped dye, attached to each fiber in the bundle. Temporal response of each optical fiber sensor in the bundle was monitored during and after exposure of the sensor array to vapors. Development of microbead sensor arrays has also been described by Patano et al. [25]. Microbead arrays are developed by making micron sized wells on the surface of a bundle of optical fibers and filling the wells with bead sensors. The bead sensors consist of micro spheres in which a fluorescent indicator is attached to a polymeric or porous silica bead.

Another class of chemical sensors developed by employing optical fibers is biosensors. Biosensors are detection devices that use biological components to identify analytes of interest. These analytes of interest may not be a biological species. The biological molecules can be enzymes, antibodies, receptors, or nucleic acids and show high specificity and affinity towards the analytes. When optical fiber-based bio sensors are employed, the biological molecules indicate recognition of analytes by showing changes in optical properties like absorbance, fluorescence, bioluminescence [7]. As an example of a biosensor, alcohol oxidase was immobilized on the surface of an optical fiber sensor in order to develop a bio-sniffer for ethanol vapor [26]. Another group of biosensors includes the use of antibodies or antigens. Antibody immobilization on optical fibers for the development of immunosensors has been performed by several researchers [27]. Fiber-optic immunosensors also have been developed for the detection of protein C (PC) deficiency [28]. Optical fibers have also been employed for measuring biomedical information like pH of blood and in certain parts of the body such as stomach, and blood oxygen saturation [7].

2.2.2.2 Optical fibers for temperature sensing

Different kinds of optical fiber sensors are employed for sensing temperature like Fiber Bragg Grating (FBR) sensors [31-32], sensors based on semiconductor absorption [33-34], or Brillouin scattering [32, 35] and Fabry-Perot based sensors [16, 36-37]. Other kinds of temperature sensors include those based on the change of fluorescence lifetime and intensity upon an increase in temperature [38-39].

The main principle in the measurement of temperature by employing Fiber Bragg Grating (FBR) sensors is based on measuring a temperature dependent shift of dip in the spectrum reflected back from the Fiber Bragg Grating. The dip in reflectance spectrum occurs at a wavelength called the Bragg grating wavelength (λ_B), which is given by the relationship $\lambda_B = 2n\Lambda$, where Λ is the periodic spacing of the grating and n is refractive index of the fiber. Shift in λ_B with strain and temperature is described by the following relationship [31]:

$$\Delta\lambda_B = 2n\Lambda \left(\left\{ 1 - \left(\frac{n^2}{2} \right) [P_{12} - \nu(P_{11} + P_{12})] \right\} \varepsilon + \left[\alpha + \frac{\left(\frac{dn}{dT} \right)}{n} \right] \Delta T \right) \quad (3)$$

where α , ν , P_{12} , P_{11} , ε , and ΔT are coefficient of thermal expansion of the fiber material (silica), poisson's ratio, Pockel's or piezo coefficients of the stress-optic tensor, strain, and increase in temperature respectively. One of the methods utilized method for the interrogation of FBG sensors is based on inputting light with a very broad spectrum on to the FBG sensor and monitoring the position of narrowband dip in the spectrum reflected by the FBG. Wavelength associated with this narrowband dip in the spectrum changes upon increase in temperature according to equation 3.

The main principle in the measurement of temperature by employing Fabry-Perot cavity based sensors is to measure the change in phase shift, associated with the Fabry-Perot cavity, upon increase in temperature [16]. The phase (ϕ) associated with a Fabry-Perot cavity, due to multiple reflections at the front and back reflective surfaces, is given by the following relationship:

$$\phi = \frac{4\pi nL}{\lambda} \tag{4}$$

where n is refractive index of the fiber mode, L the length of the Fabry-Perot sensor, λ the free-space wavelength. The fractional phase shift per unit temperature can be defined by the following relationship:

$$\left(\frac{d\phi}{\phi dT}\right) = \left(\frac{dL}{LdT}\right) + \left(\frac{dn}{ndT}\right) \tag{5}$$

The temperature dependence of the phase associated with a Fabry-Perot cavity arises from the change in optical length of the cavity region due to temperature dependence of the refractive index of the medium between the two reflective surfaces. This change in refractive index occurs

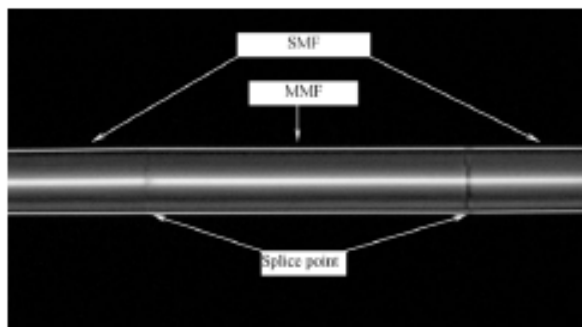


Figure 6. In-line fiber optic structure employed for temperature sensing applications based on the fusion of a single mode fiber to a multimode fiber which is further fused to a single mode fiber in order to form a Fabry-Perot Cavity [36]

due to the thermal expansion of the cavity dielectric material or due to the temperature dependence of the dielectric constants of the materials forming the reflective surfaces of the cavity. A Fabry-Perot cavity can be formed at the end-face of an optical fiber by forming a couple of reflective surfaces separated by a dielectric medium, as described by Lee et al. [16] or by fusing a single mode fiber to another single mode fiber having a different diameter [40]. An in-line Fabry-Perot cavity based fiber optic sensor, was formed by separating fibers containing reflective surfaces at their ends by a certain distance and keeping them in that position by fusing them to a hollow glass tube [37]. The reflective surfaces employed in a Fabry-Perot cavity are either metallic or thin film stack based mirrors [16, 37] or are based on reflections at the fiber face due to a change of a refractive index at the boundary [36-37]. Another variation of an in-line fiber-optic sensor was described by Huang et al. [36], in which a single mode fiber (SMF) was fused to a multi-mode fiber (MMF), which was further fused to a single mode fiber and the reflection spectrum from this Fabry-Perot cavity was measured. This structure is shown in Figure 6. The first and second reflective surfaces of this Fabry-Perot cavity sensor were formed at the SMF-MMF interface and the MMF-SMF interface respectively, due to reflection of the guided wave taking place at the interfaces. This reflection occurs because of a change in refractive indices of optical fiber waveguides at the interface boundaries. The reflectance at each of the two interfaces could be described by the relationship:

$$R = \left(\frac{n_{\text{MMF}} - n_{\text{SMF}}}{n_{\text{MMF}} + n_{\text{SMF}}} \right)^2 \quad (6)$$

where n_{MMF} and n_{SMF} are the refractive indices of the multimode and single mode fiber sections respectively. When the fundamental mode of the SMF is launched into the multimode fiber Fabry-Perot cavity, it excites the fundamental mode of the MMF along with other higher order guided modes. When the light enters the SMF from the multimode fiber, most of the power in the higher order guided modes is lost due to poor coupling of these modes into the fundamental mode of the SMF. Reflection of light at the two boundaries multiple times leads to the formation of a Fabry-Perot cavity in the MMF region. With an increase in temperature, there is a change in the optical path length in the cavity region due to a change in both the refractive index of the MMF and the length of the cavity due to thermal expansion.

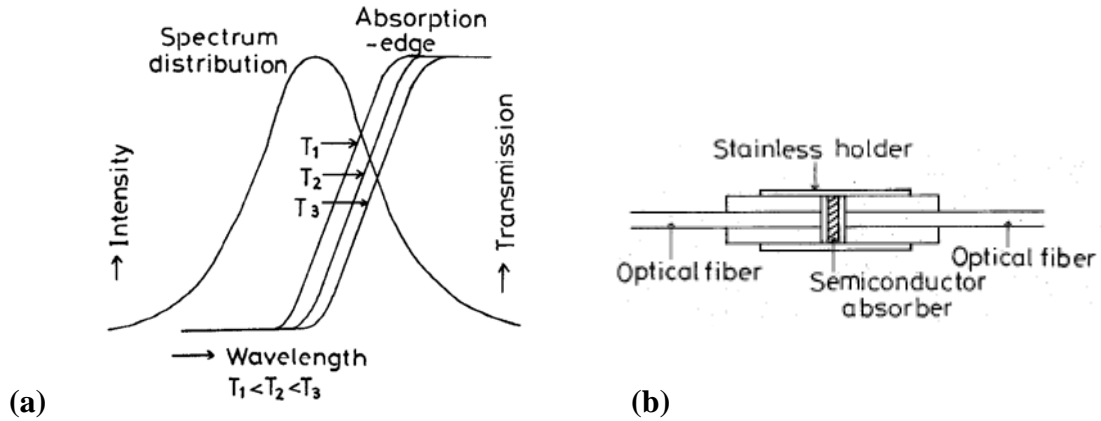


Figure 7. (a) Optical fiber temperature sensor based on temperature dependent shift in the absorption edge of the semiconductor material and (b) A semiconductor material inserted between two optical fibers to form a temperature sensor based on shift in the absorption edge of the semiconductor [33]

Another inline fiber-based Fabry-Perot intrinsic sensor was developed by Lee et al. [16]. The mirrors in the Fabry-Perot cavity were produced by fusion splicing a single-mode silica fiber to a fiber having a seven-layer quarter-wave $\text{TiO}_2/\text{SiO}_2$ stack on a cleaved fiber, cleaving the other end of the single mode fiber to get the desired interferometer cavity length, and then fusing the cleaved end to another fiber having a seven-layer quarter-wave $\text{TiO}_2/\text{SiO}_2$ stack. A novel temperature sensor based on the development on an inline Fabry-Perot cavity is described in detail in chapter 7.

Optical absorption in semiconductor materials is also employed for sensing temperature [33-34]. As the absorption edge in the transmission spectrum of a semi conducting material shifts upon an increase in temperature, the calibrated shift can be employed for temperature sensing applications. The principle of temperature sensing is shown in Fig. 7 a. The energy bandgap of semiconductors decreases with increasing temperature according to the following relationship:

$$E_g(T) = \frac{E_g(0) - \gamma T^2}{\beta + T} \quad (7)$$

where $E_g(0)$ is the band gap when the Kelvin temperature amounts to zero and γ & β are two empirical constants [34]. This decrease in semi-conductor energy bandgap leads to a red-shift in the optical absorption edge of the semiconducting material. The sensor described by Kyuma et al. [33] is shown in Figure 7 and consisted of a thin semiconductor chip, made up of polycrystalline CdTe or semi-insulating GaAs, sandwiched between two ends of optical fibers

inside a stainless pipe as the sensing region. An AlGaAs LED as the light source and an avalanche photodiode detector formed the sensor system. The decrease in transmitted light at a given wavelength, due to a temperature dependent red-shift in the optical absorption edge, is employed for sensing of temperature. Some semiconducting materials like vanadium oxides [41] also exhibit a absorption edge shift upon increase in temperature and this phenomenon could be employed for sensing temperatures. A novel fiber optic temperature sensor based on optical absorption in a semiconductor film is described in detail in chapter 7.

Separate fiber optic sensors are frequently employed for the measurement of strain and temperature in composite structures. Optimal use of an optical fiber sensor can be obtained if simultaneous measurements of strain and temperature are carried out by employing the same sensor. Several researchers have studied the development of fiber-optic sensors that can make simultaneous measurements of strain and temperature [42-44].

2.3 References

1. Fraden J., Handbook of modern sensors: physics, designs, and applications, Springer-Verlag, New York, 1996.
2. Soloman S., Sensors Handbook, McGraw-Hill Companies, 1998.
3. Morrison A. M., Coughlin K., Shine J. P., Coull B. A., and Rex A. C., "Receiver Operating Characteristic Curve Analysis of Beach Water Quality Indicator Variables", Applied and Environmental Microbiology, 69 (11), 6405–6411, 2003.
4. Arshak K., Lyons G. M., Cunniffe C., Harris J., and Clifford S., "A review of digital data acquisition hardware and software for a portable electronic nose", Sensor Review, 24 September 2003, vol. 23, iss. 4, pp. 332-344(13).
5. Gopel W., Jones T. A., Kleitz M., Lundstrom I., and Seiyama T. Eds., Chemical and biochemical sensors: Part I, in: W. Gopel, J. Hesse, J.N. Zemel Eds., Sensors, A Comprehensive Survey, Vol. 2, Wiley-VCH, Weinheim, 1991.
6. Janata J., Principles of chemical sensors, Plenum Press, New York, 1989.
7. Miguel, J., and Higuera L., Handbook of Optical Fiber sensing technology, John Wiley and Sons Ltd., 2002.
8. Ghatak, A. and Thyagarajan, K., Introduction to Fiber Optics, Cambridge University Press, Cambridge, 1998.

9. Kazousky, L., Benedetto, S., and Willner, A., *Optical Fiber Communication Systems*, Artech Book House, 1996.
10. Yu, T. S. and Yin, S., *Fiber Optic Sensors*, Marcel Dekker, Inc., 2002.
11. Ball, G. A., Meltz, G. and Morey, W. W., "Polarimetric Heterodyning Bragg-Grating Fiber Laser," *Optics Letters*, 18, 1976-1978, 1993.
12. Stewart, G. and Culshaw, B., "Optical waveguide modeling and design for evanescent field chemical sensors," *Optical and Quantum Electronics*, 26, 249-259 1994.
13. Monro, T. M., Richardson, D. J., and Bennet, P. J., "Developing holey fibers for evanescent field devices," *Electronic Letters*, 35(14), 1999.
14. Zhou, G. and Sim, L. M., "Damage detection and assessment in fibre-reinforced composite structures with embedded fibre optic sensors-review", *Smart Material and Structures*, 11, 925-939, 2002.
15. Udd, E., *Fiber Optic Sensors: An introduction for Engineers and Scientists*, John Wiley and Sons, Inc., New York, 1991.
16. Lee, C. E., Atkins, R. A., and Taylor, H. F., "Performance of A Fiber-Optic Temperature Sensor from -200-Degrees-C to 1050-Degrees-C," *Optics Letters* 13 (11), 1038-1040, 1988.
17. Schmidt, M. and Frstenau, N. "Fiber-optic extrinsic FabryPerot interferometersensors with three-wavelength digital phase demodulation," *Optics Letters*, 24, 599-601, 1999.
18. Arnold, M. A., "Enzyme-based fiber-optic sensor," *Analytical Chemistry*, 57, 565-566, 1985.
19. Blum, J. L., Gautier, S. M., and Coulet, P. R., "Luminescence fiber optic biosensor," *Analytical Letters*, 21, 717-726, 1988.
20. Healey, B. G., Li, L., Walt, D. R., "Multianalyte biosensors on optical imaging bundles," *Biotechnology and Bioelectronics*, 12, 521-529, 1997.
21. Kuang, K. S. C. and Cantwell, W. J., "In situ process monitoring of a thermoplastic-based fibre composite using optical fibre sensors," *Smart Material and Structures*, 11, 840-847, 2002.
22. Nagle, H. T. and Gutierrez-Osuna R., "The how and why of electronic noses", *IEEE Spectrum*, 1998.
23. Barnard, S. M. and Walt, D. R., "Fiber-optic Organic Vapor Sensor," *Environment Science and Technology*, 25, 1301-1304, 1991.

24. White, J., Kauer, J. S., Dickinson, T. A., and Walt, D. R., "Rapid Analyte Recognition in a Device Based on Optical Sensors and the Olfactory System," *Analytical Chemistry*, 68, 2191-2202, 1996.
25. Pantano, P. and Walt, D. R., "Ordered Nanowell Arrays," *Chemistry of Materials*, 8, 2832-2835, 1996.
26. Mitsubayashi, K., Kon, T., and Hashimoto, Y., *Biosens. Bioelectron.*, 19 (3), 193-198, 2003.
27. Wolfbeis, O. S., *Anal. Chem.* 2004, 76, 3269-3284.
28. Kwon, H. J., Peiper, S. C., and Kang, K. A., *Adv. Exp. Med. Biol.*, 510, 115-119, 2003.
29. Kapany, N. S. and Silbestrust, N., "Fiber optics spectrophotometer for in vivo oximeter," *Nature*, 208, 138-145, 1964.
30. Mignani, A. G., and Baldini, F., "Biomedical sensors using optical fibers," *Report on Progress in Physics*, 59, 1-28, 1995.
31. Kersey, A. D. and Berkoff T. A., "Fiberoptic Bragg-Grating Differential-Temperature Sensor," *IEEE Photonics Technology Letters*, 4 (10), 1183-1185, 1992.
32. Davis, M. A., and Kersey, A. D., "Simultaneous measurement of temperature and strain using fibre Bragg gratings and Brillouin scattering," *IEE Proceedings-Optoelectronics*, 144 (3), 151 - 155, 1997.
33. Kyuma, K., Tai, S., Sawada, T., and Nunoshita, M., "Fiber-optic instrument for temperature measurement," *IEEE J. Quantum Electron.*, 18 (4), 676-679, 1982.
34. Zhao, Y., Rong, M., and Liao, Y., "Fiber-optic temperature sensor used for oil well based on semiconductor optical absorption," *IEEE Sensors Journal*, 3 (4), 400 - 403, 2003.
35. Wait, P. C. and Hartog, A. H., "Spontaneous brilliounin-based distributed temperature sensor utilizing a fiber Bragg grating notch filter for the separation of the brillouin signal," *IEEE Photon. Technol. Lett.*, 13, 508-510, 2001.
36. Huang, Z. Y., Zhu, Y. Z., and Chen, X. P., "Intrinsic Fabry-Perot Fiber Sensor for Temperature and Strain Measurements," *IEEE Photonics Technology Letters* 17 (11), 2403-2405, 2005.
37. Wang, A., Xiao, H., Wang, J., Wang, Z., Zhao, W., and May, R. G., "Self-Calibrated Interferometric-Intensity-Based Optical Fiber Sensors," *Journal of Lightwave Technology*, 19 (10), 2001.

38. Zhang, Z. Y., Grattan, K. T. V., and Palmer, A. W., "A Novel Signal-Processing Scheme for a Fluorescence Based Fiber optic Temperature Sensor," *Review of Scientific Instruments* 62 (7), 1735-1742, 1991.
39. Grattan, K. T. V., Palmer, A. W., and Zhang, Z., "Development of A High-Temperature Fiberoptic Thermometer Probe Using Fluorescent Decay," *Review of Scientific Instruments* 62 (5): 1210-1213, 1991.
40. Tsai, W. H. and Lin, C. J., "A novel structure for the intrinsic Fabry-Perot Fiber-Optic temperature sensor," *J. Lightwave Technol.*, 19, 682-686, 2001.
41. Katzke H., Toledano P., and Depmeier W., "Theory of morphotropic transformations in vanadium oxides," *Physical Review B*, 68, 024109, 2003.
42. Xu, M. G., Archambault, J. L., Reekie, L., Dakin, J. P., "Discrimination between Strain and Temperature Effects using Dual-Wavelength Fiber Grating Sensors," *Electronics Letters*, 30 (13), 1085-1087, 1994.
43. Vengsarkar, A. M., Michie, W. C., Jankovic, L., Culshaw, B., Claus, R. O., "Fiberoptic Dual-Technique Sensor for Simultaneous Measurement of Strain and Temperature," *Journal of Lightwave Technology*, 12 (1), 170-177, 1994.
44. Singh, H. and Sirkis, J. S. "Simultaneously Measuring Temperature and Strain using Optical Fiber Microcavities," *Journal of Lightwave Technology* 15 (4), 647-653, 1997.

CHAPTER 3. REVIEW OF SENSORS BASED ON SURFACE PLASMONS

3. Review of Sensors based on surface plasmons

3.1 Definition of surface plasmons

Mobile electrons at the interface of two media having dielectric constants with opposite signs, e.g. the metal-air interface when excited by light can perform coherent fluctuations or collective oscillations which are called surface plasmon polaritons (SPP). Surface plasmon polaritons or waves are localized transverse magnetic (TM) electromagnetic waves traveling along the interface of two different media [1]. The field vectors of these surface plasmon waves reach their maxima at the interface and decay evanescently into both media [2]. These waves are always p-polarized, propagate parallel to the interface and are attenuated (exponentially) in the direction normal to the interface in both media [1, 3].

Consider an electromagnetic plane wave having an electric field in an x-z plane (p-polarized) at the interface of two media having an equation:

$$\vec{E} = \vec{E} \exp[i(\omega t - k_x x - k_z z)] \quad (1)$$

where k_x and k_z are propagation constants of the electromagnetic plane wave in x and z directions respectively and ω is the angular frequency of the wave traveling at the interface of the two mediums as shown in Figure 1.

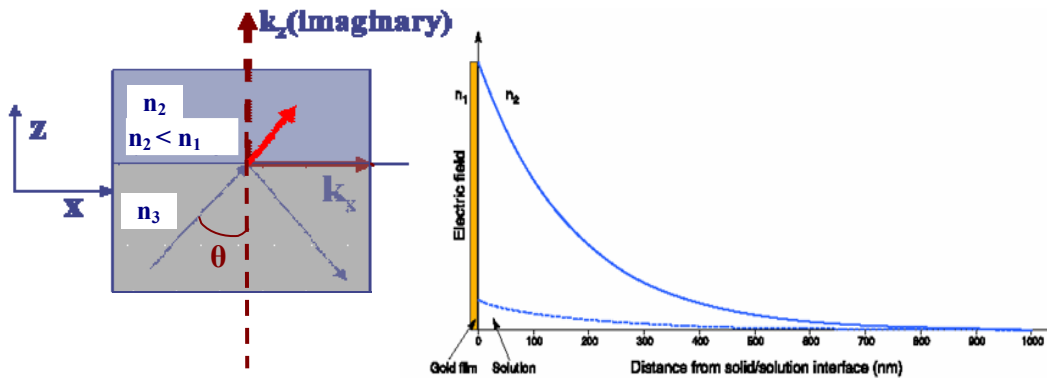


Figure 1. (a) Figure showing the phenomenon of total internal reflection. Light incident from medium 1 having refractive index n_1 is totally internally reflected for $\theta > \theta_c$. In medium 2, k_z is imaginary and k_x is real (b) Evanescent fields decaying away from a boundary with and without a thin gold layer present [17]

If k_z is imaginary in both the media, it implies that the electric field given by the relation $E = \vec{E} \exp[i(\omega t - k_x x - k_z z)]$ with the $\exp(-i k_z z)$ term is exponentially attenuated in both the media (for $z > 0$ and $z < 0$). For the surface plasmon waves to exist, the following two conditions about k_z have to be satisfied in the two mediums:

$$k_z = -i\sqrt{k_x^2 - \varepsilon_1 \frac{\omega^2}{c^2}} \quad \text{for } z > 0 \quad (2)$$

and

$$k_z = i\sqrt{k_x^2 - \varepsilon_2 \frac{\omega^2}{c^2}} \quad \text{for } z < 0 \quad (3)$$

where k_x is same in both the media and for the above conditions of k_z satisfied and on applying boundary conditions at the interface of medium 1 and 2 (of continuity of the tangential components of the E and H fields and the normal components of the D and B fields) is given by:

$$k_x = k_{SP} = \frac{\omega}{c} \sqrt{\frac{\varepsilon_1(\omega) \cdot \varepsilon_2(\omega)}{\varepsilon_1(\omega) + \varepsilon_2(\omega)}} \quad (4)$$

In order for surface plasmon waves to exist ε_1 and ε_2 should have opposite signs i.e. $\varepsilon_1 \varepsilon_2 < 0$ and the medium with dielectric constant having a negative real part (assuming medium 1) is called an active medium [3]. An active medium could be a metal with free electrons and their dielectric constant could be approximated using the Drude model. The metal dielectric constants are given by the following expressions:

$$\varepsilon_r(\omega) = 1 - \omega_p^2 \frac{1}{\omega^2 + \Gamma^2} \quad \text{and} \quad \varepsilon_{im}(\omega) = \omega_p^2 \frac{\Gamma / \omega}{\omega^2 + \Gamma^2} \quad (5)$$

where ε_r is the real part and ε_{im} is the imaginary part of the metal dielectric constant and ω_p is the free electron plasma frequency. At very high angular frequencies, the above equations reduce to the following relations:

$$\varepsilon_r(\omega) = 1 - \frac{\omega_p^2}{\omega^2} \quad \text{and} \quad \varepsilon_{im}(\omega) = \Gamma \frac{\omega_p^2}{\omega^3} \quad (6)$$

If one considers only the real dielectric constant part ($\varepsilon(\omega) = 1 - \omega_p^2/\omega^2$) and for a value of ω_p greater than ω , $\varepsilon_r(\omega)$ is negative. If medium 1 is a metal with a negative refractive index $\varepsilon_1 = \varepsilon_r(\omega)$ and medium 2 is a medium with a real dielectric constant and $\varepsilon_2 > 0$, then the

condition for surface plasmon wave formation is satisfied. Moreover for a metal with a negative dielectric constant real part, the equation:

$$k_z = -i\sqrt{k_x^2 - \varepsilon_1 \frac{\omega^2}{c^2}} \quad (7)$$

for $z > 0$ is also always satisfied as the term inside the square root is positive which makes k_z a negative imaginary number for $z > 0$ and satisfies the SPP condition. For the SPP condition:

$$k_z = i\sqrt{k_x^2 - \varepsilon_2 \frac{\omega^2}{c^2}} \quad (8)$$

to be satisfied for $z < 0$ (and assuming $\varepsilon_2 = 1$), it implies that the propagation constant in the x direction k_x is greater than $\omega/c \sqrt{\varepsilon_0}$. This implies that the propagation constant (k_x) of the incident electromagnetic radiation in the x direction has to be greater k_0 , i.e. propagation constant of light wave in air, for the excitation of surface plasmons and its value must equal k_{SP} . The relation between angular frequency of the wave traveling at the interface of the two mediums (ω) and the propagation constant (k_x) of the incident electromagnetic radiation in the x direction is called the dispersion relation (DR) and must be satisfied for the existence of surface plasmons. As only evanescent waves can have a propagation constant greater than k_0 , surface plasmons can be excited only by evanescent waves. Thus electromagnetic radiation incident on a thin metallic film from a dielectric medium is first converted to an evanescent wave and this wave excites surface plasmons at the surface of the metal. The active media could also be ionic crystals in the infrared region i.e. between 10 and 100 μm [3] or semiconductors in some other frequency range such the dielectric constant ε_1 of the medium is negative.

3.2 Description of Evanescent Waves

Evanescent waves are defined as electromagnetic waves that have a real propagation constant in the direction parallel to the interface of two media and an imaginary propagation constant perpendicular to the interface as shown in Figure 1 a. An evanescent wave decays in the direction away from the media interface in the medium having a lower refractive index, as shown in Figure 1 b. Speed of an evanescent wave is slower than the propagation speed of light in the medium next to the interface (n_1).

Evanescent waves are formed by total internal reflection of an electromagnetic plane wave that is incident at an angle θ from a medium 1, with a refractive index n_1 , onto a smooth planar

surface separating medium 1 from medium 2 (with a refractive index n_2), as shown in Figure 1.

The critical angle for total internal reflection, θ_c is given as:

$$\theta_c = \sin^{-1}(n_2/n_1) \quad (9)$$

i.e. for any angle of incidence i.e. θ more than the critical angle there is going to be total internal reflection.

Mathematically, for $\theta > \theta_c$,

$$\cos\theta'' = \sqrt{1 - \sin^2\theta''} = i\sqrt{\sin^2\theta'' - 1} = i\sqrt{(n_1/n_2)^2 \sin^2\theta - 1} \quad (10)$$

An electromagnetic plane wave (E_i) incident on the planar surface separating medium 1 and 2 and E_t , the transmitted electric field are given by:

$$E_i = A. \exp(i.(k.r - \omega t))$$

$$E_t = T_0. A. \exp(i.(k''.r - \omega t))$$

$$E_t = T_0. A. \exp(i.(k''\sin\theta''x + k''\cos\theta''z - \omega t))$$

$$E_t = [T_0. A. \exp(i.k''\sin\theta''x). \exp(-i.\omega''t)]. \exp(-M.z) \quad (\text{since } \cos\theta'' \text{ is imaginary}) \quad (11)$$

where A is the amplitude, k is the propagation constant, and ω is the angular frequency of the incident wave and T_0 is the transmission of the wave across the interface. This implies that E_t i.e. transmitted field in total internal reflection decreases in the z direction away from the boundary i.e. it is an evanescent field. Besides total internal reflection in planar surfaces (like prisms, planar interface between two media etc.), evanescent waves are also created in tapered optical fibers, and in gratings with a period smaller than light wavelength.

When light is totally internally reflected, a phase change (δ_N and δ_P) occurs in the reflected wave. δ_N and δ_P are the phase shifts of the electric-field wave components

normal and parallel to the plane of incidence of the field. This phase change depends on the incident angle θ_1 and is given by the following relations:

$$\tan \frac{\delta_N}{2} = \frac{\sqrt{n_1^2 \cos^2 \theta_1 - n_2^2}}{n_1 \sin \theta_1} \quad \text{and} \quad \tan \frac{\delta_P}{2} = \frac{n_1 \sqrt{n_1^2 \cos^2 \theta_1 - n_2^2}}{n_2^2 \sin \theta_1} \quad (12)$$

3.3 Excitation of surface plasmon waves

Excitation of surface plasmon waves could be achieved by total internal reflection of p-polarized light waves in prism couplers, optical waveguides, tapered optical fibers etc., a rough surface at which p-polarized light waves are incident, or by using a diffraction grating [1-6]. Surface plasmon polaritons are not excited if the incident optical radiation is s-polarized [1, 3-5]. Since the propagation constant of the incident optical radiation is less than that required for excitation of surface plasmon waves, a coupling mechanism has to be employed to enhance the propagation constant of the incident wave so that it matches that of the surface plasmon wave. This change in propagation constant (momentum) is achieved by employing attenuated total reflection in prism couplers, optical waveguides or optical fibers, and diffraction at the surface of gratings.

3.3.1 Excitation of surface plasmons by Attenuated Total Reflection (ATR)

Total internal reflection (TIR) can lead to formation of evanescent waves being generated and these waves could be used to excite surface plasmon waves. The Otto configuration shown in Figure 2 is used to generate surface plasmon waves by employing a prism and an air gap between the prism and a metal (e.g. silver) surface. When the angle of incidence of light (θ) at the glass-air interface is greater than the critical angle, total internal reflection occurs and an evanescent transmitted wave is generated in the air gap between the prism and the metal. The wave propagating in air between the prism and the metal is an evanescent wave. This requires gap between the glass prism and the metal surface to be ~ 100 nm or the order of wavelength of light wave propagating in air or [3].

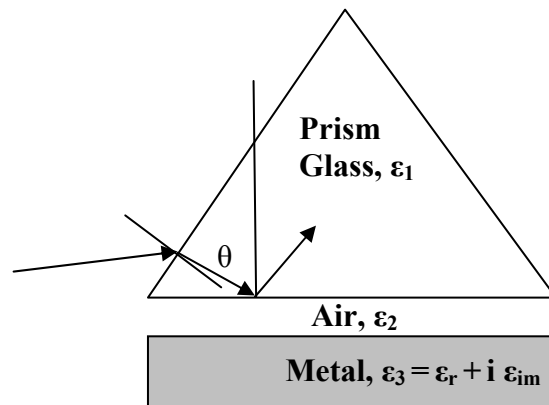


Figure 2. Otto configuration employed for surface plasmon generation

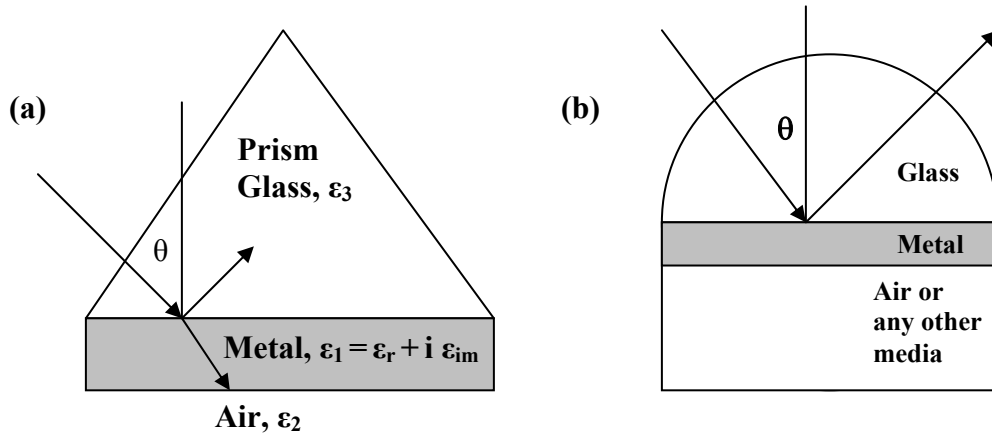


Figure 3. Kretschmann configuration (a) and Kretschmann-Raether configuration (b) to generate evanescent waves to excite surface plasmon waves at the metal air interface employing attenuated total internal reflection (ATR)

The Kretschmann configuration shown in Figure 3 is another configuration that is used to generate evanescent waves through the total internal reflection process. In this configuration a thin metal film ($< \lambda/10$) is deposited directly on the prism and the total internal reflection at the glass-metal boundary leads to generation of evanescent waves that could be used to excite surface plasmon resonance at the metal-air boundary. Variation of the angle of incidence ‘ θ ’ of the input radiation allows matching of the wave vector of the incident light and that of the surface plasmon polaritons via excitation of evanescent waves. At the angle θ_{SP} , the value of wave vector or the propagation constant ‘ k_x ’ of light parallel to the direction of the metal layer matches the value of k_x required for the excitation of surface plasmon polaritons i.e. k_{SP} , which is equal to $k_x = (\omega/c) / (\sqrt{\epsilon_d} \sin \theta_{SP})$.

3.3.2 Generation of surface plasmons by using diffraction gratings

The value of the propagation constant of the incident wave is increased to match that of the surface plasmon waves by using diffraction grating couplers as shown in Figure 4 [2]. When a grating coupler is used to generate surface plasmon waves, the value of wave vector or the propagation constant of the waves in direction of propagation of light is increased from k_0 , i.e. $\omega/c \sqrt{\epsilon_0}$ where ϵ_0 is the dielectric constant of the medium next to the grating, by a certain value which is a function of the grating period i.e. $k_x = k_0 + 2\pi n/d$ where n is an integer and d is the period.

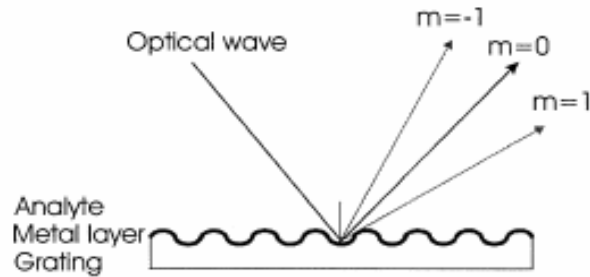


Figure 4. A grating coupler employed to excite surface plasmon modes by the process of diffraction [2]

3.3.3 Generation of surface plasmons in optical waveguides

Evanescent fields are also generated in planar and cylindrical optical waveguides and these fields can be used to excite surface plasmon waves, at the metal-surrounding interface. In planar optical waveguides, light is guided until it enters a region which has a thin metal over layer. The evanescent electromagnetic field penetrates the metal layer and interacts with the analyte on top of the metal layer. Surface plasmon waves are excited in optical waveguides if the surface plasmon wave and the guided mode in the planar waveguide are phase matched as shown in Figure 5.

Excitation of surface plasmons in optical fibers can be treated in a manner similar to the case of optical waveguides. The only difference would be that optical fibers are cylindrical waveguides and have different waveguide modes as compared with the planar waveguides. In planar waveguides only TE and TM modes exist whereas in the optical fibers TE, TM, EH, and HE modes exist. The modes responsible for propagation of the surface plasmon waves in optical fibers are the TM, EH, and the HE modes. In order to excite surface plasmon waves in thin gold films via the evanescent waves, either the gold layer has to be right next to the waveguide layer in which light is propagating or one has to ensure that the geometry of the structure allows evanescent fields to excite plasmon waves. Hence, either the cladding of the optical fiber is removed or its geometry is altered before deposition of the gold film on the fiber.

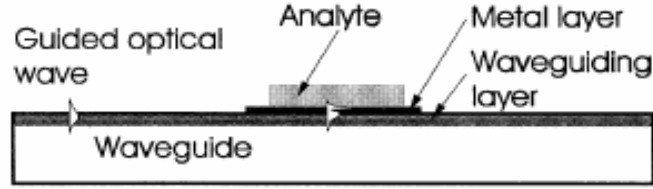


Figure 5. A planar waveguide structure used for sensing employing surface plasmon resonance [2]

3.4 Field enhancement due to Surface Plasmon excitation

Weber et al. have discussed enhancement of optical electric fields at gold, silver, and copper metal surface due to surface-plasmon excitation [4]. Excitation of a surface plasmon wave from an incident plane wave is shown in Figure 6 where the dashed lines represent a plane wave coupler, which could be a prism, a grating, or roughness. Electromagnetic fields of a surface plasmon mode excited by an incident p-polarized plane wave to ensure optimum coupling of the incident radiation by the prism or grating coupler and are given by the following equations:

$$H_{SP} = H_y \exp[i(k_x x - \omega t)]. \exp[-k_{z1} z] \hat{y} \quad \text{for } z > 0$$

$$H_{SP} = H_y \exp[i(k_x x - \omega t)]. \exp[k_{z2} z] \hat{y} \quad \text{for } z < 0 \quad (13)$$

and

$$E_{SP} = \frac{c}{\omega} H_y \exp[i(k_x x - \omega t)]. \exp[-k_{z1} z]. \frac{1}{\epsilon_1} (ik_{z1} \hat{x} - k_x \hat{z}) \quad \text{for } z > 0$$

$$E_{SP} = \frac{c}{\omega} H_y \exp[i(k_x x - \omega t)]. \exp[-k_{z1} z]. \frac{1}{\epsilon_1} (ik_{z1} \hat{x} - k_x \hat{z}) \quad \text{for } z < 0 \quad (14)$$

where H_y is the amplitude of the magnetic field and

$$k_x = \frac{\omega}{c} \sqrt{\frac{\epsilon_1 \epsilon_2}{\epsilon_1 + \epsilon_2}} \quad \text{for } z > 0 \quad \text{and} \quad \text{for } z < 0 \quad (15)$$

and

$$k_{z1} = \frac{\omega}{c} \sqrt{\frac{-\epsilon_1^2}{\epsilon_1 + \epsilon_2}} \quad \text{for } z > 0 \quad \text{and} \quad k_{z2} = \frac{\omega}{c} \sqrt{\frac{-\epsilon_2^2}{\epsilon_1 + \epsilon_2}} \quad \text{for } z < 0 \quad (16)$$

for the surface plasmon wave to be excited. The time averaged power flow in the mode propagating in the x direction per unit length in the y direction is calculated by evaluating the real part of the Poynting vector, taking its dot product with the unit vector, and integrating from z equal to $-\infty$ to ∞ and is given by:

$$P_{SP} = \frac{c}{8\pi} \int_{-\infty}^{\infty} \Re(\mathbf{E}_{SP} \times \mathbf{H}_{SP}^*) \cdot \hat{x} dz \quad (17)$$

Employing the equality of power dissipated in the metal per unit mode area with the net power added to the metal per unit area by coupling with the incident plane wave, one gets the formula for the ratio of the square of the modulus of the electric field of the excited surface plasmon mode at $z = 0$ and the square of the modulus of the electric field vector in the incident radiation ($|E_{SP}(0)|^2 / |E_0|^2$) which can be calculated from the following relation:

$$\frac{|E_{SP}(0^+)|^2}{|E_0|^2} = \frac{2 \cos \theta \epsilon_2'^2 (1-R)}{\epsilon_1'^{1/2} \epsilon_2'' (-\epsilon_2' - \epsilon_1)^{1/2}} \quad (18)$$

where $\epsilon_2 = \epsilon_2' + i\epsilon_2''$ and $\epsilon_2' < -\epsilon_1$ and $\epsilon_2'' \ll -\epsilon_2'$ and R is the power reflectance resulting from either specular reflection of the incident beam at the coupler or re-radiation of the surface plasmon. Raether [7] provided a relation for the magnetic field of the surface plasmons at the interface of the metal layer and the medium surrounding the metal layer ($H_y(2/1)$), where 1 is the metal layer and 2 is the medium surrounding the metal layer, and the incoming field intensity ($H_y(0/1)$), where 1 is the metal layer and 0 is the medium from which light is incident onto the metal layer.

$$\frac{|H_y(2/1)|^2}{|H_{y0}(0/1)|^2} = \frac{t_{01}^p t_{12}^p \exp(ik_{z1}d_1)}{1 + r_{01}r_{12} \exp(2ik_{z1}d_1)} \quad (19)$$

where k_{z1} is the propagation constant of the field in the z direction in the metal layer (layer 1) and d_1 is the thickness of the metal layer. t_{01}^p and t_{12}^p are the Fresnel coefficients at the boundaries of media 0 & 1 and 1 & 2 respectively. The equation 19 has a maximum for the minimum value of thickness of the metal layer d_1 and the maximum value of the square of the magnetic and electric-field enhancements are given by:

$$T_{max}^H = \frac{|H_y(2/1)|^2}{|H_{y,0}(0/1)|_{max}^2} = \frac{1}{\epsilon_0} \frac{2|\epsilon_1'|^2}{\epsilon_1''} \frac{a}{1+|\epsilon_1'|} \quad (20)$$

and

$$T_{\max}^{\text{el}} = \frac{|E(2/1)|^2}{|E_0(0/1)|_{\max}^2} = \frac{1}{\varepsilon_2} \frac{2|\varepsilon_1'|^2}{\varepsilon_1''} \frac{a}{1+|\varepsilon_1'|} \quad (21)$$

where ε_0 , ε_2 , ε' , and ε'' are the dielectric constant of the medium '0' from which light is incident on the metal surface, dielectric constant of the medium '2' next to the metal, real part of the metal dielectric constant, and the imaginary part of the metal dielectric constant respectively.

The term 'a' in equations 20 and 21 is given by the following relationship:

$$a = |\varepsilon_1'|(\varepsilon_0 - 1) - \varepsilon_0 \quad (22)$$

Raether [7] reported that the maximum enhancement in the electric field intensity given by equation 21 is approximately 250 for a 700 nm light incident on a silver film from a quartz medium having a dielectric constant of 2.2, with the medium '2' on the other side of the silver film being air ($\varepsilon_0 = 1$). It is reported by Weber et al. [4] that when the electric field enhancement is calculated using the formula mentioned above, the results are consistent with experimental data obtained for prism couplers and grating couplers (e.g. with a grating of spacing $d=800$ nm) for evaporated silver, gold and copper films exposed to air. For a perfect coupler on the surface of a silver film, the maximum increase of the square of the electric fields is calculated to be approximately 300 for incident light energy in 2-3 eV range.

3.5 Surface plasmon resonance condition

3.5.1 Derivation of surface plasmon resonance condition

Simon et al. [1] and Yamamoto [5] have calculated reflectivity R for an optical field incident at an angle on a three layer system of a prism, a metal layer, and air as shown in Figure 7. As discussed earlier, in the Kretschmann configuration, an electromagnetic wave (p-polarized plane wave) in a glass prism is incident on a metal film at the hypotenuse face of the glass prism at an angle greater than θ_c i.e. the critical angle for total internal reflection [1]. Simon et al. have described the procedure to evaluate reflectivity (R) of the electromagnetic wave that is incident on the glass-metal interface (as shown in Figure 7) by applying boundary conditions (of continuity of tangential components of E and H fields and normal components of D and B fields across the boundary) at the interfaces of metal and air and metal and glass in the three layer configuration (i.e. at boundaries $z=0$ and $z=-d$ in Figure 7).

The equation of the electric field (E field) of the electromagnetic wave incident on the glass-metal boundary at an angle θ_1 is given by the following plane wave equation:

$$\begin{aligned}\hat{E}_{inc} &= \hat{E}_1^i \exp[i(\frac{\omega}{c})(x \sin \theta_1 - z \cos \theta_1)(n_1)]. \exp[-i\omega t] \\ &= (\hat{x} \cos \theta_1 + \hat{z} \sin \theta_1). E_1^i. \exp[i(\frac{\omega}{c})(x \sin \theta_1 - z \cos \theta_1)(n_1)]. \exp[-i\omega t]\end{aligned}\quad (23)$$

where E_1^i is the amplitude of the incident electric field vector \hat{E}_1^i . The magnetic field (H field) of the electromagnetic wave is given by:

$$\hat{H}_{inc} = \hat{y} \frac{n_1}{\mu_0 c}. E_1^i. \exp[i(\frac{\omega}{c})(x \sin \theta_1 - z \cos \theta_1)(n_1)]. \exp[-i\omega t] \quad (24)$$

For the sake of convenience, one could write the electric and magnetic field equations without writing the time dependence. Thus the incident electric field could be written as:

$$\hat{E}_{inc} = \hat{E}_1^i \exp[i(\frac{\omega}{c})(x \sin \theta_1 - z \cos \theta_1)(n_1)] \quad (25)$$

which can be written as:

$$\hat{E}_{inc} = (\hat{x} \cos \theta_1 + \hat{z} \sin \theta_1). E_1^i. \exp[i(\frac{\omega}{c})(x \sin \theta_1 - z \cos \theta_1)(n_1)] \quad (26)$$

The transmitted electric field without the time term dependence is given by:

$$\hat{E}_t = \hat{E}_3 \exp[i(\frac{\omega}{c})(x \sin \theta_1)(n_1)]. \exp[(\frac{\omega}{c}).(\sqrt{n_1^2 \sin^2 \theta - 1})z] \quad (27)$$

which can be written in terms of magnitude of \hat{E}_3 as:

$$\hat{E}_t = (\hat{x} \cos \theta_3 + \hat{z} \sin \theta_3). E_3. \exp[i(\frac{\omega}{c})(x \sin \theta_1)(n_1)]. \exp[(\frac{\omega}{c}).(\sqrt{n_1^2 \sin^2 \theta - 1})z] \quad (28)$$

The reflected electric field without the time dependence term is given by:

$$\begin{aligned}\hat{E}_{reflected} &= \hat{E}_1^r \exp[i(\frac{\omega}{c})(x \sin \theta_1 + z \cos \theta_1)(n_1)] = \\ &= (-\hat{x} \cos \theta_1 + \hat{z} \sin \theta_1). E_1^r. \exp[i(\frac{\omega}{c})(x \sin \theta_1 + z \cos \theta_1)(n_1)]\end{aligned}\quad (29)$$

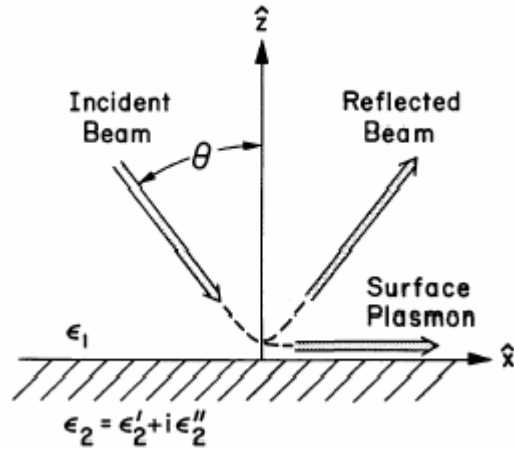


Figure 6. Excitation of a surface plasmon wave with a plane-wave coupler (prism, a grating, or random roughness) which is shown by dashed lines [7]

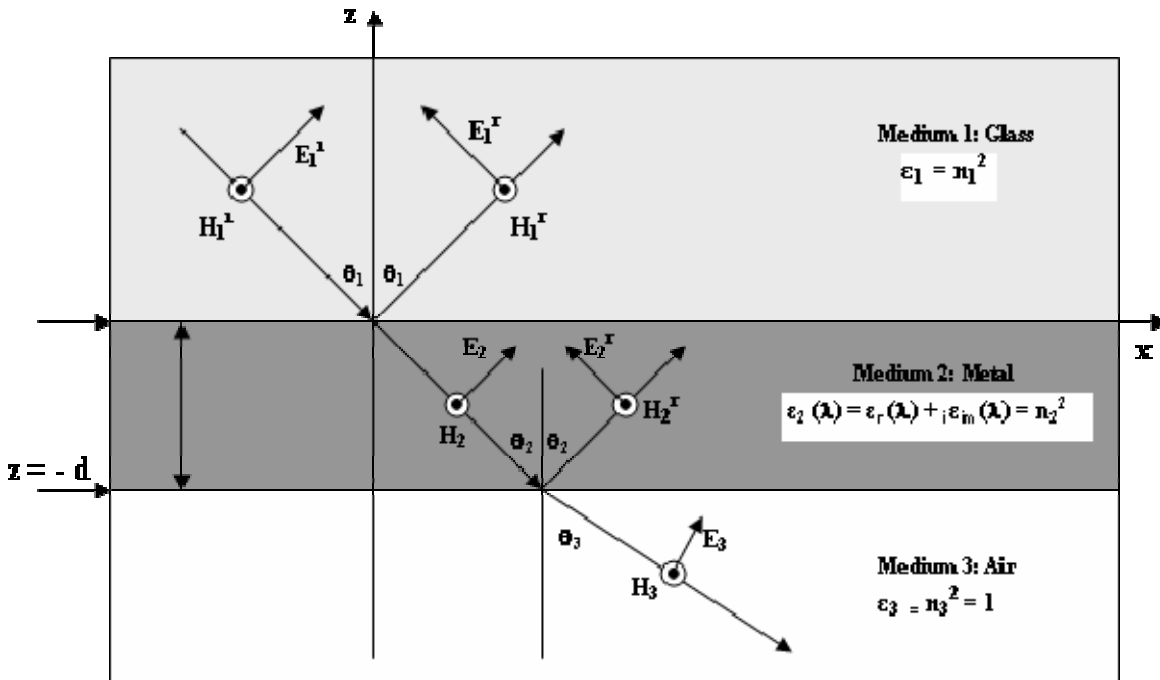


Figure 7. Geometry depicting excitation of surface plasmon waves at the Metal-Air interface through attenuated total reflection (ATR). Electric and magnetic fields of the reflected and transmitted radiation in the three media are shown. Thickness of the metal film (d) is $\sim 10\text{-}50$ nm for excitation of surface plasmons

and the electric field inside the metal layer without the time dependence term is given by:

$$\begin{aligned} \hat{E}_{\text{metal_layer}} &= \hat{E}_2 \exp[i(\frac{\omega}{c})(x \sin \theta_1)(n_1)]. \exp[-z.i \frac{\omega}{c} \sqrt{n_2^2 - n_1^2 \sin^2 \theta_1}] + \\ \hat{E}_2^r &\exp[i(\frac{\omega}{c})(n_1)x \sin \theta]. \exp[z.i \frac{\omega}{c} \sqrt{n_2^2 - n_1^2 \sin^2 \theta_1}] \end{aligned} \quad (30)$$

On application of boundary conditions of the continuity of the continuity of tangential components of E and H fields at the boundaries $z = 0$ and $z = -d$, one could obtain the amplitude of all the electric and magnetic fields in mediums 1, 2, and 3 in terms of amplitude of the incident electric field E_1^i . The ratio of the amplitude of the reflected electric field in medium 1 and the incident electric field in medium 1 i.e. $\frac{E_1^r}{E_1^i}$ is given by the following expression:

$$\frac{E_1^r}{E_1^i} = \frac{r_{12} + r_{23} \cdot \exp(-2kd)}{1 + r_{12} \cdot r_{23} \cdot \exp(-2kd)} \quad (31)$$

where d is the thickness of the metal film (generally between 10-50 nm for the excitation of surface plasmons in metallic films of silver), and r_{12} and r_{23} are the Fresnels reflection coefficients at the interface of mediums 1 and 2 and mediums 2 and 3 respectively and are given by the following expressions:

$$r_{12} = \frac{n_2 \cos \theta_1 - n_1 \cos \theta_2}{n_2 \cos \theta_1 + n_1 \cos \theta_2} \text{ and } r_{23} = \frac{n_3 \cos \theta_2 - n_2 \cos \theta_3}{n_3 \cos \theta_2 + n_2 \cos \theta_3} \quad (32)$$

Thus reflectivity R of the radiation from the metallic film can be calculated from the square of $\frac{E_1^r}{E_1^i}$ and is given by the expression:

$$R = \left| \frac{E_1^r}{E_1^i} \right|^2 = \left| \frac{r_{12} + r_{23} \cdot \exp(-2kd)}{1 + r_{12} \cdot r_{23} \cdot \exp(-2kd)} \right|^2 \quad (33)$$

Using Snell's law i.e. $n_1 \sin \theta_1 = n_2 \sin \theta_2 = n_3 \sin \theta_3$ and putting the value of r_{23} defined above, the following value of r_{23} is obtained in terms of incident angle θ_1 :

$$r_{23} = \frac{n_3^2 \sqrt{n_1^2 \sin^2 \theta_1 - n_2^2} - n_2^2 \sqrt{n_1^2 \sin^2 \theta_1 - n_3^2}}{n_3^2 \sqrt{n_1^2 \sin^2 \theta_1 - n_2^2} + n_2^2 \sqrt{n_1^2 \sin^2 \theta_1 - n_3^2}} \quad (34)$$

The value of r_{23} is infinity for the denominator of the above term equaling zero. When this happens we get the following equation:

$$n_1 \sin \theta_1 = \sqrt{\frac{n_2^2 n_3^2}{n_2^2 + n_3^2}} \quad (35)$$

For this condition r_{23} tends to infinity and this implies that the value of R given above tends to its minimum value at this condition. As the propagation constant of the incident wave (k_1) equals $n_1 \sin \theta_1$, the above condition for the value of $n_1 \sin \theta_1$ is the condition for excitation of surface plasmon waves at the metal-air boundary.

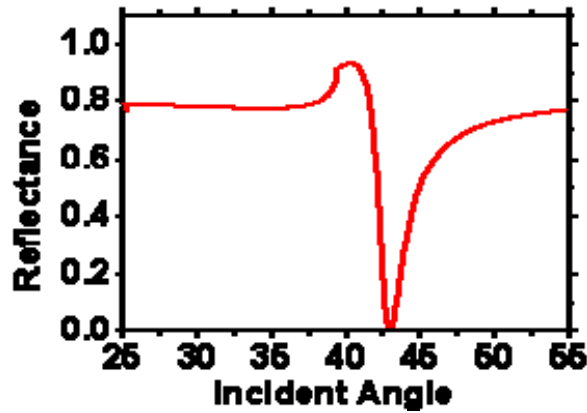


Figure 8. Surface plasmon resonance curve indicating minima in reflectance from a metallic thin film on varying the angle (for a fixed wavelength) of incident radiation

In the case of attenuated total reflection (say in the Kretschmann configuration), at an angle θ_1 above the angle for total internal reflection, a sharp minimum in reflected light (reflectivity R) is observed. This minimum in reflectivity of the radiation that is incident upon a metal film, due to excitation of surface plasmon waves, is called the surface plasmon resonance. The condition for the excitation of surface plasmons shows the relationship between angle of the incident optical fields θ_1 and refractive indices n_1 , n_2 , and n_3 (square roots of the dielectric constants ϵ_1, ϵ_2 , and ϵ_3 respectively) of the glass, metal (their dielectric constant is a function of wavelength of the input radiation), and air respectively. Any change in value of the angle of the incident light without changing any of the other quantities like wavelength of the incident light or the refractive index of the layer next to the metal layer would lead to equation 2.47 not being satisfied and thereby existence of no surface plasmon resonance. Hence, the geometric and polarization requirements on incident light, for the excitation of plasmon resonance, are more

stringent in continuous thin films than in the case of metallic nanoparticles. Moreover, surface plasmon waves have to be excited by evanescent waves and not propagating light due to a phase mismatch between the propagating light and surface plasmon waves.

Variation in any one of the two quantities - wavelength of the incident light and dielectric constant of the layer next to the metal film layer, for a given angle of incidence, can lead to a shift in the position of the plasmon resonance related dip and this could be employed for sensing refractive index of the layer next to the metal layer. The minimum in reflectivity, as shown in Figure 8, results from the absorption of resonantly enhanced plasmon mode at the metal-air boundary. The energy from the incident radiation is transferred to the surface plasmon waves propagating parallel to the metal-air boundary, thereby causing a minimum in the reflected radiation. The effect of excitation of surface plasmon waves on reflectivity of the incident radiation can be observed only for metals having an absorptive part (i.e. ϵ'') of the complex dielectric constant of the metal ($\epsilon_2' + i \epsilon_2''$). If $\epsilon_2'' = 0$, reflectivity R remains at unity for all angles of the incidence of the radiation and no effect of surface plasmon resonance on reflectivity can be observed.

Some of the metals that have a negative real part of the refractive index and exhibit surface plasmon resonance are silver, gold, copper, aluminum etc. Silver has the highest ratio of modulus of the real (ϵ_r) and imaginary parts (ϵ_i) of its dielectric constant ($|\epsilon_r/\epsilon_i| \approx 37.96$ for silver, 20.38 for copper, and 7.33 for gold) and is theoretically the best candidate for plasmon related sensors and other devices due to a higher field enhancement and a narrower resonance peak in the surface plasmon resonance (SPR) reflection spectra.

3.5.2 Interrogation of surface plasmon resonance

Different mechanisms used to interrogate surface plasmon resonance are:

- Angular Interrogation
- Wavelength Interrogation
- Intensity Measurement

The application of these mechanisms to interrogate attenuated total reflection based (Kretschmann or Otto configurations) SPR is described below. In angular interrogation, for a given thickness of a metallic film, the minimum in the reflectivity occurring at a certain angle for an incident radiation (surface plasmon resonance) can be detected by changing the angle of incident radiation keeping the wavelength fixed (see Figure 9a). In wavelength interrogation, the

minimum in the reflectivity occurring at a certain wavelength can be monitored by keeping the angle of the incident radiation fixed while varying the wavelength of the radiation (see Figure 9b).

The intensity of electric fields near the resonance points could also be monitored. If the wavelength and the angle of incidence are fixed around the values required for producing surface plasmon resonance, then monitoring change in intensity of the fields with time, for a change in the refractive index of the medium around the sensor, could help in detecting deviations from the resonance condition. If both the wavelength (λ) and the angle of incidence (θ) of an incident electromagnetic wave are kept constant and the thickness of the metal film (d) is varied, one can still observe a minimum in the reflectivity R at a given value of metal film thickness [1]. According to Abeles et al. [3], surface plasmon resonance could be observed occurring at approximately 44.6 degrees in a Kretschmann configuration for a 21.4 nm aluminum film, having a refractive index $-15 + i3.24$ at the incident radiation wavelength of 327 nm, deposited on a glass prism by varying the angle of incidence of the input radiation from 40 degrees to 50 degrees.

Wavelength interrogation, angular interrogation and intensity measurement techniques are also employed in grating and waveguide-based SPR. Angular interrogation is used in cylindrical waveguide (optical fiber) based SPR by changing the angle of a monochromatic laser or LED beam with respect to the optical fiber axis and monitoring the intensity of the transmitted light. In planar and cylindrical (optical fiber) optical waveguide based SPR systems, generally wavelength interrogation techniques are employed as they are easy to evaluate. Moreover, as the optical fiber could easily bend or deform, monitoring SPR using angular interrogation may not be a very accurate interrogation mechanism.

3.6 Plasmon resonances due to light scattering and absorption by metallic particles

The origin of plasmon resonances of metallic nanoparticles are collective oscillations of the conduction band electrons in the nanoparticles, which are called Localized Surface Plasmons (LSPs). LSPs can be excited when light is incident on metallic nanoparticles having a size much smaller than the wavelength of the incident light. At a suitable wavelength, resonant dipolar and multipolar modes can be excited in the nanoparticles, which lead to a significant enhancement in absorbed and scattered light and enhancement of electromagnetic fields inside and near the

particles. Hence, the LSPs can be detected as resonance peaks in the absorption or scattering spectra of the metallic nanoparticles.

Mie scattering [8-9] explains the resonant light scattering by metallic nanoparticles in a dielectric medium and is described in detail in this section. The mathematical explanation provided in this section is for the case of spherical metallic nano-particles only. Mie theory involves analytical solution of the Maxwell's equations for the spherical particles without any approximations. Theory based on quasi-static approximations is also described briefly in this section. It has been reported by Raether et al. [7] that the enhancement of electromagnetic field intensity inside and near metallic nanoparticles, due to excitation of localized surface plasmons in the particles, is of the order of $\sim 3-4$ and is much greater than that in the case of surface plasmon resonance in continuous thin films. Mathematical evaluations for other cases such as ellipsoidal geometry of the metallic nanoparticles or for the case of nano-particles present on a planar dielectric surface are described in literature [9-10], and will not be discussed in detail in this document.

Excitation of LSPs due to metallic nano-particles of different non-spherical geometries – ellipsoidal and triangular has been described in literature [11]. Different sizes of nanoparticles, that are associated with LSP excitation, have been described in literature [9, 12] to be lying in the range of 5-150 nm. Excitation of LSPs is highly dependent on the size and geometry of the metallic nanoparticles and refractive index of the medium or surface surrounding or in contact

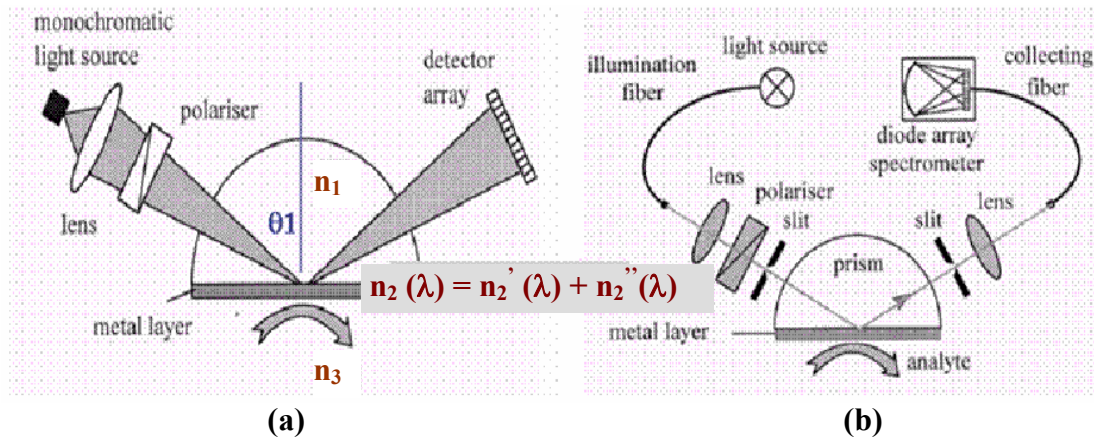


Figure 9. Methods to detect surface plasmon resonance using a Kretschmann-Raether configuration (a) by changing θ_1 (angle of incidence) for a fixed λ (wavelength) or (b) by changing λ for a fixed θ_1

with the nano-particles [9, 11-12]. The particle geometry affects the wavelength at which a peak in the absorption or scattering spectra occur and also the intensity & width of resonant absorption and scattering peaks associated with LSPs.

In the case of metallic nanoparticles, the geometric and polarization requirements on the incident light are relaxed as compared with continuous thin films used in attenuated total reflection sensors. Moreover, unlike surface modes in SPR which are not excited by propagating light due to a phase mismatch between the propagating light and surface plasmon waves, LSPs can be excited by propagating light.

Futamata et al. [13] calculated the enhancement in the electric field intensity, i.e. $|E_{loc}/E_0|^2$ to be equal to ~ 289 , for light incident on a single silver nanoparticle in air at a wavelength of 480 nm. In the above equation, E_{loc} is the localized electric field in the vicinity of the nanoparticle and E_0 is the incident electric field. This is higher in value as compared with the enhancement achieved at 480 nm wavelength of incident light in the case of surface plasmon resonance, where light is incident on a silver film from a quartz medium having a dielectric constant of 2.2, with the medium on the other side of the silver film being air.

3.6.1 Mie Resonance Theory

When a single sphere (or oblate spheroid particle), having a dielectric constant ϵ_1 is placed in a medium with dielectric constant ϵ_2 and an electromagnetic field is applied on the sphere, the electric and magnetic field spatial distributions are obtained by analytically solving Maxwell's equations. The solution for scattering electric and magnetic fields, as described by Okamoto [9], is given by the following expressions:

$$\begin{aligned} E_s &= \sum_{n=1}^{\infty} i^n \frac{2n+1}{n(n+1)} E_0 (ia_n N_{e1n} - b_n M_{o1n}) \\ H_s &= \frac{k}{\omega\mu} \sum_{n=1}^{\infty} i^n \frac{2n+1}{n(n+1)} E_0 (ib_n N_{o1n} - a_n M_{e1n}) \end{aligned} \quad (36)$$

where M and N are given by:

$$M \begin{Bmatrix} e \\ o \end{Bmatrix} = \frac{m}{\sin \theta} \begin{Bmatrix} -\sin m\phi \\ \cos m\phi \end{Bmatrix} P_n^m(\cos \theta) z_n(r) e_\theta - \begin{Bmatrix} \cos m\phi \\ \sin m\phi \end{Bmatrix} \frac{dP_n^m(\cos \theta)}{d\theta} z_n(r) e_\phi \quad (37)$$

$$N\left\{e\right\}_o = \frac{m}{\sin \theta} \left\{ \begin{matrix} -\sin m\phi \\ \cos m\phi \end{matrix} \right\} P_n^m(\cos \theta) \frac{1}{r} \frac{d}{dr} [rz_n(r)] e_\phi + \left\{ \begin{matrix} \cos m\phi \\ \sin m\phi \end{matrix} \right\} \frac{dP_n^m(\cos \theta)}{d\theta} \frac{1}{r} \frac{d}{dr} [rz_n(r)] e_\theta + \left\{ \begin{matrix} \cos m\phi \\ \sin m\phi \end{matrix} \right\} n(n+1) P_n^m(\cos \theta) \frac{z_n(r)}{r} e_r \quad (38)$$

and

$$j_n(r) = \sqrt{\frac{\pi}{2r}} J_{n+1/2}(r), y_n(r) = \sqrt{\frac{\pi}{2r}} Y_{n+1/2}(r) \quad (39)$$

where J_v and Y_v are Bessel functions of the first and second kind, respectively. The constants a_n and b_n are obtained by applying appropriate boundary conditions of continuity of the tangential components of the E and H fields and the normal components of the D and B fields at the boundary (at the surface of a sphere). The values of a_n and b_n are given by the following expressions:

$$a_n = \frac{m \psi_n(mx) \psi_n'(x) - \psi_n(x) \psi_n'(mx)}{m \psi_n(mx) \xi_n'(x) - \xi_n(x) \psi_n'(mx)} \quad (40)$$

and

$$b_n = \frac{\psi_n(mx) \psi_n'(x) - m \psi_n(x) \psi_n'(mx)}{\psi_n(mx) \xi_n'(x) - m \xi_n(x) \psi_n'(mx)} \quad (41)$$

where x is given by the product of k_0 (given by $k_0 = 2\pi/\lambda$ where λ is the wavelength of the EM wave) and r_1 i.e. the radius of the sphere. The other terms used in the above expression are given by the following relations:

$$m = \sqrt{\frac{\epsilon_1}{\epsilon_2}}, \psi_n(r) = j_n(r)r, \xi_n(r) = j_n(r)r - iy_n(r)r, \text{ and } z_n(r) = j_n(r) + iy_n(r) \quad (42)$$

The scattering cross-section (C_{sca}), which is defined as ratio of the total scattered power to the energy density of the external field, and extinction cross-section (C_{ext}) are given by the following terms:

$$C_{sca} = \pi r_1^2 Q_{sca} = \frac{2\pi}{k^2} \sum_{n=1}^{\infty} (2n+1) (|a_n|^2 + |b_n|^2) \quad (43)$$

$$C_{ext} = \pi r_1^2 Q_{ext} = \frac{2\pi}{k^2} \sum_{n=1}^{\infty} (2n+1) \text{Re}(a_n + b_n) \quad (44)$$

where Q_{sca} and Q_{ext} are the scattering efficiency and extinction efficiencies, respectively. The absorption cross-section is defined as the difference of the extinction and the scattering cross-sections i.e.

$$C_{\text{abs}} = C_{\text{ext}} - C_{\text{sca}} \quad (45)$$

When the scattering cross-section (C_{sca}) and absorption cross-section (C_{abs}) values are obtained for a metallic sphere (having a wavelength-dependent complex dielectric constant) is plotted against wavelength, a Mie resonance peak is observed at certain wavelengths. The wavelength at which the peak or dip occurs is a function of the radius of the sphere, and the dielectric constants of the sphere and the surrounding media. Hence one could detect the refractive index of the surrounding medium by observing a shift in the Mie resonance wavelength. The equations of Mie theory become more complex if the sphere lies on or above a substrate (as shown in Figure 10) or if multiple spheres are present on top of a substrate.

Approximate values of the scattering cross-section (C_{sca}) and the absorption cross-section (C_{abs}) could also be determined by using quasi-static field approximation, implying that the external electromagnetic field is static, with no retardation effects, but oscillates temporarily as $e^{-j\omega t}$. The quasi-static approximations are valid only if the diameter of the sphere is much smaller than the wavelength of the incident field.

3.6.2 Absorbance spectra of oblate spheroid particles (Quasi-static Approximation)

Meriaudeau et al. [14] have described a theoretical model to calculate the absorbance spectra of metallic (gold) oblate spheroid particles. This theoretical model makes assumptions that the individual metallic particles do not interact with neighboring particles and that dipole approximation could be applied for the calculation of the absorbance. Theoretically the value of absorbance was calculated using the formula:

$$A = \log_{10} \left(\frac{1}{1 - N\sigma} \right) \quad (46)$$

where N is the density of metal (gold) islands per unit surface area and σ is the polarizability of the metallic sphere (dipole approximation has been assumed). The relations for polarizability (σ_s for s-polarized and σ_p for p-polarized), for incident electric fields that are s-polarized or p-polarized, are given by the following relations are:

$$\sigma_s = \frac{4\pi\omega}{c} \text{Im} \left(\frac{2a^3 \sqrt{(1+\eta_0^2)} (\varepsilon(\omega) - 1)}{3Q_{1,1}(i\eta_0) (\varepsilon(\omega) - \varepsilon_{1,1}(i\eta_0))} \right)$$

$$\sigma_p = \frac{4\pi\omega}{c} \text{Im} \left(\frac{2a^3 \sqrt{(1+\eta_0^2)} (\varepsilon(\omega) - 1) \cos^2(\theta)}{3Q_{1,1}(i\eta_0) (\varepsilon(\omega) - \varepsilon_{1,1}(i\eta_0))} + \frac{-a^3 \eta_0 (\varepsilon(\omega) - 1) \sin^2(\theta)}{3Q_{1,0}(i\eta_0) (\varepsilon(\omega) - \varepsilon_{1,0}(i\eta_0))} \right) \quad (47)$$

where $\varepsilon(\omega)$ is the frequency dependent, complex dielectric constant of the oblate spheroid particle (metal), θ is the angle of incidence of the incident radiation, $Q_{1,0}$ and $Q_{1,1}$ are the Legendre polynomials $Q_{l,m}$ for $l = 1, m = 0$ and $l = 1, m = 1$ respectively, and η_0 is related to R , i.e. the ratio of the minor axis of the oblate spheroid to its major axis, by the following expression:

$$\eta_0 = \frac{R}{\sqrt{(1-R^2)}} \quad (48)$$

The terms $\varepsilon_{1,0}$ and $\varepsilon_{1,1}$ are given by the following expression:

$$\varepsilon_{1,0} = 1 + \frac{1}{(1+\eta_0^2)(\eta_0 \cot^{-1} \eta_0 - 1)}$$

$$\varepsilon_{1,1} = 1 - \frac{2}{(1+\eta_0^2)(\eta_0 \cot^{-1} \eta_0 - \eta_0^2)} \quad (49)$$

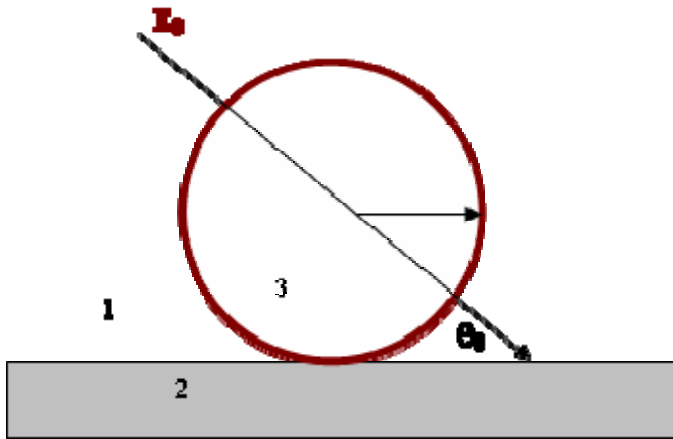


Figure 10. A sphere on a substrate, with an electric field incident at an angle to the surface of the substrate. Mediums 1, 2, and 3 are the surrounding medium, substrate, and the sphere respectively

The value of absorbance calculated by the above formula did not take into account, the presence of a substrate underlying the metallic particles. Moreover, it also did not take into account, the dielectric constant of an over layer (like the MgF_2 over layer) or the medium to be sensed. The value of $\epsilon_{1,0}$ and $\epsilon_{1,1}$ were modified to take these effects into accounts. Details of the resonance arising due to a particle (having a spherical or oblate spheroid shape) or a number of particles, with or without an underlying substrate, have been described earlier in this section. The theoretical model described above was used by Meriaudeau et al. [14] to calculate the effects of varying the refractive index of the surrounding medium and the thickness of the MgF_2 over layer, on the value of absorbance, and the results are shown in Figures 11a and 11b respectively.

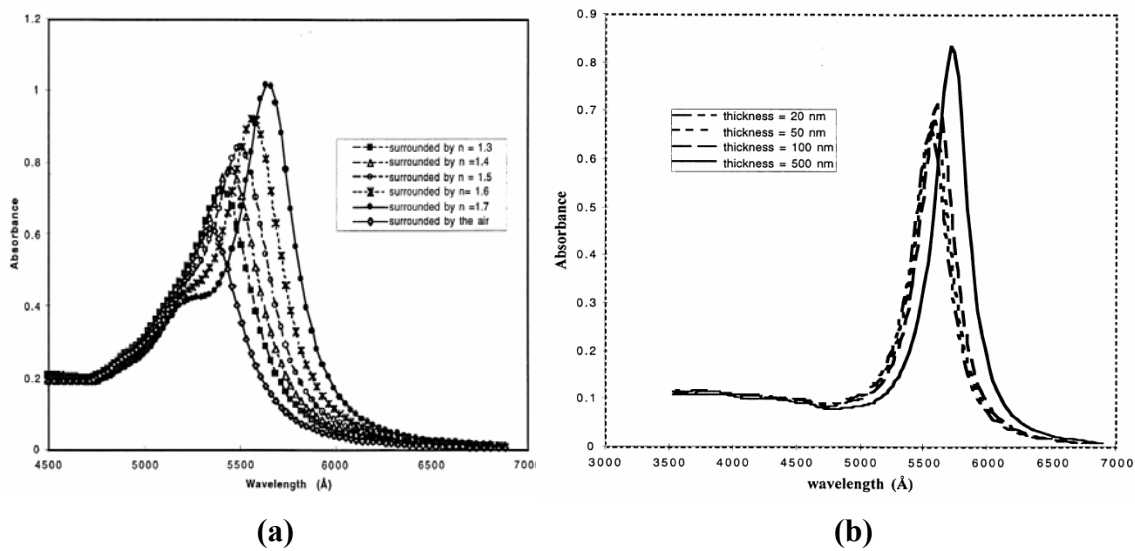


Figure 11. Theoretical model by Meriaudeau et al. was used to calculate the (a) Effect of varying the refractive index, of the medium surrounding a gold-coated fiber optic sensor, on the value of absorbance and (b) Effect of varying the thickness of the MgF_2 over layer on a gold-coated fiber optic sensor, on the value of absorbance [14]

3.7 Non fiber-based SPR Chemical and biological sensors

3.7.1 Fundamentals of chemical sensing employing SPR

Surface plasmon waves are evanescent waves that have an electric field that penetrates some distance into the lower refractive index medium. Moreover, the magnitude of the evanescent electric and magnetic fields in the case of surface plasmon waves is much higher than in the case of evanescent fields without surface plasmon waves. Hence sensors employing surface plasmon

waves are more sensitive to change in refractive index of the medium next to the metal surface as compared to sensors employing just evanescent field sensing.

As described earlier, surface plasmon resonance can be detected using several mechanisms like the detection of reflected light (reflectivity R) in the Otto and Kretschmann configurations. For a given thickness of a metallic film, surface plasmon resonance (SPR) can be detected by changing the angle of incident radiation keeping the wavelength fixed or by keeping the angle of incident radiation fixed while varying the wavelength of the radiation. As the condition for SPR given by equation 35 involves the refractive index of the medium 3, it can be visualized that the propagation constant $k_x = n_1 \sin \theta_1$ and thus the angle of the incident radiation θ_1 for surface plasmon resonance shift as the value of n_3 is changed (angular interrogation method). Hence, surface plasmon resonance can be used for detecting change in refractive index of a medium surrounding a thin metallic film deposited on the surface of a glass prism i.e. using Kretschmann configuration or on the surface of a tapered glass optical fiber (both glass prism and tapered optical fiber have an evanescent field generated and that is used to excite surface plasmon waves). Similarly, if one varies the wavelength of the input radiation, the dielectric constant n_2 is varied and the point where the value of the right hand side of equation 35 is equal to the fixed value, $n_1 \sin \theta_1$, surface plasmon resonance is excited (wavelength interrogation process). One could also monitor the intensity of electric fields near the resonance points (This is called the intensity measurement).

Surface plasmon resonance based optical sensors primarily consist of an optical system, a transduction medium, and electronics for data processing and for signal detection using optoelectronics (like photodiodes, photodetectors etc.) [15]. The transduction medium transforms changes in quantities of chemical or biological molecules into changes in the refractive index which may be determined by optical interrogation of surface plasmon resonance using ATR, diffraction, or waveguide processes. The optical system in a surface plasmon resonance sensor contains a source of optical radiation (diode laser, LED, or a white light lamp) and an optical structure (prism, grating, waveguide, or optical fiber) in which surface plasmon waves are excited and interrogated.

Homola et al. [15] have defined the sensitivity of SPR sensors as a derivative of the monitored SPR parameter with respect to the parameter being determined i.e. the refractive index, concentration etc. of the medium next to the metal layer. Sensors using ATR prism

coupling have higher sensitivity as compared to ones using grating couplers as shown in Table 1. Moreover wavelength interrogation SPR sensors have higher sensitivity at higher wavelengths. Other parameters of an SPR sensor that are important are its resolution, i.e. the minimum change in a parameter to be determined which can be resolved by a device, and the operating range, i.e. range of values of the parameter to be determined which can be measured by the sensor.

Most commonly used surface plasmon active metals are gold and silver. Silver leads to the formation of more sensitive surface plasmon sensing devices as compared to gold due to a large ratio of modulus of the real and imaginary parts of its refractive index. The electromagnetic field of a surface plasmon wave is less attenuated in the case of silver (due to lower value of loss term in its dielectric constant) and is distributed in an asymmetric manner such that majority of the field is concentrated in the dielectric next to the metal layer, thereby helping in detection of chemicals. As the stability of silver to oxidation is poor, methods for protecting thin silver films against oxidation have been developed like coating the metal layers with protective over layers of materials like Ta_2O_5 [15]. Besides the penetration depth of the evanescent fields, another important parameter for surface plasmon sensors is the propagation length. For an incident optical radiation having a wavelength of 630 nm, the propagation length of the surface plasma waves at the metal-water interface (water being the medium around the metal layer) for silver as the metal layer is 19 microns and for gold is 3 microns and the 90 % of the fields are concentrated in the dielectric in the case of silver as compared to 85% in the case of gold.

3.7.2 Chemical and biological sensors based on Attenuated total reflection (Kretschmann or Otto configurations)

Kano et al. [16] employed Kretschmann configuration to detect the change in refractive index in the medium surrounding the metal film deposited on the hypotenuse of a glass prism. They have reported use of surface plasmon resonance occurring at around 68 degrees (refractive index of a 44 nm silver film being $0.0666 + i4.045$ at a wavelength of 632.8 nm) to differentiate between two samples of water - one being pure (non absorbing) and the other contaminated (absorbing). They observed that when the medium surrounding the metal film was changed from pure water, with a refractive index = 1.33, to contaminated water, with a refractive index = $1.33 + i0.002$, a change in the surface plasmon resonance angle was observed. They also changed the thickness of the silver film deposited on the glass prism in order to obtain the value of thickness

of the films required for maximum enhancement of sensitivity for the absorbance measurement. They reported that when SPR was used to detect absorbance by changing the value angle of the of incident radiation, peak absorbance of 2.30 was observed at an angle of 68.3 degrees. The value of absorbance was many times higher (by a factor of ~ 30) than the value of absorbance obtained (0.00795) when only attenuated total internal reflection was employed to sense absorbance with the same refractive index of the medium surrounding the glass prism.

Prism-based SPR sensors using angular interrogation have been used extensively by BIAcore [17] and Karlsson et al. [18] have reported a refractive index resolution better than 3×10^{-7} RIU (Refractive Index Unit). A wavelength interrogation based planar surface plasmon sensor (employing the prism ATR principle) has been reported by Pfeifer et al. [19] that has a sensitivity of about 6400 nm RIU^{-1} . This device called Jena SPR relies on sensing change in resonance wavelength when bio-molecular interactions occur at the sensing layer above a metal film deposited on the hypotenuse of a glass prism. It was seen that there was a change in response (shift of wavelength being 0.178 nm for one pixel shift shown in the graph) when sucrose solution with 15% concentration in HEPES (N-2-hydroxyethylpiperazine-N'-2-ethanesulphonic acid) is injected into a flow cell having only HEPES after around 10 seconds and when it is flushed out after around 70 seconds. The experimental measurements made on this sensor for detecting the presence of 15% sucrose solution (in HEPES) showed that on injection of the sugar solution to the flow cell, there was a shift in wavelength of 141 nm. As there is a difference of refractive index of 0.022 between the HEPES and the sucrose solution in HEPES, the sensitivity of the sensor was calculated to be 6400 RIU^{-1} . This device was used to detect

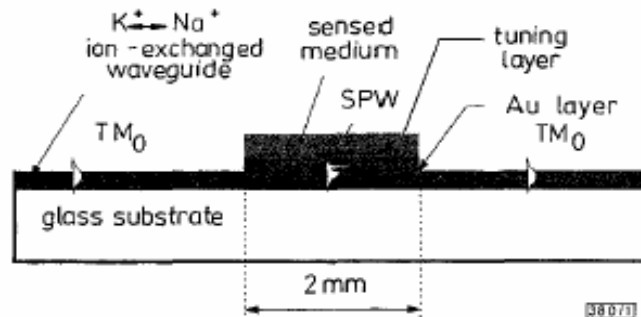


Figure 12. Schematic of a planar waveguide used for SPR sensing [2]

Table 1. Sensitivities and resolutions of different interrogation procedures and different kinds of coupling systems [2]

Detection approach	Angular interrogation		Wavelength interrogation		Intensity measurement	
	Sensitivity (deg RIU ⁻¹)/ Resolution (RIU) ^b		Sensitivity (nm RIU ⁻¹)/ Resolution (RIU) ^c		Sensitivity (% RIU ⁻¹)/ Resolution (RIU) ^d	
	$\lambda = 630$ nm	$\lambda = 850$ nm	$\lambda = 630$ nm	$\lambda = 850$ nm	$\lambda = 630$ nm	$\lambda = 850$ nm
Prism coupler-based SPR sensor	191 5×10^{-7}	97 1×10^{-6}	970 2×10^{-5}	13 800 1×10^{-6}	3900 5×10^{-5}	15 000 1×10^{-5}
Grating coupler-based SPR sensor	43 2×10^{-6}	39 2×10^{-6}	309 6×10^{-5}	630 3×10^{-5}	1100 2×10^{-4}	4400 5×10^{-5}

binding of Ni₂₊ ions to a matrix of Nitrilotriacetic acid. Pfeifer et al. [19] also describe the functioning of a BIAcore 2000 equipment which can detect myoglobin using a CM-5 chip. The chip carries a hydrogel of carboxymethylated dextran activated with EDC and NHS and monoclonal antibodies were aminocoupled to the chip surface. Mu et al. [20] have reported the development of an optical biosensor for monitoring antigen recognition based on surface plasmon resonance. This sensor uses fixed angle of incidence for interrogation while the wavelength of the incident light is in the range of 400 to 800 nm (wavelength interrogation procedure). This sensor employs the attenuated total reflection of radiation from a bio recognition surface which consists of thin gold layer deposited on glass on which sensing membranes of avidin specifically bound to biotin are self assembled on the gold layer.

3.7.3 Chemical and biological sensors based on planar optical waveguides

Surface plasmon resonance sensors using planar optical waveguides have been described by Ctyroky et al. [2, 21] and Homola et al. [15]. In optical waveguides, light is guided till it enters a region which has a thin metal over layer. The evanescent electromagnetic field penetrates the metal layer and interacts with the analyte on top of the metal layer. Surface plasmon waves are excited in optical waveguides by if the surface plasmon wave and the guided mode in the planar waveguide are phase matched (See Figures 5 and 12).

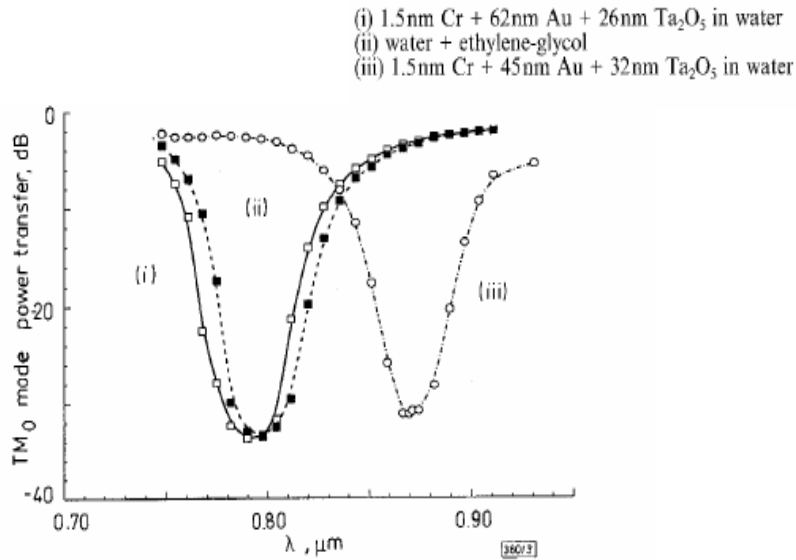


Figure 13. Shift in the SPR resonance wavelength on changing the thickness of the gold layer and the Ta₂O₅ over layer [2]

Homola et al. [2] have described a planar waveguide based SPR sensor used to sense the refractive index of the medium around the sensor as shown in Figure 12. This sensor consists of a K⁺-Na⁺ ion-exchanged BK-7 glass waveguide with a thin gold layer (40-60 nm thick) deposited in the middle of the waveguide. This sensor works on the principle of resonant coupling between the TM modes of the ion exchanged waveguide (TM₀, TM₁, and TM₂ modes) and the surface plasmon wave of the gold layer. The effect of thickness of a Ta₂O₅ over layer (on top of the gold layer) on the wavelength of surface plasmon resonance is studied. This over layer acts as a protective layer for the gold layer and also can be used as a tuning layer by changing its thickness to change the resonant wavelength of the SPR sensor. One can also see the effect of gold layer and the medium, on the resonant wavelength, in Figure 13.

3.7.4 Chemical and biological sensors based on gratings

The development of a surface plasmon resonance immunosensor based on a diffraction grating was described by Cullen et al. [22-23]. The diffraction gratings were developed by first spin-coating a photoresist on an optical glass flat and then exposing the glass to an interference pattern produced by an argon ion laser. The photoresist was developed to form a diffraction grating of a photo-resist, which was then ion-milled into the surface of the glass. The gratings had a sinusoidal profile with a grating constant of 556 nm and amplitudes of 40 nm for a subsequent coating of gold evaporated onto the surface of the grating. Chromium and gold were

thermally evaporated onto the glass gratings. Various immunological molecules were immobilized onto the surface of the gold-coated grating and binding of analytes to these immobilized molecules was monitored by using the angular SPR interrogation method. A shift in the surface plasmon polariton-related resonance (in the reflectivity-incident beam angle curve) curve, with the binding of the analyte to the immobilized molecule, was used to monitor the reaction of the analyte with the immobilized molecules. Grating based SPR sensors are also described in a paper by Homola et al. [15].

3.8 Surface plasmon resonance-based optical fiber sensors

Most of the currently available surface plasmon sensors (like the BIAcore 1000/ BIAcore 2000 or the Jena SPR-device) depend on bulk-optic implementation of the ATR (attenuated total reflection) method. This requires the use of relatively large prisms and lenses and this does not allow surface plasmon sensing elements to be miniaturized [24]. Developing surface plasmon sensors on optical fibers allows development of small sized, portable SPR sensors that could be easily employed for large area distributed sensing or remote sensing applications. In this section we will be discussing four types of fiber-based SPR sensors:

- Side Polished SPR sensors, based on side-polished single-mode optical fiber
- Etched optical fiber sensors where the etched section has an SPR layer
- Tapered Optical Fiber SPR sensors with metal-coated tapered optical fibers
- Fiber tip sensors where the geometry of the fiber tip is modified

This subsection reviews the developments of these technologies and describes the important features of the different kinds of sensors developed.

3.8.1 SPR sensors based on side-polished single-mode optical fiber

One method of preparing an optical fiber for SPR sensing is to mount the fiber in a block such that a portion of the fiber can be polished to remove enough of the cladding such that the evanescent wave will be able interact with the plasmon sensing layer. In this subsection, we describe the review the work done in previous literature on side-polished SPR fiber-optic SPR sensors.

A fiber optic surface plasmon resonance sensing device based on spectral interrogation of the device has been described by Slavik et al. [25]. In this device, surface plasmon waves

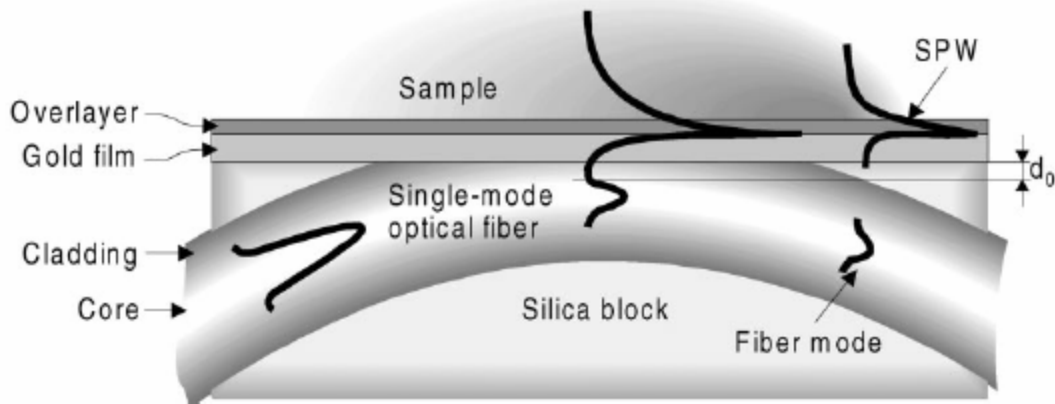


Figure 14. Surface plasmon resonance sensing structure based on a side-polished single-mode fiber [25]

are excited by a guided mode propagating in the fiber if phase matching of the two waves takes place. As the propagation constant of the surface plasmons waves depends on the refractive index of the analyte (called sample in Figure 14) in contact with the metal layer, the wavelength at which the resonant attenuation of the fiber mode occurs depends on the refractive index of the analyte. Slavik et al. [25] reported that variations in the refractive index of the analyte can be determined either by measuring changes in the transmitted optical power at a fixed wavelength or by measuring shifts in the resonant wavelength i.e. wavelength at which resonant attenuation of the fiber mode occur (the spectral mode). The Fiber optic SPR sensing element was fabricated using a single-mode optical fiber and the fiber was side polished close to the fiber core in order to attain $d_0 = 500$ nm. d_0 is the distance between the core-cladding boundary and the thin tantalum pentoxide over layer of thickness of 19 nm, by vacuum evaporation (see Figure 14). As only TM-polarized radiation in a fiber can excite surface plasmon waves, change in polarization of the radiation occurring due to fiber bending and twisting can adversely affect coupling of the fiber guided mode to the surface plasmon waves.

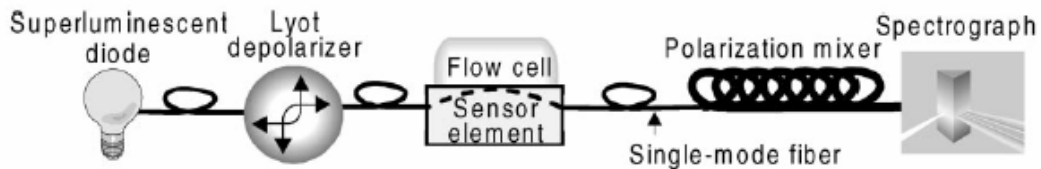


Figure 15. Surface plasmon resonance sensing system consisting of the light source, the depolarized, the flow cell, polarization mixer, and the spectrograph [25]

In order to solve this problem of change of states of polarization of the fiber modes, the fiber sensing device described by Slavik et al. [25] uses depolarized radiation for sensing. The configuration of the developed SPR Fiber optic sensor system developed by Slavik et al. [25] is shown in Figure 15 where light from a superluminescent diode coupled into the SPR sensing element through a Lyot depolarizer (made up of two pieces of bow-tie highly birefringent fiber) was input into a spectrograph through a polarization mixer. In order to study the characteristics of the fiber optic sensor developed by Slavik et al. [25], mixtures of diethyleneglycol and water of known refractive indices were made to flow across the sensor element surface and the temporal response of the resonant wavelength was recorded. In this sensor, a sensor sensitivity of 3100 nm/RIU was recorded and a resolution of 5×10^{-7} RIU for the static mode (sensor being held in place without movement) and 5×10^{-5} RIU for the dynamic mode (sensor movement allowed) was reported.

Homola et al. [26] have proposed the development of a humidity based on a surface plasmon resonance. The proposed sensor is based on a bent side-polished single-mode optical fiber embedded in a substrate. Part of cladding of the optical fiber is removed by mechanical polishing and an intermediate dielectric layer (Al_2O_3), a metal (silver) layer, and a transducing medium magnesium fluoride layer are deposited in this region. The evaporated magnesium fluoride films are porous in nature and adsorb water vapor when exposed to air. This results in a change in refractive index of the transducing layer which lies next to the metal layer.

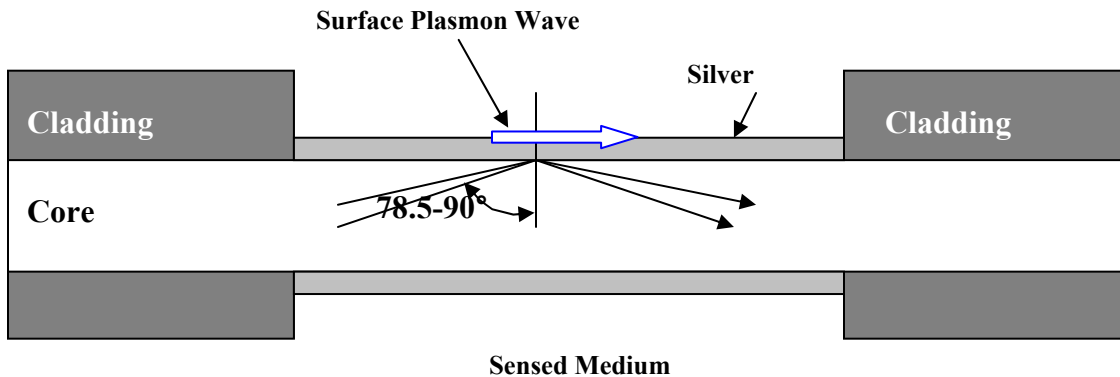


Figure 16. Sensing element, based on Surface Plasmon Resonance, consisting of a silver film deposited on the core of an optical fiber in a region where cladding has been removed [27]

3.8.2 SPR Sensors based on metal-coated unclad fibers

In these SPR sensors, the sensing element consists of a multimode optical fiber with an exposed core coated with a thin metal layer supporting surface plasma waves (SPW). Jorgenson et al. [27] developed the first surface plasmon resonance based fiber-optic chemical sensor by depositing a thin metal layer onto the exposed core of an optical fiber as shown in Figure 16. The SPR sensing surface was formed by etching cladding and the jacket from a certain length of the optical fiber and depositing a silver film onto a 400 μm core of the fiber, outer diameters of the cladding and the jacket being 600 μm and 760 μm respectively. Three sensors were developed by removing 6 mm, 10 mm, and 18 mm respectively, of the cladding and the jacket layers, from the middle section of three optical fibers. An electron beam evaporator was used to deposit a 55nm thick silver film onto core of the fiber, which was rotated during the deposition. This multimode fiber, with a numerical aperture of 0.36, allowed several internal angles of incidence of the radiation to be propagated through it, the different incident angles corresponding to modes of the electromagnetic radiation propagating through the fiber. The fiber supported internal propagating angles of the radiation within a range of 78.5° to 90° , the angles being measured with respect to the normal at the interface of the core and the silver film. Wavelength interrogation was employed to evaluate this sensor i.e. a change in refractive index of the medium surrounding the sensing surface was detected by observing a shift in the resonance wavelength of the light transmitted through the optical fiber sensor. A tungsten-halogen lamp acted as a source of radiation which was focused onto an optical fiber tip by a lens.

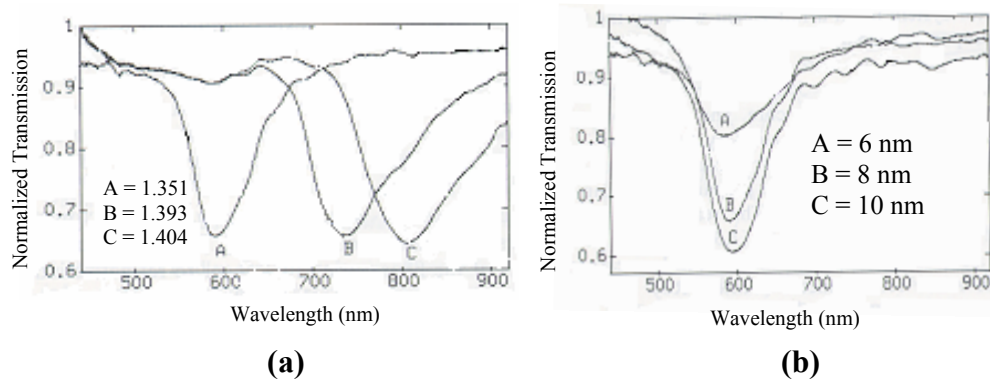


Figure 17. Spectra of a fiber optic surface plasmon resonance based sensor indicating (a) Shift in resonance point of the normalized intensity curves to higher wavelengths on increasing the refractive index of the surrounding medium and (b) Increase in depth of the surface plasmon resonance spectra on increasing length of the SPR sensing area [27]

The metal-coated sensing region of the optical fiber was enclosed in a 3 ml flow cell having an inlet and an outlet port. Six samples of high-fructose corn syrup diluted with ionized water were prepared, with each sample having a different concentration of the high-fructose corn syrup and thereby a different refractive index. The real part of the refractive index for the six samples was 1.333, 1.351, 1.364, 1.381, 1.393, and 1.404 respectively. The transmitted spectral intensity distribution was measured for each of these six solutions surrounding the fiber optic sensor in the

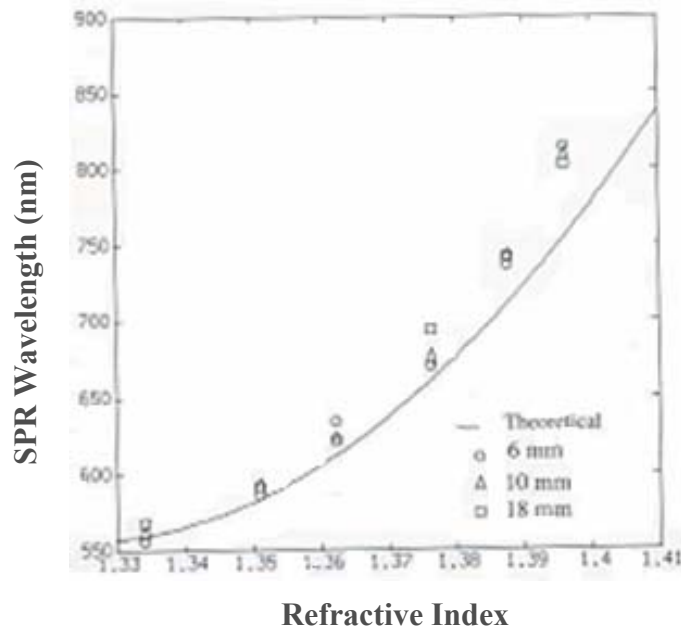


Figure 18. Theoretical and experimental values of the surface plasmon resonance coupling wavelength as a function of the refractive index of the fructose sample solutions surrounding the exposed core SPR-based fiber optic sensor [27]

flow cell and the values of transmitted intensity obtained were normalized with the values when the flow cell contained only air. It was observed that the resonance dip in the normalized transmitted intensity vs. wavelength curve shifted towards higher wavelength values for higher values of the refractive index of the solution surrounding the fiber optic sensor in the flow cell, see Figure 17a. It was also observed that a sensor with a longer length of the sensing area i.e. the region where the core is exposed and coated with metal exhibits a deeper resonance in the normalized transmitted intensity vs. wavelength curve, as shown in Figure 17b. In order to calculate the sensitivity and the resolution of the fiber optic sensors, Jorgenson et al. [27] calculated the SPR coupling wavelengths, i.e. the wavelengths at which the surface plasmon resonance related dip occurs in the normalized transmitted intensity vs. wavelength curve, for the

6 mm, 10mm, and 18 mm exposed core sensors, and plotted the SPR coupling wavelengths against the refractive indices of the chemicals surrounding the sensor element in the flow cell, as shown in Figure 18. The sensitivity of the sensors, in nm/RIU was calculated by calculating the slope of the non-linear SPR wavelength response curve shown in Figure 18. The optical resolution of the spectrograph was assumed to be 0.5 nm and the resolution of the sensor was calculated to be 2.5×10^{-4} at a wavelength of 500 nm and 7.5×10^{-5} at a wavelength of 900 nm.

Lin et al. [28] have described the development of SPR-based fiber optic chemical and biological sensors which have thin layers of gold [28] or silver [28] deposited directly on the core of optical fibers in regions where fiber cladding was selectively removed. A 21 cm multimode step-index silica/silicone optical fiber was taken and a section of cladding 15mm in length was removed at the middle of the optical fiber. A gold film of 40-70 nm thickness was deposited on the exposed core of the optical fiber via thermal evaporation to obtain a sensing segment as shown in Figure 19a. In this sensor, main principle of sensing involves excitation of surface plasmon waves at the interface of the gold film and the layer surrounding it for a certain internal incident angle. A new method proposed to interrogate this SPR sensor involved illuminating the input end of the optical fiber, with a monochromatic light beam of 658 nm from a laser diode, at an external incident angle α as shown in Figure 19b.

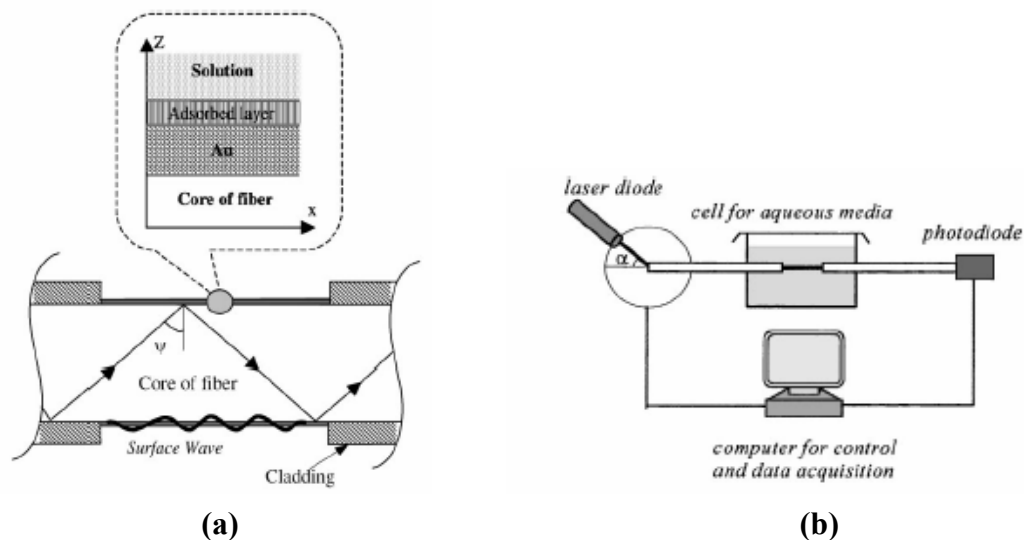


Figure 19. (a) Sensing segment of an SPR-based optical fiber sensor having a gold layer deposited on the exposed core and (b) Experimental setup to interrogate the SPR-based fiber optic chemical sensor [28]

3.8.3 SPR sensors based on tapered optical fibers

As it has been described earlier, tapering of optical fibers leads to the creation of an evanescent field with light escaping the core of the optical fiber as the electromagnetic radiation proceeds from the untapered section to the tapered section. As it has been described earlier in this section, an evanescent field is required to generate surface plasmon waves at the interface of a thin metal layer and the surrounding medium. The evanescent field generated due to creation of taper in the optical fiber could be used to excite surface plasmon waves in continuous and discontinuous metallic films deposited on the surface of the tapered optical fibers.

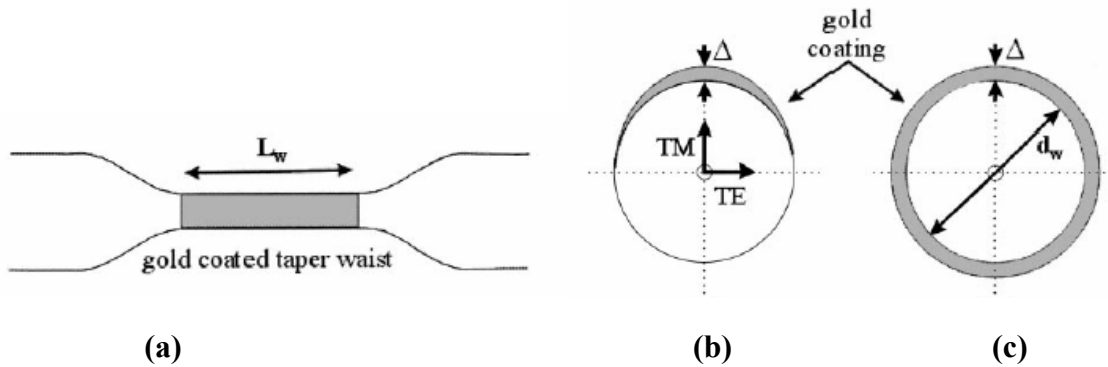


Figure 20. (a) Gold coated tapered optical fiber with length of the taper waist being L_w and the diameter of the waist being d_w ; (b) Asymmetric sensor device; (c) Quasi-circular sensor device with a uniform coating of gold on the waist of the optical fiber taper [29]

Diez et al. [29] and Tubb et al. [30] have described the development of refractive index sensors based on excitation of surface plasmon resonance in metal coated tapered optical fibers. Tapered optical fibers were developed by stretching single mode optical fibers while applying heat to them via a traveling flame oxybutane gas burner, a procedure described by Kenny et al. [31]. Adiabatic tapers, having a loss less than 0.1 dB, were developed such that waist of the taper had a diameter (d_w) of about 30 μm and a length (L_w) between 4 and 20 mm, as shown in Figure 20a. A layer of gold, 23nm to 32 nm thick was thermally deposited onto the waist of the tapered optical fiber by using thermal deposition. Quasi-circular sensors, i.e. ones having a uniform gold coating on the taper waist, were fabricated by depositing gold onto the waist of the tapered fiber three times and rotating the optical fiber by 120 degrees after the first and the second deposition (see Figure 20 c). Asymmetric sensors were developed by carrying out one deposition of gold, without rotating the fiber, to get coating on only one side of the taper waist (see Figure 20 b). In order to interrogate the devices, white light from a halogen lamp was used as the source and the

output of the optical fiber sensor was incident on an optical spectrum analyzer. The transmission spectra were recorded for different refractive indices of the medium surrounding the optical fiber. Commercially available Cargille liquids, of different refractive indices, were used to provide media with different refractive indices.

It was observed by Diez et al [29] that there was a single dip in the transmission spectra of a quasi-circular sensor. This dip could be attributed to coupling of the fundamental guided mode of the tapered fiber waist and a hybrid surface plasmon mode (with azimuthal order, $m=1$) bound to the thin metallic layer, thereby lowering the intensity of the transmitted light. It was also observed that there was a shift in the wavelength at which the dip occurs when the refractive index of the medium surrounding the fiber sensor was changed. When the center wavelength of the resonance dip was plotted against the refractive index of the surrounding medium, it was seen that there was an almost linear relation between dip wavelength and the refractive index.

Villatoro et al. [32] have described the development of a palladium-coated tapered optical fiber sensor for sensing gaseous hydrogen. The procedure used to develop the sensor is the same as that described by Diez et al. [28] with palladium replacing gold in the hydrogen sensor. A palladium coated sensor was developed having a taper diameter of 20 microns, taper length of 15 mm, and a palladium coating thickness of 12nm. Both symmetric and asymmetric sensors were developed. The mechanism of sensing in this sensor depends upon change of dielectric constant of the metal on adsorption of hydrogen onto palladium to form a hydride, thereby causing a shift in the surface plasmon resonance excited at the boundary of the palladium metal and the surrounding medium. In order to interrogate this sensor, a gaseous mixture of hydrogen and nitrogen is input into a flow cell containing this palladium-coated tapered section of the optical fiber and the change in normalized power transmitted (T) through the fiber was recorded as a function of time as the concentration of hydrogen in the gaseous mixture was increased. The normalized power (T) transmitted through the tapered fiber optic sensor is the ratio of the power transmitted when hydrogen is present in the mixture of gases injected into the flow cell (I), and the power transmitted when 0% hydrogen was present in the gaseous mixture injected into the flow cell (I_0). An LED having a 3 μ W power and a 1.6 μ m wavelength was used as a light source and the output light was input into a photo detector. The normalized transmitted power, i.e. $T = I/I_0$ It was observed that when the taper waist diameter is decreased from 30 microns to 20 microns, there is an increase in the relative power transmitted through the

hydrogen sensor for concentrations of hydrogen in the gas surrounding the sensor less than 4%. It was observed that this sensor was highly sensitive and also highly specific to hydrogen. The sensor described by Villatoro et al. [32] was reversible and had very fast response and recovery times. The fast response times of the sensor are associated with the rapid adsorption of hydrogen by the sensor and the fast recovery times are associated with the rapid desorption of hydrogen from the sensor. It was seen that when the concentration of hydrogen in the medium surrounding the sensor was reduced from 10.5 % to 0%, there was a fast drop in the value of the transmitted intensity from around 1.6 to 1, the recovery time being approximately 75 seconds.

Villatoro et al. [32] also described a theoretical relationship between I and I_0 :

$$I = I_0 \exp (2\Delta\gamma L_{in}) \quad (50)$$

where L_{in} is the interaction length given by the length of the waist of the taper L_w defined by Diez et al. [29], $\Delta\gamma = \gamma_{Pd} - \gamma_{PdH}$ where γ_{Pd} is the attenuation constant associated with the metal-coated tapered optical fiber when there was no hydrogen is present and γ_{PdH} is the attenuation constant associated with the metal-coated tapered optical fiber in the presence of hydrogen. The value of γ_{PdH} and therefore the value of $\Delta\gamma$ depends on the concentration of hydrogen present in the mixture of gases surrounding the fiber optic sensor.

One of the problems associated with the tapered optical fiber sensors based on surface plasmon resonance is that they are very fragile and are thereby difficult to employ for chemical sensing in environments that are subjected to strains or bending. One has to make a compromise between the sensitivity of the sensor and the robustness if one increases the diameter of the tapered fiber region in order to make the sensor more robust. This is because the sensors that have a thicker tapered region will have a lower magnitude of evanescent field emanating from the fiber thereby decreasing the sensitivity of the sensor to changes in refractive index of the medium surrounding the sensor.

3.8.4 Surface plasmon resonance sensors having a sensing section at the tip of the optical fiber

Surface plasmon resonance-based chemical and optical sensors could be developed by depositing continuous or discontinuous metallic layers at the tip of an optical fiber and using the metal-coated probes for sensing changes in refractive index around the tip. Having a tapered region on the fiber tip enables sensing in remote areas and also allows the possibility of

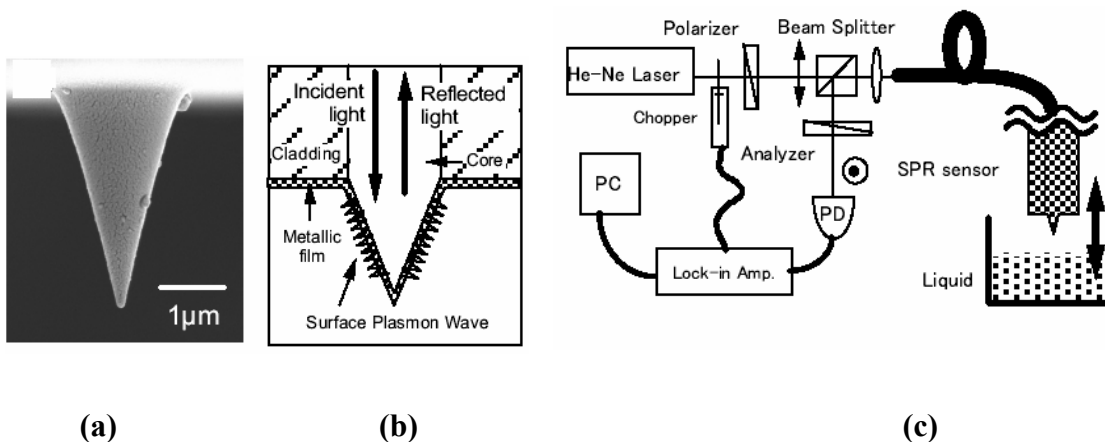


Figure 21. (a) Micrograph of a metal-coated tapered optical fiber probe developed by chemical etching of the fiber tip; (b) Schematic of a metal-coated tapered optical fiber probe used for SPR sensing; (c) Experimental setup employing polarization spectroscopy to interrogate the surface plasmon resonance based sensor [33]

developing disposable sensors at the fiber tip. Some of the sensors developed for chemical and biological sensing are described below.

The technique used for near-field scanning electron microscopy has been applied by Kurihara et al. [33] for developing an SPR-based chemical and biochemical fiber-optic sensor. A near-field scanning electron microscopy probe used for making this sensor was fabricated by tapering the tip of an optical fiber using chemical etching and then coating the tapered tip with a

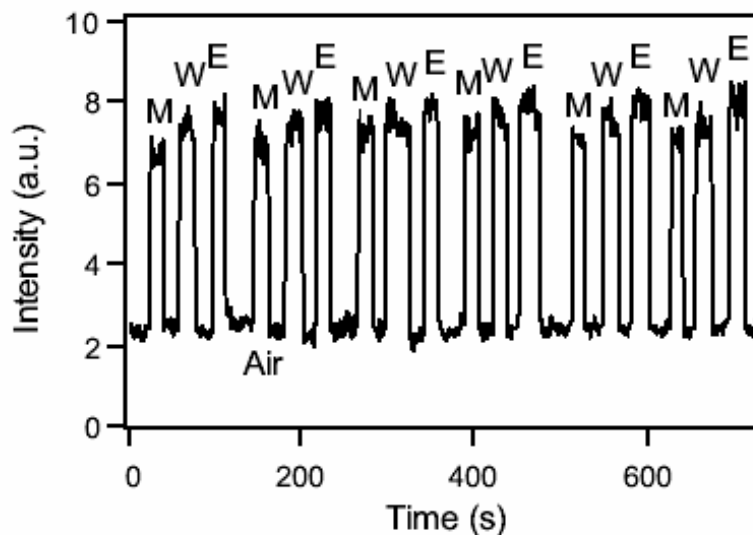


Figure 22. Temporal response of the SPR-based fiber optic sensor showing change in intensity of light detected by the photodiode when the medium surrounding the fiber tip was changed from air (A) to Methanol (M), Water (W), and Ethanol (E) repetitively [33]

thin gold layer (~ 40 nm thickness). The process of taper formation involved immersing flattened tip of a silica-based single mode optical fiber into a buffered hydrogen fluoride solution so that the end of the fiber is etched into a tapered core and a flattened cladding configuration (as shown in Figures 21a and b) based on the differential in the etching rates between the core and the cladding. Size of the optical fiber tapered tip was ~ 3 μm . Gold film was deposited on the tapered fiber tip by using sputtering equipment (Hitachi E-1030). Interrogation of this fiber optic sensor was based on the principle of polarization spectroscopy as shown in Figure 21c. Light beam from a singlemode He-Ne laser (operation at 632.8 nm) was linearly polarized by a polarizer and coupled into an optical fiber after it passed through a beam splitter. It was observed that this beam excited surface plasmon resonance at the surface of the metal layer and the medium surrounding the tapered fiber tip as shown in Figure 21 b. Excitation of SPR resulted in polarization rotation such that the beam reflected back from the tip was elliptically, and not linearly, polarized. This reflected beam traveled in the direction opposite to the incident beam through the optical fiber, changed its direction at the beam splitter, passed through an analyzer, and was incident upon a photo detector connected to a lock-in-amplifier. Working principle of this fiber optic sensor probe involved measuring intensity of the radiation detected by the photodiode with time and noting a change in intensity when the refractive index of the medium, into which the probe was inserted, was changed. Figure 22 shows change in

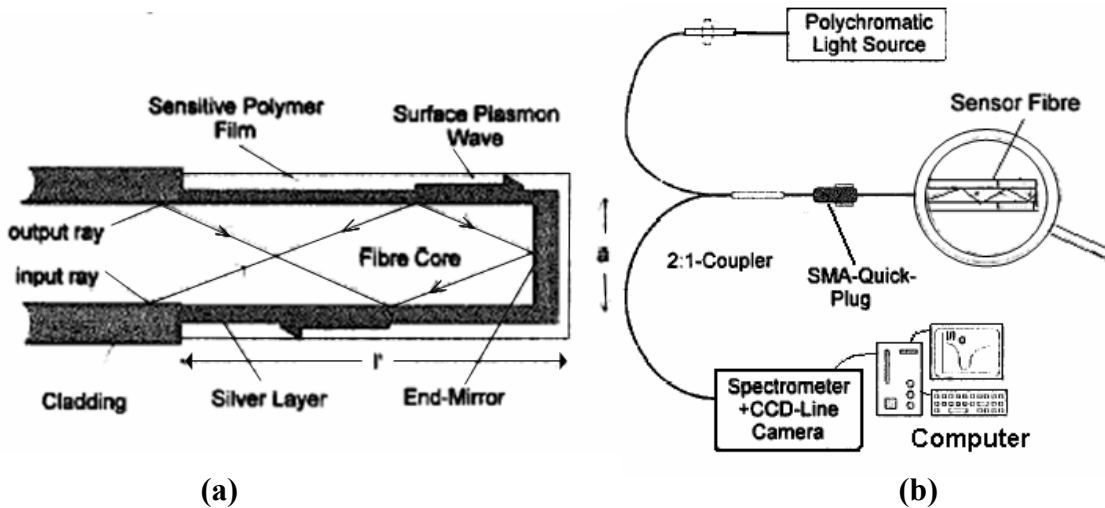


Figure 23. (a) An SPR based optical fiber sensor with a silver film deposited on the unclad core of the fiber, (b) Interrogation mechanism of the sensor employing a 2 by 1 coupler to input light into the sensor from a polychromatic light source and carry the output radiation, reflected from the chromium mirror at the end of the fiber tip, to the spectrometer [34]

intensity of radiation detected by the photodiode, as a function of time, when the medium around the fiber optic sensor tip was changed repetitively from air (refractive index = 1.000) to methanol (refractive index = 1.329), water (refractive index = 1.333), and ethanol (refractive index = 1.362). The minimum detection limit of this optical fiber sensor was calculated to be 4×10^{-3} .

Niggemann et al. [34], Jorgenson et al. [27], and Kunz et al. [35] have developed surface plasmon resonance-based optical fiber sensors that have a sensing section consisting of an unclad core of an optical fiber at the end of the fiber. A thin layer of silver is deposited on the unclad section at the end of the fiber by thermal vacuum deposition. A chromium mirror was deposited at the tip of the fiber in these sensors. In the sensor described by Niggemann et al. [34], a thin layer of a gas sensitive polymer layer is deposited, as shown in Figure 23a, so that the presence of organic solvent vapors like tetrachloroethene could be detected. Surface plasmon waves are excited at the end section of the silver coated multimode fiber by radiation from a polychromatic source. A 2 by 1 coupler is used to couple light into the fiber and also to collect radiation reflected back from the chromium mirror. This reflected radiation is input into a spectrometer as shown in Figure 23b. It was described by Niggemann et al. [34] that adsorption of tetrachloroethene vapors on a thin gas-sensitive polydimethylsiloxane film (The polymer film had an optimal refractive index range of 1.4 -1.45 and an optimal thickness range of 100-250 nm) deposited on the silver-coated fiber tip, changes the refractive index of the polymer film. The spectrum of the reflected light collected by the spectrometer shows a dip in the received intensity at a certain wavelength, the dip occurring due to surface plasmon resonance. Change in refractive index of the polydimethylsiloxane film, occurring due to adsorption of the tetrachloroethene vapors, causes a shift in the wavelength at which the SPR related dip occurs. This shift in the minima of the intensity vs. wavelength curves was a function of the concentration of tetrachloroethene present in an air- tetrachloroethene gaseous mixture surrounding the fiber sensor. The response time of this sensor was determined by plotting the wavelength at which the minimum of the Intensity vs. wavelength curve occurs against time, when the medium surrounding the sensor is changed from pure air to 1300 ppm tetrachloroethane. The sensor response time was found to be only 2.5 seconds. It was also observed that when the sensor was exposed to tetrachloroethane vapors, sensitivity of the sensor

increased from 0.004 nm/ppm to 0.011 nm/ppm on increasing the thickness of the polydimethylsiloxane film from 60 nm to 225 nm.

3.9 Optical fiber sensors based on plasmon resonances of metallic particles

Meriaudeau et al. [14] have reported the development of a fiber optic chemical sensor based on surface plasmon excitation on a discontinuous metallic (gold) film deposited on the core of an optical fiber. In this sensor, cladding is removed from a section of the optical fiber and a very thin layer (4 nm) of gold is evaporated onto the unclad portion of the fiber, as shown in Figure 24. This leads to the formation of a discontinuous metal-island film, consisting of irregularly shaped particles, on the core of the fiber. This sensor is different from the sensors described earlier in section 3.7.2 as in those sensors a continuous film was deposited on the core of the optical fiber. Hence, in this sensor, localized surface plasmon waves are excited on the metal islands in the discontinuous film instead of exciting these waves at the interface of a continuous metallic film and the surrounding medium. In order to develop this sensor, a 10 cm optical fiber with a silica core (1000 μm diameter), a doped silica cladding (1250 μm outer diameter), and a plastic coating (1850 μm outer diameter) was taken and the plastic coating was removed using a razor blade. This fiber was then placed in a 48 % hydrofluoric acid solution for 2 hours, such that only an inch length of the cladding was removed by chemical etching. A 4nm gold layer was deposited symmetrically on the unclad section of the fiber by placing the fiber in an electron-beam evaporator and rotating the fibers during the gold evaporation process. The rate of electron-beam evaporation was 0.4 nm/sec and the pressure of the chamber was 2×10^{-6} Torr.

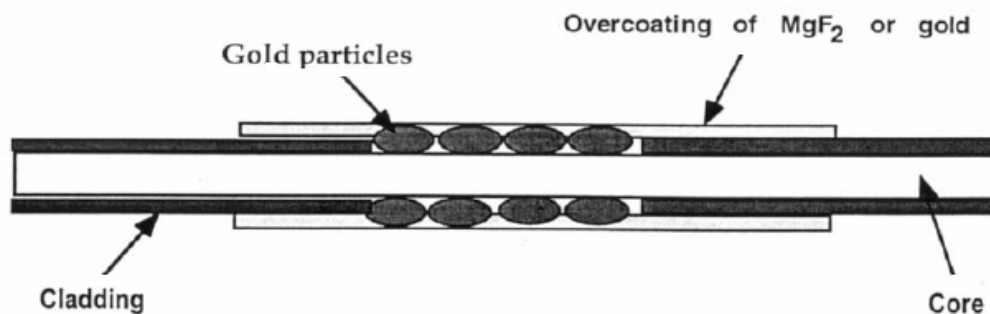


Figure 24. Optical fiber sensor consisting of a section where the cladding is removed and a 4 nm annealed gold film is deposited. An over coating of MgF₂ is provided to prevent light from coupling out when the refractive index of the medium being sensed is higher than that of the fiber core [14]

Then the fiber was annealed at different temperatures in order to change the shape of the gold particles deposited on the core of the fiber. It was reported that annealing of the fiber leads to a change in shape of the particles in the metal-island film, from an irregular shape to one like an oblate spheroid [14].

In order to interrogate the fiber optic sensor developed by the process described by Meriaudeau et al. [14], light from a xenon arc lamp white light source was incident on a monochromator and the light exiting from it was focused on the entrance of the optical fiber sensor using a microscope objective. The Monochromator was scanned from a wavelength of 400 to 900 nm. The gold particle-coated unclad section of the optical fiber was immersed in liquids whose refractive index was to be sensed. Light exiting the other end of the optical fiber sensor was incident on a silicon photodiode, which calculated the intensity I_t transmitted through a gold-coated fiber optic sensor. The intensity of light transmitted through a reference fiber, i.e. a fiber having no gold coating, was also calculated and noted as I_0 . The value of Absorbance (A) was calculated using the formula, $A = \log(I_0/I_t)$. Various liquids, having a real refractive index

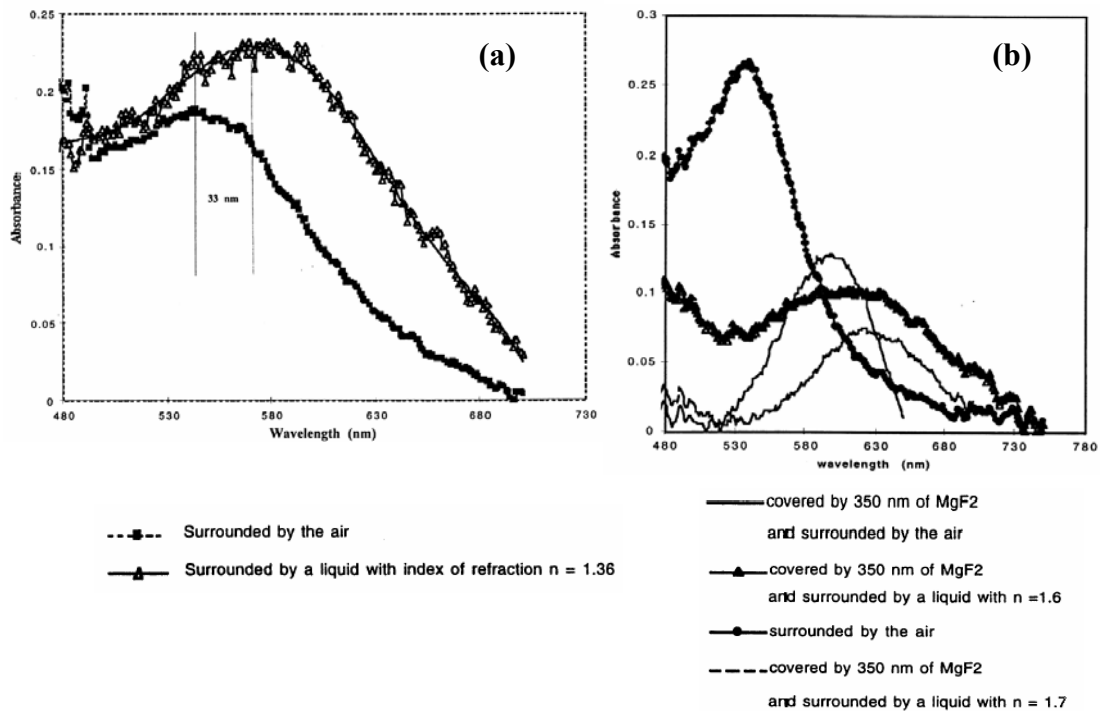


Figure 25. Experimental absorbance curves for a fiber optic sensor with a 4-nm gold film annealed 4 min at 600 °C (a) Peak resonance shifts to higher wavelength when the refractive index of the medium surrounding the fiber optic sensor is changed from 1 to 1.36. (b) The absorbance curves for a 350 nm cover layer deposited on top of the gold layer and varying the refractive index of the surrounding medium from 1 to 1.7 [14]

between 1.3 and 1.7, were selected for this experiment. It was observed by Meriaudeau et al. [14] that the resonance absorbance peak for a 4 nm discontinuous gold film, annealed at 600 °C for 4 minutes, shifts to higher wavelengths when the medium surrounding the fiber optic sensor has a refractive index of 1.36 instead of that of air (Figure 25a). It can be seen in Figure 25a that the peak in the absorbance occurs at 543 nm when the medium surrounding the sensor was air (refractive index of 1) and it occurs at around 577 nm, when the medium surrounding the sensor has a refractive index of 1.36. The absorbance curves for fibers with MgF₂ deposited on the gold-coated fiber are shown in Figure 25b. The annealed gold particle-coated fiber was over coated with MgF₂ to prevent light in the core of the fiber from being coupled out when the index of refraction of the medium being sensed is higher than that of the core of the optical fiber. It can be seen that coating with MgF₂ enables measurement of absorbance spectra even for liquids having high index of refraction (for values as high as 1.7) [14, 36].

3.10 References

1. Simon, H. J., Mitchell, D. E., and Watson, J. G., "Surface plasmons in silver films - A novel undergraduate experiment," *Am. J. Phys.* 43(7), 630–636, 1975.
2. Homola, J., "On the sensitivity of surface plasmon resonance sensors with spectral interrogation," *Sens. Actuators B* 41, 207-211, 1997.
3. Abeles, F., and Lopez-Rios, T., in *Surface Polaritons*, edited by V. M. Agranovich and D. L. Mills North-Holland, Amsterdam, 1982.
4. Weber, W. H. and Ford, G. W., "Optical electric-field enhancement at a metal surface arising from surface-plasmon excitation", *Optics letters*, 6(3), 122-124, 1981.
5. Yamamoto, M., "Surface Plasmon Resonance (SPR) Theory: Tutorial", <http://www.scl.kyoto-u.ac.jp/~masahiro/sprtheory.html>.
6. Homola, J., Ctyroky, J., and Skalsky, M., Hradilova, J., and Kolarova, P., "A surface plasmon resonance based integrated optical sensor", *Sensors and Actuators B*, 38–39, 286-290, 1997.
7. Raether, H., "Surface plasmons on smooth and rough surfaces and on gratings," Springer-Verlag, Berlin, 1988.
8. Mie G., "Beitrage zur Optik truber Medien speziell kolloidaler Metallosungen," *Ann. Phys.*, 25, 377, 1908.
9. Okamoto T., "Near-Field Spectral Analysis of Metallic Beads" in *Near-Field Optics and Surface Plasmon Polaritons*, edited by Kawata, S., Springer-Verlag Berlin, Heidelberg, 2001.

10. Van de Hulst H. C., "Light scattering by small particles," Ed., John Wiley and Sons: New York, 1957.
11. Mcfarland, A. D., and Van Duyne, R. P., "Single Silver Nanoparticles as Real-Time Optical Sensors with Zeptomole Sensitivity," *Nano Lett.*, 3, 1057, 2003.
12. Dhawan, A., and Muth, J. F., "Plasmon resonances of gold nanoparticles incorporated inside an optical fibre matrix," *Nanotechnology* 17, 2504-2511, 2006.
13. Futamata, M., Maruyama, Y., and Ishikawa, M., "Local Electric Field and Scattering Cross Section of Ag Nanoparticles under Surface Plasmon Resonance by Finite Difference Time Domain Method," *J. Phys. Chem. B*, 107(31), 7607 – 7617, 2003.
14. Meriaudeau, F., Downey, T., Passian, A., Wig, A., Buncick, M. C., and Ferrell, T. L., "Fiber optic sensor based on surface plasmon resonance," *Sens. Actuators B*, 54, 106-117, 1999.
15. Homola, J., Yee, S. S., and Gauglitz, G., "Surface plasmon resonance sensors: review," *Sensors and Actuators B: Chemical*, 54(1-2), 3-15, 1999.
16. Kano, H., and Kawata, "Surface-plasmon sensor for absorption-sensitivity enhancement", *Appl. Opt.* 33, 5166-5170, 1994.
17. Karlsson, R., Stahleberg, R., "Surface plasmon resonance detection and multispot sensing for direct monitoring of interactions involving low-molecular-weight analytes and for determination of low affinities", *Anal. Biochem.*, 228, 274–280, 1995.
18. BIAcore, www.biacore.com.
19. Pfeifer, P., Aldinger, U., Schwotzer, G., Diekmann, S., and Steinrücke, P., "Real time sensing of specific molecular binding using surface plasmon resonance spectroscopy", *Sens. Actuators B*, 54, 166-175, 1999.
20. Mu, Y., Zhang, H., Zhao, X., Song, D., Wang, Z., Sun, J., Li M., and Jin, Q., "An Optical Biosensor for Monitoring Antigen Recognition Based on Surface Plasmon Resonance Using Avidin-Biotin System," *Sensors*, 1, 91-101, 2001.
21. Ctyroky, J., Homola, J., and Skalsky, M., "Tuning of spectral operation range of a waveguide surface plasmon resonance sensor," *Electron. Lett.*, 33, 1246-1248, 1997.
22. Cullen, D. C., Brown, R. G., and Lowe, C. R., "Detection of immunocomplex formation via surface plasmon resonance on goldcoated diffraction gratings," *Biosensors*, 3, 211–225, 1987
23. Cullen, D. C. and Lowe, C. R., "A direct surface plasmon-polariton immunosensor: preliminary investigation of the non-specific adsorption of serum components to the sensor interface", *Sensors and Actuators B*, 1, 576–579, 1990.

24. Slavik, R., Homola J., and Ctyroky J., "Miniaturization of fiber optic surface plasmon resonance sensor", *Sensors and Actuators B*, 51, 311–315, 1998.
25. Slavik, R., Homola J., Ctyroky J., and Bryndab E., "Novel spectral fiber optic sensor based on surface plasmon resonance", *Sensors and Actuators B*, 74, 106-111, 2001.
26. Homola J., "Optical fiber sensor based on surface plasmon excitation," *Sensors and Actuators B*, 29, 401-405, 1995.
27. Jorgenson, R.C. and Yee, S. S., "A fiber optic chemical sensor based on surface plasmon resonance", *Sensors and Actuators B*, 12, 213-220, 1993.
28. Lin, W. B., Lacroix, M., Chovelon, J. M., Jaffrezic-Renault, N., Gagnaire, H., "Development of fiber-optic sensor based on surface plasmon resonance on silver film for monitoring aqueous media", *Sensors and Actuators B*, 75, 203-209, 2001.
29. Diez, A., Andres, M. V., and Cruz, J. L., "In-line fiber-optic sensors based on the excitation of surface plasmon modes in metal-coated tapered fibers, *Sensors and Actuators B*, 73, 95-99, 2001.
30. Tubb, A. J. C., Payne, F. P., Millington, R. B., Lowe, C. R., "Single mode optical fiber surface plasmon wave chemical sensor," *Sensors and Actuators B*, 41, 71-79, 1997.
31. Kenny, R. K., Birks, T.A. and Oakley, K. P., "Control of optical fiber taper shape", *Electron. Lett.*, 77, 1654–1656, 1991.
32. Villatoro, J., Diez, A., Cruz, J.L., and Andres, M.V., "In-line highly sensitive hydrogen sensor based on palladium-coated single-mode tapered fibers," *IEEE Sensors Journal*, 3(4), 533- 537, 2003.
33. Kurihara, K., Ohkawa, H., Iwasaki, Y., Tobita, T., Niwa, O., and Koji Suzuki K., "Microscale Fiber-Optic Chemical and Biochemical Sensors based on NSOM Technology", *Analytical Sciences*, 2001, 17, I433.
34. Niggemann, M., Katerkamp, A., Pellmann, M., Bolsmann, P., Reinbold, J., and Cammann K., "Remote sensing of tetrachloroethene with a micro-fibre optical gas sensor based on surface plasmon resonance spectroscopy", *Sensors and Actuators B*, 34, 328-333, 1996.
35. Kunz, U., Katerkamp, A, Reinhard, R, Spener, F, Cammann, K., "Sensing fatty acid binding protein with planar and fiber-optical surface plasmon resonance spectroscopy devices," *Sensors and Actuators B-Chemical* 32 (2), 149-155, 1996.
36. Meriaudeau, F., Wig, A., Passian, A., Downey, T., Buncick, M. C., and Ferrell, T. L., "Gold island fiber optic sensor for refractive index sensing," *Sens. Actuators B*, 69, 51-57, 2000.

**CHAPTER 4. IN-LINE OPTICAL FIBER STRUCTURES FOR EXPANSION
AND RE-FOCUSING OF GAUSSIAN BEAMS**

4. In-line optical fiber structures for expansion and re-focusing of Gaussian beams

4.1 Chapter Summary

Novel in-line optical fiber structures based on fused single-mode, coreless, and graded index optical fibers, are proposed in this chapter such that these fused fiber segments form miniature optical systems. The purpose of developing these in-line structures is to make mechanically robust sensors where there is increased interaction area with the environment in comparison with other fiber optic sensors such as those formed by tapering fibers, or utilizing the tips of optical fibers.

4.2 Background

Graded index optical fiber (GIF) lenses have been used to improve the coupling efficiency of light from lasers and LEDs to optical fibers and planar waveguides [1-5]. Graded index fiber lenses can be used for focusing, diverging, or collimating an incident Gaussian beam depending on the length of the graded index fiber lens used [2]. A graded index fiber-based optical fiber lens structure was described by Rahman et al. [2] and the efficiency of coupling of light originating from a laser diode to a single mode fiber was determined. It was determined that the coupling efficiency of light into the single mode fiber was dependent not only on the refractive indices of the different optical components but also on the lengths of the different graded index optical fiber lenses. In this chapter, the concept of using short lengths of graded index fibers as lenses is extended to diverge and converge light beams within a continuous optical fiber, such that light can be made to interact with the environment and then be collected to sense the interaction. In this case, the sensing region between the graded index fiber lenses is a coreless optical fiber.

In most fiber optic applications the light in an optical fiber is confined to the core of the waveguide and the cladding layer is made thick to minimize the interaction of light with the environment. The thickness of the cladding also serves an important role of providing mechanical strength to the fiber. However, evanescent wave and surface plasmon optical sensors require the electromagnetic wave to extend beyond the glass/air interface and to interact with the environment. Although sensors based on these techniques are sensitive, they become very fragile as the cladding diameter is generally reduced to dimensions less than 20 μm . Other

fiber sensors have been constructed that use just the tip of the optical fiber. This limits the interaction area, and usually requires the signal to be monitored in reflection. In this work, a novel scheme based on coupling light into a coreless optical fiber, has been developed in order to expand light to the cladding surface of the optical fiber. It is proposed that this scheme would lead to a greater interaction length of guided light with the environment. It also allows more mechanically robust sensors to be developed.

Before fabricating the in-line fiber optic structures based on fused segments of graded index, coreless, single mode, and multimode fibers, we developed a theoretical model to determine the optimal lengths of the different segments in the fused in-line structure. The theoretical model described in this chapter considers guided light emanating out of a single mode fiber. A Gaussian profile of the beam is assumed to be propagating in the different optical fiber sections. As the Gaussian beam propagates in the coreless optical fiber section, it expands such that parts of the beam are reflected from the coreless fiber-air boundary due to total internal reflection. Analysis of reflection of the Gaussian beam in hollow metal waveguides has been previously reported by Casperson et al. [6-7]. Here a similar but more thorough analysis is performed to understand the total internal reflection behavior of Gaussian beams in coreless optical fibers at the air-coreless fiber boundary.

When light travels and the beam expands in the coreless fiber segment, there are multiple total internal reflections at the coreless fiber-air boundaries. These multiple reflections cause the Gaussian profile of the beam to become distorted for a characteristic distance, but as the beam continues to propagate, the Gaussian beam profile recurs. The distance it takes for the recurrence of the Gaussian beam in the coreless optical fiber is analytically calculated in our calculations and then compared with a beam propagation simulation. Examples of in-line fiber optic structures involved in our analysis are shown in Figure 1.

Understanding the expansion and reassembly of the Gaussian beam within the coreless fiber segment is important for three principle reasons:

- a) Control of the angle of beam expansion can be used to determine the location and extent of the region of fiber where the evanescent wave can be coupled to the environment.

- b) To optimize critical parameters such as the quality factor of the surface plasmon resonance, the polarization, and the incident angle of the light at the environmental interface.
- c) The light throughput of the entire structure can be optimized by the relative placement of the receiving fiber, which is determined by the length and diameter of the coreless region.

4.3 Principle and Analysis

In order to effectively expand a Gaussian light beam to the surface of the optical fiber, the first structure examined is structure A, which is shown in Figure 1. In this structure, a single mode fiber (SMF1) is fused to a graded index fiber (GIF1), which is in turn fused to a coreless fiber (CLF). In the proposed scheme, the coreless fiber is cleaved at a certain length and then fused to another graded index fiber (GIF2), which is fused to a second single mode fiber, SMF2. The first graded index fiber is cut to a certain length, ‘ a ’, such that it acts like a diverging lens, whereas the second graded index fiber is cut to a length, ‘ c ’, such that it acts like a converging lens.

A ray matrix transformation analysis of the complex beam parameter is used to determine the shape of the light beam leaving the in-line optical fiber structure. In a Gaussian beam, the complex beam parameter, $q(z)$, is defined by the following relation:

$$\frac{i}{q(z)} = \frac{1}{R(z)} - \frac{j\lambda}{\pi n w(z)^2} \quad (1)$$

where $R(z)$ is the radius of curvature of the Gaussian beam, λ is the free-space wavelength and n is the refractive index of the medium in which the Gaussian beam is traveling. The ray matrix transformation analysis of $q(z)$ from an input plane to an output plane is give by:

$$q_2(z) = \frac{Aq_1(z) + B}{Cq_1(z) + D} \quad (2)$$

where $q_1(z)$ is the complex beam parameter of the beam input into an optical structure, which is defined by a given ABCD matrix, and $q_2(z)$ is the complex beam parameter of the beam exiting from the optical structure. If there are multiple optical components in series with each other, then the overall ABCD matrix for the whole system of optical components is the product of the

ABCD matrices for the individual components. The ABCD matrices to describe each of the optical components and the interfaces between the different components are given below

$$\begin{aligned}
 M0 &= \begin{bmatrix} 1 & 0 \\ 0 & \frac{nao}{nsmfc1} \end{bmatrix}, & M1 &= \begin{bmatrix} \cos(g_a \ a) & \frac{\sin(g_a \ a)}{g_a} \\ -g_a \sin(g_a \ a) & \cos(g_a \ a) \end{bmatrix}, & M2 &= \begin{bmatrix} 1 & 0 \\ 0 & \frac{ncl}{nao} \end{bmatrix}, \\
 M3 &= \begin{bmatrix} 1 & \frac{b}{ncl} \\ 0 & 1 \end{bmatrix}, & M4 &= \begin{bmatrix} 1 & 0 \\ 0 & \frac{nco}{ncl} \end{bmatrix}, & M5 &= \begin{bmatrix} \cos(g_c \ c) & \frac{\sin(g_c \ c)}{g_c} \\ -g_c \sin(g_c \ c) & \cos(g_c \ c) \end{bmatrix}, & M6 &= \begin{bmatrix} 1 & 0 \\ 0 & \frac{nsmfc2}{nco} \end{bmatrix} \quad (3)
 \end{aligned}$$

where M0 is the ABCD matrix describing the interface between the single mode fiber and GIF1 and nao and $nsmfc1$ are the refractive indices of the axis of the graded index fiber and the core of the single mode fiber respectively. M1 and M5 are the matrices describing the graded index fibers, i. e. GIF1 and GIF2. Here g_a , and g_c are the focusing parameters of GIF1 and GIF2 respectively whereas ‘ a ’ and ‘ c ’ are the lengths of the first and second graded index fibers respectively. The focusing parameters of the graded index fibers are dependent on the radii ra and rc of the first and second graded index fiber cores, and are given by the relationship:

$$g_a = (\sqrt{2} \cdot \sqrt{\delta_a}) / ra \text{ and } g_c = (\sqrt{2} \cdot \sqrt{\delta_c}) / rc \quad (4)$$

where δ_a and δ_c can be defined as the percentage difference of the refractive index between fiber core and that of the cladding, for GIF1 and GIF2 respectively. In our calculations, a graded index fiber with a δ_a value of 0.03 (i.e. 3%) and a core diameter of 62.5 microns was selected. M2 is the matrix describing the interface between the GIF1 and the coreless fiber nao and ncl being the refractive indices of the axis of the graded index fiber and the coreless fiber respectively. M3 is the matrix describing the expansion of the Gaussian beam in the coreless fiber. M4 is the matrix describing the interface between the GIF2 and the coreless fiber, nco and ncl being the refractive indices of the axis of the second graded index fiber and the coreless fiber respectively. M6 is the matrix describing the interface between the second single mode fiber and GIF2, nco and $nsmfc2$ being the refractive indices of the axis of the second graded index fiber and the core of the second single mode fiber respectively. The overall ABCD matrix for the whole system of optical components is the product of the ABCD matrices for the individual components and is given by the term: $M_net := M0 \cdot M1 \cdot M2 \cdot M3 \cdot M4 \cdot M5 \cdot M6$. The complex beam parameters of the light beam entering the second single mode fiber were determined from the A, B, C, and D parameters of the matrix M_net by employing equation 2.

Subsequently, the waist of the beam and the radius of curvature of the Gaussian beam entering SMF2, was calculated.

In order to calculate the appropriate length of the first graded index fiber, i. e. ‘ a ’, the product of the matrices M_0 and M_1 was computed and the A, B, C, and D terms of the matrix

$M_{01} = M_0 \cdot M_1$ determined. Subsequently, the beam waist of the Gaussian beam inside the first graded index fiber lens was calculated and plotted for different values of ‘ a ’, as shown in Figure 2. In order to form a converging lens from the first graded index fiber GIF1, one needs to use a length of the graded index fiber such that the beam waist is increasing in that section, i.e. the slope of the beam waist vs. ‘ a ’ curve is positive, as shown in Figure 2. Thus lengths between ‘ a ’ = 0 and 200 μm , 400 and 600 μm , 800 and 1000 μm , 1200 and 1400 μm , or between 1600 and

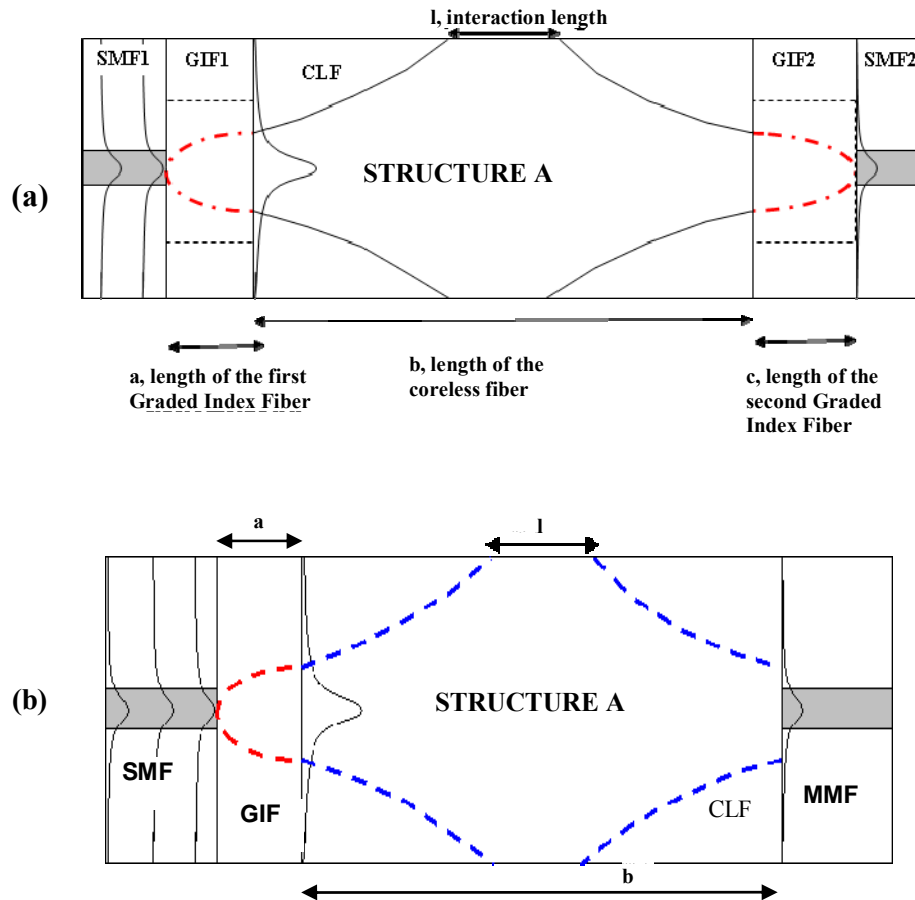


Figure 1. (a) Schematic of Structure A, i.e. an in-line optical fiber structure to expand a Gaussian light beam in the coreless optical fiber and to couple maximum amount of light back into the SMF (single mode optical fiber) using GIF (graded index fiber) lenses and (b) Slight variation of structure A with a multimode fiber (MMF) replacing the combination of graded index fiber and the single mode fiber

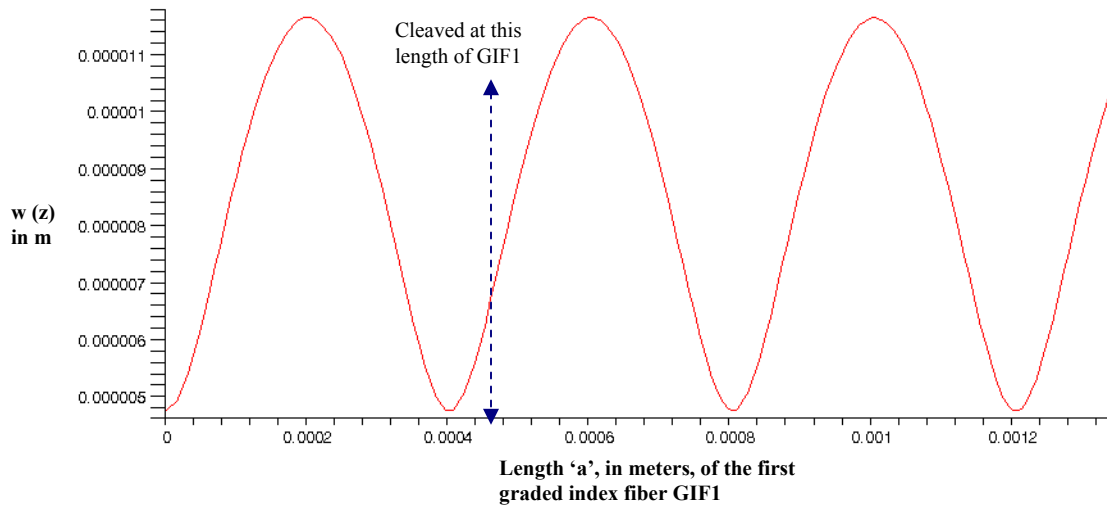


Figure 2. Plot of the half beam waist i.e. $w(z)$, in meters, vs. the length ' a ', in meters, of the first graded index fiber GIF1 in structure A

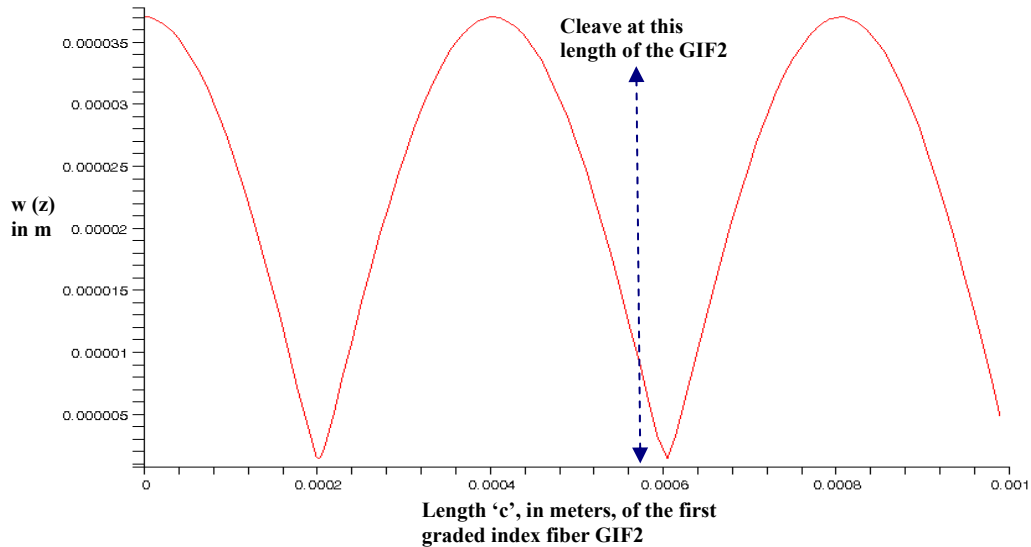


Figure 3. Plot of the half beam waist i.e. $w(z)$, in meters, vs. the length ' c ', in meters, of the second graded index fiber GIF2 in structure A

1800 μm are suitable. The GIF1 length between 400 and 600 μm or between 1600 and 1800 μm is probably preferable since it is easier to cleave of a length greater than 400 μm instead of cleaving a short length between 0 and 200 μm .

Further, the SIF1-GIF1-CLF in-line fiber structure was evaluated and the matrix product $M_{0123} = M_0 \cdot M_1 \cdot M_2 \cdot M_3$ obtained. The beam waist of the Gaussian beam in the coreless fiber was obtained by determining the ABCD terms from the matrix M_{0123} . This allowed estimation of the appropriate length of GIF1 such that the Gaussian beam expanded to the surface of the 125 μm diameter coreless fiber, for the shortest distance in the coreless fiber. The half-waist of the Gaussian beam at the surface of the coreless fiber was taken to be 62.5 μm . Lengths of 452 μm or 1722 μm were calculated as the appropriate GIF1 length, considering the factors mentioned above.

Then, the CLF-GIF2-SMF2 fiber in-line fiber structure was considered and the matrix product $M_{456} = M_4 \cdot M_5 \cdot M_6$ evaluated to obtain the ABCD matrix terms, and subsequently the beam waist of the light wave entering the single mode fiber SMF2. This is done in order to estimate the length of the second graded index fiber, i. e. GIF2, such that the beam waist at the end of the coreless fiber can be optimally focused to the core of the second single mode fiber SMF2. The half-waist of the Gaussian beam at the entrance of the second single mode fiber, i. e. SMF2, was plotted against the length ' c ' of the second graded index fiber GIF2, as shown in Figure 3. In order to form a converging lens, the length ' c ' was estimated by selecting a point on the curve shown in Figure 3 such that there is a negative slope of the curve between the beam half-waist and ' c '. Lengths of 186 μm or 588 μm were obtained as the appropriate GIF2 lengths but 588 μm length was selected as it is easier to cleave a greater length of the GIF2 fused to the coreless fiber.

In structure A, it was assumed that the Gaussian beam has wave front normals almost parallel to the fiber axis, when the beam entered the coreless fiber. Hence, it was assumed that that the beam's waist approximately exists at that point. In our calculations, the beam waist at the start of the coreless fiber was taken to be 20% of the diameter of the coreless fiber, with details of the Gaussian beam analysis being described in detail in section 4.4. Another variation of structure A is using a multimode fiber (MMF) instead of the combination of GIF2 and SMF2. The MMF has a large core diameter of 62.5 μm and thereby a large area to capture the light coming out of the coreless section of the fiber.

Another structure called structure B, as shown in Figure 4, is proposed in which another set of a coreless fiber (CL1) and a graded index fiber (GIF2) were used. The aim of employing this set was to first expand and then make the wave-front normals, of the Gaussian light beam, parallel to the fiber axis before it entered the second coreless fiber. This allowed the beam entering the coreless fiber section to be more collimated. The length ‘ $a1$ ’ of the first graded index fiber, that diverges the light beam coming out of the single mode fiber SMF1 to a certain waist diameter, was first determined. Then the beam is allowed to expand even further in the first coreless fiber, CL1. Subsequently, the light beam enters the second graded index fiber GIF2, which serves to make the wavefront normals of the light beam parallel to the fiber axis. This was done by selecting the length ‘ $a2$ ’ of the second graded index fiber GIF2, such that the waist of the Gaussian beam coming out of GIF2 lies exactly at the end of the beginning of the second coreless fiber, CL2. For the Gaussian beam computations, it was assumed that the beam waist diameter at the beginning of CL2 was 20% in size of the coreless fiber diameter of 125 micron. Lengths of the first graded index fiber, the first coreless fiber, and the second graded index fiber were calculated to be 500, 1206.2, and 220 microns respectively. Following nine ABCD matrices describe the optical components and the interfaces between the different components described in Figure 4:

$$\begin{aligned}
M2_0 &= \begin{bmatrix} 1 & 0 \\ 0 & \frac{na1o}{nsmfc1} \end{bmatrix}, & M2_1 &= \begin{bmatrix} \cos(g_a1 \ a1) & \frac{\sin(g_a1 \ a1)}{g_a1} \\ -g_a1 \sin(g_a1 \ a1) & \cos(g_a1 \ a1) \end{bmatrix}, & M2_2 &= \begin{bmatrix} 1 & 0 \\ 0 & \frac{ncl1}{nao1} \end{bmatrix}, \\
M2_3 &= \begin{bmatrix} 1 & \frac{b1}{ncl1} \\ 0 & 1 \end{bmatrix}, & M2_4 &= \begin{bmatrix} 1 & 0 \\ 0 & \frac{na2o}{ncl1} \end{bmatrix}, & M2_5 &= \begin{bmatrix} \cos(g_a2 \ a2) & \frac{\sin(g_a2 \ a2)}{g_a2} \\ -g_a2 \sin(g_a2 \ a2) & \cos(g_a2 \ a2) \end{bmatrix}, \\
M2_6 &= \begin{bmatrix} 1 & 0 \\ 0 & \frac{ncl2}{na2o} \end{bmatrix}, & M2_7 &= \begin{bmatrix} 1 & \frac{b2}{ncl2} \\ 0 & 1 \end{bmatrix}, & M2_8 &= \begin{bmatrix} 1 & 0 \\ 0 & \frac{na3o}{ncl2} \end{bmatrix}, \\
M2_9 &= \begin{bmatrix} \cos(g_a3 \ a3) & \frac{\sin(g_a3 \ a3)}{g_a3} \\ -g_a3 \sin(g_a3 \ a3) & \cos(g_a3 \ a3) \end{bmatrix}, & M2_10 &= \begin{bmatrix} 1 & 0 \\ 0 & \frac{nsmfc2}{na3o} \end{bmatrix}
\end{aligned} \tag{5}$$

where $M2_0$ is the ABCD matrix describing the interface between the single mode fiber and GIF1 and $na1o$ and $nsmfc1$ are the refractive indices of the axis of the graded index fiber and the core of the first single mode fiber respectively. $M2_1$ is the matrix describing the first graded

index fiber, GIF1. Here g_{a1} and ' $a1$ ' are the focusing parameter of the graded index fiber and the length of the first graded index fiber, respectively. The focusing parameters of the first, second, and third graded index fibers are dependent on the radii $ra1$, $ra2$ and $ra3$ of the first, second, and third graded index fiber cores, and are given by the relationship:

$$g_{a1} = \left(\sqrt{2}\sqrt{\delta_{a1}}\right)/ra1, \quad g_{a2} = \left(\sqrt{2}\sqrt{\delta_{a2}}\right)/ra2, \quad \& \quad g_{a3} = \left(\sqrt{2}\sqrt{\delta_{a3}}\right)/ra3 \quad (6)$$

where δ_{a1} , δ_{a2} , and δ_{a3} can be defined as the percentage difference of the refractive index between fiber core and that of the cladding, for GIF1, GIF2, and GIF3 respectively. In our calculations, a graded index fiber with a δ_{a1} value of 0.03 (i.e. 3%) and a core radius of 31.25 microns was selected. $M2_2$ is the matrix describing the interface between the GIF1 and the first coreless fiber CL1, with $na1o$ and $ncl1$ being the refractive indices of the axis of the first graded index fiber and the first coreless fiber respectively. $M2_3$ is the matrix describing the expansion of the Gaussian beam in the first coreless fiber. $M2_4$ is the matrix describing the interface between CL1 and GIF2, with $na2o$ and $ncl1$ being the refractive indices of the axis of GIF2 and CL1 respectively. $M2_5$ is the matrix describing the second graded index fiber GIF2. $M2_6$ is the matrix describing the interface between the GIF2 and CL2, with $na2o$ and $ncl2$ being the refractive indices of the axis of GIF2 and CL2 respectively. $M2_7$ is the matrix describing the expansion of the Gaussian beam in the second coreless fiber, i. e. CL2. $M2_8$ is the matrix describing the interface between CL2 and GIF3, with $ncl2$ and $na3o$ being the refractive indices of CL2 and the axis of GIF3 respectively. $M2_9$ is the matrix describing the third graded index fiber, GIF3. $M2_10$ is the matrix describing the interface between GIF3 and the second single-mode fiber, i. e. SMF2, with $nsmfc2$ and $na3o$ being the refractive indices of SMF2 and the axis of GIF3 respectively.

In order to calculate the optimal length of ' $a3$ ', the CL2-GIF3-SMF3 fiber in-line structure was evaluated. The matrix product $M8910 = M2_8 \cdot M2_9 \cdot M2_10$ was determined to obtain the ABCD terms and subsequently the beam waist of the fiber entering the single mode fiber SMF2. The appropriate length ' $a3$ ' was estimated by following the same procedure that was employed for determination of length ' c ' in the case of structure A. A length of 588 nm was obtained as the appropriate GIF3 length.

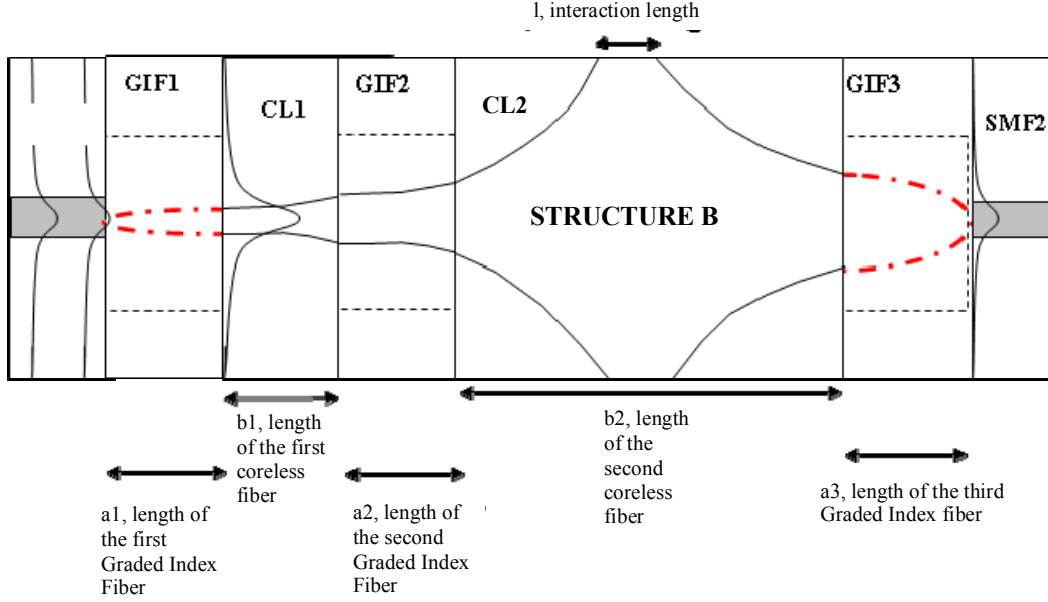


Figure 4. Schematic of Structure B, i.e. an in-line optical fiber structure to expand a Gaussian light beam in the second coreless optical fiber and to couple light back into the single mode optical fiber

Ray tracing analogues of structures A and B are shown in Figure 5, which highlights the role of graded index fibers as lenses that help in expansion and collection of the propagating light and that of the coreless fiber as the environmental interaction volume, i.e. the region in which a Gaussian light beam is expanded to the coreless fiber-environment boundary and interacts with the environment.

The fields for the LP₀₁ (EH₁₁) guided mode of the step-index single mode optical fiber, having a cladding radius of 62.5 μm and the core radius varying between 2 and 4.5 microns, were determined by using the boundary conditions of continuity of the tangential components of the E and H fields. The electric and magnetic field distributions as a function of the radius r involve Bessel functions. As an example, the different equations employed for the determination of the transverse electric field (E_ϕ) are given below:

$$E_\phi = (-u_1 \cdot A_1) \left[\frac{J_1(u_1 \cdot r) \cdot \beta}{u_1 \cdot r \cdot k_0 \cdot n_1} + J'_1(u_1 \cdot r) \right] \quad r < r_1$$

$$E_\phi = (-w_2 \cdot B_2) \cdot \left[\frac{K_1(w_2 \cdot r) \cdot \beta}{w_2 \cdot r \cdot k_0 \cdot n_1} + K'_1(w_2 \cdot r) \right] \quad r > r_1$$

$$A_1 = 1 \text{ (for normalization) and } B_2 = -[(u_1^2)/(w_2^2)] \cdot \{J_1(U)/K_1(W)\} \cdot A_1$$

$$\begin{aligned}
u_1 &= \sqrt{k_0^2 n_1^2 - \beta^2}, \quad w_2 = \sqrt{\beta^2 - k_0^2 n_2^2}, \\
U &= r_1 \sqrt{k_0^2 n_1^2 - \beta^2}, \quad W = r_1 \sqrt{\beta^2 - k_0^2 n_2^2}
\end{aligned} \tag{7}$$

where β is the propagation constant of the LP₀₁ mode traveling in the optical fiber (the dielectric cylindrical waveguide), n_1 is the refractive index of the core, n_2 is the refractive index of the cladding, r_1 is the radius of the core, and k_0 is the free space propagation constant of light i.e. $k_0 = 2\pi/\lambda$.

In our calculations, the refractive indices of the core and the cladding of the single mode fiber were taken as 1.5362 and 1.5306 respectively. The plot of tangential component of the electric field (E_ϕ) plotted against the radius r is given in Figure 6, for the case of an optical fiber with a core radius of 4.15 μm . An optical fiber with a core radius of 4.15 μm behaves as a single mode fiber for the wavelength of light being greater than ~ 1420 nm. Calculations of electromagnetic fields in the single mode fiber were also carried out by taking the core radius to be 2 μm . A Gaussian curve was fitted to the guided LP₀₁ mode in order to determine the mode field diameter in the single mode optical fiber. Mode field diameter is calculated as the region of the fiber, which contains approximately 87% of the overall intensity of the light beam. Hence, one can obtain the waist of the beam that enters the in-line optical fiber structures. As an example, the mode field diameter for the optical fiber with a core diameter of 8.3 μm was calculated to be 9.32 μm and this was selected as the beam waist of the beam exiting SMF1.

Another complex in-line structure, called structure C, was also evaluated to expand and collect light from and into the single mode fibers. This structure, shown in Figure 7, allows a more collimated beam of the correct diameter to enter the coreless fiber section CL2. The lengths of the different fiber sections in structure C were estimated in the same manner as those of structures A and B. In structure C, the second coreless fiber section, i. e. CL2, consists of two parts CL2a and CL2b. CL2a is the length that allows the Gaussian beam to expand further in the coreless region to a point where its diameter is equal to a certain value, which was taken as 50 μm in some of the calculations. The radius of curvature of the beam at the end of section CLa was calculated and was very high, almost infinite, thereby ensuring that the beam is collimated to some extent. This fairly collimated Gaussian beam of 50 μm diameter is input into the subsequent section CL2b, where it expands to the boundary of the coreless fiber and the

environment, and gets reflected multiple times as discussed later in sections 4.4 and 4.5. The different lengths of the graded index and coreless fiber sections are given in Table 1.

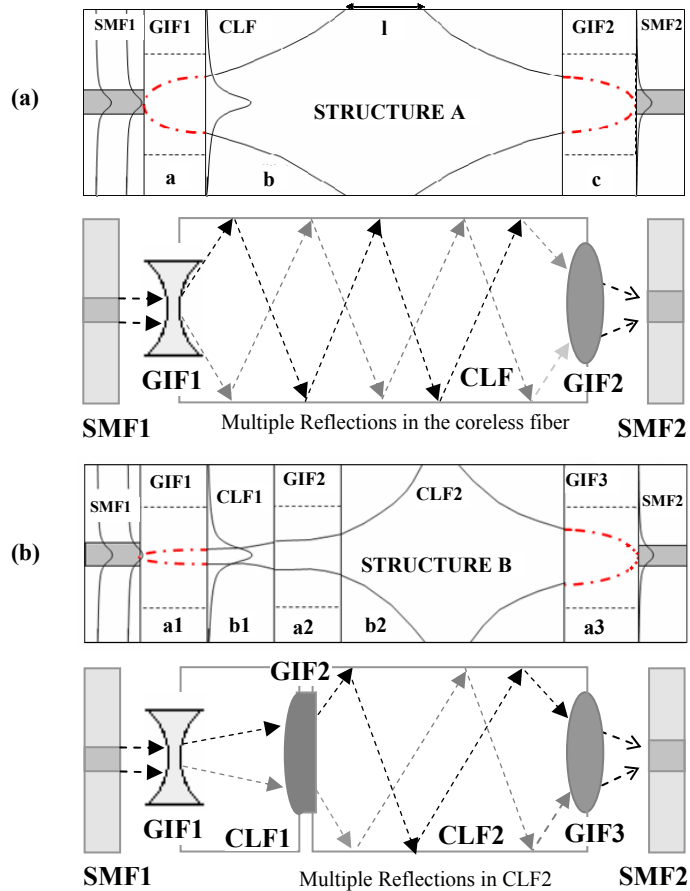


Figure 5. (a) Ray tracing analogue of structure A, which uses graded index optical fibers as lenses to expand and collect a Gaussian beam and a coreless fiber as an environmental interaction volume with a corresponding (b) Ray tracing schematic of structure B, which uses multiple graded index and coreless fiber elements. The angles of incidence are exaggerated in the figure, and remain greater than the critical angle of the glass/air interface

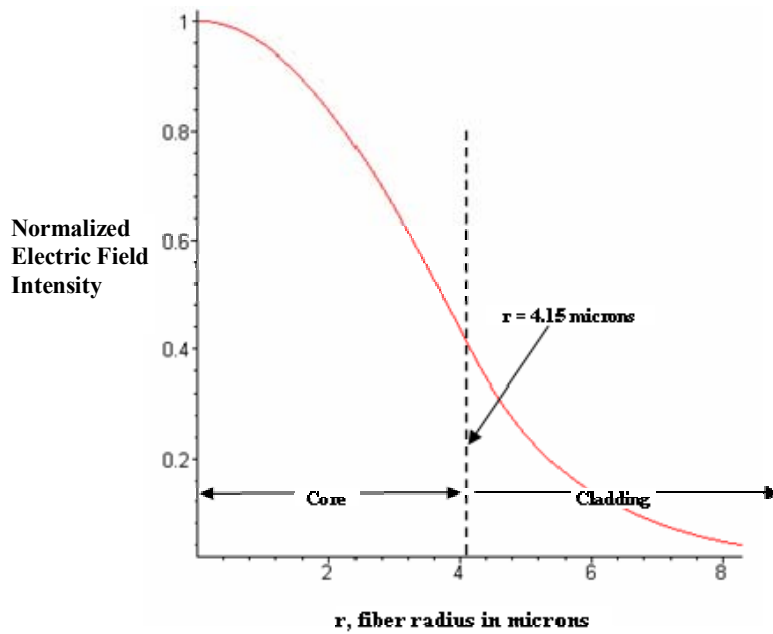


Figure 6. Plot of tangential component of the electric field (E_{ϕ}) for LP01 mode

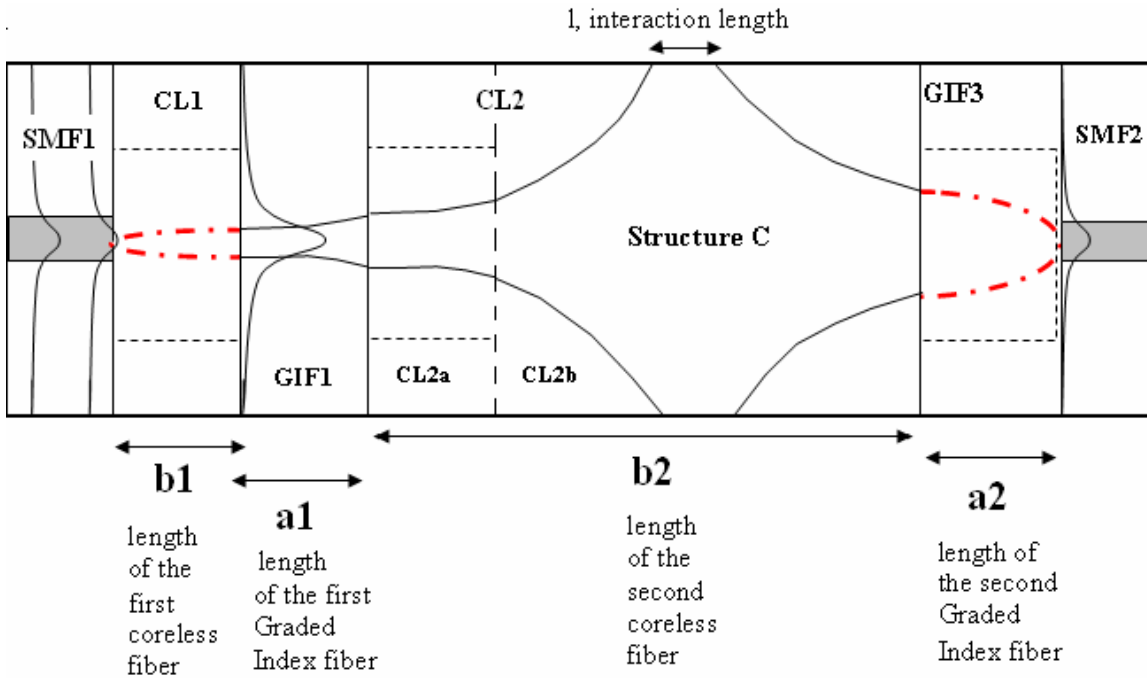


Figure 7. Schematic of Structure C, i.e. in-line optical fiber structure to expand a Gaussian light beam in the second coreless optical fiber and to couple light back into the single mode optical fiber

Table 1. Calculation Of Lengths of coreless and Graded-Index Fiber Segments In The In-Line Fiber Optic Structures

Structure	a (mm)	b (mm)	c (μm)	a1 (μm)	b1 (μm)	a2 (μm)	b2 (mm)	a3 (μm)
A	1.7	36.07	588	-	-	-	-	-
B	-	-	-	950	520	900	41.3	588
C	-	-	-	610	475	588	35.2	-

4.4 Derivation of Gaussian beam intensity considering multiple beam reflections

The Electric field profile for a linearly polarized wave propagating in the z direction in a cylindrical or rectangular waveguide is given by:

$$e(x,y,z) = E(x, z) \cdot \exp(-j\beta_0 z) \quad (8)$$

where β_0 is the propagation constant in a uniform dielectric medium and x,y, and z describe the Cartesian coordinates [7]. The relation for the amplitude of a Gaussian beam propagating in a waveguide, between two metallic surfaces, has been derived by Casperson et al [6-7]. The electric field in equation 8 was substituted into the Helmholtz wave equation and a paraxial wave approximation was considered. The amplitude of electric field in equation 8 is given by E(x,z), which has a Gaussian profile. The Gaussian beam described here is considered to be on-axis and its amplitude is given by the following relationship:

$$E(R, Z) = \sqrt{\frac{\sqrt{2}}{W_0 \sqrt{\pi(1+Z^2)}}} \cdot \exp\left(\frac{(-R^2 - i.Z.R^2)}{W_0^2.(1+Z^2)}\right) \cdot \exp\left(\frac{i.\tan^{-1}(Z)}{2}\right) \quad (9)$$

where W_0 is the normalized beam waist size i.e. $W_0 = w_0/d$, $R = x/d$, and $Z = z/z_0$, where d is the diameter of the fiber and z_0 is the Rayleigh length. The relation for Rayleigh length in terms of beam waist size and the wavelength (λ) is given as: $z_0 = (n\pi (w_0)^2)/\lambda$.

In our work, the relation given in equation 9 was applied to an optical fiber, which is a cylindrical waveguide, by replacing 'x' by 'r', the distance in the radial direction. The term described in equation 9 was obtained by normalizing the intensity of the Gaussian beam according the following integral [7]:

$$\int_{-\infty}^{\infty} I(X, Z) dX = 1 \quad (10)$$

On reflection of an electromagnetic wave from the boundary, the reflected wave differs from the incident wave by a change of phase. The changes of phase for the s and p polarizations are given by the following relationships [8]:

$$\phi_s = 2 \tan^{-1} \left(\frac{\sin^2 \theta_1 - \sin^2 \theta_c}{1 - \sin^2 \theta_1} \right)^{1/2} \quad \text{and} \quad \phi_p = -\pi + 2 \tan^{-1} \left[\left(\frac{\sin^2 \theta_1 - \sin^2 \theta_c}{1 - \sin^2 \theta_1} \right)^{1/2} \left(\frac{n_1}{n_2} \right)^2 \right] \quad (11)$$

For grazing reflection, i.e. reflection at small angles between the incident light and the reflecting surface, $\theta_1 \sim 90$ degrees. This implies that for s polarization the change of phase is 180

degrees and for p polarization, it is 0 degrees. Hence for s polarization, every reflection of the Gaussian beam at a reflecting surface leads to a phase change of π , implying a change in sign of the reflected beam amplitude. In case of p polarization, there is no phase change associated with total internal reflection at incident angles close to 90 degrees. Hence, amplitude of a p-polarized beam does not change sign when it undergoes grazing total internal reflection. Casperson et al. had described grazing reflection of the Gaussian beam from metallic surfaces [6-7]. In our work, reflections considered were total internal reflections from the coreless fiber-environment boundary of the optical fibers. The expression for the net electric field profile was derived, considering the superposition of the incident and the reflected Gaussian electric fields, the reflection being total internal reflection from the coreless fiber-environment boundary. Thus for s polarization, the net electric field profile is given by the following relationship that considers a phase change of 180 degrees at each total internal reflection point:

$$E_s = E(R, Z) + \sum_{n=1}^{n=M} \{(-1)^n \cdot \exp(j \cdot n \cdot \theta_s) \cdot E((n + (-1)^n R), Z)\} \\ + \sum_{n=1}^{n=M} \{(-1)^n \cdot \exp(j \cdot n \cdot \theta_s) \cdot E((-n + (-1)^n R), Z)\} \quad (12)$$

For p polarization, the net electric field profile, as a superposition of the incident and the reflected Gaussian beam electric fields is given by the following relationship, considering a phase change of 0 degrees at each total internal reflection point:

$$E_p = E(R, Z) + \sum_{n=1}^{n=M} \{(-1)^n \cdot \exp(j \cdot n \cdot \theta_p) \cdot E((n + (-1)^n R), Z)\} \\ + \sum_{n=1}^{n=M} \{(-1)^n \cdot \exp(j \cdot n \cdot \theta_p) \cdot E((-n + (-1)^n R), Z)\} \quad (13)$$

The intensity of the Gaussian beam, with s or p polarizations, is given as the product of the electric field and its conjugate at a given point X, Z:

$$I_{s,p} = E_{s,p} \times E_{s,p}^* \quad (14)$$

In this work, the intensity profile for the s and p-polarized light in an optical fiber was calculated considering multiple total internal reflections at the core-cladding boundary. These profiles were plotted as a function of the X, the radial distance from the center of the fiber normalized to the diameter of the optical fiber. The intensity profile for different values of Z was plotted, which gives us an idea about the change of beam shape as the beam propagates down the optical fiber. In most of our calculations, a Gaussian beam with a waist size of about 20 percent of the fiber diameter was injected into a coreless fiber, and the distance it takes for the Gaussian

beam to recur estimated. The coreless fiber sections, defined as CLF and CL2 in structures A and B, act as the sensor interaction volumes for the interaction of evanescent wave with the environment.

4.5 Results and Discussion

In this work, intensity profiles for s and p-polarized light in an optical fiber were calculated taking into consideration, the multiple total internal reflections at the coreless fiber-environment boundary. Plots of these profiles were obtained as a function of the X, i. e. the radial distance from the center of the fiber normalized to the diameter of the optical fiber. The intensity profile was plotted for different values of Z to get an idea about the change of beam shape as the beam propagated down the optical fiber. The Rayleigh length was calculated to be approximately 2248 microns. It can be seen in Figure 8 that the Gaussian beam with a waist size of 0.2 times the fiber diameter, i.e. 25 microns, undergoes multiple total internal reflections at the coreless fiber-environment boundary as it propagates. This changes the Gaussian profile into a non-Gaussian profile, for a certain distance. It was observed at a distance of around 7.98 times z_0 , which is approximately 17.9 mm, the Gaussian beam profile recurs inside the coreless fiber. In the

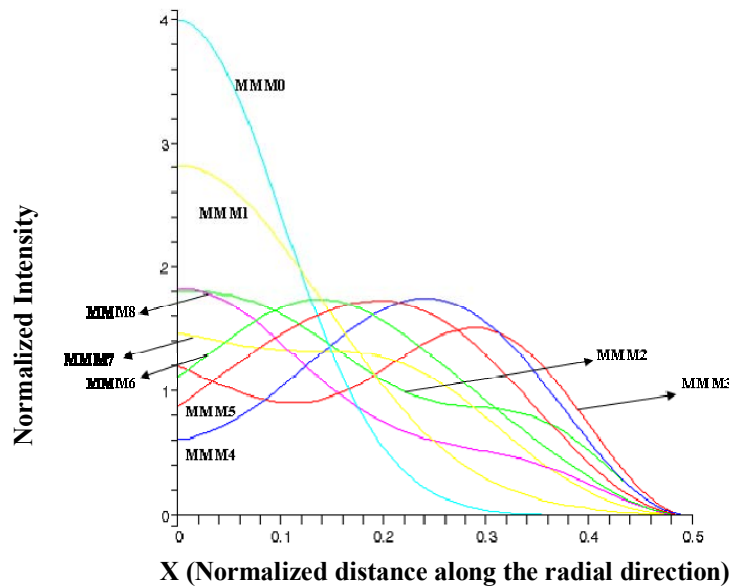


Figure 8. Plot of the normalized Gaussian beam intensity profiles for different values of Z, MMM0 is at $Z=0$, MMM1 at $Z = z_0$, MMM2 at $Z = 2z_0$, MMM3 at $Z = 3z_0$, MMM4 at $Z = 4z_0$, MMM5 at $Z = 5z_0$, MMM6 at $Z = 6z_0$, MMM7 at $Z = 7z_0$, MMM8 at $Z = 8z_0$, where z_0 is the Rayleigh length

structure B, a Gaussian beam enters the coreless region with its beam front normals parallel to the fiber axis. Hence one can take this to be the waist of our beam with a waist size of 25 microns. In structure A, the beam front normals are not parallel to the fiber axis and an approximation is made that the Gaussian beam waist is laying at the start of the coreless fiber. Length of interaction, of the beam propagating inside the coreless fiber sections in structures A and B, with the environment was estimated using two procedures. In the first procedure, the start point of interaction was measured as the point when the Gaussian Beam starts to change its profile from Gaussian to non-Gaussian, with greater intensity near the coreless fiber-environment interfaces than the fiber axis. Our calculations show that this begins to happen after $1.6 z_0$, which is 1.6 times the Rayleigh length as shown in Figure 9. Subsequently, the distance after which the intensity profile completes the process of reformation of the Gaussian beam was calculated and our calculations show that this happens after a length of $7.98 z_0$ as shown in Figure 8. Hence the interaction length is the length between the start and end points of the interaction and was estimated to by $6.38 z_0$, which is 14.34 mm. One can also observe from Figure 10 that the process of re-construction of the Gaussian beam starts after a distance of $4.2 z_0$ from the start of the coreless fiber. The second procedure uses the same process for determination of the end point of the interaction but is different in determining the start point. In this procedure, the start point

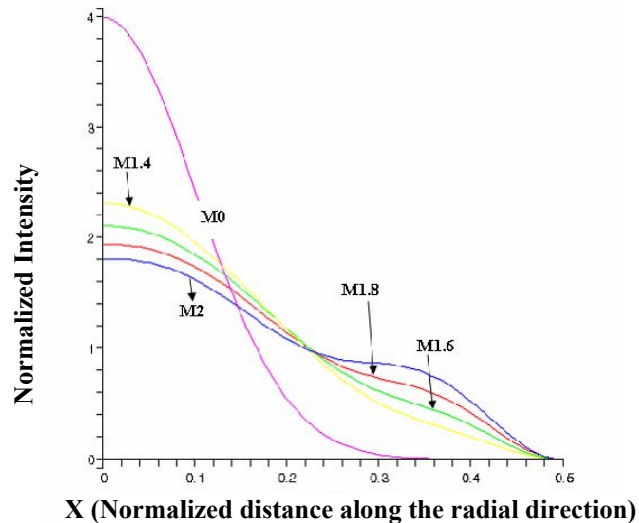


Figure 9. Plot of the normalized Gaussian beam intensity profiles for different values of Z , M_0 is at $Z=0$, $M_{1.4}$ at $Z = 1.4z_0$, $M_{1.6}$ at $Z = 1.6z_0$, $M_{1.8}$ at $Z = 1.8z_0$, M_2 at $Z = 2z_0$, where z_0 is the Rayleigh length. As Z is increased from $Z=0$ to $Z=2$, at $Z = 1.6z_0$, we observe a start of divergence from the Gaussian profile indicating the start of the interaction region

is estimated as the distance after which the beam propagating in the coreless fiber reaches the surface of the coreless fiber-environment interface. This is estimated using Gaussian beam expansion in the coreless fiber medium taking its refractive index to be ~ 1.5 . It was determined that the start point occurred 1016.3 microns after the start of the coreless fiber. But 382 microns of the coreless fiber are needed just for the beam to have a size of 0.2 times the fiber radius i.e. equal to 25 microns, which is assumed to be the waist in case of the structure A. Therefore, the length of coreless fiber in which the beam expands from the beam waist to the surface of the fiber is 1016 microns minus 382 microns, which is equal to 634 microns. Hence, the interaction length is taken to be $7.98 z_0$, i. e. point of the end of the Gaussian beam interaction, minus 634 microns which is equal to 17.3 mm. The interaction length, calculated using the procedure described in this section, is same for CLF and CL2 in structures A and B respectively. The calculation of the distance after which the beams recurs as well as the interaction length gives an idea of the length of the coreless fiber needed for fabrication of the in-line structures shown in Figures 1 and 4. In structure B, the minimum length of CL2 to be selected is just $7.98 z_0$, which is approximately 17.9 microns. In structure A the minimum length of CLF is $7.98 z_0$ plus the length, required for the Gaussian beam to expand to a half-waist size of 25 microns from its size at the end of the first graded index fiber, which was calculated to be 382 microns. Hence, in the case of the structure A, the total length of the coreless fiber required was found to be 18.28 mm.

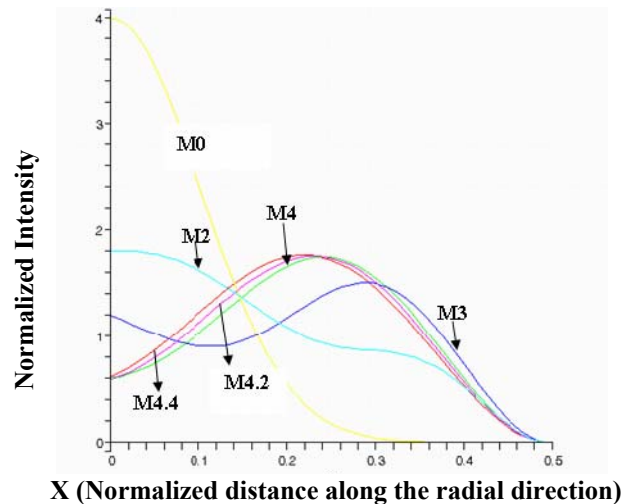


Figure 10. Plot of the normalized Gaussian beam intensity profiles for different values of Z , M_0 is at $Z=0$, M_2 at $Z = 2z_0$, M_3 at $Z = 3z_0$, M_4 at $Z = 4z_0$, $M_{4.2}$ at $Z = 4.2z_0$, $M_{4.4}$ at $Z = 4.2z_0$, where z_0 is the Rayleigh length. Estimation of the distance after which the interaction region ends in the coreless fiber is carried out

Waist of the beam at the end of the coreless fiber section was evaluated by considering the recurred profile of the Gaussian beam after 7.98 z_0 length of the coreless fiber and then calculating the radius of the region within which 86.6 percent of the overall intensity of the light beam was present. The area under the recurred Gaussian beam at the end of 7.98 z_0 was found to be 0.382; and 0.866 times this area was obtained when the value of X was equal to 0.3. Hence, the beam waist at the end of the coreless fiber was obtained as 0.3 times 125 microns, which is equal to 37.5 microns.

4.6 Beam Propagation Method Simulations on the In-line fiber Optic Structures

Beam Propagation Method was employed to study the in-line fiber optic structures, that were developed to make the electromagnetic light wave propagating in the core of the single mode or multimode fibers to reach the surface of the coreless fiber. Use of a numerical tool like the Beam Propagation Method allowed analysis of the light propagation and reflection in the coreless fiber sections and in the graded index fibers. A commercially available software called Beam-Prop from R-Soft was employed for the Beam Propagation Method calculations. The effect of overlap of the electromagnetic fields upon reflection at the boundaries of the coreless fiber sections was studied. Graded-index fiber structures that were employed for expansion and collection of the propagating light wave, were also evaluated using the beam propagation method.

Beam Propagation method approximates the wave equation for monochromatic waves by using scalar field and paraxial approximations [9-13]. The scalar-field approximation neglects the polarization effects and the paraxial approximation considers light propagation for a very narrow range of angles, mainly grazing incidence. The approximated equations are then solved numerically. The scalar field assumption, i.e. neglecting the polarization effects allows the electromagnetic wave equation to be written as the Helmholtz monochromatic wave equation, given by the following relationship:

$$\frac{\partial^2 \mathbf{E}}{\partial^2 x} + \frac{\partial^2 \mathbf{E}}{\partial^2 y} + \frac{\partial^2 \mathbf{E}}{\partial^2 z} + k^2 \mathbf{E} = 0 \quad (16)$$

Time dependence of the propagating electric field $e(x, y, z, t)$ can be separated by using the relationship $e(x, y, z, t) = E(x, y, z)e^{-j\omega t}$, where the k is the wave number that is dependent only on the spatial coordinates $x, y,$ and z and is given by the relationship $k = k_0 n$, where $k_0 = 2\pi/\lambda$, i.e. the free space wave number, λ is the free space wavelength, and n is the refractive index of

the medium, which is again dependent only on the spatial coordinates x , y , and z . One can also define another field $S(x, y, z)$, as a slowly varying field. This field propagates along the z -direction and varies slowly with z . The slowly varying field S can be defined by using the relationship:

$$S(x, y, z) = E(x, y, z) e^{-jk'z} \quad (17)$$

where k' is a reference wave number that can be written as $k' = k_0 n'$, n' being the reference refractive index. By putting equation 17 in equation 16, the Helmholtz wave equation can be reduced to the following relationship:

$$\frac{\partial^2 S}{\partial^2 x} + 2jk' \frac{\partial S}{\partial z} + \frac{\partial^2 S}{\partial^2 y} + \frac{\partial^2 S}{\partial^2 z} + (k^2 - k'^2) \cdot S = 0 \quad (18)$$

By employing the paraxial approximation in the above equation, i. e. by ignoring the $\partial^2 S / \partial^2 z$ term considering that the variation of the field S with z is slow in the case of the paraxial approximation, one obtains the final Beam Propagation Method equation in the three dimensional (x, y, z) space:

$$\frac{\partial^2 S}{\partial^2 x} + 2jk' \frac{\partial S}{\partial z} + \frac{\partial^2 S}{\partial^2 y} + (k^2 - k'^2) \cdot S = 0 \quad (19)$$

Elimination of the second derivative term in z reduces the problem from a second order boundary value problem to a first order initial value problem leading to a shorter calculation time for numerical calculations. In order to convert equation 19 into a form that could be employed for numerical calculation of the field $S(x, y, z)$, Beam Propagation Method employs the finite-difference approach based on the well-known Crank-Nicholson structure [13]. In this method, the field $S(x, y, z)$ in the x - y plane is represented only at discrete points on a grid, and at discrete planes in the z direction, which is the propagation direction. If one knows the field at one z plane, discretization of equation 19 using the finite-difference approach allows determination of the field at the next z plane. This propagation step is then repeated to determine the field throughout the x, y, z structure. Results for the Beam Propagation Method calculations for structures A and B are given in section 4.6.1.

4.6.1 Beam Propagation Simulation Results

R-Soft was employed for the Beam Propagation Method analysis of structures A and B described in sections 4.3 - 4.5. The mode propagating in the single mode fiber was calculated

using the software by inputting the dimensions of the single mode fiber, i.e. 125 μm cladding diameter and 4 μm core diameter, and the core and cladding refractive indices. These calculations were also carried out for the case of core diameter being 8.3 μm . The Gaussian-like field profile emanating from the single mode fiber section was then taken as the input for the subsequent graded index fiber section and the field through the length of the graded index fiber was calculated and plotted. The field profile at the end of the graded index fiber section was further input into the coreless fiber section and this process was continued for all sections of the fiber.

In Figure 11, one can observe the expansion of the light wave propagating in the continuous in-line structure consisting of a single mode fiber fused to a graded index fiber of 1700 μm length, which is further fused to a coreless fiber. The light wave in the single mode fiber can be observed to be concentrated in the fiber core and is expanded via the graded index fiber cut at the appropriate length. The expansion of the beam further in the coreless fiber and its reflection at the coreless fiber-air boundary are also shown in Figure 11. Figure 12 highlights the reflection and super positioning of the electric fields propagating in the coreless fiber after reflections at the fiber-air boundary. One can observe that the incident beam superposes with the reflected beams multiple times as was considered in sections 4.4 and 4.5 in the analytical calculations employed to estimate the shape of the beam propagating in the coreless fiber after a certain propagation distance.

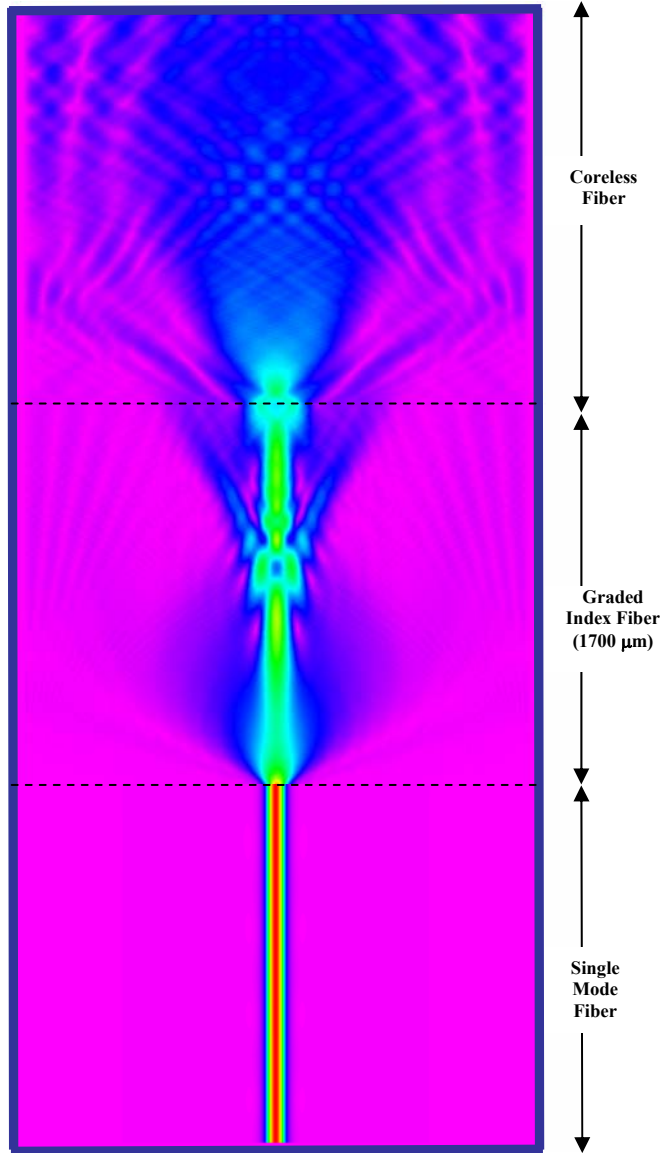


Figure 11. Field profile in a single mode fiber, a graded index fiber cut at a length of 1700 μm , and input into a coreless fiber

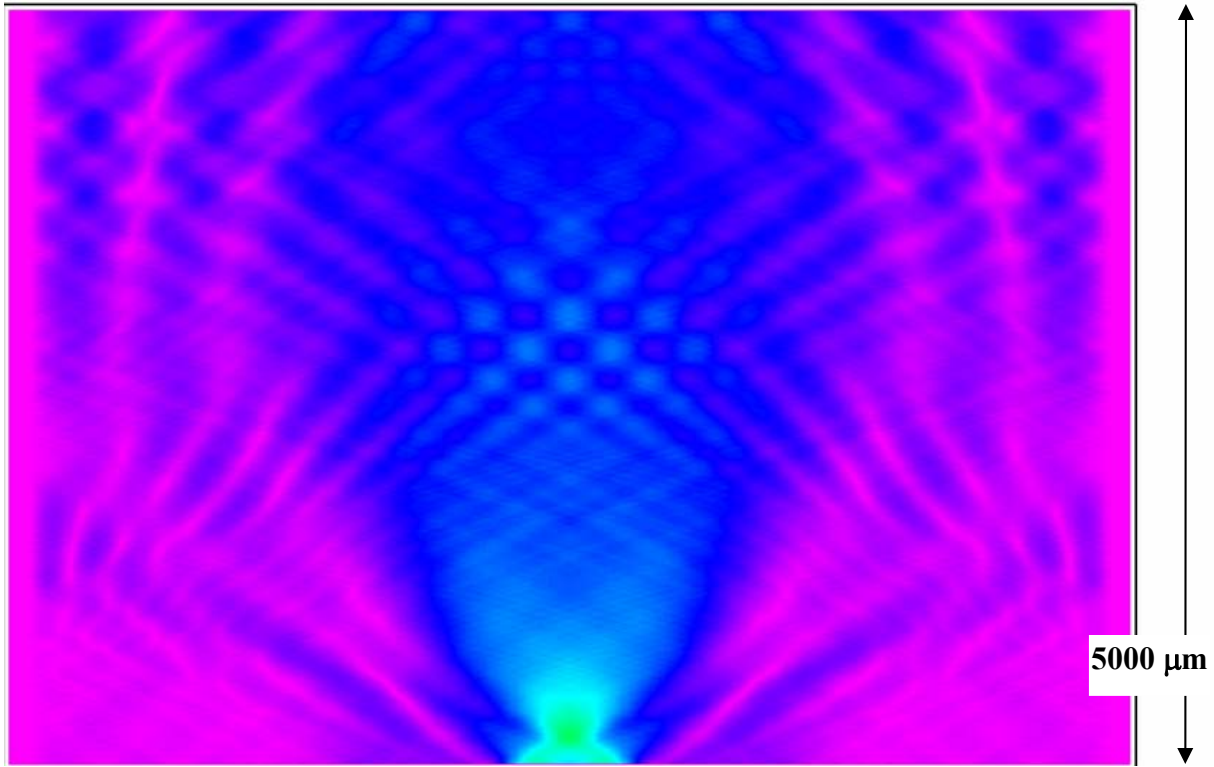


Figure 12. Field profile in a coreless fiber section 5000 um in length showing the expansion of a Gaussian beam to the fiber-air boundary and the superposition of beams being reflected at the boundary

4.7 Conclusions

In this chapter, novel in-line optical fiber structures based on fused single-mode, coreless, and graded index optical fibers, have been proposed and modeled. These structures were proposed to increase the level of interaction of propagating light with the environment for forming evanescent environmental sensors. In this chapter, two structures were proposed to make the light beam propagating in an optical fiber to interact with the atmosphere. In the first proposed structure, a Gaussian beam emanating from a single mode optical fiber (SMF) is expanded to the surface of a coreless optical fiber using a graded index optical fiber lens so as to increase the interaction of light with the atmosphere. In the coreless fiber, there are multiple total internal reflections of the Gaussian beam at the coreless fiber-air boundaries and the distance it takes for the recurrence of the Gaussian beam in the coreless optical fiber was estimated, using Gaussian beam optics calculations. Analytical calculations were performed to estimate the length of the graded index optical fiber required for maximum beam expansion in the coreless fiber and the length of another graded-index fiber lens, that is required to focus the Gaussian beam down to the dimensions of the collector single mode optical fiber. Another in-line optical fiber structure, comprising of three graded index lenses and two coreless fibers that are fused to each other and to the single mode optical fibers, was also proposed in this chapter. The second graded index fiber serves to make the light beam wave-front normals parallel to the fiber axis as it enters the second coreless fiber. The beam expands in the second coreless fiber and undergoes multiple reflections from the coreless fiber-air interface. The distance it takes for the recurrence of the Gaussian beam in the coreless optical fibers and the length of a third graded index fiber lens, that would be required to refocus the beam to the mode field diameter of the second single mode fiber, was analytically calculated. In this chapter, the use of Beam Propagation Method was described to study the propagation of the Gaussian beam in the coreless and graded index sections of the fiber.

4.8 References

1. Faiz A. R., and Chuah H. T., Ghafouri-Shiraz H., "Coupling Efficiency Between a Laser Diode and a Conically Lensed Single Mode Fibre," Proceedings of TENCON 2000, 3, 66 – 70, 2000.
2. Rahman F. A., Takahashi K. and Teik C. H., "A scheme to improve the coupling efficiency and working distance between laser diode and single mode fiber, Optics Communications, 208, 103-110, 2002.
3. Shah V., Curtis L., Vodhanel R. S., Bour D. P. and Young W. C., "Efficient power coupling from a 980 nm Broad Area laser to a single mode fibre using a wedge shaped fibre endface", Journal of Lightwave Technology, Vol. 8 (9), 1313-1318, 1990.
4. Shiraishi K., Ohnuki H., Hiraguri N., Matsumura K., Ohishi I., Morichi H., and Kazami H., "A lensed-fiber coupling scheme utilizing a graded-index fiber and ahemispherically ended coreless fiber tip", Journal of Lightwave Technology, 15(2), 356-363, 1997.
5. Edwards C. A., Presby H. M., and Dragone C., "Ideal microlenses for laser to fibre coupling", Journal of Lightwave Technology, Vol. 11(2), 252-257,1993.
6. Casperson L.W., "Recurring beams in hollow metal waveguides: paraxial approximation", Applied Optics, 41 (30), 6410-6415, 2002.
7. Casperson L.W., "Gaussian beams in hollow metal waveguides", J. Opt. Soc. Am. A, 17(6), 1115-1123, 2000.
8. Hadley G. R., "Low-truncation-error finite difference equations for photonics simulation I: beam propagation", J. Lightwave Technol. 16, 134 (1998).
9. Rao H., Scarmozzino R., and Osgood Jr. R. M., "A bidirectional beam propagation method for multiple dielectric interfaces", Photon. Technol. Lett. 11,830 (1999).
10. Yamauchi J., Shibayama J., and Nakano H., "Modified finite-difference beam propagation method based on the generalized Douglas scheme for variable coefficients", Photon. Technol. Lett. 7, 661 (1995).
11. Hoekstra H. J. W. M., Krijnen G. J. M., and Lambeck P. V., "Efficient interface conditions for the finite difference beam propagation method", J. Lightwave Technol. 10, 1352 (1992).
12. Feit M. D. and Fleck J. A., "Computation of mode properties in optical fiber waveguides by a propagating beam method", Applied Optics, 19, 1154 (1980).
13. Yevick D. and Hermansson B., "Efficient beam propagation techniques", J. Quantum Electron. 26, 109 (1990).

**CHAPTER 5. FIBER-OPTIC CHEMICAL SENSORS:
END-FACE AND IN-LINE SENSORS**

5.0 Fiber-optic chemical sensors: End-face and in-line sensors

In this chapter, development of novel fiber optic chemical sensors is described. Several ways of forming sensitive and robust chemical sensor and biosensors based on plasmon resonances of metallic islands and nanoparticles are demonstrated. As the refractive index of the medium around the sensors was varied, a shift in the plasmon resonance related dip in the transmission spectrum was observed.

The first kind of sensor described in this chapter is fiber-tip sensor based on excitation of localized surface plasmons at the tip of an optical fiber. Evaluation of this sensor in the reflection and transmission modes is described. The second sensor demonstrated in this chapter is based on the approach described in chapter 4 where optical fiber elements are fused together to form an optical system within the fiber. This results in an in-line optical fiber structure that is mechanically robust, provides a large interaction length for high sensitivity, and is compatible with standard chemistries for optical affinity sensing of biological compounds. The fiber optic sensors were tested by placing them placed in mediums of different refractive indexes to evaluate their chemical sensing capability. These sensors were also evaluated by monitoring their optical response to the binding of biomolecules such as Biotin and Streptavidin to the sensor surface.

At the end of the chapter, a method of forming sensor systems from the individual fiber optic systems is described. In order to form sensor systems, the individual optical fiber-based sensors can then be integrated into substrates like textile fabrics. Optical fibers can be woven or knitted into a fabric in a manner similar to conventional single filament yarns made from polymers. Optical fibers can also be embedded into non-woven materials by the processes of electro-spinning, melt blowing, or spun bonding. These textile-based substrates are flexible and conformable and can potentially be used to form large-area distributed sensing systems. The textile format potentially allows the deployment and re-deployment these sensor systems, with a large number of sensors embedded over a large area by unrolling and rolling up the sensor fabric like a carpet.

5.1 Different optical fiber structures for sensing applications

The main objective is to develop surface affinity sensors that employ plasmon resonances of metallic nanoparticles and islands, as a means of transducing the input optical signal. By using the localized surface plasmon one can avoid some of the polarization restrictions inherent in using

thin films. Instead of scanning the angle of incidence, the spectrum can be measured and light scattering or absorption resonance as a function of wavelength, obtained. Different structures that were developed to form sensors for chemical and biomolecules are shown in Figures 1 - 3. In Figure 1, use of end-face of the optical fiber as the sensing region, is shown. This is a simple method for LSP-based sensing and geometry of the fiber tip can also be altered. However, the interaction volume is very small. It also usually requires the fiber to be interrogated in the reflection mode. In this study, fiber tip based sensors were evaluated in the transmission mode. Gold nanoparticles were deposited on the tip of the optical fiber as shown in Figure 1 and light propagating in the optical fiber excited LSP in the gold nanoparticles. In order to form in-line fiber optic sensors using the fiber tip, a platform to hold the sensor fiber and a collector fiber very close to each other, was developed as shown in Figure 2. A V-groove having a width (of the top of the groove) almost equal to the fiber diameter was etched out in a silicon substrate by using standard photolithography and etching techniques. The sensor and collector fibers were placed in the V-groove, their tips at a distance ~ 10 μm from each other, and held in that position using two magnets as shown in Figure 2.

A second structure developed was a fiber taper, which is shown in Figure 1b. Tapering the fiber allows the guided wave to escape the core of the fiber due to the fiber geometry and interact with the environment. This guided wave, after interaction with the environment, gets coupled back into the other end of the optical fiber. This allows in-line sensing of the medium around the fiber taper. The light escapes the taper is evanescent in nature, it can excite surface plasmons in a thin gold film on the tapered region and also in gold nanoparticles in that region. The fiber taper provides a larger interaction volume, but it significantly reduces the mechanical strength of the fiber since the diameter is typically reduced to less than 20 μm . Hence employing this fiber sensor for large-area distributed sensing in tough environments is not possible.

In order to form chemical sensors that are sensitive yet robust, a third approach that allows fabrication of optical elements within the optical fiber to control the way light in the fiber interacts with environment or fiber interface, was employed. Novel fiber structures, called structures A and B, were developed to form an in-line sensing mechanism that is able to overcome the problem associated with fragile tapered fiber sensors. These structures are shown in Figures 3a and b. Structure A is the simplest structure formed by fusion splicing a section of a coreless fiber to two pieces of continuous multimode fibers. In this sensor, different modes

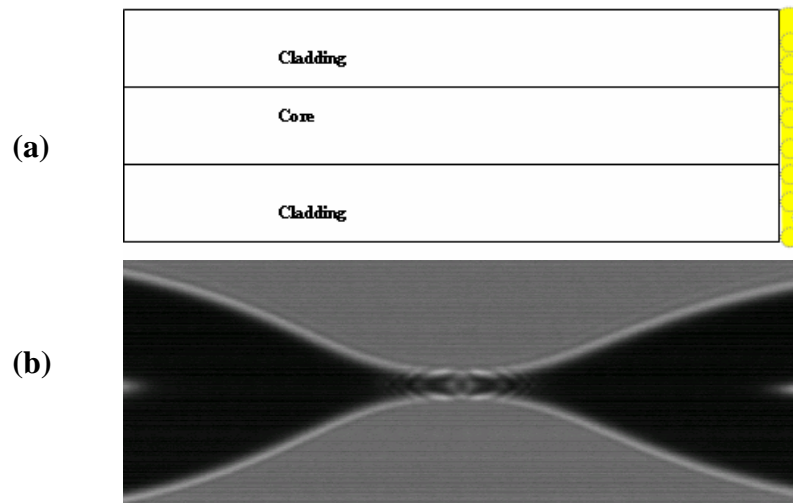


Figure 1. (a) Deposition or formation of gold nanoparticles on the fiber tip, and (b) Tapered optical fiber employed for evanescent and surface plasmon sensing

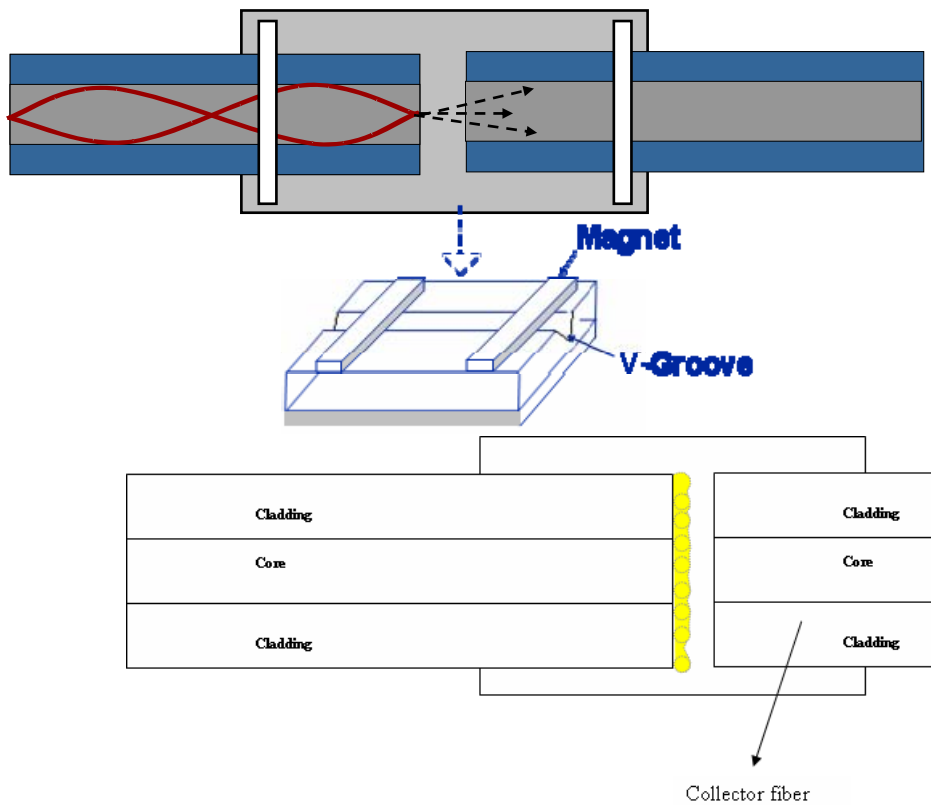


Figure 2. A schematic of the silicon piece, having a V-groove, employed to hold the optical fiber for sensing a change of refractive index of the medium around the sensor

propagating in the multimode fiber expand to the surface of the coreless fiber in the central region and after reflection from the coreless fiber-environment boundary, get coupled back into the second multimode fiber fused to the coreless fiber. The evanescent waves at the coreless fiber-environment boundary excite plasmon resonance in the metallic nanoparticles formed on the surface of the coreless fiber section, as shown in Figure 3a. Resolution of a sensor involving structure A is lower as compared with the fiber tip plasmon sensors. This can be explained by the fact that there are a lot of modes emanating from the multimode fiber section of this structure, thereby leading to light being incident, on the nanoparticles on the surface of the coreless section of the fiber, at several angles. Several angles of incidence of light on the nanoparticles leads to plasmon resonance related dips in the transmission due to each incident angle, thereby leading to a broad cumulative plasmon resonance related dip in the transmission spectrum. When the plasmon resonance related dip is broad, it is difficult to detect the shift in the dip due to a change in the refractive index of the medium around the sensor by a small amount.

A substantially more efficient structure was constructed by using multiple optical elements [1] as shown in Figure 3b. This structure, called structure B, consisted of four optical elements - a single mode fiber as the light input fiber, a graded index fiber as a diverging lens, a coreless fiber as an environmental interaction volume, and a multimode fiber as light collector fiber, that were fused together to form a continuous fiber. Development of this structure enables a Gaussian wave traveling in a single mode fiber to be expanded to the surface of the coreless fiber, thereby allowing interaction of the light wave at the coreless fiber/environment boundary with the nanoparticles at the surface and with the environment. When the Gaussian beam traveling in the coreless optical fiber expands to the surface of the fiber, it folds back into the fiber multiple times, due to total internal reflection. A schematic demonstrating this is shown in Figure 4. The evanescent wave just outside the coreless fiber excites LSP in the gold nanoparticles on the surface of the fiber. The wavelength at which the localized surface plasmon occurs is dependent on the refractive index of the medium surrounding the nanoparticles and this medium can be sensed by monitoring the plasmon resonance related wavelengths for the different media around the fiber.

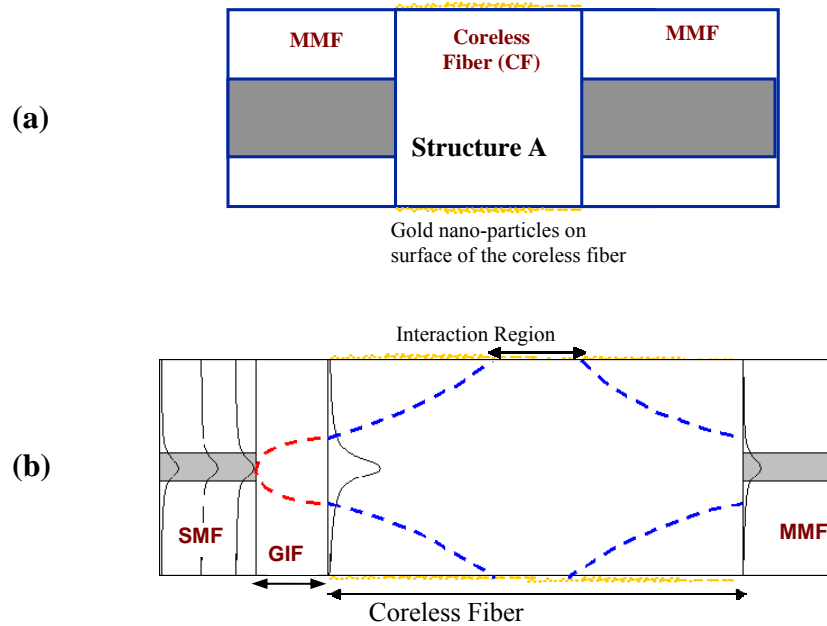


Figure 3. Gold nano-particles are formed on the surface of (a) A fused MMF-CF-MMF structure and (b) A fused SMF-GIF- CF-MMF structure

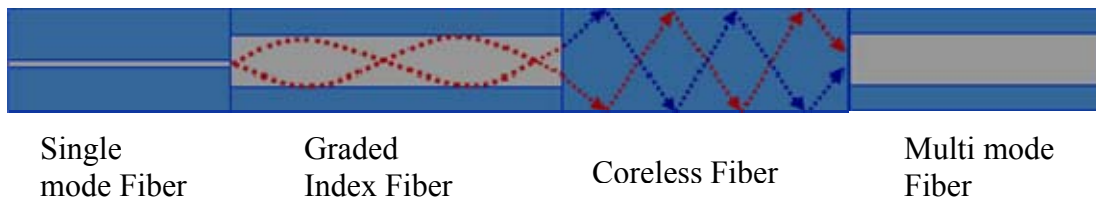


Figure 4. Ray Tracing schematic of Structure B, which is an in-line fiber structure consisting of single mode, graded index, coreless, and multimode fibers to expand the Gaussian beam to the surface of the coreless fiber

5.2 Experimental

5.2.1 Development of nanoparticles

5.2.1.1 Nanoparticle development by annealing of very thin metallic films

In order to form metallic nanoparticles, very thin metallic films (gold or silver) were first deposited on the substrates (glass or sapphire) and subsequently annealed. Two processes were employed for annealing the thin metallic films in order to form nanoparticles from the films – thermal annealing and application of plasma arcs. Thermal annealing of fibers coated with thin metallic films were placed in a homemade micro-coil furnace with the annealing temperature varying between 200-600 °C. In the case of plasma arc annealing, controlled low energy plasma arcs were applied on the thin gold films using a Sumitomo fusion splicer.

The thin metallic films (thickness varying between 4 -10 nm) deposited on the substrates by employing the electron beam (E-beam) deposition process were almost discontinuous in nature. Upon annealing the films, the metal (gold or silver) reflow of the metal takes place thereby forming nanoislands and nanoparticles.

Before developing nanoparticles on the tip or surface of silica-based optical fibers, nanoparticle formation was carried out on planar substrates. Very thin metal films of varying thickness (4 - 10nm) were deposited on planar silica and sapphire substrates. On thermally annealing the thin metal films deposited on these fibers at different temperatures, varying between 250 °C and 600 °C, metal islands and metal nanoparticles were formed on the films. The formation of nanoparticles is indicated by appearance of a reddish film color and a plasmon resonance-related peak in the absorbance spectra, as shown in Figure 5. When absorbance spectra of the annealed gold films was taken in media having different refractive indices, the plasmon resonance-related peak shifted to higher wavelengths, as shown in Figure 5, indicating the applicability of metallic nanoparticles for chemical sensing.

The thin gold films were also deposited on the tip, unclad, coreless, or tapered regions of optical fibers and subsequently annealed. E-beam deposition was employed to deposit the thin metal films and cleaved fibers were mounted on special fiber holders so that their end-face was in the direction of the plume of gold during the E-beam evaporation process. Thus, optical fiber tips with gold films having thicknesses varying between 4 and 10 nm, were obtained. The thin gold films deposited on fiber tips were annealed at different temperatures by employing a micro-coil heated shown in Figure 6. The micro-coil heater consisted of a high-resistance wire element

wound around a hollow ceramic tube. Temperature inside the hollow ceramic tube was controlled by resistive heating of the coil upon varying the current in the coil from 0.2 A to 2.6 A. A thermocouple was placed inside the hollow tube to measure the temperature inside the tube as the current in the coil was varied. The fiber tip, with a thin gold film (4-10 nm) on its surface was annealed by placing the fiber inside the micro-coil heater for times varying between 10-30 min. Upon annealing, the transmission spectrum showed a plasmon resonance related dip, as shown in Figure 7, which indicates the development of gold nanoparticles on the tip of the fibers.

The annealing of the gold films was also carried out using controlled, low-intensity plasma arcs. A fusion splicer was used to arc-anneal the gold-coated fiber tips, as shown in Figure 8. It was observed that the plasmon resonance related dip in transmission spectra appeared upon arcing, as shown in Figure 9, and that the dip become sharper and moved to lower wavelengths as the number of applied arcs was increased. A combination of thermal and arc annealing processes was also employed and the thin gold films on fiber tips were first thermally annealed and subsequently plasma arc annealed. It was observed that very sharp plasmon resonance related dips could be obtained by following this procedure and also that the dip moved to a lower wavelength, as shown in Figure 10. This could be attributed to a change in size or shape of nanoparticles when subsequent plasma arcs were applied.

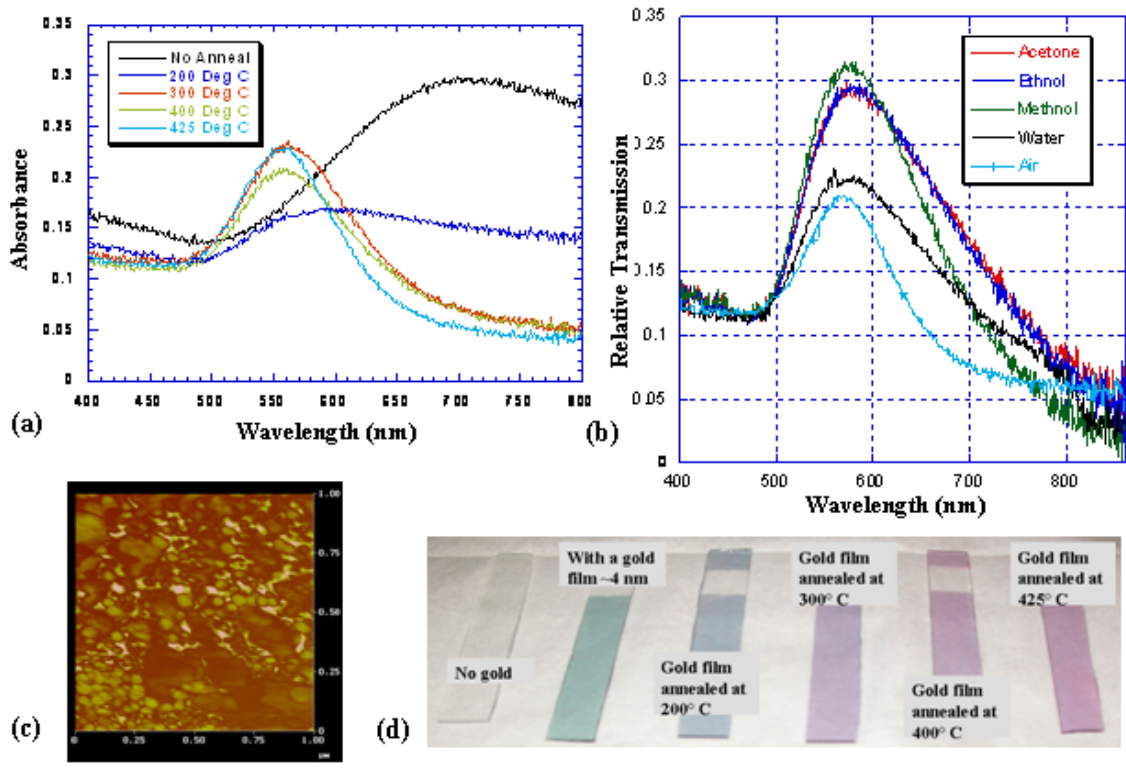


Figure 5. (a) Absorbance vs. wavelength plot for annealed and unannealed, 4-10 nm thick gold films on a glass substrate, (b) Plasmon resonance related peak shifts when placed in media having different refractive indices, (c) AFM picture of an annealed gold film deposited on a glass substrate after annealing at 400 Deg C, and (d) Change of color of the gold films upon annealing at different temperatures

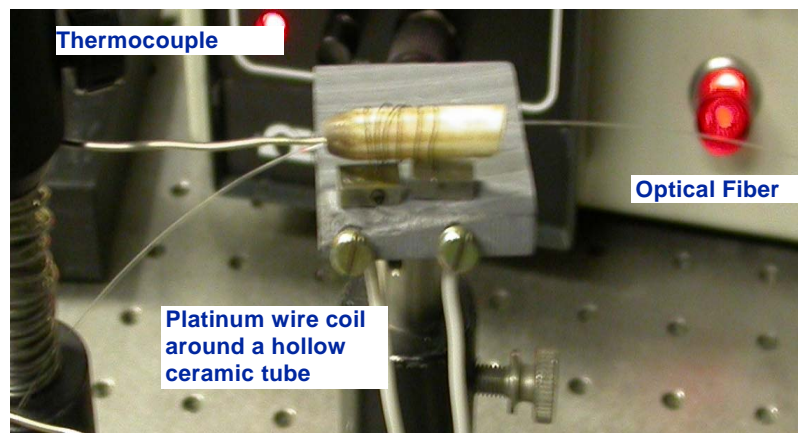


Figure 6. (a) Micro-heater used for annealing gold films on fiber tips to form nanoparticles

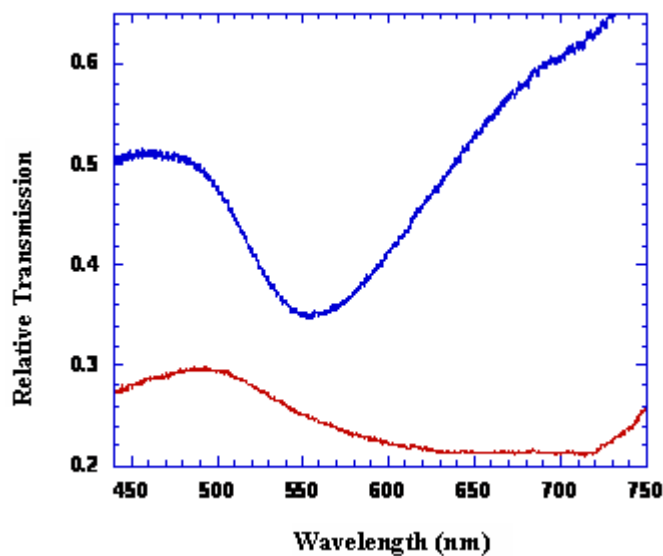


Figure 7. Effect of annealing on transmission spectra of thin gold film on fiber tips before (red) and after (blue) annealing

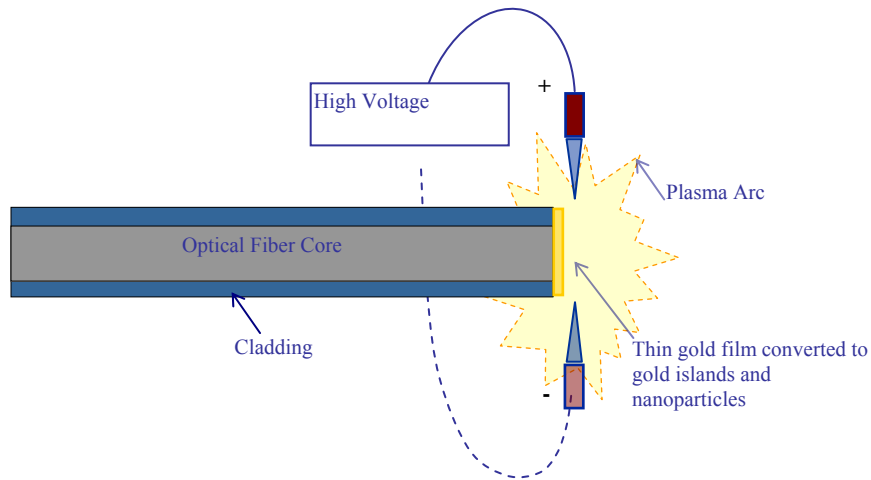


Figure 8. Plasma arc annealing of 4-10 nm gold film on the optical fiber tip using a fusion splicer

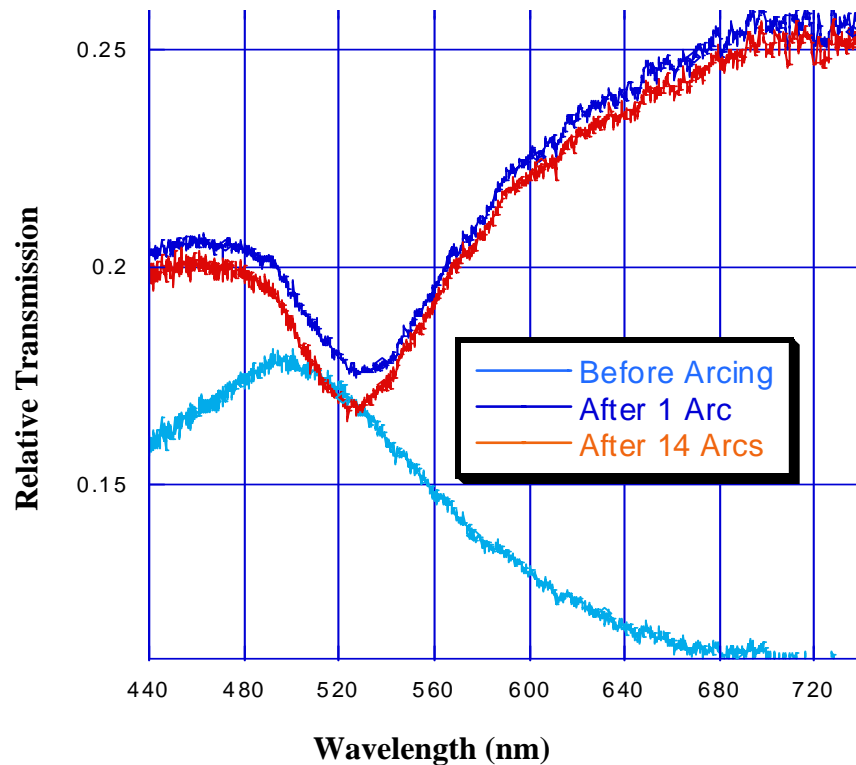


Figure 9. (a) Appearance of a plasmon resonance related dip in the transmission spectra upon application of plasma arcs to a gold coated (8 nm) fiber tip, (b) Plasmon resonance related dip becomes sharper when both thermal annealing and plasma arc are applied to the fiber tip

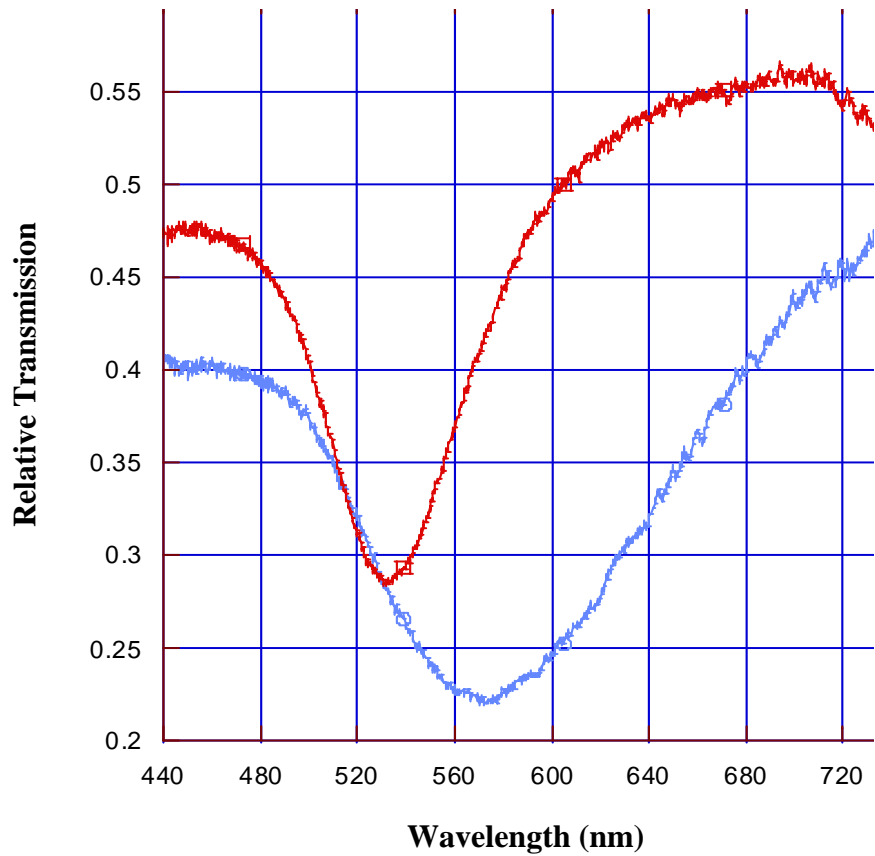


Figure 10. (a) Appearance of a plasmon resonance related dip in the transmission spectra upon application of plasma arcs to a gold coated (8 nm) fiber tip as shown by the blue curve, (b) Plasmon resonance related dip becomes sharper when both thermal annealing and plasma arc are applied to the fiber tip, as shown by the red curve

5.2.1.2 Formation of nanoparticles using citrate reduction

Chemical synthesis of gold nanoparticles was also carried out by citrate reduction of sodium tetrachloro aurate [2]. Employing this process for nanoparticle formation can potentially allow better control of nanoparticle size as compared with annealing of thin gold films. However, the application of the colloidal nanoparticles is not as straightforward as it is for physical deposition methods.

The process of forming gold nanoparticles and attaching them to the tip of the optical fibers is described in Figure 11. In order to form gold nanoparticles, 100 ml of 0.254 mM aqueous solution of sodium tetrachloro aurate was taken and heated to 95° C in a beaker. 1 - 3 ml of 33.3 mM aqueous solution of sodium citrate was added to the beaker, while stirring the solution in the beaker for 10 minutes. Then the solution was taken off of the heater and cooled to room temperature. It was observed that the color of the solution changed to red, pink, or purple depending on the volume of sodium citrate added. This is because of the different average nanoparticle sizes obtained, resulting in different nanoparticle related plasmon resonances, on varying the molar ratio of sodium citrate to sodium tetrachloro aurate by varying the volume of sodium citrate (1 - 3 ml) added to the 100 ml sodium tetrachloro aurate solution. Nanoparticle suspensions of different colors obtained by this process were stored in different closed glass containers at 4° C. Storage of the nanoparticle suspensions at cold temperatures prevents aggregation of the nanoparticles to form particles of larger size. These suspensions remained stable for days in the cold storage and were taken out of the cold storage only when they had to be deposited on a substrate.

In order to attach the gold nanoparticles to the surface or tip of the optical fibers, the SiO₂ surface of the glass was modified by treating it with a solution of APTMS (3-aminopropyltrimethoxysilane) in ethanol. Before the attachment of the gold nanoparticles, the surface of the sensor region of the optical fibers was cleaned with a Pirhana solution a solution containing 30 % hydrogen peroxide and sulphuric acid in the ratio 1:3. After cleaning the fiber sensor region, the tip of the fibers, in case of tip-based fiber sensors, were dipped in a 10% v/v solution of APTMS in ethanol to form a monolayer of APTMS on the surface of the fiber tip. The modified fiber tips were rinsed with deionized water, dried with nitrogen, and then placed in an aqueous solution containing nanoparticles of a given color which was used to estimate the average particle size for around 20 minutes. Optical transmission spectra, of white light through

the optical fibers containing nanoparticles on their tips, was measured by using a SpectraPro®-500 spectrograph having a Spectradrive stepping motor scan controller and is shown in Figure 12. In Figure 12, one can observe a plasmon resonance related dip in the transmission spectrum at a wavelength of ~ 530 nm.

This process also enabled attachment of nanoparticles to the surface of fiber tips or the inline fiber optic structures described in chapter 4 without disturbing the measurement setup employed to evaluate the fibers. In the case of tip-based or the inline fiber sensors, the reference transmission signal through the sensor fibers, with the surface of the sensor regions of the optical fibers modified with APTMS as described above, was measured by employing a white light

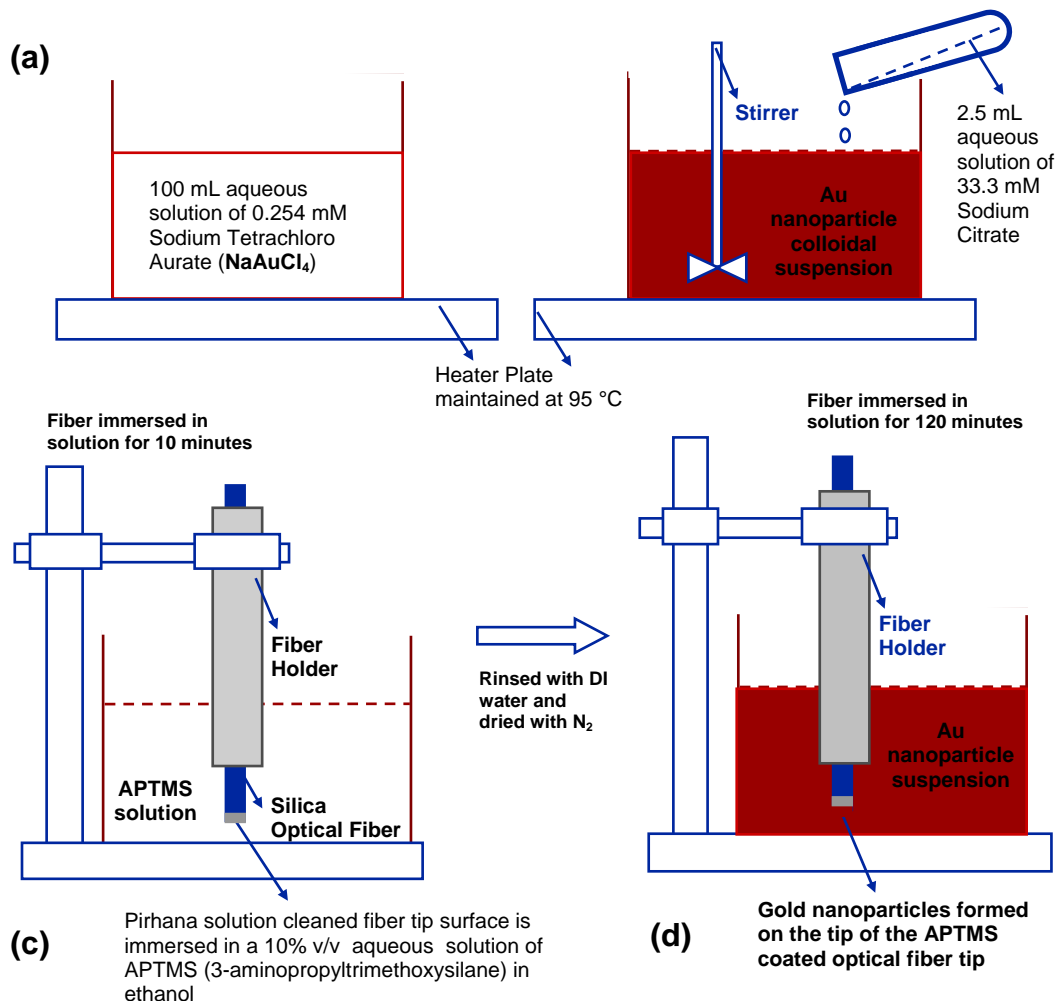


Figure 11. Citrate reduction process to form gold nanoparticles (~ 20 - 120 nm) on the tip of the optical fiber

source and then a suspension containing gold nanoparticles can be dropped on the sensor region of the optical fiber such that the particles would adhere to the fiber surface without moving the optical fibers or the alignment in the measurement setup. This enables a very accurate measurement of the reference signal as the fiber alignment and bending is kept the same for the case of the fibers with and without nanoparticles on their surface. After the nanoparticles are attached to the optical fiber surface, the fluids to be sensed were flowed into a fluid chamber surrounding the sensor region of the optical fiber.

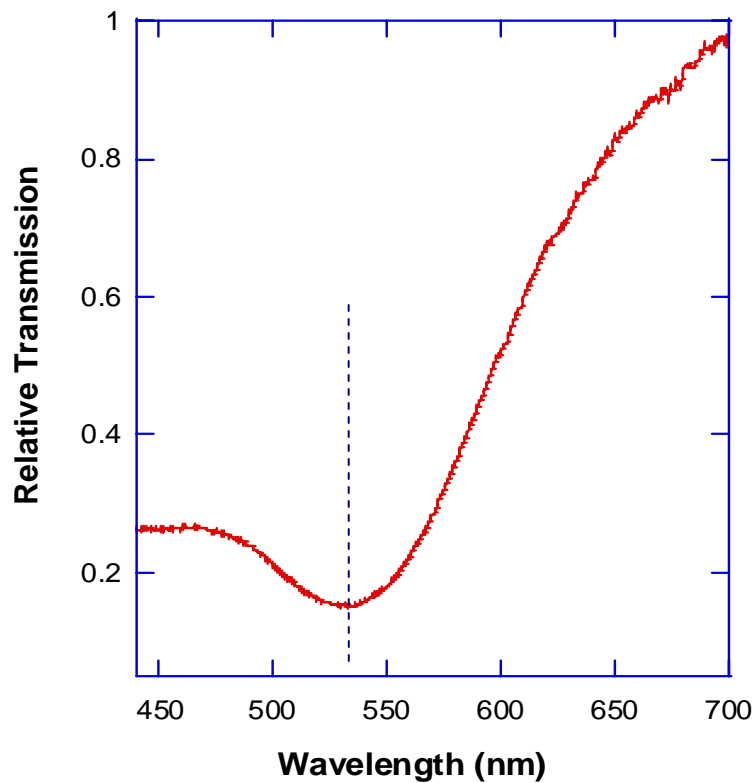


Figure 12. Transmission spectrum of an optical fiber having gold nanoparticles (~ 20 - 120 nm), formed by citrate reduction, deposited on its tip

5.2.1.3 Development of metallic nanoparticles using Focussed Ion Beam Milling (FIB)

In order to form metallic nanoparticles, nanorods, and nano-sized islands on optical fibers in a more controlled manner as compared to the processes described in sections 5.2.1.1 – 5.2.1.3, these nanostructures were formed by employing focused ion beam lithography to either pattern out the metallic nanoparticles and nanorods or to anneal a thin metallic films to form metal islands.

In order to form gold nanoparticles and nanorods on optical fiber tips, 50 and 100 nm gold films were deposited on the tip of step-index multimode and graded-index silica optical fibers by employing electron-beam (E-beam) evaporation. An electron beam, with a current varying between 75 and 85 mA, was directed towards a crucible containing gold slugs, and gold particles evaporated from the slugs were deposited on the tip of the optical fibers. The optical fibers were positioned such that their tips faced the plume of evaporated gold particles emanating from the crucible. The thickness of the film deposited on the fibers was measured by a quartz crystal monitor. The multimode optical fibers employed in this work were F-MLD fibers obtained from Newport Corporation with a 100 μm core and a 140 μm cladding diameter. The graded index fibers employed in this work were obtained from 3 M Corporation and had a 62.5 μm core and a 125 μm cladding diameter. The single mode and four mode fibers employed in this work had core diameters of 4 μm and 8 μm respectively, with the cladding diameter being 125 μm for both types of the fibers. The single mode fibers were obtained from 3 M Corporation and the four mode fibers were obtained from Corning Corporation. Before depositing the gold films on the fiber tips, ends of the optical fibers were cleaved using a diamond cleaver. A fiber holder made from brass was employed to hold the fibers during the deposition process in a manner that the fiber tips remained normal to the direction of the plume. The evaporation of gold was carried out at a rate varying between 0.08 nm s^{-1} and 0.14 nm s^{-1} at a chamber pressure of 2.7×10^{-6} Torr. In order to deposit gold in a uniform manner, the sample holder was rotated during the electron-beam evaporation process. Planar glass substrates were also placed right next to the optical fibers so as to accurately monitor the thickness of the gold film deposited on the fiber tip. A Dektak proflometer was employed after the deposition to monitor thickness of the film deposited on the glass and the results were compared with the value from the quartz monitor.

In order to form an ordered array of nanoparticles and nanorods on the tip of the optical fiber, Focused Ion Beam (FIB) milling was employed. A Hitachi D3100 Focus Ion Beam (FIB)

milling machine with a Gallium ion source normally used for transmission electron micrograph sample preparation was used to pattern the gold films on the fiber tips. Typical Gallium ion beam parameters were 40 keV, 0.01 nanoAmps at a magnification of 8000 times. The instrument is equipped with software and a beam blanker that accepts a 512 by 512 image file with 8 bit grayscale, that allow the desired pattern to be milled by rastering the ion beam and controlling the duration and beam current appropriately.

A special fiber mount, that could be attached to the sample mount in the Hitachi D3100 equipment, was developed in order to hold the gold-coated fiber tip in place during the FIB process. Figures 13 and 14 show periodic arrays of circular and triangular nanoparticles respectively, formed on the surface of a planar glass substrate by employing focused ion beam lithography. SEM micrograph of a multimode optical fiber, with an array of elliptical nanoparticles on its tip, is shown in Figures 15. FIB can also be employed to anneal gold films deposited on the tips of optical fibers to form nano-sized gold islands in a more controllable manner. 50 and 100 nm thick gold films were deposited on single and multimode optical fibers and FIB, with beam currents varying between 0.1 and 0.7 nA, was employed to form gold nanoislands on the fiber tip as shown in Figures 16 and 17. The control of beam current as well as the focused nature of the beam allows FIBL to be an effective means of forming gold nanoislands. Transmission spectrum, with a dip that can be attributed to plasmon resonances of the gold nanoislands, is shown in Figure 16b.

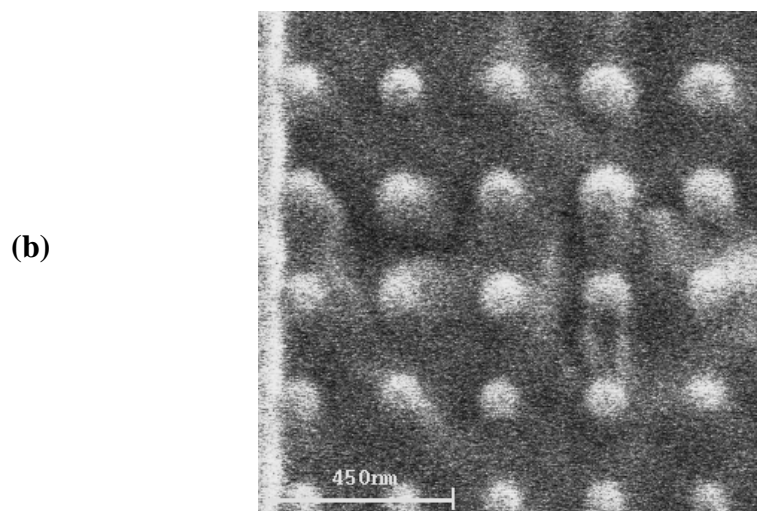
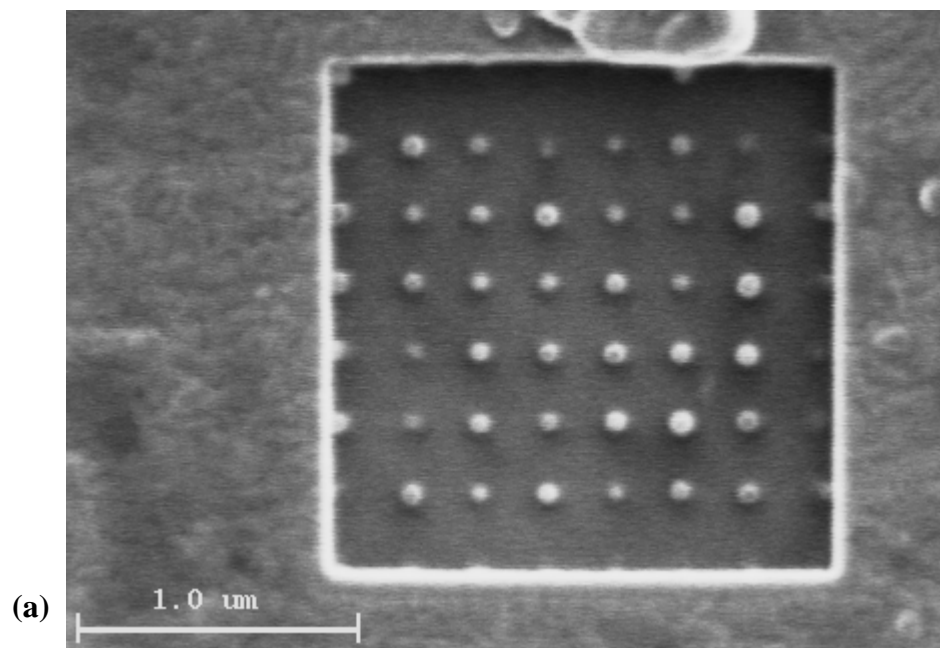


Figure 13. Development of circular gold nanoparticles on a glass substrate by employing Focussed Ion Beam lithography (FIBL). FIBL was applied to a 50 nm gold film on a glass substrate to pattern the array of these nanostructures. The diameter of the nanostructures was measured as (a) ~ 80 nm and (b) ~ 100 nm

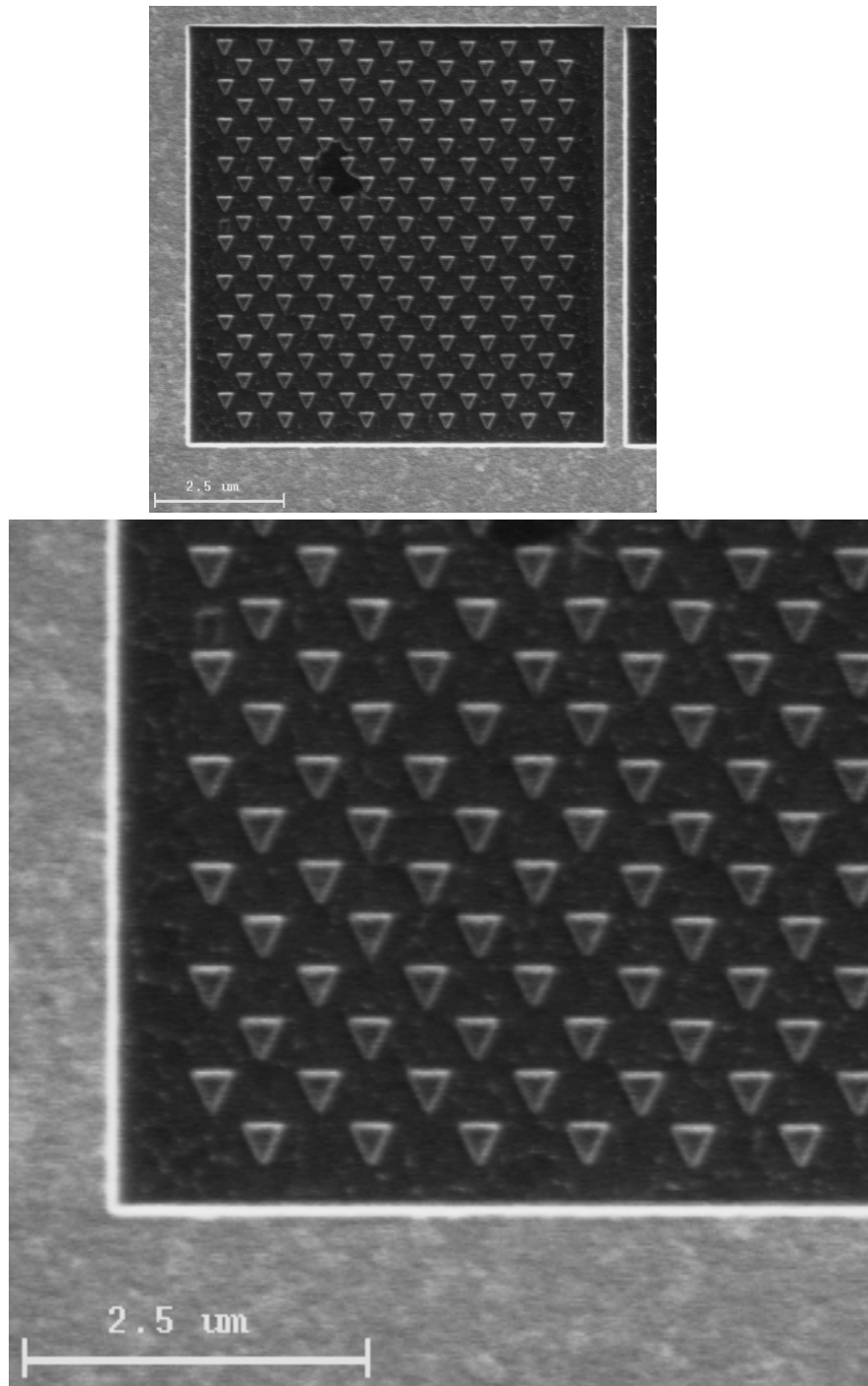
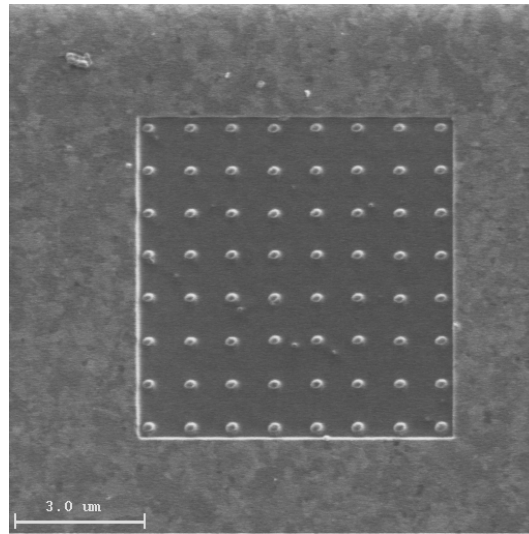


Figure 14. Development of triangular gold nanoparticles on a glass substrate by employing Focussed Ion Beam lithography (FIBL). FIBL was applied to a 50 nm gold film on a glass substrate to pattern the array of these nanostructures

(a)



(b)

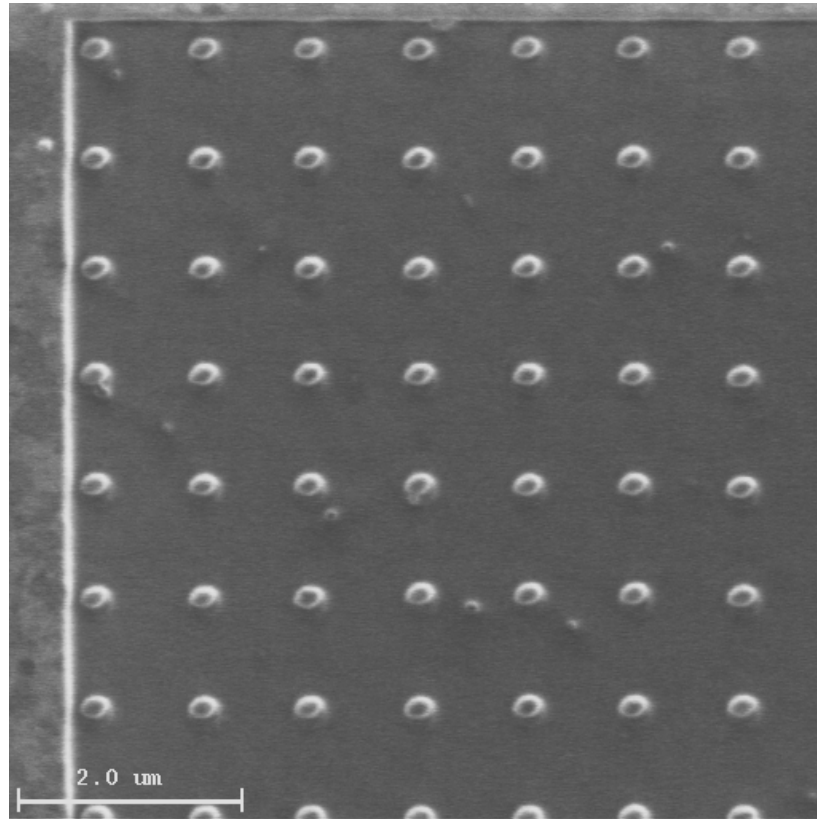


Figure 15. Development of elliptical gold nanoparticles on the tip of a multimode optical fiber by employing Focussed Ion Beam lithography (FIBL). FIBL was applied to a 50 nm gold film deposited on the tip of the optical fiber. The long axis of the nanostructures was measured to be ~ 250 nm while the short axis was ~ 150 nm

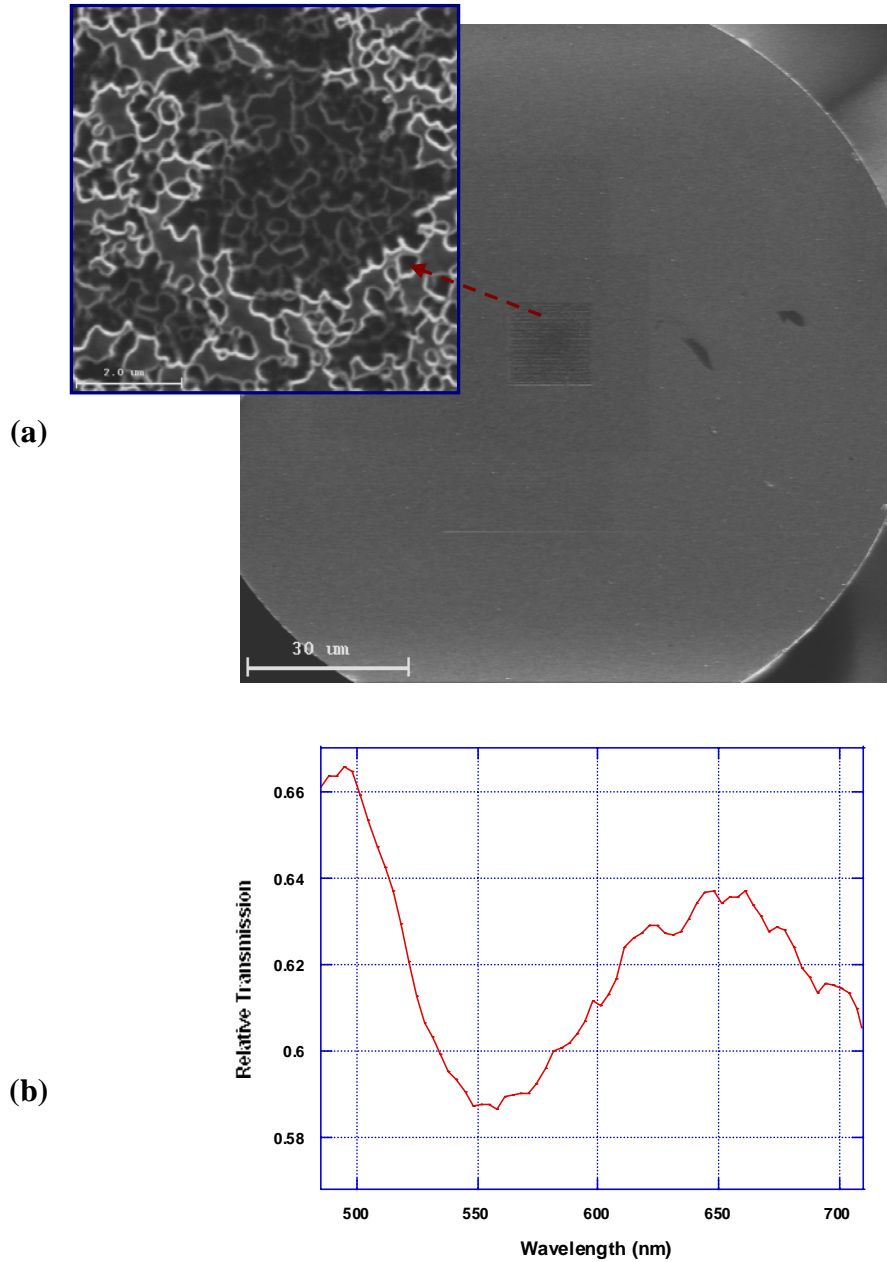


Figure 16. (a) Development of gold nanoislands on the tip of a multimode optical fiber by employing Focussed Ion Beam lithography (FIBL). FIBL was applied to a 100 nm gold film deposited on the tip of the optical fiber, and (b) Relative transmission spectrum of a multimode fiber with gold nanoislands on the tip

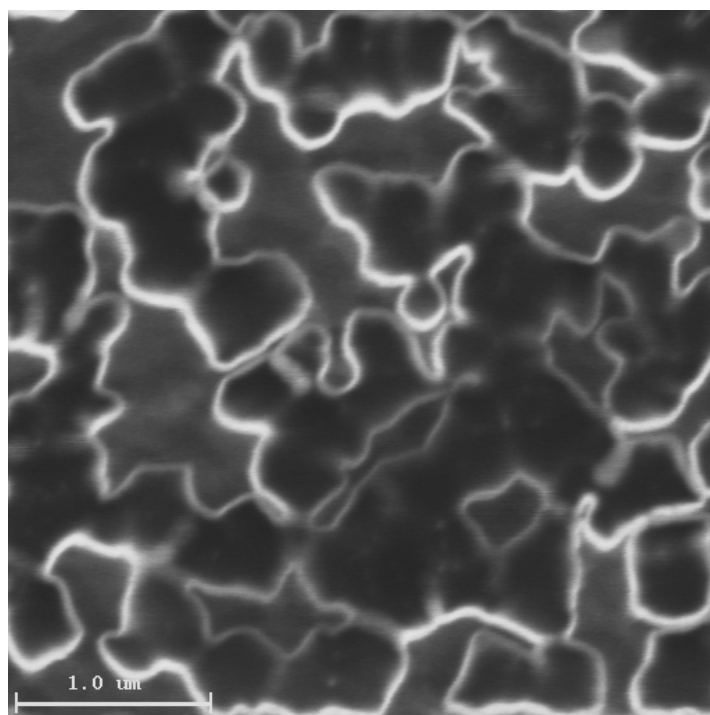
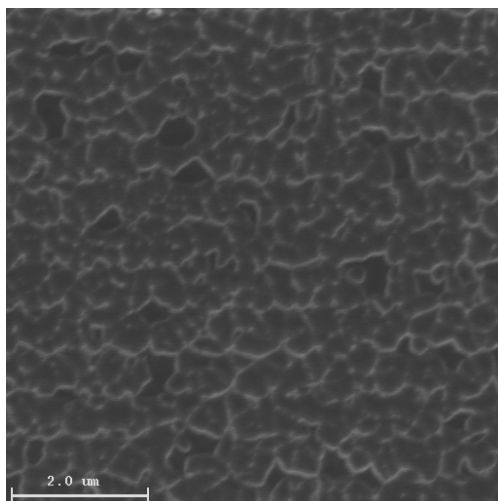


Figure 17. Development of gold nano-islands on the tip of a multimode optical fiber by employing Focussed Ion Beam lithography (FIBL). FIBL was applied to a 100 nm gold film deposited on the tip of the optical fiber

5.2.2 Development and evaluation of the sensor structures

The sensor shown in Figure 1a was developed by stripping and cleaving F-MLD multimode fibers obtained from Newport Corporation with a 100 μm core and a 140 μm cladding diameter and then evaporating a very thin gold film (4-8 nm) on the fiber tips. Electron-beam evaporation process was employed for carrying out the gold film depositions. An electron beam, with a current varying between 65 and 85 mA, was directed towards a crucible containing gold slugs, and thickness of the film deposited on the fibers was measured by a quartz crystal monitor. Optical fibers were attached to the electron beam substrate holder by employing a fiber holder made from a thick aluminum foil. The evaporation of gold was carried out at a chamber pressure of 3×10^{-6} Torr. In order to form nanoparticles, the thin gold films deposited on fiber tips were annealed using the different procedures described in section 5.2.1. Thermal annealing of the nanoparticles was carried out by employing a micro-coil heater as described earlier in section 5.2.1.1. The annealing of the gold films was also carried out using controlled, low-intensity plasma arcs using a Sumitomo Electric fusion splicer as described earlier in section 5.2.1. In order to evaluate the fiber tip based sensor in transmission mode, a sensor arrangement was developed by placing the nanoparticle-containing fiber and the collector fiber inside a V-groove etched in a silicon piece, of a size smaller than a dime. The arrangement, held together by two small magnets on top of the fibers and a metal piece below the silicon piece, was dipped in different fluids to measure the response of the sensor to change in refractive indices.

The fiber taper structure shown in Figure 1b was developed by using the Sumitomo fusion splicer. Commercial software was employed to pull the optical fiber clamps at a precise rate as a controlled plasma arc was applied to develop the fiber taper.

The sensor structure described in Figure 1a was evaluated for its sensing capability by inserting the fiber holder, with the sensor and collector fibers held in place as shown in Figure 2, into several mediums having refractive indices higher than that of air such as water, methanol, and ethanol. Optical transmission, of white light through the fiber sensors, was measured by using a SpectraPro®-500 spectrograph having a Spectradrive stepping motor scan controller.

In order to form the inline structure A, a multimode fiber was fusion spliced to a cleaved end of a coreless fiber. The coreless fiber was then cleaved after a length of 35.3 mm using a diamond scribe and pull assembly developed by us. The cleaved end of the coreless fiber was fusion spliced to another multimode fiber, which served as the collector fiber. The length of the

coreless fiber was determined by employing calculations that are described by Dhawan et al. [1] and in chapter 4. A schematic showing application of an optical fiber structure, such as structure A, for chemical sensing is shown in Figure 18. The composite fiber structure B, based on the calculations described by Dhawan et al. [1], was developed by first fusing GIF1 to SMF1 using a fusion splicer. The first graded index fiber, i.e. GIF1, was cleaved at approximately 1622 μm length by using a microscope setup and a diamond scribe. Then a coreless fiber was fused and then cleaved at an appropriate length. This length depended on the desired level of interaction of the propagating light with the environment and varied between 17.6 mm and 35.3 mm. A multimode fiber was then fused to the SMF1-GIF1-CLF arrangement. 8 nm gold films were then deposited on the surface of the coreless fiber segments of structures A and B and annealed at 330 $^{\circ}\text{C}$ for 10 minutes forming nanoscale gold islands and nanoparticles on the surface of the coreless fiber. The sensor structures A and B were evaluated for their sensing capability by inserting the in-line fiber sensors into several mediums having refractive indices higher than that of air such as water, methanol, and ethanol. Optical transmission, of white light through the in-line fiber sensors, was measured by using the spectrometer described above. Similarly, silver nanoparticles were formed on the tips of optical fibers by depositing a 4 nm film of silver on the tip of multimode fibers, obtained from Newport and having a cladding diameter of 140 μm and the core diameter of 100 μm , by employing electron beam evaporation and by annealing the film using plasma arcs to form silver nano-islands on the tip of the optical fiber.

5.3 Results and Discussion

Absorbance spectrum of a fiber tip-based sensor, formed by thermal annealing of an 8 nm gold coated fiber fiber tip, is shown in Figure 19. It was observed that in air, the position of the plasmon resonance related peak was ~ 530 nm. When de-ionized water (DI) was inserted into the fiber sensor chamber shown in Figure 18, the peak position shifted to ~ 542 nm - a shift of approximately 13 nm corresponding to a change of refractive index of 0.33, implying that that value of change in peak wavelength per unit change in refractive index (RIU) was ~ 40 nm/RIU. The transmission spectrum of a fiber tip-based sensor, formed by plasma arc annealing of a gold coated fiber tip, is shown in Figure 20. It was observed that in air, the position of the plasmon resonance related dip was ~ 526 nm. In methanol, having a refractive index of 1.33, the plasmon resonance related dip moved to 541 nm and when it was placed in acetone, having a refractive

index of 1.36, the plasmon resonance related dip moved to 545 nm, showing a dip wavelength shift of 4 nm for a 0.03 shift in the refractive index indicating a sensitivity of ~ 133 nm/RIU. The position of the plasmon resonance related dip in the transmission spectra when the medium surrounding the sensor was water was 540.4, a position similar to that for methanol. One has to note the refractive indices of methanol and DI water are 1.33 and 1.329 respectively. The transmission spectrum of a fiber tip-based sensor, formed by a combination of thermal and plasma arc annealing of an 8 nm gold coated fiber tip, is shown in Figure 21. It was observed that in air, the position of the plasmon resonance related dip was ~ 535 nm and it moved to ~ 547.5 nm when the medium surrounding the fiber tip was changed to water. One can observe in Figure 21 that the dips in the transmission spectra are sharper as compared with the sensors shown in Figures 19 and 20, indicating that it is easier to detect the resonance shifts on varying the refractive index of the media surrounding the optical fiber sensors.

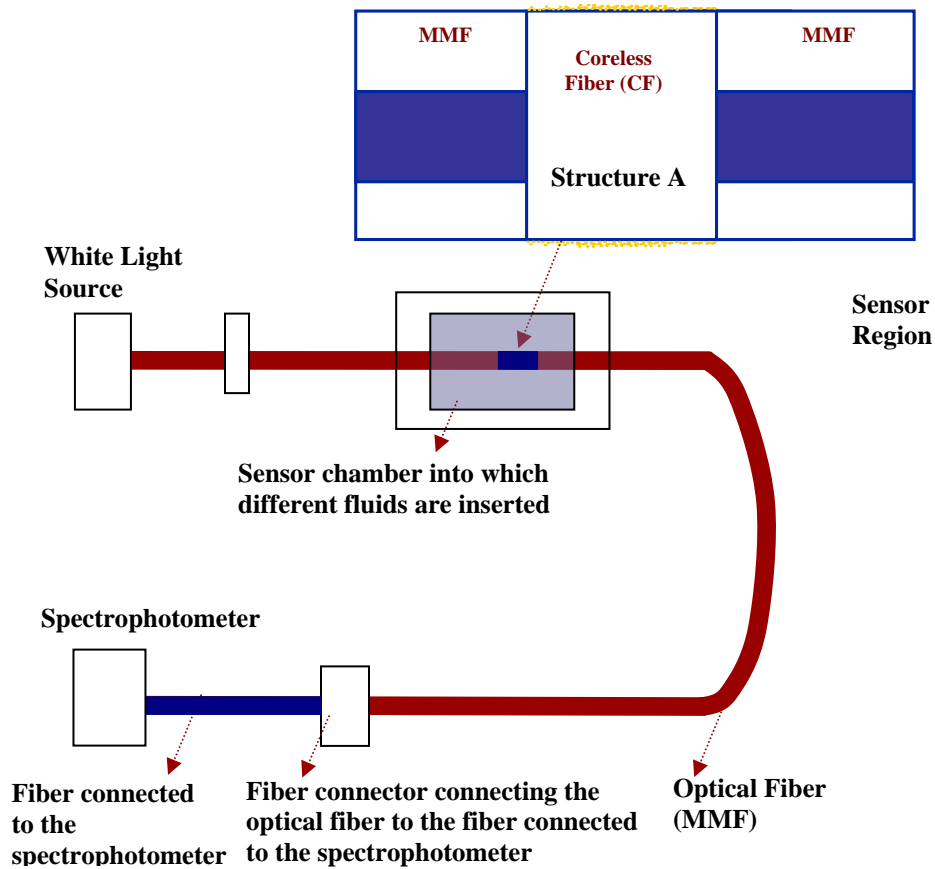


Figure 18. Schematic showing a measurement set-up for an in-line fiber optic sensor, where the sensor region consists of a nanoparticle-coated coreless fiber

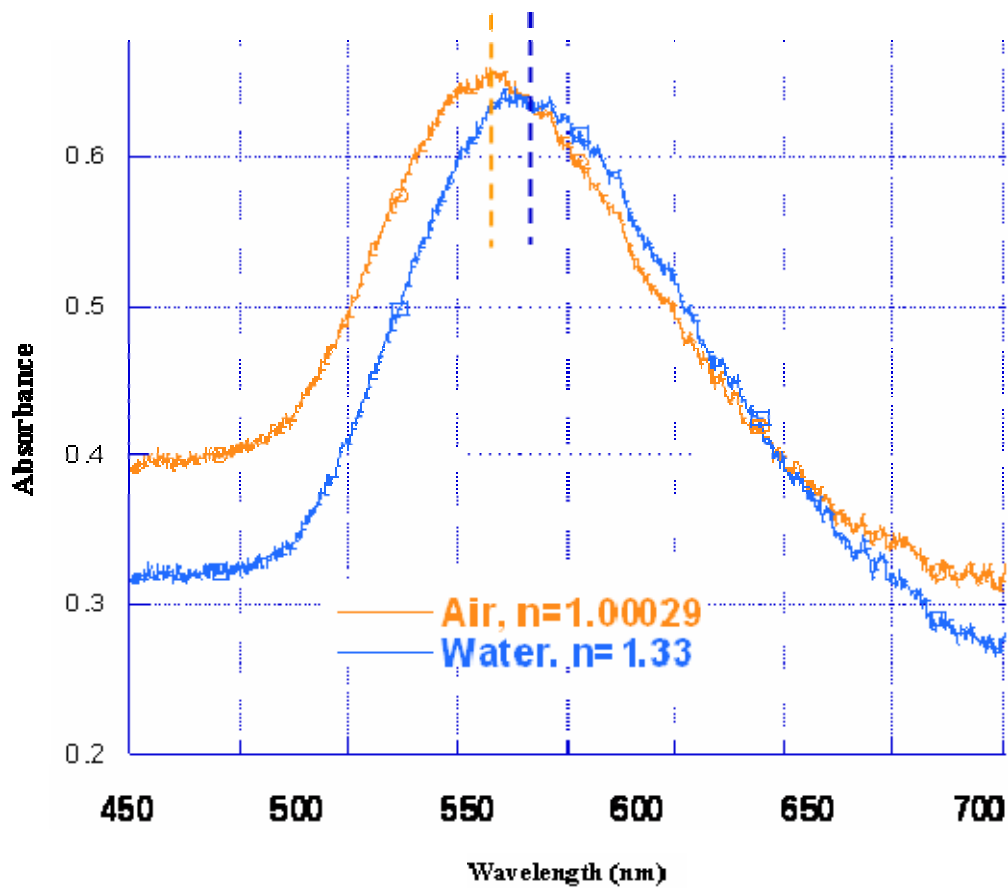


Figure 19. Shift in absorbance spectra when a fiber tip containing gold nano-particles, formed by thermal annealing, is placed in water

Although the fiber tip based sensors are fairly sensitive, they have to be precisely aligned under a microscope before they are used. Moreover, stress applied to either the sensor or the collector fiber could cause the alignment of the fiber tips to be changed.

Optical transmission spectrum of the two nanoparticle coated in-line fiber structures, i.e. structures A and B, showed a plasmon resonance related dip indicating the formation of nanoparticles on the fiber surface, see Figure 22. When the sensor fibers were dipped in water (a change of refractive index of ~ 0.33 as compared to air) and media of a refractive index higher than air, there was a shift in the spectral position of the plasmon resonance related dip towards higher wavelengths. The spectral response of a sensor formed by using structure B is shown in Figure 22. When the structure B based sensor was inserted in water, a peak shift of 42 nanometers per refractive index unit was obtained. In the case of structure A, a peak shift between 80-120 nanometers per refractive index unit was obtained for different samples that were prepared under similar conditions. The shift in the resonance related dip for structure A was higher than that for structure B but the plasmon resonance related dip was very broad for structure A. Hence, the peak position could not be as accurately determined for the structure A sensor as compared with the structure B sensor.

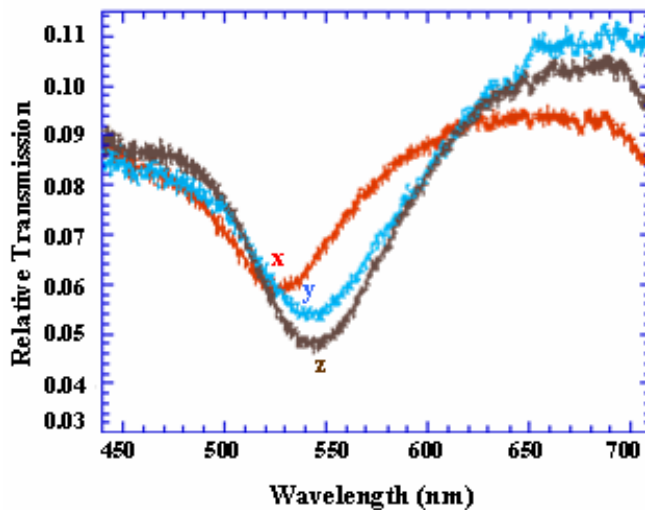


Figure 20. Shift in transmission spectrum when a fiber tip containing gold nanoparticles, formed by plasma arc annealing, is placed in air with refractive index ~ 1 (x), in methanol with refractive index ~ 1.33 (y), and acetone with refractive index ~ 1.36 (z)

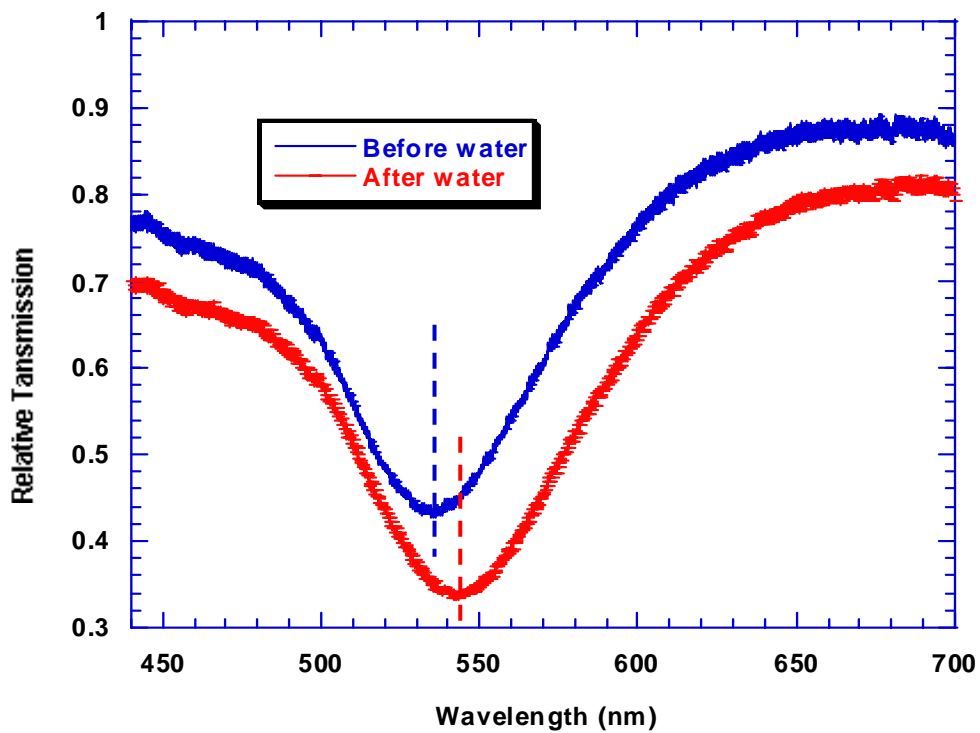


Figure 21. Shift in transmission spectrum when a fiber tip containing gold nanoparticles, formed by a combination of thermal annealing and plasma arcing, is placed in water

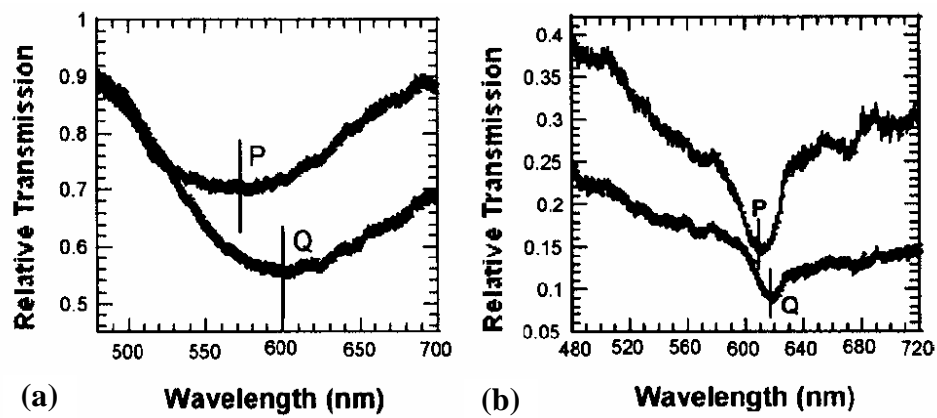


Figure 22. Shift in plasmon-resonance related dip when (a) fused MMF-CF-MMF structure and (b) fused SMF-GIF-CF-GIF-MMF fibers with gold nanoparticles formed on the coreless section of the fibers, were placed in water (Plot Q) as compared with when it was in air (Plot P) [1]

5.4 Optical fiber sensors for sensing of biomolecules

A conventional surface plasmon biosensor, as shown in Figure 23a, employs a Kretschmann configuration in which a prism is used to couple light to a thin gold film on its surface [3-6]. This enables excitation of surface plasmons on the surface of the gold film [3-6]. As the angle of incident light is changed, for a fixed wavelength of incident light, a dip in the reflection spectrum appears at an angle when the condition for surface plasmon resonance (SPR) is satisfied. When the refractive index of the medium above the gold film changes, the position of the dip changes as the condition for surface plasmon resonance is satisfied at a different angle of incidence for the new refractive index of the medium above the gold film. This change in the refractive index next to the gold film could be due to attachment of certain biomolecules to binding sites located on the surface of the gold film. Figures 23a and b show the attachment of protein molecules to protein binding sites on the gold film thereby causing a change in the angle at which the plasmon resonance related dip in the reflectance spectrum occurs. Similarly, if the angle of incidence is maintained the same and the wavelength of the incident light is varied, a dip in the reflection spectrum appears at a wavelength when the SPR condition is met. In this work, localized surface plasmon (LSP) resonance based on scattering and absorption of light by metallic nanoparticles and islands on the surface of optical fiber structures is employed for the detection and sensing of biomolecules.

The Biotin/Streptavidin system was chosen for initial studies since it has a large free energy of association [7], and is stable under reasonable temperatures and pH ranges. Since it is also used as a test system, it permits sensing results to be compared with other sensor systems. The Biotin molecule works well with gold via thiol bonding and the Streptavidin molecule can also be designed to be selectively receptive to a variety of other molecules, toxins or proteins. Monitoring the binding response over time also allows reaction kinetics, and concentrations to be determined.

In order to carry out measurements for sensing biomolecules, Biotin-HPDP ((N-(6-(Biotinamido)hexyl)-3'-(2'-pyridyldithio)-propionamide) was obtained from Pierce Biotechnology. It was attached to gold nanoparticles on the surface of the in-line sensor fibers and the fiber tips by first reducing the Biotin-HPDP using a reducing agent Dithiothreitol to form free thiol groups that are available for attachment to the gold nanoparticles. Streptavidin, obtained from the bacteria *Streptomyces Avidinii*, was obtained from Sigma Aldrich. In order to

form the Biotin-HPDP solution, 1 mg of Biotin-HPDP was dissolved in 100 ul of DMSO to get a concentration of 10 mg/ml. A solution of Dithiothreitol was separately prepared and 100 ul of that solution was added to the Biotin-HPDP solution to get a net Dithiothreitol concentration of 50 mM. After around 4 minutes the disulfide bond in the Biotin-HPDP is reduced by the reducing agent and the solution turns yellow in color. Fiber tip sensors and the in-line fiber optic sensors were immersed in a 2 ml mixture of water and methanol (1:1) in a small boat-shaped fluid cell. The reduced Biotin-HPDP solution was then added to the water-methanol mixture. Right after the reduced Biotin solution was added to the solution containing the sensor, optical transmission as a function of time, of white light through the fiber-tip and in-line fiber sensors, was measured by using a spectrometer. Biotin-HPDP was allowed to react with the gold nanoparticles for upto 2 hours and a transmission spectrum through the fiber sensors was taken every minute. After binding of the thiol group of the reduced Biotin-HPDP with the gold nanoparticles is complete, a wash buffer (a dilute PBS buffer solution with a pH of 7.2) was flowed into the fluid cell to wash away the Biotin-HPDP that is not bonded to the gold nanoparticles. Then, a solution of Streptavidin was made by dissolving 0.15 mg of Streptavidin in 150 ul of 7.2 pH PBS buffer solution. This solution was then added to the fluid cell with the fiber sensors so as to surround the fiber sensors completely. Right after the Streptavidin solution was added to the fluid cell holding the fiber sensor, optical transmission of white light through the fiber-tip and in-line fiber sensors was measured by using a spectrometer. Streptavidin molecules were allowed to react with the Biotin molecules that were in turn bound to the gold nanoparticles via the thiol bond, for upto 4 hours and a transmission spectrum through the fiber sensors was taken every 5 minutes.

The fiber tip sensor, employed in the transmission mode, and the inline fiber optic structures were also employed for affinity sensing of biomolecules such as Biotin and Streptavidin. The chemical bond between Biotin and Streptavidin is extremely strong with a large free energy of association. Figure 24 shows a schematic explaining the binding mechanism of Biotin-HPDP to gold nanoparticles. When the reducing agent Dithiothreitol breaks the disulfide bond in Biotin-HPDP, the free thiol (-SH) group of Biotin-HPDP attaches to the gold molecule. As Biotin has a high affinity for Streptavidin, one can chemically conjugate different biological molecules such as antibodies to Streptavidin and then react the Streptavidin with the Biotin. An example of such an antibody that can be chemically conjugated to Streptavidin is Immunoglobulin IgG, as shown

in Figures 24a - c. Thus an affinity sensor, that can specifically sense the presence of antigens such as anti-IgG, can be developed. The Streptavidin molecule can be modified, via conjugation to other biomolecules, to make it selectively receptive to a variety of other molecules, toxins and proteins. Thus Biotin-Streptavidin based optical sensing systems can not only sense the concentration of biological agents and contaminants, they can also study the chemical kinetics of the different reactions taking place in the environment being sensed. Shift in plasmon resonance related dip wavelength, upon the addition of Biotin to a fluid cell containing the in-line sensor based on structure A, is shown in Figure 25. The spectral readings were taken every minute after the addition of Biotin to the fluid cell. It can be seen that there was no shift in the plasmon resonance related dip position after 4 minutes. Subsequently, the response of Streptavidin addition to the Biotin coated fiber sensor was evaluated. Value of the wavelength, at which the plasmon resonance-related dip occurs, was plotted vs. time for the in-line fiber optic biosensor and is shown in Figure 25b. Development of biosensors on in-line optical fiber structures can enable continuous online monitoring of biological agents present in the environment around the sensors. These fiber sensors can be conveniently inserted into water filtration systems to sense the presence of harmful agents or contaminants.

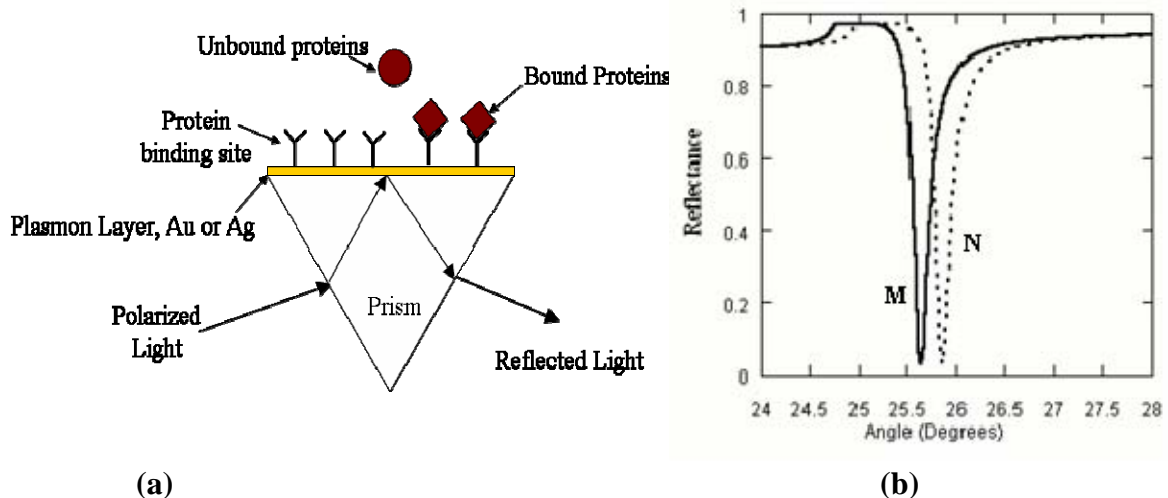


Figure 23. (a) Prism configuration for detecting refractive index change due to protein binding and (B) Shift in plasmon resonance angle at a given wavelength is employed to sense presence or concentration of chemical and biological molecules; Refractive index of the medium above the gold film changes when biomolecules, e.g. proteins, bind to the binding sites (curve N) as compared to the case with no binding

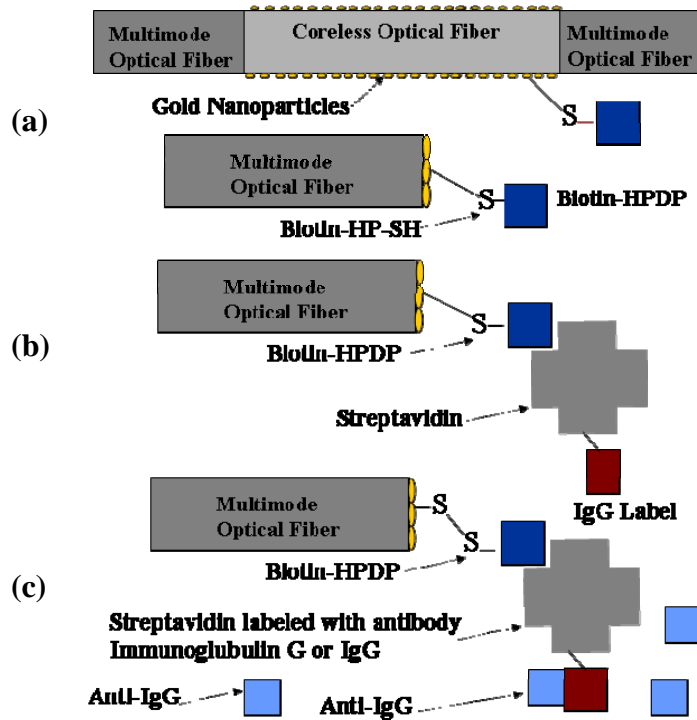


Figure 24. A schematic of employing Biotin-Streptavidin Chemistry (High affinity interaction: $K_a = 10^{15} \text{ M}^{-1}$) for detection and sensing of biological agents (anti-IgG for example) and contaminants

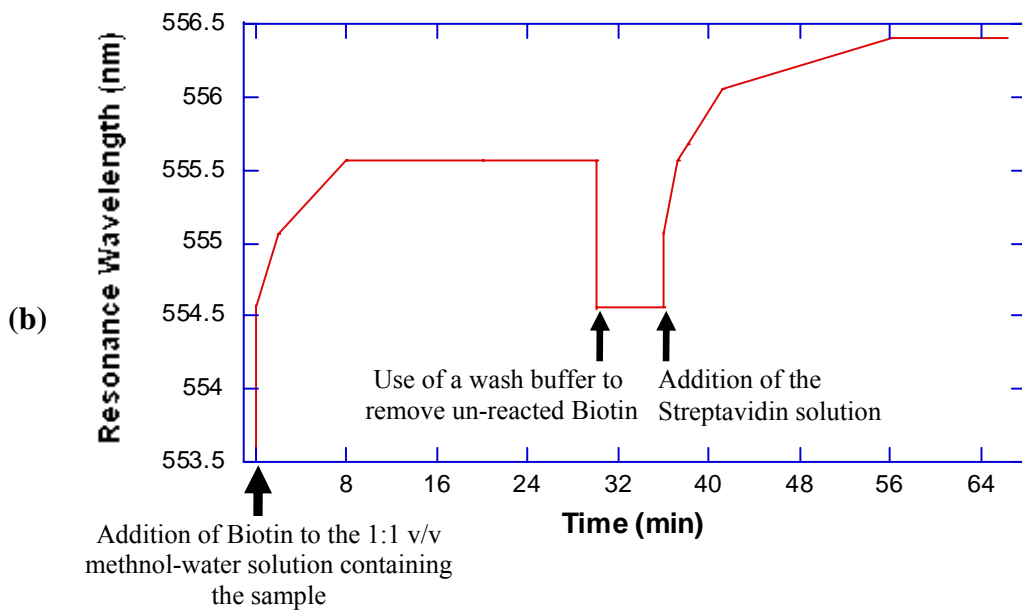
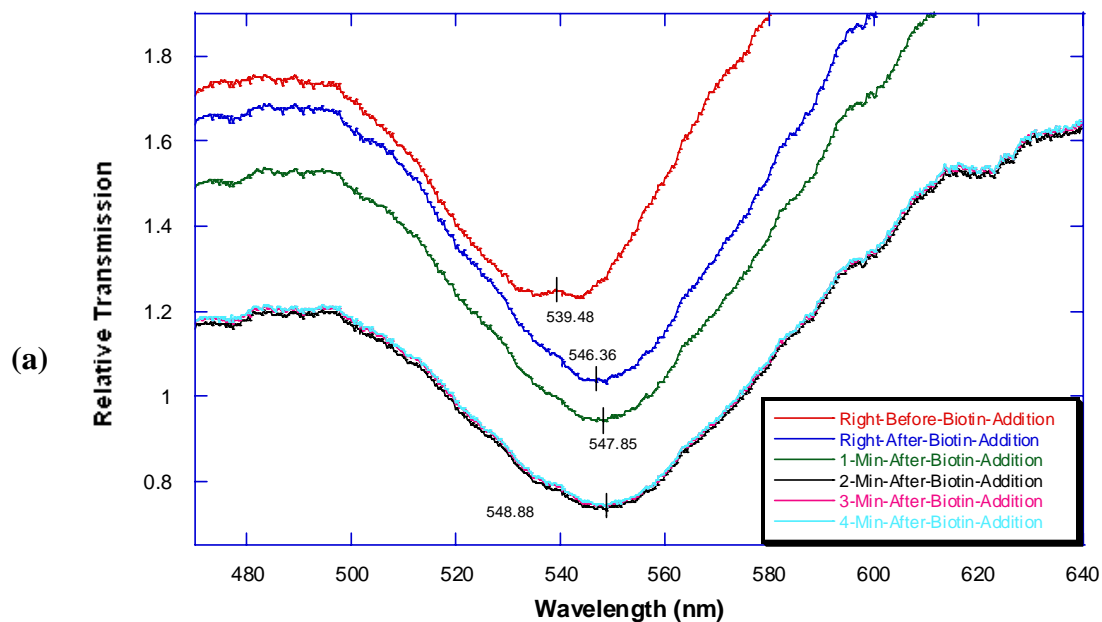


Figure 25. (a) Shift in plasmon resonance peak wavelength upon addition of Biotin, (b) Response of Streptavidin addition to a Biotin coated fiber; The value of the wavelength at which plasmon resonance-related dip occurs was plotted vs. time for an in-line fiber optic biosensor based on structure A

5.5 Development of a sensor system to sense chemicals/biomolecules

As a means of incorporating the fiber sensors into systems, incorporation of in-line fiber sensors into non-woven fabrics was explored. In order to incorporate an in-line sensor into a textile fabric, a spun-bonded base fabric was taken and an in-line fiber sensor was placed on top of it. Subsequently, non-woven fibers of polyurethane were electrospun on top of the optical fiber sensor to hold the sensor fiber in its position, thereby incorporating it in a non-woven fabric matrix. The electro-spinning was carried out at a voltage of 18 KV using a solution of polyurethane in the solvent DMP. Embedding optical fiber based chemical and biological sensors into non-woven fabric based water filters allows the development of an in-line water monitoring system. An example of such a non-woven fabric structure, with an embedded optical fiber, is shown in Figure 26a. Figure 26b shows an SEM micrograph of electrospun fibers holding the fiber optic sensor in its position on top of a base spun-bonded fabric. As electrospun fibers have very fine diameters, in the sub-micron range, they provide high surface area for adsorption of fluids from the surface of the fabric to the surface of the optical fiber sensor. These non-woven fabric filters, containing the embedded fiber optic sensors, can either be placed at the mouth of water-carrying pipes or can form a lining on the inner walls of the pipes. One can obtain continuous information about the contamination levels of drinking water if biosensors, developed on optical fibers to detect the presence of antigens or biochemical agents, are embedded into water monitoring systems. Thus one can be in a position to prevent outbreaks of drinking water based diseases or a biological agent attack.

Future extensions of the work include using the sensors for gas monitoring and multiplexing multiple in-lines sensors on the same fiber. An example of forming more than one in-line fiber optic sensor on the same fiber is shown in Figure 27. The fiber containing the multiple sensors can be incorporated into a textile fabric as shown in the schematic in Figure 27a. The two different sensors on the same fiber, i.e. sensors X and Y in Figure 27a, can be developed by first fusing two coreless fiber sections to multimode fibers and coating these coreless fiber sections with different metallic nanoparticles like gold and silver. Optical transmission spectrum through an optical fiber, with two different metallic nanoparticles on the surface of its coreless region, is shown in Figure 27b. One can observe two plasmon resonance related dips, due to LSP excitation in gold and silver nanoparticles at different wavelengths [8-10], in the overall transmission spectrum of the fiber. When refractive index of the local environment around sensor

X at position 1 is changed from n_1 to n_2 , with refractive index of the environment around sensor Y remaining constant at n_1 , there is a shift in only one of the plasmon resonance-related dips i.e. the dip associated with that of sensor X. Thus one can sense the presence of chemicals in a very large area by forming multiple sensors on the same optical fiber, each sensor being based on a certain metallic nanoparticle, and incorporating the fiber in a large area fabric as shown in Figure 27a. This fabric based sensor system has an advantage that it can be quickly deployed at or removed from a given location. This fabric based sensor system could be deployed in the form of carpets or wallpapers in rooms for gas sensing applications.

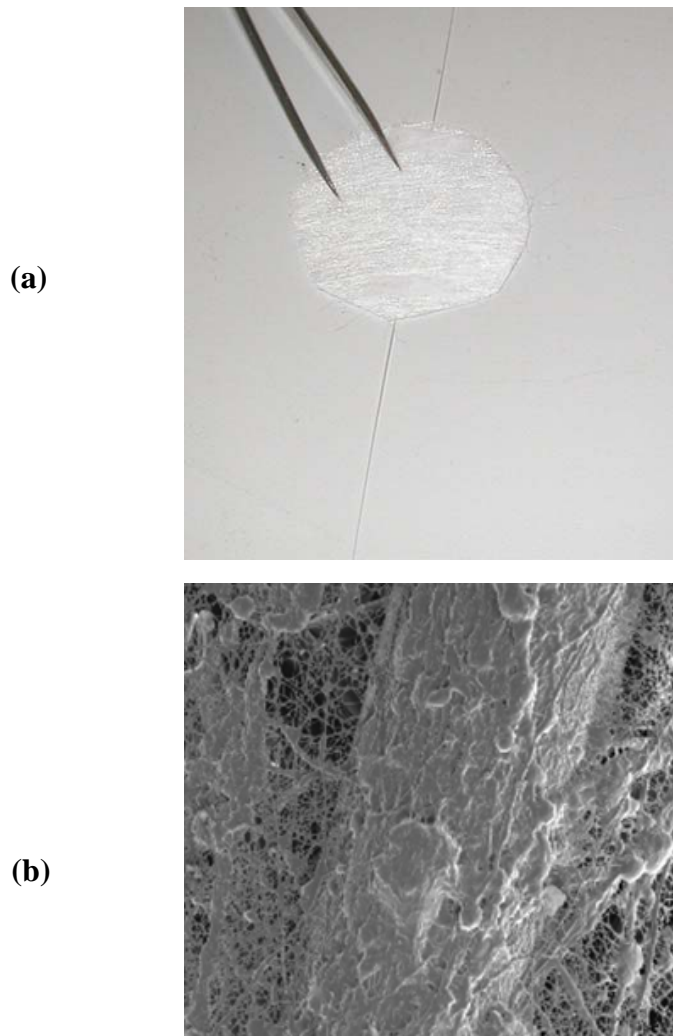


Figure 26. (a) Incorporation of optical fiber into nonwoven-textile filter that can be placed in an in-line water monitoring system, and (b) SEM micrograph of electrospun nonwoven fibers used to sandwich an optical fiber sensor in between a spun-bonded nonwoven fabric and the electrospun fibers

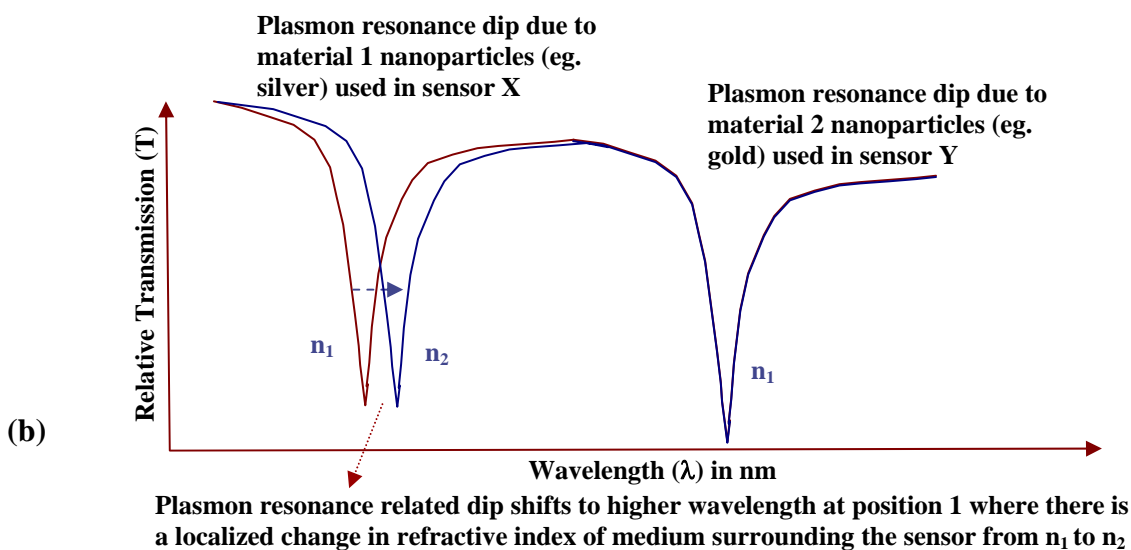
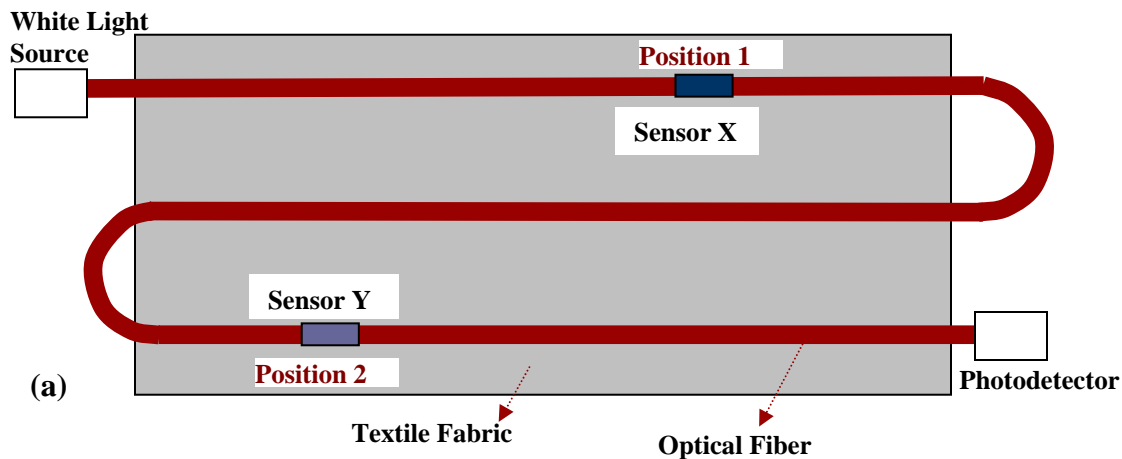


Figure 27. (a) Schematic of fiber optic fiber sensor system consisting of multiple sensors placed on the same optical fiber, which is integrated into a textile fabric. Sensor X is an in-line fiber optic sensor with a structure similar to structure B that has the coreless fiber region coated with silver nanoparticles and sensor Y is an in-line fiber optic sensor with a structure similar to structure B that has the coreless fiber region coated with gold nanoparticles and (b) Shift in plasmon resonance related peak associated with sensor X material (silver) upon exposure to a fluid of refractive index n_2 , when the original refractive index of the medium surrounding sensor is n_1 . Refractive index of the medium around sensor Y is assumed to be always at n_1

5.6 Conclusions

Sensors were developed on optical fibers by incorporating metallic nanoparticles on the surface of optical fibers. Several ways of forming sensitive and robust chemical sensors based on plasmon resonances of metallic islands and nanoparticles were demonstrated. Development of in-line optical fiber structures, involving single mode or multimode optical fibers fused to an arrangement of coreless and graded index fibers, enabled us to expand the light propagating in the core of the optical fiber to reach the surface of a coreless fiber and effectively interact with nanoparticles on the fiber surface and the environment. Moreover, these optical fiber sensors and devices can be embedded into non-woven or woven textiles to be used in carpets, tents, wallpapers, nets, etc. These sensors were evaluated by monitoring their optical response to binding of Biotin/Streptavidin to the sensor surface and by placing the sensors into mediums of different refractive indexes.

5.7 References

1. Dhawan A. and Muth J. F., In-line fiber optic structures for environmental sensing applications, *Opt. Lett.* 31, 1391-1393, 2006.
2. Mitsui K., Handa Y., and Kajikawaa K., "Optical fiber affinity biosensor based on localized surface plasmon resonance," *Applied Physics Letters*, 85 (18), 4231-4233, 2004.
3. Simon H. J., Mitchell D. E., and Watson J. G., Surface plasmons in silver films - a novel under-graduate experiment, *Am. J. Phys.*, 43 630, 1975.
4. Green R. J., Frazier R. A., Shakesheff K. M., Davies M. C., Roberts C. J., and Tendler S. J. B., Surface plasmon resonance analysis of dynamic biological interactions with biomaterials, *Biomaterials* 21, 1823-1835, 2000.
5. Homola J., Yee S. S., and Gauglitz G., Surface plasmon resonance sensors: review, *Sens. Actuators B* 54, 3, 1999.
6. Homola J., On the sensitivity of surface plasmon resonance sensors with spectral interrogation, *Sens. Actuators B* 41, 207, 1997.
7. Mu Y., Zhang H., Zhao X., Song D., Wang Z., Sun J., Li M., and Jin Q., An Optical Biosensor for Monitoring Antigen Recognition Based on Surface Plasmon Resonance Using Avidin-Biotin System, *Sensors*, 1, 91-101, 2001.
8. Stratton A., *Electromagnetic Theory*, New York: McGraw-Hill, 1941.

9. Van de Hulst H. C. Ed., Light scattering by small particles, John Wiley and Sons: New York, 1957.

10. Born M. and Wolf E., Principles of Optics 7th ed., Cambridge University Press: New York 1999.

**CHAPTER 6. IN-LINE DEVICES BASED ON THE INCORPORATION OF METALLIC
NANOPARTICLES INSIDE OPTICAL FIBERS**

6.0 In-line devices based on the incorporation of metallic nanoparticles inside optical fibers

Metallic nanoparticles were incorporated into the core of standard telecommunications grade optical fibers. This creates a simple, yet robust, platform which can be used to investigate the properties of nanoparticles, for sensing, spectroscopy, and optical switching applications. The optical response of gold nanoparticles embedded in the optical fiber matrix, was evaluated as a function of temperature and the use of the structure as an inline fiber-optic temperature sensor is described. A red-shift in the localized surface plasmon (LSP) resonance-related peak, as well as broadening of the plasmon resonance, was observed upon increasing temperature of the nanoparticle-containing fiber. The shift and broadening of the plasmon resonance was attributed to the temperature dependence of dielectric constants of metallic nanoparticles and the silica matrix and to plasmon-phonon interactions. Plasmon resonance of silver nanoparticles formed on the tip or optical fibers was also evaluated. Analytical calculations for the determination of wavelength-dependent absorption and extinction cross-sections of gold or silver nanoparticles embedded inside in an optical fiber (silica) matrix were also carried out.

6.1 Introduction

In order to incorporate the gold nanoparticles into the core of silica optical fibers, a discontinuous thin gold film was deposited on the cleaved tips of the fibers, thermal annealing of the film was used to form nanoparticles from this film, a protective fused silica layer was then deposited on the nanoparticles, and the fiber was fused to a bare cleaved fiber to form a continuous fiber.

Using the procedures developed in Chapter 5 metallic thin films between 4 and 10 nm thick were deposited on the fiber tips. AFM scan of a thin (8 nm) gold film, that was annealed at 400 °C, is shown in Figure 1b. One can observe from this figure that gold nanoparticles and islands are formed upon annealing the gold thin film. After optimizing the conditions for nanoparticle formation, thin gold films deposited on fiber tips were annealed at different temperatures by employing a micro-coil heater. Upon annealing, the transmission spectra showed a plasmon resonance related peak, shown in Figure 2, which indicates the development of metal islands and metal nanoparticles on the tip of the fibers. The annealing of the gold films was also carried out using controlled, low-intensity plasma arcs. A Type-36 Sumitomo Electric fusion splicer was used to arc-anneal the gold-coated fiber tips, as shown in Figure 3. It was observed that the

plasmon resonance related dip in transmission spectra appeared upon arcing, as shown in Figure 4, and that the dip become sharper and moved to lower wavelengths as the number of applied arcs was increased. A combination of thermal and arc annealing processes was also employed and the thin gold films on fiber tips were first thermally annealed and subsequently plasma arc annealed. It was observed that very sharp, plasmon resonance-related dips could be obtained by following this procedure and also that the dip moved to a lower wavelength, as shown in Figure 5. This could be attributed to a change in size or shape of nanoparticles, which were first formed by thermal annealing, when subsequent plasma arcs were applied. Transmission spectra of an optical fiber, containing nanoparticles on its tips, were obtained by using a fusion splicer to align the coated fiber with a uncoated collector fiber.

The optical fiber, containing nanoparticles on its tip, was fused with another optical fiber so as to incorporate the nanoparticles inside the fiber matrix by employing a fusion splicer. It was observed that application of fusion plasma arc to the nanoparticle containing tip caused fusion of the gold nanoparticles to form a blob of gold at the fiber interface. Thus, the nano-sized nature and functionality was not present in this case. In order to prevent the gold nanoparticles from fusing to each other, a protective over-layer of silicon dioxide (SiO_2) was first deposited on the nanoparticle containing tip and the over-coated tip was then fused to another optical fiber using a fusion splicer.

SiO_2 thin films were deposited on tips of optical fibers employing the channel spark pulsed electron deposition (PED) process. In the case of channel spark pulsed electron deposition, short pulses of electron current are employed for ablating the target instead of short pulses of light that are employed in pulsed laser deposition [1]. In our study, fused silica targets were employed for SiO_2 thin film deposition. As fused silica targets are optically transparent to ultraviolet light, the pulsed laser deposition (PLD) process is not as efficient as the channel spark PED process. In PED, a short pulse of electrons, having a width of approximately 70 ns, is produced in a hollow cathode at a gas pressure between 5 and 30 mTorr. A ceramic spark channel is employed to confine the resulting plasma so as to allow efficient transfer of charge to the tip of the channel. In our study, the channel tip was placed about 5 mm from the target and an accelerating potential of 15 kV was employed. The PED of SiO_2 was carried out in an oxygen environment with the gas flow rate and the chamber pressure being 15 sccm and 17 mTorr respectively. As shown in Figure 6, the channel spark electron beam impacts the fused silica target at a 45° angle with the

target surface normal resulting in high energy ablation of the target. In pulsed electron deposition, stoichiometry of the target material is preserved in the film within 5% of its original value in the target. In the case of oxide thin films, the stoichiometric balance can also be maintained by controlling the partial pressure of a reactive gas. Optical fiber samples were attached to the rotary sample holder with the help of a fiber holder made from a thick aluminum foil. Fibers were held together in the fiber holder, which was then attached to the rotary sample holder, as shown in Figure 6. The optical fibers were positioned such that their tips faced the plume emanating from the ablated fused silica target. During the pulsed electron deposition, the fused silica target was rotated and rastered for uniform ablation, and the sample holder was rotated.

Figure 7a shows the picture of an optical fiber tip, containing nanoparticles on its surface, which is over-coated with a fused silica layer. The thickness of the fused silica layer was estimated from a micrograph of the coated fiber tip and was found to be approximately 4 μm . It can be observed in Figure 7b that the SiO_2 over-coating helped to retain the shape of the plasmon resonance-related dip in the transmission spectra indicating that the size and shape of the

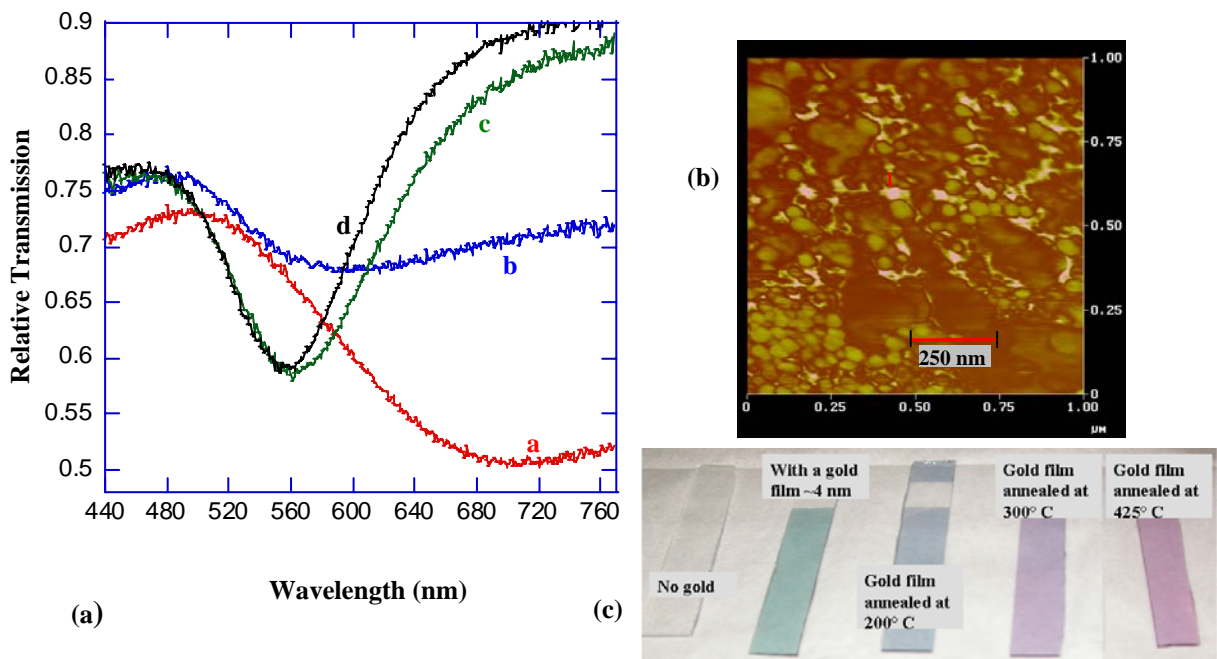


Figure 1. (a) Relative Transmission vs. wavelength plot for unannealed and annealed gold films, (b) AFM picture of an annealed (400 °C) gold film, and (c) Change of color of the thin gold films on glass slides upon annealing. The relative transmission is taken with respect to an uncoated substrate

nanoparticles was not significantly altered by the fusion arcing due to the protective over-layer. In our study, the fusion splicer was employed for different purposes including precise alignment of two fibers, for producing reduced plasma arc for rapid thermal annealing of gold films deposited on the fiber tips, for proper characterization of the nanoparticle containing tips, and for fusing two fibers to form a continuous fiber of constant diameter.

After incorporation of nanoparticles inside the silica optical fiber matrix, experimental evaluations of the effect of temperature on plasmon resonances of gold nanoparticles in the matrix were carried out by passing an optical fiber containing gold nanoparticles through a micro-coil heater setup. A schematic of the setup, employed for measuring the temperature dependence of localized surface plasmons, is shown in Figure 17a. For measuring the temperature dependence below room temperature, a bath containing ice-water (273 K) and liquid nitrogen (77 K) was prepared and the nanoparticle containing fiber was placed in it as optical transmission through the fiber was measured.

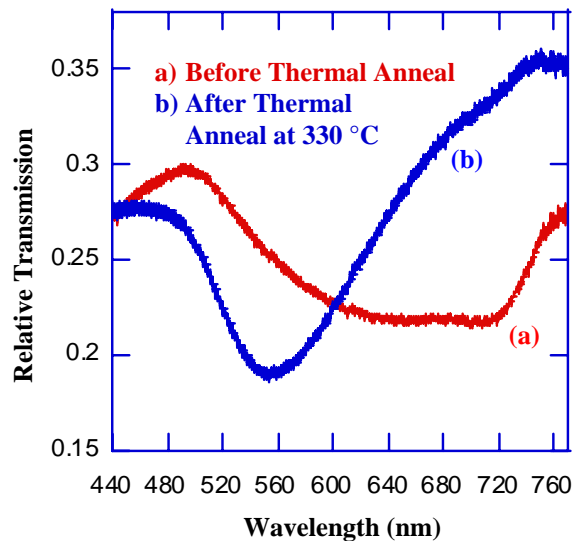


Figure 2. Effect of annealing on the transmission spectra of thin silver film on fiber tips (a) before and (b) after annealing

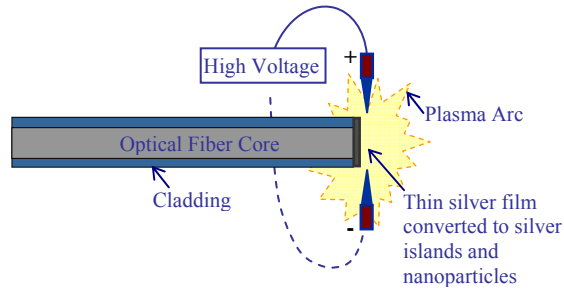


Figure 3. Plasma arc annealing of gold film on the optical fiber tip using a fusion splicer

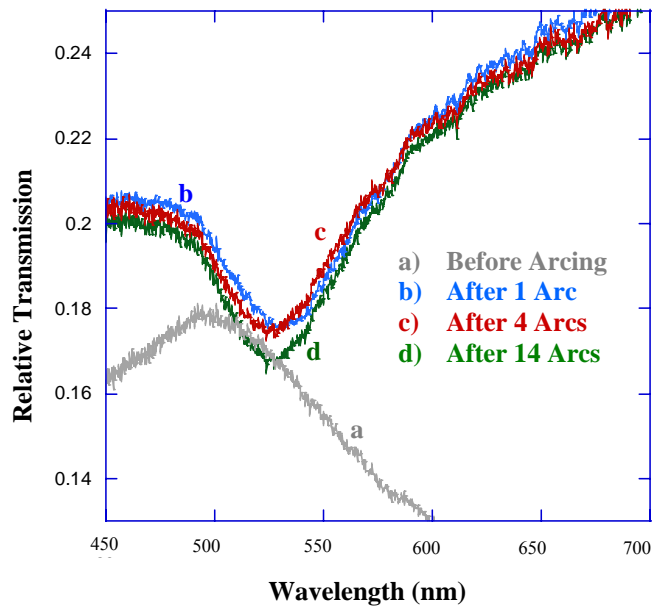


Figure 4. Appearance of a plasmon resonance related dip in the transmission spectra upon application of plasma arcs to a gold coated (8 nm) fiber tip

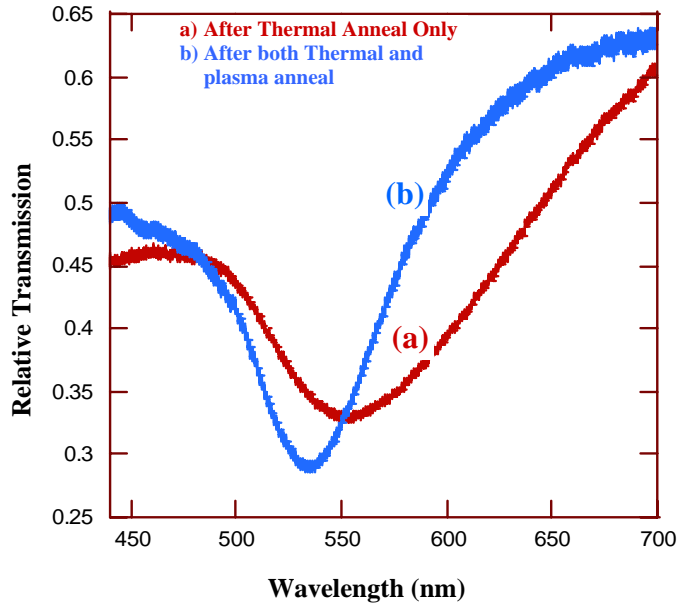


Figure 5. Plasmon resonance related dip becomes sharper when both thermal annealing (330° C) and plasma arc are applied to the fiber tip

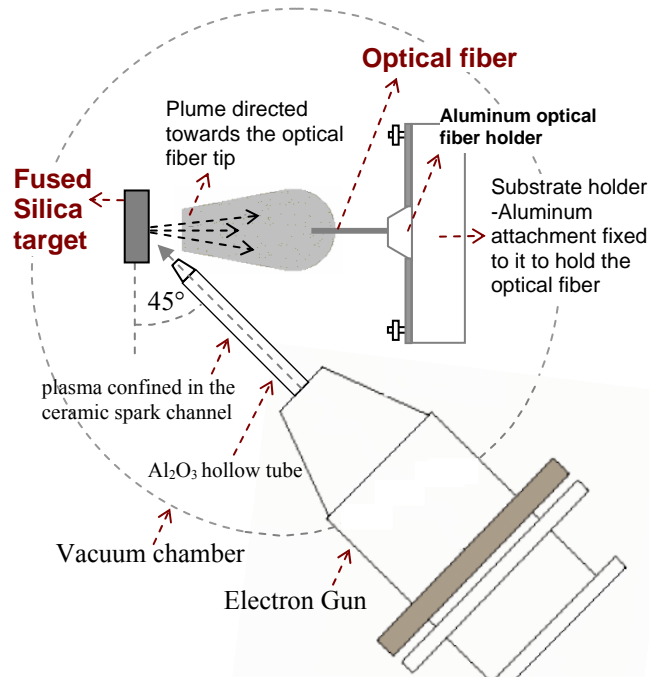


Figure 6. Schematic of a pulsed electron deposition system employed for depositing silicon dioxide on tip of an optical fiber

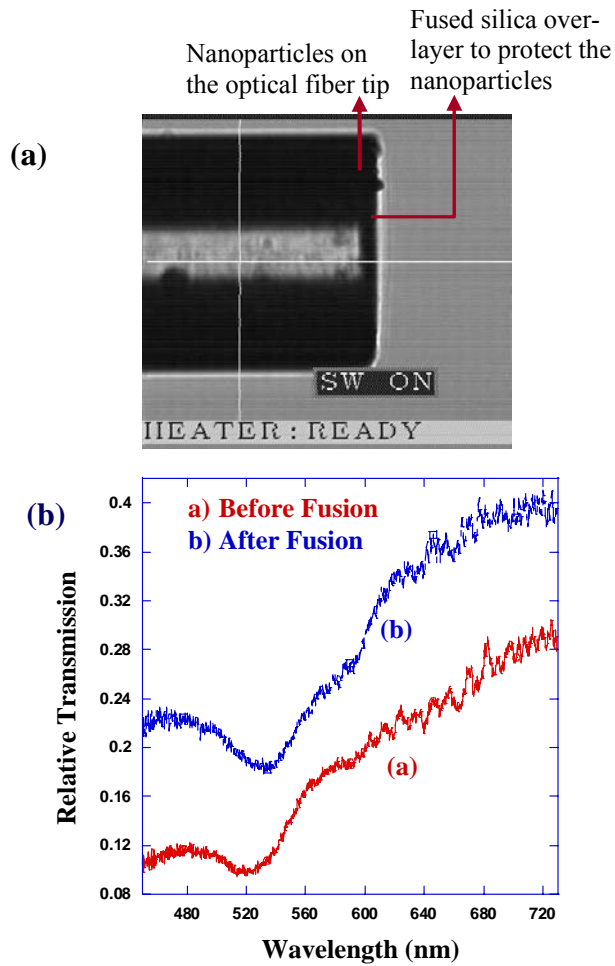


Figure 7. (a) Image of a fiber tip with a layer of nanoparticles and coated with fused silica and (b) Plasmon resonance related dip in the transmission spectrum is preserved when nanoparticles on the fiber tip are covered by a fused silica protective layer before fusion to another optical fiber

6.2 Analytical calculations

6.2.1 Determination of absorption and scattering cross-sections based on Mie Theory

Mie theory provides mathematical description of resonant light scattering and absorption by metallic nanoparticles [2-4]. Resonant light scattering and absorption and excitation of plasmon resonances on interaction of light with metallic nanoparticles, is dependent on the size and shape of the nanoparticles [2]. Analytical calculations, for evaluating the extinction cross-section (C_{ext}) of gold and silver nanoparticles embedded in a silica matrix, were carried out based on Mie theory.

According to Mie theory, when a single sphere (or oblate spheroid particle), having a dielectric constant ε_1 is placed in a medium with dielectric constant ε_2 and an electromagnetic field is applied on the sphere, the electric and magnetic field spatial distributions can be obtained by analytically solving Maxwell's equations. The solution for scattering electric and magnetic fields, as described by Okamoto [4-5], is given by the following expressions:

$$\begin{aligned} E_s &= \sum_{n=1}^{\infty} i^n \frac{2n+1}{n(n+1)} E_0 (ia_n N_{e1n} - b_n M_{o1n}) \\ H_s &= \frac{k}{\omega\mu} \sum_{n=1}^{\infty} i^n \frac{2n+1}{n(n+1)} E_0 (ib_n N_{o1n} - a_n M_{e1n}) \end{aligned} \quad (1)$$

where M and N are given by:

$$M \begin{Bmatrix} e \\ o \end{Bmatrix} = \frac{m}{\sin \theta} \begin{Bmatrix} -\sin m\phi \\ \cos m\phi \end{Bmatrix} P_n^m(\cos \theta) z_n(r) e_\theta - \begin{Bmatrix} \cos m\phi \\ \sin m\phi \end{Bmatrix} \frac{dP_n^m(\cos \theta)}{d\theta} z_n(r) e_\phi \quad (2)$$

$$N \begin{Bmatrix} e \\ o \end{Bmatrix} = \frac{m}{\sin \theta} \begin{Bmatrix} -\sin m\phi \\ \cos m\phi \end{Bmatrix} P_n^m(\cos \theta) \frac{1}{r} \frac{d}{dr} [r z_n(r)] e_\phi + \begin{Bmatrix} \cos m\phi \\ \sin m\phi \end{Bmatrix} \frac{dP_n^m(\cos \theta)}{d\theta} \frac{1}{r} \frac{d}{dr} [r z_n(r)] e_\theta + \begin{Bmatrix} \cos m\phi \\ \sin m\phi \end{Bmatrix} n(n+1) P_n^m(\cos \theta) \frac{z_n(r)}{r} e_r \quad (3)$$

and

$$j_n(r) = \sqrt{\frac{\pi}{2r}} J_{n+1/2}(r), y_n(r) = \sqrt{\frac{\pi}{2r}} Y_{n+1/2}(r) \quad (4)$$

where J_ν and Y_ν are Bessel functions of the first and second kind, respectively. The constants a_n and b_n are obtained by applying appropriate boundary conditions of continuity of the tangential components of the E and H fields and the normal components of the D and B fields at the

boundary (at the surface of a sphere). The values of a_n and b_n are given by the following expressions:

$$a_n = \frac{m\psi_n(mx)\psi_n'(x) - \psi_n(x)\psi_n'(mx)}{m\psi_n(mx)\xi_n'(x) - \xi_n(x)\psi_n'(mx)} \quad (5)$$

and

$$b_n = \frac{\psi_n(mx)\psi_n'(x) - m\psi_n(x)\psi_n'(mx)}{\psi_n(mx)\xi_n'(x) - m\xi_n(x)\psi_n'(mx)} \quad (6)$$

where x is given by the product of k_0 (given by $k_0 = 2\pi/\lambda$ where λ is the wavelength of the EM wave) and r_1 i.e. the radius of the sphere. The other terms used in the above expression are given by the following relations:

$$m = \sqrt{\frac{\epsilon_1}{\epsilon_2}}, \quad \psi_n(r) = j_n(r)r, \quad \xi_n(r) = j_n(r)r - iy_n(r)r, \quad \text{and} \quad z_n(r) = j_n(r) + iy_n(r) \quad (7)$$

The scattering cross-section (C_{sca}), which is defined as ratio of the total scattered power to the energy density of the external field, and extinction cross-section (C_{ext}) are given by the following terms:

$$C_{sca} = \pi r_1^2 Q_{sca} = \frac{2\pi}{k^2} \sum_{n=1}^{\infty} (2n+1)(|a_n|^2 + |b_n|^2) \quad (8)$$

$$C_{ext} = \pi r_1^2 Q_{ext} = \frac{2\pi}{k^2} \sum_{n=1}^{\infty} (2n+1) \text{Re}(a_n + b_n) \quad (9)$$

where Q_{sca} and Q_{ext} are the scattering efficiency and extinction efficiencies, respectively. The absorption cross-section is defined as the difference of the extinction and the scattering cross-sections i.e.

$$C_{abs} = C_{ext} - C_{sca} \quad (10)$$

In our calculations of the scattering cross-section (C_{sca}), the absorption cross-section (C_{abs}), and the extinction cross-section (C_{ext}), we applied the summation upto the fourth term i.e till the $n=4$ term. The terms with $n>4$ in the summation in equation can be neglected as they are very small in magnitude as compared with the terms from $n=1$ to $n=4$.

6.2.2 Absorption and scattering cross-sections based on Quasi-static Theory

Based on the Quasi-static theory, the extinction cross-section of a metallic nanoparticle is particle geometry dependent and is defined for ellipsoidal shaped nanoparticle by the following expression:

$$C_{\text{ext}} = \frac{24\pi^2 a_1 a_2 a_3}{\lambda} \frac{(\epsilon_2)^{3/2} \epsilon_{1b}}{(3\epsilon_2 - 3\epsilon_2 L_i + 3\epsilon_{1a} L_i)^2 + 9L_i^2 \epsilon_{1b}^2} + \frac{128\pi^5 \epsilon_2^2 a_1^2 a_2^2 a_3^2}{3\lambda^4} \left(\frac{(\epsilon_{1a} - \epsilon_2)^2 + (\epsilon_{1b})^2}{(3\epsilon_2 - 3\epsilon_2 L_i + 3\epsilon_{1a} L_i)^2 + 9L_i^2 \epsilon_{1b}^2} \right) \quad \text{and } \epsilon_1 = \epsilon_{1a} + j\epsilon_{1b} \quad (11)$$

where ϵ_1 is the refractive index of the metallic nanoparticle, ϵ_2 is refractive index of the medium containing the nanoparticles, and L_i is a depolarization factor when the external field is parallel to the i^{th} -axis, where $i = 1, 2, \text{ or } 3$, of the ellipsoid and a_1, a_2 , and a_3 are the semi-axis of the ellipsoid. L_i is defined by:

$$L_i = \frac{a_1 a_2 a_3}{2} \int_0^\infty \frac{ds}{(s + a_i^2) \sqrt{(s + a_1^2)(s + a_2^2)(s + a_3^2)}} \quad (12)$$

In the context of ellipsoidal metallic nanoparticles deposited on optical fibers, the fiber axis direction axis was assumed to be in the direction of the semi-axis a_3 of the ellipsoidal metallic particle. Moreover, in the theoretical calculations described above, the external field was taken to be parallel to the semi-axis a_1 . In case the particles are perfect spheres, $L_i = 1/3$, $a_1 = a_2 = a_3 = a$ and the extinction coefficient is given by:

$$C_{\text{ext}} = \frac{24\pi^2 a^3}{\lambda} \frac{(\epsilon_2)^{3/2} \epsilon_{1b}}{(2\epsilon_2 + \epsilon_{1a})^2 + \epsilon_{1b}^2} + \frac{128\pi^5 \epsilon_2^2 a^6}{3\lambda^4} \frac{(\epsilon_{1a} - \epsilon_2)^2 + (\epsilon_{1b})^2}{(2\epsilon_2 + \epsilon_{1a})^2 + \epsilon_{1b}^2} \quad (13)$$

This Quasi-static theory is useful and has been employed in our calculations since the temperature dependence of plasmons can be easily integrated.

Results of calculations base on Mie theory for gold nanoparticles in a silica matrix are shown in Figure 8 and those for silver nanoparticles are shown in Figure 9.

6.2.3 Temperature dependence of absorption and scattering cross-sections of metallic nanoparticles in an optical fiber matrix

The Drude-Sommerfeld [5-9] model, based on the intraband contribution to the dielectric function in a noble metal free electron gas, was used to describe the real and imaginary parts of dielectric constant of the metallic nanoparticles, i.e. ϵ_{1a} and ϵ_{1b} . These dielectric constants are dependent on both temperature and wavelength of the incident light and thereby lead to the temperature dependence of the extinction cross-section (C_{ext}). They are given as:

$$\varepsilon_{ia}(T) = 1 - \frac{\omega_p^2(T)}{\omega^2 + \omega_c^2(T)} \quad (14)$$

$$\varepsilon_{ib}(T) = \frac{\omega_p^2(T)\omega_c(T)}{\omega(\omega^2 + \omega_c^2(T))} \quad (15)$$

The term ω_c in the equations 14 and 15 is the electron collision frequency. The origin of temperature dependence of plasma oscillation frequency (ω_p) is the temperature dependence of the density and the effective mass of electrons. As the temperature dependence of effective mass of electrons is very small, the electron effective mass is assumed constant. Temperature dependent plasma oscillation frequency is given by:

$$\omega_p(T) = \sqrt{\frac{e^2 \left(\frac{N(T_0)}{1 + 3\gamma(T - T_0)} \right)}{m^* \varepsilon_0}} \quad (16)$$

where $N(T_0)$ is the density of electrons at a reference temperature, which was taken as room temperature (300 K) in our study and γ is the thermal linear expansion coefficient. The electron collision frequency (ω_c), also known as the damping constant associated with the free electron plasma oscillations, is also dependent on temperature and is described as:

$$\omega_c(T) = \frac{\omega_p^2 \varepsilon_0}{\sigma(0)} \left[\frac{1}{10} + \left(\frac{T}{T_0} \right)^5 \int_0^{T_0/T} \frac{y^4}{e^y - 1} dy \right] + \frac{1}{12} \pi^3 \frac{\Gamma \Delta}{\hbar E_F} \left[(k_B T)^2 + \left(\frac{\hbar \omega}{2\pi} \right)^2 \right] + \frac{A V_F}{d} \quad (17)$$

The first term in equation 17 is associated with the frequency of phonon-electron scattering ($\omega_{c\phi}$) and the second term is related to frequency of electron-electron scattering (ω_{ce}). The third term is due to the nano-particle size effect, when the particle size becomes smaller than the mean free path of the electrons. In equation 17, E_F is the electron Fermi energy (5.51 eV for gold), T_0 is the Debye temperature (185 K for gold), \hbar is the Planck's constant, k_B is the Boltzmann constant, $\sigma(0)$ is dc conductivity ($\sim 1.32 \times 10^8 \Omega\text{-m}$ for gold at $T = T_0$), Γ is a constant giving the average over the Fermi surface of the scattering probability (0.55 for gold), Δ represents the fractional unklapp scattering (0.77 for gold), V_F is the Fermi velocity (1.39×10^6 m/sec for gold), and A is a proportionality constant associated with the size effect of the nanoparticles. For Isotropic scattering, the value of A is taken to be equal to unity whereas it is taken to be 0.75 if the scattering is diffusive [6]. The term d in equation 17 is the particle radius,

i.e. a in the case of a spherical particle and a_i ($i = 1, 2, \text{ or } 3$) for an ellipsoidal particle, where i is the direction of the ellipsoid axis to which the external field is parallel. The expression for electron collision frequency (ω_c) that is employed in our calculations is based on models described by McKay et al. [9], Holstein [10] and Lawrence [11]. The derivation for the phonon-electron scattering frequency ($\omega_{c\phi}$) employs the Debye model for the phonon spectrum and is valid assuming $E_F \gg \hbar\omega \gg k_B T$ and $E_F \gg \hbar\omega \gg k_B T_0$. Along with the temperature dependence of metallic nanoparticles, the dielectric constant of silica i.e. ϵ_2 is also a function of both temperature (T) and wavelength of the incident radiation (λ) [12-14]. Ghosh et al. [12] modeled the temperature dependence of silica by using the following relationship, which was employed by us for calculation of C_{ext} in equation 11:

$$\begin{aligned} \epsilon_2(\lambda, T) = & (1.31552 + T \times 0.690754 \times 10^{-5}) + \frac{(0.788404 + T \times 0.235835 \times 10^{-4})(\lambda^2)}{\lambda^2 - (0.0110199 + T \times 0.584758 \times 10^{-6})} \\ & + \frac{(0.91316 + T \times 0.548368 \times 10^{-6})(\lambda^2)}{\lambda^2 - (100)} \end{aligned} \quad (18)$$

In this study, the extinction cross-sections for both ellipsoidal and spherical particles, embedded in a silica matrix, were calculated and plotted as a function of wavelength and temperature. The results of these analytical evaluations of extinction coefficients of gold nanoparticles, having spherical and ellipsoidal geometries, in a silica (SiO_2) matrix are shown in Figures 10a and b. One can observe in both the figures that the plasmon resonance-related peak shifts to higher wavelengths upon as temperature was increased. Moreover, the width of the plasmon resonance-related peak also increased upon increasing the temperature and this could be attributed to the temperature dependence of the electron collision frequency (ω_c), which is a sum of phonon-electron and electron-electron scattering frequencies. It was observed from the theoretical calculations that the effect of temperature, on the shift and broadening of the plasmon resonance-related peak in the extinction spectra, resulted primarily from the temperature dependence of the dielectric constant of the metallic nanoparticles (including phonon-electron scattering effects). The temperature dependence of the refractive index of the matrix, i.e. silica, was also accounted for in the calculations and its contribution to the shift and broadening of the plasmon resonance-related peak was found to be negligible. Similar calculations were carried out for silver nanoparticles and the results are shown in Figures 11 and 12. The plots of extinction cross-section of ellipsoidal silver nanoparticles are given in Figure 11a and Figure 12.

Extinction cross-section calculations were also carried out for a system consisting of silver and gold nanoparticles, both surrounded by silica matrix, and laying in series. An example of such a system is gold and silver nanoparticles embedded inside an optical fiber matrix, but at two different spatial positions. The gold and silver nanoparticles are assumed to be spatially separated from each other with an optical fiber in between them. If the temperature around only gold nano-particles is varied from 300 to 623 K, keeping the temperature around the silver nanoparticles constant at 300 K, only the plasmon resonance related peak associated with the gold nanoparticles shifts to higher wavelengths whereas the peak associated with silver nanoparticles remains constant. This is shown in Figure 13 for spherical nanoparticles and in Figure 13b and Figure 14 for ellipsoidal nanoparticles of two different sizes.

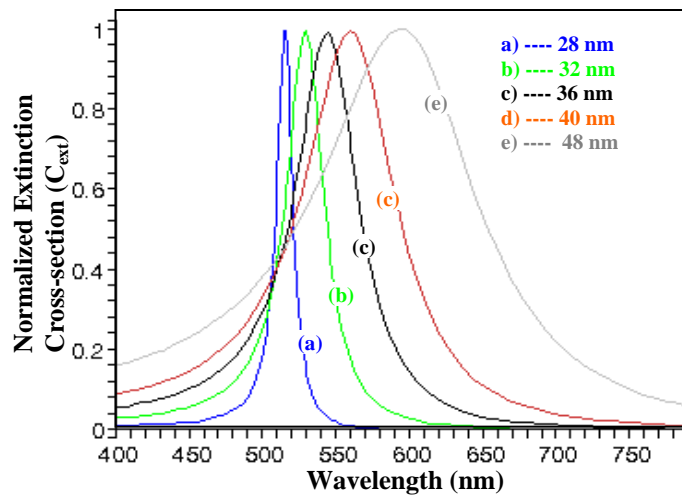


Figure 8. Analytical calculations results for extinction cross-section for gold nanoparticles. Calculations based on Mie theory showing the effect of particle size on the normalized plasmon peak shape and position – The normalization here was done to make the peaks to have a value 1 so as to effectively compare the plots

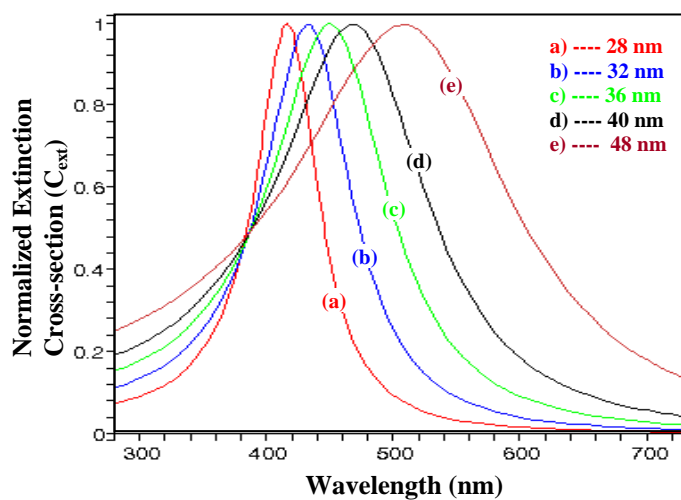


Figure 9. Analytical calculations results for extinction cross-section for silver nanoparticles. Calculations based on Mie theory showing the effect of particle size on the normalized plasmon peak shape and position – The normalization here was done to make the peaks to have a value 1 so as to effectively compare the plots

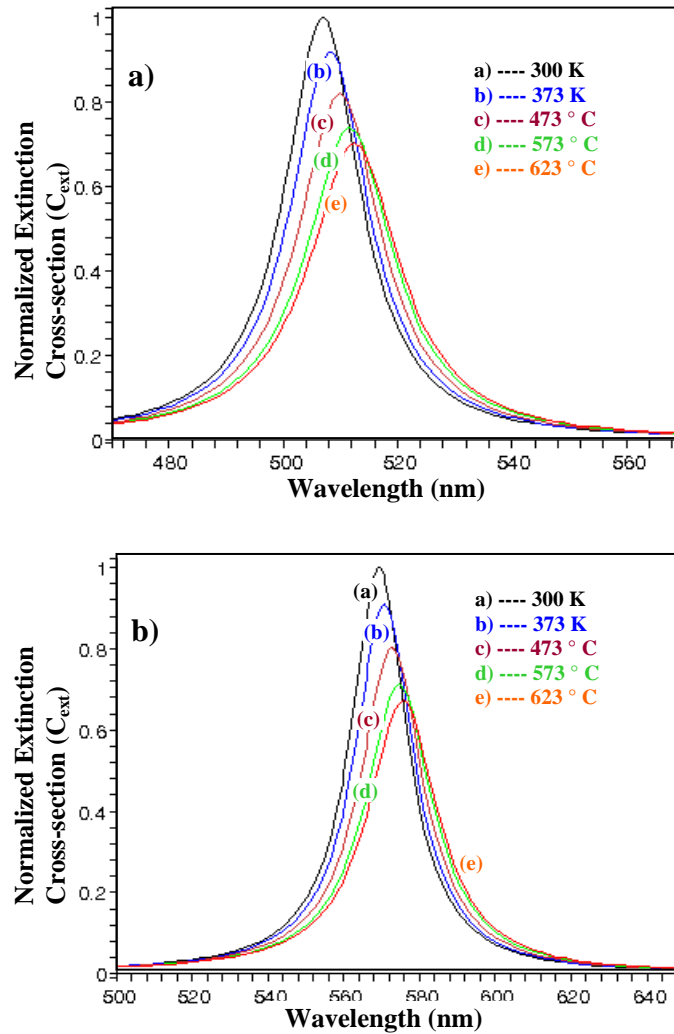


Figure 10. Analytical calculations results for extinction cross-section. (a) Quasi-static model for spherical gold nanoparticles with radius of 34 nm in a silica matrix and (b) Quasi-static model for ellipsoidal gold nanoparticles with $a_1 = 39$ nm, $a_2 = 34$ nm, and $a_3 = 34$ nm, showing the effect of increasing temperature on position of the plasmon resonance-related peak and on peak broadening

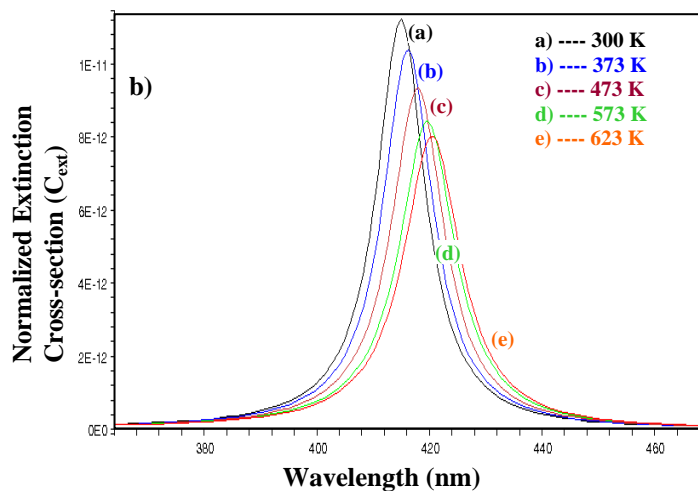
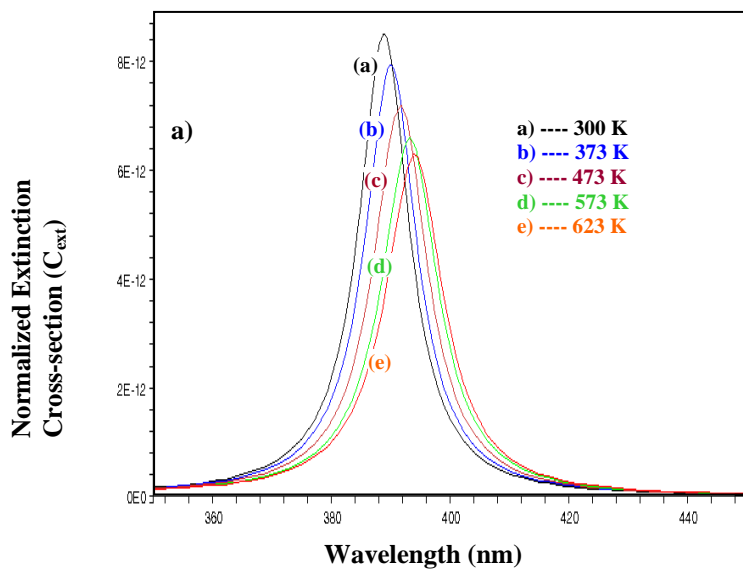


Figure 11. Analytical calculations results for extinction cross-section. (a) Quasi-static model for spherical silver nanoparticles with radius of 34 nm in a silica matrix and (b) Quasi-static model for ellipsoidal silver nanoparticles with $a_1 = 39$ nm, $a_2 = 34$ nm, and $a_3 = 34$ nm, showing the effect of increasing temperature on position of the plasmon resonance-related peak and on peak broadening

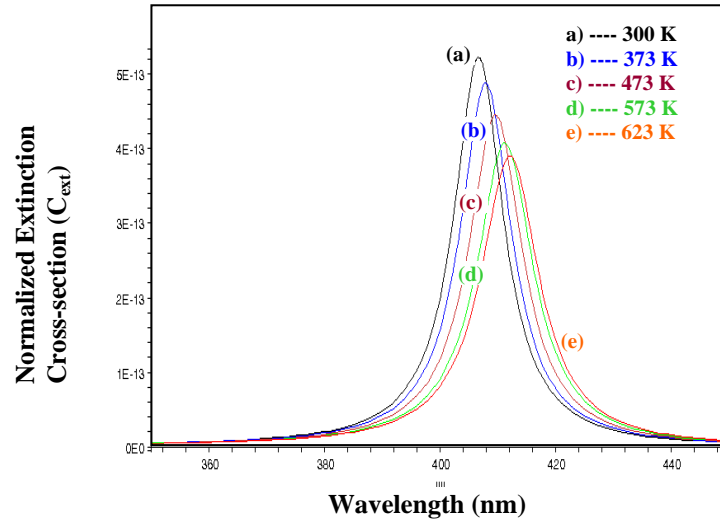


Figure 12. Analytical calculations results for extinction cross-section. Quasi-static model for ellipsoidal silver nanoparticles with $a_1 = 22$ nm, $a_2 = 20$ nm, and $a_3 = 20$ nm, showing the effect of increasing temperature on position of the plasmon resonance-related peak and on peak broadening

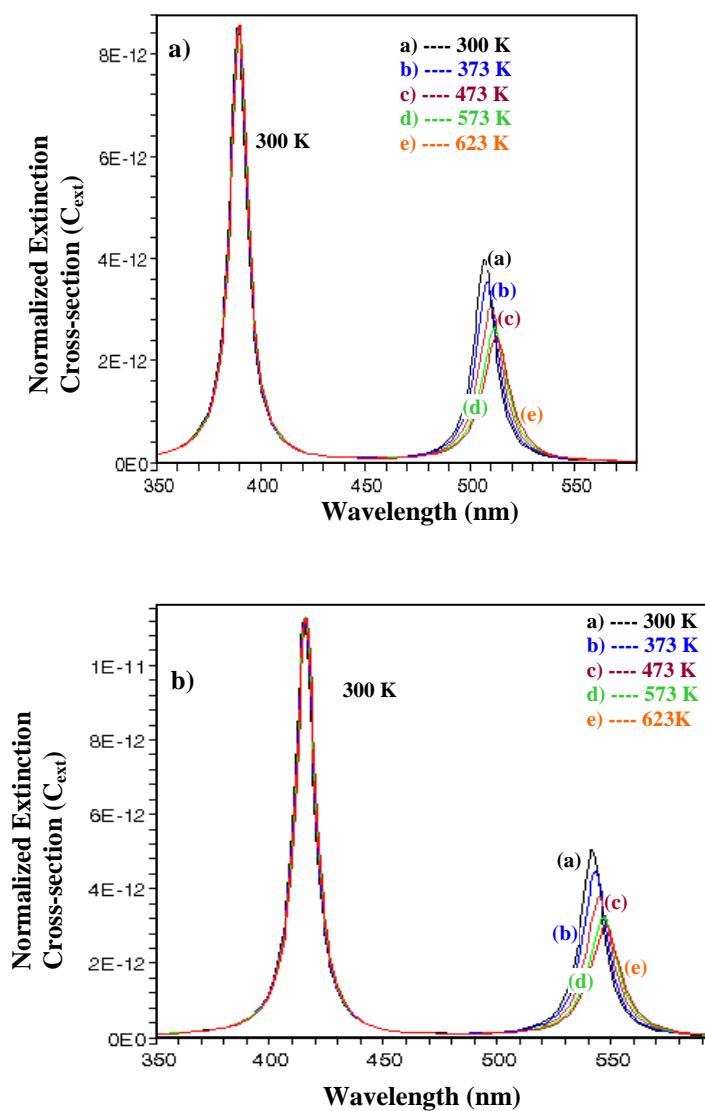


Figure 13. Analytical calculations for extinction cross-section showing the effect of increasing temperature on position of the plasmon resonance-related peak and on peak broadening (a) Quasi-static model for spherical gold and silver nanoparticles, with radii of 34 nm, at different locations in a silica matrix and (b) Quasi-static model for ellipsoidal gold and silver nanoparticles, with $a_1 = 39$ nm, $a_2 = 34$ nm, and $a_3 = 34$ nm, at different locations in a silica matrix

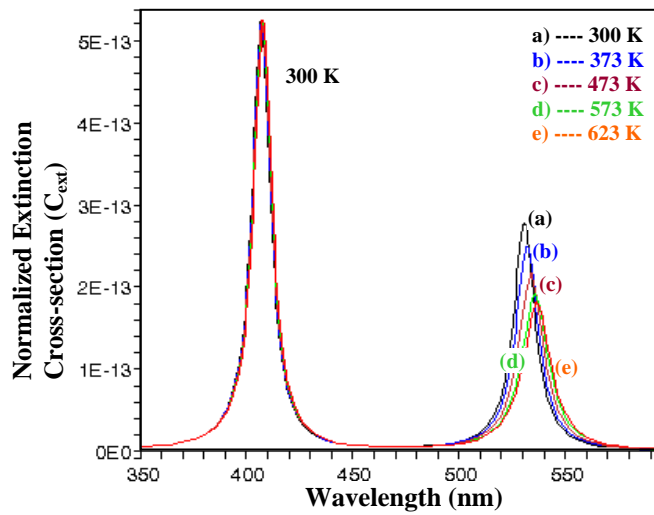


Figure 14. Analytical calculations for extinction cross-section showing the effect of increasing temperature on position of the plasmon resonance-related peak and on peak broadening using the Quasi-static model for ellipsoidal gold and silver nanoparticles, with $a_1 = 22$ nm, $a_2 = 20$ nm, and $a_3 = 20$ nm, at different locations in a silica matrix

6.2.4 Design of a distributed temperature sensor

As a novel way of holding the optical fiber sensors and to allow them to be incorporated into bridges or rubber conveyor belts for temperature monitoring, we have placed these sensors into non-woven textile structures that could be incorporated into concrete or rubber. In order to embed the fiber optic sensors in a non-woven fabric matrix, the sensor was placed on top of a base spun-bonded fabric and non-woven fibers are electrospun on top of the sensor to hold the sensor in its position in the non-woven fabric matrix. In this way, one can obtain continuous information about the temperature at different points in a structure such as bridge. This information, coupled with the level of strain at the different positions on the structures such as bridges, is important for real-time monitoring of these structures. Future extensions of the work include using the sensors for temperature monitoring and multiplexing multiple in-lines sensors on the same fiber. An example of forming more than one in-line fiber optic sensor on the same fiber is shown in Figure 15. The fiber containing the multiple sensors can be incorporated into a textile fabric as shown in the schematic in Figure 15.

The two different sensors on the same fiber, i.e. sensors X and Y in Figure 15, can be developed by first coating the tip of a multimode fiber with a thin film of metal 1 (gold) and subsequently annealing the film to form gold nanoparticles. This fiber tip, containing gold nanoparticles is then coated with a fused silica overlayer using pulsed electron deposition as described earlier in this chapter. Then, a cleaved end of another multimode fiber is fusion spliced to the fused silica coated fiber tip. The free end of the second multimode fiber is then cleaved and coated with a thin film of metal 2 (silver). Nanoparticles are formed on the fiber tip in a manner similar to the process described for gold and the fiber tip with silver nanoparticles and coated with fused silica, is then fused to a third multimode optical fiber. Optical transmission spectrum through an optical fiber, with two different metallic nanoparticles on the surface of its coreless region, is shown in Figure 16. One can observe two plasmon resonance related dips, due to LSP excitation in gold and silver nanoparticles at different wavelengths [2, 5], in the overall transmission spectrum of the fiber. When temperature of the local environment around sensor X at position 1 is changed from T_1 to T_2 , with temperature of the environment around sensor Y remaining constant at T_1 , there is a shift in only one of the plasmon resonance-related dips i.e. the dip associated with that of sensor X. Thus one can sense the presence of temperature in a very large area by forming multiple sensors on the same optical fiber, each sensor being based on

a certain metallic nanoparticle, and incorporating the fiber in a large area fabric as shown in Figure 15. This fabric based sensor system has an advantage that it can be quickly deployed at or removed from a given location. This fabric based sensor system could be deployed in the form of carpets or wallpapers in rooms for temperature monitoring applications.

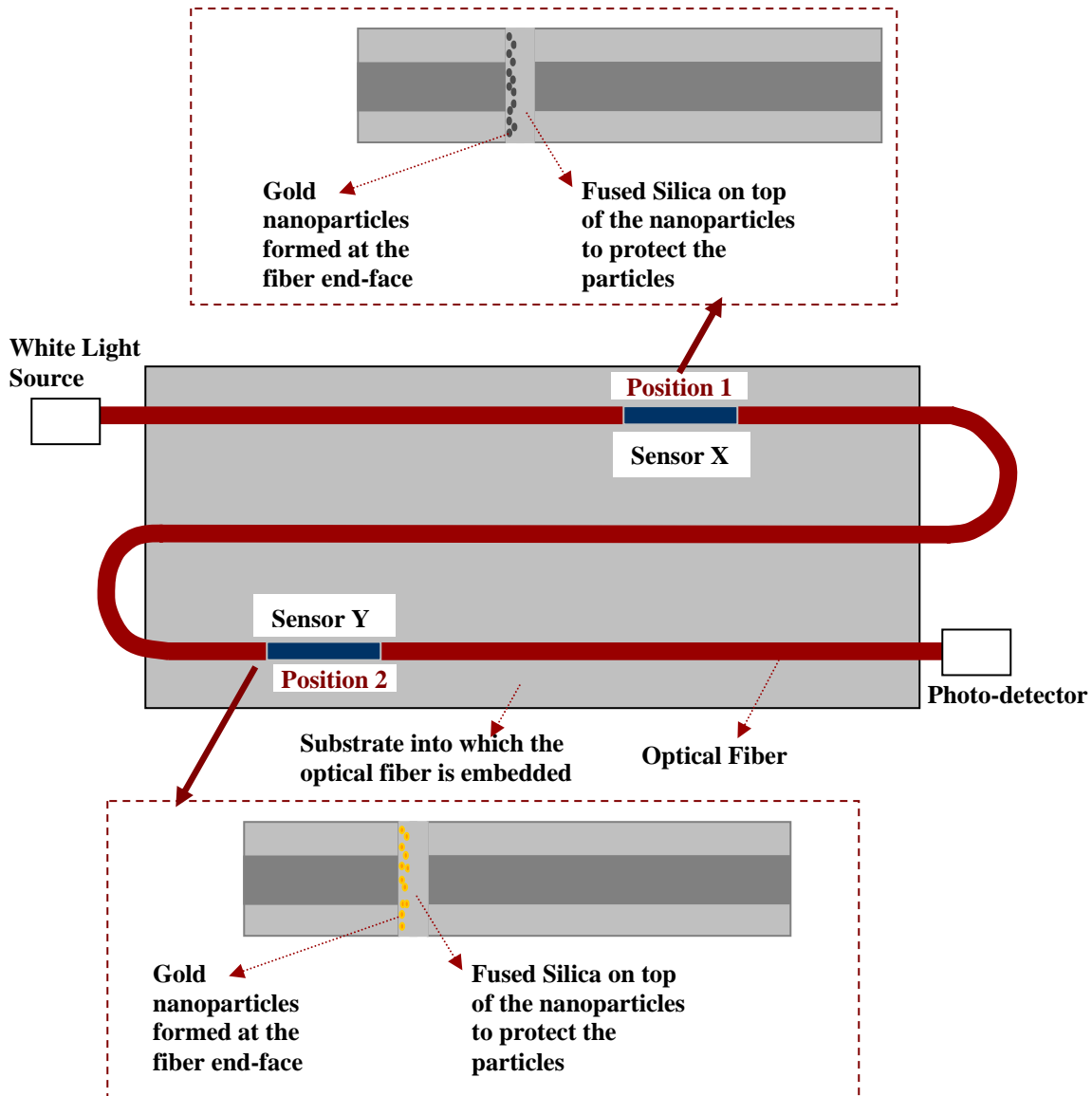


Figure 15. Schematic of fiber optic fiber sensor system consisting of multiple sensors placed on the same optical fiber, which is integrated into a textile fabric. Sensor X is an in-line fiber optic sensor with silver nanoparticles inside the fiber and sensor Y is an in-line fiber optic sensor with gold nanoparticles inside the fiber. Change of temperature in the localized environment around sensor X, i.e. at position 1, is sensed by sensor X, while sensor Y is spatially separated from the region in which the refractive index change occurs

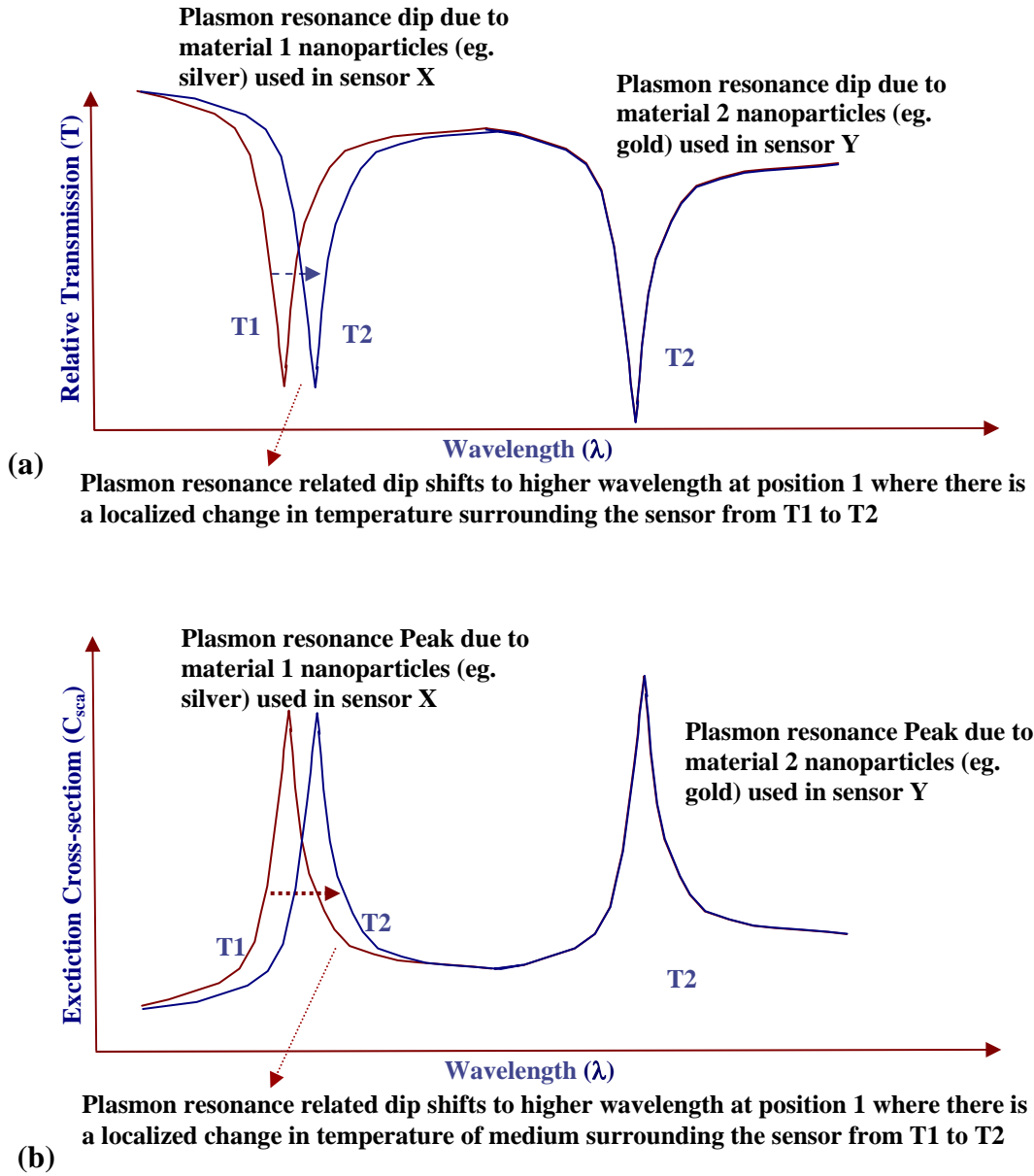


Figure 16. Schematic showing a shift in plasmon resonance dip or peak in the (a) transmission spectra and (b) Extinction Cross-section associated with sensor X material (silver nanoparticles inside the optical fiber) upon change of temperature from T1 to T2 at position 1 while the temperature at position 2 is kept constant at T1

6.3 Experimental Results and Discussion

Mathematically, resonant light scattering and absorption by metallic nanoparticles has been explained by Mie theory [2-4] and by employing dipole approximations [5]. Plasmon resonance wavelength depends on the size, shape, and dielectric constant of the nanoparticles and on the dielectric constant of the medium surrounding the nanoparticles [15-17]. The dependence of plasmon resonance wavelength on the refractive indices of the metallic nanoparticles and the matrix surrounding these nanoparticles, was exploited in our study. As these refractive indices and localized plasmon oscillations are dependent on temperature, the development of a fiber-optic temperature sensor that is based on sensing the shift in the plasmon resonance wavelength with temperature was carried out.

When the nanoparticles were formed on the optical fiber tip and the fiber was fused to another optical fiber, it was observed that while the overall efficiency of light throughput increased, the width of the surface plasmon absorption peak also increased. The fact that the plasmon resonance was retained after fusion splicing to form a continuous fiber indicates that the nanoparticle size and shape were not significantly altered due to the protective silica over-layer covering the nanoparticles. The slight broadening of the resonance and slight degradation in signal to noise was attributed to changing the collection efficiency of light to the spectrometer with the fused fiber. The fused fiber cases collect light scattered for a wider distribution of angles resulting in broadening of the spectrum.

The results of the experimental evaluations of the effect of temperature on plasmon resonances of gold nanoparticles in a silica optical fiber matrix showed that on increasing the temperature of the micro coil heater from 300 K to 600 K, a shift in the plasmon resonance-related dip in the transmission spectra was observed, as shown in Figure 17b. This was attributed to the temperature dependence of the Drude dielectric constant of metallic nanoparticles since the temperature dependence of refractive index of the silica matrix is negligible in comparison. An important observation was that on lowering the temperature back to 300 K from 603 K, the plasmon resonance-related dip shifted back to the original position of the dip before heating the fiber. This showed that there were negligible changes to the size and shape of the nanoparticles upon increasing the temperature from 300 K to 600 K. Figure 17c shows the effect of cooling the fibers to lower temperatures using ice-water and liquid nitrogen, whereas Figure 17d shows the

effect of temperature on the localized surface plasmon resonance-related peaks. We observed that the experimental data is qualitatively in agreement with our calculations.

Using Mie theory, one can attempt to determine the size range of the particle as shown in Figures 8 and 9. From the spectral data shown in Figure 17b and the AFM micrograph shown in Figure 1b, we see that the approximate particle size of 30-40 nm agrees both with the calculated Mie theory and the experimental data. While a wide range of particles sizes were observed in the AFM scan with large islands that may not significantly contribute to the resonance, and a distribution of particle sizes that broaden the resonance, the approximate average size of the nanoparticles was 34 nm. From the AFM data it also appears that the particles are not perfect spheres but may be slightly flattened and ellipsoidal. This coupled with the observation that Mie theory alone seems to overly broaden the spectra as compared with the experimental spectra, leads us to consider a theory that accommodates the ellipsoidal nature of the particles. Ellipsoidal particles tend to exhibit larger red shifts while retaining a narrower resonance. As a practical matter it is useful to note that while the precise shape and orientations of the nanoparticle are not known to high precision, the theoretical calculations are in qualitative agreement with experiment and are useful for understanding trends in behavior.

6.4 Conclusions

A method, for incorporating nanoparticles of different materials into the core of an optical fiber to study their optical characteristics or to be used as sensors, was developed. Specifically, the dependence of localized surface plasmons on temperature was employed to make an optical fiber based temperature sensor that could be used for remote monitoring of temperatures in different media. The scheme may also be useful in fiber optic sensor systems such as Bragg Grating Sensors where it would be advantageous to have a in line temperature sensor that doesn't require demodulation. Another advantage of incorporating the nanoparticles inside the fiber matrix, as opposed to depositing thin metallic films and nanoparticles on the fiber surface is that the metallic nanoparticles are protected from harsh physical and chemical environments. In the case where nanoparticles or films are on the fiber surface, physical or chemical erosion can occur due to exposure of the films to the environment thereby necessitating coating of metallic surfaces with over layers in order to avoid inconsistent sensing results. The silica matrix protects the metallic nanoparticles in our sensors. An extension of this work is to place metallic

nanoparticles, having different plasmon resonances, at different positions along the length of the optical fiber allowing temperature to be sensed at different points.

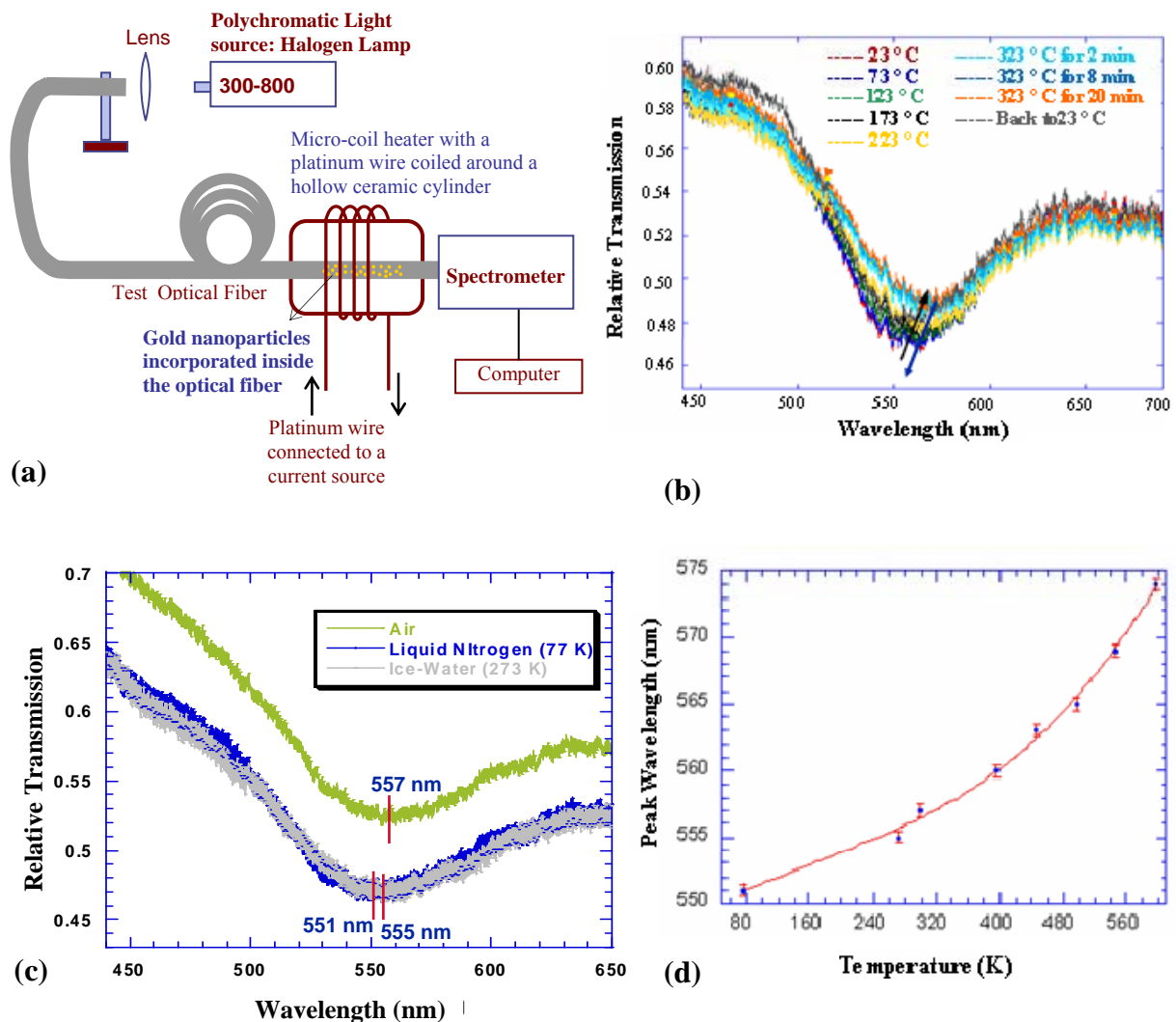


Figure 17. (a) Schematic of the arrangement employed for measurement of the effect of temperature on the plasmon resonances of metallic nanoparticles incorporated inside an optical fiber, (b) Measured shift in the plasmon resonance related dip upon heating, (c) Shift in plasmon peak to lower wavelengths upon cooling using ice-water and liquid nitrogen, and (d) Effect of increasing the temperature on the position of the plasmon resonance-related peak

6.5 References

1. Stark R., Christiansen J., Frank K., Mucke F. and Stetter M., IEEE Trans. Plasma Sci., 23 258, 1995.
2. Mie G., Ann. Phys., 25, 377, 1908.
3. Van de Hulst H. C. (ed), Light Scattering by Small Particles (New York: Wiley), 1957.
4. Born M. and Wolf E. (ed), Principles of Optics 7th edn (New York: Cambridge University Press), 1999.
5. Okamoto T., Near-field spectral analysis of metallic beads Near-Field Optics and Surface Plasmon Polaritons ed S Kawata (Berlin: Springer), 2001.
6. Kreibig U., J. Phys. F: Met. Phys., 4, 999, 1974.
7. Chiang H. P., Yeh H. T., Chen C. M., Wu J. C., Su S. Y., Chang R., Wu Y. J., Tsai D. P., Jen S. U., and Leung P. T., Opt. Commun., 241, 409, 2004.
8. Chiang H. P., Wang Y. C., Leung P. T., and Tse W. S., Opt. Commun., 188, 283, 2001.
9. McKay J. A. and Rayne J. A., Phys. Rev. B, 13, 673, 1976.
10. Holstein T., Phys. Rev., 96, 535, 1954.
11. Lawrence W. E., Phys. Rev. B, 13, 5316, 1976.
12. Ghosh G., Endo M. and Iwasalu T., J. Lightwave Technol., 12, 1338, 1994.
13. Ghosh G., IEEE Photon. Technol. Lett., 6, 431, 1994.
14. Malitson I. H., J. Opt. Soc. Am., 55, 1205, 1965.
15. Liu J. and Lu Y. J., Am. Chem. Soc., 125, 6642, 2003.
16. Mcfarland A. D. and Van Duyne R. P., Nano Lett., 3, 1057, 2003.
17. Sadowski J. W., Lekkala J. and Vikholm I., Biosens. Bioelectron., 6, 439, 1991.

**CHAPTER 7. INCORPORATION OF FABRY-PEROT CAVITIES AND VANADIUM
OXIDE FILMS INSIDE OPTICAL FIBERS FOR TEMPERATURE
SENSING AND OPTICAL SWITCHING APPLICATIONS**

7.0 Incorporation of Fabry-Perot cavities and vanadium oxide films inside optical fibers for temperature sensing and optical switching applications

Novel fiber optic temperature sensors were formed by depositing vanadium oxide thin films on the tips of optical fibers, and by incorporating vanadium oxide materials into the core of optical fibers. Temperature sensors were also developed by incorporating Fabry-Perot cavities on the tips or inside the optical fibers. These Fabry-Perot cavities were based on a 3-4 μm thick fused silica layer between two partially reflective surfaces that were formed by depositing two 50-75 nm gold films. It was found that the properties of the initially amorphous vanadium oxide could be controllably converted to crystalline VO_x compounds via the plasma arc of a fiber fusion splicer, or by thermal annealing. These crystalline VO_x compounds could then be over coated with SiO_2 , then fused with another fiber to form an in-line fiber optic sensor. It was found that the VO_x when annealed formed a well defined optical absorption edge was formed and the spectral position of the absorption edge varied with temperature in a reproducible way. The fabrication method used is also suitable for the formation of VO_2 within the core of the optical fiber which has potential for fabricating an in-line optical switch based on the insulator to metal phase transition of vanadium dioxide. Dependence of the optical transmission spectrum, of the Fabry-Perot cavities formed on the fiber tips and inside the optical fibers, on temperature was evaluated. It was observed that this transmission spectrum changed substantially as a function of temperature. Temperature dependence of the optical transmission spectrum, of the fiber-optic Fabry-Perot cavities, can be attributed to a change in the optical length of the cavity region and to the temperature dependence of the dielectric constants of the gold films forming the partially reflective surfaces of the cavity. The change in the optical length, of the cavity region, as a function of temperature can be attributed to the temperature dependence of the dielectric constant of the medium, i. e. fused silica, between the two partially reflective surfaces or to the thermal expansion of the cavity dielectric material.

7.1 Introduction

Temperature is a very important physical variable to monitor and control in the manufacture of chemicals, polymers & polymer products, and drugs, in oil refining, in the food processing industry, and in biomedical applications [1-5]. In sensors such as flow, strain, humidity, and

pressure sensors, there is an effect of temperature on the measured properties. Hence, it is important to measure temperature accurately so that the effect of temperature could be compensated and decoupled from the actual measured values [4]. Moreover, it is important to accurately sense temperature in structures such as bridges and buildings as changes in temperature could effect the expansion or contraction of these structures. As remote sensing and large area distributed sensing are important characteristics for some of these applications, it is important to develop temperature sensors on a platform, such as an optical fiber, such that these sensors could be easily incorporated into other materials or structures [3, 6]. Some of the attributes of good temperature sensors include high sensitivity and response times, ability to withstand high temperatures, compact size, and low weight. In temperature sensing applications, it is also important to isolate the effect of temperature, on the optical spectrum of a sensor optical fiber, from other factors such as losses due to connectors and light absorption in the fiber [3]. Hence, this chapter describes the development of robust and sensitive fiber-optic temperature sensors such that these sensors can be easily deployed for large area distributed sensing applications. Other advantages of employing fiber optic temperature sensors include their immunity to electromagnetic interference and that these sensors can often be used in harsh chemical environments. One way of forming sensor systems from fiber-optic sensors is to integrate multiple fiber optic sensors into flexible and conformable substrates such as textile fabrics and then deploy the fabrics [7, 8].

A wide variety of approaches have been used to construct fiber optic temperature sensors including the use of fiber Bragg gratings [9-10], the measurement of fluorescence lifetimes [11-12], Fabry-Perot Cavities [13, 14-15], monitoring the shift in the absorption edge of semiconductors such as GaAs or Si [16-17], Brillouin scattering [10, 18], and more recently monitoring the shift and broadening of surface plasmon resonance [19-20]. This chapter describes the use of vanadium oxide films, incorporated on the tip or in the core of the optical fiber, as temperature sensors. The development of temperature sensors, based on the incorporation of Fabry-Perot cavities on the tips or inside the optical fibers, is also described in this chapter.

Two kinds of temperature sensors are described in this chapter – the first one based on the incorporation of semiconducting materials, such as vanadium oxide films, on the tip or inside an

optical fiber and the second based on the formation of Fabry-Perot cavities on the tip or inside an optical fiber.

7.1.1 Vanadium oxide based inline fiber optic sensors

In semiconductors, the spectral position of the optical absorption edge is dependent on the band gap which is dependent on the temperature. Known as the Varshni effect [21-22], this temperature dependence typically follows the form:

$$E_g(T) = \frac{E_g(0) - \gamma T^2}{\beta + T} \quad (1)$$

where $E_g(0)$ is the band gap when the Kelvin temperature amounts to zero and γ & β are two empirical constants [21-22]. The decrease in semiconductor energy bandgap with temperature leads to a red-shift in the optical absorption edge of the semiconducting material.

Optical absorption in semiconductor materials has been employed for sensing temperature [16-17, 21-22]. As the absorption edge in the transmission spectrum of a semi conducting material shifts upon an increase in temperature, the calibrated shift can be employed for temperature sensing applications. The sensor described by Kyuma et al. [16] consisted of a thin semiconductor chip, made up of polycrystalline CdTe or semi-insulating GaAs, sandwiched between two ends of optical fibers inside a stainless pipe as the sensing region. Since the semiconductor bandgap is dependent on the expansion of the crystal lattice as a function of temperature, these sensors are precise and reproducible. However the magnitude of the change with temperature of spectral position of the band gap of compound semiconductors can be relatively small around room temperature. Furthermore, in examining the choice of materials that would be suitable for deposition and incorporation onto the fiber optic tips and into the cores of the optical fiber Si and GaAs have the possibility of oxidizing, having a stoichiometric imbalance respectively.

As an alternative material that is known to exhibit large changes in its optical properties near room temperature, vanadium oxide compounds were considered. The temperature sensors described in this chapter were developed by incorporating thin films of a semiconductor material such as vanadium oxide on tip of the optical fibers as well as inside the optical fiber matrix. Optical fibers containing vanadium oxide films can be employed for sensing temperature based on a change in the transmission spectrum, including a band-edge shift, of the optical fiber structures as temperature surrounding the sensor region of the optical fiber is varied.

Incorporating vanadium oxide films inside an optical fiber matrix allows the formation of continuous inline optical fiber sensor structures that are robust.

Vanadium oxide (VO_x) thin films are useful for a variety of applications ranging from smart windows, temperature sensors and bolometers, storage devices, ultra-fast optical switches, and as catalysts [23-26]. The vanadium oxide material system is complex consisting of many different phases of different valence states of vanadium in the oxide as shown in Figure 1 [23-24]. The value of 'x' in the different vanadium oxide (VO_x) phases varies between 1 and 2.5 and some of the common vanadium oxide phases are the VO, VO_2 , V_2O_3 , and V_2O_5 phases [23-24]. It has to be noted that the vanadium dioxide (VO_2) phase of VO_x exhibits a first order phase transition between semiconducting and metallic state at $\sim 68^\circ\text{C}$ [23]. This phase transition could also be produced by illuminating a vanadium dioxide film with a laser. This semiconductor to metal phase transition leads to a deformation of the lattice structure of vanadium oxide from monoclinic to tetragonal or rutile structure. The optical constants in the metallic phase are different from those in the semiconductor phase as shown in Figure 2. In the semiconductor phase, the lattice parameters of the cell are $a = 5.75 \text{ \AA}$, $b = 5.42 \text{ \AA}$, $c = 5.38 \text{ \AA}$, the space group being $\text{P}2_1/\text{c}$. In the metallic phase, the lattice parameters of the cell are $a = 4.55 \text{ \AA}$, $b = 4.55 \text{ \AA}$, $c = 2.88 \text{ \AA}$, the space group being $\text{P}4_1/\text{mmm}$ [23]. The phase transition has an effect on the electrical and optical properties of the vanadium oxide film. Upon phase transition, the material transforms from being semiconducting and transparent to being conductive (metallic) and reflecting in the infrared region. Thus, one can employ a red or an infrared light source and monitor the change in the transmission intensity through a vanadium oxide thin film as it undergoes semiconductor to metal transition. Moreover, one can also monitor the shift in the temperature-dependent band edge in the blue - green region of the visible spectrum to sense changes in temperature.

There are a wide variety of methods employed for producing vanadium oxide films [27-30] including sol gel process, hydrothermal process, oxidation of vanadium metal, and pulsed laser deposition. In order to develop VO_x films on the tip of optical fibers, pulsed laser deposition was employed to develop these films on the tip of the optical fiber and these films were subsequently annealed to develop polycrystalline VO_x films. The annealing processes involved the application of controlled plasma arcs to the VO_x films deposited on the fiber tips to develop crystallinity in the otherwise amorphous as-deposited films. The advantage of employing a non-equilibrium

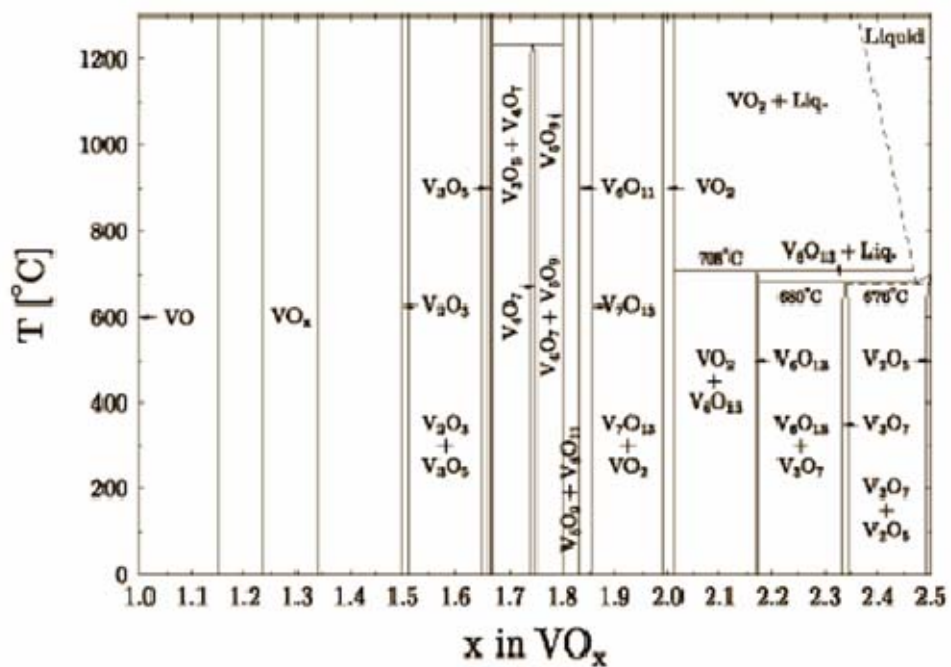


Figure 1. Phase diagram for vanadium oxide (VO_x) showing multiple phases of VO_x , with x varying between 1 and 2.5

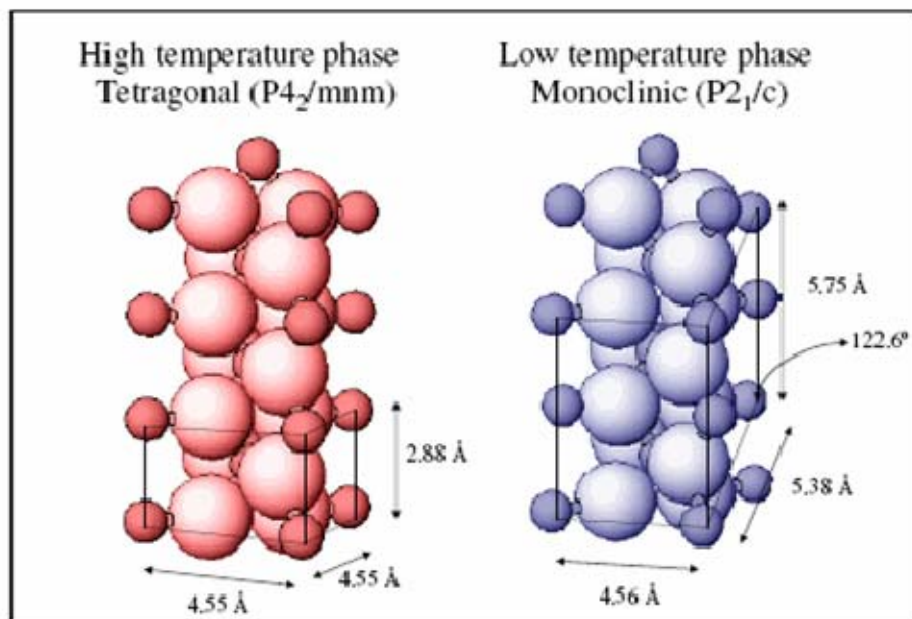


Figure 2. Structures and lattice constants for the monoclinic (low temperature, semi conducting) and tetragonal (high temperature, metallic) phases of vanadium dioxide

process such as pulsed laser deposition is that the stoichiometry of the vanadium oxide targets can be varied and appropriate deposition conditions optimized with relative ease.

7.1.2 Fabry-Perot cavity based inline fiber optic sensors

The main principle in the measurement of temperature by employing Fabry-Perot cavity based sensors is to measure the change in phase shift, associated with the Fabry-Perot cavity, upon increase in temperature [30]. The phase (ϕ) associated with a Fabry-Perot cavity, due to multiple reflections at the front and back reflective surfaces, is given by the following relationship:

$$\phi = \frac{4 \cdot \pi \cdot n \cdot L}{\lambda} \quad (2)$$

where n is refractive index of the fiber mode, L the length of the Fabry-Perot sensor, λ the free-space wavelength. The fractional phase shift per unit temperature can be defined by the following relationship:

$$\frac{d\phi}{\phi dT} = \frac{dL}{LdT} + \frac{dn}{ndT} \quad (3)$$

Hence, the temperature dependence of the phase associated with a Fabry-Perot cavity arises from the change in optical length of the cavity region due to temperature dependence of the refractive index of the medium between the two reflective surfaces. This change in refractive index occurs due to the thermal expansion of the cavity dielectric material or due to the temperature dependence of the dielectric constants of the materials forming the reflective surfaces of the cavity. A Fabry-Perot cavity can be formed at the end-face of an optical fiber by forming a couple of reflective surfaces separated by a dielectric medium, as described by Lee et al. [30] or by fusing a single mode fiber to another single mode fiber having a different diameter [31]. An in-line Fabry-Perot cavity based fiber optic sensor, was formed by separating fibers containing reflective surfaces at their ends by a certain distance and keeping them in that position by fusing them to a hollow glass tube [15]. The reflective surfaces employed in a Fabry-Perot cavity are either metallic or thin film stack based mirrors [13, 15] or are based on reflections at the fiber face due to a change of a refractive index at the boundary [14-15]. Another variation of an in-line fiber-optic sensor was described by Huang et al. [14], in which a single mode fiber (SMF) was fused to a multi-mode fiber (MMF), which was further fused to a single mode fiber and the reflection spectrum from this Fabry-Perot cavity was measured. The first and second

reflective surfaces of this Fabry-Perot cavity sensor were formed at the SMF-MMF interface and the MMF-SMF interface respectively, due to reflection of the guided wave taking place at the interfaces. With an increase in temperature, there is a change in the optical path length in the cavity region due to a change in both the refractive index of the MMF and the length of the cavity due to thermal expansion.

Another inline fiber-based Fabry-Perot intrinsic sensor was developed by Lee et al. [13]. The mirrors in the Fabry-Perot cavity were produced by fusion splicing a single-mode silica fiber to a fiber having a seven-layer quarter-wave $\text{TiO}_2/\text{SiO}_2$ stack on a cleaved fiber, cleaving the other end of the single mode fiber to get the desired interferometer cavity length, and then fusing the cleaved end to another fiber having a seven-layer quarter-wave $\text{TiO}_2/\text{SiO}_2$ stack.

7.2 Experimental

7.2.1 Development of vanadium oxide based fiber optic sensors

In this study, amorphous vanadium oxide thin films were deposited on the cleaved tips of optical fibers and annealed to make these films polycrystalline. Moreover, vanadium oxide films were incorporated inside silica optical fibers by depositing these films on the cleaved tips of optical fibers, annealing the films to develop some crystallinity in them, depositing a protective fused silica layer on the annealed vanadium oxide films, and then fusing the fiber to a bare cleaved fiber in order to form a continuous fiber.

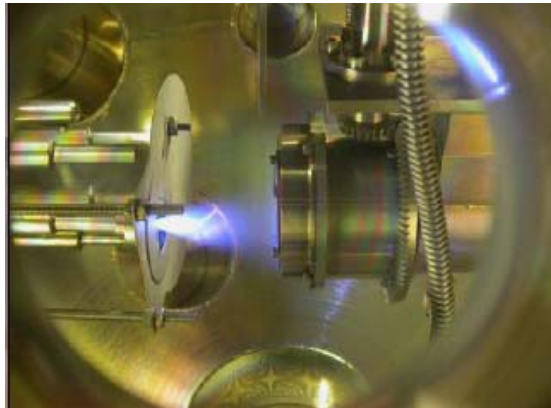
In order to deposit vanadium oxide films on the fiber tip, pulsed laser deposition (PLD) process was employed. High energy pulses from a Lambda-Physik KrF excimer laser, with a wavelength of 248 nm, were incident on a hard vanadium oxide target and the plume, produced due to the ablation, was incident on the surface of optical fiber tips facing the plume. One inch diameter, polycrystalline V_2O_3 targets were prepared from V_2O_3 powder (~120 mesh, 99.995% pure) by pressing under 5000 PSI, and sintering in air at 650 °C for 9 hours. Sintered targets were then polished until they have a smooth surface. Before depositing the vanadium oxide films on the fiber tips, ends of the optical fibers were cleaved using a diamond cleaver. Optical fibers were then attached to the PLD substrate holder by employing a fiber holder made from a thick aluminum foil. The fiber sample, mounted on the substrate holder and the target were loaded in the PLD chamber, which was pumped down to a base pressure of $\sim 1.4 \times 10^{-7}$ Torr before carrying out the deposition. A capacitance manometer and throttled gate valve were used

to maintain oxygen pressure at 5 mTorr during the deposition process. Low temperature growth was carried out maintaining the substrate at room temperature. Figure 3 shows the PLD deposition of a vanadium oxide film. The target was rotated and rastered for a uniform distribution of pulses on the target surface. During the growth, the pulsed laser was operated at ~ 150 mJ/pulse, the pulse frequency being 10 Hz. The substrate holder was rotated during growth for film uniformity. The optical fibers employed in our work were F-MLD multimode fibers obtained from Newport Corporation with a 100 μm core and a 140 μm cladding diameter.

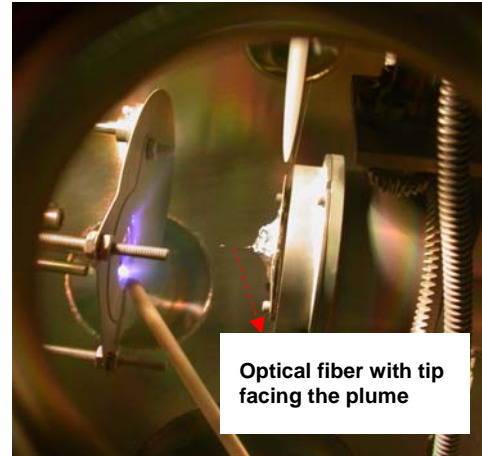
After the deposition, some of the vanadium oxide-coated optical fibers were removed from the PLD chamber and annealed by employing two processes - thermal annealing and plasma arc annealing, to make the films polycrystalline. Thermal annealing process was carried out by placing the vanadium oxide-coated fiber tips in a micro-coil heater, which was heated to 350 $^{\circ}\text{C}$, for 20 minutes. The annealing of the vanadium oxide films was also carried out using controlled, low-intensity plasma arcs. A Type-36 Sumitomo Electric fusion splicer was used to arc-anneal the vanadium oxide-coated fiber tips, as shown in Figure 4a. A schematic, illustrating the formation of a tip based fiber sensor with PLD deposited vanadium oxide on the fiber tips, is shown in Figure 5a. Figure 5b shows an optical microscope image of an optical fiber with vanadium oxide on its tip after annealing of the film by the application of controlled plasma arcs.

Optical transmission measurements were made on vanadium oxide coated optical fibers, for both the as-deposited and annealed vanadium oxide films, using a SpectraPro®-500 spectrograph having a Spectradrive stepping motor scan controller. The vanadium oxide-coated optical fiber tips and a light collector fiber were aligned inside a micro-coil heater shown in Figure 5c, and the effect of temperature on the transmission spectrum of the vanadium oxide film was evaluated. Similar measurements were carried out on an uncoated silica optical fiber and these served as reference spectral measurements.

Incorporation of vanadium oxide (VO_x) inside the optical fiber involved taking an optical fibers with an annealed vanadium oxide film on its tip and depositing a 3-4 μm layer of fused silica on the film. This silica-coated fiber was fused to an uncoated optical fiber to form a continuous optical fiber structure containing VO_x inside the fiber matrix. A schematic, illustrating the formation of a continuous inline fiber sensor with PLD deposited vanadium oxide inside the optical fiber matrix, is shown in Figure 6a. Figure 6b shows an optical microscope image of an optical fiber an annealed vanadium oxide film incorporated inside an optical fiber



(a)



(b)

Figure 3. (a) Pulsed laser deposition to deposit Vanadium oxide on the tip of an optical fiber, and (b) Pulsed electron deposition of fused silica on top of an annealed Vanadium oxide film so as to protect the film before fusion to another fiber

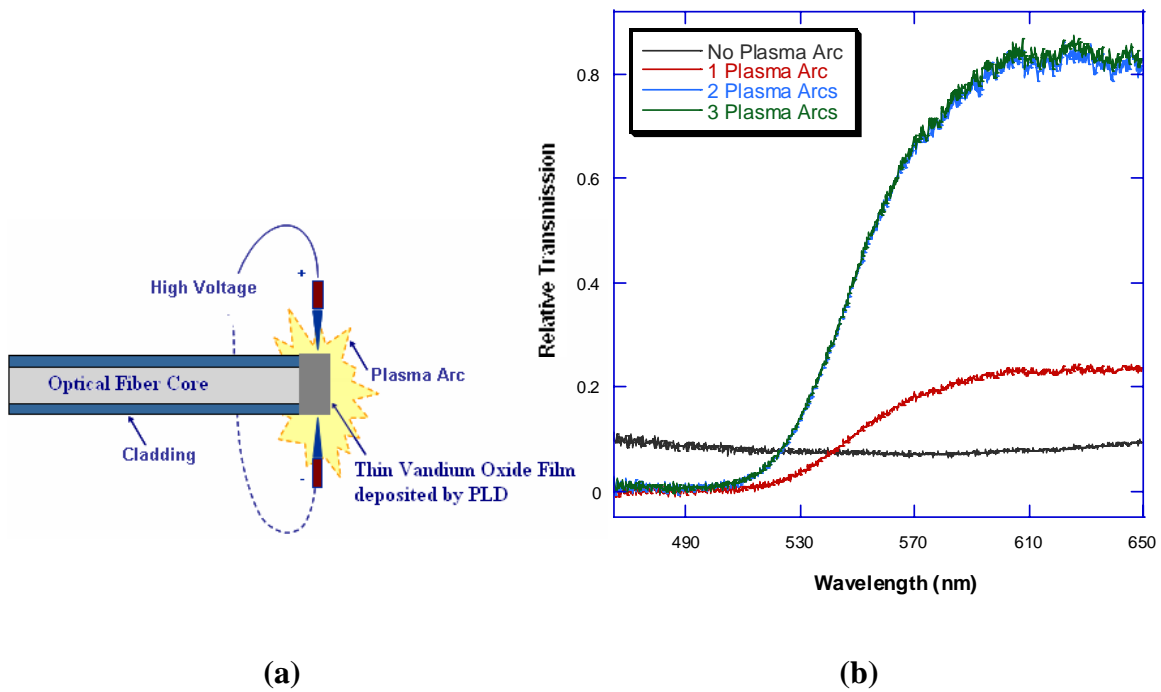


Figure 4. (a) Application of plasma arcs to the Vanadium Oxide film deposited on the tip of an optical fiber, and (b) Effect of application of plasma arcs to the Vanadium Oxide film deposited on the tip of an optical fiber; An increase in the absorption edge was observed upon application of subsequent plasma arcs indicating the increase in crystallinity of the film

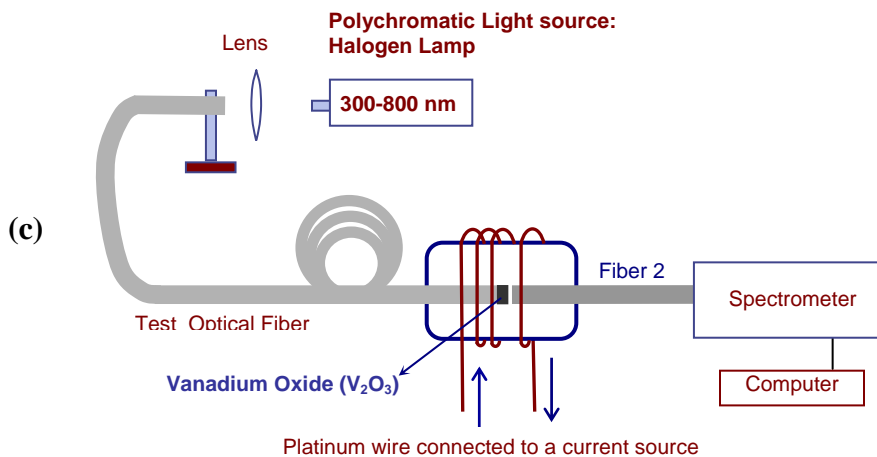
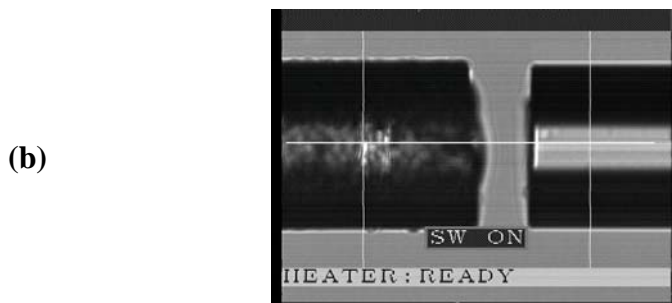
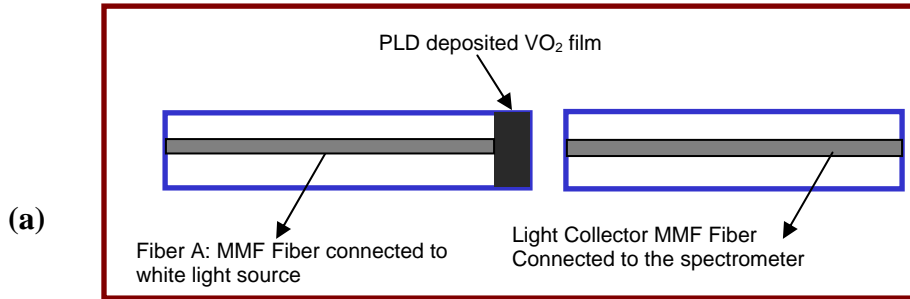


Figure 5. (a) Schematic showing the formation of a tip based fiber sensor with vanadium oxide deposited on the tip of the fiber by using pulsed laser deposition, (b) A fiber with vanadium oxide on its tip after annealing of the film by the application of controlled plasma arcs, and (c) Schematic of the setup employed for evaluation of temperature dependence of the spectrum of the optical fiber containing the Vanadium oxide film on the tip of the optical fiber

matrix to form a continuous in-line fiber optic temperature sensor. Temperature dependence of the transmission properties of the fiber containing vanadium oxide inside the fiber matrix was evaluated by placing these fibers in a micro-coil heater as shown in Figure 6c.

7.2.2 Development of Fabry-Perot cavity based fiber optic sensors

Fabry Perot cavities were developed on the tip of multimode optical fibers by coating the tip of the optical fiber with a 75 nm gold layer employing e-beam deposition. The thickness was calculated, using simulations, such that the reflectance was in the range of 70%-75%. This gold layer formed the first reflective surface of the cavity as shown in Figures 7 a-c. The gold layer was over-coated with a 3-4 μm thick layer of fused silica using the pulsed electron deposition system. A second partially reflecting layer of gold, with a thickness of 75 nm, was then deposited. Asymmetric cavities were formed by depositing the second reflective layer having dissimilar thickness as compared with the first surface.

Three different variations of Fabry-Perot cavities on optical fibers are shown in Figures 7 a-c. The Fabry-Perot cavities shown in Figures 7a and b were formed on the tip of an optical fiber. When the Fabry-Perot cavity shown in Figure 7b is fused to another optical fiber by employing a fusion splicer, one can obtain an inline structure shown in Figure 7c, where the Fabry-Perot cavity is incorporated inside the optical fiber. The light transmitted through the Fabry-Perot cavity was collected using a collector fiber aligned to the Fabry Perot cavity fiber as shown in Figure 8. A white light lamp was employed as the light source and light was coupled into the optical fiber containing the Farby-Perot structure by using a lens arrangement. Optical transmission, of light through the fiber sensors, was measured by using a SpectraPro®-500 spectrograph having a Spectradrive stepping motor scan controller.

7.3 Results and Discussion

7.3.1 Vanadium oxide based inline fiber optic sensors

One can observe in Figure 4a that a novel process of annealing the vanadium oxide films, deposited on the tips of optical fibers, was employed in our work. This process involved application of low intensity plasma arcs on the tip of the optical fiber as shown in the Figure. This process can be considered analogous to rapid thermal annealing of thin films. One can observe in Figure 4b that before the application of plasma arcs, the vanadium oxide film was completely amorphous as indicated by the lack of a sharp band edge. On the application of one

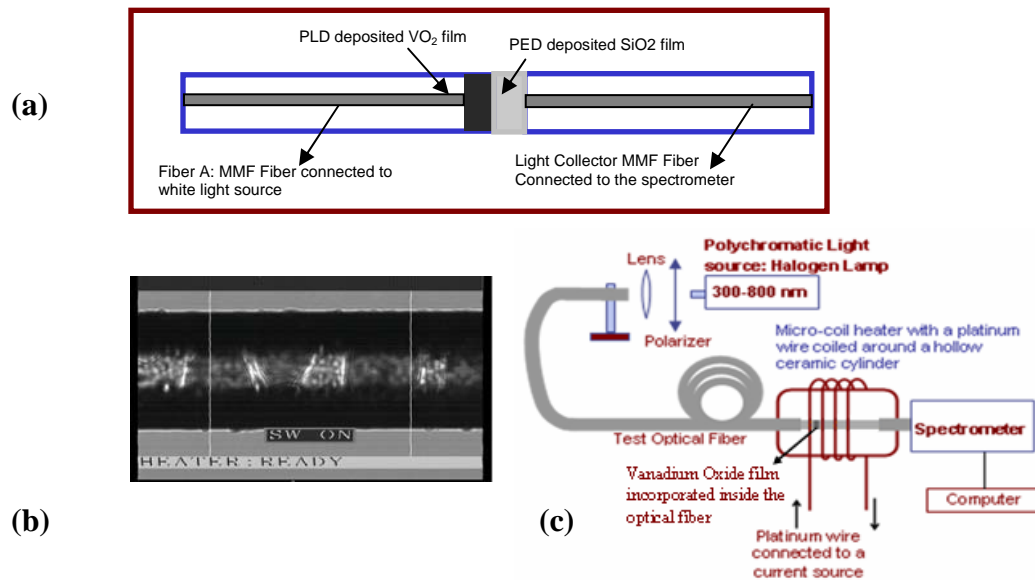


Figure 6. (a) Schematic showing the formation of an inline fiber sensor with vanadium oxide incorporated inside the optical fiber matrix, (b) A fiber with an annealed vanadium oxide film incorporated inside an optical fiber matrix to form a continuous in-line fiber optic temperature sensor, and (c) Schematic of the setup employed for evaluation of temperature dependence of the spectrum of the optical fiber containing the vanadium oxide film inside the fiber matrix

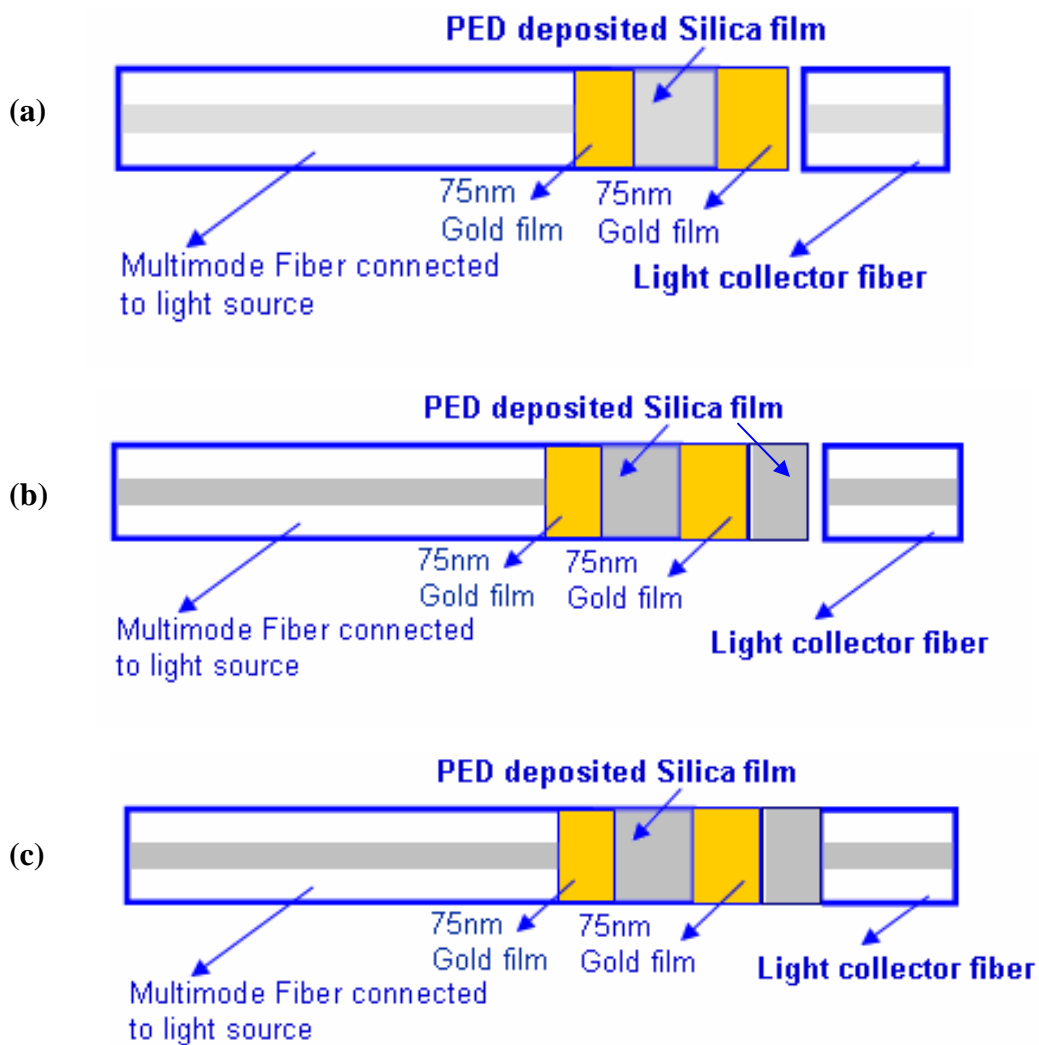


Figure 7. A schematic showing electric and magnetic fields of the reflected and transmitted radiation, when a light wave is incident from a dielectric medium such as silica on a thick metallic film, thickness of the metal film 'd' is ~50 - 75 nm

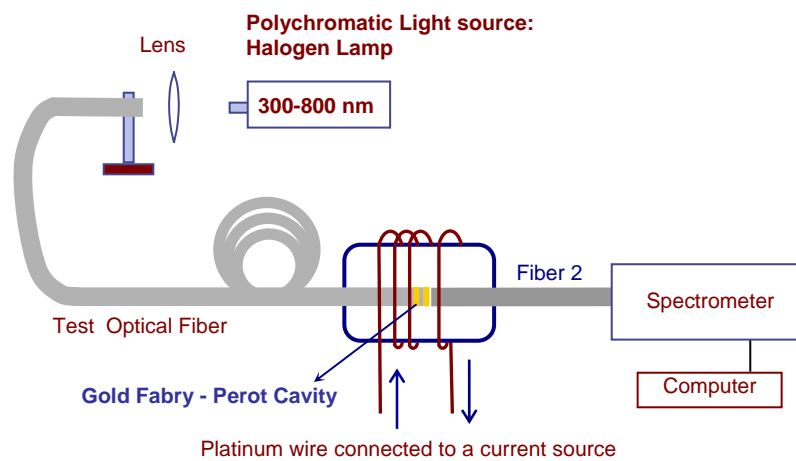


Figure 8. Schematic of the setup employed for evaluation of temperature dependence of the spectrum of the optical fiber containing the Fabry-Perot cavity on the tip or inside the optical fiber

plasma arc, the band edge slope changes but the film is still amorphous. It can be seen in Figure 4b that on application of 2 or 3 plasma arcs, the film has a sharper band edge indicating a polycrystalline character of the vanadium oxide film. Moreover, the shape of the transmission spectrum and the position of the band edge indicate that the dioxide phase of vanadium oxide is achieved on annealing the film, though further studies need to be carried out to investigate the exact phase of the vanadium oxide film on the fiber tip upon plasma arc annealing.

The annealed vanadium oxide film was evaluated for its transmission spectrum, as the temperature surrounding the optical fiber tip was increased, by employing a setup shown in Figure 5c and employing a white light source. The effect of temperature on spectrum of an optical fiber, containing an annealed vanadium oxide film on the fiber tip, is shown in Figure 9a. It was observed that there was a substantial decrease in the optical transmission, especially in the red region of the visible spectrum, as the temperature of the micro-coil heater was increased. The indication of large changes of transmission with temperature in the red region of the visible spectrum are also indicative of the vanadium dioxide (VO_2) phase being formed. It can also be observed from Figure 9a that the transmission spectrum increased as the temperature of the micro-coil heater was decreased. Figure 9b shows the effect of temperature on the optical transmission of an optical fiber, containing an annealed vanadium oxide film on its tip, evaluated at 561 nm wavelength of input radiation. One can observe a substantial decrease in the intensity of the transmitted light as the temperature surrounding the fiber tip is increased. On decreasing the temperature of the micro-coil heater, there is an increase in the intensity value, but the value of relative transmission during the decreasing of temperature is lower than the value when the temperature was increased. One can also monitor a shift in the absorption edge upon increasing the temperature of the vanadium oxide film, as shown in Figure 10, in order to sense the temperature of the surrounding medium. Figure 10 shows transmission spectra that are normalized to the relative transmission intensity of a room temperature sample at ~ 700 nm wavelength. One can observe in Figure 10 that as the temperature of the film increases, there is a shift in the band edge toward the right. A band edge shift of ~ 20 nm was observed when the relative transmission was 0.35. It can also be seen that lowering the temperature back to room temperature causes the band edge to nearly return to the original position, i. e. the band edge position before the heating experiment was carried out. The shift in absorption edge with temperature can be explained by the temperature dependence of the bandgap energy. As the

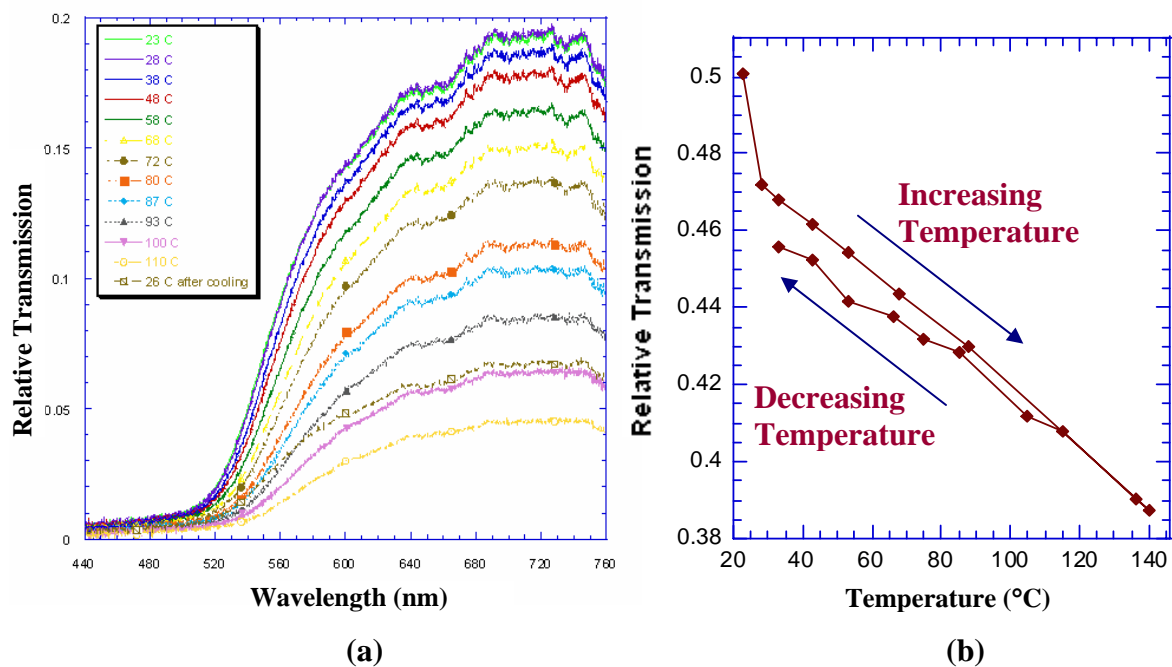


Figure 9. (a) Effect of temperature on Spectrum of an optical fiber containing an annealed Vanadium oxide film on the fiber tip, and (b) Effect of temperature on the optical transmission of an optical fiber, containing an annealed vanadium oxide film on its tip, evaluated at 561 nm wavelength of input radiation

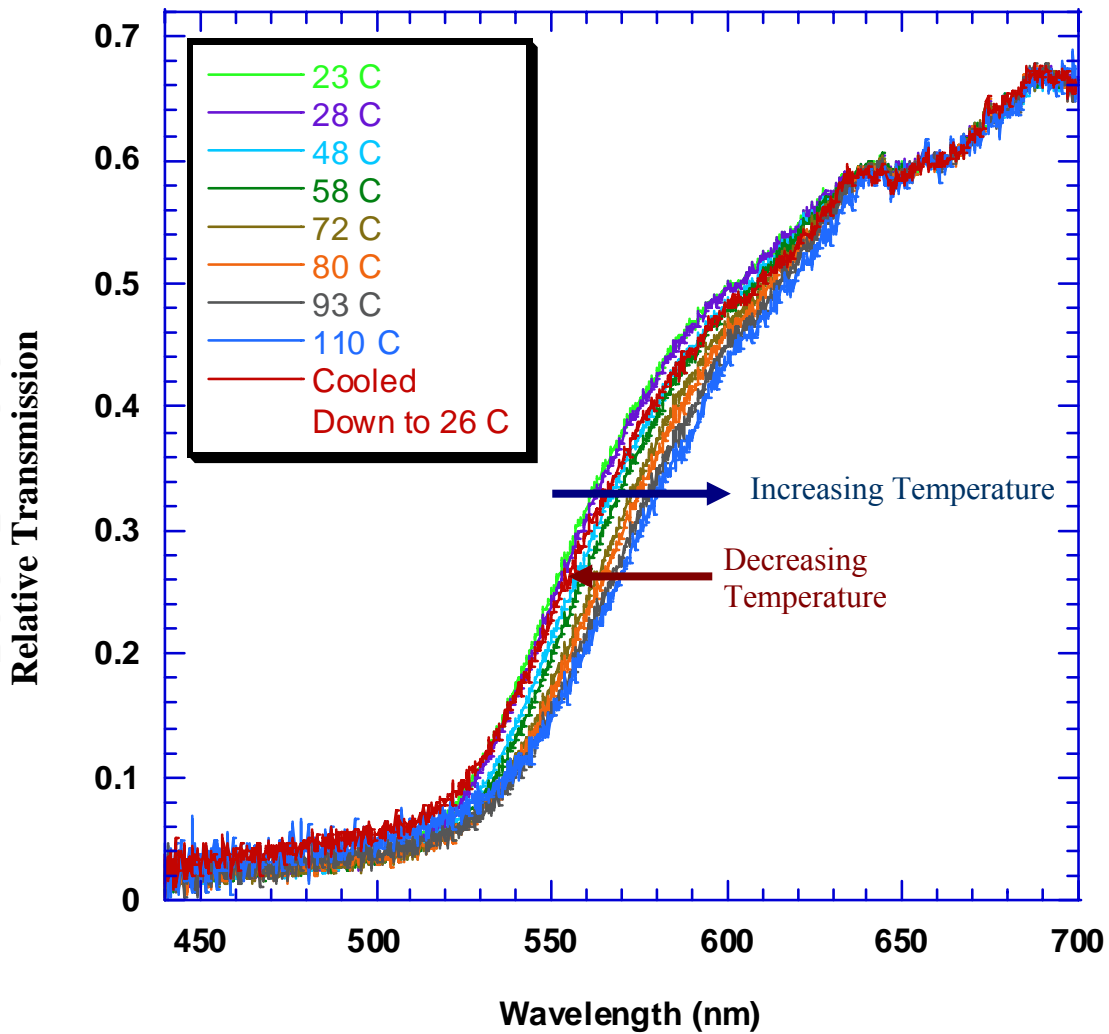


Figure 10. Effect of temperature on the normalized spectrum of the optical fiber, containing vanadium oxide film on the tip of the optical fiber, indicating a shift in the band edge upon increase in temperature around the optical fiber. The band edge comes back to nearly the original position upon cooling back to room temperature. The spectrum was normalized to the intensity of the room temperature spectrum at ~ 700 nm wavelength

absorption coefficient of the vanadium oxide film is dependent on the bandgap energy, the absorption coefficient and therefore the intensity of light transmitted through the oxide film are functions of temperature.

Figure 11 shows the temperature-dependent transmission spectrum of a continuous inline fiber containing a vanadium oxide film inside the fiber matrix. This inline fiber was formed by fusing a fiber, containing vanadium oxide on its tip and over-coated with fused silica, to another optical fiber. It was observed that there was a substantial shift in the band edge upon heating the film and that the band edge nearly comes back to the original position on lowering the film temperature back to room temperature. A band edge shift of ~ 16 nm was observed, at a relative transmission value of 0.4, when the temperature surrounding the sensor was increased from 23 °C to 140 °C. This result can be compared with the fiber optic sensors described by Barmenkov et al. [36], who reported a ~ 12 nm shift in the band edge at a transmittance of 0.4, when the temperature of the glass plate, containing semiconductor CdS and CdSe nanocrystals, was increased from 10 °C to 140 °C.

In the case of the optical fiber containing a vanadium oxide film inside the fiber matrix, it was observed that the transmission spectrum does not decrease with temperature in the red region of the spectrum. This could be attributed to the vanadium oxide film, inside the fiber matrix, having a phase other than the dioxide phase. This could be the result of further annealing of the vanadium oxide film when the fiber containing vanadium oxide on its tip was fused to another optical fiber.

7.3.2 Fabry-Perot cavity based inline fiber optic sensors

The temperature dependence of the transmission spectrum of the fiber optic Fabry-Perot (FP) cavity is shown in Figure 12. One can see a substantial change in the transmission spectrum as the temperature surrounding the FP cavity was varied from room temperature to ~ 140 degrees C and then decreased back to room temperature. One can observe that there is a decrease in intensity of the light transmitted as well as a shift in the position of the peaks when the temperature surrounding the Fabry-Perot cavity is varied. It can also be observed from Figure 12 that the shift of peak position, as a function of temperature, is not the same for all the peaks. The shift in peak position can be attributed to the temperature dependence of the dielectric constant of the medium, i. e. fused silica, between the two reflective surfaces. The temperature and

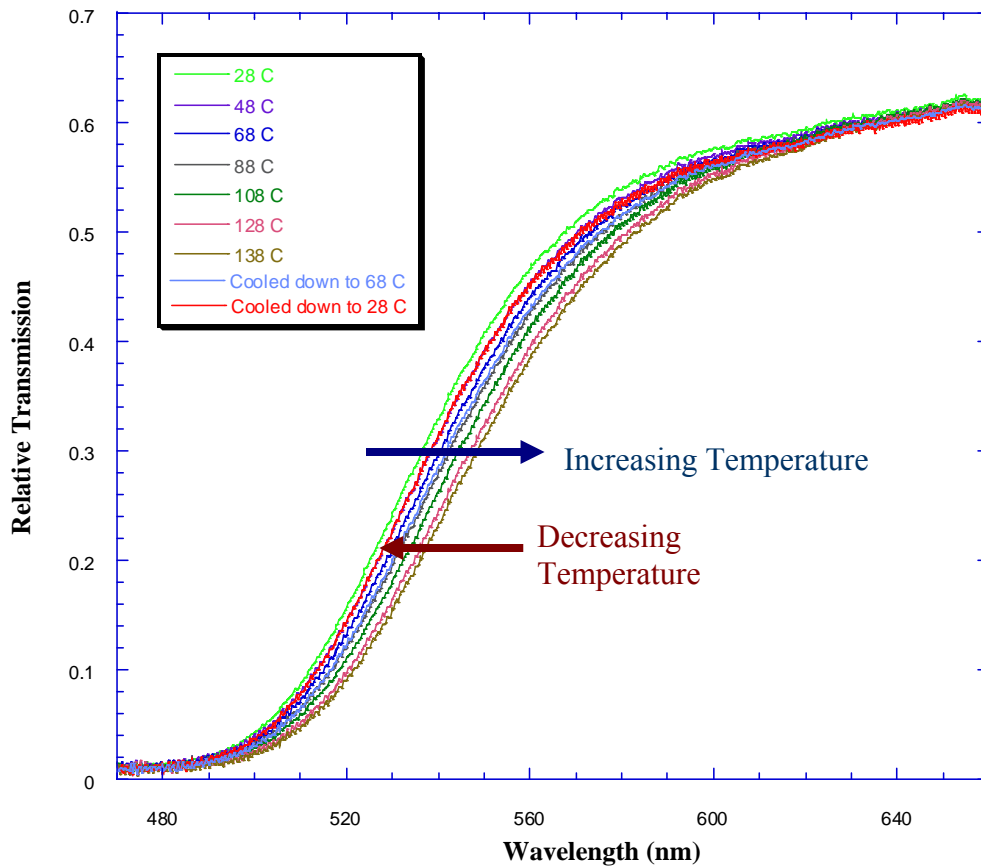


Figure 11. Effect of temperature on the spectrum of the optical fiber containing a vanadium oxide film inside the optical fiber matrix, indicating a shift in band edge upon increase in temperature around the optical fiber

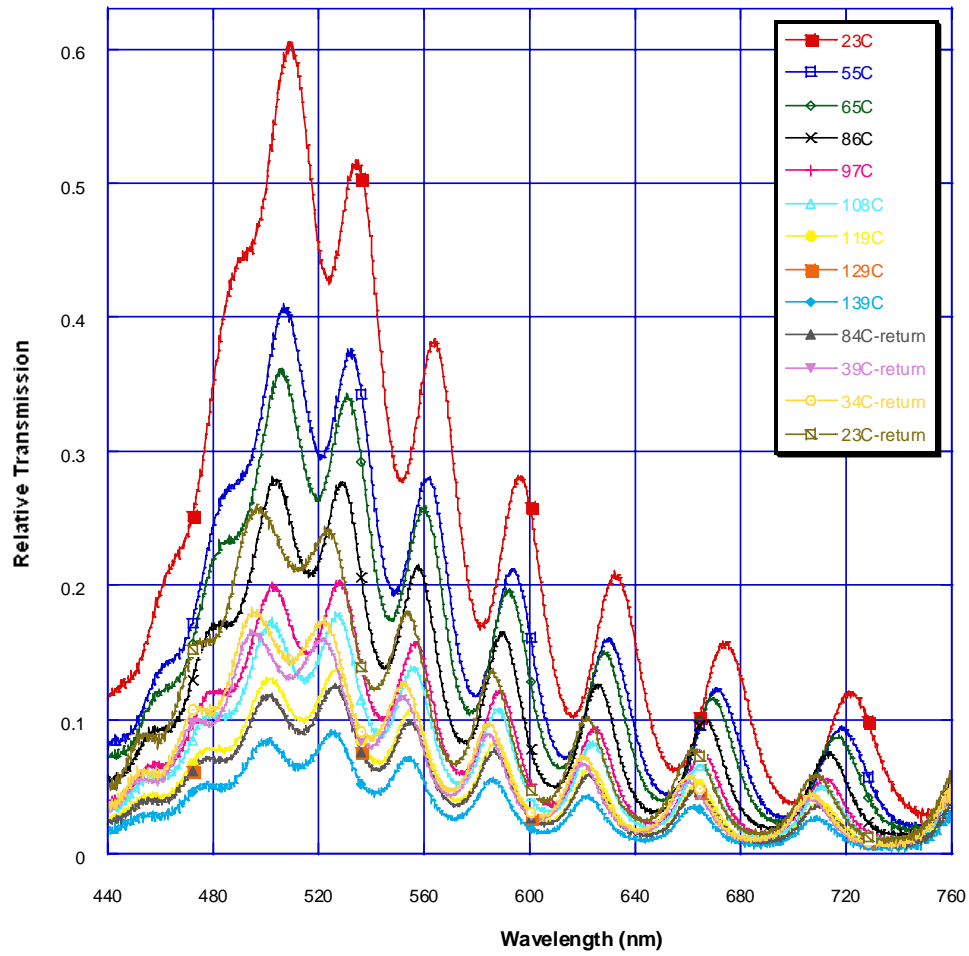


Figure 12. Effect of temperature on the transmission spectrum of the Fabry-Perot cavity

wavelength dependence of the dielectric constant (and refractive index) of silica can be described by the following relationship which was modeled by Ghosh et al. [32]:

$$\begin{aligned} \varepsilon_2(\lambda, T) = & (1.31552 + T \times 0.690754 \times 10^{-5}) + \frac{(0.788404 + T \times 0.235835 \times 10^{-4})(\lambda^2)}{\lambda^2 - (0.0110199 + T \times 0.584758 \times 10^{-6})} \\ & + \frac{(0.91316 + T \times 0.548368 \times 10^{-6})(\lambda^2)}{\lambda^2 - (100)} \end{aligned} \quad (4)$$

The optical length of the cavity is also dependent on the thermal expansion of the cavity dielectric material, but this can be ignored as the magnitude of its effect is less than that of the change of the refractive index of silica with temperature.

The decrease in intensity, of the light transmitted through the Fabry-Perot cavity, as the temperature surrounding the cavity is increased, can be attributed to the temperature dependence of the dielectric constants of the gold films forming the reflective surfaces of the cavity. The Drude-Sommerfeld [20, 33] model, based on the intraband contribution to the dielectric function in a noble metal free electron gas, was used to describe the real and imaginary parts of dielectric constant of the metallic nanoparticles, i.e. ε_{1a} and ε_{1b} . These dielectric constants are dependent on both temperature and wavelength of the incident light and thereby lead to the temperature dependence of the light transmitted through the Fabry-Perot cavity. They are given as:

$$\varepsilon_{1a}(T) = 1 - \frac{\omega_p^2(T)}{\omega^2 + \omega_c^2(T)} \quad (5)$$

$$\varepsilon_{1b}(T) = \frac{\omega_p^2(T)\omega_c(T)}{\omega(\omega^2 + \omega_c^2(T))} \quad (6)$$

The term ω_c in the equations 5 and 6 is the electron collision frequency. The origin of temperature dependence of plasma oscillation frequency (ω_p) is the temperature dependence of the density and the effective mass of electrons. As the temperature dependence of effective mass of electrons is very small, the electron effective mass is assumed constant. Temperature dependent plasma oscillation frequency is given by:

$$\omega_p(T) = \sqrt{\frac{e^2 \left(\frac{N(T_0)}{1 + 3\gamma(T - T_0)} \right)}{m^* \varepsilon_0}} \quad (7)$$

where $N(T_0)$ is the density of electrons at a reference temperature, which was taken as room temperature (300 K) in our study and γ is the thermal linear expansion coefficient. The electron

collision frequency (ω_c), also known as the damping constant associated with the free electron plasma oscillations, is also dependent on temperature and is described as:

$$\omega_c(T) = \frac{\omega_p^2 \epsilon_0}{\sigma(0)} \frac{\left[\frac{1}{10} + \left(\frac{T}{T_\theta} \right)^5 \int_0^{T_\theta/T} \frac{y^4}{e^y - 1} dy \right]}{\int_0^1 \frac{y^5}{(e^y - 1)(1 - e^{-y})} dy} + \frac{1}{12} \pi^3 \frac{\Gamma \Delta}{\hbar E_F} \left[(k_B T)^2 + \left(\frac{\hbar \omega}{2\pi} \right)^2 \right] \quad (8)$$

The first term in equation 8 is associated with the frequency of phonon-electron scattering ($\omega_{c\phi}$) and the second term is related to frequency of electron-electron scattering (ω_{ce}). The third term is due to the nano-particle size effect, when the particle size becomes smaller than the mean free path of the electrons. In equation 8, E_F is the electron Fermi energy (5.51 eV for gold), T_θ is the Debye temperature (185 K for gold), \hbar is the Planck's constant, k_B is the Boltzmann constant, $\sigma(0)$ is dc conductivity ($\sim 1.32 \times 10^{-8} \Omega\text{-m}$ for gold at $T = T_\theta$), Γ is a constant giving the average over the Fermi surface of the scattering probability (0.55 for gold), and Δ represents the fractional unklapp scattering (0.77 for gold). The expression for electron collision frequency (ω_c) that is employed in our calculations is based on models described by McKay et al. [33], Holstein [34] and Lawrence [35]. The derivation for the phonon-electron scattering frequency ($\omega_{c\phi}$) employs the Debye model for the phonon spectrum and is valid assuming $E_F \gg \hbar \omega \gg k_B T$ and $E_F \gg \hbar \omega \gg k_B T_\theta$.

The intensity of light transmitted through the Fabry-Perot cavity, formed on the tip of an optical fiber, was evaluated at a wavelength of 633 nm and plotted as a function of the temperature surrounding the cavity, as shown in Figure 13. One can observe from Figure 13 that there was a substantial decrease in the relative transmission, from 0.2 to 0.015, on increasing the temperature surrounding the FP cavity from 23 °C to 140 °C. Moreover, a linear response of the sensor can be observed in the 23 °C to 95 °C range. Taking the slope of the plot shown in Figure 13, a decrease in the relative transmission from 0.2 to 0.06 takes place - $\sim 70\%$ decrease in the value of relative transmission - when the temperature was increased from 23 °C to 95 °C. This result can be compared with the fiber optic sensors described by Barmenkov et al. [36]. Barmenkov et al. [36] observed band edge shifts in the optical transmission of semiconductor CdS and CdSe nanocrystal doped glasses as the temperature surrounding the sensor was increased. They coupled light from a 635 nm, 40 μW laser having a spectral width of ~ 30 nm, to a glass plate doped with the CdS and CdSe nanocrystals by employing a multimode optical fiber

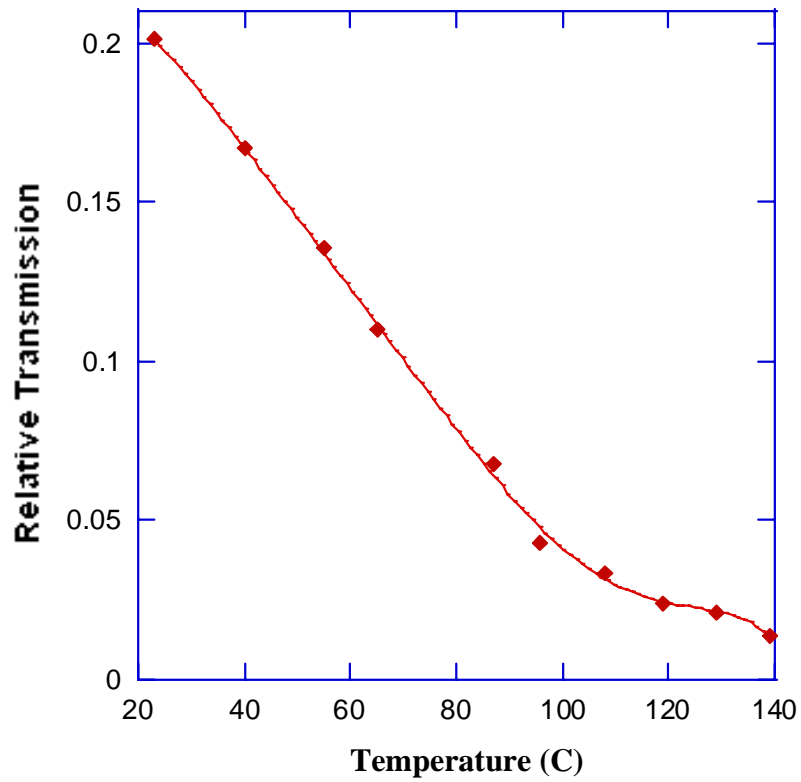


Figure 13. Decrease in temperature on the transmission spectrum of the Fabry-Perot cavity evaluated at a wavelength of 633 nm

and collected light transmitted through the plate with another multimode optical fiber. They measured the voltage signal, detected by a photodetector, as the temperature surrounding the sensor was increased from -20 to 120 °C. They reported a 8.3% decrease in the voltage signal when the temperature was decreased from 23 °C to 95 °C.

7.4 Conclusions

Optical fibers containing vanadium oxide films, on their tips and inside the fiber matrix, were employed for sensing temperature. The sensing mechanism was based on monitoring the shift in the transmission spectrum, either change in intensity at a given wavelength or a band-edge shift, of the optical fiber structures as a function of temperature. Amorphous vanadium oxide films were deposited on the tips of optical fibers using pulsed laser deposition and plasma arc annealing, of these vanadium oxide-coated tips, was carried out to develop crystallinity in the films. These fiber tips, having the polycrystalline vanadium oxide films on their surface, were over-coated with fused silica using pulsed electron deposition and then fused to another optical fiber to form a robust fiber optic structure. It was observed that there was a significant change in the optical transmission spectrum and a band edge shift when temperature of the optical fibers, having vanadium oxide films inside the fiber matrix or on the fiber tip, was increased from room temperature to around ~140 °C and then decreased back to room temperature. Dependence of the optical transmission spectrum, of the Fabry-Perot cavities formed on the fiber tips and inside the optical fibers, on temperature was also evaluated and it was observed that this transmission spectrum changed substantially as a function of temperature. This was attributed to a change in the optical length of the cavity region due to the temperature dependence of the dielectric constant of the material forming the cavity, i. e. fused silica, and to the temperature dependence of the gold films forming the partially reflective surfaces.

7.5 References

1. R. A. Bianchi , F. Vinci Dos Santos , J. M. Karam , B. Courtois , F. Pressecq and S. Sifflet “CMOS-compatible smart temperature sensors ,” *Microelectronics Journal*, 29 (9), 627-636, 1998.
2. G. C. M. Meijer, “An accurate biomedical temperature transducer with on-chip microcomputer interfacing,” *IEEE Journal of Solid State Circuits*, 23 (6), 1405-1410, 1988.
3. Y. Zhao and Y. Liao, “Compensation technology for a novel reflex optical fiber temperature sensor used under offshore oil well,” *Optics Communications*, 215 (1-3), 11-16, 2003.
4. F. R. Riedijk and J. H. Huijsing, “An integrated absolute temperature sensor with sigma-delta A/D conversion,” *Sensor and Actuators A24*, 249-256, 1996.
5. R. A. Bianchi , F. Vinci Dos Santos , J. M. Karam , B. Courtois , F. Pressecq and S. Sifflet “CMOS-compatible smart temperature sensors,” *Microelectronics Journal*, 29 (9) 627-636, 1998.
6. Ph. M. Nellen, P. Mauron, A. Frank, U. Sennhauser, K. Bohnert, P. Pequignot, P. Bodor and H. Brandle, “Reliability of fiber Bragg grating based sensors for downhole applications,” *Sensors and Actuators A: Physical*, Volume 103 (3), 364 - 376, 2003.
7. A. Dhawan, T. Ghosh, and J. Muth, “Incorporating Optical Fiber-Based Sensors Into Fabrics,” *Proceedings of the Materials Research Society Conference, Symposium H*, March, 2005.
8. A. Dhawan, J. F. Muth, D. J. Kekas, and T. K. Ghosh, “Optical nano-textile sensors based on the incorporation of semiconducting and metallic nanoparticles into optical fibers,” *Proceedings of the MRS Conference*, December, 2005.
9. A. D. Kersey and T. A. Berkoff, “Fiberoptic Bragg-Grating Differential-Temperature Sensor,” *IEEE Photonics Technology Letters*, 4 (10), 1183-1185, 1992.
10. M. A. Davis and A. D. Kersey, “Simultaneous measurement of temperature and strain using fibre Bragg gratings and Brillouin scattering,” *IEE Proceedings-Optoelectronics*, 144 (3), 151 - 155, 1997.
11. Z. Y. Zhang, Grattan and A. W. Palmer, “A Novel Signal-Processing Scheme for a Fluorescence Based Fiber optic Temperature Sensor,” *Review of Scientific Instruments*, 62 (7), 1735-1742, 1991.
12. K. T. V. Grattan, A. W. Palmer, and Z. Zhang, “Development of A High-Temperature Fiberoptic Thermometer Probe Using Fluorescent Decay,” *Review of Scientific Instruments*, 62 (5), 1210-1213, 1991.

13. C. E. Lee, R. A. Atkins, and H. F. Taylor, "Performance of A Fiber-Optic Temperature Sensor from -200-Degrees-C to 1050-Degrees-C," *Optics Letters*, 13 (11), 1038-1040, 1988.
14. Huang, Z. Y., Zhu, Y. Z., and Chen, X. P., "Intrinsic Fabry-Perot Fiber Sensor for Temperature and Strain Measurements," *IEEE Photonics Technology Letters*, 17 (11), 2403-2405, 2005.
15. A. Wang, H. Xiao, J. Wang, Z. Wang, W. Zhao, and R. G. May, "Self-Calibrated Interferometric-Intensity-Based Optical Fiber Sensors," *Journal of Lightwave Technology*, 19 (10), 2001.
16. K. Kyuma, S. Tai, T. Sawada, and M. Nunoshita, "Fiber-optic instrument for temperature measurement," *IEEE J. Quantum Electron.*, 18 (4), 676-679, 1982.
17. Y. Zhao, M. Rong, and Y. Liao, "Fiber-optic temperature sensor used for oil well based on semiconductor optical absorption," *IEEE Sensors Journal*, 3 (4), 400 - 403, 2003.
18. P. C. Wait, and A. H. Hartog, "Spontaneous Brillouin-based distributed temperature sensor utilizing a fiber Bragg grating notch filter for the separation of the Brillouin signal," *IEEE Photon. Technol. Lett.*, 13, 508-510, 2001.
19. A. K. Sharma and B. D. Gupta, "Influence of temperature on the sensitivity and signal-to-noise ratio of a fiber-optic surface-plasmon resonance sensor," *Applied Optics*, 45 (1), 151-161, 2006.
20. A. Dhawan and J. F. Muth, "Plasmon resonances of gold nanoparticles incorporated inside an optical fibre matrix," *Nanotechnology*, 17, 2504-2511, 2006.
21. Y. Varshni, "Temperature Dependence of the Energy Gap in Semiconductors," *Physica*, 34, 149-154, 1967.
22. J. I. Pankove, *Optical Processes in Semiconductors*, Prentice-Hall, New Jersey, 1971.
23. S. Lysenko, A. J. Rua, V. Vikhnin, J. Jimenez, F. Fernandez, and H. Liu, "Light-induced ultrafast phase transitions in VO₂ thin film," *Applied Surface Science*, 252, 5512-5515, 2006.
24. P. Jin and S. Tanemura, "V_{1-x}Mo_xO₂ thermochromic films deposited by reactive magnetron sputtering," *Thin Solid Films*, 281 - 282 (1 - 2), 239 - 242, 1996.
25. H. Katzke, P. Toledano, and W. Depmeier, "Theory of morphotropic transformations in vanadium oxides," *Physical Review B*, 68, 024109, 2003.

26. X. J. Wang, H. D. Li, Y. J. Fei, X. Wang, Y. Y. Xiong, Y. X. Nie, K. A. Feng, "XRD and Raman study of vanadium oxide thin films deposited on fused silica substrates by RF magnetron sputtering," *Applied Surface Science*, 177, 8, 2001.
27. Y. P. Zhang, C. J. O'Connor, A. Clearfield, R.C. Haushalter, "An organically templated layered vanadium oxide: Hydrothermal synthesis, single-crystal structure, and magnetic properties of $(\text{H}_3\text{N}(\text{CH}_2)_3\text{NH}_3)[\text{V}_4\text{O}_{10}]$," *Chemistry of Materials*, 8, 595, 1996.
28. D. P. Partlow, S. R. Gurkovich, K. C. Radford, and L. J. Denes, "Switchable vanadium-oxide films by a Sol-Gel Process," *Journal of Applied Physics*, 70 (1), 443, 1991.
29. R. Lopez, L. A. Boatner, and T. E. Haynes, L. C. Feldman, R. F. Haglund, Jr., "Synthesis and characterization of size-controlled vanadium dioxide nanocrystals in a fused silica matrix," *Applied Physics Letters*, 92 (7), 4031, 2002.
30. D. H. Kim and H. S. Kwok, "Pulsed-Laser deposition of VO_2 Thin-Films," *Applied Physics Letters*, 65 (25), 3188, 1994.
31. W. H. Tsai and C. J. Lin, "A novel structure for the intrinsic Fabry-Perot Fiber-Optic temperature sensor," *J. Lightwave Technol.*, 19, 682-686, 2001.
32. G. Ghosh, M. Endo, and T. Iwasalu, "Temperature-dependent Sellmeier coefficients and chromatic dispersions for some optical-fiber classes," *J. Lightwave Technol.*, 12, 1338, 1994.
33. J. A. McKay and J. A. Rayne, "Temperature-dependence of infrared absorptivity of noble-metals," *Phys. Rev. B*, 13, 673, 1976.
34. T. Holstein, "Optical and infrared volume absorptivity of metals," *Phys. Rev.*, 96, 535, 1954.
35. W. E. Lawrence, "Electron-electron scattering in low-temperature resistivity of noble-metals," *Phys. Rev. B*, 13, 5316, 1976.
36. Yu. O. Barmenkov, C. Sifuentes, and A. N. Starodumov, "CdS and CdSe semiconductor nanocrystal doped glasses and their application in fiber-optic sensors," *Revista Mexicana De Fisica*, 46 (2), 64-66, 2000.

CHAPTER 8.
FABRICATION OF SURFACE PLASMON ENGINEERED
FIBER-OPTIC PROBES USING AN ARRAY OF
SUB WAVELENGTH APERTURES

8.0 Fabrication of surface plasmon engineered fiber-optic probes using an array of sub wavelength apertures

Ordered arrays of nanoholes with sub wavelength diameters, and sub micron array periodicity were fabricated on the tips of gold-coated optical fibers using focused ion beam (FIB) lithography. This provided a convenient platform for evaluating extraordinary transmission and possible implementations of nanohole structures for sensors. A variety of optical fiber types: single mode and multimode with step and graded index refractive index profiles were investigated with variety of tip geometries including etched and tapered tips. Significant enhancement of light, transmitted through the fiber optic probes, was observed at certain wavelengths and was found to be dependent on the surrounding refractive index.

8.1 Introduction

There has been substantial interest in the development of surface plasmon engineered structures [1], where the excitation of collective oscillations of electrons by light can be used to make new classes of optoelectronic devices. Interaction of light with sub-wavelength structures such as metallic nanostructures can lead to excitation of surface plasmon waves at the interface of the metal and the medium surrounding the nanoparticles. Surface plasmons are collective oscillations of the conduction band electrons inside or on the surface of metallic thin films, nanoparticles and nano-sized apertures in optically thick metallic films. The excitation of surface plasmon waves in these structures depends not only on the dimensions of the metallic structures but also on the refractive indices of metals and the medium next to the metals. Plasmon resonances of metallic nanoparticles have been employed in the past for the development of chemical and biological sensors [2-3].

The observation of extraordinary transmission of light through sub wavelength apertures has been especially interesting [4, 5]. Controlling the size and periodicity of the an array of sub-wavelength apertures, or by controlling the surface topography of metal around a nano-scale hole, one can engineer the structure to transmit light of desired wavelength through the aperture with the efficiency much greater than what would be predicted by diffraction theory. To date, these investigations have been investigated on flat substrates such as glass or sapphire substrates [6, 7], or free standing metal films [8]. Ebbesen et al. [4], Kim et al. [7], Ghaemi et al. [9], and

Lezec et al. [10] demonstrated enhanced transmission of light through a periodic array of sub-wavelength circular holes in thick silver and gold films. The extraordinary light transmission through the array of nanoholes has been attributed to excitation of surface plasmon waves in the thick metallic films containing the arrangement of nanoholes. Thick metallic films, with an ordered array of nanoholes on it, act like two-dimensional diffraction gratings. Surface plasmon waves are excited, on both sides of thick metallic film, when the propagation constant of the diffraction grating like arrangement of nanoholes matches that of surface plasmon waves [11].

The phenomenon of extraordinary transmission of light through a periodic arrangement of holes is observed mainly in metals, such as gold and silver, which have characteristics like a negative real part of the dielectric constant (ϵ_r) and a high ratio ($|\epsilon_r / \epsilon_{im}|$) of the magnitude of the real and the imaginary parts of the dielectric constant ($\epsilon_r + i \epsilon_{im}$). Gao et al. [12] demonstrated that extraordinary transmission of light through sub wavelength apertures occurs due to excitation of surface plasmon waves in metallic materials having an ordered array of nano-sized holes and does not occur in a material such as silicon. Kim et al. [13] have demonstrated extraordinary transmission of light through a periodic array of holes of non-circular geometries such as elliptical and triangular geometries and have highlighted the dependence of the position of the extraordinary transmission peaks to be polarization dependent.

Initial theories on transmission of light through sub-wavelengths apertures in an opaque material, when the apertures are significantly smaller than the wavelength of incident light, describe the magnitude of transmission to be inversely proportional to the fourth power of the ratio between the hole's radius and the wavelength of the incident light [4, 7, 9]. Ebbesen et al. [4] first demonstrated extraordinary transmission of light through sub-wavelength apertures in a thick silver film and found that the transmission was several orders of magnitude larger than the theory described above. This extraordinary transmission was attributed to the excitation of surface plasmon resonance when the propagation constant of the surface plasmon waves was matched with that of a two-dimensional Bragg grating formed by the ordered array of nanoholes. In the case of excitation of surface plasmons in thin metallic films, matching of the momentum (and wave vector) of an incident photon with that of the surface plasmon waves leads to the plasmon excitation. The excitation of surface plasmons on the surface of thin continuous metallic films is possible only if the light is incident on the surface of the metal at a certain angle to satisfy the dispersion relation for matching the wave vectors of the surface and plasmon waves.

In the case of a periodic array of holes in a optically thick metallic film, the plasmons can be excited by photons incident at normal incidence due to zero order diffraction of the photons that permits an increase in the effective momentum (and the wave number) associated with the incident photons due to the addition of certain multiples of grating momentum wavevectors for the array [4]. In the case of a square array of nanoholes in an optically thick metallic film, the relationship between the wavevectors of the surface plasmon waves (k_{SP}), the component of the incident photon wavevector in the plane of the periodic array grating (k_x), and the periodicity ‘A’ of the square array grating in x and y directions is given as:

$$k_{SP} = k_x \pm m P_x \pm n P_y \quad (1)$$

where m and n are integers and P_x and P_y are grating momentum vectors in the x and y directions in the plane of the grating formed by the periodic array of nanoholes in the optically thick metal film. In the case of normal incidence of light, the component of the incident photon wavevector in the plane of the periodic array grating (k_x) is zero but equation 1 is satisfied due to the integral multiples of the grating momentum wavevectors defined in equation 1. Hence, the zero order diffraction converts the incident photons to plasmons on one side of the metal film, there is coupling of surface plasmon modes from one side of the metal film to the plasmons on the other side of the film.

For a square array of holes at normal incidence of light, the peak positions due to the excitation of surface plasmons is given by the following relationship [4]:

$$\lambda_{\max}(m, n) = \frac{A}{\sqrt{m^2 + n^2}} \sqrt{\frac{\epsilon_{\text{metal}} \epsilon_s}{\epsilon_{\text{metal}} + \epsilon_s}} \quad (2)$$

where A is the periodicity of the holes in the metal array, m and n are the scattering orders from the array, ϵ_{metal} and ϵ_s are respectively the dielectric constants of the metal and the surrounding dielectric medium respectively. Thus, one can observe that the wavelength at which the peak position occurs for each mode depends not only on the periodicity of the holes but also on the dielectric constant of the medium surrounding the array of nanoholes. If the two dielectric mediums on the two sides of the metallic film are different, there are two peaks as given in equation 2, each corresponding to a value of dielectric constant ϵ_s on either side of the metal. The light incident on one side of the metallic film containing the nanohole array excites surface plasmons on that side, is tunneled to the other side of the optically thick metallic film, and excites surface plasmons on that side. The transmission spectrum through this film shows peaks

at different wavelengths with the peak positions corresponding to surface plasmon excitation on the two sides, which have different refractive indices, of the optically thick metallic film. In the discussion of the experimental results the peaks in transmission are identified by the indices (m,n) in equation 2.

Hence, the transmission spectrum through a periodic array, of nanoholes in metallic film, changes as refractive index of the media next to the array of periodic nanoholes is varied. Since the surface plasmon phenomena can be mediated by the refractive index of the surrounding medium, this suggests that these structures like sub wavelength apertures in thick metallic films, can be used as sensors sensitive to the surrounding refractive index. For example, the advantage of studying arrays of sub-wavelength apertures in free standing metal films is that the refractive index is balanced on either side of the film. In this condition the extraordinary transmission of light is enhanced compared to situations where the refractive index is not matched [14]. On flat substrates, depositing a dielectric on sub wavelength metallic structures has been used to demonstrate shifts in the wavelength and efficiency of transmitted light [15]. However, free standing metal films are fragile and inconvenient to work with. Flat substrates are robust and easily fabricated, however the very small size of the nano-hole structures often leads to difficulties in optical alignment as well issues in base lining the optical spectrum, especially if pinholes or scratches mar the gold surface.

Recently there has been interest in the use of localized surface plasmon resonances for fiber optic sensing [16, 17]. In this chapter, we investigate the fabrication of surface plasmon engineered structures on optical fiber tips by the focused ion beam milling and show that these structures are very sensitive to refractive index changes and can be designed to operate at designed wavelengths. Using the tips of optical fibers as the platform, for investigating surface plasmon engineered structures, turns out to be convenient for a variety of reasons:

- a) Optical alignment is easy, and the structures can be easily identified.
- b) Once light is coupled into the fiber, the confinement of the light to the core of the fiber is well understood and efficient.
- c) Etching of the fiber tip with hydrofluoric acid clearly allows the core of the fiber be identified allowing the position of the sub wavelength aperture array to be accurately placed.

- d) Modern focused ion beam milling tools allow generation of arbitrary metallic structures on the nano- to micro-scale with the ability to grey scale the depth of the milling allowing the surface topography of the metal to be controlled in a desired way.

In this chapter, we describe the development of optical fiber probes having extraordinary light transmission at certain wavelengths by forming a periodic array of sub-wavelength holes in a thick gold film deposited on the tip of an optical fiber. We demonstrate that there is a change in the transmission of the fiber optic probes when refractive index of the medium surrounding the gold-coated optical fiber tips, having the periodic arrangement of nano-sized holes, is varied. Hence, these fiber optic probes can be employed for chemical sensing applications based on the detection of refractive index change around the fiber tip. The fiber tips developed by us were evaluated in transmission mode and both single mode and multimode fibers were employed. These optical fiber probes can be employed for in-vivo sensing of concentrations of chemical and biological molecules surrounding the fiber tip. Position and width of the peaks, associated with extraordinary transmission of light through the nano-sized holes, can be tailored by controlling the size, shape, and periodicity of the nano-sized holes [9-10]. This allows control of sensitivity and spectral range of the optical chemical sensors developed on the optical fiber. Extra-ordinary transmission of light in adiabatically tapered optical fibers, coated with a thick layer of gold and having a periodic square array of nanoholes on the tip, was also evaluated.

Although this chapter is limited in scope to the demonstration of these fiber-optic probes by sensing of refractive index around the fiber tip, the use of the fiber optic tip as a platform for surface plasmon engineered structures also suggests they could be employed as optical filters or for optical switching applications.

8. 2 Experimental

In order to form optical fiber probes with extraordinary transmission characteristics, 100 and 180 nm gold films were deposited on the tips of step-index single mode or multimode and graded-index silica optical fibers by employing electron-beam (E-beam) evaporation.

The multimode optical fibers employed in this work were F-MLD fibers obtained from Newport Corporation with a 100 μm core and a 140 μm cladding diameter. The graded index fibers employed in this work were obtained from 3 M Corporation and had a 62.5 μm core and a 125 μm cladding diameter. The single mode and four mode fibers employed in this work had

core diameters of 4 μm and 8 μm respectively, with the cladding diameter being 125 μm for both types of the fibers. The single mode fibers were obtained from 3 M Corporation and the four mode fibers were obtained from Corning Corporation. Gold was also deposited on tapered step-index multimode fibers that were developed by employing a Sumitomo Electric fusion splicer and a tapering software to precisely control the power and the pull distance of the fiber clamps during the tapering process.

Before depositing gold films on the fiber tips, these tips were prepared by stripping the polymer jacket, which was followed by cleaving the fiber with a commercial handheld fiber cleaver to obtain a smooth mirror like surface. The fiber tip were then inspected and cleaned of particulate if necessary. In the case of fibers with small cores, such as single mode and four mode optical fibers, etching the fiber in a buffered 49% hydrogen fluoride oxide etch was found to be very useful in determining where to place that nano-hole array. Typically the duration of the etch was 4 to 8 minutes and the fiber tips were then rinsed in deionized water and blown dry with nitrogen. One could observe the difference between the core and cladding regions of the single and four mode optical fibers by looking under an optical microscope. Even after the fiber tips were coated with a gold film, one could identify the core and the cladding regions as shown in the SEM micrographs in Figures 1a and b. One can observe from Figure 1b that the diameter of the core of the optical fiber tip, coated with a 180 nm gold film, is approximately 4 microns.

After preparation of the optical fibers, electron beam evaporation of the gold was used to coat the fiber tips. Gold was chosen as the metal since it is highly conductive, easily evaporated and is resistant to oxidation. An electron beam, with a current varying between 75 and 85 mA, was directed towards a crucible containing gold slugs, and gold particles evaporated from the slugs were deposited on the tip of the optical fibers. The optical fibers were positioned such that their tips faced the plume of evaporated gold particles emanating from the crucible. A fiber holder made from brass was employed to hold the fibers during the deposition process in a manner that the fiber tips remained normal to the direction of the plume. The evaporation of gold was carried out at a rate varying between 0.08 nm s^{-1} and 0.14 nm s^{-1} at a chamber pressure of 2.7×10^{-6} Torr. In order to deposit gold in a uniform manner, the sample holder was rotated during the electron-beam evaporation process. The thickness of the gold films was measured by a quartz crystal monitor inside the electron beam deposition chamber. Planar glass slides, that were shadow masked, were also placed right next to the optical fibers in the electron beam deposition

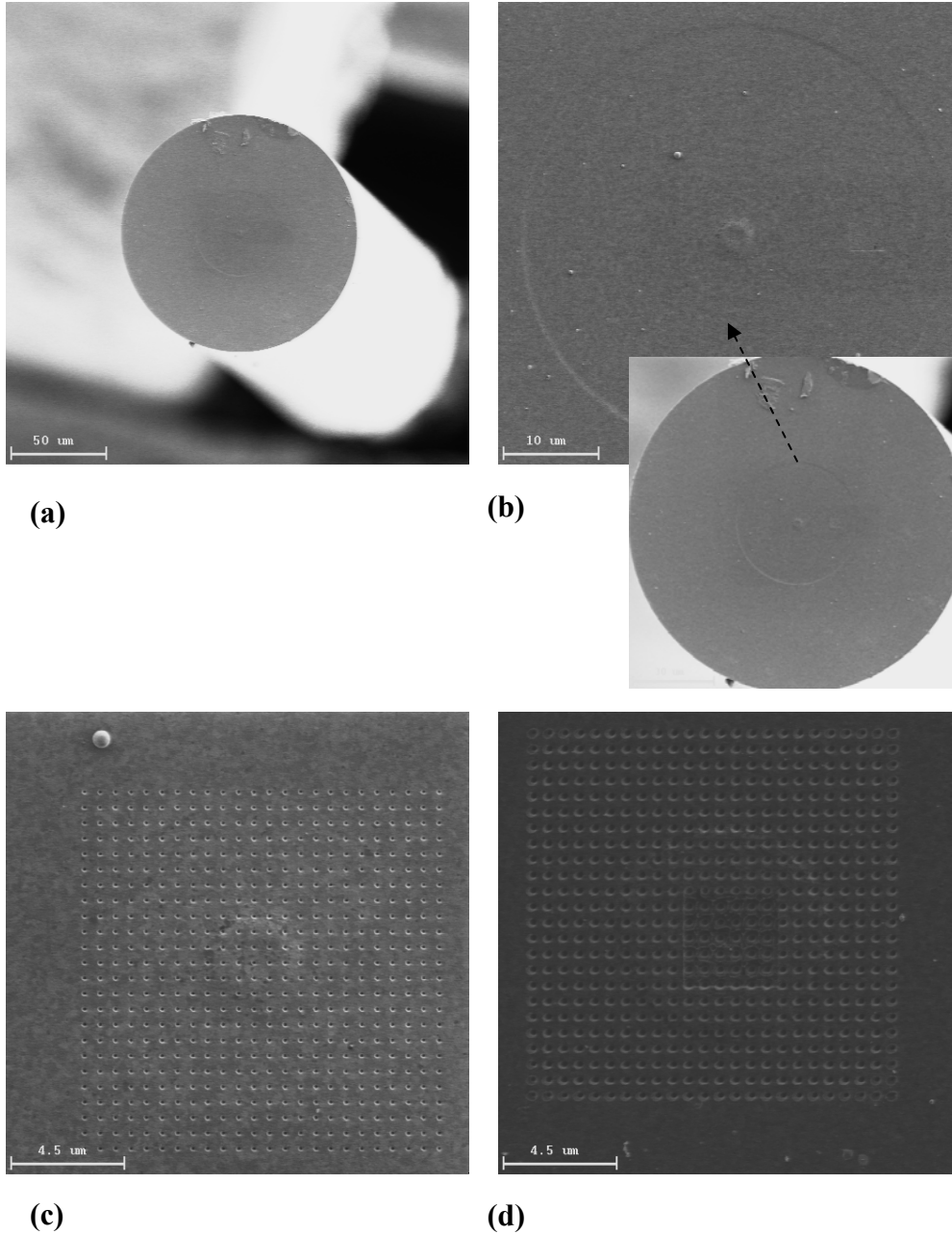


Figure 1. SEM micrograph showing a 180 nm gold film having a periodic square array of nanoholes on the tip of an optical fiber tip: (a) A cleaved end-face of a single mode optical fiber etched with HF and having a 180 nm of gold on it, (b) Close up of the single mode optical fiber, coated with 180 nm gold, showing that the $\sim 4 \mu\text{m}$ core region can be identified due to the HF etching. The inset shows the whole fiber (c) A 24 by 24 array of nanoholes on the core region of the optical fiber tip, and (d) An array of nanoholes on the tip of a four mode optical fiber having a $8 \mu\text{m}$ core region

chamber, so as to accurately monitor the thickness of the gold film deposited on the fiber tip. A Dektak profilometer was employed after the deposition, to monitor thickness of the film deposited on the glass, and the results were compared with the value from the quartz crystal monitor.

A Hitachi D3100 Focus Ion Beam (FIB) milling machine with a Gallium ion source normally used for transmission electron micrograph sample preparation was used to pattern an array of nano-sized holes on the gold films on the fiber tips. A special fiber mount, that could be attached to the sample mount in the Hitachi D3100 equipment, was developed in order to hold the gold-coated fiber tip in place during the FIB process. Typical Gallium ion beam parameters were 40 keV, 0.01 nanoAmps at a magnification of 8000 times. The instrument is equipped with software and a beam blanker that accepts a 512 by 512 image file with 8 bit grayscale, that allow the desired pattern to be milled by rastering the ion beam and controlling the duration and beam current appropriately.

SEM micrographs of a multimode optical fiber, with an array of nanoholes on its tip, are shown in Figures 2 a-d. In this particular sample, a 24 by 24 array of holes was formed and the hole diameter and the center-to-center distance between neighboring holes were selected to be 180nm and 612 nm respectively. Ordered array of nanoholes, having the same dimensions and spacing as in the case of cleaved optical fibers, were also formed on the tips of the gold-coated tapered optical fibers as shown in Figures 3 a-d. Figure 1c shows an array of nanoholes on the core region of the optical fiber tip indicating that the array lies exactly on top of the core region so that the light can effectively interact with the nanohole array grating. Figure 1d shows an array of nanoholes formed on the core of a four mode optical fiber.

Optical transmission measurements were performed using a tungsten halogen lamp as the light source, and a $\frac{1}{4}$ meter spectrometer, with a 600 line per inch grating a cooled CCD spectrometer and a multimode optical fiber input. To investigate the effect of changing the refractive index of the medium surrounding the fiber tip a sensor chamber was fabricated by machining a small metal block that kept the sensor fiber and collecting fiber aligned, while allowing liquids to be applied and removed. The setup, employed for making these measurements, is shown in Figure 4. Light from a white light source (300-800 nm) was focused on to the tip of a fiber and the other end of the fiber was placed inside the sensor chamber. The optical transmission was measured by a collector fiber that was aligned to the gold-coated fiber

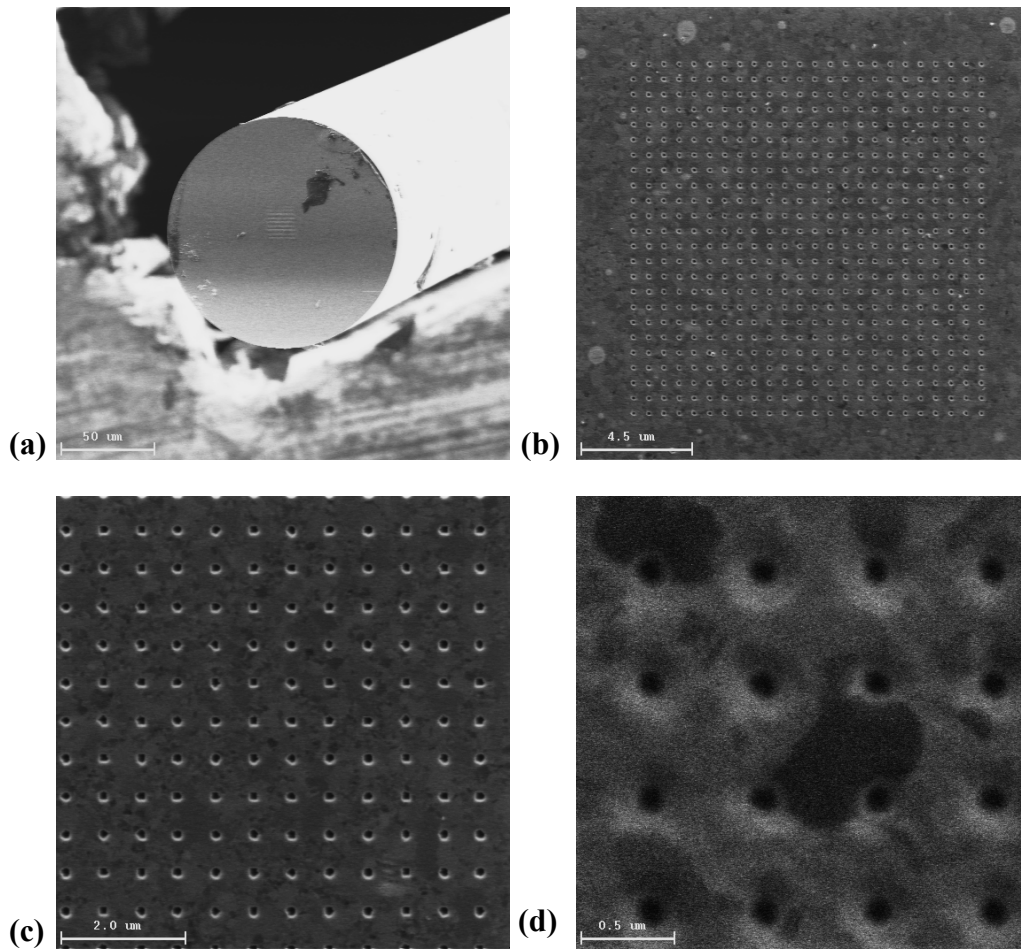


Figure 2. SEM micrograph showing a 180 nm gold film having a periodic square array of nanoholes on the tip of an optical fiber tip: (a) A cleaved end-face of a step-index multimode fiber with a thick layer of gold and a periodic array of nanoholes, (b) A 24 by 24 array of nanoholes on the optical fiber tip, (c) and (d) close-up view of nanoholes on the fiber optic tip

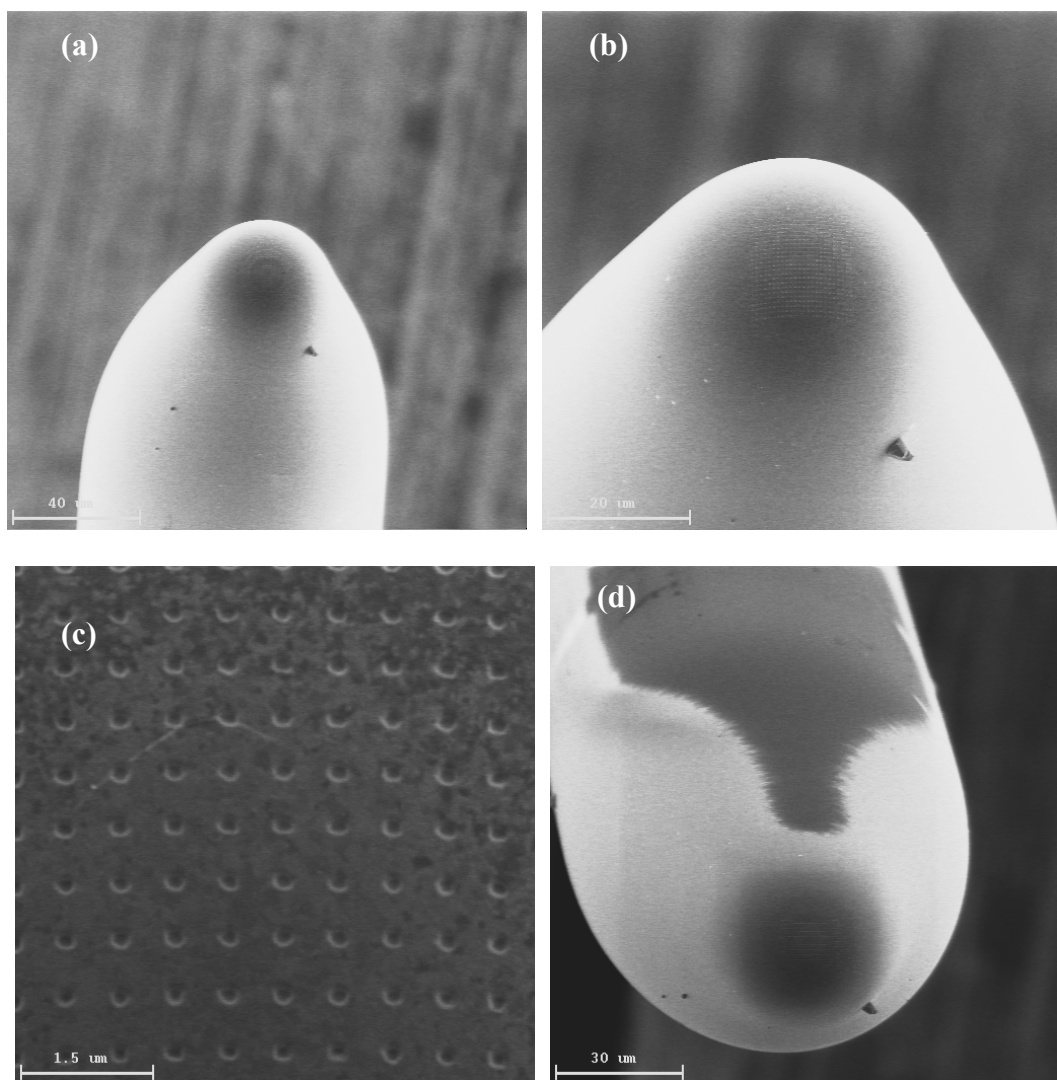


Figure 3. SEM micrograph showing a 180 nm gold film having a periodic square array (24 by 24) of nanoholes on the tip of an optical fiber tip: (a) and (b) Nanohole array on the tip of a tapered multimode fiber, (c) close-up view of nanoholes on the tapered fiber optic tip and (d) tapered multimode fiber (top fiber view) having the nanohole array

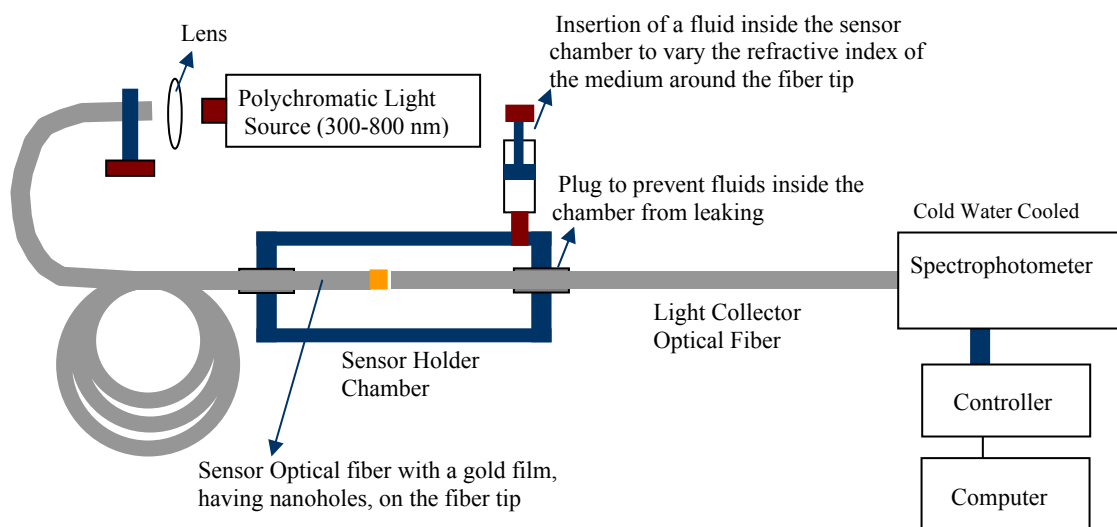


Figure 4. Schematic showing the setup used to evaluate the spectrum of the array of nanoholes in transmission mode. The sensor holder chamber can be filled with a medium of different refractive indices in order to study the effect of medium refractive index on the optical transmission of the gold-coated fiber having nano-sized holes

tip with a space, approximately 300 μm between the fiber tips. In order to measure the effect of changing the refractive index of the medium around the optical fiber probe tip, fluids such as water were inserted into a sensor chamber containing the fiber tip having the nanohole array.

8.3 Results and discussion

Transmission spectrum of a 24 by 24 square nanohole array in a 180 nm gold film on the tip of a multimode optical fiber is shown in Figure 5. The diameter of the nano-sized holes was 180 nm and the spacing between the holes 612 nm and 420 nm, as shown in Figures 5a and 5b respectively. In Figure 5a, one can observe a peak at ~ 498 nm. This peak occurs due to photoluminescence of the gold film, resulting from electron transitions between the d-bands in metal and the Fermi level in conduction band. It was observed that the wavelength and intensity of this peak are not dependent on the shape or size of the nanohole array or on the refractive index of the medium around the nanohole array. In Figure 5a, the peak at 612 nm can be attributed to the (1, 0) scattering order of the nanohole array grating, which is surrounded by air. In this multimode fiber sample, the media surrounding the gold film containing the nanohole array are air and glass with refractive indices 1 and ~ 1.5 respectively. The third peak at around 650 nm can be attributed to the (1, 1) scattering order of the nanohole grating and corresponding to glass as the medium (refractive index ~ 1.5) next to the nanohole array in the gold film. The second and the third peaks are dependent on the structure of the nanohole array, size and shape of the nanoholes, and the refractive index of the media on either side of the nanohole array. It can be seen in Figure 5a that the heights of the second and the third peaks are 48 % and 53 % of the height of the first peak at 494 nm. In Figure 5b, one can observe a peak at ~ 500 nm due to photoluminescence of the gold film, resulting from electron transitions between the d-bands in metal and the Fermi level in conduction band. In Figure 5b, the peak at 570 nm can be attributed to the (1, 0) scattering order of the nanohole array grating, with air as the refractive index of the medium surrounding the gold film. The third peak at around 710 nm can be attributed to the (1, 1) scattering order of the nanohole grating and corresponding to glass as the medium (refractive index ~ 1.5) next to the nanohole array in the gold film. It can be seen in Figure 5b that the heights of the second and the third peaks are 82 % and 93 % of the height of the first peak at 500 nm.

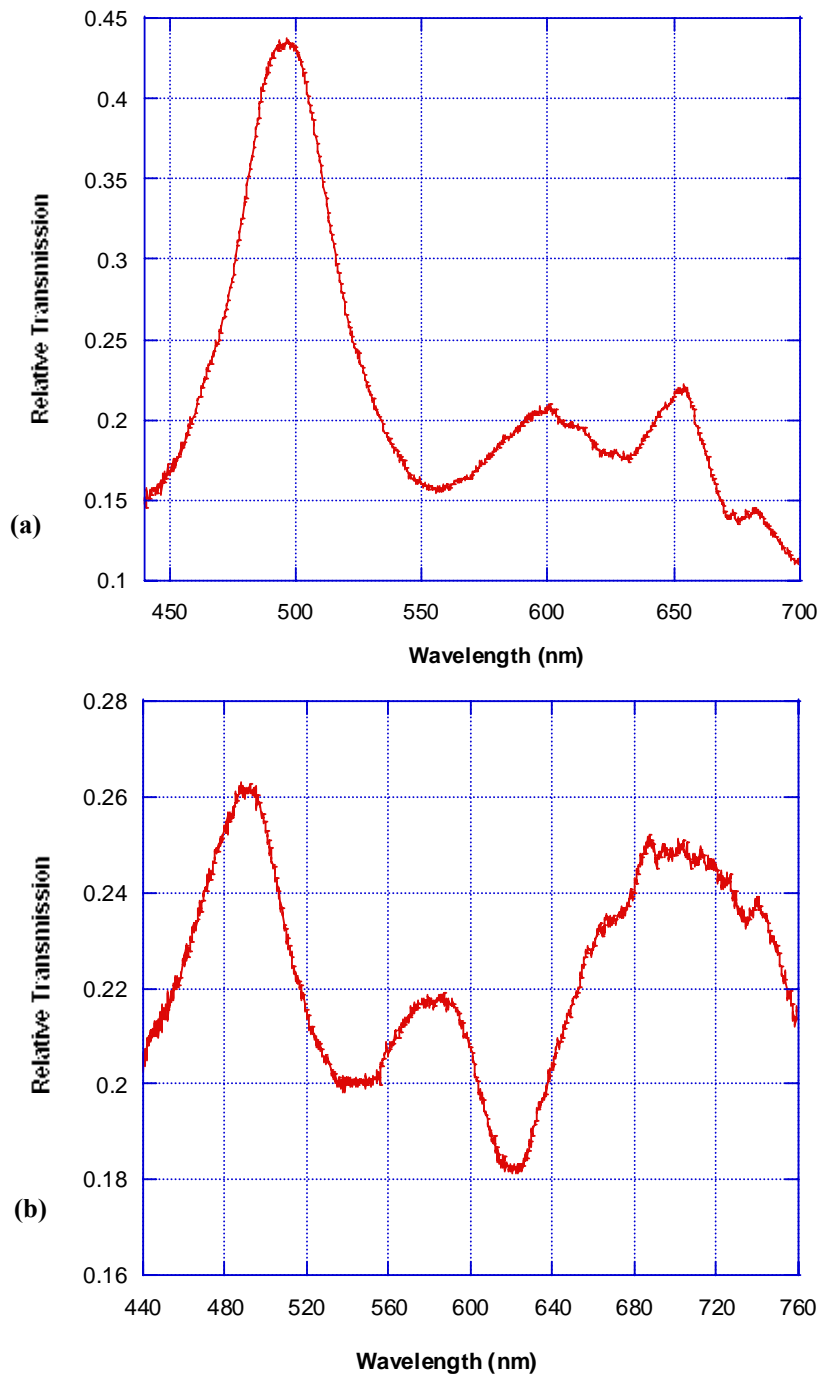


Figure 5. Transmission spectrum of a 24 by 24 square nanohole array in a 180 nm gold film on the tip of a multimode optical fiber, having a 100 μm core. The spacing between the holes was (a) 612 nm and (b) 420 nm. The transmission spectra was evaluated using a white light source and a Spectra©500 spectrophotometer

One can observe in Figure 6 that there was a change in the transmission spectrum as the medium surrounding the multimode fiber tip, having 180 nm gold on its tip and a 24 by 24 array of nanoholes in the gold film, was changed from air (refractive index ~ 1.00029) to water (refractive index ~ 1.329). The spacing between the nanoholes in this array was 612 nm and the hole size was 180 nm. One can observe that the peak which was observed at 612 nm in air is not present when water is inserted in the chamber surrounding the optical fiber tip. This can be attributed to the fact that this peak, labeled as peak A in Figure 6, corresponds to the (1, 0) diffraction order of the nanohole array grating when the nanohole array is surrounded by air and in this peak moves to a much higher wavelength when the nanohole array is inserted into water. It is also observed that the peak shown as peak B in Figure 6 moves to a slightly higher wavelength when the medium refractive index is changed from air to water. Peak B can be attributed to the (1, 1) scattering order of the nanohole grating with silica as the medium next to the nanohole array in the gold film. The change in this peak's spectral position, on changing the refractive index of the medium on the other side of the gold film, can be attributed to a change in coupling of plasmons, from one side of the optically thick gold film to the other, on changing the medium in front of the fiber tip from air to water. Similarly, when the fiber samples with a spacing of ~ 420 nm between the nanoholes in the array were evaluated, the disappearance of peak A was observed when the medium next to the nanohole array was changed from air to water. Peak A in Figure 7 occurs at ~ 560 nm and corresponding to the (1, 0) diffraction order of the nanohole array grating when the medium next to the nanohole array is air. When the medium is replaced with water, this peak is not present around 560-600 nm region and therefore is not present at 560 nm when the medium surrounding the fiber tip is replaced with water. This principle of observing change in peak position or intensity, on varying the refractive index of the medium next to the gold film nanohole array, can be employed to sense the presence of different chemical or biological agents surrounding the optical fiber tip.

In order to get a more controlled interaction of the light modes propagating in the optical fiber with the nanohole array in the gold film, we also developed these arrays on single mode and four mode optical fiber tips that were coated with a 180 nm gold film. In these fiber optic probes, the diameters of the holes were ~ 180 nm and the spacing between the nanoholes was 600 nm, as shown in Figure 1. It can be observed in Figure 1d that the number of holes covering the core region, which has a diameter of ~ 8 μm , of a four mode optical fiber is ~ 170 . The transmission

spectrum this fiber optic probe, having a 8 μm core diameter and an array of nanoholes on a 180 nm gold film deposited on the four mode fiber tip, is shown in Figure 8. This transmission spectrum was normalized to the peak, related to the transition of electrons between the d-bands in metal and the Fermi level in conduction band, occurring at ~ 495 nm wavelength. It can be observed a very sharp peak, with an intensity $\sim 90\%$ of the intensity of the peak related to the transition of electrons between the d-bands in metal and the Fermi level in conduction band, and corresponding to the (1, 0) diffraction order of the nanohole array grating appears at ~ 560 nm. When water was inserted into the chamber, containing the four mode fiber aligned to a collector optical fiber as shown in Figure 4, this peak occurring at 560 nm disappears as can be seen in Figures 9a and b. When water on the fiber tips and in the chamber was dried using a

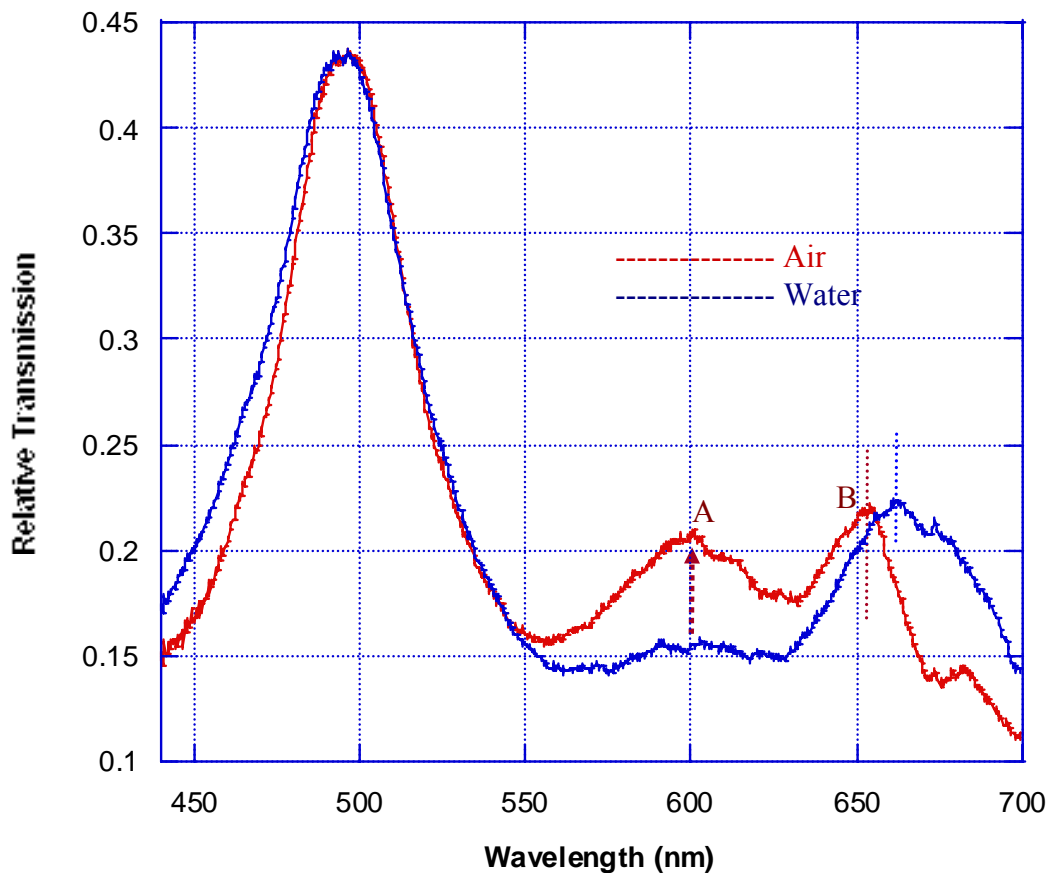
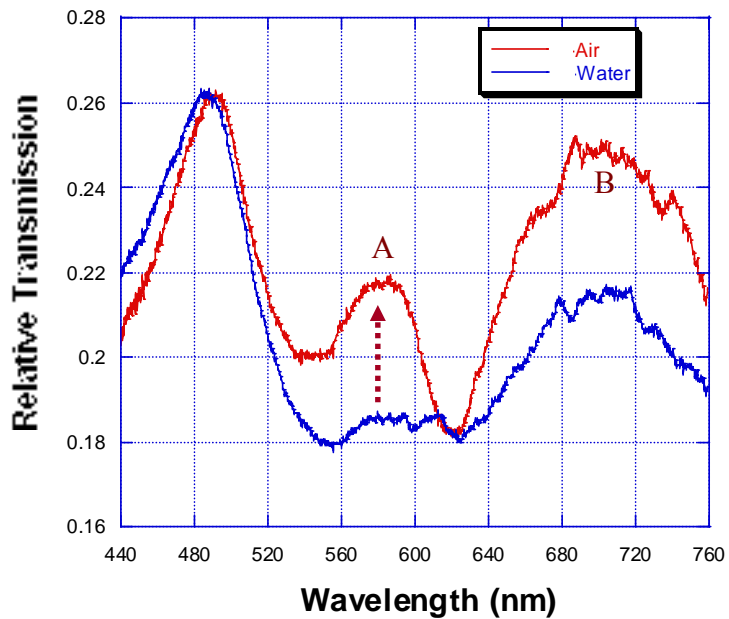


Figure 6. Transmission spectra of a 180 nm gold film having a 24 by 24 square nanohole array on the tip of a multimode fiber. The transmission spectrum was evaluated in the wavelength range 440 -760. One can observe a change in the spectrum and a substantial decrease in normalized transmission at 600 nm wavelength upon changing the medium surrounding the fiber tip from air to water; The transmission spectra was evaluated using a white light source and a Spectra©500 spectrophotometer. The spacing between the holes was 600 nm



(b)

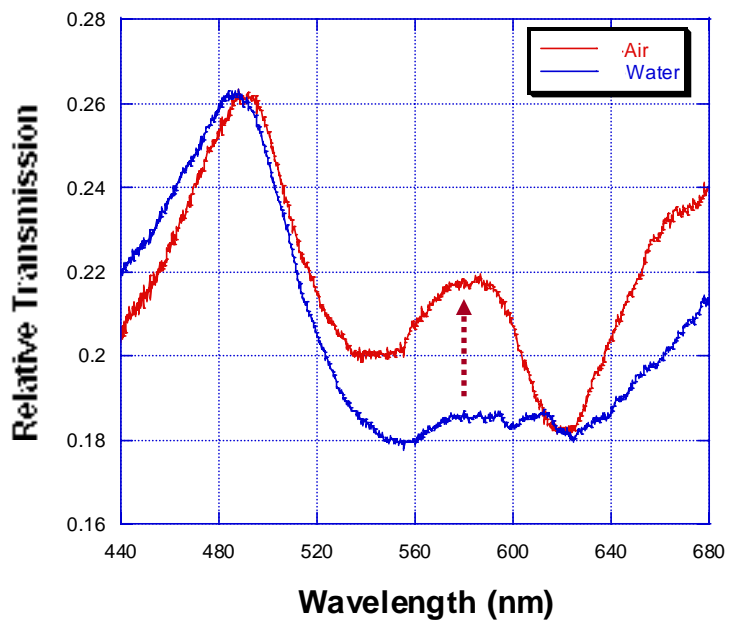


Figure 7. Transmission spectra of a 180 nm gold film having a 24 by 24 square nanohole array on the tip of a multimode fiber. The transmission spectrum was evaluated in the wavelength range 440 -760 nm. One can observe a change in spectrum and a substantial decrease in the normalized transmission at 580 nm wavelength, upon changing the medium surrounding the fiber tip from air to water; The transmission spectra was evaluated using a white light source and a Spectra©500 spectrophotometer. The spacing between the holes was 420 nm

nitrogen gun with a very low flow rate, so that the alignment of the optical fibers is not affected at all, one can observe the reappearance of the peak. When water is added again to the chamber, the peak appeared again as shown in Figures 9a and b. Instead of using a white light source, one could also use a 560 nm laser diode and monitor the change in intensity of the light as the refractive index of the medium surrounding the fiber sensor is varied.

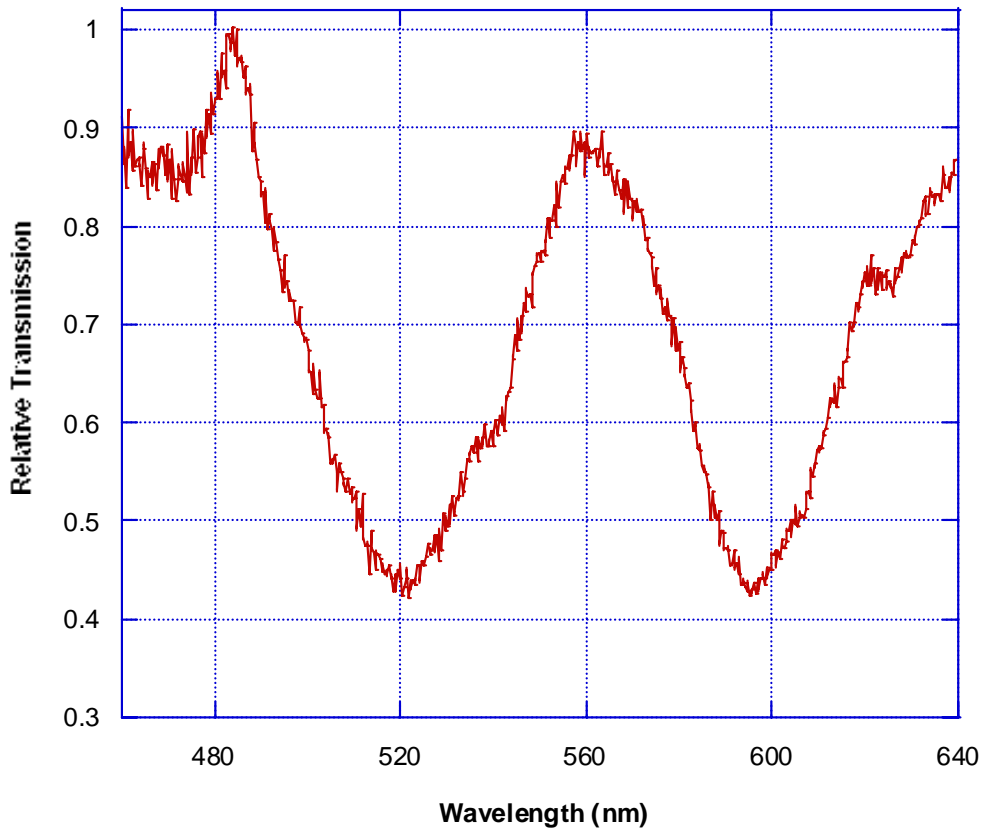


Figure 8. Transmission spectrum, normalized to the D-band absorption related peak, of a 24 by 24 square nanohole array in a 180 nm gold film on the tip of a 4 mode optical fiber, having a 8 μm core diameter. The spacing between the holes was 612 nm. The transmission spectra was evaluated using a white light source and a Spectra©500 spectrophotometer

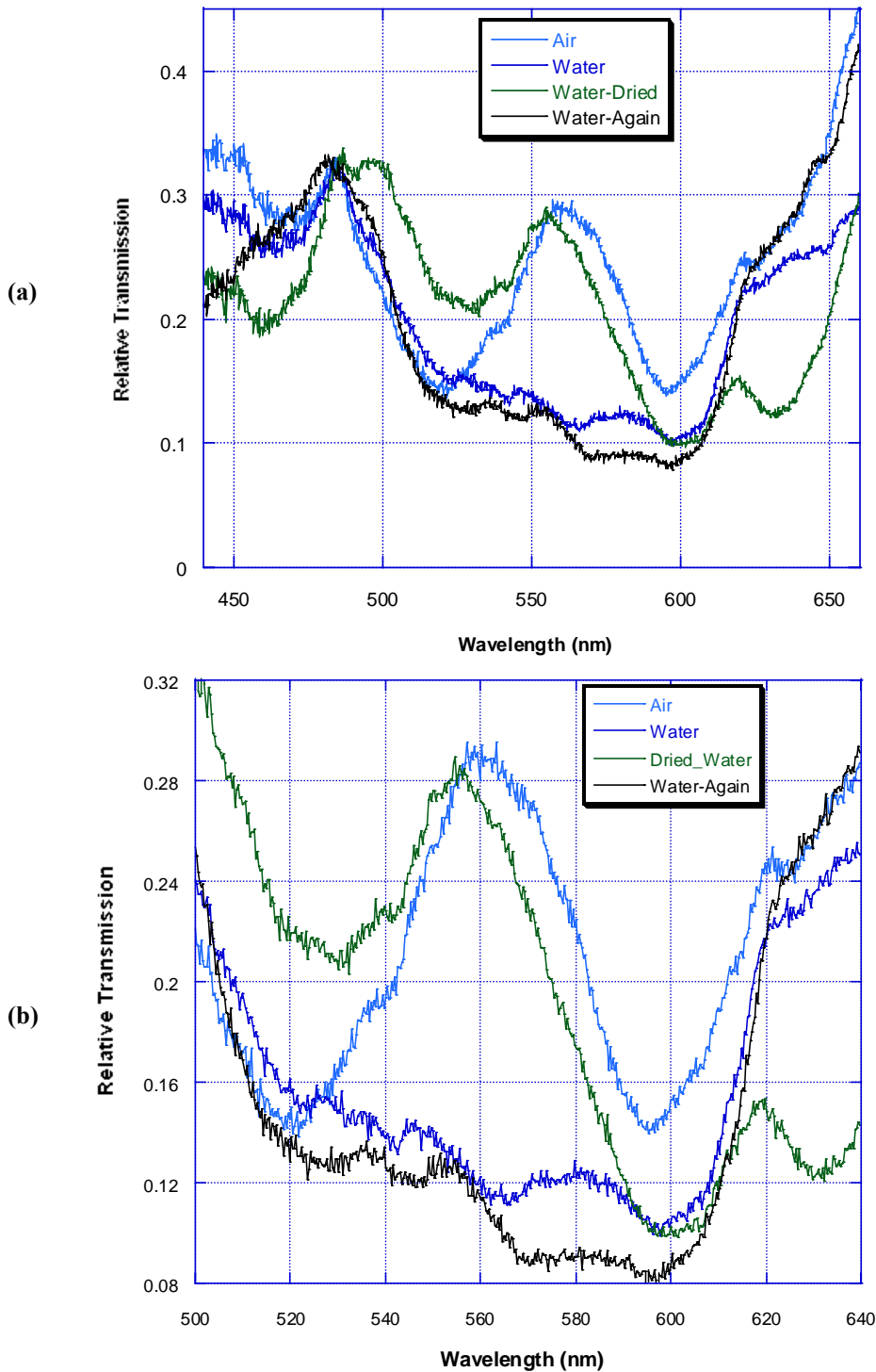


Figure 9. Transmission spectra of a 24 by 24 square nanohole array on the tip of a 4-mode optical fiber, having a 8 μm core, that is coated with a 180 nm gold film as the localized environment around the fiber tip is varied. The spacing between the holes was 612 nm. The transmission spectra was evaluated using a white light source and a Spectra©500 spectrophotometer

8.4 Conclusion

Ordered arrays of nanoholes were developed on the tips of gold-coated optical fiber tips by employing the focused ion beam (FIB) lithography. Transmission spectrum of these optical fibers, with a periodic array of nanoholes developed on 130 and 180 nm gold films deposited on the fiber tip, was evaluated for single mode and multimode fibers using a spectrometer. A square array of holes was formed and periodicity of the holes was varied from 420 nm to 612 nm. Moreover, adiabatically tapered single mode and multimode fibers were also coated with a 180 nm thick layer of gold and a periodic square array of nanoholes was formed on the tapered fiber tip using FIB. Significant enhancement of light, transmitted through the fiber optic probes, was observed at certain wavelengths.

8.5 References

1. W. L. Barnes, A. Dereux and T. W. Ebbesen, "Surface plasmon subwavelength optics," *Nature* 424, 824-830 (2003).
2. J. Matsui, K. Akamatsu, N. Hara, D. Miyoshi, H. Nawafune, K. Tamaki and N. Sugimoto, "An SPR sensor chip for sensitive detection of small molecules using molecularly imprinted polymer with embedded gold nanoparticles," *Anal. Chem.* 77, 4282 (2005).
3. A. D. McFarland and R. P. Van Duyne, "Single Silver Nanoparticles as Real-Time Optical Sensors with Zeptomole Sensitivity," *Nano Lett.* 3, 1057 (2003).
4. T. W. Ebbesen, H. J. Lezec, H. F. Ghaemi, T. Thio, and P. A. Wolff, "Extraordinary optical transmission through sub-wavelength hole arrays," *Nature* 391, 667-669 (1998).
5. A. Benabbas, V. Halté, J.-Y. Bigot, "Analytical model of the optical response of periodically structured metallic films," *Opt. Express* 13 (22), 8730-8745 (2005).
6. J. H. Kim and P. J. Moyer, "Thickness effects on the optical transmission characteristics of small hole arrays on thin gold films," *Opt. Express* 14, 6595-6602 (2006).
7. T. J. Kim, T. Thio, T. W. Ebbesen, D. E. Grupp, and H. J. Lezec, "Control of optical transmission through metals perforated with subwavelength hole arrays," *Opt. Lett.* 24, 256-258 (1999).
8. H. Cao and A. Nahata, "Resonantly enhanced transmission of terahertz radiation through a periodic array of subwavelength apertures," *Opt. Express* 12 (6), 1000-1004 (2004).
9. H. F. Ghaemi, T. Thio, D. E. Grupp, T. W. Ebbesen, and H. J. Lezec, "Surface plasmons enhance optical transmission through subwavelength holes," *Phys. Rev. B* 58, 6779-6782 (1998).

10. H. J. Lezec, and T. Thio, "Diffracted evanescent wave model for enhanced and suppressed optical transmission through subwavelength hole arrays," *Opt. Express* 12, 3629-3651 (2004).
11. A. Degiron and T. W. Ebbesen, "The role of localized surface plasmon modes in the enhanced transmission of periodic subwavelength apertures," *J. Opt. A: Pure Appl. Opt.* 7, S90–S96 (2005).
12. H. Gao, J. Henzie, and T. W. Odom, "Direct Evidence for Surface Plasmon-Mediated Enhanced Light Transmission through Metallic Nanohole Arrays," *Nano Lett.* 6, 2104-2108 (2006).
13. J. H. Kim and P. J. Moyer, "Thickness effects on the optical transmission characteristics of small hole arrays on thin gold films," *Opt. Express* 14, 6595-6602 (2006).
14. A. Krishnan, T. Thio, T.J. Kim, H.J. Lezec, T.W. Ebbesen, P.A. Wolff, J. Pendry, L. Martin-Moreno, and F.J. Garcia-Vidal, "Evanescently coupled resonance in surface plasmon enhanced transmission," *Opt. Commun.* 200, 1-7 (2001).
15. J. Dintinger, S. Klein, and T. W. Ebbesen, "Molecule-Surface Plasmon Interactions in Hole Arrays: Enhanced Absorption, Refractive Index Changes, and All-Optical Switching," *Adv. Mater.* 18, 1267-1270 (2006).
16. A. Dhawan and J.F. Muth, "In-line fiber optic structures for environmental sensing applications," *Optics Letters* 31, 1391-1393 (2006).
17. A. Dhawan and J.F. Muth, "Plasmon resonances of gold nanoparticles incorporated inside an optical fibre matrix," *Nanotechnology* 17, 2504-2511 (2006).

CHAPTER 9.
CONCLUSIONS

9. Conclusions

In this thesis we have described the development of novel fiber-optic sensors such that these sensors could be incorporated into textile fabrics or polymeric film substrates with relative ease. Developing novel inline sensors enables making these sensors more robust and therefore easier to incorporate into textile substrates. Incorporation of multiple optical fibers, with each fiber containing one or more sensor on it, into textile fabrics such as non-woven or woven fabrics can help to form a large area array of these sensors that is flexible, conformable, and easily deployable in the form of carpets, tents, wallpapers fabrics, geo-textiles, or upholstery.

The fiber optic sensors developed in this work were environment sensors and were employed to sense temperature and the change in refractive index of the medium surrounding the sensor. The change of refractive index was the result of a change of chemical around the sensor or adsorption of biological molecules on the surface of the sensor. The chemical and biological sensors described in this thesis are surface affinity sensors that employ plasmon resonances of metallic nanoparticles, islands, and nanoholes, as a means of transducing the input optical signal, are described. Novel methods of forming nanostructures on planar substrates and optical fibers, like focused ion beam lithography, annealing of continuous gold films by employing a focused ion beam, plasma arcs or high temperature, and nanosphere lithography, were also demonstrated in this work.

In order to form robust fiber optic sensors, novel in-line optical fiber structures were designed and developed based on fused single-mode, coreless, and graded index optical fibers. The aim of these in-line structures was to increase the level of interaction of propagating light with the environment for forming evanescent environmental sensors. We carried out analytical and numerical calculations based on Gaussian beam optics and the Beam Propagation Method (BPM) respectively, to determine the dimensions of the different elements of the fused inline fiber optic structures. We applied the inline fiber-optic structures, with metallic nanoparticles on the surface of the coreless sections of these structures, to detect changes in refractive index of the medium surrounding the sensors. We also developed fiber optic sensors based on metallic nanoparticles formed on the tips of optical fibers. Applicability of the fiber optic sensors for biosensing was carried out by monitoring their optical response to binding of biomolecules such as Biotin and Streptavidin to the sensor surface. In this study, the fabrication of ordered arrays of nanoholes with sub wavelength diameters, and sub micron array periodicity on the tips of gold-

coated optical fibers, was also carried out. We employed focused ion beam (FIB) milling to develop the array of nanoholes. Optical fibers provided a convenient platform for evaluating extraordinary light transmission through the array of nanoholes and possible implementations of nanohole structures for sensors. Significant enhancement of light, transmitted through the fiber optic probes, was observed at certain wavelengths and was found to be dependent on the surrounding refractive index. We demonstrated that the sensors, developed by employing extraordinary light transmission characteristics of a nanohole array on the fiber tip, had high levels of sensitivity for detecting changes in bulk refractive index of media around the sensors.

We also incorporated metallic and semiconducting nanoparticles and films inside standard telecommunications grade optical fibers. The optical response of gold nanoparticles, embedded in the optical fiber matrix, was evaluated as a function of temperature; and the use of the structure as an inline fiber-optic temperature sensor is described. A red-shift in the gold nanoparticle related localized surface plasmon resonance-related peak, as well as broadening of the plasmon resonance, was observed upon increasing temperature of the nanoparticle-containing fiber. We developed temperature sensors by incorporating vanadium oxide thin films on the fiber tips as well as inside the optical fiber matrix. Amorphous vanadium oxide films were deposited on the tips of optical fibers using pulsed laser deposition and annealed by employing low intensity plasma arcs. Some of the fiber tips, having the crystalline vanadium oxide films on their surface, were over-coated with fused silica using pulsed electron deposition and then fused to another optical fiber to form a robust fiber optic sensor structure, with a constant diameter of 125 μm . Optical fibers containing vanadium oxide films were employed for sensing temperature based on the shift in the transmission spectrum, including a band-edge shift, of the optical fiber structures as a function of temperature.

Finally, in this thesis, we described ways of developing sensor systems from the individual fiber optic sensors by integrating these sensors into textiles such as woven, knitted, or non-woven fabrics. In this study, optical fiber sensors were incorporated into non-woven fabrics by employing electro-spinning of nanofibers on top of the fiber-optic sensors, to embed the sensors into a non-woven fabric matrix.

In future work, we propose the development of arrays of metallic nanoparticles and other nanostructures, such as nanorods, nanowires, and nanoholes, on the tips of optical fibers by employing techniques such as Deep UV lithography and E-Beam lithography. We propose

employing metals such as silver and copper along with gold, as well as semiconductors such as vanadium oxide (VO_x) and indium gallium zinc oxide (InGaZnO) to form the array of nanostructures on the optical fiber tips. We also propose development of these nanostructures on the surface of the coreless regions of the inline fiber optic structures, described by us in chapters 4 and 5, by employing FIB, Deep UV lithography and E-Beam Lithography. One may need to flatten the surface of the coreless section of the inline fiber structures by mechanical polishing, to effectively employ these processes for developing metallic and semiconducting nanostructures on the fiber surface. We also propose employing the nanohole tip sensors, described in chapter 8 of this thesis, to sense the presence of biological agents such as proteins and antigens along with their use as chemical sensors. Moreover, further work on applying the sensor structures described in chapter 5, for bio-sensing applications needs to be carried out. The application of some of the sensor structures for the detection of basic biological molecules such as Streptavidin and Biotin was demonstrated in this work, but more elaborate work needs to be carried out to apply the sensors to detect the presence and concentration of antigens, antibodies, or proteins. In order to develop inline temperature sensors, one could also explore other processes such as ion-implantation to incorporate metallic and vanadium oxide nanoparticles inside the optical fiber matrix.

PART II

**MECHANICAL ANALYSIS OF
ELECTRONIC TEXTILE CIRCUITS**

CHAPTER 1

INTRODUCTION AND OVERVIEW

1.1 Introduction of fabric based electrical circuits

Conventional printed circuit boards are usually made from metal-clad organic laminated materials and have a conductive wiring pattern inscribed on them by using photolithography or electron beam lithography. It is desirable to have circuits and circuit boards that are flexible and conformable for several applications such as wearable electronics, hand-held electronic devices, flexible displays, and laptops. Flexible circuit boards could be developed by printing circuit patterns on flexible polymeric films or by developing them on textile substrates, which offer higher flexibility in bending compared with polymeric films.

Several processes have been employed by researchers to fabricate fabric based circuits including embroidery, weaving & knitting, and printing or deposition & chemical patterning on textile substrates [1]. Orth et al. [2] and Post et al. [3-4] reported electrical circuits on textile substrates developed by employing embroidery of conductive threads on fabrics made of insulating materials. Some other processes that have been reported include deposition of conducting materials and subsequent etching, reducing, or physical removal of the conductive materials from certain regions. The conductive material that is not removed forms a patterned electrical circuit or a region of higher conductivity. Other processes include in-situ formation of conductive polymeric films on fabric substrates and subsequent patterning of the films using one of the techniques described above [5-6].

One of the disadvantages of embroidery or machine sewing as a means of circuit formation is that one cannot form multi-layered circuits involving conductive threads traversing through different layers as is possible in the case of woven circuits. In sewing conductive threads on fabric substrates, high levels of stress and friction are encountered by the conductive threads due to bending and shear and the tortuous path they have to traverse to form a secure stitch. These stresses can lead to yarn breaks and splices to fix the discontinuities in sewn conductor lines may lead to undesirable additional impedance in fabric circuits. One of the problems associated with patterning of circuits from thin conductive films, either polymeric or metallic, deposited on fabric substrates is that use of an etching agent for forming a circuit pattern leads to non-uniform etching, as some of the etching liquid is absorbed by the threads of the underlying substrate fabric [1].

Another problem with deposition of conductive films on fabric substrates is that bending

of such a fabric may lead to electrical discontinuities at certain points. This problem also exists in printed electrical circuits as conductive materials such as inks or pastes with metallic particles as fillers [7] printed on fabric substrates are stiff and are prone to cracking on bending.

Woven fabrics are well suited for the formation of fabric based circuits due to their structural order and flexibility. In woven fabrics, warp and weft threads can be individually addressed by employing a jacquard weaving machine that allows the formation of complex fabric designs. Hence, very complex circuit designs can be developed on jacquard weaving machines. Moreover, multilayered fabric structures can be formed by the weaving process which can allow the formation of multilayered fabric circuits that have conductive threads traversing from one layer or circuit plane to another according to a circuit design. The ability to form multilayered fabric circuits allows reduction in the density of conductive lines in each layer or circuit plane thereby leading to better signal integrity of these circuits. Moreover, woven fabric based circuits have greater flexibility and conformability than circuits printed on textile substrates or polymeric films and are therefore well suited for the development of applications such as wearable electronic clothing.

A woven fabric-based electrical circuit has been described by Dhawan et al. [8-10] as a network of conducting and non-conducting orthogonal threads that have been arranged and interlaced according to a given fabric design. The conductive threads act as electrical signal carriers in woven circuits whereas the non-conducting threads provide appropriate separation between the conductive threads. Electronic devices can be attached at different locations on this fabric circuit which provides coupling between the devices based on the circuit design. Dhawan et al. [8-10] and Cottet et al. [11] have reported the formation of fabric-based circuits by weaving of conductive and non-conductive threads.

Several issues related to woven fabric circuits that have been investigated by researchers include the formation of effective interconnects between orthogonal conductive threads at crossover points, the formation of disconnects at certain locations along a conducting yarn so as to control the signal path in the circuitry, and the attachment of electronic devices to conducting elements integrated in the fabric. Different techniques can be employed to form interconnections at the crossover point of orthogonal

conductive threads like resistance welding, adhesive bonding, air splicing, and soldering [8 -10]. The techniques that have been employed for the development of disconnects in fabric circuits include cutting of conductive threads using micro-cutters, resistance welding at higher current levels, and laser ablation [12]. The attachment of devices could be carried out either using physical contact between snap-connectors, conducting yarns, and electronic devices or by employing soldering or thermal bonding techniques.

1.2 Importance of studying the bending behavior of woven fabric based electrical circuits

In previous work, researchers have addressed issues relating to the improvement of electrical characteristics of fabric-based electrical circuits, like achieving reliable & robust interconnect formation and improving signal integrity [8 -10]. They have also studied the mechanical characteristics of fabric circuits like their strength, washability and weatherability [13, 14].

Another important mechanical characteristic of fabric circuits is their bending rigidity. A garment made from a conductive fabric could be too stiff and uncomfortable to wear if it contains too many or too rigid conductive elements or crossover point interconnects. One application of fabric circuits includes embedding or developing lightweight and flexible electronics, like transmitters, receivers, displays, and some signal processing devices in the fabrics worn by the soldiers, such that there is a substantial reduction in the weight of electronics carried by the soldiers. Flexible electronics, with a good conformability can also be beneficial for military applications such as formation of large area sensor arrays on a camouflage fabrics that could conform to shape of the surface on which it is laid. Conformability and fabric drape are of great importance in these applications and are dependent on the bending rigidity of the fabric. Along with the military applications, wearable electronics could be applied to several other fields such as biomedical engineering, medicine, homeland security/public safety, transportation, and to consumer products. One application to the field of medicine is the incorporation of electronic devices, such as heart rate measurement devices, thermometers, perspiration and other sensors, into fabrics of patients such that real time monitoring of their physiological characteristics, could be transmitted to a doctor at a remote location.

Conformability and flexibility of fabric circuits is also desirable in some other applications such as flexible displays and fiber based power generation systems.

As described in the previous section, different techniques can be employed to form interconnections at the crossover point of orthogonal conductive threads like resistance welding, conductive adhesive bonding, and soldering. In the case of resistive welding, interconnects formed at the crossover point can restrict the movement of yarns during fabric bending making the overall fabric more rigid if the density of the weld points in the fabric is large. In case the crossover point interconnects are formed by soldering or chemical adhesive bonding, the bending stiffness of the fabric circuit increases together with fabric weight due to the weight of the material, solder or the conductive adhesive, dispensed to form a crossover point interconnect.

Not much work has been carried out previously to study the bending rigidity of woven fabric based electrical circuits and no theoretical model has previously been developed to explain the bending stiffness of fabric circuits based on the number of conductive elements or crossover points present in the woven circuit. The present work addresses the problem of stiffness of fabric-based electrical circuits and attempts to quantify the effect of incorporating rigid elements such as conducting threads into a woven fabric based electrical circuits. Although the models described in this thesis are employed to understand the bending behavior of fabric circuits, these models could also be applied for determining the bending rigidity of other fabrics with rigid metallic threads woven into the fabric structure.

1.3 Thesis Overview

In the second chapter of this thesis, a critical review of published literature on textile-based electrical and optical devices and systems is presented. A section of this chapter focuses on the development of fabric-based electrical circuits, fabric antennas & fiber-based transistors, and describes the methodologies for attachment of electrical and electronic devices to conductive textiles.

In the third chapter, the key elements of a model employed to determine fabric bending rigidity are described. This chapter explains the procedure to determine fabric

bending rigidity based on an energy method that incorporates fabric structural parameters.

In the fourth chapter a theoretical model, that explains the effect of incorporating a certain number of rigid threads in a fabric, in the warp and weft directions, along with flexible threads on the bending rigidity of the fabric, is presented. Theoretical calculations were carried out for conductive fabrics with an arrangement of non-conductive threads. The theoretical models were compared with experimental measurements.

In the fifth chapter, the elastica-based theoretical model described in chapter 3 is applied to fabrics containing multiple welded, fused, or soldered interconnects at the crossover point.

1.4 References

1. T. K. Ghosh, A. Dhawan, and J. F. Muth, "Formation of electrical circuits in textile structures", in *Intelligent Textiles and Clothing*, Edited By H. Mattila, June 2006.
2. M. Orth and E. R. Post, "Smart fabric, or wearable clothing," *Proc. of the First International Symposium on Wearable Computers*, 13-14, Oct 1997.
3. E. R. Post, M. Orth, P. R. Russo, and N. Gershenfeld, "E-broidery: Design and fabrication of textile-based computing," *IBM Systems Journal*, 39(3 & 4), 840-860, 2000.
4. E. R. Post and M. Orth, "Smart Fabric, or Washable Computing," *Proc. First International Symposium on Wearable Computers*, Cambridge, MA, *Proc. of the IEEE Computer Society*, 167-168, 1997.
5. A. R. DeAngelis, A. D. Child, and D. E. Green, "Patterned conductive textiles," *US Patent 5624736*, 1995.
6. H. H. Kuhn, and W. C. Kimbrell, "Electrically conductive textile materials and method for making same," *US Patent 4803096*, 1987.
7. D. P. Cadogan and L. S. Shook, "Manufacturing and Performance Assessments of Several Applications of Electrotiles and Large-Area Flexible Circuits," *Proceedings of the Materials Research Society Conference Symposium D*, Boston, 2002.
8. A. Dhawan, T. K. Ghosh, A. M. Seyam, and J. F. Muth, "Woven Fabric-based Electrical Circuits Part I: Evaluation of Interconnect Methods," *Textile Research Journal*, 74 (10), 913-919, 2004.

9. A. Dhawan, T. K. Ghosh, A. M. Seyam, and J. F. Muth, "Woven Fabric-based Electrical Circuits Part II: Yarn and fabric structures to reduce crosstalk noise in woven fabric-based circuits," *Textile Research Journal*, 74 (11), 955-960, 2004.
10. A. Dhawan, T. K. Ghosh, A. M. Seyam, and J. F. Muth, "Woven Fabric-based Electrical Circuits," *Proc. of Textile Technology Forum, IFAI and the Textile Institute, Charlotte, NC*, 2002.
11. D. Cottet, J. Grzyb, T. Kirstein, and G. Tröster, "Electrical Characterization of Textile Transmission Lines," *IEEE Transactions on Advanced Packaging*, 26 (2), 182-190, 2003.
12. A. Dhawan, T. K. Ghosh, J. Muth, and A. Seyam, "Methods and systems for selectively connecting and disconnecting conductors in a fabric," *US Patent 6852395*, 2002.
13. J. Slade, P. Wilson, B. Farrell, J. Teverovsky, D. Thomson, J. Bowman, M. Agpaoa-Kraus, W. Horowitz, E. Tierney, and C. Winterhalter, "Mechanical Testing of Electrotexile Cables and Connectors," *Proceedings of the Materials Research Society Conference Symposium D, Boston*, 736, D3.2, 2002.
14. J. Slade, P. Wilson, B. Farrell, J. Teverovsky, D. Thomson, J. Bowman, M. Agpaoa-Kraus, W. Horowitz, E. Tierney, and C. Winterhalter, "Improving Electrotexile Wearability Using Stiffness Testing Methods," *Proceedings of the Materials Research Society Conference Symposium D, Boston*, 736, D3.3, 2002.

CHAPTER 2

BACKGROUND AND LITERATURE REVIEW

DEVELOPMENT OF FIBER AND FABRIC BASED ELECTRICAL AND OPTICAL DEVICES AND SYSTEMS

Abstract

In recent years, research and development of flexible and conformable electronics and optical devices has gained momentum. Development of flexible electronics, optical, and opto-electronic devices on textile structures i. e. on fibers, yarns, and fabrics can provide a means of making these devices light-weight, flexible and conformable. Textiles offer opportunities to incorporate sensors and other devices, either by developing these devices on the textile substrates or by attaching them to an arrangement of conducting elements incorporated into the textile substrates, to form large-area electrical and electronic systems. The continuous nature of textiles allows development of large area electronic products with relative ease and at relatively low costs. In this chapter, an attempt has been made to critically review the numerous publications in the literature and patents on textile-based electrical and optical devices and systems. A section of this chapter focuses on the development of fabric-based electrical circuits, fabric antennas & fiber-based transistors, and describes the methodologies for attachment of electrical and electronic devices to conductive textiles. The objectives of reviewing current and previous research and development in the area of fabric circuits are to shed light on the different applications of fabric circuits and to explain why it is important to carry out a detailed study on the electrical and mechanical behavior of fabric circuits. In subsequent chapters, we will describe the study of mechanical properties; mainly fabric bending behavior, of fabric based electrical circuits. This literature review provides a foundation for carrying out further research to study the electrical and mechanical properties of fabric based electrical circuits. Other sections describe the development of fiber or fabric based sensors, sensor systems, and actuators, fabric based power generation and storage devices, and heating systems based on textiles.

2.1 Introduction

In recent years, development of fibers or fiber assemblies (Textile structures) with built-in electrical or optical functionality has been an active area of research. The research and development activities are primarily driven by the motivation of creating multifunctional fiber assemblies that can sense, actuate, communicate, compute, etc. The potential for developing light-weight, flexible and conformable electronic devices on textile products is very significant. Textile substrates offer tremendous opportunities to deploy sensors and other devices, built-in or embedded into the fabric-based network, to create large-area electrical and electronic systems. The convergence of electronics, electrical engineering and textiles technologies has the potential to combine the positive attributes of each technology, the speed and computational capacity of modern electronics, with the flexible, conformable, and continuous nature of textiles. The hierarchical nature (fiber – yarn – fabric – product, etc.) of textile structures makes it particularly suitable for fabrication of electrical devices. Research in the field of fabric-based electrical and electronic devices started in the 1970s, however, the most significant developments have been made in the last 10 years. The research carried out in this area has already been applied to develop commercial products for civilian and military use. It is envisioned that the preliminary research in fiber-based electrical and electronic devices will pave the way for the development of fully integrated electronic textiles (or Electotextiles) with transistors and integrated circuits, sensors and other electronic devices, batteries, solar cells etc. built into the textile (fiber, thread and fabric) structures.

In this paper, an attempt has been made to critically review the numerous publications in the literature and patents on mostly fiber-based (or textile-based) electrical and optical devices and systems. Obviously, these include some of today's commercial products as well as product concepts based on the potential of electotextiles. Section 2.2 provides an overview of the conventional printed circuit boards and multichip modules, discusses the recent developments in fabric-based circuits, and describes the methodologies for attachment of electrical and electronic devices to conductive textiles. This section also describes the research being carried out to develop electronic devices (transistors and integrated circuits) on thin films and thread-like structures. An overview of the research and development in the area of fabric-based antennas is also provided in section 2.2. The

third chapter focuses on sensors, sensor systems, and actuators that could be developed and/or deployed on fibers or fabrics. Fiber-based pressure sensing, environment sensing, strain sensing, and temperature sensing systems are discussed. An overview of optical fiber sensors describing the research involved in integrating these sensors into textiles and composites is also provided in section 2.3. Section 2.4 describes the development power generation and storage devices (batteries, solar cells etc.) on flexible substrates and their integration into textile fabrics or other products. Section 2.5 describes the use of fibers for developing flexible heaters and heating systems. Although newer applications of electrotiles are emerging at a very fast rate, the review provided in sections 2.2-2.5 envisages capturing most of the significant developments so far, in this important area.

2.2 Research in the development of fabric based circuits and devices

2.2.1 Fabric-based circuits and circuit boards

Printed circuit boards (PCBs) are used in the formation of most modern electronic products and devices. Conventional printed circuit boards are multi-layered structures that have a conductive wiring pattern inscribed on different layers of insulating substrates to make interconnects between different electronic or power devices attached to them [1-4]. In the current state of the art technology, PCBs are usually made from organic laminated materials like epoxy or phenolic resins embedded with reinforcement like glass. PCBs have copper foil (or other metals like aluminum) attached to their outer surfaces and these substrates are called copper clad industrial laminates. The interconnect patterns on each copper clad laminate are inscribed using photolithography or electron beam lithography. Copper is mainly used as the wiring/interconnection material in PCBs as it has high electro-migration resistance and low resistivity (as compared to materials like aluminum). The interconnections between different layers (i.e. layers of power, ground, and signal planes) of a printed circuit board include mechanically drilled, blind and buried vias [1-2]. These layers are separated by insulating layers as shown in Figure 1. The closeness of the ground, power, and signal planes and also the separation between signal lines within the signal plane determine the impedance of the signal lines in each of the wiring planes. It also determines the extent of interference between signals on different lines.

The conventional printed circuit boards are made from rigid materials, hence they cannot be bent or flexed beyond a certain point. Flexible circuit boards and multi-chip modules are desirable in many applications in the field of electronics for example if a lot of electronic circuitry has to be placed in a small area (in a spacecraft or airplane) or in hand-held keypads, PDAs, laptops etc. Polymer-based flexible circuit boards have been developed in the past, with not only the dielectric material being polymeric but also the wiring being made from conductive polymers. More flexibility has been provided to the circuit board in certain new developments in which textile based materials are used for the formation of circuit boards – either fabric based printed circuit boards have been constructed by defining certain printed patterns on a flexible (fabric based) substrate or circuit boards/bread boards have been fabricated with conductive and non-conductive fibers arranged in different parts of the fabric with the conductive fibers acting as signal carriers and the non-conductive fibers acting as the insulators. All of these developments and inventions have been described in this section in detail with focus on constructions of these flexible circuit boards, their manufacturing procedures and applications.

In a patent by Leiby et al. numbered US5906004 [5], a conducting textile fabric and clothing has been reported. This conducting fabric provides wired coupling or interconnect between portable electronic devices connected to (and integrated within) the textile fabric and also wireless coupling with a remote electronic device. A woven textile fabric having conductive fibers in the warp direction only, has been described in this patent [5]. It has been described that holographic fibers (fibers that selectively absorb or reflect different wavelengths of light using layers of transparent optical media with different indices of refraction) could be used in conducting fabric networks for developing flexible display screens (see Figure 2). A holographic fiber described in Figure 2 consists of a central core, labeled as 26, which is light absorbing. The central core is coated with layers of optical media that have different refractive indices. In one of the configurations proposed in this patent, the different layers labeled as 28, 30, 32, and 34 in Figure 2, have refractive indices n_1 , n_2 , n_1 , and n_2 respectively. When light is incident on the holographic fiber, a part of the light gets transmitted to the core of the fiber and gets absorbed by the central core layer and a part of the light is reflected back from the multi-layered optical fiber. This reflected light will have a specific color

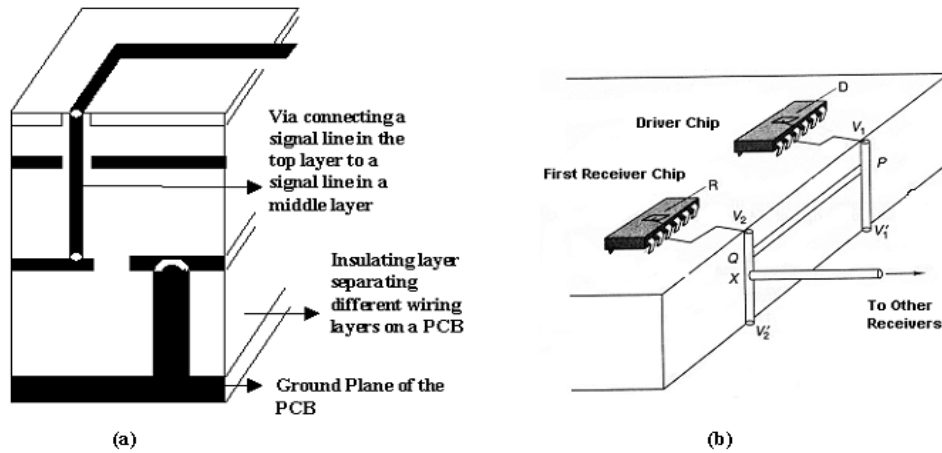


Figure 1. (a) 3-D sectional view of a multilayered printed circuit board showing interconnections between different layers that are achieved by using vias. Separation between the different interconnect, ground, and power planes is achieved by using insulating mediums between the different layers; (b) Interconnection between a driver chip and several receiver chips using

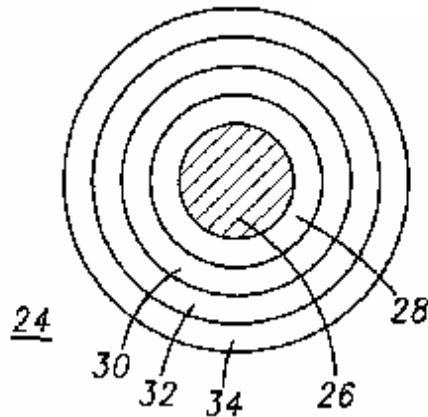


Figure 2. Cross-section of a holographic fiber showing the different layers with different cross-sections

corresponding to wavelength of the radiation reflected by the holographic fiber. Another textile fabric, which has conductive fibers or yarns woven in both warp and weft directions, has been described in this patent [5]. This fabric served as an antenna in a certain segment of a garment to have wireless communication between an electronic device placed on the conductive fabric and a remote electronic device.

Dhawan et al. [6-11] have reported the formation of fabric-based circuits by arranging and interlacing conductive and non-conductive threads according to a given fabric design. Multilayered conductive fabrics were produced on a rapier weaving machine (equipped with a jacquard shedding system) using conducting (copper and/or steel) and non-conducting threads. Development of interconnections, between different orthogonal conductive threads to route the signals in these circuits, was carried out. Different techniques were identified and explored as potential methods to form interconnects at crossover points of woven circuits. Evaluation of resistance welding as a method of formation of crossover point interconnects in woven fabric-based electrical circuits has been discussed [6, 8, 9]. Two kinds of resistance welding processes i.e. top-bottom probe welding and parallel gap welding were used to form crossover point interconnects in fabrics containing steel and copper threads. To evaluate the effectiveness of resistance welding, DC resistance values of conductive threads in and outside the fabric were measured. It was observed that the resistance across a crossover point of two woven (welded and unwelded) copper yarns was found to be higher than that of a copper thread (not woven into the fabric). In all cases, the DC resistance values of the welded samples were found to be less than those for woven copper samples without any weld. Scanning Electron Microscope (SEM) images of resistance-welded and unwelded fabric samples of copper and steel conductive threads were obtained in order to analyze the nature of the crossover point interconnects (Figure 3). In addition to crossover point interconnects, woven electrical circuits require formation of disconnects or cuts at predetermined locations along a conducting yarn so as to control the current path in the circuitry. Disconnects can be formed by creating a fabric with "floats" at certain points. These floats could be selectively cut by appropriate cutters to form the disconnects. Dhawan et al, also reported introduction of disconnects using properly set up parallel gap resistance welding technique [9].

Researchers working in the area of electronic textiles realize that there are numerous challenging issues to be addressed like achieving reliable and robust interconnect formation, improving signal integrity (crosstalk noise) , maintaining textile characteristics (lightweight, flexibility, strength, conformability, etc.), providing efficient means of power generation/harvesting, addressing washability and weatherability for wearable electrotexiles [12, 13, 14]. In order to study and evaluate AC signal crosstalk noise in woven circuits, Dhawan et al. used AC signals varying between 10 KHz-15 MHz on woven transmission lines (called aggressor lines) and evaluated the effect of these signals on the neighboring quiet lines (carrying no signal) [7, 12, 13]. They observed that the magnitude of crosstalk noise increased as the spacing between the conducting lines is decreased, see Figure 4. Moreover, as the frequency of the signals transmitted through the aggressor line is increased, the magnitude of the crosstalk noise also increased. Coaxial transmission line-like thread structures were developed by wrapping an insulated conductive thread with a conductive thread and twisted-pair thread structures were developed by twisting two insulated copper threads. Dhawan et al also observed that there was a significant reduction in crosstalk noise when twisted-pair (see Figure 4) and coaxial yarns were used to form these circuits.

Development and application of electronic textile acoustic arrays, for use in accurate tracking and location of targets via beam-forming and triangulation, has been carried out [15, 16]. Primary advantages of these fabric-based large-area acoustic sensor arrays are their ability to flex and conform to their surroundings, ability to be camouflaged to suit their surroundings, light weight, and ease of deployment. The fabric-based acoustic array serves as a passive SONAR and can detect gun shots, vehicle and troop movement. Grant et al. [16] produced a 5x4 element prototype acoustic array on a 3m x1m fabric substrate (Figure 5). This acoustic array was developed by weaving of conductive elements in a large area textile substrate and subsequent attachment of microphones at certain locations.

Research is also being carried out to develop active Parafoil fabrics [12]. Parafoils can be dropped precisely to a desired target if their lift to drag ratio can be controlled during deployment. One way of changing the lift to drag ratio is to change the porosity and thereby air permeability of the parafoil fabric. Different concepts for actively

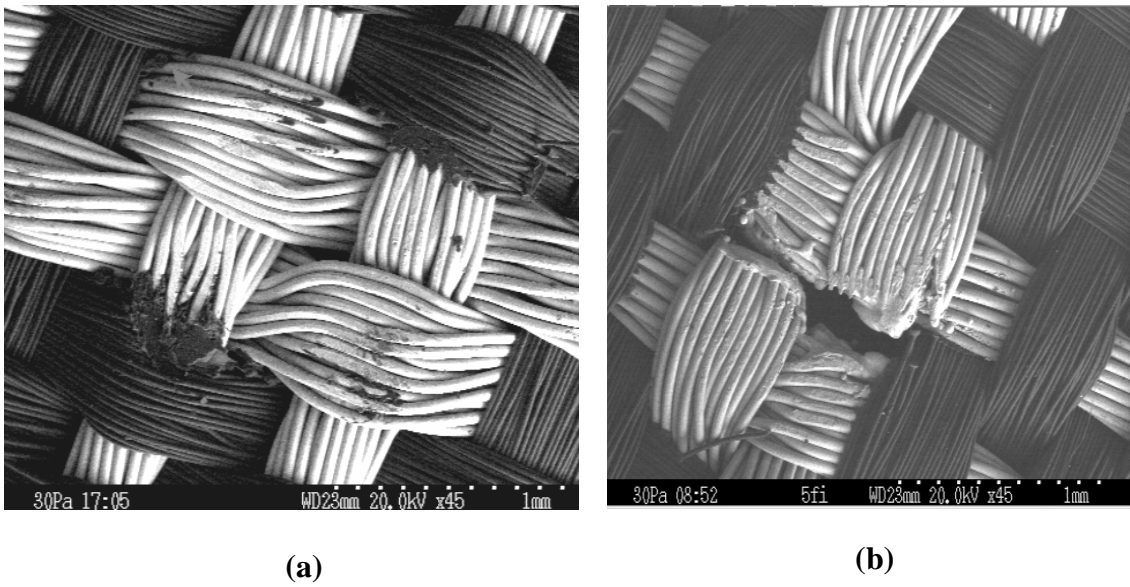


Figure 3. SEM micrographs of copper (light) and polyester (dark) threads: Plan view of a welded interconnect using (a) top-bottom probe resistance welding, (b) parallel-gap resistive welding

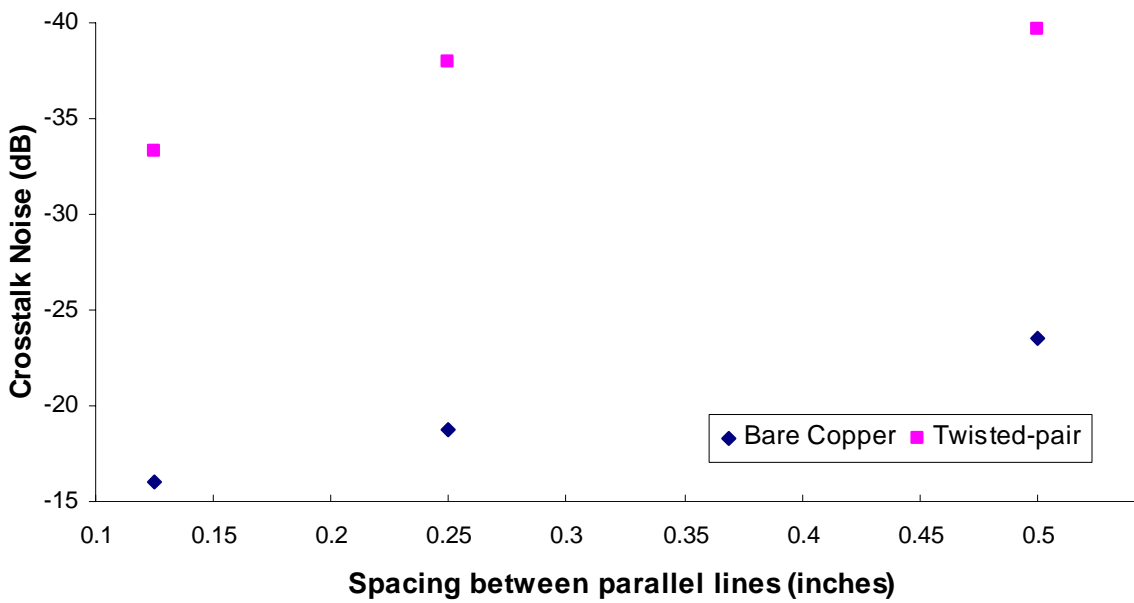


Figure 4. Crosstalk noise between woven interconnect lines for a 1 Volt signal (1 MHz frequency) sent into an aggressor line: Crosstalk noise vs. spacing between the twisted pair and bare copper lines

changing the air permeability of parafoil fabrics are being developed and investigated. Electroactive materials are being used to develop fabric structures that can change porosity or surface characteristics to modify the lift to drag ratios of Parafoils.

Kirstein et al. [17, 18, 19] have studied the electrical performance of fabric-based signal transmission lines. They have applied methods of microwave technology to evaluate the frequency response of textile transmission lines and to develop a theoretical model to describe signal transmission in textiles [18]. Conducting threads woven into fabrics (as transmission lines) were polyester yarns (16.7 and 33.4 Tex) twisted with an insulated copper filament (40 μm diameter). The woven fabrics had these copper yarns in warp and/or weft directions. Configurations similar to coplanar waveguides (on printed circuit boards) were developed in the woven circuits by weaving the copper-polyester yarns in the warp direction, see Figure 6. In coplanar waveguides, the signal lines are surrounded by ground lines in order to prevent parasitic coupling between neighboring signal lines at high frequencies. In the case of fabric-based coplanar waveguides, one, two, and three signal (S) lines were woven with one or two ground (G) lines on each side of the signal lines to form GS, GSG, GSSG, and GSSSG configurations of signal and ground transmission lines. The conductive threads (ground or signal lines) were separated from each other by any number of non-conductive threads. Electrical parameters (e.g., line impedance, insertion loss, far end crosstalk, etc.), for the different configurations of woven coplanar waveguides using time and frequency domain analysis, were evaluated. It was reported that when the GSSSG configuration was used (i.e. more number of signal lines), the value of coplanar waveguide impedance was lower as compared to the GSSG or GSG configurations. Moreover, it was observed that the impedance of the woven transmission lines showed variation with time and this was attributed to irregularities in the fabrics. The measured impedance results were compared to those predicted using electromagnetic field solver simulations and a close match was found between the two [17]. Based on the measured values of impedance, inductance, capacitance, and resistance for the different transmission lines, a theoretical transmission line model was also developed through simulation using the SPICE software [18]. Crosstalk noise (noise induced on a quiet line or a signal line due to change in signal on neighboring signal-carrying lines) between two neighboring signal lines was evaluated and it was reported

that the value of crosstalk reduced substantially if the neighboring signal lines were separated by a ground line [17].

In a patent by Jayaraman et al. numbered US6145551 [20], a process for the development of a woven garment with intelligence capabilities, has been described. One of the intelligence capabilities of the garment described in the patent is the ability to monitor one or more vital signs (like blood pressure, pulse rate, cardiac output, and respiratory rate) of human body and the other is the ability to monitor garment penetration by a ballistic material. These two intelligence capabilities are achieved by including sensing components in the weave of the garment. The garment called the sensate liner [20-22] consists of integrated optical fibers (a tubular fabric [23] is woven and these optical fibers run in a spiral along the length of the fabric) that run from the optical signal transmitter to a receiver (see Figure 7). The receiver (shown in Figure 8) receives the signal and sends an acknowledgement back to the transmitter. If there is any penetration of the fabric by a bullet, the signal going to the receiver is reflected back from the point of penetration and reaches the transmitter back. The time that the signal takes to get back from the receiver is known and hence if any signal reaches the sender before that time implies that the signal was disrupted by a penetration (e.g, bullet), and hence rebounded back to the sender. The time that the signal takes to get back to the sender for this signal is noted and with a fixed velocity of the optical signal in that optical fiber medium, the distance or location on the fabric where the bullet penetration took place, can also be determined. All the information collected about the location of bullet penetration on the fabric is transferred to a computer called the personal status monitor. In this fabric, one also has electrically conducting fibers woven into the fabric and running in the longitudinal direction. These fibers transfer electrical signals from sensors, interconnected at different points of the fabric/garment, to the computer or the personal status monitor. If the signals from the sensors are outside the normal range or if there is a penetration alert, the readings are transmitted using the transmitter.

Lebby et al. describe a communicative wristwatch in a patent, US6158884 [24]. The wristwatch reportedly consists of a wristband made up of woven conductive fibers/yarns and an electronic unit and a power source integrated into the woven wristband. The wristband has conductive and non-conducting fibers woven orthogonal to one another to

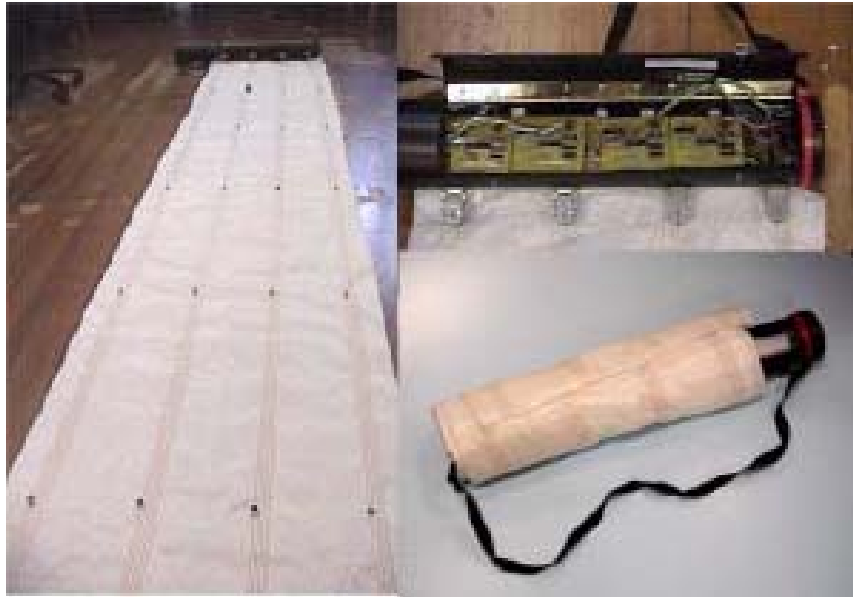


Figure 5. Portable, woven fabric-based acoustic sensor array with 20 microphones attached to twisted pair wires woven into the fabric

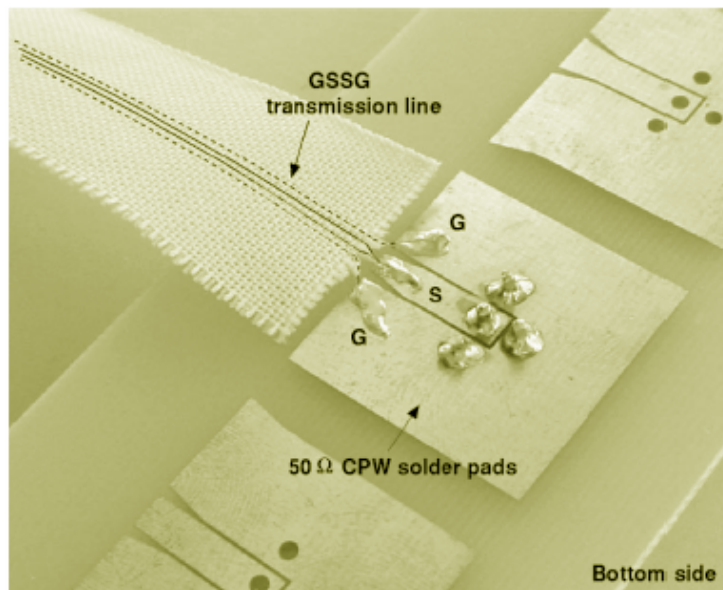


Figure 6. Woven, fabric-based coplanar waveguide-like transmission line with signal (S) lines surrounded by ground (G) lines

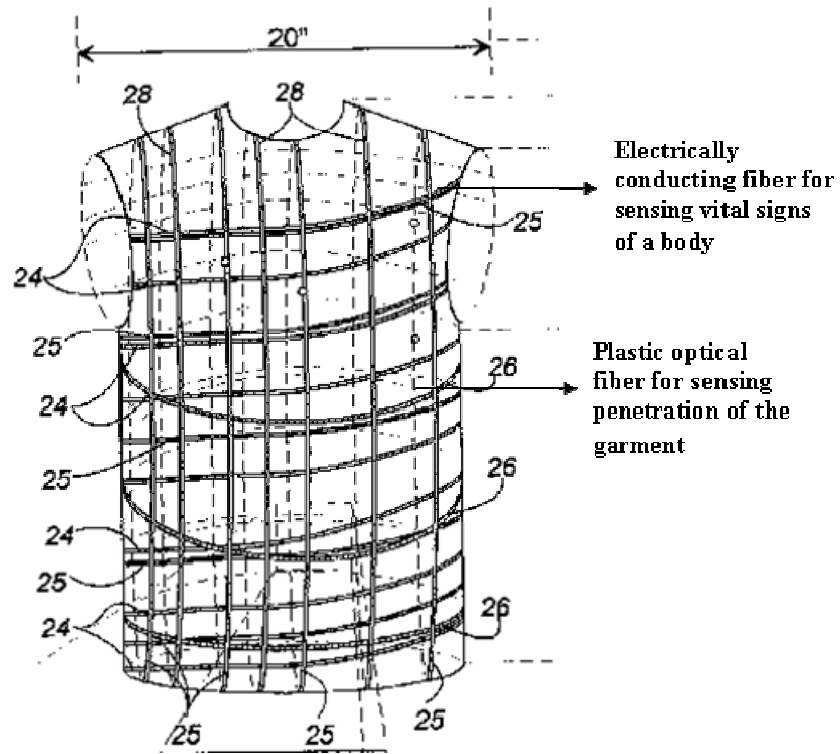


Figure 7. A Sensate Liner – a woven garment with intelligence capability

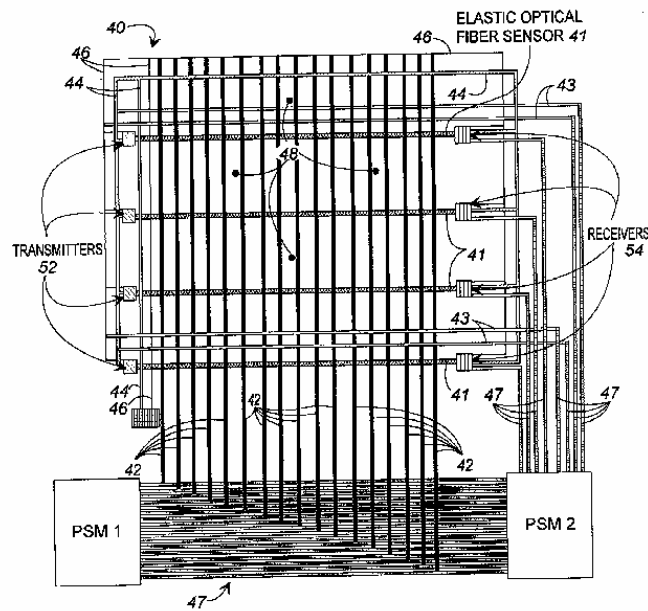


Figure 8. Signal transmission in a sensate liner

define a simple grid (shown in Figure 9). The conductive fibers/yarns provide wired coupling between an electronic unit (which consists of a transceiver for transmitting and receiving messages, a watch to display time, a microphone, and a speaker) and the power source and with all other components attached to the wristband. The woven conductive fabric can also act as an antenna for transmission and receipt of signals. The communicative watch may have a micro-processing unit, a memory, a microscanner, a micro-recorder, a smart card storage and reader device, a cellphone or a pager integrated within the electronic unit. According to the claims, these components could also be integrated within the wrist band conducting fabric and can be interconnected to the electronic unit and the power source by using the conductive fibers and yarns, see Figure 10. One of the other components attached to the wristband can be a display device used for the display of informative data. The display device could be integrated into the wrist band by using holographic optical fibers.

In a patent by Piper, numbered US4463323 [25], a woven transmission cable has been described which includes a plurality of warp elements interwoven with a weft elements. The main characteristics of this transmission cable are low characteristic impedance even when the signals are transferred at high frequencies, see Figure 11. This structure can be considered to be an important building block for the development of a fabric circuit board. It includes conducting fiber/yarn elements, woven in an orthogonal manner, into a fabric along with non-conducting fiber/yarn elements. A number of conductive warp elements are ground conducting fibers/yarns (labeled as 10 in Figure 11) and are woven parallel to the signal conducting warp yarns (labeled as 12 in Figure 11) in a manner that each of the signal conductors is separated from the other by one or two ground conducting yarns. An input signal going into the signal conductors is split at the input between the signal conductor pairs and combined at the output to give a single output signal as shown in Figure 12. The placement of the ground conductors relative to signal conductors can be changed so as to control the characteristic impedance of the transmission cable. The placement of the ground conductors in between signal conductors eliminates differential impedance and even cross-talk between neighboring lines and as these phenomena are more pronounced at higher frequencies, the transmission cable structure mentioned is suitable for transmitting high frequency signals. A fabric based

electronic network like a flexible fabric circuit board could be developed based on the same arrangement of signal and ground conductors as described above and this could considerably reduce differential impedance and crosstalk noise [26] in neighboring lines.

In a patent by Yoshida et al. numbered US4929803 [27], a planar conductive fabric-like piece with electrical anisotropy, has been described (see Figure 13). This conductive fabric-like piece has groups of non-conducting and conducting lines arranged in orthogonal directions. The individual conducting lines are kept separate from each other and form a planer conductive piece with electrical anisotropy. The conductive lines may be placed either next to each other or by placing one insulating line (fiber or yarn) in between two signal lines to prevent them from shorting. This may become important if the density of lines in the piece becomes very high. The conducting lines may be metallic yarns or wires, conducting polymeric yarns or carbon fibers and the insulating lines may be nylon or Teflon fibers or yarns. Electrical anisotropy of this yarn is achieved as this fabric-like piece allows currents to flow in one direction (in the direction of the conducting yarns/fibers) but not in the orthogonal direction (which has only insulating yarns).

In a patent by DeAngelis et al. numbered US5624736 [28], a conductive textile has been described in which a conductive polymer film is patterned on selected areas of a fabric, according to a given design. Firstly, a conductive polymer film is coated all over a woven or knitted fabric substrate. The conductive polymers used were polypyrrole, polyaniline and polythiophenes or their substituted derivatives. The sheet resistance of the deposited polymeric film, measured by using a standard test method (AATCC test method 76-1982), was found to be less than 1000 Ω /square. After coating the whole fabric (shown in Figure 14a and Figure 14b) with a conducting polymer, a mask was applied (in the form of a dispersion, emulsion or a solution) selectively in certain areas of the fabric to form a desired pattern. The mask (made up of polyvinylidene chloride, polyvinyl chloride or paraffin) is resistant to a chemical etching agent. In the unmasked areas, the conductive polymer degrades on application of the etching material. Thus one gets a design or pattern of conductive polymer on a flexible textile substrate. The area of the fabric having the conductive polymer has high conductivity and the uncovered area has low conductivity. The mask or protective coating on top of the conducting polymer

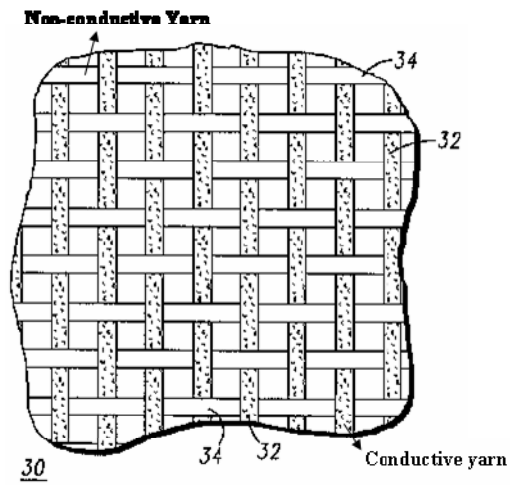


Figure 9. Conductive and Non-conductive fibers woven orthogonally to construct a smart strap

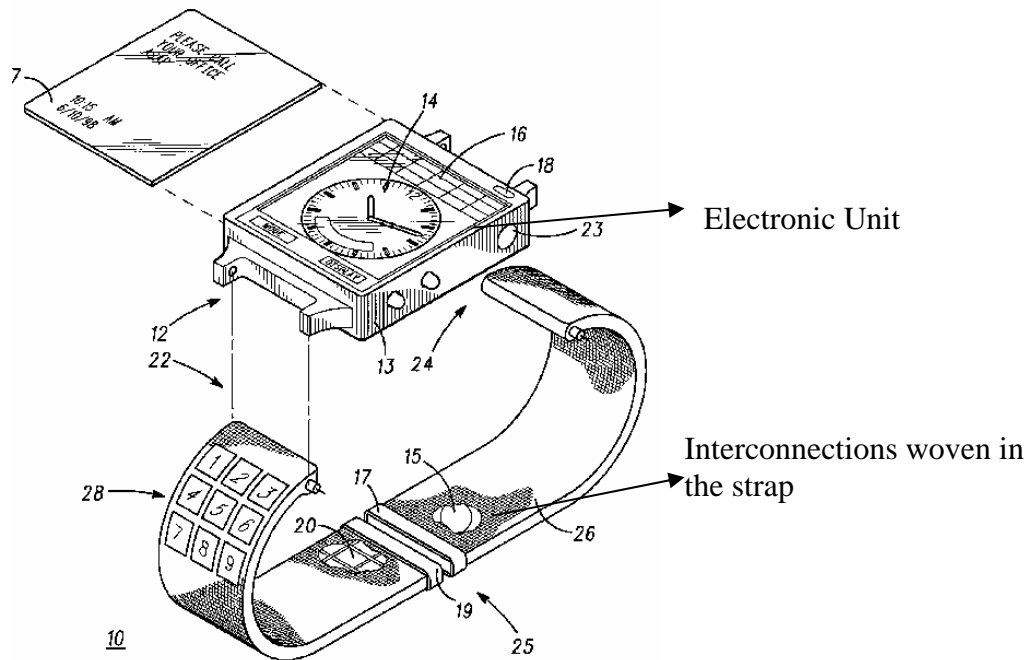


Figure 10. A communicative wrist watch

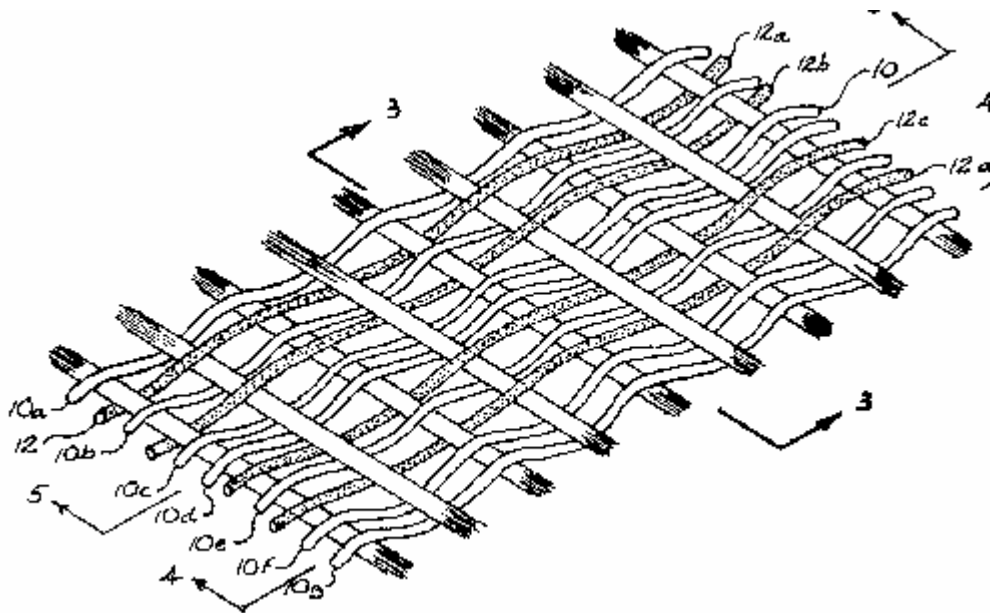


Figure 11. Woven transmission cable

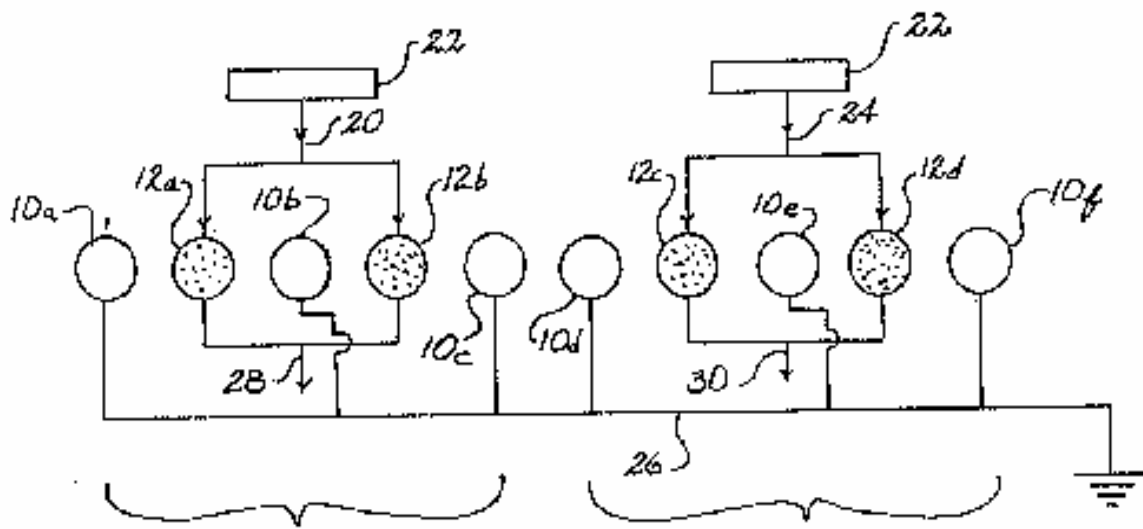


Figure 12. The input signal is split at the input of signal yarns 12a and 12 b separated by the ground yarn 10b

film (that is not etched out) has a second function as well, that is to serve as an air or moisture barrier, thereby increasing the stability of the conductive polymer under the protective film. The product and procedure mentioned in this patent could be used to develop conductive wiring designs on a textile substrate leading to the formation of a flexible textile-based circuit board.

Kuhn et al. [29] have described an electrically conductive fabric material made from a conductive polymer in patent number US 4803096. Placing a fiber, yarn or a fabric in an aqueous solution of an oxidatively polymerizable material and an oxidizing agent produces this conductive fabric. This results in a film of conductive polymer being formed on the surface of the textile material. A patent by Pittman et al. numbered US5102727 [30] describes an electrically conductive textile fabric having a conductivity gradient. This is achieved by varying the relative concentration of high and low conductivity yarns during the construction of the fabric. In case of a woven fabric, the number of high conductivity yarns per inch is varied (relative to the number of low conductivity yarns per inch) in both the warp and the weft directions. This conductive fabric with a conductivity gradient is useful in radar absorbing applications when it is incorporated into the body of a military aircraft or other armored vehicle. Having a conductivity gradient allows for a smooth transition around sharp edges or changes on surface angles to minimize the radar profile of an aircraft and avoid detection and identification. Weaving non-conductive warp yarns along with a combination of conducting and non-conducting weft yarns produces the conductive fabric being discussed. The concentration of conducting yarns in the weft (relative to the number of non-conductive yarns) can be varied as one moves from the top of the fabric to the bottom of the fabric as shown in Figure 15. In this figure, the number of conducting yarns in the weft (relative to the number of non-conductive yarns) in region A is greater than those in region A' which has a higher concentration of conductive yarns than in region A''. Alternate method to produce the conductivity gradient involves varying the number of conductive monofilaments relative to non-conductive monofilaments in each twisted weft yarn, see Figure 16. The number of non-conductive filaments relative to the conductive filaments in this yarn can be varied to get different levels of conductivities of the yarns. A woven fabric (as shown in Figure 16) can be constructed with three regions

D, D' and D''. The number of conductive filaments in the weft yarn cross-section (as shown in Figure 16) decreases as one moves from region D to D' and further down to D'', thereby creating the conductivity gradient.

Gregory et al., in a patent (US5162135 [31]), also describes a conductive textile fabric having a conductivity gradient. In this approach, a fabric having a coated conductive polymeric film is treated with a solution containing a chemical reducing agent to reduce its conductivity. By selectively reducing portions of the conducting polymer in varying degrees, a conductivity gradient is produced along the length of the fabric. The fabric substrate on which the uniform polymeric film is formed, may consist of woven, non-woven or knitted fabric made from nylon, polyethyleneterephthalate, and aromatic polyamide fibers and yarns. The polymeric film being described above is made up of conductive polymers like polypyrrole and polyaniline (doped). The solution containing the reducing agent is applied (by spraying or dipping in the solution bath) to the polymeric film on the textile substrate for varying conditions time, concentration and temperature at different portions of the fabric. Thus, conductivity of different parts of the film is changed in varying degrees to produce an anisotropic material. The reducing agent used for the above purpose is zinc formaldehyde sulfoxylate.

A patent by Adams et al. numbered US5316830 [32] describes a fabric having a non-uniform electrical conductivity. The fabric is coated with a conductive polymeric coating and the coating is selectively removed from certain areas to form a pattern. The areas, from which the conducting film coating is removed, have lower conductivity than the areas with the film coating. The process involves use of high velocity water jets directed at the coated fabric to produce a pattern of conductive portions on a fabric as shown in Figure 17. The conductive polymer is removed from cross-shaped patterned region, not affecting the conducting polymer in the remaining region. Even in the cross-shaped region, more conducting polymeric film is removed from the yarns in the warp direction of the woven fabric than in the filling direction as the fabric travels (into the water-jet) in the warp direction. The process can lead to the formation of a flexible textile-based circuit board. This patent also describes the formation of electrically conductive fabrics having a conductivity gradient as is shown in Figure 18. In this fabric, conducting polymeric coating has been removed in certain areas shown in square shapes and the

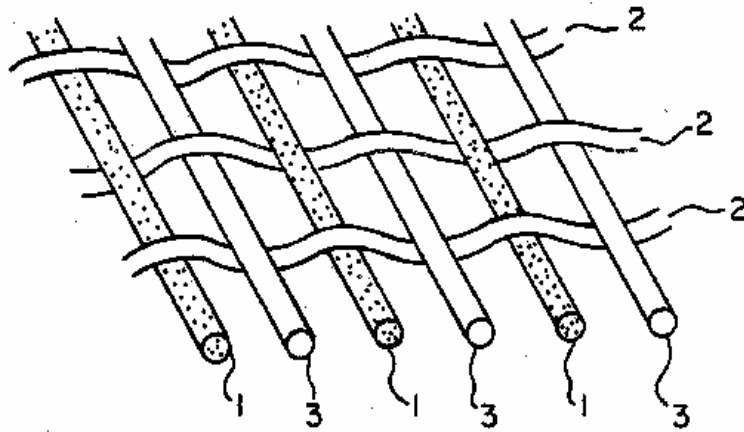


Figure 13. Schematic view of a planar conductive piece with electrical anisotropy

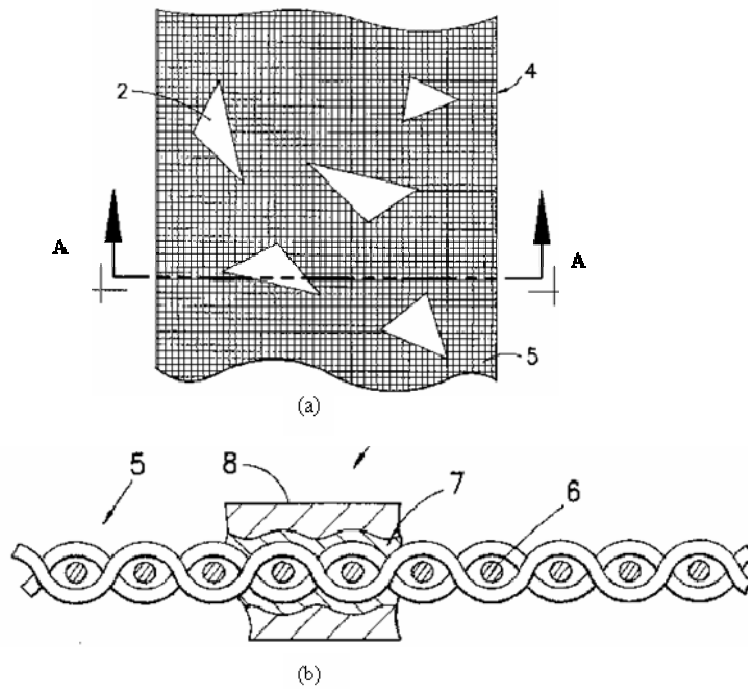


Figure 14. a) A woven fabric treated with a chemical etching agent to remove the conductive polymer coating from unprotected areas; b) Cross-section of the fabric shown in figure 16 (a) cut along line AA

conductivity in these regions is lower than the areas where the polymeric coating exists, thus, the average per square conductivity increases as one moves from left to right. Even in the regions where the polymeric film is removed, the conductivity in the direction of the fabric travel is lower than in the orthogonal direction. The amount of removal of the coating within a specified region of a fabric can also be varied by applying water jet at different parts of that region for a varying duration. A three dimensional conductivity variation can be obtained in a textile based structure by placing different fabrics, each of which has sections where conductive polymeric film has been removed, on top of one other such that each of those sections lie on top of each other. As conductivity varies within each section, placing these sections on top of each other leads to variation of conductivity in three dimensions. The fabric substrate (on which the uniform polymeric film is formed) may consist of woven, non-woven or knitted fabric made from nylon, polyethyleneterephthalate, and aromatic polyamide fibers and yarns. The polymeric film being described above is made up of conductive polymers like polypyrrole and polyaniline (doped).

Onai et al., in a patent (US4889963 [33]), describe a flexible electrically conductive sheet containing a woven fabric of stainless steel fibers impregnated with a synthetic resin material. Portions of the stainless steel fibers are exposed on the surfaces of the synthetic resin material and are used for dissipating electrostatic charge from any charged object contacting the exposed steel fibers. This structure can also be used for making a pattern for the exposed conducting fibers on this conductive sheet and contacting different layers of these conducting sheets at certain desired points as in a multi-layered circuitry.

In a patent by Triplett et al. numbered 5802607 [34], a fencing jacket made from electrically conducting yarns has been described. The fencing jacket consists of a fabric constructed by weaving electrically conducting threads in the weft direction and non-conductive threads in the warp direction. It registers a score when the conducting yarns of the jacket are hit by a fencing wire and is used in electronically scored fencing competitions. The conductive threads used in this fabric are silver-coated nylon yarns. These yarns are more flexible than wires or metallic yarns and provide enough conductivity to send a signal to register a score, whenever the jacket is hit.

Post et al. [35, 36] and Orth et al. [37] have described the development of e-broidery or electronic embroidery as the patterning of conductive textiles by numerically controlled sewing or weaving processes as a means of creating computationally active textiles. Computational textiles have been defined as washable multilayer electronic circuitry constructed on textile substrates, using conductive yarns and suitably packaged components. They have described applications of textile-based circuitry like row and column fabric keyboard, an electrical dress, a musical jacket incorporating an e-broidered keypad and fabric buses, and a musical ball with e-broidered pressure sensors. The row and column fabric keyboard consists of two layers of highly conductive metallic organza and non-conducting rows separated by an insulating layer of nylon netting. When pressed at the right point, the two conducting layers make contact through spaces in the nylon netting and current flows from a row electrode to a column electrode. A microcontroller is connected to the organza of the keyboard using gripper snaps. They also report a musical jacket from denim into a wearable musical instrument, allowing the wearer to play notes by integrating directly into the jacket an embroidered fabric keypad, a sequencer/synthesizer, amplifying speakers, and batteries to power the above subsystems. A fabric bus was sewn from conductive organza to connect all the components attached to this musical jacket (as shown in Figure 19). Another application developed by Post et al [35] is a keypad made by e-broidery (known as the No-Soap Radio) and was designed to transmit data to a nearby AM/FM radio (via near-field electrostatic coupling). When the user touches a symbol on the keypad, the microcontroller capacitively senses the contact and then transmits a particular audible tone by FM-modulating a 455 kHz square-wave carrier in software and presenting the resulting signal on all of the keys connected to the circuit. They have also discussed the development of flexible multichip module which consists of semi-flexible circuit elements that may be embedded in textile products to form a sensor readout network. Their primary method of circuit patterning was numerically controlled embroidery using conductive threads used to stitch patterns that define circuit traces, component connection pads, or sensing surfaces.

Azoulay [38] has discussed anisotropy in electric properties of a fabric containing conductive yarns or fibers,. A 2/1 twill weave fabric was constructed by weaving a

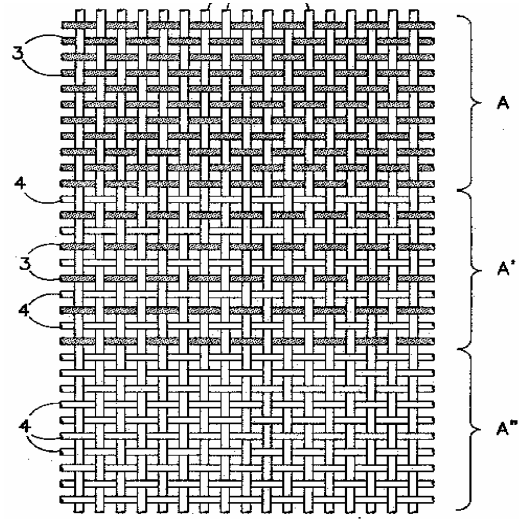


Figure 15. Electrically conductive fabric with conductivity gradient

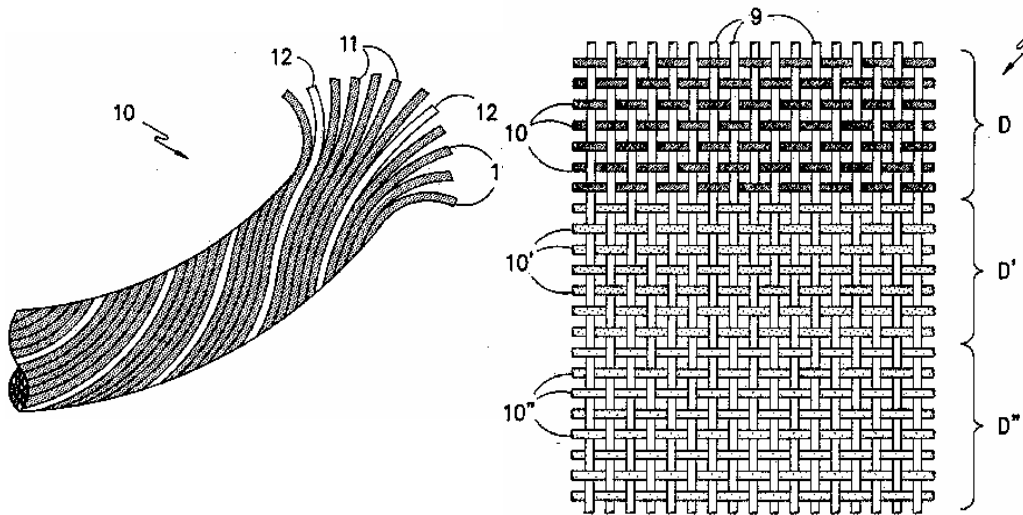


Figure 16. Electrically conductive fabric with conductivity gradient by varying the number of conductive filaments in the yarn cross-section

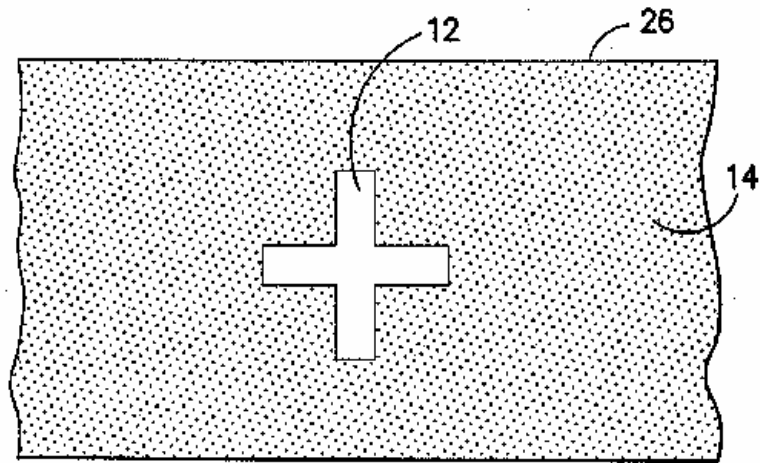


Figure 17. Schematic view of a textile fabric coated with a conductive polymeric film, which is removed selectively from the cross-shaped region shown

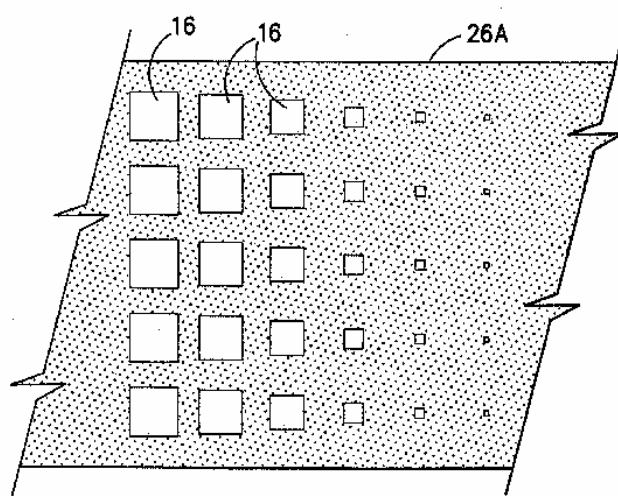


Figure 18. Formation of electrically conductive fabrics having a conductivity gradient



Figure 19. Musical jacket which has the embroidered fabric keypad (shown on the right), a sequencer/synthesizer, amplifying speakers, and batteries

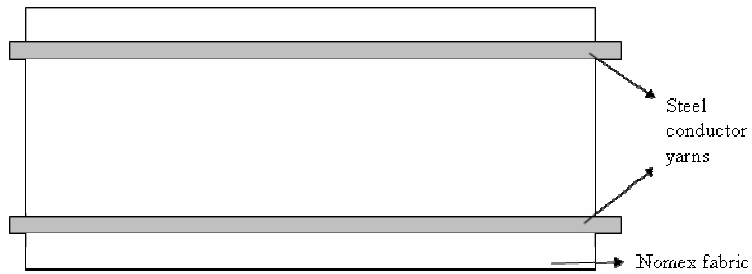


Figure 20. Top view of the fabric webbing developed by Gorlick

conductive filling yarn (containing 10% conductive fibers) with a non-conductive yarn in the warp direction. Surface resistivity measurements in different directions of the fabric showed that there was anisotropy in the surface resistivity of this fabric. This could be attributed to the weave pattern of the fabric i.e. twill weave pattern. The fabric face consists mainly of warp (67% which non-conductive) and has a surface resistivity which is by many orders of magnitude higher than that of the back side, which has more conductive filling fiber (67%) when the resistivity is measured in the direction of the weft. This fabric was used to dissipate the charge accumulated (on the body or clothing of a person) in order to avoid electrostatic discharge.

Gorlick [39], proposed a means of connecting conventional electronics with conductive fabrics using electric suspenders i.e. a fabric power bus and data network for wearable digital devices. A conductive fabric webbing is woven out of Nomex yarns with two pairs of stainless steel conductors woven directly into the webbing as shown in Figure 20. Each conductor is a bundle of twenty fine stainless steel wires. Suspenders made from this fabric webbing can be transformed into a shared low voltage, DC power bus for digital wearable devices. The electronic devices can be attached to these suspenders (the conductors of the fabric webbing) by using electrical surface connectors like ball and socket connectors.

2.2.2 Device Attachment

One of the greatest challenges in the field of electronic textiles is the attachment of integrated circuits and devices to the conducting elements integrated in the fabric. In order to minimize the use of rigid circuit boards and multi-chip modules in electronic textiles, individual chip (integrated circuit) packages can be directly connected or bonded to the conductive threads. Post et al. [35] explored several methods for producing device-fabric interconnects and found that soldering of devices to the conducting threads in the fabric, bonding the electronic components using conductive adhesives, or stapling components into conductive stitched circuits were not very effective processes in producing these interconnects. Gripper snaps can be used as effective connectors between the fabric and the electronic devices, though they may provide low connection densities. In order to form flexible and conformable device interconnections, Post et al. [35] have designed packages called plastic threaded chip carrier packages that have long

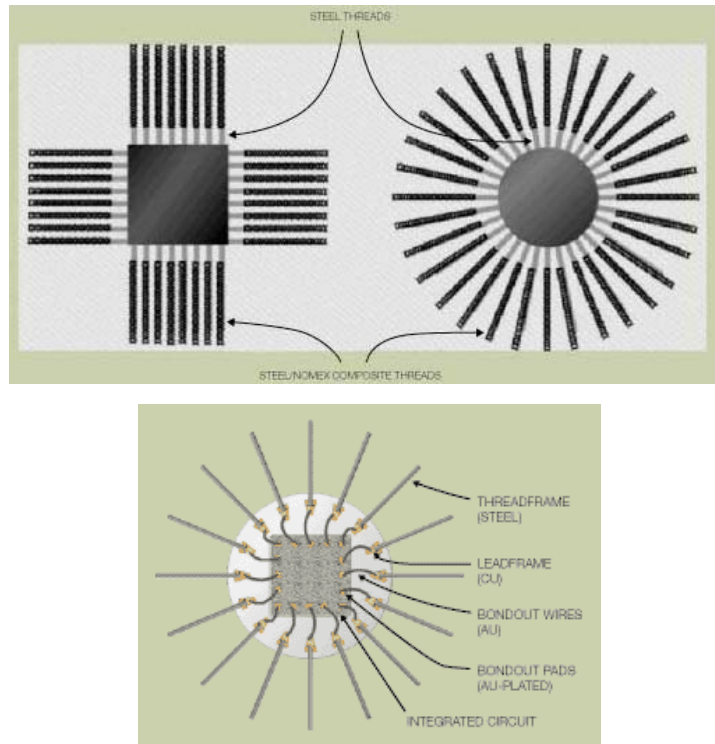


Figure 21. Square and round PTCC (Plastic Threaded Chip Carrier)

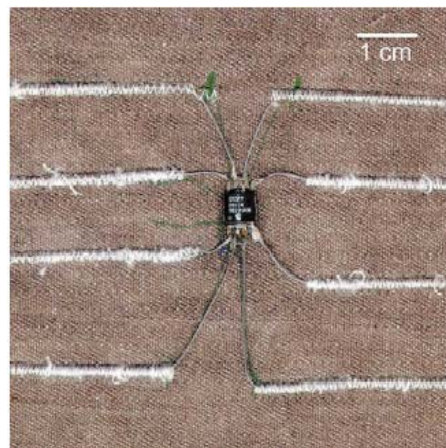


Figure 22. Plastic threaded chip carrier package prototype attached to a fabric substrate

conducting threads that lead out from the package instead of the rigid leads. The leads of the plastic thread chip carrier packages can be woven or stitched into the fabric circuitry as shown in Figure 21. In order to manufacture threaded packages, a bare die or integrated circuit was taken and fine gold wires were thermo-compression bonded onto gold plated bond pads of the integrated circuit chip. The other end of the fine gold wire was connected to a copper lead frame. Flexible and conformable conductive threads (100 continuous steel fibers, 5 μm each) were micro-spotwelded to the lead frame stubs and the structure is sealed in a plastic carrier. A picture of a prototype plastic thread chip carrier package, attached to conductive yarns embroidered onto a fabric substrate, is shown in Figure 22.

Electronic device attachment to conductive elements of a woven fabric has been discussed by Jung et al. [40]. They have suggested new methods to form interconnections between integrated circuits and the conductive fabrics as these two have a very different scale of feature sizes - integrated electronic circuits with feature sizes on the micrometer scale and textile and garment technologies with dimensions in the order of millimeters. In one of the interconnect methods proposed by them, bonding wires are used to connect integrated circuits and conductive threads (with insulation) woven into narrow fabric strips. In order to prepare the endings of the conductive threads, insulation of the woven conductive threads is first removed by laser treatment and tiny metal contact plates are soldered to the threads. Then, insulated bonding wires are used to connect the metal plates to the integrated circuit (an audio module) bond pads (Figure 23). In another interconnect method; a flexible circuit board with structured electrodes is used to act as an interface between the woven conductive threads and the integrated circuit (Figure 24). The integrated circuit (audio module) is attached to the flexible circuit board. Conducting threads are connected to the electrodes and pads on the flexible circuit board by soldering.

2.2.3 Transistors on thin films/threads

In the area of flexible electronics, one of the most significant research developments is the fabrication of transistors on thin films that could be slit into narrow films and woven into a fabric (Figure 25). Research work in this area is being carried out at Princeton, North Carolina State, and North Texas Universities [41, 42]. Fabrication of

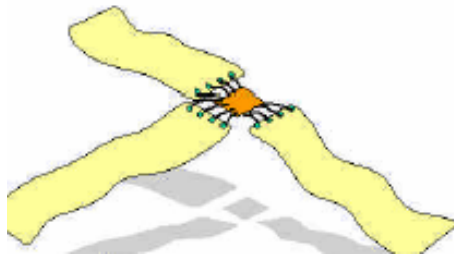


Figure 23. Wire bonding of narrow fabric strips containing conducting threads to an integrated circuit

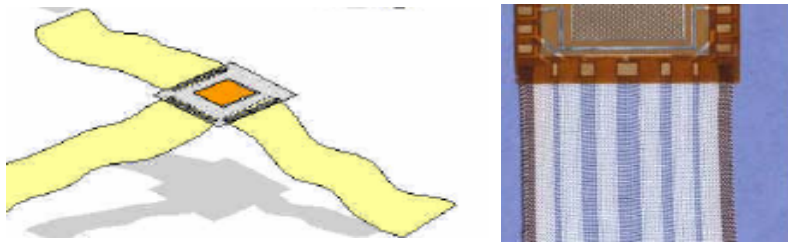


Figure 24. Flexible circuit board used to form interconnects between an integrated circuit and the conducting threads woven into narrow fabric strips



Figure 25. Strips of thin film transistors woven into a fabric and interconnected to form a desired logic circuitry

these transistors (called TFTs or Thin Film Transistors) is done on amorphous silicon. Layers of n-doped and intrinsic amorphous silicon are deposited on silicon nitride deposited at a low temperature (150° C) on flexible Kapton films and the transistors are formed on the amorphous silicon. Plasma Enhanced Chemical Vapor Deposition (PECVD) process is used for the deposition of amorphous silicon and silicon nitride. The gate, source and the drain contacts (gold contact pads) of the transistor are deposited by using thermal deposition, see Figure 26. All the patterning is done using conventional photolithography. The films with transistors formed on it, are cut (slit film technique) into thin strips (using plasma etching) which are then woven into a fabric structure. Interconnections between the different transistors are made using conductive strips (Kapton film strips which have gold and chromium deposited on them by electron beam deposition) to demonstrate digital logic functionality (Figure 25). These transistors have a very high threshold voltage of 4V; their gate leakage current is 4 pA and the ratio of currents in the “On” state to that in the “Off” state is equal to 10^7 . In the ongoing work in the area of thin film transistors, an attempt is being made to reduce the threshold voltage and the gate leakage current. The development of these transistors is significant because it proves that if good quality transistors could be fabricated on thin films (or on threads in the future) and these thin films (or threads) could be woven into a fabric (with the different transistors being interconnected to each other by conductive elements or threads woven into the fabric), an all fabric-based integrated circuit could be formed at a relatively high manufacturing speed of large-scale fabric production.

Inoue et al. [43] have developed organic (Pentacene-based) thin film transistors on plastic substrates (Polycarbonate) by using Tantalum oxide as the gate insulator. The structure of these thin film transistors is shown in Figure 27. A stacked structure of 50-nm-thick Al and 200-nm-thick Tantalum was used for the gate electrode and the gate insulator (Tantalum oxide) was developed by anodizing the Tantalum metal deposited as the gate electrode. Pentacene was used as the organic semiconductor and the thickness of its layer was 50 nm. These organic thin film transistors reportedly exhibit excellent characteristics like a high current On/Off ratio and a low value of threshold voltage (1.1 V). Development of organic thin film transistors from poly (3-hexylthiophene) (P3HT)

has been reported by Park et al. [44]. Work on organic thin film transistors on flexible substrates has also been reported by Yoshida et al. [45) and Bonfiglio et al. [46].

2.2.4 Fabric-based Antennas

There are several kinds of antennas [47-54] like loop antennas, helical antennas, whip antennas, patch antennas, thin wire dipole antennas, cylindrical dipole antennas, and biconical antennas [52]. Devices like mobile phones conventionally use helical or whip antennas that are positioned on top part of the device. Important parameters of antennas are: electric and magnetic fields (E and H fields), radiation patterns and beam widths, radiation intensity, directivity (and directional gain), gain, efficiency, impedance (includes radiation resistance and loss resistance of the antenna), range, coupling factor, quality factor, and loop inductance [52]. Radiation intensity at a given point can be defined as the power radiated from an antenna per unit solid angle and is obtained by multiplying the radiation density (real power density radiated from an antenna) by the square of the distance of that point from the antenna. Directivity of an antenna in a given direction is an important parameter and is defined as the ratio of the radiation intensity in that direction to the radiation intensity of a reference antenna. Different kinds of antennas (loop, dipole, etc.) have different levels of directivity. One of the most important parameter in case of antennas is the antenna radiation efficiency, which takes into account signal reflection, conduction and dielectric losses at the input terminals of the antenna and within the structure of the antenna. The radiation efficiency of a transmitter antenna can be defined as the ratio of the power transmitted by the antenna to the power supplied by the power source.

Loop antennas (loop shape being circular, rectangular, triangular, etc.) with small circumferences have very small values of radiation resistance as compared to their loss resistance. Hence these loop antennas with small circumferences have poor radiation capabilities and can't be effectively used for wireless communications. The radiation resistance of an antenna loop can be increased by increasing the circumference of the loops and the number of turns in the loop. Loop antennas are generally used as signal receivers, and not as transmitters [52, 53]. The dipole antennas made from thin wires are used for communication that does not require a broad range of frequencies. For such applications, Biconical and cylindrical dipole antennas are used.

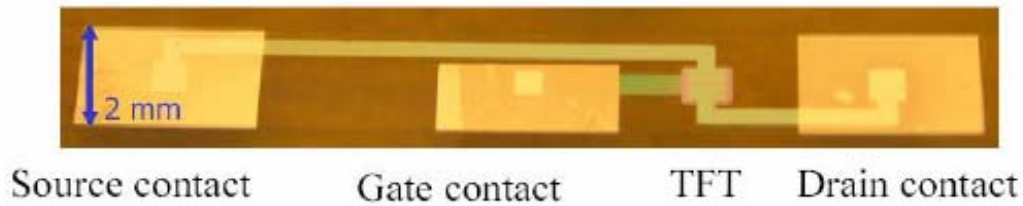


Figure 26. Source, Gate, and Drain gold contacts for a thin film transistor (TFT) developed on a Kapton thin film

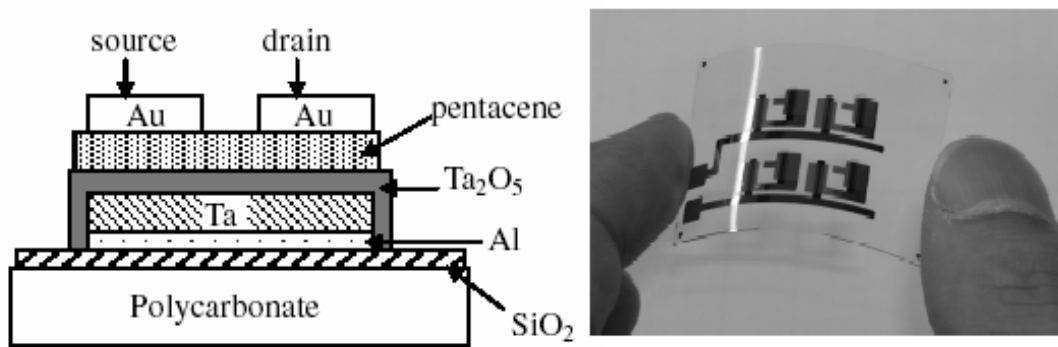


Figure 27. Structure of an organic thin film transistor developed on a flexible plastic substrate

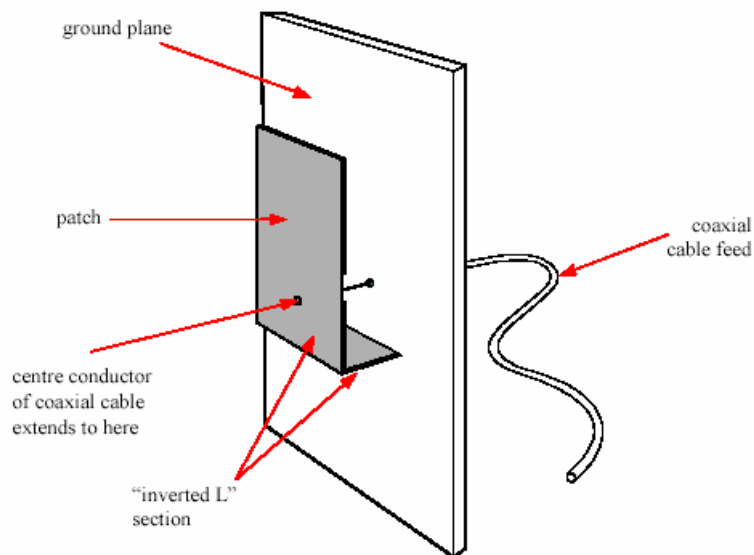


Figure 28. Planar Inverted F Antenna consisting of an inverted L section of a conducting patch, a ground plane, and a coaxial cable feed

In the work being carried out on textile-based antennas, Massey [47] has reported the development of patch or planar inverted F antennas that could be integrated within clothing [47-49]. Planar inverted F antennas have a configuration as shown in Figure 28. The inverted F antenna consists of a conducting patch which is connected to the center conductor of a coaxial feed cable. The conducting patch has an inverted L section (shown in Figure 28) that is connected to the ground plane. A fabric-based planar inverted F antenna (as shown in Figure 29) consists of a conducting fabric patch, which is formed by electroless plating of a rip-stop nylon fabric with copper. The ground plane is also formed from the copper-plated fabric while the patch and the ground plane are separated from each other by a thin foam layer. The short between the conducting patch and the ground plane is formed through a slot in the foam spacer layer. The advantage of providing a ground plane in the patch antenna is that it isolates the electromagnetic fields of the patch antenna from the user's body [48]. The center conductor of the coaxial cable feeding the signal (transmitter antenna) or carrying the received signal (receiver antenna) is connected from the side to the conducting fabric patch. The outer conductor of the cable is connected to ground.

In case of small sized loop antennas, (e.g. used in pagers) the electrical loss resistance is much larger than the radiation resistance. In order to improve loss characteristics of a loop antenna, one needs to have large sized loops, which is possible in case in the case of fabric-based antennas [47-49, 51]. Building the antennas into the fabric also allows the formation of flexible, conformable, light-weight antennas.

Massey [47] has reported that fabric-based patch antennas have an efficiency of 70-80% when the antenna is not worn and about 50% when the antenna is worn. The efficiency of the antennas can be increased by having a good impedance match between the feed coaxial cable and the antenna to avoid the reflection losses or return losses [47]. The return losses in the fabric-base patch antenna are better than 6dB in the GSM antenna band (frequency range 880-960 MHz). The impedance of the antenna depends on the distance between the location where the coaxial cable joins the patch (called the feed point) and short between the patch and the ground plane. In the GSM patch antennas, the feed point is 20 mm away from the short for a good impedance match [47, 48]. The textile-based patch antenna could be formed from conducting threads that are knitted or

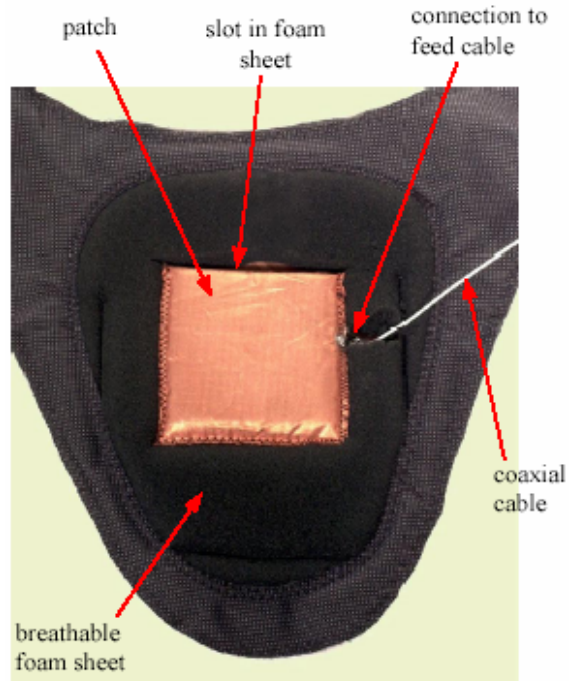


Figure 29. Fabric-based Planar Inverted F Antenna consisting of a conducting fabric patch made from an electroless copper plated fabric



Figure 30. A model of a crossed loop (Merenda) antenna

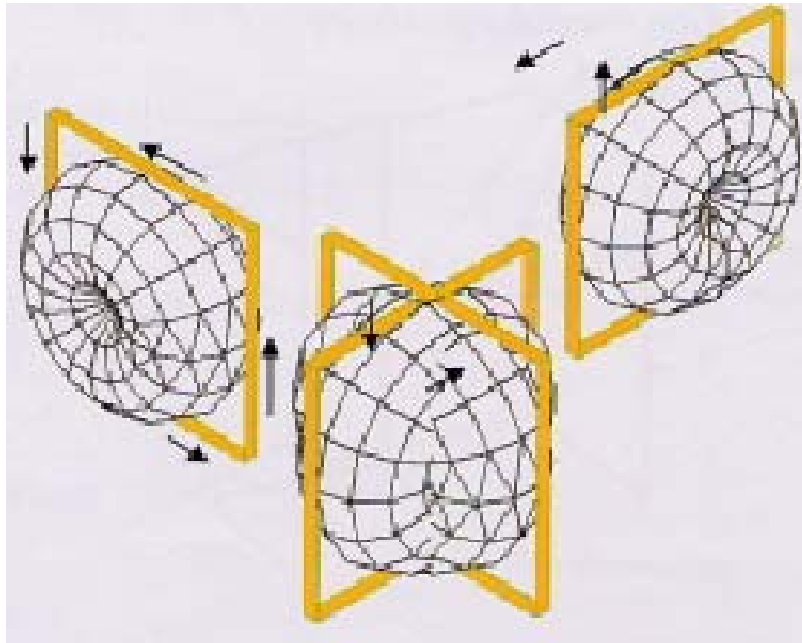


Figure 31. Radiation pattern of loop antennas (unidirectional pattern) as compared to that of a crossed-loop antenna (omnidirectional pattern)



Figure 32. Fabric implementation of a crossed-loop antenna, consisting of conducting elements woven into narrow fabrics that are integrated into a vest

woven into a fabric. Massey [47] reported that these antennas could also be developed by coating or electroless plating of woven or knitted fabrics. The performance of patch antennas formed from the electrolessly plated woven fabrics (low loss conducting fabrics) was found to be the best. The patch antennas could be integrated into the clothing of the user at certain locations on the user's garment like the shoulders, outside of the upper arm [47] or on the back side of the user [48].

Slade et al. [50] have described the development of fabric-based dual loop antennas that operate in the 30-88 MHz frequency range. These antennas are designed such that they use 15 times less power than the conventional antenna technology and support broadband waveforms. These antennas (shown in Figure 30) consist of two large-sized loops that are orthogonal to each other (crossed-loops); thereby producing a radiation pattern (Figure 31) that is omni-directional. It is important to note that the radiation pattern of the dual loop antenna is very close to spherical. A fabric-based implementation of a dual loop antenna as a vest with integrated conductive elements in it is shown in Figure 32. The development of dual loop fabric antennas have also been described by Massey et al. [51]. The design of these antennas (Merenda antennas) was done by BAE Systems and the textile implementation was done by Foster-Miller, Inc. Small loop antennas that could be integrated into a fabric were developed for receiving and transmitting signals in the 225-400 MHz frequency range. These small antennas could be integrated into the collar, pocket, or flap of a battle dress uniform.

Fabric-based antennas are flexible, conformable, and allow formation of very large sized loops and ground planes. These antennas may have limitations in terms of durability, wash resistance, abrasion resistance, or flex resistance and these issues are being investigated by several researchers to understand the viability of integrating these antennas on textile-based materials [50, 51, and 54].

2.3 Sensors and Actuators

Textile materials (fiber, yarn, fabric, etc.) based sensors and actuators have been of considerable interest recently. The vast amount of published work in this area is a testament to the growing interest in fiber/textile based sensing. In this sub-section,

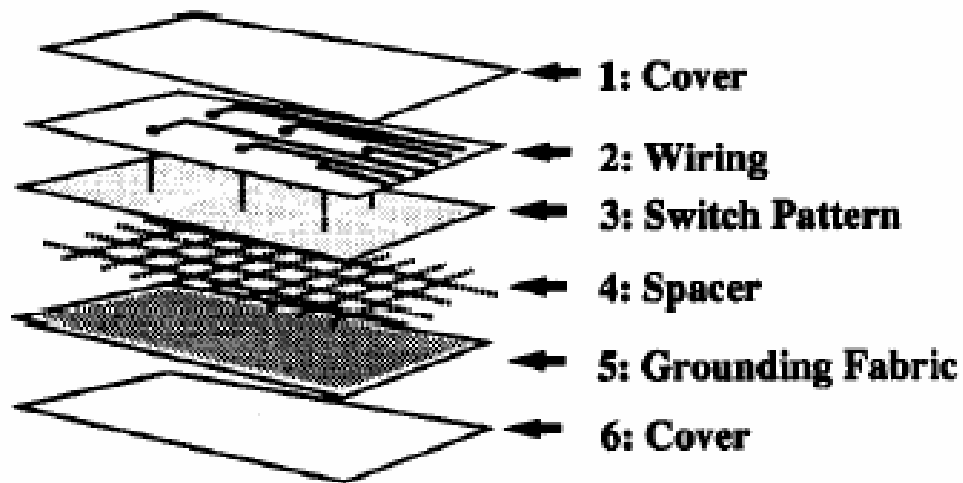


Figure 33. Structure of a tactile sensor made of an electrically conductive fabric

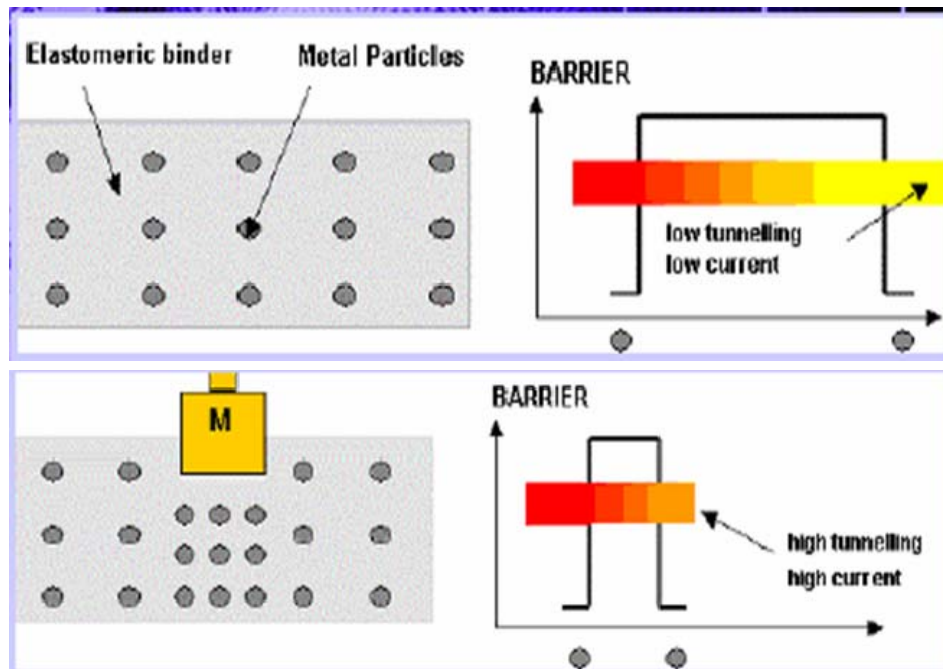


Figure 34. Softswitch Technology used for the formation of interactive fabrics: Metal particles present in the elastomeric binder are brought close to each other on application of pressure thereby allowing conduction through the elastomeric binder by the process of quantum tunneling

development of textile materials-based pressure, environment, and strain sensors and sensing systems are discussed. In Section 2.3.4, properties and actuation mechanisms of electroactive materials and the research being carried out to develop fiber actuators are discussed.

2.3.1 Pressure/tactile Sensing Systems

Inaba et al. [55] described a conducting fabric based tactile sensor system in which a garment made from the sensing fabric covers the entire body of a robot. This fabric helps the robot to sense the touch of an object or a human being. These fabric-based tactile sensors in the sensor suit are distributed on the entire body of the robot and a network of conducting fibers/strings conveys the sensed signals to the sensor processor. The sensor suit has 192 sensing regions and each of these works as a switch, i.e. it allows current to flow (resistance is lowered) where ever pressure is applied on the garment in that region. The sensor fabric consists of six fabric layers, see Figure 33. In addition to the cover layers, the second fabric contains wiring that connects each of the sensor units to the sensor processor and the third, fourth and the fifth layers constitute the arrangement that provides the switching action for the sensor unit. Layer four has a reticulate structure and works as a spacer between layers 3 and 5. The third layer of the fabric is made of polyester and coated with copper or nickel is at the desired sensor points according to the switch pattern. The fifth layer is also an electrically conductive fabric made by electroplating copper/nickel (approximately 15 g/mm^2) to get a uniform conductivity. Layer 3 has distributed segments of the electrically conductive fibers and each of these fibers is connected to the video multiplexer by an electrically conductive string or wiring on the second layer. In case of a touch the tactile sensor or the six-layer fabric structure behaves like an on-switch. An electrical contact is made between the switch pattern on the Layer 3 and the ground (Layer 5) thereby completing the circuit. The electrical signal produced upon sensing of touch is multiplexed on a video signal to produce sensor images.

Jones at SOFTswitch Ltd. [56] has developed a Soft switch technology that enables textile surfaces to become touch sensitive for the purposes of developing user interface through pressure sensing. The mechanism of conduction in the Soft switch fabrics is due to ‘field induced quantum tunneling’ provided by a unique composite material. The

composite material is made of metal particles embedded in an elastomeric binder. The amount of tunneling conduction can be increased by mechanically distorting the composite as the metal particles move closer to each other on application of pressure thereby decreasing the width of the potential barrier and allowing greater quantum tunneling conduction (Figure 34). Soft switch fabrics show a very broad resistance change when compressed. This allows the fabric to change from an insulating state to a highly conductive state under the control of fingertip pressure. The change in resistance can be customized according to application. The switch could be used for occupancy sensing based on seat pressure mapping, and tactile sensing in automotives, airlines, home furnishings, and floors. These flexible fabric sensors could be incorporated into textile products to allow grip pressure and impact loading in different sports to be objectively monitored. It could also be used for developing wearable electronic products for industrial and defense applications. A high mobility suit called an I-suit, that incorporates soft switch controls into the fabric, has been developed for planetary surface operations.

A patent filed by Sandbach of ElekSen Ltd. (USP 6452479 [57]) describes the development of a position sensor that is arranged to detect the position of applied pressure. This position sensor consists of a two layers of electrically conductive fabrics with conduction in all directions along the layer. A partially insulating layer is sandwiched between these two conducting layers and consists of conducting fibers surrounded by an insulating material. When pressure is applied at a certain point of this three layer laminate structure, the conducting fibers in the middle layer get locally compressed and thus provide a local circuit connection or conductive path to be established between the two conducting outer layers at the position of applied pressure. ElekSen Ltd. has developed a sensor called ElecTex based on the patent described above. This sensor can determine the position of application of pressure. Interpreting software is used to identify the location of switch areas. ElecTex can also be used to measure the amount of the pressure applied with pressure response range over which reliable data can be accessed being 3.5kPa to 207kPa. These precise electrical measurements are then translated into digital signals, which could control electronic devices attached to the sensors. Because of their flexible fabric construction, ElecTex sensors can be used in a

wide variety of products – for sensing in automobiles, mobile phones, and health care applications. Logitech Ltd. partnered with ElekSen to produce a fabric keyboard for

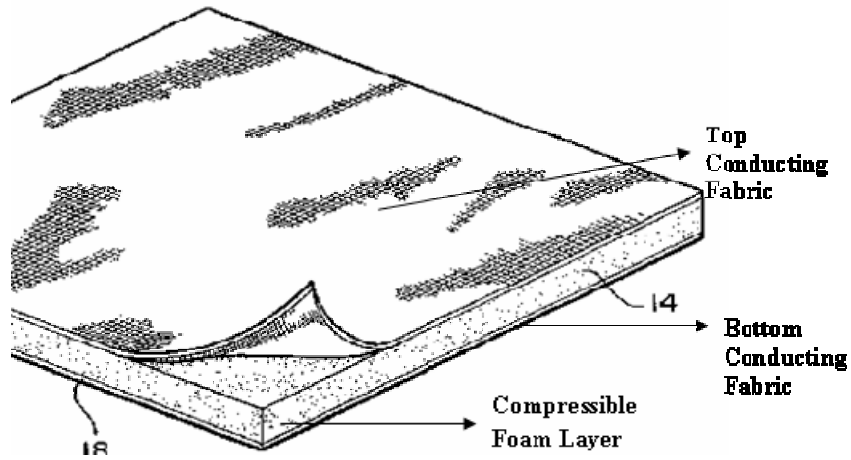


Figure 35. Capacitive weight sensor formed by placing a foam layer between two conducting fabric layers

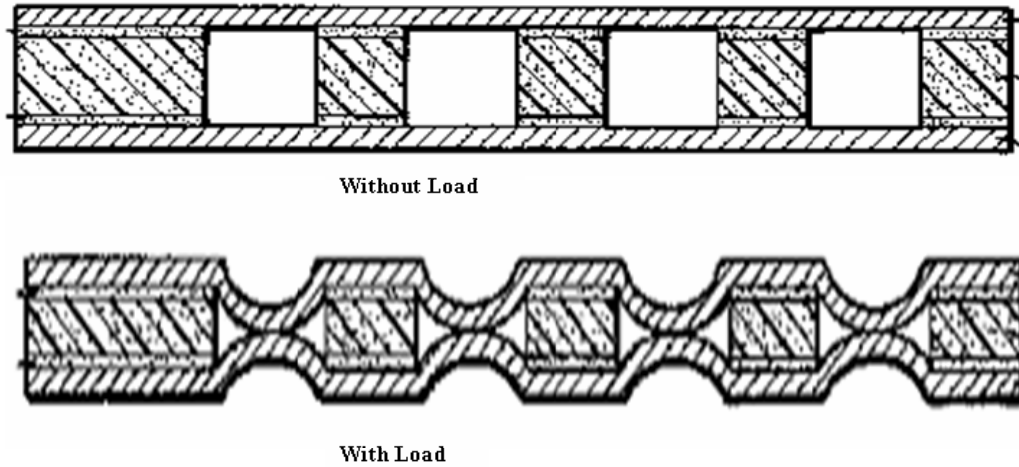


Figure 36: Weight sensor formed by creating apertures in a foam layer between two conducting fabric layers

PDAs (Personal Digital Assistant). Manufactured from the ElekTex fabric, this device provides ability to easily interact with PDAs.

In another patent by Sandbach et al. (USP 6437258 [58]), a laminate conducting fabric sensor has been described. It consists of two conducting planes (with strips of conductive lines) separated by a mesh of insulating fibers. On application of pressure, the outer conducting planes are brought into mechanical contact through the insulating mesh. The amount of current flowing as a result of this contact varies depending upon the actual position of the plane where the mechanical interaction takes place.

Gilbert et al. (USP 5878620 [59]), described a fabric based weight sensor for automotive seats. The sensor includes a compressible, preferably foam layer disposed between two conductive fabric layers. The capacitance between the conductive fabrics is measured to determine whether an object is placed on the sensor, see Figure 35. When pressure is applied to the top fabric the foam layer is compressed and this changes the thickness of the dielectric between the two conductive fabric layers forming the capacitor. As the capacitance is inversely proportional to the thickness of the dielectric layer, decrease in thickness increases the capacitance by a certain amount and thereby detects the amount of load. This patent also describes the development of a weight sensor that employs change in resistance measurements to determine the amount of load on the sensors. In this application apertures are formed through a compressible foam layer sandwiched between two layers of conductive fabric. When a pressure is applied to the sensor, the top conductive fabric contacts the bottom fabric layer at the points where apertures are present, see Figure 36. The contact between the top and bottom conductive fabrics leads to either a switching operation or a reduction in the resistance (proportional to the load/weight) measured across the fabric. One application area where such weight sensors could be used is the controlled deployment of automotive airbags depending on occupant weight.

In a patent by Karplus numbered US4255973 [60], a digital pressure sensor for measuring fluid pressures at high temperatures has been described. This sensor includes an electrically conducting fiber coupled to the fluid by a force disc that causes tension in the fiber to be a function of fluid pressure. The fiber is caused to vibrate in a magnetic field to produce an electrical signal from a positive-feedback amplifier at the resonant

frequency. The change in tension in the fiber (dependent on the fluid pressure) causes changes in the mechanical resonant frequency of fiber. The fluid pressure can thus be measured by measuring the resonant frequency of the fiber.

2.3.2 Environment Sensing Systems

2.3.2.1 Chemical Sensing

There has been an increased interest in incorporating chemical and biological sensors into textile substrates because of the increased proliferation and threat of chemical and biological warfare agents. These sensors could be incorporated into uniforms of soldiers to detect these threats and provide an early warning. El Sherief et al. [61] have reported integration of fiber optic chemical and biological sensors into soldier uniforms. A miniature chemical sensor has been developed for the detection of the presence of Organophosphate dimethylmethylphosphonate (DMMP) gas. Development of the sensor includes replacing the cladding materials of an optical fiber with reactive materials like polypyrrole and polyaniline (Figure 37). The cladding material made from silica is etched with hydrofluoric acid to remove the cladding of the optical fiber in certain regions. Polypyrrole is synthesized chemically or electrochemically and deposited selectively in these etched regions. Exposure to DMMP changes refractive index of the reactive material (polypyrrole) and thereby reduces the transmitted intensity of light signal through the optical fiber, see Figure 38. To improve the sensor sensitivity when exposed to DMMP vapor, polypyrrole cladding was doped with naphthalene-disulphonic acid (NDSA).

Development of optical fiber-based environment, chemical and vapor sensors have also been reported [62, 63-75] by many others. The active sensing region of these sensors may be located at the end of the optical fiber (end fiber configuration), on the side of the optical fiber in side-fiber configuration or in porous sections in the fiber (interrupted fiber configuration). In side-fiber configuration the cladding of the optical fiber is removed in the active region and the sensing is carried out by the evanescent field of the optical fiber.

Sensing of oxygen, carbon dioxide, and ammonia (in gaseous form and dissolved in a liquid) has been carried out using fiber optic sensors [63, 64, 66-68]. The most commonly used optical sensing methodology for sensing gaseous and dissolved oxygen is the dynamic quenching of luminescence by oxygen [62, 63]. pH sensors (ion sensors) based

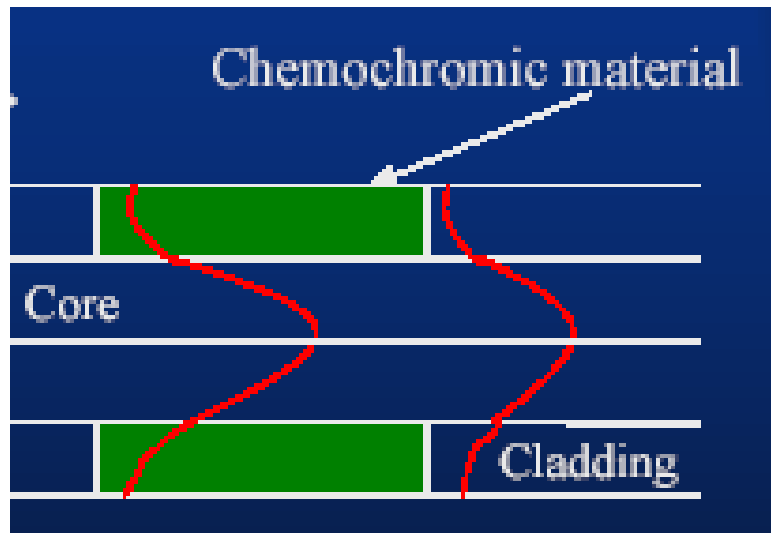


Figure 37. Optical fiber sensor developed for the detection of toxic gases by removing a part of the optical fiber cladding and replacing it with a chemochromic material

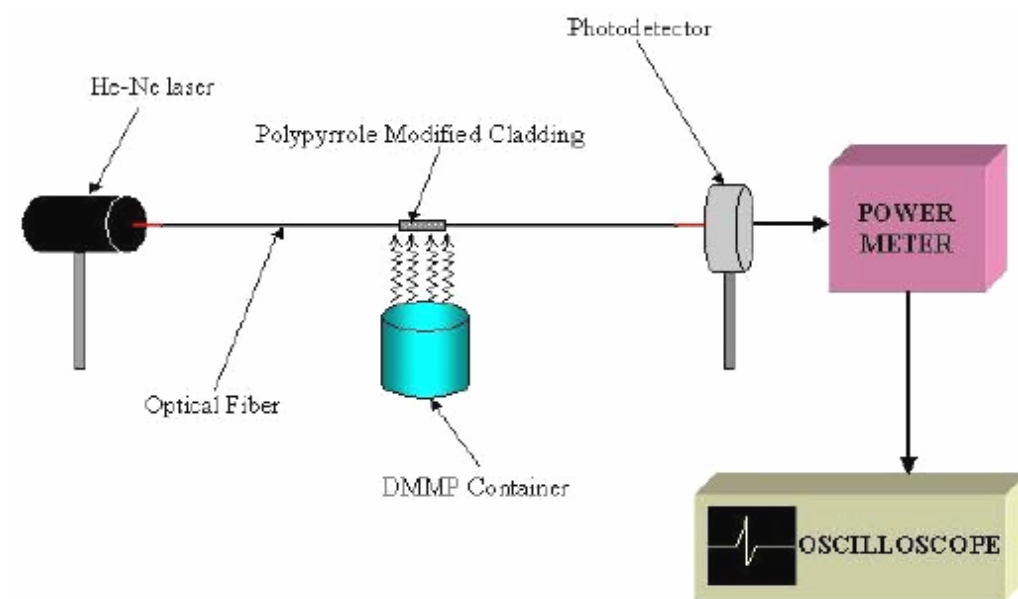


Figure 38. Optical fiber-based sensor system for the detection of DMMP as environmental stimulant

on optical fibers have also been reported in literature [65, 69, 70, 75]. Sensing of organic compounds like chlorinated hydrocarbons and volatile organic compounds has also been reported [62, 71-74]. Sensing of organic compounds is based on spectroscopic techniques and changes of refractive indices of polymer coatings on optical fibers on exposure to the analytes (organic compounds) [71-74].

Collins et al. [76] have described the development of conductive polymer-coated fabrics for sensing of chemicals and toxic vapors. Fabrics offer a large surface area for chemical sensing which leads to improved sensitivity and dynamic range of these sensors. Woven fabrics were developed from polyester and nylon yarns coated with polypyrrole (doped with naphthalene-disulphonic acid or anthraquinone-2-sulfonic acid). These conductive polymer-coated fabrics were exposed to several toxic gases (like Dimethyl methylphosphate or DMMP, ammonia, or nitrogen dioxide) and change of resistivity of these conductive fabrics (with exposure to the toxic gases) was monitored. It was observed that the resistance of NDSA-doped polypyrrole coated polyester fabric decreased when the fabric was exposed to chemical warfare agent, DMMP. It was also observed that the response of the conductive fabric-based sensor to DMMP was reversible and the resistance increased when the toxic gas was removed (as shown in Figure 39).

Development of optical fiber-based chemical and vapor sensors has led to the development of fiber-based electronic noses [77-80]. Electronic and optical noses comprising of optical fiber-based arrays of conductive polymer sensors have been developed in the past [62, 77, 81] to sense and identify individual gases and vapors from a mixture. These electronic noses consist of arrays of cross-reactive sensors, in which each sensor responds to several analytes. The analytes are discriminated from each other based on the unique temporal response patterns from the sensors [62, 81]. Hatfield et al. [81] have reported the development of an array of conducting polymer-based vapor sensors. They investigated the response of a 20-sensor array to the homologous series of n-alcohols (methanol to 1-pentanol). This array consisted of ten different conducting polymers like polypyrrole, polythiophene and polyaniline derivatives (heterocyclic molecules) deposited in pairs. These polymers display reversible changes in conductivity when exposed to polar volatile chemicals. Barnard et al. [77] have described the

development of a polymer-based optical fiber vapor sensor. This sensor was developed by entrapping a dye Nile Red in a polymer (dimethylsilicone) attached to the distal tip of a single mode optical fiber. The fluorescence change of the optical fiber sensors on exposure to vapors (benzene, toluene, ethyl benzene, xylene, and gasoline) was monitored. An optical fiber-based nose was developed [78] by taking a bundle of nineteen optical fibers with a different polymer sensing layer (polymer with an entrapped dye) attached to each fiber in the bundle. Temporal response of each sensor (optical fiber with a polymer deposited at the end) in the bundle was monitored during and after exposure of the sensor array to vapors. Development of microbead sensor arrays (optical fiber nose) has been described by Micheal et al. [79] and Patano et al. [80]. Microbead arrays are developed by making micro sized wells on the surface of a bundle of optical fibers and filling the wells with bead sensors (bead sensors consist of micro spheres (beads) in which a fluorescent indicator is attached to a polymeric or porous silica bead). These optical fiber-based vapor (or gas) sensors or sensor arrays could be incorporated into a fabric (by weaving or knitting the optical fibers into the fabric) to form fabric-based sensor arrays or optical noses.

2.3.2.2 Sensing of Biomedical Information

Biomedical sensors measure biomedical parameters by locating optical fiber probes in contact with the human skin or by placing them inside the human body. Optical fibers are used for measuring biomedical information like blood pH [82], stomach pH [83-84], blood oxygen saturation [85], for monitoring breathing conditions [86], in oncology [87], in skin condition monitoring [88], in ophthalmology [89], stroke analysis and treatment [62, 90], atherosclerosis analysis using fiber optic near field spectroscopy [91], blood pressure monitoring, and temperature monitoring [92-93].

In a patent by Leiby et al. numbered US6080690 [94], a woven textile fabric with integrated sensing elements has been reported (Figure 40). The fabric or clothing made from it is intended to assist a wearer in the monitoring of his/her biomedical information and surrounding environmental conditions. The biomedical information may include one obtained by monitoring the heart, the blood, and bodily fluids. The measurements taken use non-invasive procedures like skin analysis, body moisture analysis, and body temperature analysis and include information obtained through thermocouples and optical

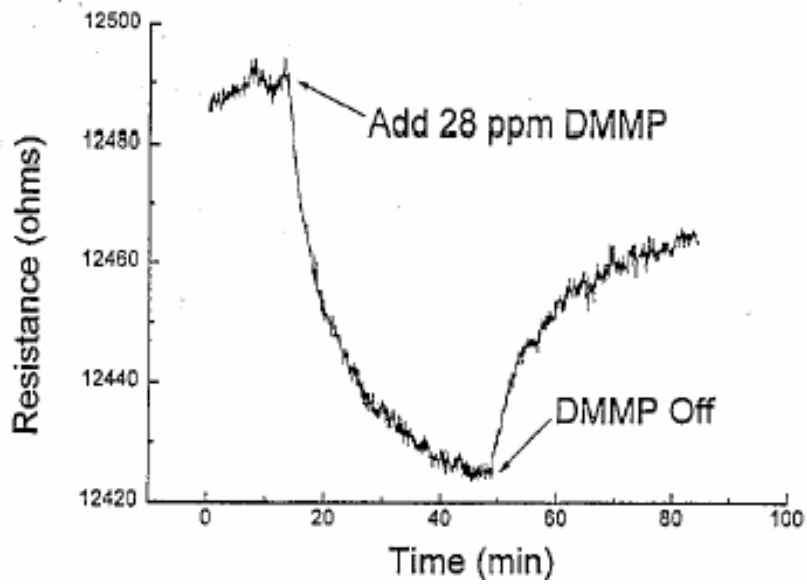


Figure 39. Decrease in the measured resistance of the NDSA-doped polypyrrole coated polyester fabric on exposure to DMMP. The resistance increases on removal of DMMP showing a reversible process

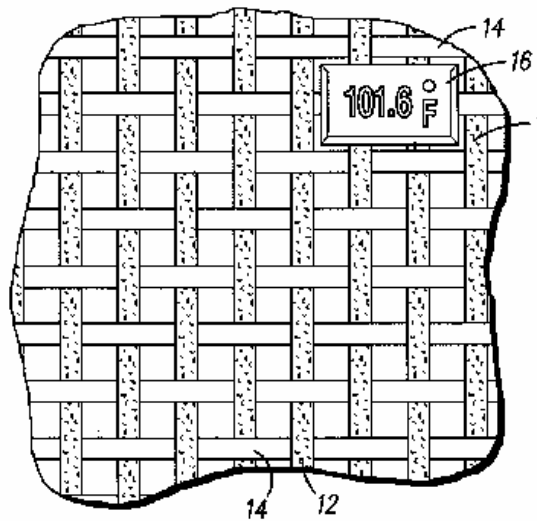


Figure 40. Woven textile fabric with integrated sensing elements like a temperature sensing unit

measurements. Sensors integrated into such a fabric could be used to measure environmental conditions existent upon the wearer and in order to control these conditions, heating and cooling bands in closed loop control with the sensors could be integrated into the fabric. According to the patent [94] the fabric has an arrangement of conducting fibers or yarns in a woven network, so as to transmit signals from integrated sensing elements to a monitoring electronic device integrated within some part of the fabric (wired interconnect). According to the patent [94], individual electronic components such as semiconductor chips, a power source or a controller for receiving sensed information can be interconnected to the conducting fibers in the fabric. The monitoring device can have wireless coupling with a remote electronic device located away from the fabric or clothing described above.

In a patent by Jayaraman et al., numbered US 6381482 [95], a woven or knitted conductive fabric network has been described which includes a flexible information infrastructure integrated within the fabric for sensing, processing, and transmitting biomedical information regarding the wearer. The fabric consists of a base fabric and an information infrastructure component which includes electrically conductive textile fibers, sensors and connectors for the sensors. These sensors can be used for monitoring physical aspects of the wearer, for example body vital signs, such as blood pressure, heart rate, EKG, pulse rate, respiration rate, temperature, voice, and allergic reaction. The electrically conducting fibers are woven into the fabric running in the longitudinal direction. These fibers transfer electrical signals sensed by sensors, interconnected at different points of the fabric/garment, to the computer or the personal status monitor. The signals from the sensors can be compared with the normal range for the body vital signs and if there are any deviations in readings from the normal, these readings can be transmitted using the transmitter.

2.3.2.3 Context Awareness

Application of context awareness to wearable electronics has been discussed in several papers [96-105]. Context awareness can be defined as making the electronic devices carried by people in everyday life more aware of the environment and activity of the users. The information can be used to modify the functionality of the devices to suit

the activities and situation of their wearers. Context awareness can be achieved by using sensors that can feed information into the electronic devices carried by the user.

Randell et al. [96] described a method of determination of context awareness [95, 102-104, 106-107] using location sensing (Global Positioning Systems or GPS). A guide, with a GPS as a location sensor to determine the location of a tourist (and render web pages related to the location), is one such application of these sensors on wearable clothings. This tourist guide has been implemented on a jacket (called a Cyber Jacket) which is equipped with a processor programmed with a web server, a GPS receiver, and a display. The Jacket with the location sensors incorporated in it does not provide a positional accuracy within ten meters due to difficulties receiving an adequate signal with body mounted antennas. In order to prevent inadequate rendering of the web pages in this jacket, accelerometers have been used along with the location sensors to help the context awareness system to determine what the user is doing in addition to location of the user. The accelerometers are movement sensors that can detect activity (walking, sitting standing, etc.). In the sensor system described above, the main processor is switched off when there is a steady state movement of the user (recorded by the accelerometers placed on the jacket). The accelerometers are programmed by the main processor to power up the main processor when a change in movement occurs like from walking to sitting. It can thus switch the main processor on and display the location and web information on the display. Sensor information (RMS and average values of gravitational force corresponding to the x and y axis of an accelerometer) was gathered at a frequency of 5 Hz and allows determination of whether a person is running, sitting, and standing, or walking. The values measured by the sensors were found to be person and clothing specific and the accelerometers had to be calibrated to compensate for the inclination and orientation of the device in the user's clothing. Calibration for clothing is also done with an accelerometer sewn and integrated into users clothing. These accelerometers could be integrated into clothing such as shirt or shorts, along with heart rate monitors to obtain some useful training information for athletes.

Schmidt et al. [100] have described the use of wearable Radio Frequency Identification Device (RFID) tag readers for increased human computer interaction for

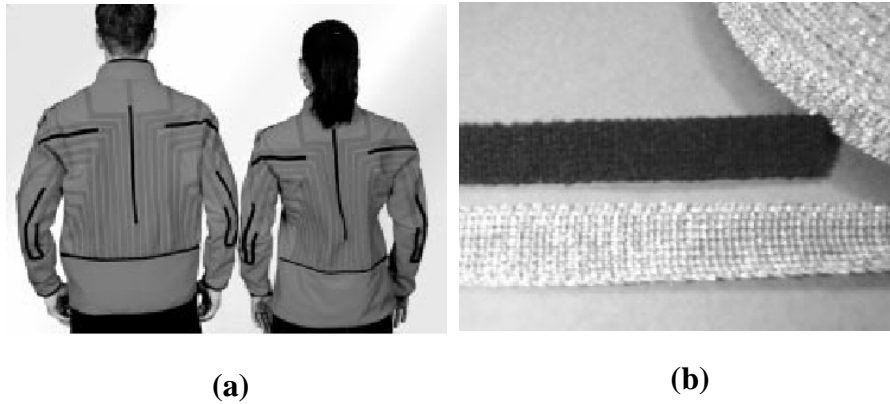


Figure 41. (a) Sensor jacket with integrated stretch sensors to determine the movement of limbs of the wearer of the jacket (b) A strip of the knitted stretch sensor used to form the sensor jacket

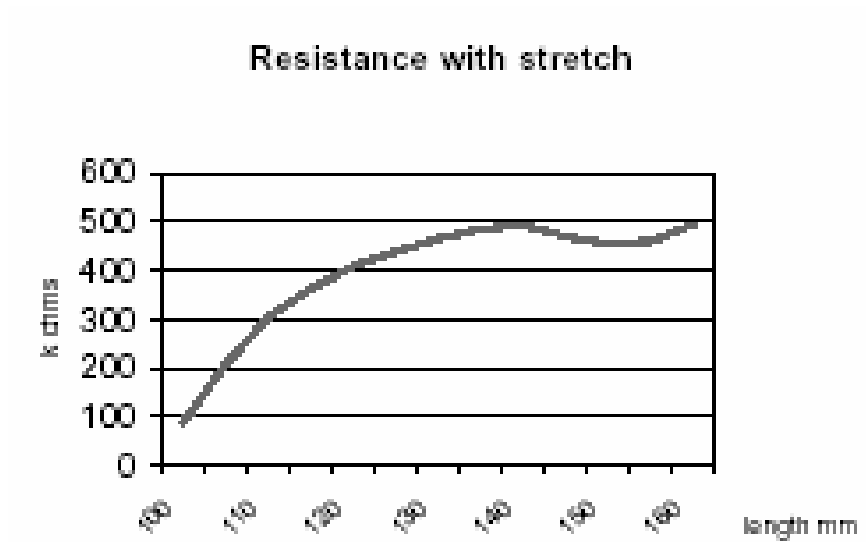


Figure 42. Increase in resistance of the knitted fabric-based stretch sensor on application of stretch

users of wearable computing. They developed a system with a portable RFID reader and an antenna coil integrated into a glove. This RFID system provides increased human computer interaction for wearable computers as the RFID reader can detect the presence of RFID tags or responders and the information read could be mapped to a URL on the internet using a software.

2.3.3 Strain sensors

Among other types of sensors, optical fiber-based sensors and sensing systems have been employed for the measurement of strain and its distribution. Types of fiber optic sensors used for accurate strain measurements are intensity-modulated sensors, spectrally based sensors, interferometric sensors, and Fiber Bragg Grating (FBG) sensors.

Intensity-modulated fiber optic strain sensors [108-109, 110-123, 124] are based on modulation of light intensity in a multimode optical fiber on application of strain. There is a loss of light intensity when any portion of the optical fiber is strained. These sensors are easy to construct and do not require complex instrumentation and signal processing. An interferometric strain sensor [108, 110, 124] measures phase changes on application of mechanical strain either in a single-mode optical fiber or developed between two optical fibers. They have higher levels of sensitivity as compared to the Intensity-modulated fiber optic strain sensors. Fiber Bragg grating (FBG) sensors have been used for strain sensing [62, 108-109, 110-123, 124-125]. When a FBG strain sensor is subjected to the external load, induced changes in the Bragg wavelength (mechanism of FBG sensors described in section 3.2.2) can thus be related to mechanical strain. The major advantages of FBG strain sensor are high failure strain, ease of multiplexing, and its small size. One limitation of these sensors is that they are sensitive to both strain and temperature simultaneously thereby creating a problem in independent measurement of these two parameters. A optical fiber grating tapered cavity sensor has been developed by Du et al. [119] which encodes strain (independent of temperature) into its spectral profile. The sensor possesses two spectral peaks within its main reflection band and the power difference between the two spectral peaks changes linearly with strain while it is independent of temperature. A number of other methods to obtain independent measurements of strain and temperature have been reported [126-128].

Fiber optic sensors embedded in fiber-reinforced composite structures have been used for in situ damage detection and assessment [108, 110, 112, 115, 125, 129-133]. These sensors are used for detecting damage, its nature and precise location in composite materials. Fiber optic sensors can be easily integrated into composite structures to access interior material and structure locations where other sensing methods cannot easily probe. Use of in situ fiber optic sensors allows damage detection and assessment without performing any destructive tests. Damage in a composite may arise primarily from impact loads or stress loads, leading to changes in strength and moduli of these materials. Damage usually appears in the form of three major mechanisms, namely, matrix cracks, delamination and fracture of reinforcing fibers. Matrix cracking generally appears relatively early in the loading because the tensile strength of the matrix materials is lowest. That is usually followed by the onset of delamination and fracture of reinforcing fibers at an advanced stage of loading. Fiber optic strain sensors can be used to measure these changes by measuring the changes in optical properties of the fiber (intensity, wavelength, and phase). These optical properties are in turn related to the axial strain of these fibers. Embedded sensors must have a good adhesion with the matrix of the composite so that the axial strain experienced by them is the same as that of the host structure in the direction of the optical fiber [108, 115-118, 130-131]. Reliability of fiber Bragg grating sensors embedded in textile-reinforced composites has been studied by Tao et al. [115] and Tang et al. [116].

El Sherif et al. [134] have incorporated fiber optic strain sensors into textile structures for the detection of static and dynamic loads in parachute canopy and suspension lines. They used two types of embedded fiber optic sensors; the Fiber Bragg Grating (FBG) [135-142] and the Modal Power Distribution (MPD). These fiber optic strain sensors are woven into the parachute canopy fabric. Detection of dynamic loads on the parachute canopy and suspension lines can be determined by measuring the change in wavelength of the transmitted light signal (through the optical fibers) on application of strain to the fabric incorporating the optical sensor.

Individual fiber optic strain sensors provide information on strain levels (and damage) in certain localized sites in a composite. This information is useful in applications where it is sufficient to know if the composite structure had sustained

impacts above certain thresholds levels. However, to evaluate damage on large composite structures, the induced strain distribution must be determined. Spatial distribution of strains within the host structure at impact sites can be determined by employing sensor networks or multiplexed fiber optic sensors. Distributed sensor systems [62, 108-109, 84-97] can be used for strain distribution determination in reinforced composites. These systems are based on sensor arrays multiplexed by optical time-domain reflectometry and wavelength division multiplexing [62, 109, 143-148]. The optical time domain reflectometry technique involves sending a light pulse from one end of a single fiber optic sensor and its reflection back to the same fiber end from certain reflective locations along the fiber. The time of flight (sending and coming back) is used to determine strains in the composites. Individual sensors within a network can be arranged in either series or a parallel topology.

A wearable sensor jacket has been developed from knitted fabric-based stretch sensors [97]. This jacket helps in determining context awareness by measuring movement of certain limbs of the body. The conformable fabric-based stretch sensors can be positioned or integrated into the jacket to measure upper limb and body movement. These sensors (shown in Figures 41a and 41b) measure stretch from resistive changes in knitted strips. These sensor strips gave a linearly increasing asymptotic resistance with stretch (shown in Figure 42). These sensors supply information about the user's activity to other electronics worn by the user (like displays) so that it leads to an improved behavior of these electronics related to the activity of the users. The aim of the Sensor Jacket is to detect the posture and movements of the user by using knitted stretch sensors and conductive interconnections thereby forming a completely fabric worn sensor system.

2.3.4 Actuators

Actuators produce change in shape or dimensions in response to application of thermal, electrical, chemical or other stimulation. Many of the actuator materials currently being studied are polymers and for obvious reasons fabrication of these polymers in fiber form is of interest. Some of the relevant materials that could be used to produce actuation are piezoelectric materials, ferroelectric materials, dielectric elastomers, ionic polymer-metal composites, conducting polymers, shape memory alloys, and carbon nanotubes have been used in the past to form actuators. These materials produce actuation or change their shape

in response to application of thermal, electrical, chemical or other stimulation. Some of the important properties considered for development of actuators from these materials are: levels of stress/strain on actuation, the strain rate, hysteresis, excitation field (i.e. voltage) required to produce the actuation, and the cycle life of the material (ability to withstand a given number of actuation cycles). Some of the above mentioned active materials that could be used to produce fiber-based actuation systems are described below. In this section, research being carried out to develop actuators and actuator systems based on fibers, is described.

Hutchison et al. [149] have reported the development of fiber and film actuators based on conducting polymers. These actuators consist of liquid (NaNO_3) or solid electrolytes (hydro gel containing NaNO_3) in the vicinity of doped conducting polymer (metal-coated or uncoated) electrodes. The principle of actuation involves oxidation or reduction reactions at the electrolyte/electrode interface. These oxidation and reduction reactions lead to expansion and contraction of the conducting polymer (e.g. polypyrrole). The actuation force generated varies with the type of dopant used (see Figure 43). Different configurations of polypyrrole electrodes used to develop these actuators included electrochemically deposited polypyrrole films, platinum-coated polypyrrole films, and fibers with polypyrrole coated on platinum-coated polyester fibers. In one configuration of a fiber actuator, fibers with polypyrrole coated on platinum-coated polyester fibers were combined into a bundle. Bundling of fiber (as shown in Figure 44) actuators causes an increase in the surface area of polypyrrole thereby increasing the rate of ion diffusion to and from the polypyrrole electrodes. This causes an increase in the rate of redox reactions taking place at the electrode-electrolyte interface thereby causing an increase in the achievable force density. The force per unit width was found to be 5 N/mm and the stress generated was 5MPa for the total area of the device. The mechanism of electrochemical actuation in conducting polymers (polypyrrole doped with polyvinyl sulfate and para-toluene sulfonate) is discussed in a paper by Gandhi et al. [150]. The performance and work capacity of a conducting polymer film actuator made of polypyrrole (doped with benzenesulfonate anions) is also discussed in a paper by Della Santa et al. [151]. They discuss that during reduction (on application of voltage during cyclic voltametry on a doped polypyrrole sample immersed in electrolyte bath of sodium

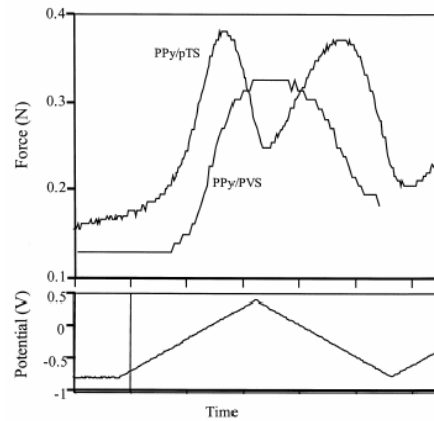


Figure 43. Force changes observed for free-standing films of PPy (polypyrrole) with two different counterions: pTS (*para*-toluene sulfonic acid) and PVS (polyvinylsulfonate) . Applied potential was varied between -0.8 V to 0.4 V

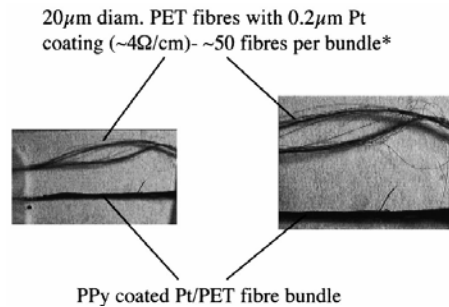


Figure 44. Polypyrrole coated (below) and uncoated (above) Pt/PET fiber bundle

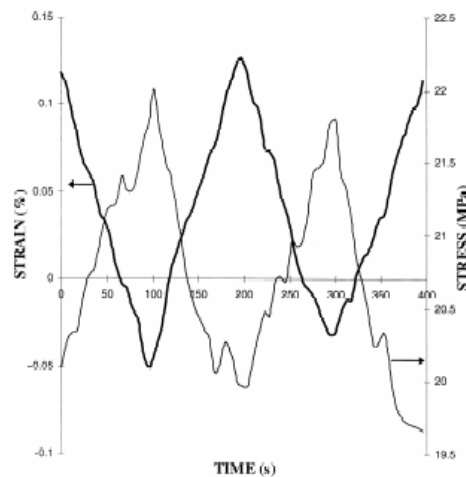


Figure 45. Evaluation of doped-polyaniline fiber/solid polymer electrolyte/copper fiber-based actuator: Isometric stress and Isotonic strain vs. time during short wave pulse (period 200 s) stimulation between the electrodes

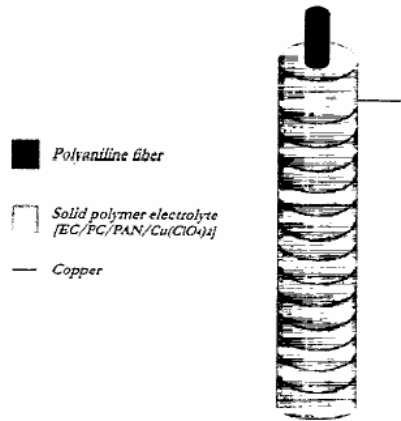


Figure 46. A dry fiber actuator based on polyaniline fiber, a solid polymer electrolyte, and copper wire

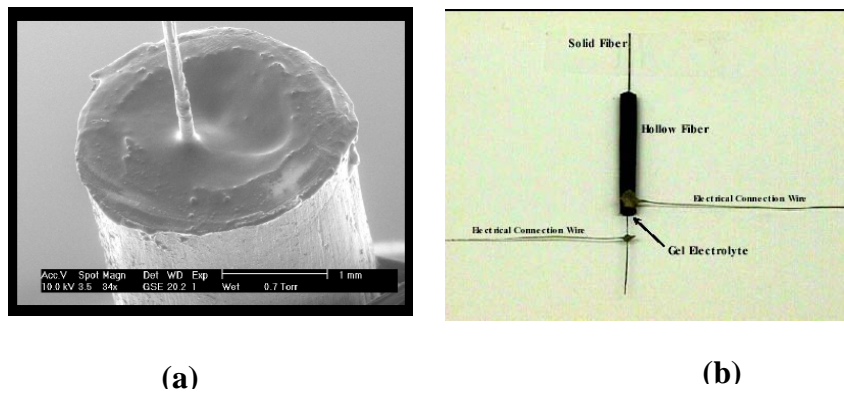


Figure 47. (a) Polyaniline hollow fiber containing a polyaniline conducting fiber at its core and filled with gel electrolyte between the two conducting surfaces and (b) Electrical connections to the outer (hollow polyaniline fiber) and inner conducting (solid polyaniline fiber) fibers to form an electrochemical actuator

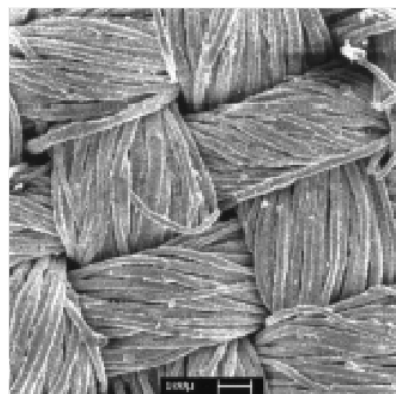


Figure 48. SEM micrograph showing a woven wool fabric with Polypyrrole chemically deposited on it

benzenesulfonate in acetonitrile and water) one observes contraction of the polymeric film due to de-doping of benzenesulfonate anions and an elongation due to intake of sodium ions by the film.

Rossi et al. [152] have described the development of spun conductive fibers (polyaniline fibers) that show electromechanical actuation. The actuating polyaniline fibers were spun according to a procedure described by Tzou et al. [153]. In the work carried out by Rossi et al. [152], wet spun polyaniline fibers were drawn (draw ratio being 2) and doped with a 1 M HClO₄ solution through immersion for 24 hours. In order to evaluate the conducting polymer fibers for their electromechanical behavior, these fibers were immersed in a 1 M electrolyte bath composed of HClO₄/distilled water with the lower end of the fiber clamped and connected to a gold electrode and the upper end connected to a motion transducer. A potentiostat-galvanostat provided voltage or current waveforms between the Polyaniline fiber (working electrode) and a Platinum counter electrode. Evaluation of the electro-active fiber activation i.e. changes in its length with the application of voltage or current was carried out by stimulations by means of cyclic voltammetry, square-wave potential, and a square-wave current excitations. In this paper, Rossi [152] also describes the development of dry fiber actuators. A Polyaniline fiber having a diameter of 200 μm doped with HClO₄ was embedded into an elastomeric solid polymer electrolyte matrix having a thickness of 50 μm. A thin layer of polypyrrole was grown on top of the solid polymer electrolyte jacket to form a dry fiber actuator. In another method, a metallic counter electrode was developed by winding a 100 μm diameter copper wire on the solid polymer electrolyte jacket as a helix. A square wave pulse (with a period of 200 s) was applied between the doped polyaniline fiber electrode and the copper wire counter electrode and the results are shown in Figure 45. Rossi [154] has described different limitations of the conducting polymer based fiber actuators like slow response time (which is dependent on the rate of ion diffusion) and a low strain in the axial direction. In this paper Rossi [154] also describes how radial strain in such fiber actuators could be converted to axial strain using a radial to axial strain transducer. Development of cylindrical actuators made from dielectric elastomers and compliant electrodes is also described in this paper [154]. Carpi et al. [155] have modeled cylindrical actuators made from dielectric elastomers having compliant electrodes

assuming that electrostatic pressures exerted by the electrodes are constant during actuation. This electromechanical model correlates the axial and radial strain developed in the cylindrical actuator to the applied voltage. This model was experimentally validated using silicone elastomer and carbon grease compliant electrodes.

Mazzoldi et al. [156] have described the development of a dry fiber actuator based on spun polyaniline fibers. The three main elements of this dry fiber actuator were the HClO₄ doped polyaniline fiber as the working electrode, a solid polymer electrolyte as an electrolyte between the electrodes, and a 100 μm diameter copper wire wound in a spiral around the solid polymer electrolyte as the counter electrode. Mazzoldi et al. [156] have reported that in order to spin polyaniline fibers, undoped polyaniline in powder form was dissolved in N-N` dimethylpropylene urea (20-25% by wt.). For extrusion an air-driven piston (15 cc. chamber volume), a filter with pores of 11-17 μm and a spinneret were used. The extruded fiber was then immersed in a coagulation water bath and rolled up on a cylinder at a speed of 4-6 m/s. Finally the fiber resided in a second water bath for 30 minutes. The fiber was then drawn at 160-180 °C with draw ratio ranging from 1 to 3. The doping was achieved by immersion of the fiber in 1M HClO₄ for 24h and drying in an oven at 50 °C for 1h. The solid polymer electrolyte was prepared by using propylene carbonate (PC), ethylene carbonate (EC), polyacrylonitrile and cupric perchlorate having a molar percentage of 38, 38, 13, and 11 % respectively. The cupric perchlorate salt was dissolved in the EC/PC solution (kept at 50-60 °C) and mixture was stirred continuously. Polyacrylonitrile was added to mixture and after its dissolution; the mixture temperature was raised to at 100 °C. After an hour of stirring, the solution was cooled very slowly to obtain a transparent, elastomeric, solid electrolyte. The dry polyaniline fiber-based actuator described above is shown in Figure 46.

In another paper, Rossi et al. [157] have reported the use of wet-spun polyaniline fibers for the development of dry fiber-based actuators. Doped wet spun polyaniline fibers were covered with a solid polymer electrolyte, which was in turn covered with a thin polypyrrole layer. The polyaniline fiber and the polypyrrole outer layer serve as the electrodes of the fiber actuator. In another paper, Rossi et al. [158] have described the development of actuating fibers composed of bundles (with hexagonally packed fibers forming the bundle) of hollow polyaniline fibers with a metal wire placed in the center of

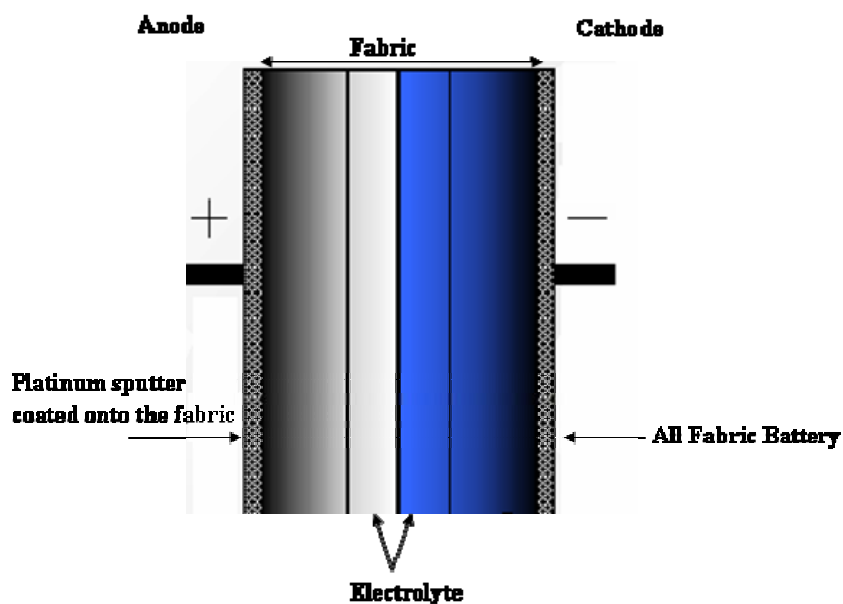


Figure 49. Schematic of an all textile-based battery comprising of a conducting fabric cathode and anode. The middle layer of the fabric holds an electrolyte to form an all-fabric battery system

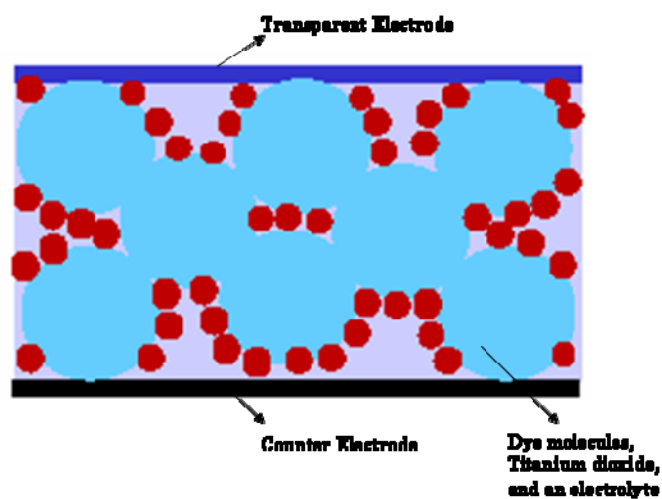


Figure 50. Dye sensitized solar cell consisting of dye molecules and titanium oxide enclosed between two electrodes

the individual hollow fibers and a thin layer of solid polymer electrolyte filling the gap between the metal wire and the inner boundaries of the hollow polyaniline fibers.

Shahinpoor et al. [159] have reported the development of fiber actuators using platinum-coated polyacrylonitrile fibers. Activated polyacrylonitrile fibers expand and contract when immersed in basic and acidic solutions, respectively. When polyacrylonitrile fibers were placed in an electrochemical cell, electrolysis of water in such a cell produced hydrogen ions at the platinum-coated polyacrylonitrile anode, thereby locally decreasing the pH around the polyacrylonitrile fiber. This caused the platinum-coated polyacrylonitrile fiber to contract. Reversing the electric field in the electrochemical cell caused the platinum-coated polyacrylonitrile fibers to elongate.

Mattes [160] has described the development of doped polyaniline fiber-based actuators that use ionic liquid electrolytes like 1-butyl-3-methylimidazolium tetrafluoroborate or propylene carbonate. In another actuator described by Mattes [160], a conducting hollow polyaniline fiber is used to develop the actuator. This hollow fiber contains another conductive polyaniline fiber at its core and the gap between the two conductors is filled with a gel-electrolyte (see Figures 47a and 47b). This actuator [160] generates a stress around 0.94 MPa and a strain of 1%.

As described above, the strain levels obtained in conducting polymer based fiber actuators is not very high (around 1%). Conducting polymer and carbon nanotube based fibers could be developed for use in electro active fiber applications that require high levels of stress to be generated. Other electroactive materials like dielectric elastomers could also be applied to achieve high levels of strain. Work done in the area of fiber-based actuators could be extended to develop fabric-based actuation systems by incorporating fiber actuators into woven and non-woven fabrics.

2.4 Fibers/Fabrics in Energy Storage & Generation

Energy generation and/or storage are essential for any textile based electrical system. In the past, conducting fibers have been used to form battery separators and electrolyte withholding fabrics. Battery electrodes have also been produced from conducting fibers and fabrics. In recent years, some research has been carried out to develop complete textile-based batteries or energy harvesting systems. Electrical energy can be generated

by converting solar energy to electrical energy (using solar cells) or may be stored by employing chemical means (batteries)

Inherently conducting polymers are being developed for wearable energy storage systems [161]. Fabric batteries and photovoltaics have been developed utilizing Ionic Liquid Electrolytes that could be incorporated into textile membranes [161]. Fabric-based electrodes have been used in these batteries to form flexible and conformable battery systems. These textile-based electrodes are formed by coating conducting polymeric materials on fabrics or by in-situ or vapor phase polymerization of the monomers of conductive polymers on fabric substrates. [161] Vapor phase polymerization of polypyrrole was carried out on FeCl_3 imbibed wool fabrics to give a thin and uniform conductive coating having a conductivity of $0.1 \text{ S}\cdot\text{cm}^{-1}$. Polyester was coated using in situ polymerization of pyrrole. Dopants like polystyrene sulfonate (PSS) were added to polypyrrole to increase the polymer conductivity and also gave high values of capacitance of the coated fabrics. Polypyrrole was deposited on wool, lycra, cotton, and polyester and it was seen that wool and cotton conductive fabrics showed higher conductivity as compared to that of lycra [161]. A SEM micrograph of a woven wool fabric, with polypyrrole chemically deposited on it, is shown in Figure 48. Ionic liquids like hexafluorophosphate, tetrafluoroborate and alkylmethylimidazolium were used in this battery as electrolytes. Hexafluorophosphate was found to be an ideal ionic electrolyte as it exhibits low vapour pressure (i.e. doesn't evaporate) and has a conductivity of around 10^{-2} Scm^{-1} . Innis et al [161] have also described the development of an all textile-based battery (Figure 49) using n-dopable polypyrrole/polystyrene sulfonate electro-polymerised on graphite fiber substrate as an anode and polypyrrole electropolymerised on graphite fiber substrate as the cathode. Platinum contacts were sputter coated on the polymeric electrodes. A solution cast polymer gel based on polycarbonates, LiClO_4 , and polyaniline blends has been used as an electrolyte. The electrolyte is incorporated in a textile layer between two layers of the textile electrodes to form an all textile-based battery.

Development of a solid polymer-based rechargeable lithium ion battery has been described by Livolsi [162]. This battery contains a solid polymer electrolyte (formed by

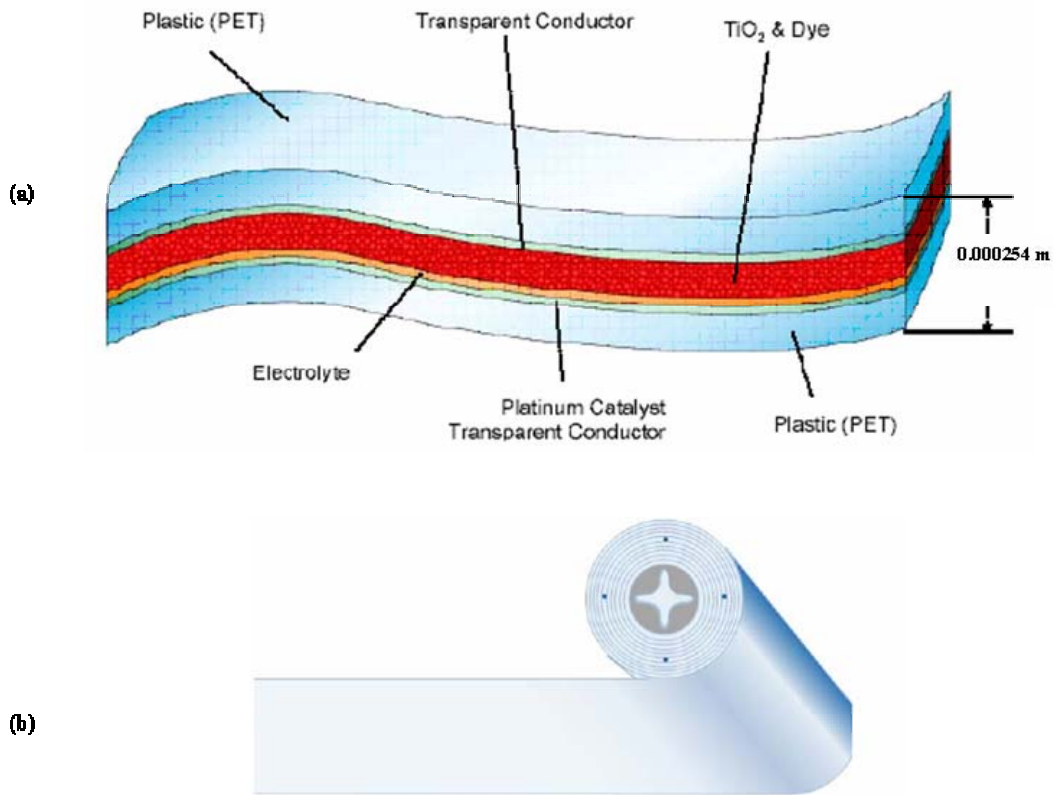


Figure 51. (a) Dye Sensitized Solar Cell developed on (b) a flexible substrate or a fabric that could be rolled up

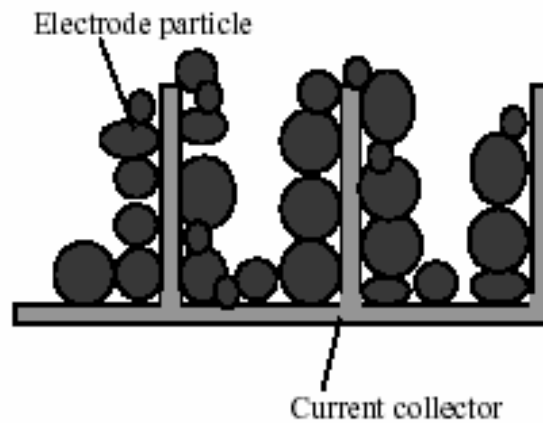


Figure 52. Schematic of a microstructured current collector leading to an increased surface area

mixing three polymers, plasticizer, and lithium salt). In situ polymerization (of low molecular weight monomers) is carried out on a synthetic fabric (in situ polymerization enhances handling and manufacturing). In this flexible battery, the anode consists of carbon, a binder, lithium salt, and plasticizers on a copper foil, the cathode consists of lithium cobalt oxide, a binder, lithium salt, and plasticizers on an aluminum foil substrate and the solid polymer electrolyte (polymerized on a fabric substrate) is sandwiched between the two electrodes. This battery provides over 1000 charge-discharge cycles with greater than 80% capacity.

A thin-film solid state lithium ion battery has been described by McDermott et al [163]. This flexible thin film (components deposited on very thin films) battery is reportedly rechargeable, has the capability to support thousands of charge-discharge cycles, has low self discharge characteristics and is meant for low power applications.

Flexible and conformable solar cells can be developed by using coatings of organic dyes and titanium dioxide particles on plastic sheets or woven fabrics [164-165]. Highly efficient thin film dye sensitized solar cells or DSSCs (composed of titanium dioxide particles) have been used to convert solar energy to electricity [164-167]. The principle of formation of these solar cells involves enclosing organic dyes and titanium dioxide nanoparticles between two conductive electrodes as shown in Figures 50 and 51 [164]. It can be seen in Figure 51 that there is a layer of electrolyte present between the organic dye and titanium dioxide mixture and the lower electrode. The overall thickness of the configuration shown in Figure 51 is 0.000254 m. The top conductive electrode is transparent and allows light to pass through it and react with the organic dye molecules. There is charge generation due to the absorption of light by the dye molecules. The charge generated is transferred to the titanium dioxide nanoparticles and collected by the electrodes thereby producing electrical energy from solar energy. These solar cells are produced at extremely low costs due to the use of inexpensive raw materials [164, 166] and can be used for producing light weight and wearable solar energy harvesting plastic sheets (Figure 51b) and textiles. The energy Conversion efficiency of these devices is 7.1-7.9% with current densities greater than $12\text{mA}/\text{cm}^2$. These solar cells have proven to have better efficiency in cloud cover than the conventional solar cells. It has also been reported that these batteries have an energy density of 400 WHr/Kg, which is four times

that of conventional rechargeable batteries. These conformable solar batteries can be incorporated into garments or in giant area fabrics such as shelters, tents, truck covers, and parachutes to produce hundreds of kilowatts of power.

Chittibabu et al. [166] describe the development of a dye sensitized solar cell that contains an ionic liquid based gel electrolyte. In order to develop DSSCs on flexible (film or fabric-based) substrates on a continuous basis, it is important to develop solid or quasi-solid electrolytes (non-liquid) to avoid problems of leakage and to allow convenient application of the electrolyte gels on to the films. The ionic liquid based gel electrolyte was developed by mixing a solution of poly (4-vinylpyridine) and 1-alkyl-3-methyl imidazolium iodide with a solution of lithium ions and 1-alkyl-3-methyl imidazolium iodide. In order to form the photo electrochemical cell, a suspension containing titanium dioxide particles was coated on an indium-tin-oxide coated polyester substrate. This substrate was then sensitized with a dye, the liquid ion electrolyte was applied to it, and a platinum coated transparent conducting oxide glass plate was placed on top. This liquid ion based gel electrolyte incorporated DSSC exhibited an efficiency of 5% and an open circuit voltage of 0.66 V.

Bio-derived electrically conducting polymers have also been used for the formation of energy harvesting devices [164]. Polyaniline is produced by enzymatic polymerization (using HRP or Horse Radish Peroxidase) of aniline with and without the use of a sulphonated polystyrene (SPS) template. This biological route to the synthesis of a water-soluble, truly conducting form of polyaniline is attractive as it allows for a one a step polyaniline synthesis process and produces a final product of high purity. Incorporation of a template with a specific structure, shape, and size allows fabrication of desirable architectures for a host of electronic and optical applications. Visible absorption spectra of enzymatically synthesized polyaniline with a template (SPS) shows high absorption in the range of 800-1000 nm. Polyaniline can be used for generation of charge on exposure to light which can be transferred to the electrodes thereby producing electrical energy.

2.5 Heating Systems

Conductive fibers and fabrics have been employed for development of several heating systems such as heating blankets, carpets, jackets, floor panels etc., which use

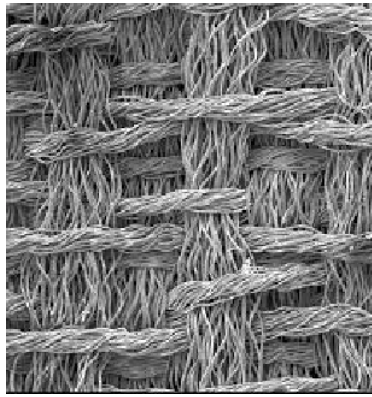


Figure 53. A metal-coated fabric used to form a microstructured electrode

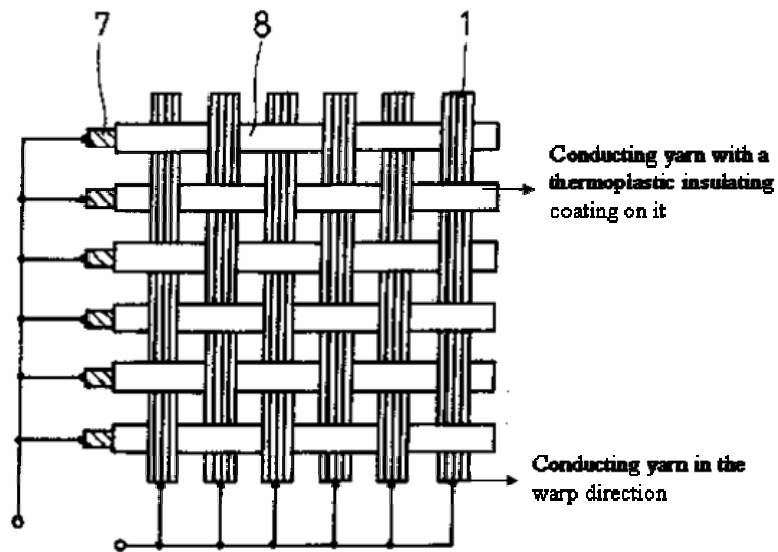


Figure 54. Weaving of conducting yarns in warp and weft direction to form an electric heating sheet for heating blankets, carpets etc.

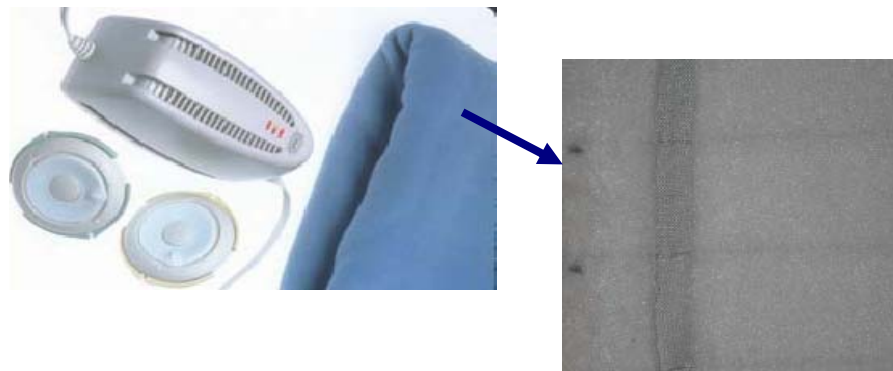


Figure 55. Polartec heating blanket developed by malden mills

passage of current through conductive elements in these applications. The passage of electric current leads to resistive heating of the conductive fibers and fabrics.

Temperature detection and control systems can be integrated into such applications to prevent over-heating and to ensure uniform heating.

In a patent by Kishimoto [168], development of a woven fabric-based conductive sheet for heating applications such as heated electric carpets, electric blankets, and floor heating has been described. Conductive wires and conductive yarns are woven into a fabric (in the weft direction) along with insulating threads (in the warp direction) to create a sheet that could be heated on application of current through the conductive wires or yarns. Weaving of flexible conductive yarns to form these electrical heating sheets makes them flexible and conformable. The conductive yarns employed could be conducting polymeric yarns or metallic yarns. In order to prevent over-heating of this sheet, weaving of insulated conducting yarns or wires in the warp direction could be carried out with bare conducting yarns in the weft direction (shown in Figure 54). The insulating coating on the thermoplastic is such that it melts on increase of temperature above a certain point leading to short-circuiting of conducting yarns in the warp and weft direction. Thus, safety of the conductive sheet can be ensured by preventing overheating. The electrically conductive sheet could also be laminated with sheets of thermo-sensitive polymeric materials for detecting the temperature of the sheet. The supply of electric current from the power source can be switched on or off depending upon the temperature detected in the sheet.

In a patent by Gurevich [169], a flexible heating element has been described. This soft, lightweight, and conformable heating element is developed from a conductive fabric, which can be heated by passing electric current. The heating element can be installed in flexible heaters that could be used for applications that involve sharp folding and compression of the heaters. The core of the heating element consists of an electrically conductive fabric due to the presence of carbon particles in the fabric. Strips of such a woven or non-woven conductive fabric are impregnated in a soft filling material that prevents moisture to be absorbed by the conductive fabric. This soft filling material may have conductive particles in it and can also lead to increase in conductivity of the fabric. The coated fabric is cut into strips of desired patterns and is then calendared between

layers of insulating polymeric sheets. Conductive adhesive is used to attach the conducting fabric to electrodes that supply current to the fabric to cause its heating.

A flexible heat blanket called the polartec heat blanket (as shown in Figure 55) has been developed by malden mills [170]. The heating elements in this blanket are electrically conducting filaments that are knitted into polyester fleece. These conducting filaments in the blanket provide an even distribution of heating throughout the entire blanket when electric current is passed through them. A flexible ribbon like power bus developed at the us army soldier systems center is used to transfer current to the conducting filaments. The temperature of the blanket can be controlled using a wireless controller.

Conductive fabrics have also been used to develop heatable wind energy turbine blades [171]. In this development, conducting fabrics are used for prevent build up of ice on the turbine blades. Ice build up on turbine blades can lower the efficiency of energy transfer from wind energy to rotational energy of the turbine by changing the aerodynamic profile. Moreover, weight of ice accumulated on the blades can increase strain on the equipment. Woven, braided or nonwoven fabrics produced from conductive fibers such as carbon fibers or metal coated carbon fibers can be used for making the heating elements in the blades. The fabric heating elements can be directly attached to the blade surface or can be incorporated in the composite structure of the turbine blades. Incorporation of conducting fabric in the composite involves lamination of the fabric between two layers of insulating resin. The conducting fabric is connected to lead wires that carry electrical current to the fabric from the power supply. The generation of heat in the conductive fabric is due to resistive heating of the conducting fibers on passage of current. The advantage of using conductive fabrics for this application is that these fabrics help to distribute heat uniformly over the surface of the blade.

Conductive fabrics have also been used as heating elements in deicing applications in aircrafts [172]. Layers of ice can accumulate on the wings and fuselage of aircrafts and can potentially affect the operation of controls and sensors of the aircraft. In order to solve this problem, a laminate consisting of a conducting fabric is bonded to the exterior surface of the aircraft (the wings and the fuselage). Controlled application of heating to the wings and fuselage of the aircraft can be used to prevent or melt the ice in these

regions. The laminate consists of a several plies that are bonded together. The outer ply of the laminate is hard, water-proof, abrasion and penetration resistant. The conducting fabric ply is a non-woven fabric developed from nickel coated graphite fibers (with a sheet resistance less than 1 ohm per square). The conductive fabric ply is connected to the power supply via an electrical bus and can be heated by passing current through it.

2.6 References

1. H. K. Bakoglu, *Interconnections and Packaging for VLSI*, Addison Wesley, 1987.
2. R. K. Poon, *Computer Circuits Electrical Design*, Prentice Hall, 1994.
3. R. R. Tummala and E. J. Rymaszewski, *Microelectronics packaging Handbook*, Van Nostrand Reinhold, 1989.
4. J. D. Plummer, P. B. Griffin, and M. D. Deal, *Silicon VLSI Technology: Fundamentals, Practice, and Modeling*, Prentice Hall, 2000.
5. M. S. Leiby, and K. E. Jachimowicz, "Textile fabric with integrated electrically conductive fibers and clothing fabricated thereof," US Patent 5906004, 1998.
6. A. Dhawan, T. K. Ghosh, A. M. Seyam, and J. F. Muth, "Woven Fabric-based Electrical Circuits Part I: Evaluation of Interconnect Methods," *Textile Research Journal*, October, 2004.
7. A. Dhawan, T. K. Ghosh, A. M. Seyam, and J. F. Muth, "Woven Fabric-based Electrical Circuits Part II: Yarn and fabric structures to reduce crosstalk noise in woven fabric-based circuits," *Textile Research Journal*, In Press, to be published in November, 2004.
8. A. Dhawan, T. K. Ghosh, A. M. Seyam, and J. F. Muth, "Woven Fabric-based Electrical Circuits," *Proc. of Textile Technology Forum, IFAI and the Textile Institute*, Charlotte, NC, 2002.
9. A. Dhawan, "Woven fabric-based electrical circuits," *Masters Thesis*, North Carolina State University, 2001.
10. A. Dhawan, T. K. Ghosh, A. M. Seyam, and J. F. Muth, "Development of Woven fabric-based electrical circuits," *Proc. of the Materials Research Society Conference Symposium D*, Boston, 2002.
11. A. Dhawan, T. Ghosh, A. Seyam, and J. Muth, "Formation of Electrical Circuits in Woven Structures," *Proc. of the International Interactive Textiles for the Warrior*

Conference organized by the Soldier and Biological Chemical Command, NASA, & DARPA, Cambridge, MA, July 9-11, 2002.

12. K. Natarajan, A. Dhawan, A. M. Seyam, T. K. Ghosh, and J. F. Muth, "Electrotextiles - Present and Future," Proc. of Materials Research Society Conference Symposium D, Boston, MA, Fall 2002.
13. J. F. Muth, E. Grant, A. Dhawan, A. Seyam, and T. Ghosh, "Signal Propagation and Multiplexing challenges in Electronic Textiles," Proc. of Materials Research Society Conference Symposium D, Boston, MA, Fall 2002.
14. E. Ethridge and D. Urban, "ElectroTextiles - Technology to Applications," Proc. Materials Research Society Conference Symposium D, Boston, MA, Fall 2002.
15. K. Luthy, J. Braly, L. Mattos, E. Grant, J. F. Muth, A. Dhawan, T. K., Ghosh, A. M. Seyam, and K. Natarajan, "An Acoustic Array as an example of a large-scale electronic fabric," Proc. of Materials Research Society Conference Symposium D, Boston, MA, Fall 2002.
16. E. Grant, K. A. Luthy, J. F. Muth, L. S. Mattos, J. C. Braly, A. Seyam, T. Ghosh, A. Dhawan, and K. Natarajan, "Developing Portable Acoustic Arrays on a Large-Scale E-Textile Substrate," Proc. of the INTEDEC conference - fibrous assemblies at the design and engineering interface, Edinburgh, UK, 2003.
17. T. Kirstein, D. Cottet, J. Grzyb, and G. Tröster, "Textiles for Signal Transmission in Wearables," Proc. of the Workshop on Modeling, Analysis and Middleware Support for Electronic Textiles (MAMSET), In conjunction with ASPLOS-X (Tenth International Conference on Architectural Support for Programming Languages and Operating Systems), San Jose, California, 2002.
18. D. Cottet, J. Grzyb, T. Kirstein, and G. Tröster, "Electrical Characterization of Textile Transmission Lines," IEEE Transactions on Advanced Packaging, 26 (2), 182-190, 2003.
19. I. Locher, T. Kirstein, and G. Tröster, "Electronic Textiles," Proc. of ICEWES Conference, Cottbus, Germany, 2002.
20. S. Jayaraman, S. Park, and R. Rajamanickam, "Full-fashioned weaving process for production of a woven garment with intelligence capability," US Patent 6145551, 1998.
21. S. Jayaraman, K. Mackenzie, and S. Park, "The wearable motherboard: a framework for personalized mobile information processing (PMIP)," Proc. of the Design Automation Conference, 2002.

22. G. Burghart, R. Eisler, S. Jayaraman, E. J. Lind, T. McKee, R. Rajamanickam, and S. Park, "A sensate liner for personnel monitoring applications," Proc. of the First International Symposium on Wearable Computers, 1997.
23. J. E. McIntyre and P. N. Daniels, Textile terms and definitions, tenth ed., The Textile Institute, 1995.
24. M. S. Lebby, K. E. Jachimowicz, and D. H. Hartman, "Integrated communicative watch," US Patent 6158884, 1998.
25. D. E. Piper, "Woven low impedance electrical transmission cable and method," US Patent 4463323, 1982.
26. P. E. Garrou and I. Turlik, Multichip Module Technology Handbook, McGraw-Hill, 1998.
27. M. Yoshida, M. Yoshikawa, Y. Yoshimoto, H. Wada, T. Suzuki, and S. Nakajima, "Planar conductive piece with electrical anisotropy," US Patent 4929803, 1989.
28. A. R. DeAngelis, A. D. Child, and D. E. Green, "Patterned conductive textiles," US Patent 5624736, 1995.
29. H. H. Kuhn and W. C. Kimbrell, "Electrically conductive textile materials and method for making same," US Patent 4803096, 1987.
30. E. H. Pittman and H. H. Kuhn, "Electrically conductive textile fabric having conductivity gradient," US Patent 5102727, 1991.
31. R. V. Gregory, W. C. Kimbrell, and M. E. Cuddihee, "Electrically conductive polymer material having conductivity gradient," US Patent 5162135, 1990.
32. L. W. Adams, M. W. Gilpatrick, and R. V. Gregory, "Fabric having non-uniform electrical conductivity," US Patent 5316830, 1992.
33. K. Onai, "Flexible electrically conductive sheet," US Patent 4889963, 1988.
34. W. W. Triplette, "Fencing jackets made from electrically conductive threads," US Patent 5802607, 1995.
35. E. R. Post, M. Orth, P. R. Russo, and N. Gershenfeld, "E-broidery: Design and fabrication of textile-based computing," IBM Systems Journal, 39(3 & 4), 840-860, 2000.
36. E. R. Post and M. Orth, "Smart Fabric, or Washable Computing," Proc. First International Symposium on Wearable Computers, Cambridge, MA, IEEE Computer Society, 167-168, 1997.

37. M. Orth and E. R. Post, "Smart fabric, or "wearable clothing," Proc. of the First International Symposium on Wearable Computers, 13-14, Oct 1997.
38. J. Azoulay, "Anisotropy in Electric Properties of Fabrics containing New Conductive Fibres," IEEE Transactions on Electrical Insulation, 23(3), 383-386, 1998.
39. M. M. Gorlick, "Electric Suspenders: A Fabric Power Bus and Data Network for Wearable Digital Devices" Proc. of the 3rd International Symposium on Wearable Computers, 114-121, 1999.
40. S. Jung, C. Lauterbach, and W. Weber, "Integrated Microelectronics for Smart Textiles," Proc. of Workshop on Modeling, Analysis and Middleware Support for Electronic Textiles (MAMSET), In conjunction with ASPLOS-X (Tenth International Conference on Architectural Support for Programming Languages and Operating Systems), San Jose, October 6, 2002.
41. B. Gnade, T. Akinwande, G. Parsons, S. Wagner, and R. Shashidhar, "Active devices on fiber: the building blocks for electronic textiles," Proc. International Interactive Textiles for the Warrior Conference, Cambridge, MA, 2002.
42. E. Bonderover, S. Wagner, and Z. Suo, "Amorphous Silicon Thin Film Transistors on Kapton Fibers," Proc. of the Materials Research Society Conference Symposium D, Boston, 2002.
43. Y. Inoue, Y. Fujisaki, Y. Iino, H. Kikuchi, S. Tokito, and F. Sato, "Low-Voltage Organic Thin Film Transistors on Flexible Plastic Substrates with Anodized Ta₂O₅ Gate Insulators," Proceedings of the Materials Research Society Conference Symposium D, Boston, 2002.
44. S. Park, J. Han, D. Moon, W. Kim, and Y. Kim, "High Performance Polymer Thin Film Transistors Array Printed on a Flexible Polycarbonate Substrate," Proceedings of the Materials Research Society Conference Symposium D, Boston, 2002.
45. M. Yoshida, S. Uemura, S. Hoshino, T. Kodzasa, S. Haraichi, and T. Kamata, "High Performance Organic Field Effect Transistor With a Novel Top-and-Bottom Contact (TBC) Structure," Proceedings of the Materials Research Society Conference Symposium D, Boston, 2002.
46. A. Bonfiglio, F. Mameli, O. Sanna, and L. Lutsen, "An Organic FET Structure for Unconventional Substrates," Proceedings of the Materials Research Society Conference Symposium D, Boston, 2002.
47. P. J. Massey, "Mobile phone fabric antennas integrated within clothing," Antennas and Propagation, Eleventh International Conference on (IEE Conf. Publ. No. 480), Volume 1, 2001, 344 -347, 2001.

48. P. J. Massey, "GSM fabric antenna for mobile phones integrated within clothing," Antennas and Propagation Society, 2001 IEEE International Sym, Volume 3, 452 - 455, 2001.
49. P. J. Massey, "Fabric antennas for mobile telephony integrated within clothing," London Communications Symposium, London, 2000.
50. J. Slade, J. Teverovsky, B. Farrell, J. Bowman, M. Agpaoa-Kraus, P. Wilson, J. Pederson, J. Merenda, W. Horowitz, E. Tierney, Carole Winterhalter, "Textile Based Antennas," Proceedings of the Materials Research Society Conference Symposium D, Boston, 2002.
51. P. J. Massey and P. Wilson, "Fabric Antennas Integrated Within Clothing," Proc. of the International Interactive Textiles for the Warrior Conference, Cambridge, MA, July, 2002.
52. C. A. Balanis, "Antenna Theory – Analysis and Design," John Wiley & Sons, Inc., New York, 1996.
53. D. H. Werner, "Exact integration procedure for vector potentials of thin circular loop antennas," IEEE Transactions on Antennas and Propagation, 44(2), 1996.
54. J. Slade, M. Agpaoa-Kraus, J. Bowman, A. Riecker, T. Tiano, C. Carey, and P. Wilson, "Washing of Electrotiles," Proceedings of the Materials Research Society Conference Symposium D, Boston, 2002.
55. M. Inaba, Y. Hoshino, K. Nagasaka, T. Ninomiya, S. Kagami, and H. Inoue, "A Full-Body Tactile Sensor Suit Using Electrically Conductive Fabric and Strings," Proc. of the IEEE/RSJ International Conference on Intelligent Robots and Systems, 450-457, 1996.
56. D. Jones, "Interactive fabrics using SOFTswitch technology," SOFTswitches ltd., Proc. of the International Interactive Textiles for the Warrior Conference organized by the Soldier and Biological Chemical Command, NASA, & DARPA, Cambridge, MA, 2002.
57. D. L. Sandbach, "Detector constructed from fabric," U.S. Patent 6452479, 2002.
58. D. L. Sandbach, "Detector constructed from fabric having planes with differing conductance," U.S. Patent 6437258, 2002.
59. S. C. Gilbert and J. E. Boyce, "Conductive fabric sensor for vehicle seats," US Patent 5878620, 1997.

60. H. H. B. Karplus, "Digital pressure transducer for use at high temperatures," US Patent 4255973, 1979.
61. M. El-Sherif, M. Li1, J. Yuan, D. El-Sherif, A. Rahman, C. Lee, and J. Fairney, "Smart textiles with embedded opto-electronic networks and sensors," Proc. of the International Interactive Textiles for the Warrior Conference organized by the Soldier and Biological Chemical Command, NASA, & DARPA, Cambridge, MA, July 9-11, 2002.
62. J. Miguel and L. Higuera, Handbook of Optical Fiber sensing technology, John Wiley & Sons, Inc., New York, 2002.
63. O. S. Wolfbeis, "Fiber-Optic Chemical Sensors and Biosensors," Analytical Chemistry, 72, 81-89, 2000.
64. I. Klimant, M. Kühl, R. N. Glud, and G. Holst, "Optical measurement of oxygen and temperature in microscale: Strategies and biological applications," Sensors and Actuators B, 38, 29-37, 1997.
65. R. Koncki and O. S. Wolfbeis, "Composite Films of Prussian Blue and N-Substituted Polypyrroles: Fabrication and Application to Optical Determination of pH," Analytical Chemistry, 70, 2544-2550, 1998.
66. M. B. Tabacco, M. Uttamlal, M. McAllister, and D. R. Walt, "An Autonomous Sensor and Telemetry System for Low-Level pCO₂ Measurements in Seawater," Analytical Chemistry, 71, 154-161, 1999.
67. C. Malins, M. Landl, P. Simon, and B. MacCraith, "Fibre optic ammonia sensing employing novel near infrared dyes," Sensors and Actuators B, 51, 359-367, 1998.
68. A. Lobnik and O. S. Wolfbeis, "Sol-gel based optical sensor for dissolved ammonia," Sensors and Actuators B, 51, 203-207, 1998.
69. T. M. Butler, B. D. MacCraith, and C. McDonagh, "TE Leaching in sol-gel-derived silica films for optical pH sensing," Journal of Non-Crystalline Solids, 224 (3), 249-258, 1998.
70. C. Malins, H. G. Glever, T. E. Keyes, J. G. Vos, W. J. Dressick and B. D. MacCraith, "Sol-gel immobilised ruthenium(II) polypyridyl complexes as chemical transducers for optical pH sensing," Sensors and Actuators B, 67, 89-95, 2000.
71. A. Abdelghani, J. M. Chovelon, N. Jaffrezic-Renault, M. Lacroix, H. Gagnaire, C. Veillas, B. Berkova, M. Chomat and V. Matejec, "Optical fibre sensor coated with porous silica layers for gas and chemical vapour detection," Sensors and Actuators B, 44, 495-498, 1997.

72. B. Mizaikoff, M. Kraft, and M. Jakusch, "Infrared fiberoptic sensors – A versatile tool for water monitoring," *Sea Technology*, 40, 25-34, 1999.
73. B. Mizaikoff, "Mid-infrared fiberoptic sensors – potentials and perspectives," *SPIE*, 3849, 7-18, 1999.
74. B. Mizaikoff, "Mid-Infrared Fiberoptic Evanescent Wave Sensors - A Novel Approach for Subsea Monitoring," *Measurement Science and Technology*, 10, 1185-1194, 1999.
75. B. D. Gupta and S. Sharma, "A long-range fiber optic pH sensor prepared by dye doped sol-gel immobilization technique," *Optics Communication*, 154, 282-284, 1998.
76. G. E. Collins, and L. J. Buckley, "Conductive polymer-coated fabrics for chemical sensing," *Synthetic Metals*, 78, 93-101, 1996.
77. S. M. Barnard and D. R. Walt, "Fiber-optic Organic Vapor Sensor," *Environment Science and Technology*, 25, 1301-1304, 1991.
78. J. White and J. S. Kauer, T. A. Dickinson and D. R. Walt, "Rapid Analyte Recognition in a Device Based on Optical Sensors and the Olfactory System," *Analytical Chemistry*, 68, 2191-2202, 1996.
79. K. L. Michael, L. C. Taylor, S. L. Schultz, and D. R. Walt, "Randomly Ordered Addressable High-Density Optical Sensor Arrays," *Analytical Chemistry*, 70, 1242-1248, 1998.
80. P. Pantano and D. R. Walt, "Ordered Nanowell Arrays," *Chemistry of Materials*, 8, 2832-2835, 1996.
81. J. V. Hatfield, P. Neaves, P. J. Hicks, K. Persaud and P. Travers, "Towards an integrated electronic nose using conducting polymer sensors," *Sensors and Actuators B*, 18, 221-228, 1995.
82. J. L. Gehrich, D. L. Lubbers, N. Opitz, D. R. Hansmann, W. M. Miller, J. K. Tusa, and M. Yafuso, "Optical fluorescence and its application to intravascular blood gas monitoring system," *IEEE Transactions on Biomedical Engineering*, 33, 117-132, 1986.
83. E. J. Netto, J. I. Peterson, M. McShane, and V. Hampshire, "A fiber-optic broad-range pH sensor system for gastric measurements," *Sensors and Actuators B*, 29, 157-163, 1995.

84. F. Baldini, P. Bechi, S. Bracci, F. Cosi, and F. Pucciani, "In vivo optical fiber pH sensor for gastro-oesophageal measurements," *Sensors and Actuators B*, 29, 164-168, 1995.
85. C. Scoggin, L. Nett, and T. L. Petty, "Clinical evaluation of a new ear oximeter," *Heart and Lung*, 6, 121-126, 1977.
86. S. Muto, H. Sato, and T. Hosaka, "Optical humidity sensor using fluorescent plastic fiber and its application to breathing-condition monitoring," *Japanese Journal of Applied Physics*, 33, 6060-6064, 1994.
87. R. A. Wolthuis, G. L. Mitchell, E. Saaski, J. C. Hartl, M. A. Afromowitz, "Development of medical pressure and temperature sensors employing optical spectrum modulation," *IEEE Transactions on Biomedical Engineering*, 38(10), 974 - 981, 1991.
88. T. Takeo and H. Hattori, "Quantitative valuation of skin surface lipids by a fiber-optic refractometer," *Sensors and Actuators B*, 29, 318-323, 1995.
89. F. Koenz, J. Ricka, M. Frenz, and F. Fankhauser, "Dynamic light scattering in the vitreous: performance of the single mode fiber technique," *Optical Engineering*, 34 (08), 2390-2395, 1995.
90. S. A. Grant and R. S. Glass, "Sol-gel-based biosensor for use in stroke treatment," *IEEE Transactions on Biomedical Engineering*, 46(10), 1207-1211, 1999.
91. J. R. Davis, D. G. Davis, R. G. Buice, and R. A. Lodder, "Biological and medical applications of near-infrared spectrometry," *Applied Spectroscopy*, 50, 18A-34A, 1996.
92. Y. Rao, D. J. Webb, D. A. Jackson, L. Zhang, and I. Bennion, "In-fiber Bragg-grating temperature sensor system for medical applications," *IEEE Journal of Lightwave Technology*, 15(5), 779-785, 1997.
93. D. J. Webb, M. Hathaway, D. A. Jackson, S. Jones, L. Zhang, and I. Bennion, "First in vivo trials of a fiber Bragg grating temperature profiling system," *Journal of Biomedical Optics*, 5(1), 45-50, 2000.
94. M. S. Leby, K. E. Jachimowicz, and J. Ramdani, "Textile fabric with integrated sensing device and clothing fabricated thereof," US Patent 6080690, 1998.
95. S. Jayaraman, S. Park, R. Rajamanickam, and C. Gopalsamy, "Fabric or garment with integrated flexible information infrastructure," US Patent 6381482, 2002.
96. C. Randell and H. L. Muller, "The Well Mannered Wearable Computer," *Personal and Ubiquitous Computing*, 6(1), 31-36, 2002.

97. J. Farrington, A. J. Moore, N. Tilbury, J. Church, and P. D. Biemond, "Wearable Sensor Badge & Sensor Jacket for Context Awareness," Proc. 3rd International Symposium on Wearable Computers, San Francisco, 107-113, 1999.
98. A. Schmidt, "Implicit Human Computer Interaction Through Context," Personal Technologies, 4(2-3), 191-199, 2000.
99. A. Schmidt, Hans-W. Gellersen, and M. Beigl, "A Wearable Context-Awareness Component - Finally a Good Reason to Wear a Tie," Proc. of the third International Symposium on Wearable Computers. San Fransico, 1999.
100. A. Schmidt, H. W. Gellersen, and C. Merz., "Enabling Implicit Human Computer Interaction - A Wearable RFID-Tag Reader," Proc. of the International Symposium on Wearable Computers, Atlanta, 2000.
101. C. Randell, "Computerized Clothing will benefit Textile Manufacturers," Technical Textiles International, 10(7), 3-27, 2001.
102. H. W. Gellersen, M. Beigl, and A. Schmidt, "Sensor-based Context-Awareness for Situated Computing," Proc. of the Workshop on Software Engineering for Wearable and Pervasive Computing SEWPC00, 22nd Int. Conference on Software Engineering ICSE 2000, Limerick, Ireland, 2000.
103. C. Randell and H. L. Muller, "Context Awareness by Analysing Accelerometer Data," Proc. of the Fourth International Symposium on Wearable Computers, IEEE Computer Society, 175-176, 2000.
104. C. Randell and H. L. Muller, "The eSleeve: A Novel Wearable Computer Configuration for the Discovery of Situated Information," Proc. of the Distributed Computing Systems Workshops, 793-796, IEEE Computer Society, 2002.
105. A. Schmidt, H. W. Gellersen and M. Beigl, "A Wearable Context-Awareness Component - Finally a Good Reason to Wear a Tie," Proc. of the third International Symposium on Wearable Computers, San Fransico, 1999.
106. A. Schmidt, M. Beigl and H. W. Gellersen, "There is more to Context than Location," Computers & Graphics Journal, 23 (6), 893-902, 1999.
107. C. Randell and H. L. Muller, "The Shopping Jacket: Wearable Computing for the Consumer," In Personal Technologies, ed. Peter Thomas, 4(4), 241-244, Springer, 2000.
108. E. Udd, Fiber Optic Smart Structures, John Wiley & Sons, Inc., New York, 1995.
109. T. S. Yu and S. Yin, Fiber Optic Sensors, Marcel Dekker, Inc., 2002.

110. G. Zhou and L. M. Sim, "Damage detection and assessment in fibre-reinforced composite structures with embedded fibre optic sensors - review," *Smart Material and Structures*, 11, 925-939, 2002.
111. G. A. Ball, G. Meltz and W. W. Morey, "Polarimetric Heterodyning Bragg-Grating Fiber Laser," *Optics Letters*, 18, 1976-1978, 1993.
112. R. M. Measures, "Smart composite structures with embedded sensors," *Composite Engineering*, 2, 597-618, 1992.
113. R. Kashyap, *Fiber Bragg Gratings*, Academic Press, 1999.
114. A. Othonos and K. Kalli, *Fiber Bragg Gratings*, Artech Book House, 1999.
115. X. Tao, L. Tang, W. C. Du, and C. L. Choy, "Internal strain measurement by fiber Bragg grating sensors in textile composites," *Composites Science and Technology*, 60, 657-669, 2000.
116. L. Q. Tang, X. M. Tao, W. C. Du and C. L. Choy, "Reliability of fiber Bragg grating sensors embedded in textile composites," *Composite Interfaces*, 5, 421-35, 1998.
117. W. C. Du, X. M. Tao, H. Y. Tam and C. L. Choy, "Fundamentals and applications of optical fiber Bragg grating sensors to textile composites," *Journal of Composite Structures*, 42, 217-230, 1998.
118. L. Q. Tang, X. M. Tao and C. L. Choy, "Effectiveness and optimization of fiber Bragg grating sensor as embedded strain sensor," *Smart Material Structures*, 8, 154-160, 1999.
119. W. C. Du, X. M. Tao, and H. Y. Tam, "Temperature independent strain measurement with a fiber grating cavity sensor," *IEEE Photonics Technology letters*, 11(5), 596-598, 1999.
120. B. Culshaw and J. Dakin, *Optical Fiber Sensors: Components and Subsystems*, Vol. 3, Artech House Books, Boston, 1996.
121. B. Culshaw and J. Dakin, *Optical Fiber Sensors: Analysis, and Future Trends*, Vol. 4, Artech House Books, Boston, 1996.
122. A. D. Kersey, M. A. Davis, H. J. Patrick, M. LeBlanc, K. P. Koo, C. G. Askins, M. A. Putnam, and E. J. Friebele, "Fiber grating sensors," *IEEE Journal of Lightwave Tech.* 15, 1442-1462, 1997.
123. Y. J. Rao, "In-fiber Bragg grating sensors," *Measurement Science and Technology*, 8, 355-375, 1997.

124. D. C. Lee, J. J. Lee, I. B. Kwon, and D. C. Seo, "Monitoring of fatigue damage of composite structures by using embedded intensity-based optical fiber sensors," *Smart Material and Structures*, 10, 285-292, 2001.
125. Y. Okabe, N. Tanaka, and N. Takeda, "Effect of fiber coating on crack detection in carbon fiber reinforced plastic composites using fiber Bragg grating sensors," *Smart Material and Structures*, 11, 892-898, 2002.
126. A. D. Kersey, M. A. Davis, H. J. Patrick, M. LeBlanc, K. P. Koo, C. G. Askins, M. A. Putnam, E. J. Friebele, "Fiber grating sensors," *Journal of Lightwave Technology*, 15 (8), 1442-1463, 1997.
127. A. D. Kersey, T. A. Berkoff, and W. W. Morey, "Fiber optic Bragg grating strain sensor with drift compensated high resolution interferometric wavelength detection," *Optics Letters*, 18, 72-74, 1993.
128. S. E. Kanellopoulos, V. A. Handerek and A. J. Rogers, "Simultaneous strain and temperature sensing with photogenerated in-fibre gratings," *Optics Letters*, 20, 333-335, 1995.
129. J. Dunphy, G. Meltz, F. Lamm, and W. Morey, "Fiber-optic strain sensor multi-function, distributed optical fiber sensor for composite cure and response monitoring," *SPIE*, 1370, 116-118, 1991.
130. J. R. Dunphy, G. Mehta, W. W. Morey, "Optical fiber Bragg grating sensors: a candidate for smart structure application," in *Fiber optic smart structures*, ed. E. Udd, John Wiley and Sons Inc, 1995.
131. D. E. Bullock, J. R. Dunphy, and G. H. Hufstetler, "Embedded Bragg grating fiber optic sensor for composite flexbeams," *Proc. of the SPIE*, 1798, 253-261, 1993.
132. B. X. Chen, M. H. Maher, and E. G. Nawy, "Fiber-optic Bragg grating sensor for non-destructive evaluation of composite beams," *Journal of Structural Engineering*, 12(12), 3456-3470, 1994.
133. E. Udd, D. V. Nelson, C. M. Lawrence, and B. A. Ferguson, "Three-axis strain and temperature fiber optic grating sensor," *Proc. of the SPIE*, 2718, 104-109, 1996.
134. M. El-Sherif, K. Fidanboyly, D. El-Sherif, R. Gafsi, J. Yuan, K. Richards, and C. Lee, "A Novel Fiber Optic System for Measuring the Dynamic Structural Behavior of Parachutes," *J. of Intelligent Material Systems and Structures*, Vol. II, No. 5, 351-359, May 2000.

135. W. C. Du, X. M. Tao, and H. Y. Tam, "Fiber Bragg grating cavity sensor for simultaneous measurement of temperature and strain," *IEEE Photonics Technology Letter*, 11, 105-107, 1999.
136. R. M. Measures, S. Huang, M. LeBlanc and M. M. Ohn, "Distributed fiber optic strain sensing based on spectral integration of Bragg grating reflection," *Proc. of the SPIE International Symposium on Optical Science, Engineering and Instrumentation*, Denver, 2294, 1996.
137. S. Huang, M. M. Ohn, R. M. Measures, "Phase-based Bragg intra-grating distributed strain sensor," *Applied Optics*, 35(7), 1135-1142, 1996.
138. A. D. Jackson, A. B. L. Ribeiro, L. Reekie, and J. L. Archambault, "Simple multiplexing scheme for a fiber-optic grating sensor network," 18(14), 1192-1194, 1993.
139. M. A. Davis and A. D. Kersey, "All-fiber Bragg grating strain sensor demodulation technique using a wavelength division coupler," *Electronics Letters*, 30, 75-77, 1994.
140. Y. J. Rao, A. B. L. Ribeiro, D. A. Jackson, L. Zhang and I. Bennion, "Combined spatial- and time-division-multiplexing scheme for fiber grating sensors with drift-compensated phase-sensitive detection," *Optics Letters*, 20, 2149-2151, 1995.
141. Y. J. Rao, D. J. Webb, D. A. Jackson, L. Zhang and I. Bennion, "In-fibre Bragg grating temperature sensor system for medical applications," *Journal of Lightwave Technology*, 15, 1997.
142. Y. J. Rao and D. A. Jackson, "Recent progress in multiplexing techniques for in-fibre Bragg grating sensors," *Proc. of the SPIE* 2895, 1996.
143. A. D. Kersey and A. Dandridge, "Multiplexed Mach-Zehnder Ladder Array with ten sensors elements," *Electron Letters*, 25(19), 1298-1299, 1989.
144. A. D. Kersey, A. Dandridge and A. B. Tveten, "Time-division multiplexing of interferometric fiber sensors using passive phase-generated carrier interrogation," *Optics Letters*, 12, 775-777, 1987.
145. A. Dandridge, "Multiplexing of interferometric sensors using phase generated carrier techniques," *Journal of Lightwave Technology*, 5, 947, 1987.
146. A. D. Kersey, "Demonstration of a Hybrid Time/Wavelength division Multiplexed Interferometric Fiber Sensor Array," *Electron Letters*, 27(7), 554-555, 1991.
147. A. B. L. Ribeiro, Y. J. Rao, L. Zhang, I. Bennion, and D. A. Jackson, "Time and spatial multiplexing tree topology for fiber optic Bragg grating sensors with interferometric wavelength shift detection," *Applied Optics*, 35, 2267, 1996.

148. G. P. Brady, A.B. Lobo Ribeiro, D. J. Webb, L. Reekie, J. L. Archambault, and D. A. Jackson, "Demultiplexing of Fibre Bragg Grating Temperature and Strain Sensors," *Optics Communications*, 111, 51, 1994.
149. A. S. Hutchison, T. W. Lewis, S. E. Moulton, G. M. Spinks and G. G. Wallace, "Development of Polypyrrole Based Electromechanical Actuators," *Synthetic Metals*, 113 (1-2), 121-127, 2000.
150. M. R. Gandhi, P. Murray, G. M. Spinks and G. G. Wallace, "Mechanism of electromechanical actuation in polypyrrole," *Synthetic Metals*, 73, 247-256, 1995.
151. A. Della Santa, D. De Rossi, and A. Mazzoldi, "Performance and work capacity of a polypyrrole conducting polymer linear actuator," *Synthetic Metals*, 90, 93-100, 1997.
152. K. T. Tzou and R.V. Gregory, "Improved Solution Stability and Spinnability of Concentrated Polyaniline Solutions Using N,N'-Dimethyl Propylene Urea as the Spin Bath Solvent," *Synthetic Metals*, 69, 109-112, 1995.
153. B. Mattes, "Electro-mechanical actuators based upon conducting polymer fibre and ionic liquid electrolytes," *Proc. International Interactive Textiles for the Warrior Conference*, Cambridge, MA, July 9-11, 2002.
154. D. De Rossi, F. Lorussi, A. Mazzoldi, W. Rocchia, and E. Pasquale Scilingo, "A strain amplified electroactive polymer actuator for haptic interfaces," *Proc. SPIE, Smart Structures and Materials 2001: Electroactive Polymer Actuators and Devices*, 4329, 43-53, 2001.
155. D. De Rossi, "Active Dressware-Wearable Kinesthetic System," *Proc. International Interactive Textiles for the Warrior Conference*, Cambridge, MA, July 9-11, 2002.
156. F. Carpi and D. De Rossi, "Dielectric elastomer cylindrical actuators: electrochemical modeling and experimental evaluation," *Materials Science and Engineering C*, 24, 555-562, 2004.
157. D. De Rossi, A. Della Santa, and A. Mazzoldi, "Dressware: wearable hardware," *Materials Science and Engineering C*, 7, 31-35, 1999.
158. A. Mazzoldi, C. Degl'Innocenti, M. Michelucci, and D. De Rossi, "Actuative properties of polyaniline fibers under electrochemical stimulation," *Materials Science and Engineering C*, 6, 65-72, 1998.
159. D. De Rossi, and A. Mazzoldi, "Linear fully dry polymer actuators," *Proc. SPIE, Smart Structures and Materials 1999: Electroactive Polymer Actuators and Devices*, Vol. 3669, 35-44, 1999.

160. H. B. Schreyer, M. Shahinpoor, K. J. Kim, "Electrical activation of PAN-Pt artificial muscles," Proc. SPIE, Smart Structures and Materials 1999: Electroactive Polymer Actuators and Devices, 3669, 192-198, 1999.
161. P. C. Innis, J. Mazurkiewicz, V. Aboutanos, J. Ding, G. M. Spinks, D. Zhou, J. Wu, G. G. Wallace, D. MacFalane, D. MacFallane, M. Forsyth, and S. Forsyth, "Inherently conducting polymers for wearable energy conversion and storage systems," Proc. International Interactive Textiles for the Warrior Conference, Cambridge, July, 2002.
162. T. Livolsi, "Technology Update on Lithium Ion Polymer," Proc. of the Wireless Symposium – Portable by Design, San Jose, Spring 2000.
163. J. McDermott and P. C. Brantner, "Thin-Film Solid-State Lithium Battery for Body Worn Electronics," Proc. of the Materials Research Society Symposium, Boston, Fall 2002.
164. L. Samuelson, F. Bruno, J. Kumar, R. A. Gaudiana, and P. Wormser, "Conformal solar cells for the soldier," Proc. International Interactive Textiles for the Warrior Conference, Cambridge, July, 2002.
165. Jin-An He, R. Mosurkal, J. Kumar, Lian Li, K. G. Chittibabu, L. A. Samuelson, "The Effect of Semiconductor and Dye Interfacial Properties in Dye-sensitized Solar Cells," Proc. of the Materials Research Society Symposium, Boston, Fall 2001.
166. K. G. Chittibabu, S. Hadjikyriacou, and L. Li, "Ionic Liquid Based Gel Electrolyte Compositions for Dye Sensitized Solar Cells," Proc. of the Materials Research Society Symposium, Boston, Fall 2001.
167. B. O'Regan and M. Grätzel, "A low-cost, high-efficiency solar cell based on dye-sensitized colloidal TiO₂ films," Nature, 353, 737, 1991.
168. Y. Kishimoto, "Electric heating sheet," US Patent 5422462, 1994.
169. A. Gurevich, "Fabric heating element and method of Manufacture," US Patent 6057530, 1996.
170. J. Hunter and D. Costello, "Out of the Lab - The Integration of Electronic Performance Textiles into the Real World," Proc. of the International Interactive Textiles for the Warrior Conference, Cambridge, July, 2002.
171. J. A., Rolls, "Device and method for heating and deicing wind energy turbine blades," US Patent 6145787, 1998.
172. O. H. Hastings, "Electrically conductive laminate for temperature control of aircraft surface," US Patent 5344696, 1992.

CHAPTER 3.

THEORETICAL MODEL TO DETERMINE EQUILIBRIUM STRUCTURE AND BENDING RIGIDITY OF A WOVEN FABRIC

Abstract

In this chapter, we describe key elements of a model employed by us to determine the fabric bending rigidity using the energy method. In order to employ the energy method to determine fabric bending rigidity, it is important to accurately predict the structure of yarns woven in a fabric. As the yarns woven into a fabric have a finite bending rigidity, yarns can be treated as elastic slender rods with a set of transverse forces acting on them at the crossover points, such that the forces are in opposite directions at the alternating crossover points. An approach to determine the equilibrium fabric structure, based on the fabric structure model developed by Ghosh et al. [1, 2], is described in this chapter. After describing the determination of equilibrium woven fabric structure, this chapter explains the procedure to determine fabric bending rigidity based on an energy method that incorporates fabric structure parameters that are previously determined for every step of fabric bending. Detailed description of the model employed by us for determining the equilibrium fabric structure and the fabric bending rigidity lays the foundation for determining the bending rigidity of a fabric circuit, having an arrangement of woven conductive and non-conductive threads along with welded or soldered crossover points. In subsequent chapters, we will describe the development of boundary conditions and equations that are specific to fabric circuits.

3.1 Introduction

Bending behavior of woven fabrics depends on bending behavior of its constituent yarns and also on inter-yarn friction primarily at the crossover points. The extent of frictional forces at the crossover points in turn is determined by the local normal pressure between the yarns. The influence of the crossover point on the bending rigidity of fabrics has been studied by Abbot et al. [3, 4] and Livesey et al. [5]. Abbot et al. [4] determined fabric bending rigidity based on the change of strain energy as a fabric is bent from a planar configuration. The strain energy of a planar fabric was determined by considering the contact pressure at the crossover points described by Pierce [6]; whereas that in a bent fabric was considered by determining the sum of the energy stored in the contact regions, the free yarn regions, and due to change in crimp of the cross yarns due to bending.. In another study, Shanahan et al. [7] proposed determination of fabric bending rigidity based on the calculation of change in strain energy of a bent fabric from that in a planar fabric but did not provide a comprehensive model or provide calculations of fabric rigidity. Ghosh et al. [1, 2, 8] provided a comprehensive theoretical model to determine the bending rigidity of a fabric in relation to that of a yarn. In the present work, the model developed by Ghosh et al. [1, 2] has been adapted, to calculate bending rigidity of a woven fabric circuit having an arrangement of conductive and non-conductive threads along with welded crossover points. In this chapter, key elements of the model employed to determine the fabric bending rigidity has been described. In order to employ the energy method to calculate fabric bending rigidity, it is important to first determine the equilibrium fabric structure.

Pierce [6], Leaf [9], and Abbot et al. [4] developed models to describe the geometry of a yarn in a woven fabric by assuming the yarns to be flexible and inextensible. In the “flexible-thread” model developed by Pierce [6], the yarns are assumed to be perfect circular cylinders and are assumed to follow a straight path in regions other than the region of the crossover point, where they are assumed to have a constant curvature. As the yarns woven into a fabric have a finite bending rigidity, yarns can be treated as elastic slender rods, with a set of transverse forces acting on them at the crossover points, such that the forces are in opposite directions at the alternating crossover points. Although Pierce [6] had first proposed the ‘elastica’ concept describing yarns in a woven fabric as

elastic rods with the local bending moment being proportional to the yarn curvature in a woven fabric, it was Konopasek et al. [10] and later Ghosh et al. [1, 2, 8] that developed comprehensive yet simple model to determine the equilibrium structure of a fabric. The model described by Ghosh et al. [1, 2, 8] was based on the determination of equilibrium warp and weft yarn structures as two planar bending curves, in two mutually orthogonal planes. In this paper, we extend the model described by Ghosh et al. [1, 2, 8] in order to determine the equilibrium yarn configurations and subsequently the bending rigidity of a fabric based circuit containing rigid conductive threads and flexible insulating threads interwoven into a fabric.

3.2 List of symbols

This section provides a list of symbols employed in the models that describe bending behavior of woven fabrics. A consistent system of nomenclature has been employed in this chapter and chapters 4 and 5, and is given below. In the list given below, the terms in the parenthesis indicate the non-dimensional parameters that are defined in section 3.3. Moreover, the subscripts, $i = 1$ and 2 are used to indicate warp and filling yarns, respectively.

d_i	Yarn Diameter
d	Sum of yarn diameters
f_{t_i} (F_{t_i})	Tensile force in yarn
f_{n_i} (F_{n_i})	Shear force in yarn
h_i (H_i)	Crimp height of yarn in a fabric
l_i (L_i)	Modular length of yarn in a fabric
m_i (M_i)	Bending moment of yarn
m_f (M_f)	Bending moment of fabric
r (R)	Radius of fabric curvature
s (S)	Length along yarn axial curves
t_x	Direction cosine of tangent with x axis
t_y	Direction cosine of tangent with y axis
uc (U_c)	Strain energy in the contact region

$u_f (U_f)$	Strain energy in the free region
$u_T (U_T)$	Total Strain energy in the fabric
$v (V)$	Radius of fabric curvature
$w^{(i)} (W^{(i)})$	Work done to deform the fabric unit cell through an angle
$x_i (X_i)$	Yarn axial curve coordinates
$y_i (Y_i)$	Yarn axial curve coordinates
A_y	Yarn Bending Rigidity
A_i	Yarn Bending Rigidity
A_F	Fabric Bending Rigidity
A_r	Ratio of A_1 and A_2
D	Sum of yarn diameters
L_r	Ratio of l_1 and l_2
β_{1i}	Contact Angles
β_{2i}	Contact Angles
κ	Local curvature of yarn in a fabric
$\kappa (\kappa_F)$	Fabric curvature
λ	Ratio of d and l_1
ψ	Fabric Bend Angle

3.3 Determination of equilibrium fabric structure

3.3.1 Assumptions made in the model

The following assumptions were made in our model to facilitate the determination of the equilibrium structure of the yarns in a woven fabric:

- (1) Yarns were assumed to be flexible and inextensible.
- (2) Yarns are assumed to be perfect cylinders.
- (3) Linear yarn bending was assumed, i. e. local bending moment of the yarn is assumed to be proportional to the yarn curvature in a woven fabric.
- (4) Yarns are assumed to have a constant curvature in the contact regions.

- (5) Yarns are assumed to be elastic slender rods, with a set of transverse forces acting on them at the crossover points, such that the forces are in opposite directions at the alternating crossover points.
- (6) Warp and weft yarn structures are considered as two planar bending curves, in two mutually orthogonal planes.
- (7) In order to determine the bending rigidity of fabric circuits, a woven conductive fabric is assumed to be consisting of series and parallel combination of various types of fabric unit cells (containing different kinds of cross-over points) as discussed later in section 4.2.2.
- (8) In the case of fabrics with welded crossover points, the value of contact angle β_2 (described in section 3.3.3) is assumed to be constant when the equilibrium fabric structure is obtained for a bent fabric, i. e. for $\psi > 0$, for all steps of fabric bending. Moreover, it is assumed in the case of welded crossover points that the normal force F_n is concentrated at the middle of the welded region.

Assumptions 1 and 2 are in accordance with earlier work by Pierce [6], Konopasek et al. [10] and Ghosh et al. [1, 2, 8]. Although Pierce [6] had first proposed the ‘elastica’ concept describing yarns in a woven fabric as elastic rods, Konopasek et al. [10] and later Ghosh et al. [1, 2, 8] employed this assumption to determine the equilibrium structure of a fabric. In our model, assumptions 1 and 2 are made to determine equilibrium warp and weft yarn structures, as two planar bending curves in two mutually orthogonal planes. We also employed assumption 3, first applied by Ghosh et al. [1, 2, 8], to determine the fabric bending behavior. The validity of this assumption was explained in detail by Ghosh et al. [1, 2, 8].

In chapter 4, the model described by Ghosh et al. [1, 2, 8] is extended to determine equilibrium yarn configurations in a woven fabric circuit; and subsequently assumption 7 is employed to determine the bending rigidity of a fabric based circuit, containing rigid conductive threads and flexible insulating threads interwoven into a fabric. This assumption is explained in detail in section 4.2.2. In chapter 5, assumption 8 is employed to evaluate the bending rigidity of a conductive fabric with welded crossover points. This process is described in detail in section 5.2.

3.3.2 Equations defining the equilibrium yarn shape in a fabric

Generalized governing equations of a bent elastica have been described by other researchers [1, 2, 8] nevertheless, for completeness, these will be derived here. A segment ds of a yarn under external forces f_t , and f_n and moment m , shown in Figure 1, is considered. Summing up the forces along the Y direction gives the relationship:

$$\begin{aligned} (f_n + df_n)(\cos(d\psi / 2)) - (f_n)(\cos(d\psi / 2)) \\ = (f_t + df_t)(\sin(d\psi / 2)) + (f_t)(\sin(d\psi / 2)) \end{aligned} \quad (1)$$

On simplifying the terms one obtains:

$$(df_n)(\cos(d\psi / 2)) = (df_t)(\sin(d\psi / 2)) + 2(f_t)(\sin(d\psi / 2)) \quad (2)$$

Considering the angle $d\psi$ is infinitesimally small, and dividing both sides by ds , equation (2) reduces to:

$$\frac{df_n}{ds} = f_t \frac{d\psi}{ds} = f_t \kappa \quad (3)$$

where κ is the curvature of the yarn. Similarly, sum of forces along X direction leads to:

$$\frac{df_t}{ds} = -f_n \frac{d\psi}{ds} = -f_n \kappa \quad (4)$$

Moreover, on summing moments about point J, one obtains:

$$\begin{aligned} (m + dm - m) &= f_n(ds) \\ \Rightarrow \frac{dm}{ds} &= f_n \end{aligned} \quad (5)$$

Assuming linear yarn bending behavior:

$$m = A_y \kappa \quad (6)$$

where, m is the bending moment of the yarn in this section, A_y is the bending rigidity of the individual yarn, and κ is the curvature of the yarn. Differentiating both sides of equation 6 with respect to 's':

$$\frac{dm}{ds} = A_y \frac{dk}{ds} = f_n \quad (7)$$

$$\Rightarrow \frac{dm}{ds} = f_n / A_y \quad (8)$$

where A_y is the bending rigidity of the individual yarn.

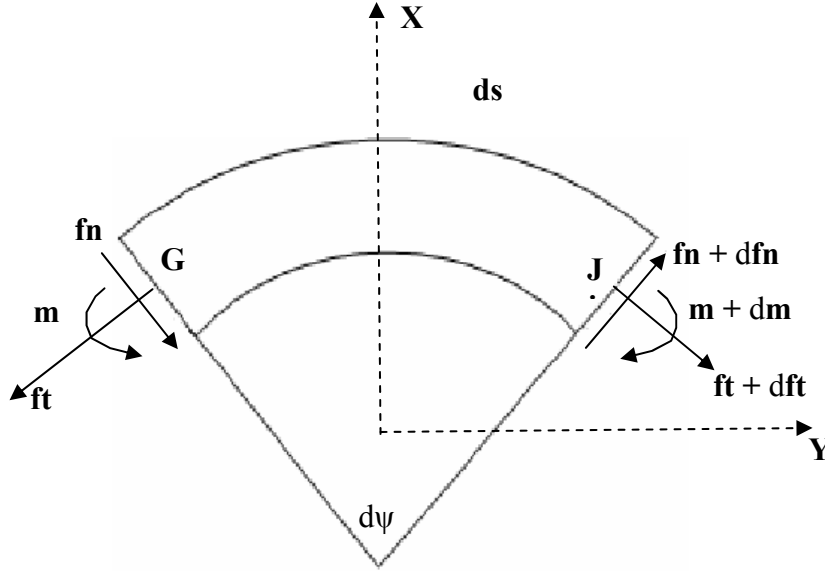


Figure 1. Free body diagram of a yarn section

Local unit tangent vectors at any point (x, y) along the length of the yarn can be given by the following relationships:

$$t_x = \frac{dx}{ds} \quad (9)$$

$$t_y = \frac{dy}{ds} \quad (10)$$

such that

$$t_x^2 + t_y^2 = 1 \quad (11)$$

Moreover, the variation of these unit tangent vectors with the axial distance could be related to the yarn curvatures by the following relations:

$$\frac{dt_x}{ds} = -\kappa t_y \text{ and} \quad (12)$$

$$\frac{dt_y}{ds} = \kappa t_x \quad (13)$$

These equations are employed to describe the parameters of both warp and weft yarns. Throughout this thesis subscripts, $i = 1$ and 2 are used to indicate warp and filling yarns, respectively. These equations were normalized to express the different terms

described in the equations in a dimensionless form. The relevant parameters in dimensionless form are:

$$\begin{aligned} Fn_1 &= \frac{fn_i}{A} l_1^2, Ft_1 = \frac{ft_i}{A} l_1^2, K_i = k_i l_1, X_i = \frac{x_i}{l_1}, \\ Y_i &= \frac{y_i}{l_1}, S_i = \frac{s_i}{l_1}, D_i = \frac{d_i}{l_1}, L_r = \frac{l_1}{l_2}, H_i = \frac{h_i}{l_1} \end{aligned} \quad (14)$$

where l_1 is the length of a warp yarn in one unit cell of a plain woven fabric as shown in Figure 2. Based on the above derivation, the following differential equations were obtained for the thread in the warp direction (labeled as thread I in Figure 2b and 3):

$$\frac{\partial}{\partial S} Fn_1(S) = K_1(S)Ft_1(S) \quad (15)$$

$$\frac{\partial}{\partial S} K_1(S) = Fn_1(S) \quad (16)$$

$$\frac{\partial}{\partial S} Ft_1(S) = -K_1(S)Fn_1(S) \quad (17)$$

$$\frac{\partial}{\partial S} ty_1(S) = K_1(S)tx_1(S) \quad (18)$$

$$\frac{\partial}{\partial S} tx_1(S) = -K_1(S)ty_1(S) \quad (19)$$

$$\frac{\partial}{\partial S} X_1(S) = tx_1(S) \quad (20)$$

$$\frac{\partial}{\partial S} Y_1(S) = ty_1(S) \quad (21)$$

$$ty_1^2(S) + tx_1^2(S) = 1 \quad (22)$$

Moreover, the following differential equations were for obtained for the threads in the weft direction (labeled a thread J Figure 2b and 3):

$$\frac{\partial}{\partial S} Fn_2(S) = K_2(S)Ft_2(S) \quad (23)$$

$$\frac{\partial}{\partial S} K_2(S) = Fn_2(S) \quad (24)$$

$$\frac{\partial}{\partial S} Ft_2(S) = -K_2(S)Fn_2(S) \quad (25)$$

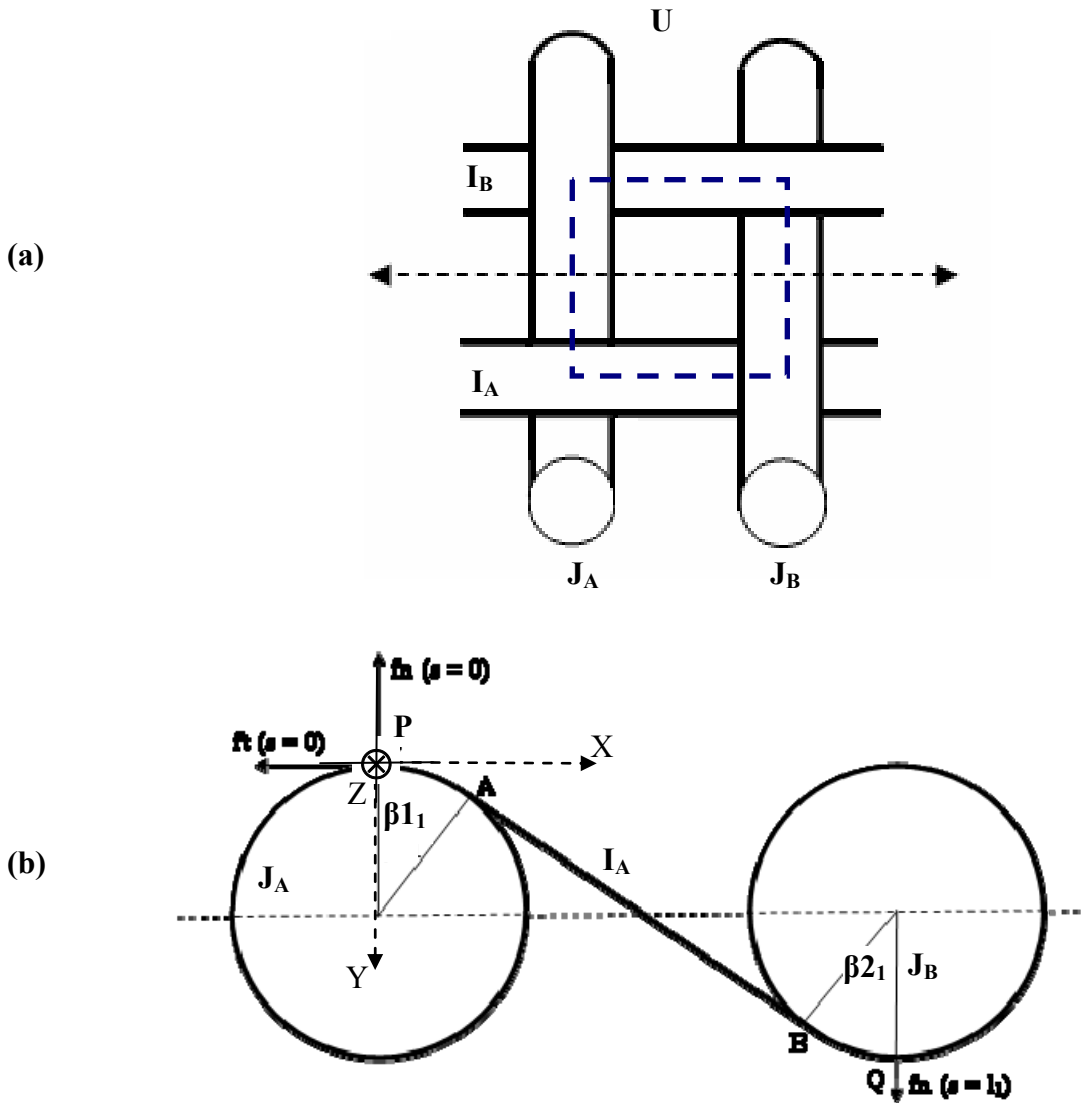


Figure 2. (a) Plan view of a plain woven fabric highlighting a unit cell, i. e. U , and (b) Sectional view of the fabric unit cell for a planar fabric, i. e. fabric with bending angle $\psi = 0$. The schematic shows a warp yarn I , going over and under two weft yarns, in the X, Y plane

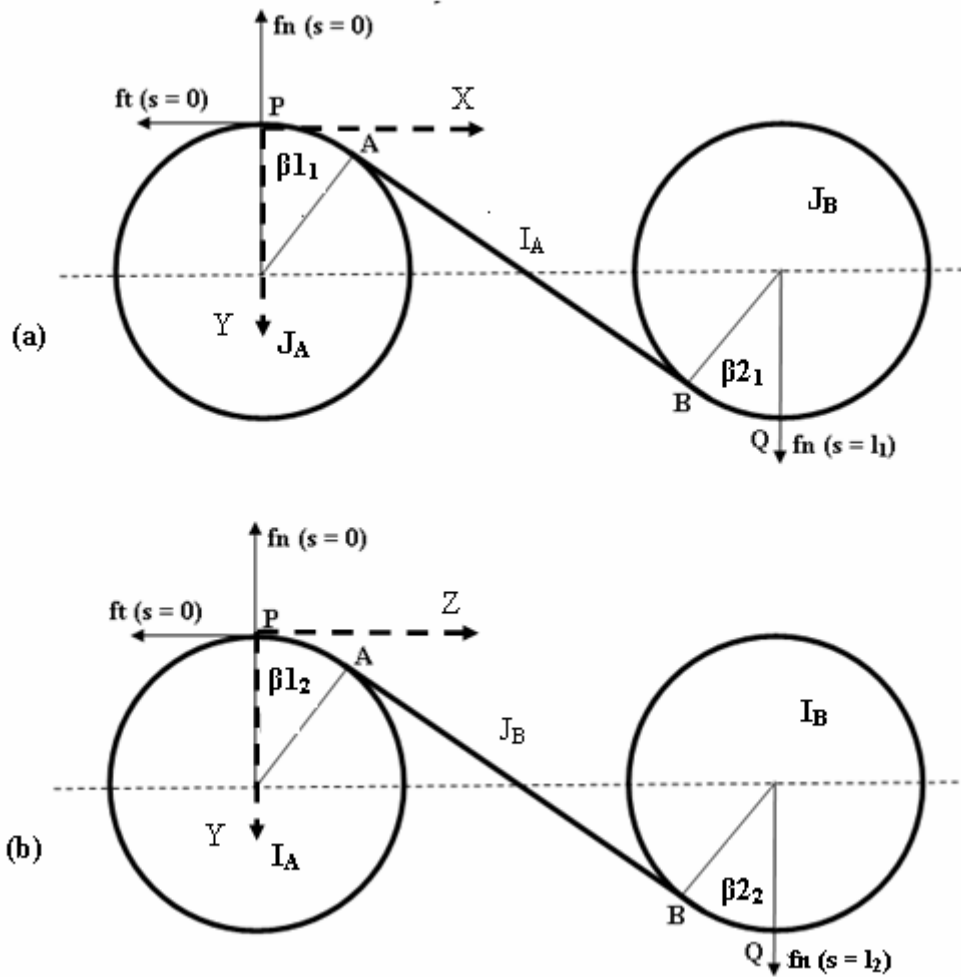


Figure 3. Schematic of equilibrium fabric configurations for planar fabrics showing the normal and tangential forces acting on the axial yarns at the crossover points (a) Equilibrium yarn configuration in the X, Y plane of bending and (b) Equilibrium yarn configuration in the Y, Z plane of bending

$$\frac{\partial}{\partial S} ty_2(S) = K_2(S)tx_2(S) \quad (26)$$

$$\frac{\partial}{\partial S} tx_2(S) = -K_2(S)ty_2(S) \quad (27)$$

$$\frac{\partial}{\partial S} X_2(S) = tx_2(S) \quad (28)$$

$$\frac{\partial}{\partial S} Y_2(S) = ty_2(S) \quad (29)$$

$$ty_2^2(S) + tx_2^2(S) = 1 \quad (30)$$

The above equations can be solved simultaneously, for appropriate boundary conditions, for both the warp and weft threads. The ratio of the bending rigidity of the warp and weft yarns, i.e. $A_r = A_1/A_2$, can be taken into account in the boundary conditions described in the following.

3.3.3 Boundary conditions required for determining the equilibrium fabric structure

In order to obtain the equilibrium fabric structure, one has to solve equations 15-30 simultaneously by applying appropriate boundary conditions to the fabric unit cell shown in Figures 3a, and 3b. Points P and Q in Figure 3 are points where the distances along the length of the yarn (warp or weft) has values, $s = 0$ and $s = l_{1,2}$, respectively, where $l_{1,2}$ is the length of the yarn in a unit cell, l_1 is the length of the warp in a unit cell and l_2 is the length of the weft yarn in the cell. Similarly, points A and B are points where the curve length parameter s has values s_1 and s_2 respectively; $s = s_1$ is the point where the yarn I in Figure 3a leaves contact with thread J_A and $s = s_2$ is the point where the yarn I makes first contact with the yarn J_B in the unit cell. The yarn I shown in Figure 3a is a warp thread wrapped over and under weft yarns J_A and J_B respectively. The yarns I are the x_1, y_1 plane as shown in Figure 3a, whereas yarns J are in the x_2, y_2 plane, which is the plane orthogonal to the x_1, y_1 plane. Similarly, one can see in Figure 3b that yarn J is a weft yarn wrapped over and under warp yarns I_A and I_B respectively.

Moreover in Figure 3, β_1 is the angle of wrap of the yarn I over the yarn J_A and β_2 is the angle of wrap of the yarn I under the yarn J_B . Hence, β_{1_1} is the angle of wrap of a warp yarn I over the weft thread J_A and β_{2_1} is the angle of wrap of a warp yarn I under the weft thread J_B as shown in the unit cell shown in Figure 3a. Similarly, in the case of a

weft yarn wrapping over and under warp yarns in the fabric unit cell, β_{12} is the angle of wrap of a weft yarn J over the warp thread I_A and β_{22} is the angle of wrap of a weft yarn J under the warp thread I_B as shown in the unit cell shown in Figure 3b. The values of s_{11} , s_{12} , s_{21} , and s_{22} are related to the values of the angle of wraps i. e. β_{11} , β_{21} , β_{12} , and β_{22} by the following relationships:

$$\begin{aligned}
 s_{11} &= \beta_{11} (d_1 + d_2)/2 \\
 s_{12} &= \beta_{12} (d_1 + d_2)/2 \\
 s_{21} &= l_1 - \beta_{21} (d_1 + d_2)/2 \\
 s_{22} &= l_2 - \beta_{22} (d_1 + d_2)/2
 \end{aligned} \tag{31}$$

Where d_1 and d_2 are diameters of the warp and weft threads respectively All of the values of distances 's' along the warp or weft threads in a unit cell were normalized with respect to the length of the warp yarn in a unit cell, i. e. l_1 , to obtain the dimensionless terms 'S' given by the following relationships:

$$\begin{aligned}
 S_{11} &= \frac{s_{11}}{l_1} = \left(\frac{\beta_{11}(d_1 + d_2)}{2} \right) \frac{1}{l_1} = \beta_{11} \frac{\lambda}{2} \\
 S_{12} &= \frac{s_{12}}{l_1} = \left(\frac{\beta_{12}(d_1 + d_2)}{2} \right) \frac{1}{l_1} = \beta_{12} \frac{\lambda}{2} \\
 S_{21} &= \frac{s_{21}}{l_1} = \frac{l_1}{l_1} - \left(\frac{\beta_{21}(d_1 + d_2)}{2} \right) \frac{1}{l_1} = 1 - \beta_{21} \frac{\lambda}{2} \\
 S_{22} &= \frac{s_{22}}{l_1} = \frac{l_2}{l_1} - \left(\frac{\beta_{22}(d_1 + d_2)}{2} \right) \frac{1}{l_1} = \frac{1}{L_r} - \beta_{22} \frac{\lambda}{2}
 \end{aligned} \tag{32}$$

where the terms λ and L_r are defined as: $\lambda = (d_1 + d_2)/l_1$ and $L_r = l_1/l_2$.

There are 14 variables in equations 15-30 – $F_{n1}(S)$, $F_{t1}(S)$, $X_1(S)$, $Y_1(S)$, $tx_1(S)$, $ty_1(S)$, & $K_1(S)$ and $F_{n2}(S)$, $F_{t2}(S)$, $X_2(S)$, $Y_2(S)$, $tx_2(S)$, $ty_2(S)$, & $K_2(S)$ and solution of these equations provides the values of these variables as a function of S.

In the case of a bent fabric, one can obtain the following relationships by adding the vertical components of the tangential and the normal forces at the boundaries $s = 0$ and $s = l_1$:

$$\begin{aligned}
 ft_1(l_1) &= fn_1(0) ((1 - \cos\psi_1)/\sin\psi_1) \\
 ft_2(l_2) &= fn_2(0) ((1 - \cos\psi_2)/\sin\psi_2)
 \end{aligned} \tag{33}$$

In case one considers the bending to be in the warp direction only, one obtains the relationships:

$$\begin{aligned} ft_1 (l_1) &= fn_1 (0) ((1 - \cos\psi_1)/\sin\psi_1), \text{ and} \\ ft_2 (l_2) &= 0 \end{aligned} \quad (34)$$

Equations 34 can be written in the normalized form as:

$$\begin{aligned} Ft_1 (1) &= Fn_1 (0) ((1 - \cos\psi_1)/\sin\psi_1), \text{ and} \\ Ft_2 (1/L_r) &= 0 \end{aligned} \quad (35)$$

Similarly, by balancing the horizontal components of normal and tangential forces in section PQ in Figure 5 and by employing equation 34, one can find the relationship between the values of fn_j and ft_j at $s = 0$, where $j = 1$ if the axial yarn is a warp thread and $j = 2$ if it is a weft thread.

$$\begin{aligned} ft_1 (0) &= -fn_1 (0) ((1 - \cos\psi_1)/\sin\psi_1) \\ ft_2 (0) &= -fn_2 (0) ((1 - \cos\psi_2)/\sin\psi_2) \end{aligned} \quad (36)$$

In case one considers the bending to be in the warp direction only, one obtains the relationships:

$$\begin{aligned} ft_1 (0) &= -fn_1 (0) ((1 - \cos\psi_1)/\sin\psi_1) \\ ft_2 (0) &= 0 \end{aligned} \quad (37)$$

Equations 37 in the normalized form can be written as:

$$\begin{aligned} Ft_1 (0) &= -Fn_1 (0) ((1 - \cos\psi_1)/\sin\psi_1) \\ Ft_2 (0) &= 0 \end{aligned} \quad (38)$$

From the force equilibrium in section PA in Figure 5, one can find the relationship between the values of fn at $s = 0$ and fn at $s = s_{1j}$, where $j = 1$ if thread I is a warp thread and $j = 2$ if thread I is a weft thread.

$$fn_1 (s_{1_1}) = fn_1 (0) \cos(\beta_{1_1}) - ft_1 (0) \sin(\beta_{1_1}) \quad (39)$$

By putting the value of $ft_1 (0)$ from equation 37 in equation 39 and writing the equation in a normalized form, one obtains the relationship, the thread I in Figures 3a and Figure 4 being a warp thread:

$$\begin{aligned} Fn_1 (s_{1_1}) &= Fn_1 (0) \cos(\beta_{1_1}) - (-Fn_1 (0) ((1 - \cos\psi_1)/\sin\psi_1)) \sin(\beta_{1_1}) \\ \Rightarrow Fn_1 (s_{1_1}) &= Fn_1 (0) (\cos(\beta_{1_1}) + ((1 - \cos\psi_1)/\sin\psi_1)) \sin(\beta_{1_1}) \end{aligned} \quad (40)$$

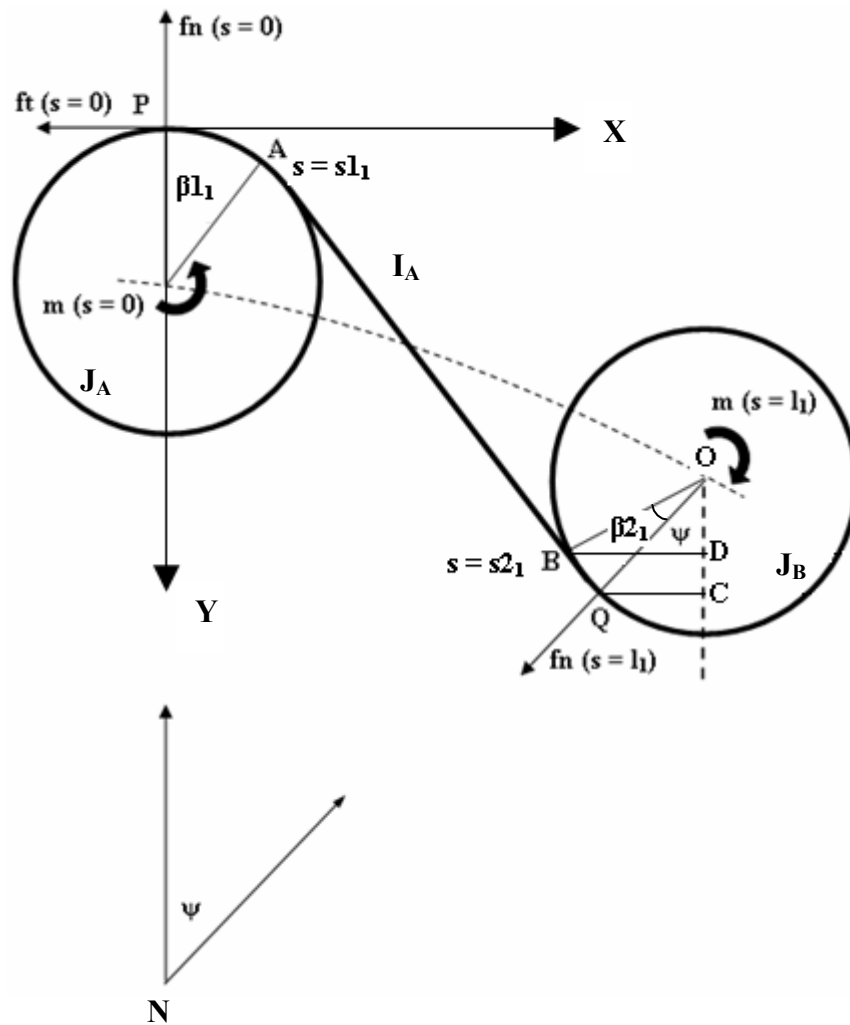


Figure 4. Schematic of equilibrium fabric configuration for a bent fabric, bent by an angle ψ . The schematic shows bending of a warp yarn, going over and under two weft yarns, in the X, Y plane

Moreover the relationship for the weft thread is given as follows:

$$fn_2(s_{1_2}) = fn_2(0) \cos(\beta_{1_2}) - ft_2(0) \sin(\beta_{1_2}) \quad (41)$$

By putting the value of $ft_2(0)$ from equation 37 and writing in the normalized form one obtains the relationship for threads J in Figures 3a and 3b being weft threads:

$$\begin{aligned} Fn_2(S_{1_2}) &= Fn_2(0) \cos(\beta_{1_2}) - 0 \times \sin(\beta_{1_2}) \\ \Rightarrow Fn_2(S_{1_2}) &= Fn_2(0) (\cos(\beta_{1_2})) \end{aligned} \quad (42)$$

Similarly, one can find the relationship between the values of ft at $s = 0$ and ft at $s = s_{1_j}$, where $j = 1$ if the axial thread is a warp thread and $j = 2$ if the axial thread is a weft thread:

$$ft_1(s_{1_1}) = fn_1(0) \sin(\beta_{1_1}) + ft_1(0) \cos(\beta_{1_1}) \quad (43)$$

and

$$ft_2(s_{1_2}) = fn_2(0) \sin(\beta_{1_2}) + ft_2(0) \cos(\beta_{1_2}) \quad (44)$$

for threads I and J in Figures 3a and 3b being warp and weft threads, respectively.

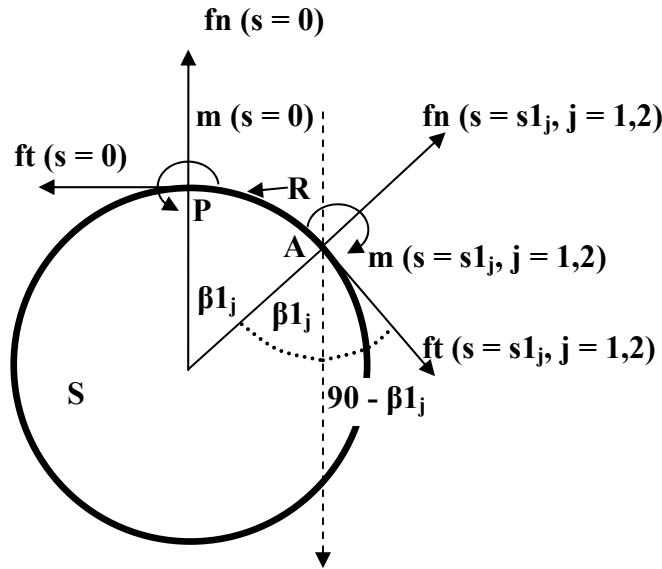


Figure 5. Schematic showing forces acting on a warp or a weft yarn going over a crossover yarn. In case the axial yarn makes a line contact with the crossover yarn the angle of wrap β_{1_j} ($j = 1$ for yarn I being a warp yarn and $j = 2$ for yarn I being a weft yarn) is greater than zero; and if it makes a point contact with the cross yarns $\beta_{1_j} = 0$

The relations given by equations 43 and 44 can be expressed in the normalized form as:

$$Ft_1 (s1_1) = Fn_1 (0) \sin(\beta1_1) + Ft_1 (0) \cos(\beta1_1) \quad (45)$$

and

$$Ft_2 (S1_2) = Fn_2 (0) \sin(\beta1_2) + Ft_2 (0) \cos(\beta1_2) \quad (46)$$

In any woven fabric, there is a geometric constraint that is required to be satisfied for the warp and weft threads to be in contact with each other whether the fabric is in the planar configuration or in the bent configuration. i. e.

$$h_1 + h_2 = d_1 + d_2 \quad (47)$$

As the values of crimp heights in the case of a planar fabric, i. e. for $\psi = 0$, equation 47 can be expressed as:

$$y_1 (l_1) + y_2 (l_2) = d_1 + d_2 = d \quad (48)$$

In non-dimensional form,

$$Y_1(l) + Y_2(1/L_r) = (d_1 + d_2)/l_1 = d/l_1 = \lambda \quad (49)$$

From the geometry shown in Figure 3, one can obtain the values of $y_1(l_1)$ and $y_2(l_2)$ in terms of the angles of wrap as:

$$\begin{aligned} y_1(l_1) &= y_1 (s2_1) + \{(d1 + d2)/2\} \{1 - \cos(\beta2_1)\} \\ y_2 (l_2) &= y_2 (s2_2) + \{(d1 + d2)/2\} \{1 - \cos(\beta2_1)\} \end{aligned} \quad (50)$$

Writing equation 50 in non-dimensional form:

$$\begin{aligned} Y_1 (1) &= Y_1 (S2_1) + \{(\lambda)/2\} \{1 - \cos(\beta2_1)\} \\ Y_2 (1/L_r) &= Y_2 (S2_2) + \{(\lambda)/2\} \{1 - \cos(\beta2_2)\} \end{aligned} \quad (51)$$

By putting the values of $Y_1 (1)$ and $Y_2 (1/L_r)$ from equation 51 into equation 49, equation 49 can be written as:

$$Y_1 (S2_1) + \{(\lambda)/2\} \{1 - \cos(\beta2_1)\} + Y_2 (S2_2) + \{(\lambda)/2\} \{1 - \cos(\beta2_2)\} = \lambda \quad (52)$$

In the case of a bent fabric that is bent by an angle ψ in the warp direction, as shown in Figure 4, the values of crimp heights are defined by the relationships:

$$h_1 = y_1 (l_1) + x_1 (l_1) \{(1 - \cos \psi)/(\sin \psi)\} \quad (53)$$

$$\text{and } h_2 = y_2 (l_2) \quad (54)$$

Hence, equation 51 can be defined in terms of the fabric equilibrium parameters x_1, y_1 and y_2 for a bent fabric (bent by an angle ψ in the warp direction) as:

$$y_1 (l_1) + x_1 (l_1) (1 - \cos \psi)/(\sin \psi) + y_2 (l_2) = d_1 + d_2 = d \quad (55)$$

which can be written in terms of normalized parameters as:

$$Y_1 (l) + X_1 (1) (1 - \cos \psi)/(\sin \psi) + Y_2 (1/L_r) = (d_1 + d_2)/l_1 = d/l_1 = \lambda \quad (56)$$

From the geometry of a bent yarn shown in Figure 4, one can obtain the values of $x_1 (l_1)$, $y_1 (l_1)$ and $y_2 (l_2)$ in terms of the angles of wrap as:

$$\begin{aligned} x_1 (l_1) &= x_1 (s_{21}) + \{(d_1 + d_2)/2\} \{\sin(\psi + \beta_{21}) - \sin(\beta_{21})\} \\ y_1 (l_1) &= y_1 (s_{21}) + \{(d_1 + d_2)/2\} \{\cos(\psi) - \cos(\psi + \beta_{21})\} \\ y_2 (l_2) &= y_2 (s_{22}) + \{(d_1 + d_2)/2\} \{1 - \cos(\beta_{21})\} \end{aligned} \quad (57)$$

In non-dimensional form:

$$\begin{aligned} X_1 (1) &= X_1 (S_{21}) + \{(\lambda)/2\} \{\sin(\psi + \beta_{21}) - \sin(\beta_{21})\} \\ Y_1 (1) &= Y_1 (S_{21}) + \{(\lambda)/2\} \{\cos(\psi) - \cos(\psi + \beta_{21})\} \\ Y_2 (1/L_r) &= Y_2 (S_{22}) + \{(\lambda)/2\} \{1 - \cos(\beta_{22})\} \end{aligned} \quad (58)$$

By putting the values of $X_1 (1)$, $Y_1 (1)$ and $Y_2 (1/L_r)$ from equation 58 into equation 56, equation 56 can be written as:

$$Y_1 (S_{21}) + \{(\lambda)/2\} \{\cos(\psi) - \cos(\psi + \beta_{21})\} + \{[X_1 (S_{21}) + \{(\lambda)/2\} \{\sin(\psi + \beta_{21}) - \sin(\beta_{21})\}] [(1 - \cos \psi)/(\sin \psi)]\} + Y_2 (S_{22}) + \{(\lambda)/2\} \{1 - \cos(\beta_{22})\} = \lambda \quad (59)$$

The different boundary conditions depend on the angle of wrap of the warp and weft yarns at the crossover points i. e. on the values of β_{11} , β_{21} , β_{12} , and β_{22} shown in Figures 3 and 4. In case the angle of wrap is zero, the contact is called a point contact. Similarly, non-zero contact angles indicate line contacts. These boundary conditions required to solve equations 15-30 are dependent on whether the contacts at points P and Q for both warp and weft are point contacts or line contacts and the boundary conditions for the different combinations of the angles of wraps are given below for both the bent and a planar fabric (with no bending). Boundary values for the bent Fabric, as shown in Figure 4, are given for the different cases below. In the boundary conditions defined below, it is assumed that the direction of bending is the warp direction i. e. yarn I is a warp and its parameters are denoted with a subscript 1, as shown in Figure 4. Each case defined below constitutes a unique boundary value problem.

Case 1 : $\beta_{11} > 0$, $\beta_{21} > 0$, $\beta_{12} = \beta_{22} > 0$

$$\begin{aligned} F_{n1} (S_{11}) / (\cos(\beta_{11}) + ((1 - \cos\psi_1)/\sin\psi_1)) \sin(\beta_{11}) &= F_{n2} (S_{12}) / (A_r \cos(\beta_{12})) \\ Y_1 (S_{21}) + \{(\lambda)/2\} \{\cos(\psi) - \cos(\psi + \beta_{21})\} + \{[X_1 (S_{21}) + \{(\lambda)/2\} \{\sin(\psi + \beta_{21}) - \sin(\beta_{21})\}] [(1 - \cos \psi)/(\sin \psi)]\} + Y_2 (S_{22}) + \{(\lambda)/2\} \{1 - \cos(\beta_{22})\} &= \lambda \end{aligned}$$

$$\begin{aligned}
X_1 (S1_1) &= \lambda \text{ ty1}(S1_1)/2 \\
X_2 (S1_2) &= \lambda \text{ ty1}(S1_2)/2 \\
Y_1 (S1_1) &= \lambda (1 - \text{tx1}(S1_1))/2 \\
Y_2 (S1_2) &= \lambda (1 - \text{tx2}(S1_2))/2 \\
K_1 (S2_1) &= -2/\lambda \\
K_2 (S2_2) &= -2/\lambda \\
K_1 (S1_1) &= 2/\lambda \\
K_2 (S1_2) &= 2/\lambda \\
\text{ty}_1 (S2_1) &= \sin (\beta2_1 + \psi)
\end{aligned} \tag{60}$$

Case 2: $\beta1_1 > 0, \beta2_1 > 0, \beta1_2 = \beta2_2 = 0$

$$\begin{aligned}
\text{Fn}_1 (S1_1) / (\cos(\beta1_1) + ((1-\cos\psi_1)/\sin\psi_1)) \sin(\beta1_1) &= \text{Fn}_2 (S1_2) / (A_r \cos(\beta1_2)) \\
Y_1 (S2_1) + \{(\lambda)/2\} \{\cos(\psi) - \cos(\psi + \beta2_1)\} + \{[X_1 (S2_1) + \{(\lambda)/2\} \{\sin(\psi + \beta2_1) - \sin(\beta2_1)\}] [(1 - \cos \psi)/(\sin \psi)]\} + Y_2 (S2_2) + \{(\lambda)/2\} \{1 - \cos(\beta2_2)\} &= \lambda \\
X_1 (S1_1) &= \lambda \text{ ty1}(S1_1)/2 \\
X_2 (S1_2) &= 0 \\
Y_1 (S1_1) &= \lambda (1 - \text{tx1}(S1_1))/2 \\
Y_2 (S1_2) &= 0 \\
K_1 (S2_1) &= -2/\lambda \\
K_2 (S2_2) &= -2/\lambda \\
K_1 (S1_1) &= 2/\lambda \\
\text{ty}_1 (S2_1) &= \sin (\beta2_1 + \psi) \\
\text{ty}_2 (S2_2) &= 0 \\
\text{tx}_2 (S1_2) &= 1
\end{aligned} \tag{61}$$

Case 3: $\beta1_1 > 0, \beta2_1 = 0, \beta1_2 = \beta2_2 > 0$

$$\begin{aligned}
\text{Fn}_1 (S1_1) / (\cos(\beta1_1) + ((1-\cos\psi_1)/\sin\psi_1)) \sin(\beta1_1) &= \text{Fn}_2 (S1_2) / (A_r \cos(\beta1_2)) \\
Y_1 (S2_1) + \{(\lambda)/2\} \{\cos(\psi) - \cos(\psi + \beta2_1)\} + \{[X_1 (S2_1) + \{(\lambda)/2\} \{\sin(\psi + \beta2_1) - \sin(\beta2_1)\}] [(1 - \cos \psi)/(\sin \psi)]\} + Y_2 (S2_2) + \{(\lambda)/2\} \{1 - \cos(\beta2_2)\} &= \lambda \\
X_1 (S1_1) &= \lambda \text{ ty1}(S1_1)/2 \\
X_2 (S1_2) &= \lambda \text{ ty2}(S1_2)/2
\end{aligned}$$

$$\begin{aligned}
Y_1 (S1_1) &= \lambda (1 - tx1(S1_1))/2 \\
Y_2 (S1_2) &= \lambda (1 - tx2(S1_2))/2 \\
K_2 (S2_2) &= -2/\lambda \\
K_1 (S1_1) &= 2/\lambda \\
K_2 (S1_2) &= 2/\lambda \\
ty_1 (S2_1) &= \sin (\psi)
\end{aligned} \tag{62}$$

Case 4: $\beta1_1 > 0, \beta2_1 = 0, \beta1_2 = \beta2_2 = 0$

$$\begin{aligned}
Fn_1 (S1_1) / (\cos(\beta1_1) + ((1 - \cos\psi_1)/\sin\psi_1))\sin(\beta1_1) &= Fn_2 (S1_2) / (A_r \cos(\beta1_2)) \\
Y_1 (S2_1) + \{(\lambda)/2\} \{\cos(\psi) - \cos(\psi + \beta2_1)\} + \{[X_1 (S2_1) + \{(\lambda)/2\} \{\sin(\psi + \beta2_1) - \\
\sin(\beta2_1)\}]\} [(1 - \cos \psi)/(\sin \psi)] &+ Y_2 (S2_2) + \{(\lambda)/2\} \{1 - \cos(\beta2_2)\} = \lambda \\
X_1 (S1_1) &= \lambda ty1(S1_1)/2 \\
X_2 (S1_2) &= 0 \\
Y_1 (S1_1) &= \lambda (1 - tx1(S1_1))/2 \\
Y_2 (S1_2) &= 0 \\
K_1 (S1_1) &= 2/\lambda \\
tx_2 (S1_2) &= 1 \\
ty_1 (S2_1) &= \sin (\psi) \\
ty_2 (S2_2) &= 0
\end{aligned} \tag{63}$$

Case 5: $\beta1_1 = 0, \beta2_1 = 0, \beta1_2 = \beta2_2 = 0$

$$\begin{aligned}
Fn_1 (S1_1) / (\cos(\beta1_1) + ((1 - \cos\psi_1)/\sin\psi_1)) \sin(\beta1_1) &= Fn_2 (S1_2) / (A_r \cos(\beta1_2)) \\
Y_1 (S2_1) + \{(\lambda)/2\} \{\cos(\psi) - \cos(\psi + \beta2_1)\} + \{[X_1 (S2_1) + \{(\lambda)/2\} \{\sin(\psi + \beta2_1) - \\
\sin(\beta2_1)\}]\} [(1 - \cos \psi)/(\sin \psi)] &+ Y_2 (S2_2) + \{(\lambda)/2\} \{1 - \cos(\beta2_2)\} = \lambda \\
X_1 (S1_1) &= 0 \\
X_2 (S1_2) &= 0 \\
Y_1 (S1_1) &= 0 \\
Y_2 (S1_2) &= 0 \\
ty_1 (S2_1) &= \sin (\psi) \\
ty_2 (S2_2) &= 0 \\
tx_1 (S1_1) &= 1
\end{aligned}$$

$$tx_2 (S1_2) = 1 \quad (64)$$

Case 6: $\beta1_1 = 0, \beta2_1 = 0, \beta1_2 = \beta2_2 > 0$

$$\begin{aligned}
Fn_1 (S1_1) / (\cos(\beta1_1) + ((1 - \cos\psi)/\sin\psi_1)) \sin(\beta1_1) &= Fn_2 (S1_2)/(A_r \cos(\beta1_2)) \\
Y_1 (S2_1) + \{(\lambda)/2\} \{\cos(\psi) - \cos(\psi + \beta2_1)\} + \{[X_1 (S2_1) + \{(\lambda)/2\} \{\sin(\psi + \beta2_1) - \sin(\beta2_1)\}] [(1 - \cos \psi)/(\sin \psi)]\} + Y_2 (S2_2) + \{(\lambda)/2\} \{1 - \cos(\beta2_2)\} &= \lambda \\
X_1 (S1_1) &= 0 \\
X_2 (S1_2) &= \lambda ty_2(S1_2)/2 \\
Y_1 (S1_1) &= 0 \\
Y_2 (S1_2) &= \lambda (1 - tx_2(S1_2))/2 \\
K_2 (S2_2) &= -2/\lambda \\
K_2 (S1_2) &= 2/\lambda \\
ty_1 (S2_1) &= \sin (\psi) \\
tx_1 (S1_1) &= 1 \quad (65)
\end{aligned}$$

Boundary values for the planar fabric i. e. the case when $\psi = 0$, as shown in Figure 3, are given below for the different values of angles of wraps $\beta1_1, \beta1_2, \beta2_1$, and $\beta2_2$. It has to be noted that in the case of a planar fabric, as the wrapping of the thread I shown in Figure 3a around threads J_A and J_B is symmetric, the angle of wrap is equal in the two cases i. e. $\beta1_1 = \beta2_1$ and $\beta1_2 = \beta2_2$. Hence the boundary conditions described below involve only $\beta1_1$ and $\beta1_2$.

Case 1: $\beta1_1 = \beta1_2 > 0$

$$\begin{aligned}
Fn_1 (S1_1) / (\cos(\beta1_1)) &= Fn_2 (S1_2) / (A_r \cos(\beta1_2)) \\
Y_1 (S2_1) + \{(\lambda)/2\} \{1 - \cos(\beta2_1)\} + Y_2 (S2_2) + \{(\lambda)/2\} \{1 - \cos(\beta2_2)\} &= \lambda \\
X_1 (S1_1) &= \lambda ty_1(S1_1)/2 \\
X_2 (S1_2) &= \lambda ty_1(S1_2)/2 \\
Y_1 (S1_1) &= \lambda (1 - tx_1(S1_1))/2 \\
Y_2 (S1_2) &= \lambda (1 - tx_2(S1_2))/2 \\
K_1 (0.5) &= 0 \\
K_2 (0.5/L_r) &= 0
\end{aligned}$$

$$\begin{aligned}
K_1 (S1_1) &= 2/\lambda \\
K_2 (S1_2) &= 2/\lambda
\end{aligned} \tag{66}$$

where $L_r = l_1/l_2$ and l_1 and l_2 are the lengths of the warp and weft respectively in each unit cell shown in Figure 3.

Case 2: $\beta1_1 > 0, \beta1_2 = 0$

$$\begin{aligned}
Fn_1 (S1_1) / (\cos(\beta1_1)) &= Fn_2 (S1_2) / (A_r \cos(\beta1_2)) \\
Y_1 (S2_1) + \{(\lambda)/2\} \{1 - \cos(\beta2_1)\} + Y_2 (S2_2) + \{(\lambda)/2\} \{1 - \cos(\beta2_2)\} &= \lambda \\
X_1 (S1_1) &= \lambda \text{ ty}_1 (S1_1)/2 \\
X_2 (S1_2) &= 0 \\
Y_1 (S1_1) &= \lambda (1 - \text{tx}_1(S1_1))/2 \\
Y_2 (S1_2) &= 0 \\
K_1 (0.5) &= 0 \\
K_2 (0.5/L_r) &= 0 \\
K_1 (S1_1) &= 2/\lambda \\
\text{tx}_2 (S1_2) &= 1
\end{aligned} \tag{67}$$

Case 3: $\beta1_1 = 0, \beta1_2 = 0$

$$\begin{aligned}
Fn_1 (S1_1) / (\cos(\beta1_1)) &= Fn_2 (S1_2) / (A_r \cos(\beta1_2)) \\
Y_1 (S2_1) + \{(\lambda)/2\} \{1 - \cos(\beta2_1)\} + Y_2 (S2_2) + \{(\lambda)/2\} \{1 - \cos(\beta2_2)\} &= \lambda \\
X_1 (S1_1) &= 0 \\
X_2 (S1_2) &= 0 \\
Y_1 (S1_1) &= 0 \\
Y_2 (S1_2) &= 0 \\
K_1 (0.5) &= 0 \\
K_2 (0.5/L_r) &= 0 \\
\text{tx}_1 (S1_1) &= 1 \\
\text{tx}_2 (S1_2) &= 1
\end{aligned} \tag{68}$$

Case 4: $\beta1_1 = 0, \beta1_2 > 0$

$$Fn_1 (S1_1) / (\cos(\beta1_1)) = Fn_2 (S1_2) / (A_r \cos(\beta1_2))$$

$$\begin{aligned}
Y_1 (S_{2_1}) + \{(\lambda)/2\} \{1 - \cos(\beta_{2_1})\} + Y_2 (S_{2_2}) + \{(\lambda)/2\} \{1 - \cos(\beta_{2_2})\} &= \lambda \\
X_1 (S_{1_1}) &= 0 \\
Y_1 (S_{1_1}) &= 0 \\
X_2 (S_{1_2}) &= \lambda t_{y2} (S_{1_2})/2 \\
Y_2 (S_{1_2}) &= \lambda (1 - t_{x2} (S_{1_2}))/2 \\
K_1 (0.5) &= 0 \\
K_2 (0.5/L_r) &= 0 \\
t_{x_1} (S_{1_1}) &= 1 \\
t_{x_2} (S_{1_2}) &= 1
\end{aligned} \tag{69}$$

As the fabric is bent, it may transition from one case to another. Hence, the conditions of angles of wrap are checked at every step of fabric bending and the boundary conditions for the appropriate case are applied to solve equations 15 - 30.

3.3.4 Solution of the boundary value problem

Hence, if the fabric construction parameters such as the yarn diameters, lengths of warp or weft in a fabric unit cell, i. e. l_1 or l_2 , and warp and weft bending stiffness, i. e. A_1 and A_2 respectively are known, then the equilibrium fabric structure can be obtained by solving the boundary value problem for the appropriate cases described above for the bent and planar fabrics. In the case of fabric bending, the fabric may transition from one case to another, which makes it important to verify for the different conditions of angles of wrap at every step of fabric bending to determine which case should be applied for the correct determination of the equilibrium fabric structure.

Equations 15-30 contain fourteen first order differential equations and eleven known boundary conditions. Hence, in order to solve the boundary value problem, one needs to guess the unknown boundary conditions at the first boundary, i. e. at $S = S_1$, and make adjustments to the guessed values such that the boundary conditions at the second boundary, i. e. at $S = S_2$, are satisfied. At each step when the guesses are made, the fourteen differential equations subject to the known and guessed boundary values are solved by employing the Fourth order Runge-Kutta-Fehlberg (RKF) method. We employed an inbuilt RKF solver in Maple 10 to solve the differential equations subject to the boundary conditions. A program written in Maple 10 was employed by us to make appropriate guesses for the unknown boundary conditions at the first boundary, i. e. $S =$

S1, and making adjustments in the guesses such that the boundary conditions at the second boundary, i. e. $S = S_2$, were satisfied. In order to solve the boundary value problem (BVP) for a bent fabric, guesses were made for the following unknown boundary conditions at the first boundary, i. e. at $S = S_1$: $tx_1(S_1)$, $tx_2(S_1)$, β_2 and $F_{n1}(0)$ for the case 1 defined in equations 60; $K_2(S_2)$, $tx_1(S_1)$, β_2 and $F_{n1}(0)$ for the case 2 defined in equations 61; $tx_2(S_2)$, $tx_1(S_1)$, β_2 and $F_{n1}(0)$ for the case 3 defined in equations 62; $K_2(S_2)$, $tx_1(S_1)$, and $F_{n1}(0)$ for the case 4 defined in equations 63; $K_1(S_1)$, $K_2(S_2)$, and $F_{n1}(0)$ for the case 5 defined in equations 64; and $K_1(S_1)$, $tx_2(S_2)$, and $F_{n1}(0)$ for the case 6 defined in equations 65. The different guessed boundary conditions in the case of the planar fabric were $tx_1(S_1)$, $tx_2(S_2)$, and $F_{n1}(0)$ for the case 1 defined in equations 66; $K_2(S_2)$, $tx_1(S_1)$, and $F_{n1}(0)$ for the case 2 defined in equations 67; $K_2(S_2)$, $K_1(S_1)$, and $F_{n1}(0)$ for the case 3 defined in equations 68; $K_1(S_1)$, $tx_2(S_2)$, and $F_{n1}(0)$ for the case 4 defined in equations 69. Newton's method was employed to solve the boundary value problem at the first boundary (i. e. at $S = S_1$) by using the known and guessed boundary conditions at this boundary and making adjustments to the guessed values such that the boundary conditions at the second boundary, i. e. at $S = S_2$, are satisfied.

Results of the boundary value problems described in this chapter are provided in subsequent chapters, i. e. chapters 4 and 5, and in Appendices 3 and 4. Specific boundary conditions and values of constants were employed for solution of the boundary value problems described in chapters 4 and 5. Chapter 4 describes the bending behavior of fabrics with yarns having different bending rigidities and sizes whereas chapter 5 involves the bending behavior of fabrics with constrained or welded crossover points.

3.4 Determination of fabric bending rigidity

In this work, we have employed the conservation of energy principle to determine the value of fabric bending rigidity. Due to deformation of the warp and weft yarns in a fabric as shown in Figure 4, there is strain energy stored in the yarns. The stored strain energy is a sum of the energy stored in the crossover regions, i. e. the region PA in Figure 4, or in the regions where the yarns take a free curvature (the region AB in Figure 4). As a fabric is bent, there is a change in the total stored strain energy in the fabric, i. e. the

energy stored in both the warp and the weft threads, and this change in the strain energy is equal to the overall work done by an externally applied bending moment to bend the fabric from a planar configuration to a bent curvature with a certain bend angle ψ .

In the yarn crossover regions, i. e. the region PA in Figure 4, the yarn I takes the curvature ($2/d$, where $d = d_1 + d_2$) of the cross yarns J_A and J_B in the x_1, y_1 plane and the yarn J takes the curvature of the cross yarns I_A and I_B in the x_2, y_2 plane. Hence, the stored strain energy in the crossover regions in the case of a bent yarn is given by the following relationships:

$$uc_1^{\text{bent}} = A_1 \frac{\beta_{2_1} + \beta_{1_1}}{d} \text{ for the warp thread} \quad (70)$$

$$\text{and } uc_2^{\text{bent}} = A_2 \frac{\beta_{2_2} + \beta_{1_2}}{d} \text{ for the weft thread} \quad (71)$$

In case of a planar fabric, angles of wrap $\beta_{1_1} = \beta_{2_1}$ and $\beta_{2_2} = \beta_{1_2}$; therefore for a planar fabric, the above relations could be written as:

$$uc_1^{\text{planar}} = A_1 \frac{2\beta_{1_1}}{d} \text{ for the warp thread} \quad (72)$$

$$\text{and } uc_2^{\text{planar}} = A_2 \frac{2\beta_{1_2}}{d} \text{ for the weft thread} \quad (73)$$

The relationship between the stored strain energy in the free region of the yarn, i. e. the region AB in Figure 4, and the yarn curvature is given by the following relationships:

$$\frac{\partial}{\partial s} uf_1(s) = \frac{A_1 (k_1(s))^2}{2}, \text{ for the warp thread} \quad (74)$$

$$\frac{\partial}{\partial s} uf_2(s) = \frac{A_2 (k_2(s))^2}{2}, \text{ for the weft thread} \quad (75)$$

One can obtain the values of stored energies in the free yarn sections for the warp thread (uf_1) and for the weft thread (uf_2) by integrating equations 74 and 75 respectively, with the integration being carried out from $s = s_{1_1}$ to $s = s_{2_1}$ for the free region of the warp thread and from $s = s_{2_1}$ to $s = s_{2_2}$ for the free region of the weft thread as given in the following relationships:

$$uf_1 = \int_{s_{1_1}}^{s_{2_1}} \frac{A_1 (k_1(s))^2}{2} ds, \text{ for the warp thread} \quad (76)$$

$$uf_2 = \int_{s1_2}^{s2_2} \frac{A_2 (k_2(s))^2}{2} ds, \text{ for the weft thread} \quad (77)$$

As one can see in equations 76 and 77, in order to obtain the value of strain energies stored in the free region of the yarn uf_1 and uf_2 , one needs to know the values of fabric curvature, i. e. $k_1(s)$ and $k_2(s)$, as a function of distance 's' along the yarn. Hence, it is important to determine the equilibrium fabric configuration for the warp and the weft threads in a manner that was described earlier in section 3.2.

The values of strain energy stored (u_j) in the crossover regions of the fabric as described in equations 70-73 or in the free regions of the fabric as described in equations 76 and 77 can be normalized by employing the following relation $U_j = u_j l_1 / A_j$ and $K_j = k_j l_1$, where $j = 1$ for the warp thread and $j = 2$ for the weft thread and l_1 is the length of a warp yarn in one unit cell of a plain woven fabric, to obtain the following relationships:

$$Uc_1^{\text{bent}} = \frac{\beta 2_1 + \beta 1_1}{\lambda} \text{ for the warp thread} \quad (78)$$

$$\text{and } Uc_2^{\text{bent}} = \frac{\beta 2_2 + \beta 1_2}{\lambda} \text{ for the weft thread} \quad (79)$$

In case of a planar fabric, angles of wrap $\beta 1_1 = \beta 2_1$ and $\beta 2_2 = \beta 1_2$; therefore for a planar fabric, the above relations could be written as:

$$Uc_1^{\text{planar}} = \frac{2\beta 1_1}{\lambda} \text{ for the warp thread} \quad (80)$$

$$\text{and } Uc_2^{\text{planar}} = \frac{2\beta 1_2}{\lambda} \text{ for the weft thread} \quad (81)$$

The relationship between the normalized stored strain energy in the free region of the yarn, i. e. the region AB in Figure 4, and the yarn curvature is given by the following relationships:

$$Uf_1 = \int_{s1_1}^{s2_1} \frac{(K_1(S))^2}{2} dS, \text{ for the warp thread} \quad (82)$$

$$Uf_2 = \int_{s1_2}^{s2_2} \frac{(K_2(S))^2}{2} dS, \text{ for the weft thread} \quad (83)$$

In order to compute the values of strain energy in equations 82 and 83 for a bent fabric, the values of the normalized warp and weft curvatures, i. e. $K_1(S)$ and $K_2(S)$, are

computed by solving the differential equations 15-30 and applying the boundary conditions 60 - 65. The values obtained for the strain energy in the free sections of the warp and weft threads in the bent fabric, by solving equations 82 and 83, are labeled as Uf_1^{bent} and Uf_2^{bent} respectively. Similarly, for the case of a planar fabric the differential equations 15 - 30 are solved by applying the boundary conditions 66 - 69 and the values of the normalized warp and weft curvatures, i. e. $K_1(S)$ and $K_2(S)$, are computed. The values obtained for the strain energy in the free sections of the warp and weft threads in the planar fabric, by solving equations 82 and 83, are labeled as Uf_1^{planar} and Uf_2^{planar} respectively. If the fabric is bent to an angle ψ , then the values of normalized stored strain energies related to the contact and free regions in the warp and weft threads can be denoted as a function of the bending angle ψ as $Uc_1^{\text{bent}}(\psi)$, $Uc_2^{\text{bent}}(\psi)$, $Uf_1^{\text{bent}}(\psi)$ and $Uf_2^{\text{bent}}(\psi)$.

The change in total stored strain energy, including that in the crossover and free regions in the warp and weft threads, of the fabric upon bending from a planar state i. e. $\psi = 0$ to an angle ψ can be written as:

$$\Delta u_{\text{Fabric}} = \{uc_1^{\text{bent}}(\psi) + uc_2^{\text{bent}}(\psi) + uf_1^{\text{bent}}(\psi) + uf_2^{\text{bent}}(\psi)\} - \{uc_1^{\text{planar}}(\psi) + uc_2^{\text{planar}}(\psi) + uf_1^{\text{planar}}(\psi) + uf_2^{\text{planar}}(\psi)\} \quad (84)$$

If the fabric is bent in k steps to an angle $\psi(k)$, such that each step of bending is a small angle $\Delta\psi = \psi^{(i)} - \psi^{(i-1)}$, the work done $w^{(i)}$ in the i^{th} step of bending is related to the bending moments $m_F^{(i)}$ and $m_F^{(i-1)}$ in the i^{th} and $(i-1)^{\text{th}}$ step of bending by the following relationship:

$$w^{(i)} = \frac{\Delta\psi}{2} (m_F^{(i)} + m_F^{(i-1)}) \quad (85)$$

For small yarn bending angles $\Delta\psi = \psi^{(i)} - \psi^{(i-1)}$, the Bernoulli-Euler relationship assuming a linear bending moment-curvature relationship, can be applied to fabric bending:

$$\Delta m_F = m_F^{(i)} - m_F^{(i-1)} = A_F^{(i)} \{k_F^{(i)} - k_F^{(i-1)}\} \quad (86)$$

where $k_F^{(i)}$ and $k_F^{(i-1)}$ are the curvature of the fabric after the i^{th} and $(i-1)^{\text{th}}$ steps of bending. Putting the value in equation 86 in equation 85 one obtains the relationship:

$$w^{(i)} = \frac{\Delta\psi}{2} (2m_F^{(i-1)} + A_F^{(i)} \{k_F^{(i)} - k_F^{(i-1)}\}) \quad (87)$$

The curvature (k_F) for a fabric bent by an angle ψ is given by the relationship:

$$k_F = 2/(v + r) \quad (88)$$

where r and v are inner and outer radii of curvature of the fabric and have the lengths NP and NQ as shown in Figure 4. They are defined by the following relationships by inputting the values from equation 57:

$$\begin{aligned} r &= x_1 (l_1) / \sin \psi \\ &= (x_1 (s2_1) + \{(d1 + d2)/2\} \{\sin(\psi + \beta2_1) - \sin(\psi)\}) / \sin \psi \end{aligned} \quad (89)$$

$$\begin{aligned} v &= x_1 (l_1) / \tan \psi + y_1 (l_1) \\ &= (x_1 (s2_1) + \{(d1 + d2)/2\} \{\sin(\psi + \beta2_1) - \sin(\psi)\}) / \tan \psi + y_1 (s2_1) + \\ &\quad \{(d1 + d2)/2\} \{\cos(\psi) - \cos(\psi + \beta2_1)\} \end{aligned} \quad (90)$$

Equations 89 and 90 can be normalized by dividing both sides of the equations by l_1 , and applying the normalizing definitions used in equation 14, to obtain the relationships:

$$\begin{aligned} R &= X_1 (1) / \sin \psi \\ &= [X_1 (S2_1) + \{(\lambda)/2\} \{\sin(\psi + \beta2_1) - \sin(\psi)\}] / \sin \psi \end{aligned} \quad (91)$$

$$\begin{aligned} V &= [X_1 (S2_1) + \{(\lambda)/2\} \{\sin(\psi + \beta2_1) - \sin(\psi)\}] / \tan \psi + Y_1 (S2_1) \\ &\quad + \{(\lambda)/2\} \{\cos(\psi) - \cos(\psi + \beta2_1)\} \end{aligned} \quad (92)$$

Equation 88 can be normalized by multiplying both sides of the equations by l_1 , and putting equations 91 and 92 into equation 88 to obtain the relationship:

$$\begin{aligned} K_F (\psi) &= 2 / \{ [X_1 (s2_1) + \{(\lambda)/2\} \{\sin(\psi + \beta2_1) - \sin(\psi)\}] / \tan \psi \\ &\quad + Y_1 (S2_1) + \{(\lambda)/2\} \{\cos(\psi) - \cos(\psi + \beta2_1)\} \\ &\quad + [X_1 (S2_1) + \{(\lambda)/2\} \{\sin(\psi + \beta2_1) - \sin(\psi)\}] / \sin \psi \} \end{aligned} \quad (93)$$

The total work done, $tw^{(i)}$, after the i^{th} step of bending is equal to the sum of the work done in the i^{th} step of bending, i. e. $w^{(i)}$, and the sum of the work done in all the steps before the i^{th} step and is given by the following relationship:

$$tw^{(i)} = w^{(i)} + \{\sum w^{(i-1)}\} \quad (94)$$

The total work $tw^{(i)}$ done after the i^{th} step of bending can be equated to the value of the change of the total strain energy stored in the fabric, i. e. Δu_{Fabric} described in equation 84, due to bending the fabric to an angle $\psi^{(i)}$:

$$\begin{aligned} tw^{(i)} &= \{\sum w^{(i-1)}\} + \frac{\Delta \psi}{2} (2m_F^{(i-1)} + A_F^{(i)} \{k_F^{(i)} - k_F^{(i-1)}\}) = \Delta u_{Fabric} (\psi^{(i)}) \\ &= \Delta u_{Fabric} = \{uc_1^{bent}(\psi^{(i)}) + uc_2^{bent}(\psi^{(i)}) + uf_1^{bent}(\psi^{(i)}) + uf_2^{bent}(\psi^{(i)})\} - \\ &\quad \{uc_1^{planar}(\psi^{(i)}) + uc_2^{planar}(\psi^{(i)}) + uf_1^{planar}(\psi^{(i)}) + uf_2^{planar}(\psi^{(i)})\} \end{aligned} \quad (95)$$

Equation 95 is solved to obtain the value of $A_F^{(i)}$ after the i^{th} step of bending. Hence, after each step of bending the value of bending rigidity of the fabric, i. e. A_F , is obtained. Equation 95 can be normalized by dividing both sides of the equation by A_1/l_1 where l_1 is the length of a warp yarn in one unit cell of a plain woven fabric and A_1 is the bending rigidity of the warp yarn and the following relationship can be obtained:

$$\begin{aligned} Tw^{(i)} &= \{ \sum W^{(i-1)} \} + \frac{\Delta\psi}{2} (2M_F^{(i-1)} + A_F^{(i)} \{ K_F^{(i)} - K_F^{(i-1)} \}) = \Delta U_{\text{Fabric}}(\psi^{(i)}) \\ &= \Delta U_{\text{Fabric}} = \{ Uc_1^{\text{bent}}(\psi^{(i)}) + Uc_2^{\text{bent}}(\psi^{(i)})/A_r + Uf_1^{\text{bent}}(\psi^{(i)}) + Uf_2^{\text{bent}}(\psi^{(i)})/A_r \} - \\ &\{ Uc_1^{\text{planar}}(\psi^{(i)}) + Uc_2^{\text{planar}}(\psi^{(i)})/A_r + Uf_1^{\text{planar}}(\psi^{(i)}) + Uf_2^{\text{planar}}(\psi^{(i)})/A_r \} \end{aligned} \quad (96)$$

During the fabric bending process, it may transition from one of the cases given in equations 60 – 65 to another case. The equilibrium fabric structure is obtained for each bending step ‘i’ and boundary conditions, corresponding to the case appropriate to the fabric at that bending step, are applied to solve equations 15 - 30. In case the fabric does transition from one case to another during the ‘i’ th step of bending, the values of the fabric curvature and the change in total strain energy are obtained for the fabric satisfying the new case but the values of total work done involves information about parameters that were computed in previous bending steps, when the fabric boundary conditions satisfied different cases.

Results of the calculations of bending rigidity of fabrics with yarns having different bending rigidities and sizes, as is the case of a fabric circuit with conductive and non-conductive threads woven into a fabric, are described in chapter 4. Results for the bending rigidity of a fabric with constrained or welded crossover points, that are required in fabric circuits for making contacts between orthogonal conductive threads, are provided in chapter 5. Different values of A_r and L_r were employed in the calculations for the bending rigidity evaluation and boundary conditions were developed to take the behavior of fabric circuits into account.

3.5 References

1. T. K. Ghosh, R. L Barker, and S. K. Batra, “On the Bending Behavior of Plain Woven Fabrics, Part I: A Critical Review,” *Journal of the Textile Institute*, 81, 255-271, 1990.
2. T. K. Ghosh, R. L Barker, and S. K. Batra, “On the Bending Behavior of Plain Woven Fabrics, Part II: The Case of Linear Yarn Bending Behavior,” *Journal of the Textile*

- Institute, 81, 272-287, 1990.
3. N. J. Abbot, M. J. Coplan, and M. M. Platt, "Theoretical considerations of bending and creasing in a fabric," *Journal of the Textile Institute*, 51, T1384, 1960.
 4. G. M. Abbot, P. Grosberg, and G. A. V. Leaf, "Elastic resistance to bending in plain woven fabrics," *Journal of the Textile Institute*, 64, 346, 1973.
 5. R. G. Livesey and J. D. Owens, "Cloth stiffness and hysteresis in bending," *Journal of the Textile Institute*, 55, T516, 1964.
 6. F. T. Pierce, "The geometry of cloth structure," *Journal of the Textile Institute*, 28, T45, 1937.
 7. W. J. Shanahan and J. W. S. Hearle, "An energy method for calculations in fabric mechanics, Part II: Examples of applications of the method to woven fabrics," *Journal of the Textile Institute*, 69, 92, 1978.
 8. T. K. Ghosh, R. L. Barker, and S. K. Batra, "On the Bending Behavior of Plain Woven Fabrics, Part III: The Case of Bi-Linear Yarn Bending Behavior and the Effect of Fabric set," *Journal of the Textile Institute*, 81, 288-299, 1990.
 9. G. A. V. Leaf, "The bending behavior of a helical filament. Part II: curvature, twist and strain energy," *Journal of the Textile Institute*, 70, 323-336, 1979.
 10. M. Konopasek, "On Large Bending and Torsional Deformations of Fibers in Space," *Textile Research Journal*, 42, 586-589, 1972.

CHAPTER 4

BENDING RIGIDITY OF WOVEN FABRIC-BASED ELECTRICAL STRUCTURES.

PART I: EFFECT OF CROSSOVER POINTS AND RIGID CONDUCTIVE YARNS IN THE WARP & WEFT DIRECTIONS

Bending Rigidity of woven fabric-based electrical structures. Part I: Effect of crossover points and rigid conductive yarns in the warp & weft directions
(A paper to be published in the Journal of Textile Institute)

Abstract

Woven fabrics, because of their structural order and flexibility, provide an excellent platform for the development of conformable electrical circuits. In a woven fabric-based electrical circuit, conducting and non-conducting orthogonal yarns are interlaced according to a predetermined circuit design. The current research addresses the influence of incorporating relatively rigid conducting elements on bending stiffness of woven fabric-based electrical circuits. Theoretical models of fabric bending rigidity are proposed to understand the effects of including rigid yarns, into woven fabrics along with the conventional flexible threads. In an approximate model to understand this effect the fabric is considered as a planar assembly of rigid and flexible threads as parallel beams placed right next to each other. Another theoretical model is developed to analyze the bending rigidity of a composite fabric, with a combination of rigid and flexible threads interwoven in the warp and weft directions, much like a fabric. In this analysis, combination of bending behavior associated with cross-over points of different combinations of conductive and non-conductive threads in a fabric circuit, are considered. The theoretical models described are compared with appropriate experimental measurements.

4.1 Introduction

Development of woven fabric based electrical circuits and circuit boards have been described by Post et al. [1, 2], Orth et al. [3], Adams et al. [4] and Dhawan et al. [5-10]. Researchers have developed fabric circuits and circuit boards by either defining conductive printed patterns on a fabric substrate or by interlacing an arrangement of conductive and non-conductive fibers into a textile fabric, with the conductive fibers acting as signal carriers and the non-conductive fibers acting as the insulators. Dhawan et al. [5-10] have reported the formation of woven fabric-based circuits by arranging and interlacing conductive and non-conductive threads according to a given fabric design.

The conductive threads act as carriers of electrical signal in woven circuits, transmitting signals from one point to another and the non-conducting threads provide appropriate separation between the conductive threads. Electronic devices could be placed at different locations on this fabric circuit which provides coupling between the devices based on the circuit design. In the work described by Dhawan et al. [5-7], single and multilayered conductive fabrics have been reported. Various others have also addressed issues related to the improvement of electrical characteristics of fabric-based electrical circuits, like achieving reliable & robust interconnect formation and improving signal integrity, as well as the mechanical characteristics of electronic textiles like their strength, washability and weatherability [11-14].

Bending behavior is an important mechanical characteristic of fabric based circuits because it determines the fabric's flexibility and in turn, its packagability. It becomes even more relevant in the case of wearable electronics. Very little work has been carried out previously to study the bending stiffness of woven fabric based electrical circuits and no theoretical model has previously been proposed.

In this paper, we first present a simplified model of fabric bending rigidity to estimate the effect of incorporation of rigid yarns, such as conductive copper or steel threads, into a woven fabric along with the regular flexible threads. In the simplified model, called the parallel beam model, the effect of crossover points on fabric bending rigidity is ignored by assuming a fabric structure consisting of parallel assembly of rigid and flexible threads in a plane. The elastica-based theoretical model described later adapts a model proposed by Ghosh et al [15-17] to include relatively rigid threads in a fabric, in the warp and/or weft directions along with flexible threads. The analysis takes into account yarns of different bending moduli as well as constraints associated with crossover points in a woven structure. Calculated results from both theoretical models described in this paper are compared with experimental measurements on a number of woven conductive fabric samples by employing the Cantilever test.

4.2 Description of the Theoretical Models

4.2.1 Parallel Beam Model of Conductive Fabrics

We first propose a simplified analysis of bending behavior of a woven fabric that consists of a combination of rigid and flexible threads. In this model, the fabric is viewed as a structure that consists of a series of parallel yarns placed next to each other and ignores the crossover points and their effect on the mechanical properties of the fabric. This model is a quick way of estimating the bending rigidity of a fabric having a certain composition of conductive and non-conductive threads.

Before evaluating the bending rigidity of a fabric, bending rigidity of individual yarns must be estimated. The analysis presented below is necessary to obtain values of bending rigidity of copper threads containing various filament diameters and number of filaments from known elastic modulus of copper. In doing so we assume that the individual fibers in a yarn are packed in a hexagonal arrangement as shown in Figure 1a. If the number of fibers in the central layer of a hexagonal closed packed yarn is x , then the maximum number of layers in the structure on either side of the central layer, is $(x-1)/2$. The area moment of inertia of the yarn can be calculated as the sum of the area moments of the fibers in each layer and applying the parallel axis theorem to obtain the net moment of inertia about the neutral axis (MM) shown in Figure 1 and is described by the equation:

$$I_{MM} = \sum_1^{(x-1)/2} \left\{ 2 \cdot \left[\frac{\pi d^4}{64} + \left(\left(\frac{\sqrt{3}}{2} di \right)^2 \cdot \left(\frac{\pi d^2}{4} \right) \right) \right] \cdot [x-i] \right\} + \left\{ \frac{\pi d^4}{64} \cdot x \right\} \quad (1)$$

where i is the layer number away from the central layer, and d is the diameter of each fiber in the yarn.

Bending rigidity of an arrangement of N beams placed parallel to each other as shown in Figure 1b, can be expressed as:

$$\text{Bending Rigidity}_{\text{parallel_beams}} = E_1 \cdot I_1 + E_2 \cdot I_2 + \dots + E_N \cdot I_N = \sum_{j=1}^N E_j \cdot I_j \quad (2)$$

where $E_1, E_2, E_3 \dots E_N$ are the elastic moduli and $I_1, I_2, I_3 \dots I_N$ are moments of inertia of the parallel beams about the neutral axis passing through the center of the arrangement of beams. A textile fabric can be viewed in terms of this simplified model by considering yarns as parallel beams, where the effect of crossover threads are ignored, as shown in Figure 1. In this model it is also assumed that the direction of bending is the direction of

the parallel yarns and that there are no threads orthogonal to the direction of the yarn bending direction. The values of yarn moment of inertia, about the neutral axis, can be calculated using equation 1. This model provides an estimate of the overall bending rigidity of a fabric, having threads with different elastic moduli and sizes, and can be applied to predict the bending rigidity of a conductive fabric containing a combination of conductive threads (e.g. copper, etc.) and nonconductive threads (e.g. polyester, etc.).

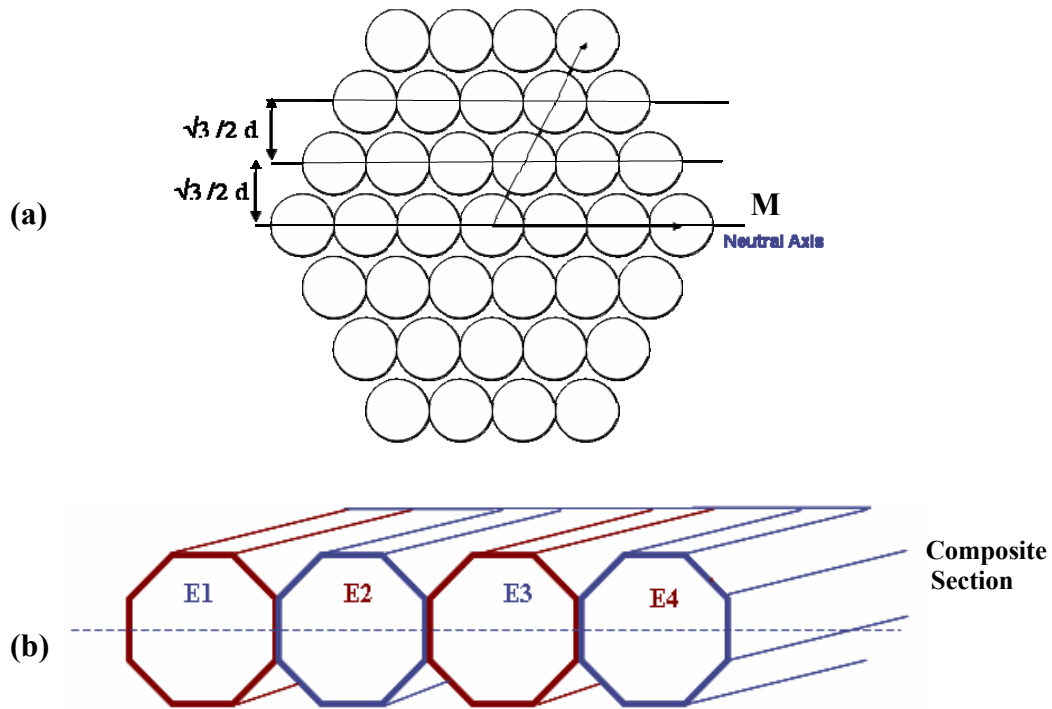


Figure 1. (a) Schematic of a yarn cross-section assuming hexagonal close packing of the fibers in the yarn, with each fiber having a diameter ‘d’ and (b) A simplified view of a woven fabric considers it to be a parallel arrangement of yarns placed next to each other, ignoring the effect of crossover yarns

4.2.2 Elastica model of conductive fabrics

In the elastica model the yarns are assumed to be inextensible, perfectly circular slender cylinders with finite bending rigidity. In order to determine the bending rigidity of the fabric, the first step is to be able to accurately predict the structure of a yarn woven in a fabric. Pierce [18], Leaf [19], and Abbot et al. [20] defined models to describe the geometry of a yarn in a woven fabric by assuming the yarns to be flexible and inextensible. In a model defined by Pierce [18] as flexible thread model, the yarns are assumed to be perfect circular cylinders that follow a straight path in regions other than the crossover point, where they were assumed to have a constant curvature. As the yarns woven into a fabric have a finite bending rigidity, they can be treated as elastic slender rods with a set of transverse forces acting on them at the crossover points, such that the forces are in opposite directions at the alternating crossover points. Although Pierce [18] had first proposed the ‘elastica’ concept describing yarns in a woven fabric as elastic rods with the local bending moment being proportional to the yarn curvature in a woven fabric, it was Konopasek [21] and later Ghosh et al. [15-17] that developed a comprehensive yet simple model to determine the equilibrium structure of warp and weft yarns in a fabric. The model described by Ghosh et al. [15-17] is based on the determination of equilibrium warp and weft yarn structures as two planar bending curves, in two mutually orthogonal planes, as the fabric is subjected to bending. In this paper, we extend the model described by Ghosh et al. [15-17] in order to determine the equilibrium yarn configurations and subsequently the bending rigidity of a fabric based circuit containing rigid conductive threads and flexible insulating threads interwoven into a fabric.

4.2.2.1 Equilibrium fabric structure

Generalized governing equations of a bent ‘elastica’ have been described by other researchers [15-17]. These equations describe the relationships between tangential and normal forces, i. e. f_t and f_n respectively, acting along the length of the yarn, the bending moment m acting at different points of the yarn, the curvature ‘ k ’, bending rigidity ‘ A_y ’ of the individual yarn, and the geometry of the yarn [15-17]. The parameters defining the geometry of a yarn in a woven fabric include the ‘ x ’ and ‘ y ’ coordinates of the different points in the yarn, the diameters ‘ d_1 ’ and ‘ d_2 ’ of the warp and weft threads respectively,

and the length ' l_1 ' of a warp yarn in one unit cell of a plain woven fabric. All these parameters are a function of ' s ', i. e. the distance along the length of the yarn (warp or weft). All the parameters described in the 'elastica' equations were normalized to obtain their dimensionless forms. The 'elastica' equations in their normalized form were described in detail in chapter 3.

In order to obtain the equilibrium fabric structure, one has to solve the 'elastica' equations [15-17] simultaneously by applying appropriate boundary conditions to the fabric unit cells described in Figures 3 and 4 of chapter 3. The different boundary conditions depend on the angle of wrap of the warp and weft yarns at the crossover points i. e. on the values of β_{11} , β_{21} , β_{12} , and β_{22} shown in Figures 3 and 4 of chapter 3. These boundary conditions required to solve the 'elastica' equations are dependent on whether the contacts at points P and Q, shown in Figure 3 of chapter 3, for both warp and weft are point contacts or line contacts and the boundary conditions for the different combinations of the angles of wraps are given below for both the bent and a planar fabric (with no bending). When a fabric is bent, it may transition from one case to another. Hence, the conditions of angles of wrap are checked at every step of fabric bending and the boundary conditions for the appropriate case are applied to solve the 'elastica' equations. Detailed boundary conditions for planar and bent fabrics have been described in chapter 3.

Hence, if the fabric construction parameters such as the yarn diameters, lengths of warp or weft in a fabric unit cell, i. e. l_1 or l_2 , and warp and weft bending stiffness, i. e. A_1 and A_2 respectively are known, then the equilibrium fabric structure can be obtained by solving the boundary value problem for the appropriate cases described above for the bent and planar fabrics. The 'elastica' equations contain fourteen first order differential equations and eleven known boundary conditions [1-2, 8]. Hence, in order to solve the boundary value problems, one needs to guess the unknown boundary conditions at the first boundary, i. e. at $S = S_1$ shown in Figures 3 and 4 of chapter 3, and make adjustments to the guessed values such that the boundary conditions at the second boundary, i. e. at $S = S_2$, are satisfied. At each step when the guesses are made, the fourteen differential equations subject to the known and guessed boundary values are solved by employing the Fourth order Runge-Kutta-Fehlburg (RKF) method. We

employed an inbuilt RKF solver in Maple 10 to solve the differential equations subject to the boundary conditions.

An important parameter that is involved in the solution of the ‘elastica’ equations is $A_r = A_1 / A_2$, where A_1 and A_2 are the bending rigidities of the warp and weft yarns respectively. The ‘elastica’ equations were solved for fabric unit cells having different values of A_r and the different parameters related to the woven fabric were obtained. These parameters - $F_{n1}(S)$, $F_{t1}(S)$, $X_1(S)$, $Y_1(S)$, $tx_1(S)$, $ty_1(S)$, & $K_1(S)$ and $F_{n2}(S)$, $F_{t2}(S)$, $X_2(S)$, $Y_2(S)$, $tx_2(S)$, $ty_2(S)$, & $K_2(S)$ - were obtained as a function of S , i. e. the distance along the length of warp or weft yarns normalized to the length l_1 of the warp yarn in a unit cell.

4.2.2.2 Determination of fabric bending rigidity

In order to determine the bending rigidity of a woven fabric, the principle of conservation of energy was employed. Due to deformation of the warp and weft yarns in a fabric as shown in Figure 4 of chapter 3, there is strain energy stored in the yarns. The stored strain energy is a sum of the energy stored in the crossover regions, i. e. the region PA in Figure 4 of chapter 3, or in the regions where the yarns take a free curvature (the region AB in Figure 4 of chapter 3). As a fabric is bent, there is a change in the total stored strain energy in the fabric, i. e. the energy stored in both the warp and the weft threads, and this change in the strain energy is equal to the overall work done by an externally applied bending moment to bend the fabric from a planar configuration to a bent curvature with a certain bend angle ψ .

In the yarn crossover regions, i. e. the region PA in Figure 4 of chapter 3, the yarn I takes the curvature $(2/d)$, where $d = d_1 + d_2$ of the cross yarns J_A and J_B in the x_1, y_1 plane and the yarn J takes the curvature of the cross yarns I_A and I_B in the x_2, y_2 plane. Hence, the stored strain energy, normalized employing the following relation $U_j = u_j \cdot l_1 / A_j$ where $j = 1$ for the warp thread and $j = 2$ for the weft thread and l_1 is the length of a warp yarn in one unit cell of a plain woven fabric, in the crossover regions in the case of a bent yarn is given by the following relationships:

$$U_{c_1}^{\text{bent}} = \frac{\beta_2 l_1 + \beta_1 l_1}{\lambda}, \text{ for the warp thread} \quad (3)$$

$$\text{and } Uc_2^{\text{bent}} = \frac{\beta_2 + \beta_1}{\lambda}, \text{ for the weft thread} \quad (4)$$

In case of a planar fabric, angles of wrap $\beta_1 = \beta_2$ and $\beta_2 = \beta_1$; therefore for a planar fabric, the above relations could be written as:

$$Uc_1^{\text{planar}} = \frac{2\beta_1}{\lambda}, \text{ for the warp thread} \quad (5)$$

$$\text{and } Uc_2^{\text{planar}} = \frac{2\beta_1}{\lambda}, \text{ for the weft thread} \quad (6)$$

The relationship between the stored strain energy in the free region i. e. the region AB in Figure 4 of chapter 3, normalized by employing the following relation $U_j = u_j \cdot l_j / A_j$ and $K_j = k_j \cdot l_j$, where $j = 1$ for the warp thread and $j = 2$ for the weft thread, and the yarn curvature is given by the following relationships:

$$Uf_1 = \int_{s_{11}}^{s_{21}} \frac{(K_1(S))^2}{2} dS, \text{ for the warp thread} \quad (7)$$

$$Uf_2 = \int_{s_{12}}^{s_{22}} \frac{(K_2(S))^2}{2} dS, \text{ for the weft thread} \quad (8)$$

As one can see in equations 7 and 8, in order to obtain the value of strain energies stored in the free region of the yarn uf_1 and uf_2 , one needs to know the values of normalized fabric curvature, i. e. $K_1(s)$ and $K_2(s)$, as a function of distance 's' along the yarn and the procedure to obtain their values was described earlier in section 4.2.2.1.

The values for the strain energy in the free sections of the warp and weft threads in the bent and planar fabrics, obtained by solving equations 7 and 8, are labeled as Uf_1^{bent} & Uf_2^{bent} and Uf_1^{planar} and Uf_2^{planar} respectively. The value of change in the total stored strain energy, including that in the crossover and free regions in the warp and weft threads, of the fabric upon bending from a planar state i. e. $\psi = 0$ to an angle ψ can be written as:

$$\Delta u_{\text{Fabric}} = \{uc_1^{\text{bent}}(\psi) + uc_2^{\text{bent}}(\psi) + uf_1^{\text{bent}}(\psi) + uf_2^{\text{bent}}(\psi)\} \\ - \{uc_1^{\text{planar}}(\psi) + uc_2^{\text{planar}}(\psi) + uf_1^{\text{planar}}(\psi) + uf_2^{\text{planar}}(\psi)\} \quad (9)$$

If the fabric is bent in k steps to an angle $\psi(k)$, such that each step of bending is a small angle $\Delta\psi = \psi^{(i)} - \psi^{(i-1)}$, the work done ' $w^{(i)}$ ' in the i^{th} step of bending is related to

the bending moments $m_F^{(i)}$ and $m_F^{(i-1)}$ in the i^{th} and $(i-1)^{\text{th}}$ step of bending by the following relationship:

$$w(i) = \frac{\Delta\psi}{2} \cdot (m_F^{(i)} + m_F^{(i-1)}) \quad (10)$$

For small yarn bending angles $\Delta\psi = \psi^{(i)} - \psi^{(i-1)}$, the Bernoulli-Euler relationship assuming a linear bending moment-curvature relationship, can be applied to fabric bending:

$$\Delta m_F = m_F^{(i)} - m_F^{(i-1)} = A_F^{(i)} \cdot \{k_F^{(i)} - k_F^{(i-1)}\} \quad (11)$$

where $k_F^{(i)}$ and $k_F^{(i-1)}$ are the curvature of the fabric after the i^{th} and $i-1^{\text{th}}$ steps of bending. Putting the value in equation 11 in equation 10, one obtains the relationship:

$$w^{(i)} = \frac{\Delta\psi}{2} \cdot (2 \cdot m_F^{(i-1)} + A_F^{(i)} \cdot \{k_F^{(i)} - k_F^{(i-1)}\}) \quad (12)$$

The value of normalized fabric curvature (K_F) for a fabric bent by an angle ψ can be obtained from the geometry of Figure 4 of chapter 3 as:

$$\begin{aligned} K_F(\psi) = & 2 / \{ [X_1 (s2_1) + \{(\lambda)/2\} \cdot \{\sin(\psi + \beta 2_1) - \sin(\psi)\}] / \tan \psi \\ & + Y_1 (S2_1) + \{(\lambda)/2\} \cdot \{\cos(\psi) - \cos(\psi + \beta 2_1)\} \\ & + [X_1 (S2_1) + \{(\lambda)/2\} \cdot \{\sin(\psi + \beta 2_1) - \sin(\psi)\}] / \sin \psi \} \end{aligned} \quad (13)$$

The total work done, $tw^{(i)}$, after the i^{th} step of bending is equal to the sum of the work done in the i^{th} step of bending, i. e. $w^{(i)}$, and the sum of the work done in all the steps before the i^{th} step and is given by the following relationship:

$$tw(i) = w^{(i)} + \{\sum w^{(i-1)}\} \quad (14)$$

The total work $tw^{(i)}$ done after the i^{th} step of bending can be equated to the value of the change of the total strain energy stored in the fabric, i. e. Δu_{Fabric} described in equation 9, due to bending the fabric to an angle $\psi(i)$:

$$\begin{aligned} tw^{(i)} = & \{\sum w^{(i-1)}\} + \frac{\Delta\psi}{2} \cdot (2 \cdot m_F^{(i-1)} + A_F^{(i)} \cdot \{k_F^{(i)} - k_F^{(i-1)}\}) = \Delta u_{\text{Fabric}}(\psi^{(i)}) \\ = & \Delta u_{\text{Fabric}} = \{uc_1^{\text{bent}}(\psi^{(i)}) + uc_2^{\text{bent}}(\psi^{(i)}) + uf_1^{\text{bent}}(\psi^{(i)}) + uf_2^{\text{bent}}(\psi^{(i)})\} - \\ & \{uc_1^{\text{planar}}(\psi^{(i)}) + uc_2^{\text{planar}}(\psi^{(i)}) + uf_1^{\text{planar}}(\psi^{(i)}) + uf_2^{\text{planar}}(\psi^{(i)})\} \end{aligned} \quad (15)$$

Equation 15 can be normalized by dividing both sides of the equation by A_1/l_1 where l_1 is the length of a warp yarn in one unit cell of a plain woven fabric and A_1 is the bending rigidity of the warp yarn and the following relationship can be obtained:

$$\begin{aligned}
Tw^{(i)} &= \{\Sigma W^{(i-1)}\} + \frac{\Delta\Psi}{2} \cdot (2.M_F^{(i-1)} + A_F^{(i)} \cdot \{K_F^{(i)} - K_F^{(i-1)}\}) = \Delta U_{Fabric}(\Psi^{(i)}) \\
&= \Delta U_{Fabric} = \{Uc_1^{bent}(\Psi^{(i)}) + Uc_2^{bent}(\Psi^{(i)})/A_r + Uf_1^{bent}(\Psi^{(i)}) + Uf_2^{bent}(\Psi^{(i)})/A_r\} - \\
&\{Uc_1^{planar}(\Psi^{(i)}) + Uc_2^{planar}(\Psi^{(i)})/A_r + Uf_1^{planar}(\Psi^{(i)}) + Uf_2^{planar}(\Psi^{(i)})/A_r\} \quad (16)
\end{aligned}$$

Equation 16 is solved to obtain the value of $A_F^{(i)}$ after the i^{th} step of bending. Hence, after each step of bending the value of bending rigidity of the fabric, i. e. A_F , is obtained.

4.2.2.3 Determination of bending rigidity of a conductive fabric

Dhawan et al. [5-10] have previously reported the formation of fabric-based circuits by arranging and interlacing conductive and non-conductive threads according to a given fabric design. Conductive threads could be incorporated into the fabric along weft and/or warp directions in various densities, their effects on fabric flexural rigidity could be very important for many applications

In order to determine the bending rigidity of a fabric circuit, the fabric circuit is assumed as a series and/or parallel combination of various types of fabric unit call (or cross-over points) as shown in Figure 2. In the example presented in Figure 2, crossover points, at the intersection of row 1 & column 1 and the one formed at the intersection of row 1 & column 2, are in series. The crossover points, at the intersection of row 1 & column 1 and the one formed at the intersection of row 2 & column 1, are in parallel with each other. In Figure 2, the direction of bending is taken as the warp direction. In order to determine the bending rigidity of the overall fabric, the bending rigidity of each row in the plane of bending is first computed by taking the crossover points to be in series with each other. This is followed by computation of the bending rigidity of the different rows, by considering them to be in parallel. If the fabric circuit is made from copper and polyester threads as shown in Figure 2, there are four different categories of crossover points in this fabric:

- a. Polyester warp weft
- b. Polyester warp & copper weft
- c. Copper warp & polyester weft
- d. Copper warp & weft

As an example, one can observe in Figure 2 that the first row consists of crossover points that fall in the categories d, c, c, d, c, and c. Bending rigidity for the different categories a-d are computed by assuming that the entire unit cell, as described earlier in

Figure 2 of chapter 3, corresponds to that category. Hence, category ‘b’ implies that a unit cell consists of two polyester warp threads and two copper weft threads. Similarly, category ‘c’ implies that a unit cell consists of two copper warp threads and two polyester weft threads. As the ratio of the bending rigidities of copper and polyester yarns is greater than 1, the appropriate values of $A_r (=A_1/A_2$, where A_1 and A_2 are the bending rigidities of the warp and weft yarns respectively) are employed for calculation of bending rigidities in the different categories described above. Different values of A_r that are assumed for the different categories for the purpose of theoretical calculations are:

- a. Polyester warp and weft: $A_r = 1$
- b. Polyester warp & copper weft: $A_r = 0.2$ or 0.5
- c. Copper warp & polyester weft: $A_r = 5$ or 2
- d. Copper warp& copper weft: $A_r = 1$

The values of A_F/A_1 , i.e. the normalized fabric bending rigidity were obtained for the different combinations described above and then the value of A_F was obtained for each of those categories by multiplying by the value of A_F/A_1 determined for that category by appropriate A_1 for the category

One can obtain a generalized formula for determining the bending rigidity of the overall fabric if the values of A_F for the different categories are given, by considering a series and parallel combination of these cells. Formula employed for the calculation of the overall bending rigidity (A_F) of a conductive fabric is derived by first taking the harmonic mean of bending rigidities of different bending elements in series, i. e. in one row along the warp direction, and then sum up the elements in parallel to be:

$$A_{F_{Fabric}} = [N_{warp} - N_{copper_warp}] * \left[\left(\frac{N_{copper_weft}}{A_{pc}} \right) + \left(\frac{N_{weft} - N_{copper_weft}}{A_{pp}} \right) \right] + [N_{copper_warp}] * \left[\left(\frac{N_{copper_weft}}{A_{cc}} \right) + \left(\frac{N_{weft} - N_{copper_weft}}{A_{cp}} \right) \right] \quad (17)$$

where N_{warp} , and N_{weft} are the number of warp and weft threads in the fabric, while, N_{copper_warp} , and N_{copper_weft} are the number of copper warp and weft threads in the fabric. It is important to note that the values of yarn bending rigidity are calculated in the same manner as was done in the case of the parallel beam model described earlier in section 4.2.1.

Based on the model described above, theoretical evaluations for the overall bending rigidity of conductive fabric samples are carried out such that the samples analyzed theoretically were similar in size to the samples evaluated experimentally. The objective of these theoretical calculations was to isolate and study the following effects:

- The effect of increasing the number of copper (rigid) threads in the warp for a given number of copper weft threads, one case being that there is no copper thread in the weft direction
- The effect of increasing the number of copper (rigid) threads in the weft direction for a given number of warp copper threads, one case being that there is no copper thread in the warp direction

Results of the theoretical calculations are given in section 4.4. The number of copper threads in the warp and the weft directions were expressed as a fraction of the total number of threads in these directions.

4.3 Experimental

In order to validate the theoretical models, conductive fabric samples with various arrangements of conductive and non-conductive threads woven in the warp or weft direction or both, were experimentally evaluated.

The experimental fabric circuits were woven on a rapier weaving machine with a programmable Jacquard shedding system. All of the fabric samples are single layer and plain woven. The conductive threads employed for these theoretical calculations are copper yarns, each yarn consisting of 29 fibers with each fiber having a diameter of 34 μm . The non-conductive threads employed for these theoretical calculations were polyester yarns, each yarn consisting of 91 fibers with each fiber having a diameter of 26 μm . These theoretical calculations are also carried out for another conductive fabric sample comprising of copper yarns, each yarn consisting of 29 fibers of 34 μm in diameter and polyester yarns containing 91 fibers of 26 μm .

In all cases the insertion order of the polyester and copper weft threads were programmed into the filling insertion controller. In order to incorporate copper threads in the warp direction, copper threads wound on separate packages were placed on a creel in the back of the weaving machine. The creel allowed for precise control of

tension in the yarns. Schematic of some of the samples that were developed are shown in Figure 4a and image of an actual sample is shown in Figure 4b.

In order to experimentally determine the bending rigidity of the woven conductive fabric structures, the cantilever bending test was employed. Cantilever bending test is described by ASTM test standards D1388 & D5372 [23]. In the cantilever bending test, 6 inch long and 1 or 3 inch wide test samples were used to determine the overhang length, as shown in Figure 5. As the fabric is slid from the planar region of the cantilever bending tester to the inclined part, making an angle θ to the horizontal, the end of the fabric sample on the planar part at point M is held by some weight where as the other end of the fabric is allowed to bend under its own weight till the end point N of the fabric touches the surface of inclined plane. The length 'l' of the fabric that hangs freely, i. e. the fabric length ON as shown in Figure 5, is called the overhang length. In the experimental evaluations of the overhang length 'l', four readings were taken for each sample – two readings, one for each end of the sample, for each side (face up and back up) of the sample.

The overhang length 'l' is related to another quantity called the bending length (L) by the following relationship [17]:

$$L = \frac{1}{2} \left(\frac{\cos(\theta/2)}{\tan(\theta)} \right)^{1/3} \quad (18)$$

where θ is the angle made by the inclined surface with the horizontal. In most Cantilever bending testers, the angle θ is $\sim 41.5^\circ$ so that relationship between the bending length and the overhang length 'l' simplifies to [22]:

$$L = \frac{1}{2} \quad (19)$$

Fabric bending rigidity, C, is subsequently calculated from bending length (L) and fabric weight per unit area (W):

$$C = WL^3 \quad (20)$$

If the value of W is expressed in units of N/m^2 and the value of bending length (L) is expressed in units of meters, then the unit of the experimentally calculated bending rigidity (C) becomes N-m. The value of the bending rigidity was normalized to the length 'l₁' of the unit cell for comparison with the values of bending rigidity determined by

employing the theoretical models described in section 4.2. Results of these experimental evaluations and their comparison with the theoretical values, calculated by employing the parallel beam model and the elastica model, are provided in section 4.4.

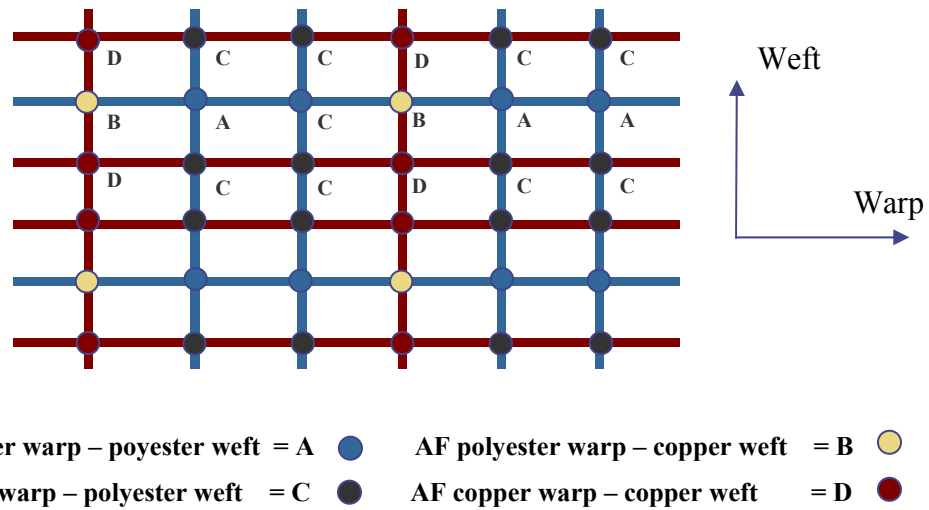
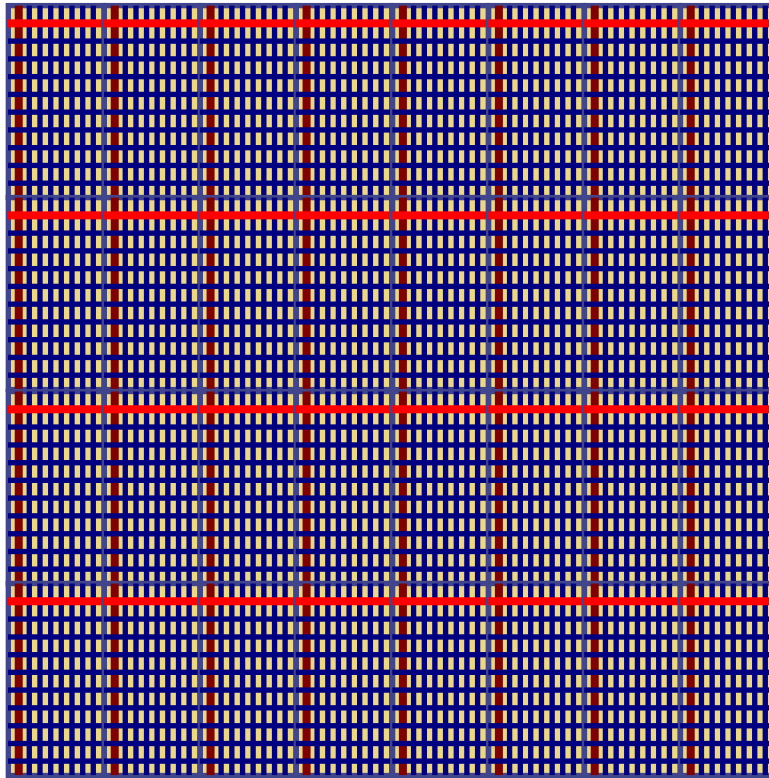


Figure 2. Schematic demonstrating the procedure employed to determine bending rigidity of fabric circuits. Bending rigidity of a fabric circuit is modeled as a series and parallel combination of the bending rigidities associated with different unit cells, each unit cell consisting of a crossover point, as shown in this figure



- Polyester Warp and Weft Threads
- Copper Weft Threads
- Copper Weft Threads

Figure 3. Part of a fabric sample that was evaluated for determining the effect, of increasing the number of copper threads in the weft direction, on the fabric bending rigidity. The number of copper threads in the warp direction was taken as 8, while the number of copper weft threads was varied in the different samples from 4 to 64. The length of the evaluated samples was 6 inches while the width was taken as either 1 inch or 3 inches. The warp density in these evaluations was taken as 32 ends per inch, while the weft density was taken as 30 picks per inch

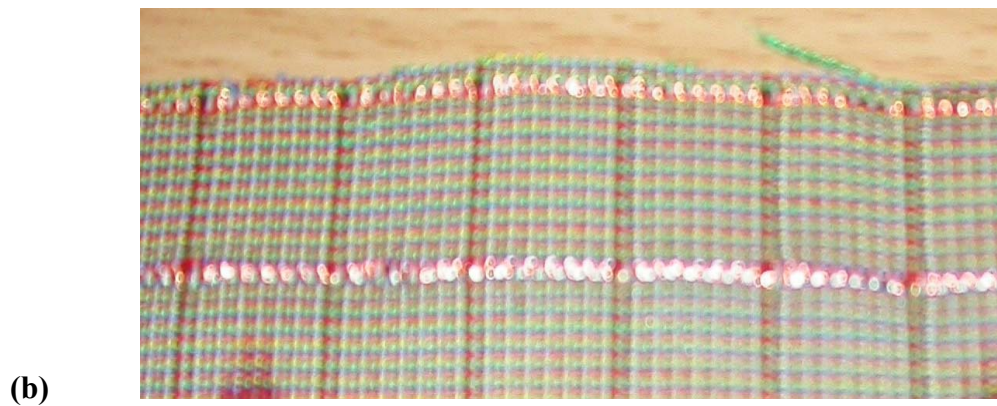
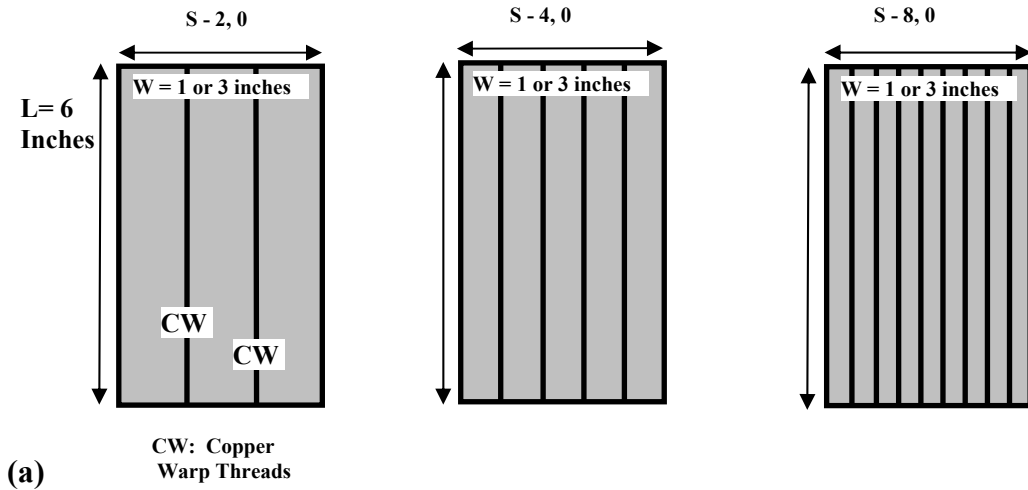


Figure 4. (a) Samples that were evaluated for the effect of increasing number of copper threads in the warp directions, with all the threads in the weft direction being polyester, and (b) Fabric sample woven on a rapier loom with a Jacquard head, having copper threads in the warp and weft directions

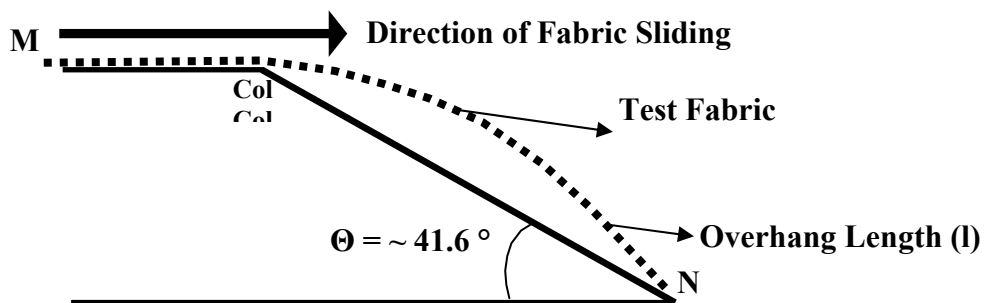


Figure 5. Schematic of the Cantilever test for bending rigidity evaluations

4.4 Results and Discussion

4.4.1 Parallel Beam Model

According to the parallel beam model described in section 4.2, the fabric structure is approximated as a series of parallel yarns placed next to each other. In order to determine the value of the bending rigidity of the fabric using equation 2, the values of yarn moment of inertia were obtained by making an assumption that the individual fibers in a yarn are packed in a hexagonal arrangement. Equation 1 was employed to determine the value of the moment of inertia for the individual yarns.

In the case of the copper yarns, having 29 fibers in each yarn with the fiber diameter being $36.46 \mu\text{m}$, and polyester yarns, having 127 fibers in each yarn with the fiber diameter being $25.16 \mu\text{m}$, the values of moment of inertia of the copper and polyester yarns were determined, using equation 1, to be $5.66 \times 10^{-17} \text{ m}^4$ and $3.53 \times 10^{-16} \text{ m}^4$ respectively, by taking the value of yarns in the middle layer 'x' to be 7 for the copper yarns and 13 for the polyester threads as shown in Figure 1. The values of yarn bending rigidity for the copper and polyester yarns were determined, using equation 2, to be $6.112 \times 10^{-6} \text{ N}\cdot\text{m}^2$ and $1.274 \times 10^{-7} \text{ N}\cdot\text{m}^2$ respectively. In the case of the copper yarns, having 29 fibers in each yarn with the fiber diameter being $34 \mu\text{m}$, and polyester yarns, having 91 fibers in each yarn with the fiber diameter being $26 \mu\text{m}$, the values of area moment of inertia of the copper and polyester yarns were determined, using equation 1, to be $3.10 \times 10^{-17} \text{ m}^4$ and $1.66 \times 10^{-16} \text{ m}^4$ respectively, by taking the value of yarns in the middle layer 'x' to be 7 for the copper yarns and 11 for the polyester threads. The values of yarn bending rigidity for the copper and polyester yarns were determined, using equation 2, to be $3.348 \times 10^{-6} \text{ N}\cdot\text{m}^2$ and $5.977 \times 10^{-7} \text{ N}\cdot\text{m}^2$ respectively. In both these cases, the ratio of the bending rigidities of the copper and the polyester yarns A_r is ~ 5 . The simplified model was employed to determine the bending rigidity of woven fabrics with certain number of copper yarns only in the warp direction with the rest being polyester yarns. The results of these theoretical calculations, for a plain woven fabric with 0, 2, 6, 8, 12, and 16 copper threads in the warp direction with the rest of the threads in the warp and weft directions being polyester threads, are shown in Figure 1. Figure 1 shows calculated values of flexural rigidity, normalized to the length of the fabric sample. A comparison between the theoretically calculated values and the

experimental data is also provided in Figure 6. All the values in the Figure 6, for both the theoretical and experimental plots, are normalized to the experimentally determined value of bending rigidity of a fabric having only polyester yarns in the warp and the weft directions. One can observe that the theoretical values of bending rigidity become increasingly higher than the corresponding experimental values with increase in the number of copper threads. The probable reason seems to be over-estimation of the copper yarn bending rigidity value.

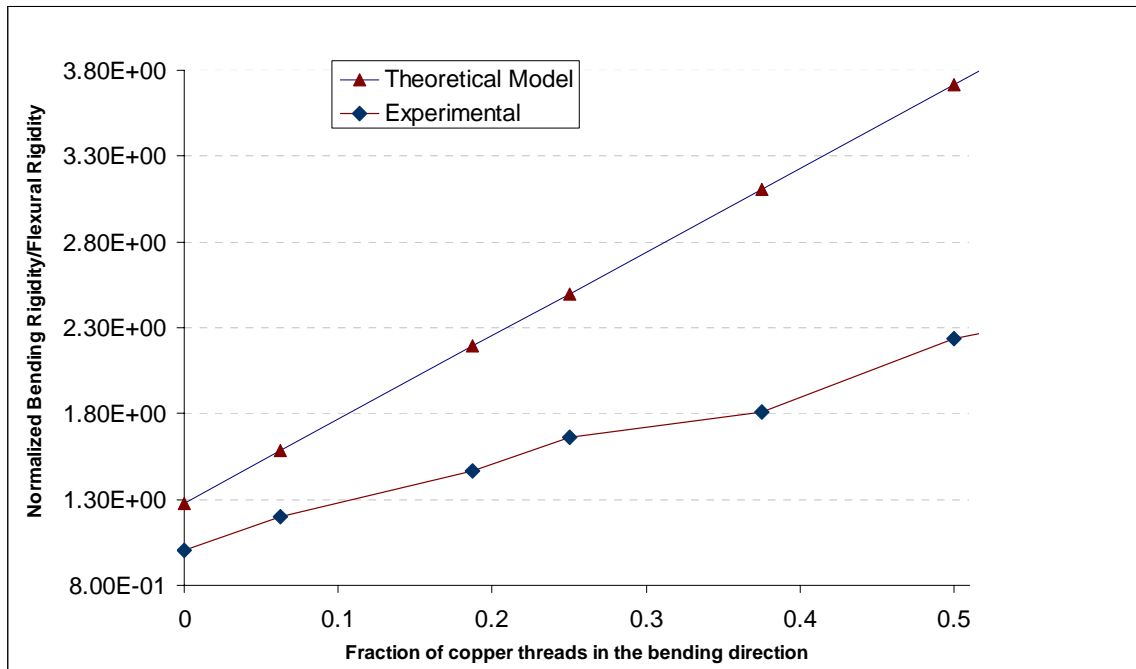


Figure 6. Experimental and calculated bending rigidity, values plotted as a function of fraction of copper threads in the direction of bending

4.4.2 Elastica Model

In order to determine the bending rigidity of the fabric using the elastic thread model, the first step was to determine the equilibrium shape of warp and weft yarns in a undeformed woven fabric. In order to determine the undeformed structure of the fabric, the ‘elastica’ equations were solved using appropriate boundary conditions. The equilibrium structure of a fabric was obtained for the planar fabric configuration, i. e. for bending angle, $\psi = 0$, (see Figure 4 of chapter 3) and for different value of bending angles for the different steps of bending. The values of the normalized fabric curvature, as obtained from equation 26, were also plotted as a function of the bending angle ψ and a

linear relationship between the bending angle ψ and the normalized fabric curvature (K_F) was obtained. Figure 7 shows the equilibrium fabric configurations, as a function of the normalized fabric curvature (K_F), for $A_r=1$.

In order to solve the boundary value problem for a conductive fabrics, the boundary conditions and equations were solved considering different ratios between the bending rigidities of the conductive and non-conductive threads employed in the fabric, i. e. for the value of $A_r = 1, 0.2, 5, 0.5$, and 2 . The evaluations were made for values of λ being 0.9 and 0.7 and value of L_r being unity.

The values of normal force at one of the boundaries, i. e. $F_{n1}(0)$, obtained for fabrics with different ratios of the bending rigidity of the warp and the weft threads (A_r) were obtained and plotted as a function of the normalized fabric curvature (K_F) as shown in Figure 8. In the different calculations, the bending direction was taken to be the warp direction. Moreover, it is observed that value of the normal force $F_n(0)$ is much higher when the value of A_r is less than unity i.e. when the warp threads are less rigid as compared with the filling yarns. This could be attributed to a higher resistance to bending imparted by the rigid filling yarns thereby resulting in a higher value of normal force at the boundaries.

The values of fabric bending rigidity, as a function of the normalized fabric curvature (K_F), were obtained for various values yarn bending rigidity, A_r , and are shown in Figure 9. It can be observed that fabric bending rigidity is much higher when the value of A_r is less than unity. This could be attributed to a higher resistance to bending imparted by the rigid cross weft threads thereby resulting in a higher value of fabric bending rigidity.

Yarn ‘elastica’ equations, subject to the appropriate boundary conditions, were solved for different values of A_r , corresponding to the different types unit cells that may be present in a fabric based circuit. These are all-polyester or all-copper fabric unit cells with $A_r = 1$, or polyester warp and copper weft unit cell with $A_r = 0.2$ (or 0.5 depending on size of the polyester and copper threads that are modeled), or copper warp and polyester weft unit cells with $A_r = 5$ (or 2 depending on size of the polyester and copper threads that are modeled), and the final case when copper (a rigid element) warp threads and copper (another rigid element) weft threads form a fabric unit cell and the value of $A_r = 1$.

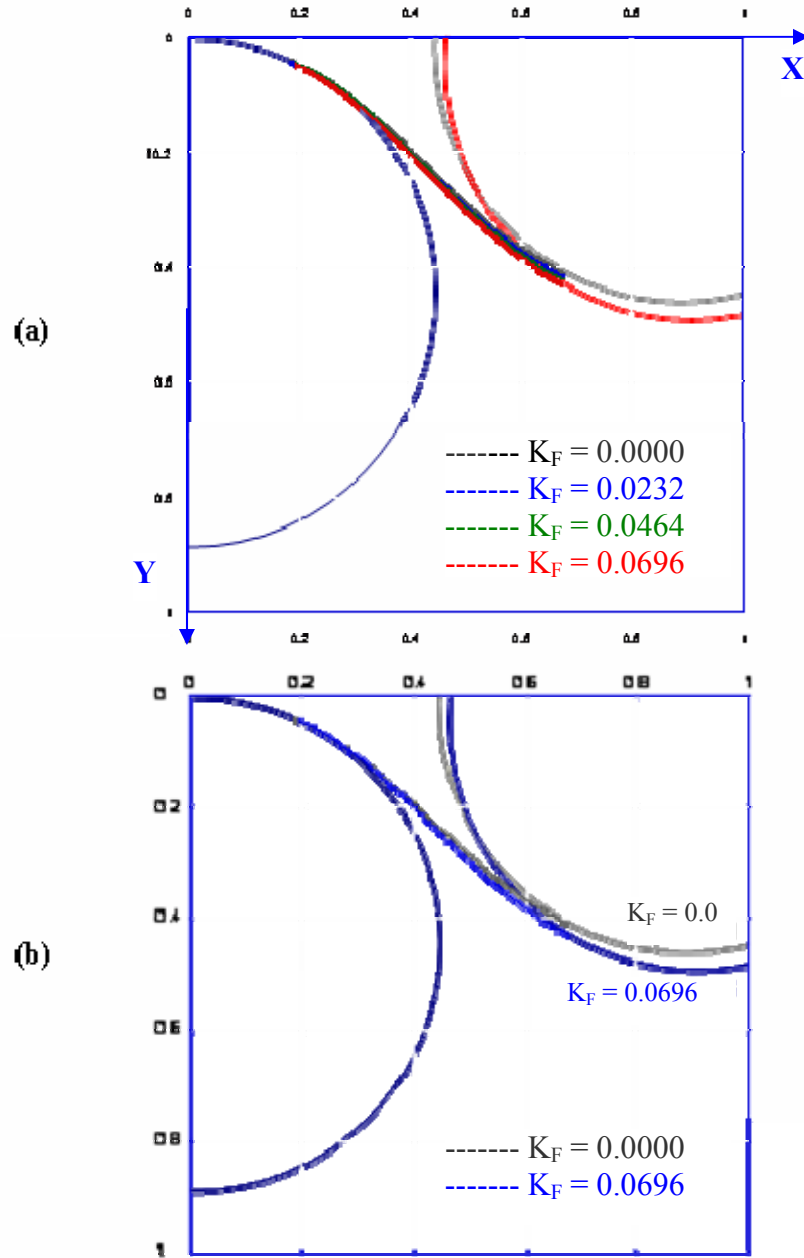


Figure 7. Equilibrium fabric configuration evaluated by solving the elastica equations described in section 4.2 for a unit cell with copper yarns in both warp and weft directions, (a) Warp yarn configuration for normalized fabric curvatures $K_F = 0.0000, 0.0232, 0.0464,$ and 0.0696 and (b) Close up view of the warp and weft yarn configurations for normalized fabric curvatures $K_F = 0.0000$ and 0.0696

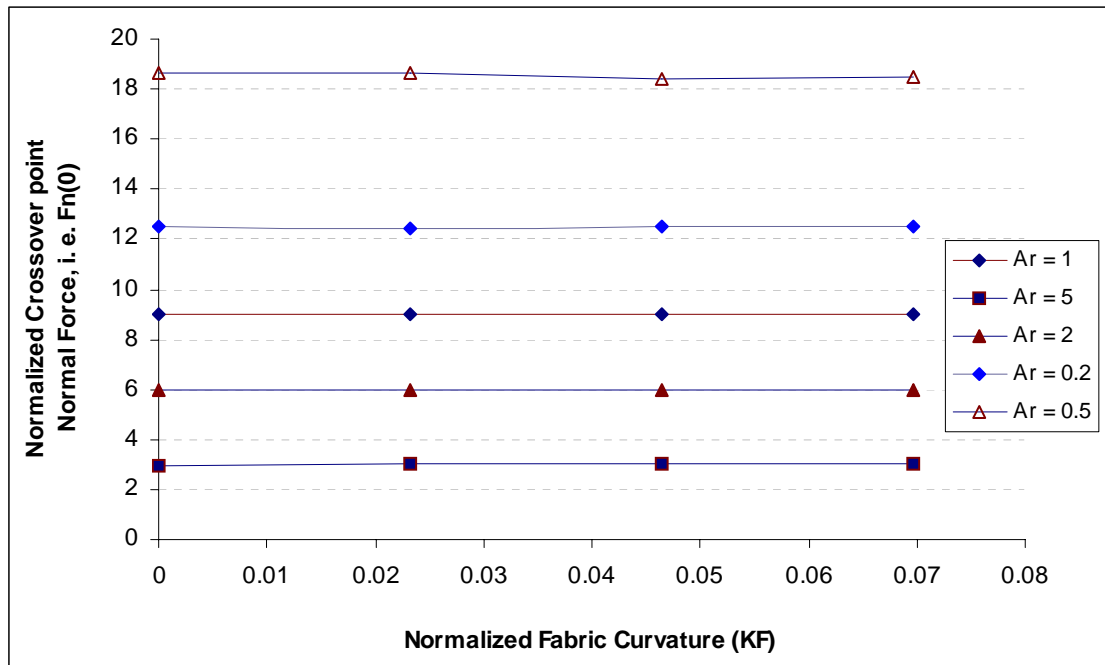


Figure 8. A plot showing values of normal force at the boundary of a fabric unit cell, i. e. $F_n(0)$, as a function of fabric bending angle. The plot shows the comparison of values evaluated for different values of A_r , i. e. ratio of bending rigidities of warp and weft threads

The values of normalized fabric bending rigidity (A_F/A_1) were obtained for the different categories described above. Equation 31 was then employed to determine the overall bending rigidity (A_F) of a conductive fabric for fabric samples with 180 total threads in weft direction and 96 total threads in the warp direction. As the pick density for the woven samples was taken as 30 picks per inch and the warp density as 32 ends per inch, the size of the samples evaluated was 6 inches by 3 inches. This size was selected because 6 inch long and 3 inch wide conductive fabric samples were fabricated for experimental evaluation of bending rigidity. The proportion of conductive copper threads in warp and weft directions was varied as values of the overall bending rigidity (A_F) of the conductive fabric were obtained. Theoretical evaluation of bending rigidity of conductive fabric samples were carried out by assuming the fabrics to be consisting of 29 fibers with each fiber having a diameter of 31.38 microns; and each polyester yarn consisting of 91 fibers with each fiber having a diameter of ~24.6 microns. The values yarn bending rigidity for copper and polyester yarns were determined using equation 2,

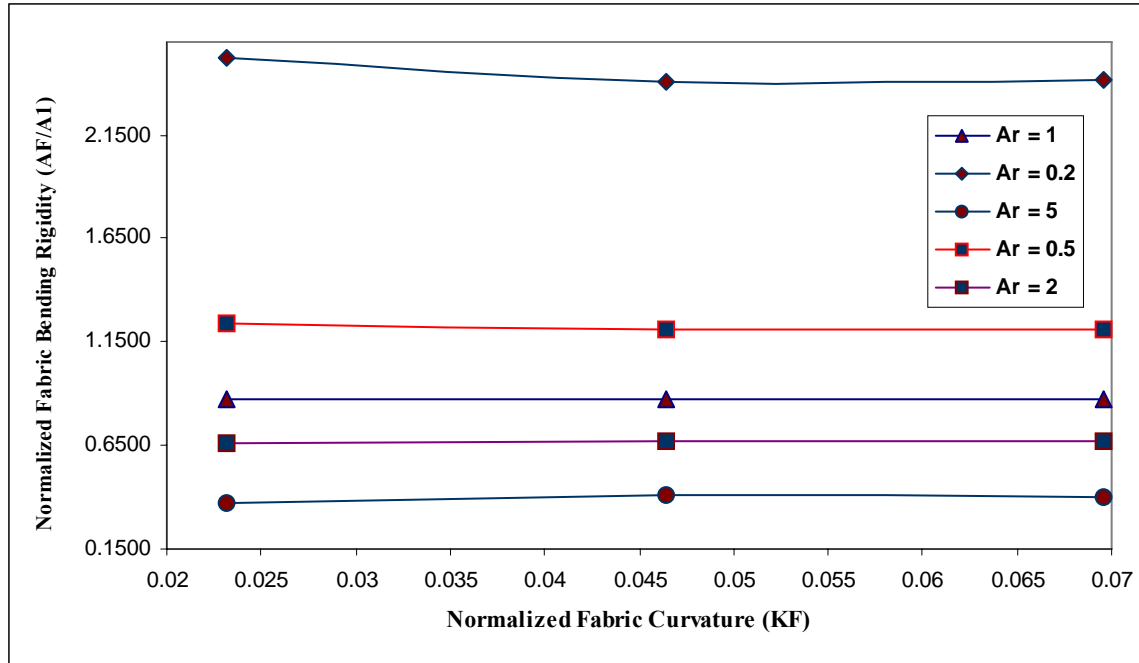


Figure 9. Plot showing normalized values of A_F/A_1 , i. e. ratio of fabric bending rigidity to yarn bending rigidity evaluated for each bending step by employing the energy method described in section 4.2, as a function of the normalized fabric curvature. The plot shows the comparison of values of A_F/A_1 evaluated for different values of A_r , i. e. ratio of bending rigidities of warp and weft threads 1

and were found to be $3.348 \times 10^{-6} \text{ N}\cdot\text{m}^2$ and $5.977 \times 10^{-7} \text{ N}\cdot\text{m}^2$ respectively, resulting in the ratio of the bending rigidities of the copper and the polyester yarns to be ~ 5 . In addition, bending rigidity values were calculated for fabrics containing rigid conductive and flexible polyester yarns, with the ratio of bending rigidity values equal to 2.

Results of varying the number of rigid conductive threads (copper yarns) in the weft direction when the density of rigid conductive threads in the warp direction is relatively low (0 and 4 copper yarns), are shown in Figures 10 and 11. Figure 10 shows these evaluations for the value of $A_r=2$ for some yarns (in the case when the copper warp yarns and polyester weft threads constitute the crossover point) and 0.5 for the others (in the case when the polyester warp yarns and copper weft threads constitute the crossover point) in a woven conductive fabric.

Figure 11 shows these evaluations for $A_r=5$ and 0.2. It can be observed in both these plots that the value of the overall bending rigidity of the conductive fabric circuit

increases as the number of copper threads in the weft direction is increased. It can be observed by comparing Figures 10 and 13 that the level of increase of the fabric bending

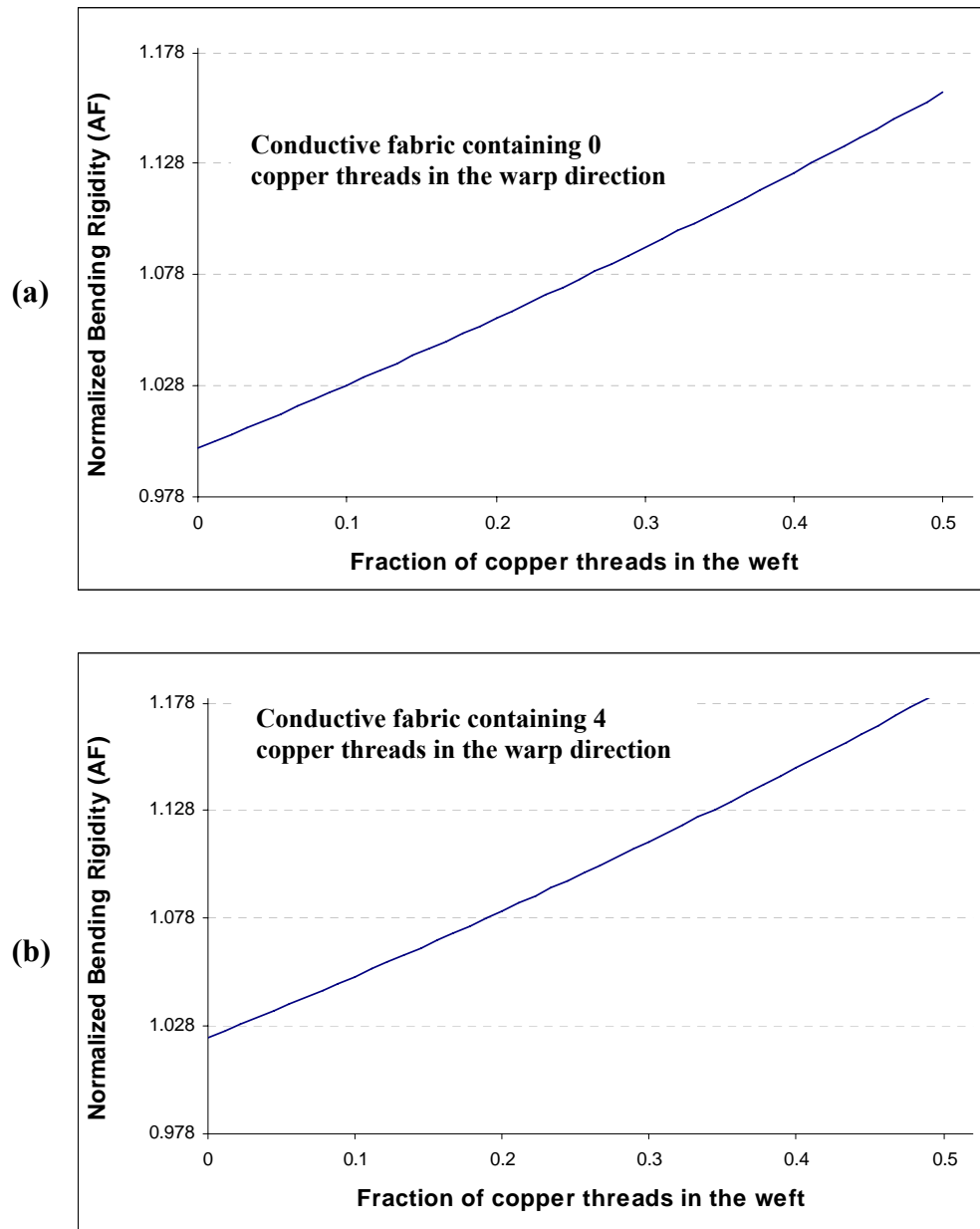


Figure 10. Plots showing the values of bending rigidities of plain woven conductive fabrics as a function of the number of copper weft threads for (a) 0 Copper warp threads and (b) 4 Copper warp threads, with the remaining threads in the warp and weft directions being polyester yarns. The ratio of the bending rigidity of the copper yarns to that of polyester yarns was taken to be 2 in these evaluations. In the fabric sample evaluated, the total number of warp threads was 96 and the total number of weft threads was 180. The normalization was carried out by dividing the value of the fabric bending rigidity by that of a fabric with no copper threads

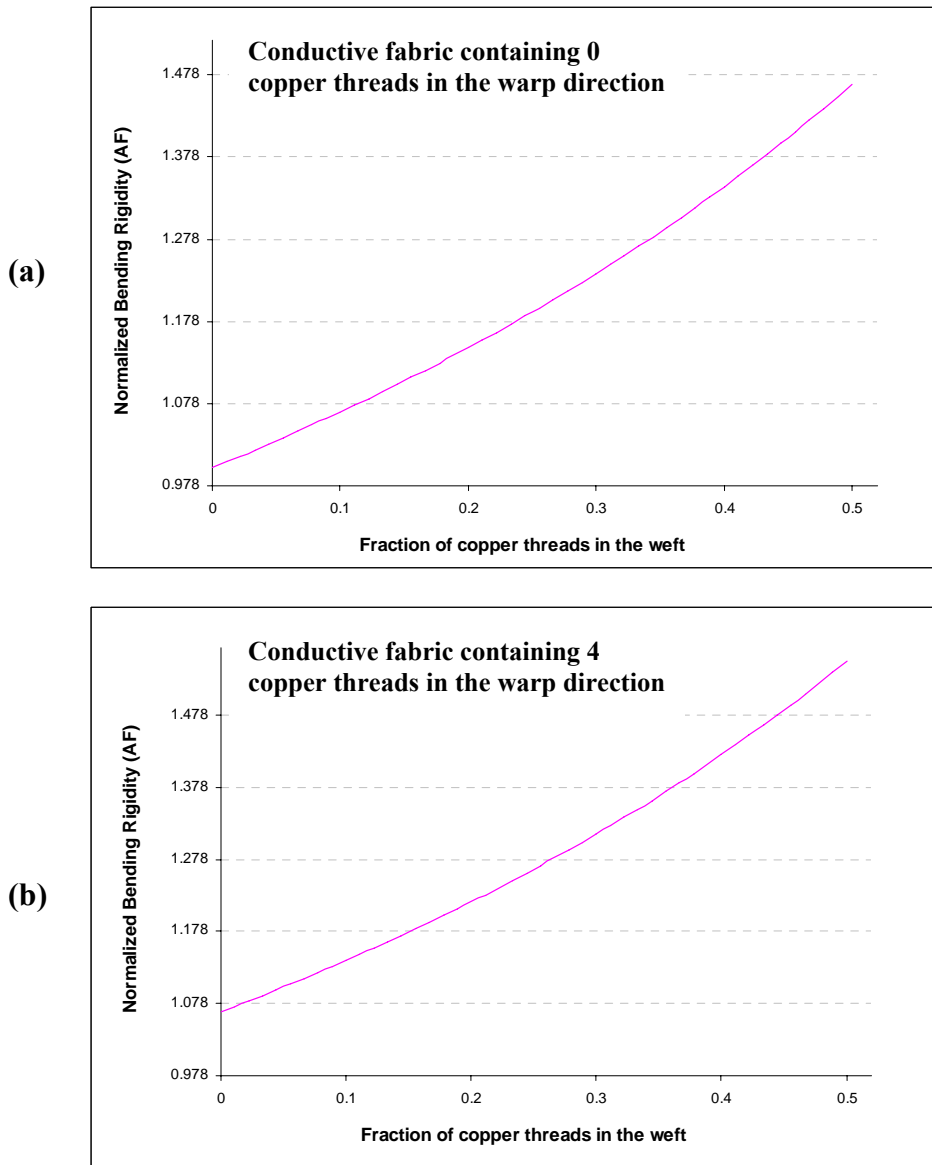


Figure 11. Plots showing the values of bending rigidities of plain woven conductive fabrics as a function of the number of copper weft threads for (a) 0 Copper warp threads and (b) 4 Copper warp threads, with the remaining threads in the warp and weft directions being polyester yarns. The ratio of the bending rigidity of the copper yarns to that of polyester yarns was taken to be 5 in these evaluations. In the fabric sample evaluated, the total number of warp threads was 96 and the total number of weft threads was 180. The normalization was carried out by dividing the value of the fabric bending rigidity by that of a fabric with no copper threads

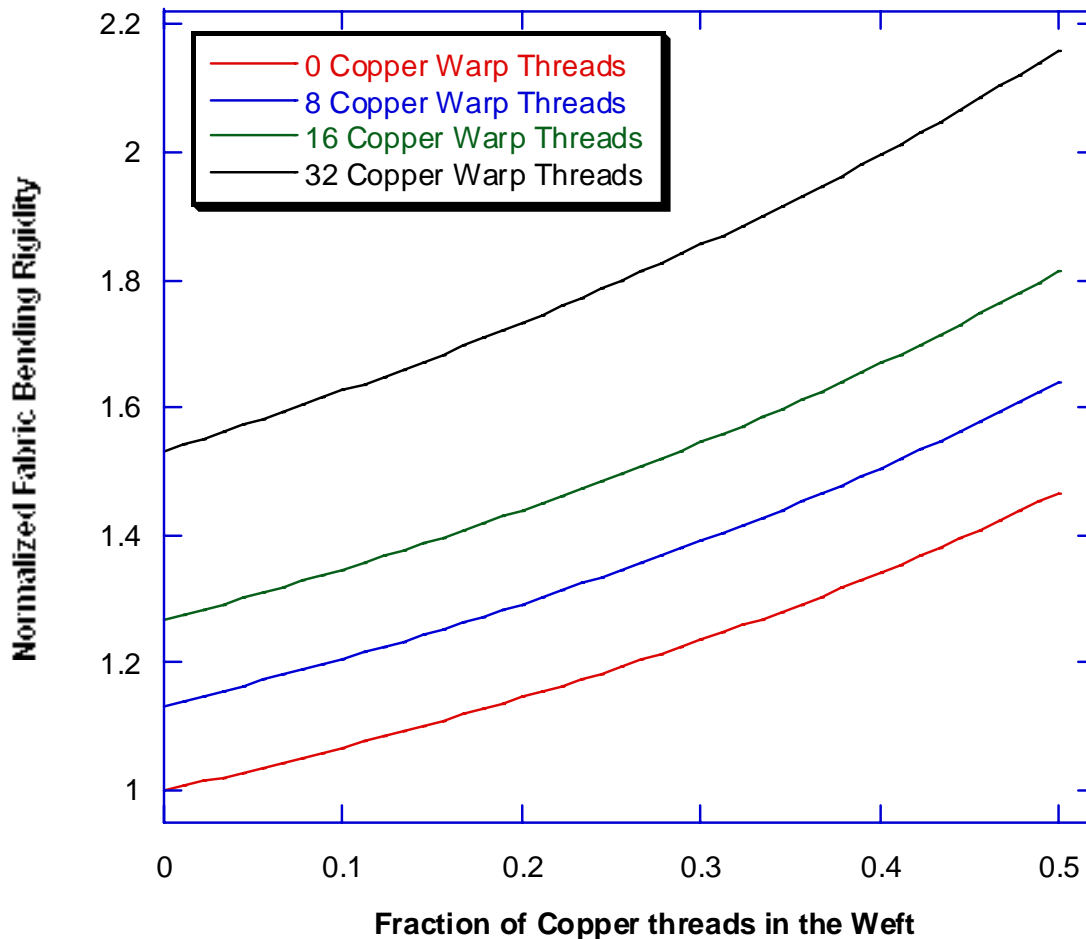


Figure 12. Plot showing the values of bending rigidities of plain woven conductive fabrics as a function of the number of copper weft threads with the fabric containing. The four fabrics evaluated had 0, 8, 16, and 32 copper threads in the warp direction. The ratio of the bending rigidity of the copper yarns to that of polyester yarns was taken to be 5 in these evaluations. In the fabric sample evaluated, the total number of warp threads was 96 and the total number of weft threads was 180

rigidity is higher in the case of fabrics where the ratio of bending rigidities of the copper and polyester yarns is 5 as compared with the fabrics in which the ratio of bending rigidities of the copper and polyester yarns is 2. This can be related to a higher value (~ 2.41) of A_F/A_I obtained for crossover points which have the A_r value equal to be 0.2 as compared to the case then the A_r value is equal to 0.5 (1.21) as is the case in some crossover points when the ratio of bending rigidities of the copper and polyester yarns is 2. It is also observed from Figures 10 and 11 that the increase in the conductive fabric bending rigidities, relative to the bending rigidity of fabrics having no conductive thread

in the weft direction, when the proportion of the conductive threads in the weft direction is increased is lower for fabrics having more threads in the warp direction. This could be attributed to the conductive fabric having a greater number of crossover points with a value of A_r greater than 1 (5 or 2 respectively in the two fabric samples evaluated) when more copper threads are present in the warp direction (the bending direction). This leads to the fabric having more fabric crossover points having a lower value of A_F/A_1 ; as the value of A_F/A_1 for a fabric with $A_r = 5$ is ~ 0.406 (for a fabric with $A_r = 2$, the value of A_F/A_1 is ~ 0.673) as compared with a fabric with $A_r = 0.2$, when the A_F/A_1 value is ~ 2.41 (or a fabric with $A_r = 0.5$, the A_F/A_1 value is ~ 1.21). Despite this observation, the magnitude of fabric bending rigidity (A_F) is higher for fabrics having a greater number of rigid copper threads in the warp direction, which is the direction of fabric bending, due to a higher value of yarn bending rigidity (A_1) associated with the copper yarns, as shown in Figure 12. Another observation that can be made from Figure 12 is that the relationship between the fabric bending rigidity and the number of copper threads in the weft direction is not linear.

In order to experimentally determine the bending rigidity of the woven conductive fabric structures, the Cantilever bending test was employed. In the Cantilever bending test, woven fabric structures were cut into 6 inches long and 1 or 3 inch wide test samples and the value of overhang length, as shown in Figure 5, was determined by sliding the fabric samples on an inclined surface in the direction shown in the figure. Cantilever bending test was performed on plain woven fabric samples having 0, 2, 4, 5, 6, and 7 copper yarns in the warp direction, the rest of the threads in the warp and weft directions being polyester threads. The results of these evaluations are provided in Figure 13, which provides a comparison between the experimental results and theoretical calculations performed for fabric samples having the same number of copper and polyester threads as the experimental samples. These results were normalized to the experimentally obtained bending rigidity value for a fabric sample having no copper thread in either warp or weft direction and the determined values were plotted as a function of the fraction of copper threads in the warp direction. In all the plots, theoretical as well as experimental, the value of fabric bending rigidity (A_F) is found to increase as the proportion of rigid copper threads in the warp direction is increased. One can observe in Figure 13 that the

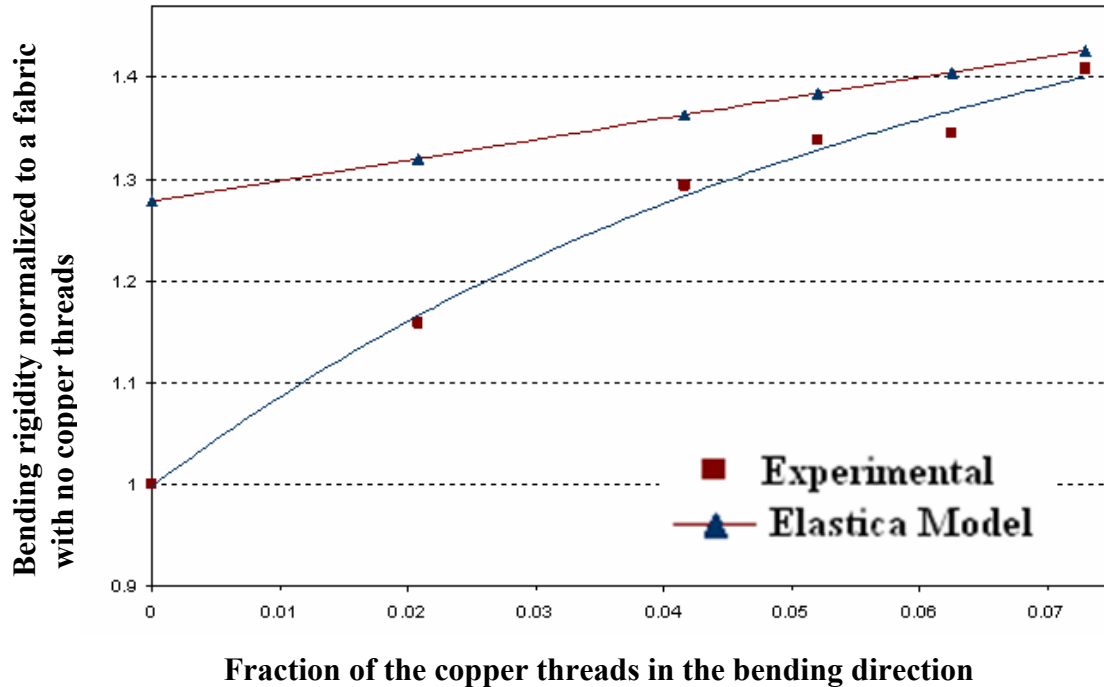


Figure 13. Comparison of fabric bending rigidity values that are evaluated experimentally and those that are determined theoretically by employing the elastica model

normalized bending rigidity values obtained theoretically, by employing the elastica model, are higher than the values determined experimentally, for all values of the proportion of copper threads as a function of total number of warp threads in the fabric sample. The theoretical results obtained by employing the elastica are close to the experimentally obtained values, especially for higher fraction of copper threads in the bending direction. These could be attributed to the fact that the elastica model considers the effect of the crossover yarns on the value of bending rigidity of the fabric resembles the actual bending behavior of the fabric. Differences in the values of bending rigidity, obtained experimentally and those obtained theoretically by employing the elastica model, can be explained by the fact that several assumptions were made in the elastica model such as yarns being circular and incompressible, which is not the actual case of yarns in the crossover point regions. Moreover, yarn bending behavior was assumed to be linear in all our theoretical evaluations, which may not be the case as the yarn bending behavior can be non-linear – more specifically bi-linear [15-17]. These considerations will be accounted for in future calculations of bending rigidity of conductive fabrics.

4.5 References

1. E. R. Post, M. Orth, P. R. Russo, and N. Gershenfeld, "E-broidery: Design and fabrication of textile-based computing," *IBM Systems Journal*, 39(3 & 4), 840-860, 2000.
2. E. R. Post and M. Orth, "Smart Fabric or Washable Computing," *Proc. First International Symposium on Wearable Computers*, Cambridge, MA, Proc. of the IEEE Computer Society, 167-168, 1997.
3. M. Orth and E. R. Post, "Smart fabric or wearable clothing," *Proc. of the First International Symposium on Wearable Computers*, 13-14, Oct 1997.
4. L. W. Adams, Jr., M. W. Gilpatrick, and R. V. Gregory, "Fabric having non-uniform electrical conductivity," US Patent 5316830, 1992.
5. A. Dhawan, T. K. Ghosh, A. M. Seyam, and J. F. Muth, "Woven Fabric-based Electrical Circuits Part I: Evaluation of Interconnect Methods," *Textile Research Journal*, October, 2004.
6. A. Dhawan, T. K. Ghosh, A. M. Seyam, and J. F. Muth, "Woven Fabric-based Electrical Circuits Part II: Yarn and fabric structures to reduce crosstalk noise in woven fabric-based circuits," *Textile Research Journal*, In Press, to be published in November, 2004.
7. A. Dhawan, T. K. Ghosh, A. M. Seyam, and J. F. Muth, "Woven Fabric-based Electrical Circuits," *Proc. of Textile Technology Forum*, IFAI and the Textile Institute, Charlotte, NC, 2002.
8. A. Dhawan, "Woven fabric-based electrical circuits," *Masters Thesis*, North Carolina State University, 2001.
9. A. Dhawan, T. K. Ghosh, A. M. Seyam, and J. F. Muth, "Development of Woven fabric-based electrical circuits," *Proc. of the Materials Research Society Conference Symposium D*, Boston, 2002.
10. A. Dhawan, T. K. Ghosh, A. M. Seyam, and J. F. Muth, "Formation of Electrical Circuits in Woven Structures," *Proc. of the International Interactive Textiles for the Warrior Conference* organized by the Soldier and Biological Chemical Command, NASA, & DARPA, Cambridge, MA, July 9-11, 2002.
11. T. Kirstein, D. Cottet, J. Grzyb, G. Tröster, "Textiles for Signal Transmission in Wearables," *Proc. of the Workshop on Modeling, Analysis and Middleware Support for Electronic Textiles (MAMSET)*, In conjunction with ASPLOS-X (Tenth International Conference on Architectural Support for Programming Languages and Operating Systems), San Jose, California, October 6, 2002.

12. D. Cottet, J. Grzyb, T. Kirstein, and G. Tröster, "Electrical Characterization of Textile Transmission Lines," IEEE Transactions on Advanced Packaging, Vol. 26, No. 2, May 2003, pages 182-190.
13. I. Locher, T. Kirstein and G. Tröster, "Electronic Textiles," Proc. of ICEWES Conference, Cottbus, Germany, December 2002.
14. J. Slade, M. Agpaoa-Kraus, J. Bowman, A. Riecker, T. Tiano, C. Carey, and P. Wilson, "Washing of Electrotiles," Proceedings of the Materials Research Society Conference Symposium D, Boston (2002).
15. T. K. Ghosh, R. L Barker, and S. K. Batra, "On the Bending Behavior of Plain Woven Fabrics, Part I: A Critical Review," Textile Institute Journal, 81, 255-271, 1990.
16. T. K. Ghosh, R. L Barker, and S. K. Batra, "On the Bending Behavior of Plain Woven Fabrics, Part II: The Case of Linear Yarn Bending Behavior," Textile Institute Journal, 81, 272-287, 1990.
17. T. K. Ghosh, R. L Barker, and S. K. Batra, "On the Bending Behavior of Plain Woven Fabrics, Part III: The Case of Bi-Linear Yarn Bending Behavior and the Effect of Fabric set," Textile Institute Journal, 81, 288-299, 1990.
18. F. T. Pierce, "The geometry of cloth structure," J. Text. Inst., 28, T45, 1937.
19. G. A. V. Leaf, "The bending behaviour of a helical filament. Part II: curvature, twist and strain energy," J. Text. Inst., 70, 323-336, 1979.
20. N. J. Abbot, M. J. Coplan, and M. M. Platt, "Theoretical considerations of bending and creasing in a fabric," J. Text. Inst., 51, T1384, 1960.
21. M. Konopasek, "On Large Bending and Torsional Deformations of Fibers in Space," Textile Research Journal, 42, 586-589, 1972.
22. P. Szablewski and W. Kobza, "Numerical Analysis of Peirce's Cantilever Test for the Bending Rigidity of Textiles," Fibres & Textiles in Eastern Europe, 11 (4), 54-57, 2003.
23. Annual Book Of ASTM Standards-Section 7: Textiles

CHAPTER 5

BENDING RIGIDITY OF WOVEN

FABRIC-BASED ELECTRICAL STRUCTURES.

PART II: EFFECT OF WELDING/SOLDERING CROSSOVER POINTS OF CONDUCTIVE THREADS WOVEN IN THE FABRIC STRUCTURE

Bending Rigidity of woven fabric-based electrical structures. Part II: Effect of welding/soldering crossover points of conductive threads woven in the fabric structure
(A paper to be published in the Journal of Textile Institute)

Abstract

Electrical circuits were developed in woven fabric substrates by interlacing conductive and non-conductive threads and by forming interconnections at crossover points of orthogonal conductive threads to achieve a desired signal path in the fabric. These crossover point interconnects can be developed by employing welding techniques such as resistive and laser welding to fuse the orthogonal conductive threads, by soldering, or by employing conductive adhesives. In this paper, the effect of crossover point interconnects on the bending stiffness of a fabric circuit is discussed. A theoretical model is developed to determine the bending rigidity of woven fabric circuits as a function of crossover point interconnect density. Energy method is employed to determine the bending rigidity of woven fabric unit cells consisting of combinations of conducting and nonconducting threads as well as constrained or unconstrained cross-over points. Bending rigidity of a woven fabric circuit is subsequently modeled as series and parallel combinations of the bending rigidities associated with the constrained/unconstrained crossover points of different combinations of conductive and non-conductive threads in a fabric circuit. To validate the theoretical model described in this paper, experimental measurements were carried out on woven fabric samples containing several crossover points that are bonded by a conductive adhesive.

5.1 Introduction

A woven fabric circuit consists of conductive and non-conductive threads interlaced according to a given circuit design such that the conductive threads act as signal carriers and the non-conductive threads provide separation between conductive threads to prevent shorting [1-7]. In a woven circuit, if an electrical signal has to be routed from one conductive thread to an orthogonal thread, the current has to flow through the crossover point of these threads. Efficient current transfer between orthogonal conductive threads is possible by means of appropriate interconnect through the use of conductive adhesive

bonding, resistive welding, soldering, air splicing, and ultrasonic bonding [1-7]. Dhawan et al. [1-6] have previously described the use of resistive welding for the formation of interconnects at the crossover point. Formation of effective crossover point interconnects also leads to a reduction in impedance and parasitic capacitance values associated with the crossover points. Fabric based electrical circuits are likely to be used in applications where they are subject to deformation, such as bending or extension, and it is preferable that the interconnects be sufficiently robust so that the DC resistances and impedances associated with the crossover points remain constant at all times. Having known values of resistances and impedances associated with the crossover point interconnects can help to design fabric circuits better as appropriate loads or impedance matching elements can be attached to these circuits.

One application of fabric circuits is to embed electronic devices, such as transmitters, receivers, displays, and some signal processing devices, into garments worn by individuals. Along with the military applications, wearable electronics could be applied to several other fields such as biomedical engineering, medicine, homeland security/public safety, transportation, and to consumer products. Conformability and drape of fabric circuits are significantly dependent on the fabric bending rigidity. Formation of crossover point interconnects, can lead to a stiffer fabric as these interconnects (welds, bonds, etc.) may restrict relative movement of yarns within it. If the formation of crossover point interconnects is carried out using conductive adhesives or solders, the added weight of the adhesives or solders can also lead to the fabric becoming more stiff. If the density of crossover point interconnects in a fabric circuit is high, the increase in bending stiffness due to these interconnects could make a wearable electronic garment, manufactured from these fabrics, uncomfortable to wear. Hence, it is important to develop fabric circuits, for wearable electronic applications, that are flexible and conformable despite the presence of rigid conductive threads or crossover point interconnects. In order to elucidate the influence of crossover point interconnects on the stiffness of the fabric circuits, a theoretical model has been developed.

In the theoretical model described in this chapter, energy method is employed to determine the bending rigidity of a woven fabric unit cell containing cross-over point interconnects. Bending rigidity of woven fabric circuits is modeled as series and parallel

combinations of the bending rigidities associated with the constrained and unconstrained crossover points involving conducting and non-conducting threads. Experimental validation of the model, described in this chapter, was carried out by characterizing bending stiffness of various woven fabric circuit samples.

5.2 Theoretical Model to determine bending rigidity of a woven fabric circuit

In an analysis presented earlier [8-10], the authors proposed an elastica based model to describe equilibrium fabric structure as well as its bending behavior. The details of the analysis can be found in reference 8; however, key elements of the model are included here for completeness. The fabric unit cell is shown in Figure 1. The equilibrium equations of the elastica based model describing the shape of the threads are,

$$\frac{\partial}{\partial S} F_{n_j}(S) = K_j(S).F_{t_j}(S) \quad (1)$$

$$\frac{\partial}{\partial S} K_j(S) = F_{n_j}(S) \quad (2)$$

$$\frac{\partial}{\partial S} F_{t_j}(S) = -K_j(S).F_{n_j}(S) \quad (3)$$

$$\frac{\partial}{\partial S} t_{y_j}(S) = K_j(S).t_{x_j}(S) \quad (4)$$

$$\frac{\partial}{\partial S} t_{x_j}(S) = -K_j(S).t_{y_j}(S) \quad (5)$$

$$\frac{\partial}{\partial S} X_j(S) = t_{x_j}(S) \quad (6)$$

$$\frac{\partial}{\partial S} Y_j(S) = t_{y_j}(S) \quad (7)$$

$$t_{y_j}^2(S) + t_{x_j}^2(S) = 1 \quad (8)$$

where the subscript j is equal to 1 for the warp and 2 for the weft threads.

The equations 1-8 are presented in their nondimensional form. Parameters F_n and F_t are normal and shear forces as shown in Figure 1, K is the curvature, and S is the independent curve length parameter. Expressed in terms of dimensional parameters these are:

$$\begin{aligned}
Fn_i &= \frac{fn_i}{A} l_1^2, Ft_i = \frac{ft_i}{A} l_1^2, K_i = k_i l_1, X_i = \frac{x_i}{l_1}, \\
Y_i &= \frac{y_i}{l_1}, S_i = \frac{s_i}{l_1}, D_i = \frac{d_i}{l_1}, L_r = \frac{l_1}{l_2}, H_i = \frac{h_i}{l_1}
\end{aligned} \tag{9}$$

where l_1 is the length of a warp yarn in one unit cell of a plain woven fabric as shown in Figure 1 and A_j is the bending rigidity of the yarns. In all cases, the small cases represent the equivalent dimensional terms. The subscript 'i' in equation 9 is equal to 1 for the warp and 2 for the weft threads. In order to obtain the equilibrium fabric structure, one has to simultaneously solve the fourteen differential equations using appropriate boundary conditions [8-10].

In the analysis presented earlier in chapter 4, equilibrium bent fabric configurations of woven circuits were determined for fabrics that contained no interconnects at the crossover points of conductive threads. In that analysis, an unconstrained change in the wrap angles was assumed as the fabric was bent (see Figure 1). In the analysis of the same fabric structure with interconnects at the crossover points of conductive threads, the angles of wrap (β_{1_1} , β_{2_1} , β_{1_2} , and β_{2_2}) are constrained and accordingly the boundary conditions are modified appropriately.

In the case of a fabric with unconstrained crossover points, the angles of wrap i.e. β_{1_1} , β_{2_1} , β_{1_2} , and β_{2_2} for a fabric bent by an angle ψ (the fabric being bent in the warp direction) were defined as:

$$\begin{aligned}
\beta_{1_1} &= \beta_{1_{10}} + \psi \\
\beta_{2_1} &= \beta_{2_{10}} - \psi \\
\beta_{1_2} &= \beta_{1_{20}} \\
\beta_{2_2} &= \beta_{2_{20}}
\end{aligned} \tag{10}$$

where $\beta_{1_{10}}$, $\beta_{2_{10}}$, $\beta_{1_{20}}$, and $\beta_{2_{20}}$ are angles of wrap for an unbent fabric.

In the case of a fabric with constrained crossover points, the angles of wrap i.e. β_{1_1} , β_{2_1} , β_{1_2} , and β_{2_2} for a fabric bent by angle ψ were defined as:

$$\begin{aligned}
\beta_{1_1} &= \beta_{1_{10}} + \psi \\
\beta_{2_1} &= \beta_{2_{10}} \\
\beta_{1_2} &= \beta_{1_{20}} \\
\beta_{2_2} &= \beta_{2_{20}}
\end{aligned} \tag{11}$$

where β_{10} , β_{20} , β_{120} , and β_{220} are angles of wrap for an unbent fabric.

The values of curve length parameters, S_{11} , S_{12} , S_{21} , and S_{22} as defined in Figure 1, are determined by the angle of wraps, β_{11} , β_{21} , β_{12} , and β_{22} . The boundary conditions, that are required to solve equations 1-8, describing the equilibrium fabric structure, depend on the angle of wrap of the warp and weft yarns at the crossover points i. e. on the values of β_{11} , β_{21} , β_{12} , and β_{22} shown in Figure 1. There are different cases of boundary conditions arising from the combination of values of β_{11} , β_{21} , β_{12} , and β_{22} . These boundary conditions were described earlier in detail by Ghosh et al. [8] and were discussed in chapter 3

In this chapter, the equilibrium structure of a fabric is obtained for the planar fabric configuration, i. e. for $\psi = 0$ and for different values of bending angle for the different steps of bending. As mentioned earlier, the boundary conditions in unbent configuration differ from those in bent configuration. As the fabric is bent, it may transition from one case to another. Hence, the conditions of angles of wrap are verified at every step of fabric bending and the boundary conditions for the appropriate case are applied to solve equations 1-7. The ‘elastica’ equations 1-7 contain fourteen first order differential equations and eleven known boundary conditions [1-2]. In order to solve the boundary value problem, one needs to guess the unknown boundary conditions at the first boundary, i. e. at $S = S_1$ shown in Figures 3 and 4 of chapter 3, and make adjustments to the guessed values such that the boundary conditions at the second boundary, i. e. at $S = S_2$, are satisfied. At each step when the guesses are made, the fourteen differential equations subject to the known and guessed boundary values are solved by employing the Fourth order Runge-Kutta-Fehlberg (RKF) method. We employed an inbuilt RKF solver in Maple 10 to solve the differential equations subject to the boundary conditions.

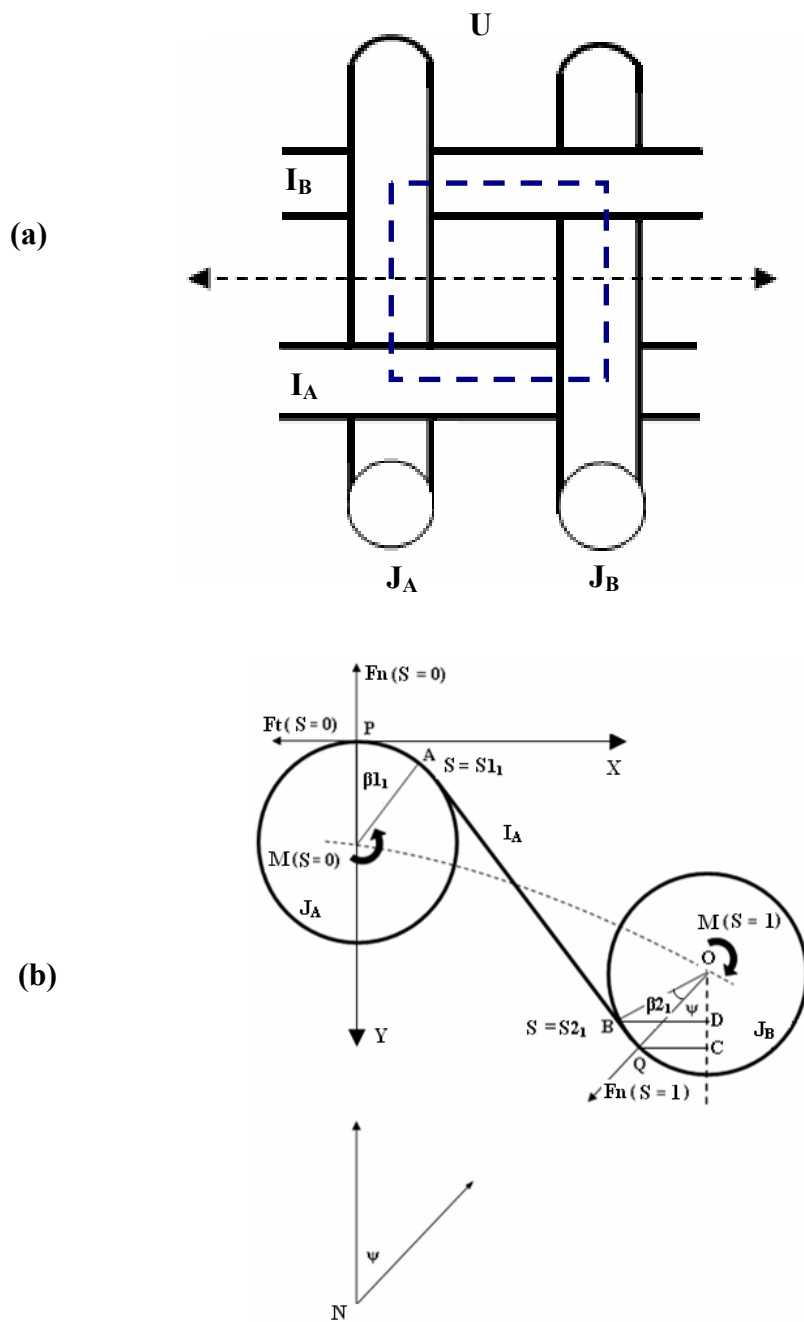


Figure 1. (a) Schematic of a part of a plain woven fabric highlighting a unit cell, and (b) Schematic of equilibrium fabric configuration for a fabric bent by an angle ψ . The schematic shows a warp yarn I , going over and under two weft yarns, in the X, Y plane

Solutions were obtained for various values of yarn bending rigidity, using $A_r = 0.2, 5, 0.5,$ and 2 . In obtaining equilibrium fabric structures for bent fabrics having no constrained cross-over points, the boundary conditions were selected such that the value of angle of wrap β_{1_1} increased and the value of angle of wrap β_{2_1} decreased, as the fabric was bent in the warp direction. These boundary conditions could be considered if both β_{1_1} and β_{2_1} are not equal to zero in the initial condition of the fabric. This boundary condition is described by equation 10 earlier in this section. In the case of constrained crossover points in a bent fabric, different boundary conditions related to the angles of wrap were considered, as described by equations 11, such that the value of β_{2_1} remains the same as the fabric is bent in the wrap direction, while the value of β_{1_1} increases.

In order to determine bending rigidity of a woven fabric, the principle of conservation of energy was employed. The total strain energy due to bending is sum of the energy stored in the crossover regions, i. e. the region PA in Figure 1b, and the free regions (region AB in Figure 1b). The change in the total strain energy is equal to the overall work done by an externally applied bending moment to bend the fabric through angle ψ . This method has been described by Ghosh et al. [8-10] and was discussed in detail in chapters 3 and 4.

In order to determine the bending rigidity of a woven fabric circuit, containing constraints at certain crossover points of orthogonal conductive threads, the fabric circuit was assumed to be a series and/or parallel combination of various types of fabric unit cells (or cross-over points) as shown in Figure 2. In the example presented in Figure 2, crossover points, at the intersection of row 1 & column 1 and the one formed at the intersection of row 1 & column 2, are in series. The crossover points, at the intersection of row 1 & column 1 and the one formed at the intersection of row 2 & column 1, are in parallel with each other. In Figure 2, the direction of bending is taken as the warp direction. In order to determine the bending rigidity of the overall fabric, the bending rigidity of each row in the plane of bending was first computed by taking the crossover points to be in series with each other. This was followed by computation of the bending rigidity of the overall fabric, consisting of several rows, by considering the different rows to be in parallel. If the fabric circuit is made from copper and polyester threads, having

constraints at certain crossover points of orthogonal copper threads as shown in Figure 2, there are five different categories of crossover points in this fabric:

- A. Unconstrained, i. e. not welded, soldered, or fused, polyester warp thread (the flexible element) and the polyester weft thread.
- B. Unconstrained polyester warp thread & copper (i.e. the rigid element) weft thread
- C. Unconstrained copper warp thread & polyester weft thread
- D. Unconstrained copper warp thread & copper weft thread
- E. Copper warp thread & copper weft thread and the crossover point is constrained by the welding, soldering, or fusion of the orthogonal copper threads

As an example, one can observe in Figure 2 that the third row consists of crossover points that fall in the categories D, C, C, E, C, and C. Bending rigidity for the different categories A-E are computed by assuming that the entire unit cell, as described earlier in Figure 2 of chapter 3, corresponds to that category. Hence, category 'B' implies that a unit cell consists of two polyester warp threads and two copper weft threads. Similarly, category 'C' implies that a unit cell consists of two copper warp threads and two polyester weft threads. As the ratio of the bending rigidities of copper and polyester yarns is greater than 1, the appropriate values of $A_r (=A_1/A_2$, where A_1 and A_2 are the bending rigidities of the warp and weft yarns respectively) are employed for calculation of bending rigidities in the different categories described above. Different values of A_r that are assumed for the different categories for the purpose of theoretical calculations are:

- A. Unconstrained polyester warp thread & polyester weft thread: $A_r = 1$
- B. Unconstrained polyester warp thread & copper weft thread: $A_r = 0.2$ (or 0.5 depending on size of the polyester and copper threads that are modeled)
- C. Unconstrained copper warp thread & polyester weft thread: $A_r = 5$ (or 2, depending on size of the polyester and copper threads that are modeled)
- D. Unconstrained copper warp thread & copper weft thread: $A_r = 1$
- E. Copper warp thread & copper weft thread: $A_r = 1$, but the crossover point is constrained (i. e. welded, fused, or bonded)

The values of A_F/A_1 , i.e. the normalized fabric bending rigidity were obtained for the different categories described above and then the value of A_F was obtained for each of those categories by multiplying by the value of A_F/A_1 determined for that category by appropriate A_1 for the category

One can obtain a generalized formula for determining the bending rigidity of the overall fabric if the values of A_F for the different categories are known, by considering a series and parallel combination of these cells. Formula employed for the calculation of the overall bending rigidity (A_F) of a conductive fabric was derived to be:

$$A_F(\text{Fabric}) = [N_{wa} - N_{cwa}] * \frac{N_{we}}{\left[\left(\frac{N_{cwe}}{A_{pc}} \right) + \left(\frac{N_{we} - N_{cwe}}{A_{pp}} \right) \right]} + \sum_{icwa=1}^{N_{cwa}} \frac{N_{we}}{\left\{ \left[(1/A_{pc}) * (N_{we} - N_{cwe}) \right] + \left[(1/A_{ccw}) * (N_{cwe}_{icwa}) \right] + \left[(1/A_{ccw}) * (N_{cwe} - N_{cwe}_{icwa}) \right] \right\}} \quad (12)$$

where N_{cwa} is the number of copper warp threads, N_{wa} is the number of warp threads in the fabric, N_{cwe} the number of copper warp threads in the fabric, N_{we} is the total number of weft threads, N_{cwe}_{icwa} is the number of constrained crossover points of orthogonal copper yarn on the $icwa^{\text{th}}$ copper warp thread. Equation 12 reduces to the following equation if constraints formed on all the copper warp threads are symmetric; i. e. number of constrained crossover points in all the warp threads is the same:

$$A_{F_{\text{Overall_Fabric_Circuit}}} = [N_{wa} - N_{cwa}] * \frac{N_{we}}{\left[\left(\frac{N_{cwe}}{A_{pc}} \right) + \left(\frac{N_{we} - N_{cwe}}{A_{pp}} \right) \right]} + [N_{c_wa}] * \frac{N_{we}}{\left[\left(\frac{N_{cwe} - N_{cwe}}{A_{cc}} \right) + \left(\frac{N_{we} - N_{cwe}}{A_{cp}} \right) + \left(\frac{N_{welded}}{A_{ccw}} \right) \right]} \quad (13)$$

where N_{welded} is the number of weft threads for which all the crossover points of copper threads are constrained.

Based on the model described above, theoretical evaluations for the overall bending rigidity of conductive fabric samples were carried out such that the samples analyzed theoretically were similar in size to the samples evaluated experimentally. The main objective of these theoretical calculations was to isolate and study the effect of increasing the density of constraints, at the crossover points of orthogonal copper threads, in a

woven fabric circuit for different densities of copper and polyester threads in warp and weft directions. The length of the samples evaluated theoretically was six inches and evaluations for two different widths, one inch and three inches, were carried out. Hence, the total number of weft threads in the samples evaluated theoretically was taken to be 180, taking the pick density to be 30 threads per inch. The total number of warp threads was taken to be 32 for the one inch wide samples and 96 for the three inch wide samples. A schematic, depicting one of the samples that were analyzed for theoretical calculations, is shown in Figure 3. Results of the theoretical calculations are described in section 5.4.

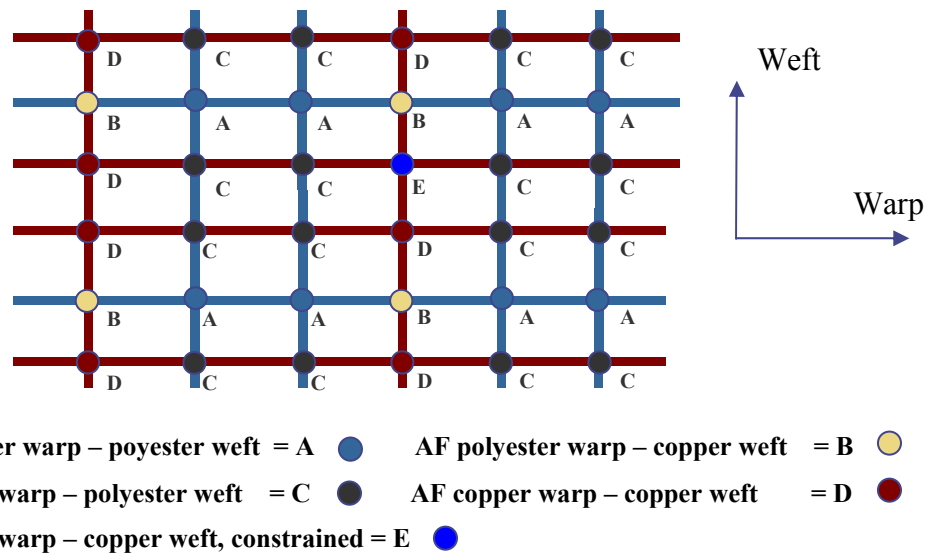


Figure 2. Schematic demonstrating the procedure employed to determine bending rigidity of fabric circuits. Bending rigidity of a fabric circuit is modeled as series and parallel combination of the bending rigidities associated with different sections, each section consisting of a crossover point, as shown in this figure

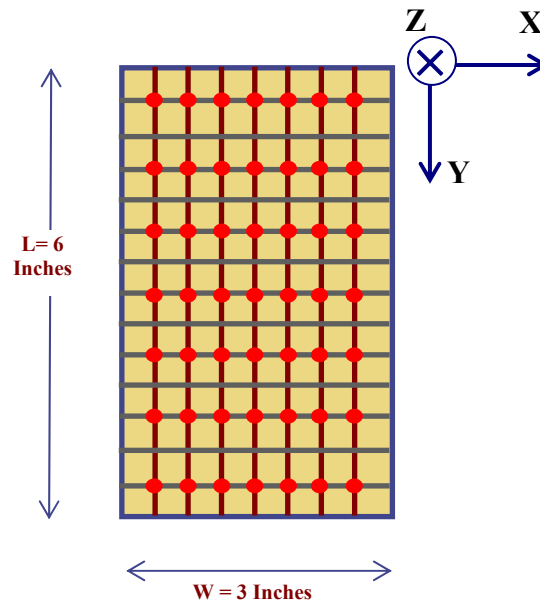


Figure 3. Fabric samples evaluated for determining the effect of increasing the number of constrained crossover points of orthogonal conductive threads. The lines shown in grey color depict weft copper threads and the lines in the brown color depict copper threads in the warp direction. The region having yellow color depicts polyester warp and weft threads. Different samples, 6 inches long and 3 inches wide, were prepared containing 7, 8, 16, 32, 64 or 96 copper warp threads out of a total of 96 warp threads and 11, 13, 22, 45, 90, or 180 copper weft threads out of a total of 180 Weft threads. The red dots in the figure depict constrained (welded, fused, or bonded) crossover points of orthogonal copper threads. The warp and weft directions are in the Y and X directions respectively and the fabric was bent in the Z direction

5.3 Experimental

In order to validate the model conductive fabric samples were woven with various arrangements of conductive (copper) and non-conductive threads in both the warp and weft directions and one or more crossover points of orthogonal copper threads were bonded by employing a conductive adhesive.

The fabric circuits were woven on a rapier weaving machine with a Jacquard shedding system. The copper threads in the warp direction were delivered from a creel positioned behind the weaving machine. The woven conductive fabrics were cut into fabric samples 6 inch long and 3 inch wide. The fabric samples evaluated experimentally in our study had 7 copper yarns in the warp direction and 11 copper yarns in the weft direction, the rest of the threads in the warp and weft directions being polyester threads. One or more crossover points of orthogonal copper yarns in these conductive fabric samples were bonded by employing a two part conductive adhesive. The two parts of the conductive adhesive were mixed and then dispensed in a very small amount by taking a tip of a syringe needle 100 micron in diameter, dipping it in the two part adhesive mixture, and then applying it to the crossover point of two copper threads, in order to form a crossover point interconnect at that crossover point. Schematic of some of the samples that were developed is shown in Figure 3 and picture of an actual sample woven in the Jacquard weaving machine is shown in Figure 4.

In order to experimentally determine the bending rigidity of the woven conductive fabric structures, the Cantilever bending test, described by ASTM test standards D1388 & D5372, was employed. In the Cantilever bending test, experimental evaluations of the overhang length 'l' were carried out and four readings were taken for each sample – two readings, one for each direction of the sample, for each side of the sample and an average value was evaluated. Fabric Bending Rigidity C is related to the overhang length 'l' by the following relationship:

$$C = W \cdot \left(\frac{1}{2} \left(\frac{\cos(\theta/2)}{\tan(\theta)} \right) \right)^{1/3} \quad (14)$$

where W is the weight per unit area of the fabric. If the value of W is expressed in units of N/m² and the value of overhang length is expressed in units of meters, then the units of the experimentally calculated bending rigidity (C) are N-m. This value of the bending

rigidity was normalized to the length of the fabric samples for comparison with the values of bending rigidity determined by employing the theoretical models described in section 5.2. The results of these experimental evaluations and their comparisons with the theoretical values, calculated in section 5.2 by employing the bending rigidity model considering the effects of the crossover point interconnects and the different types of yarns in the woven structure, are provided in section 5.4.

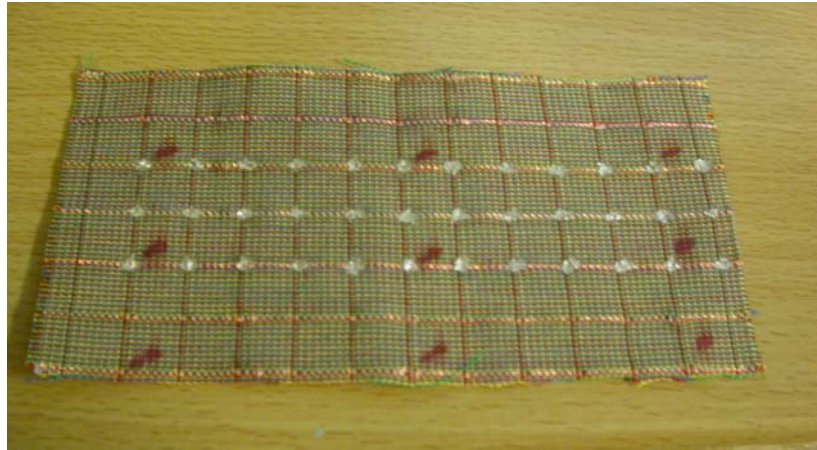


Figure 4. Fabric sample woven on a rapier loom with a Jacquard head, having copper threads in the warp and weft directions such that some of the crossover points of orthogonal copper threads were constrained by localized application of conductive adhesive

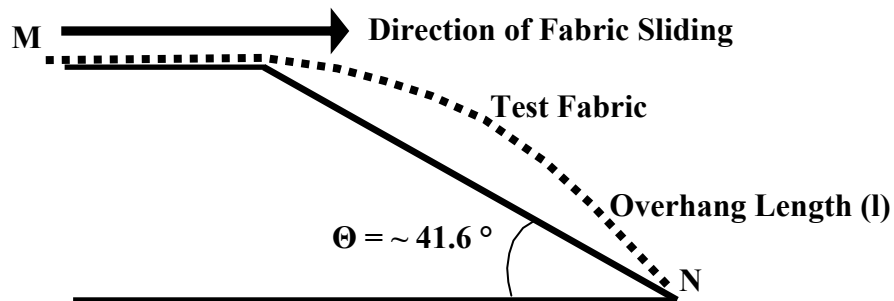


Figure 5. Schematic of the Cantilever test for bending rigidity evaluations

5.4 Results and Discussion

First part of this section discusses results of the theoretical calculations of the bending rigidity of a woven fabric circuit. This is followed by discussion of the experimental measurements that were carried out on woven fabric samples containing several crossover points that were bonded by a conductive adhesive.

It was observed from theoretical calculations that the value of A_F/A_1 was higher (~ 1.85) in the case of a constrained crossover point as compared to the unconstrained crossover point (0.86), the value of A_r and L_r being unity in both cases and λ being 0.9 (The terms A_r , L_r , and λ were defined in chapter 3). This could be attributed to a higher value of strain energy stored in the constrained crossover region when the fabric is bent as value of β_{21} (the angle of wrap of the warp yarn under the weft yarn, as shown in Figure 1) does not decrease with an increase in the bending angle ψ , while the value of β_{11} increases with the fabric bending. The strain energy stored in the free region of the axial yarns is slightly lower in the case of constrained crossover points as compared to that in the unconstrained crossover points, but the overall stored strain energy on bending the fabrics is higher for the constrained crossover points. In the case of evaluating the bending rigidity associated with a constrained crossover point, it is assumed that all four crossover points in a fabric unit cell shown in Figure 1a are constrained.

Moreover, it was observed in the case of unconstrained crossover points that the value of A_F/A_1 is higher when A_r is less than unity i. e. when the warp threads are less rigid as compared with the cross weft yarns. This could be attributed to a higher resistance to bending imparted by the rigid cross weft threads thereby resulting in a higher value of fabric bending rigidity. The value of A_F/A_1 was calculated to be 2.41 for $A_r = 0.2$, 0.406 for $A_r = 5$, and 0.86 for $A_r = 1$. Moreover, the value of free strain energy stored in the axial yarns (U_{f1}) in the direction of bending is lower than the value of free strain energy stored in the weft yarns (U_{f2}), when the value of A_r is less than unity. One also observes that when A_r is less than unity, the value of stored strain energy in the axial yarn in crossover regions of the fabric unit cell is higher than the value stored in the free yarn region.

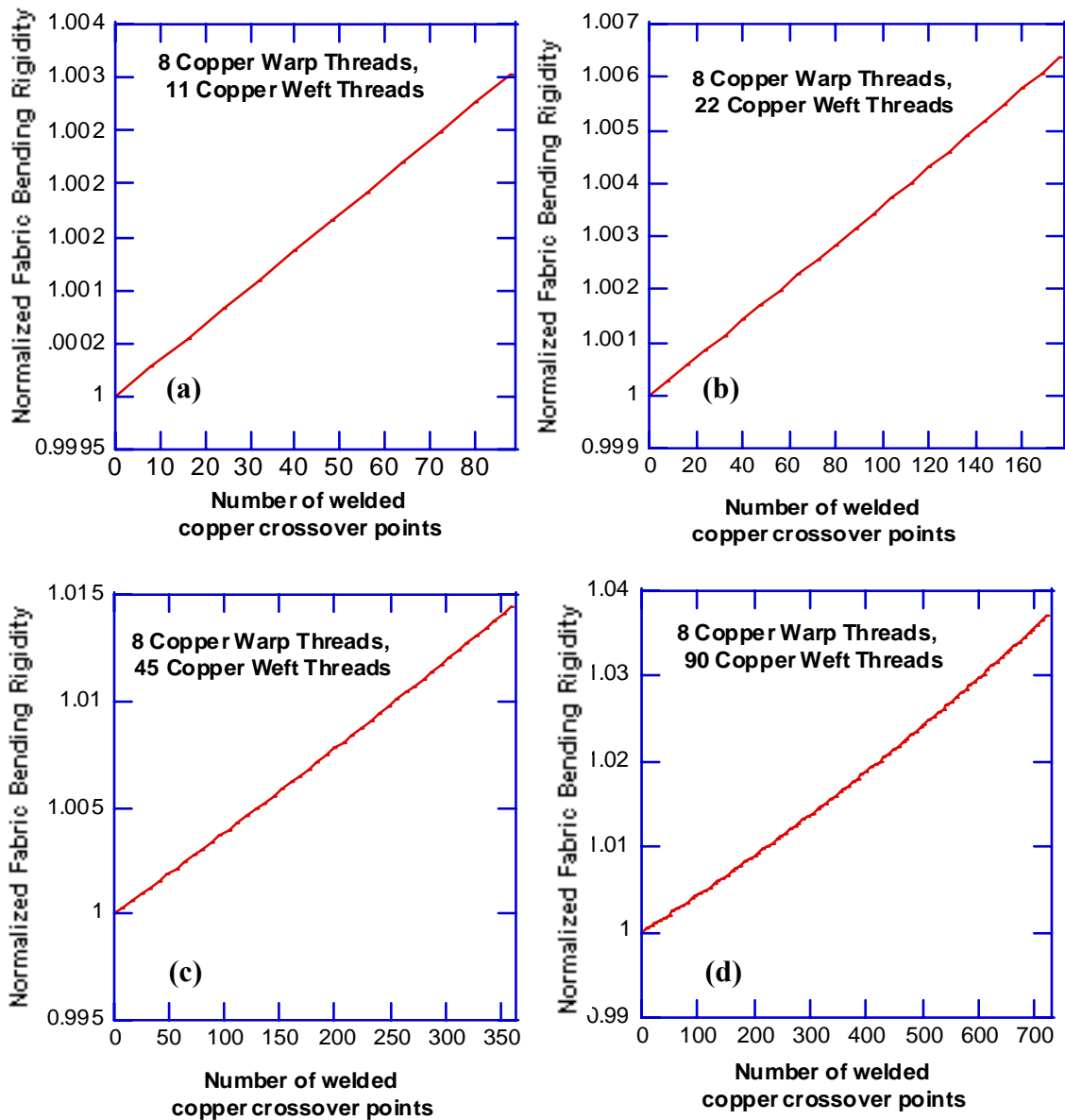


Figure 6. Theoretical values of normalized bending rigidity as the number of bonded crossover points, of orthogonal copper threads in a woven fabric circuit, is increased. All fabric samples that were evaluated had 8 copper yarns in the warp direction, the total number of warp threads in the fabric samples being 96. The normalization was carried out by dividing the theoretical value of bending rigidity of fabric samples containing bonded crossover point interconnects by the theoretical bending rigidity value of fabric circuit samples with no bonded crossover points

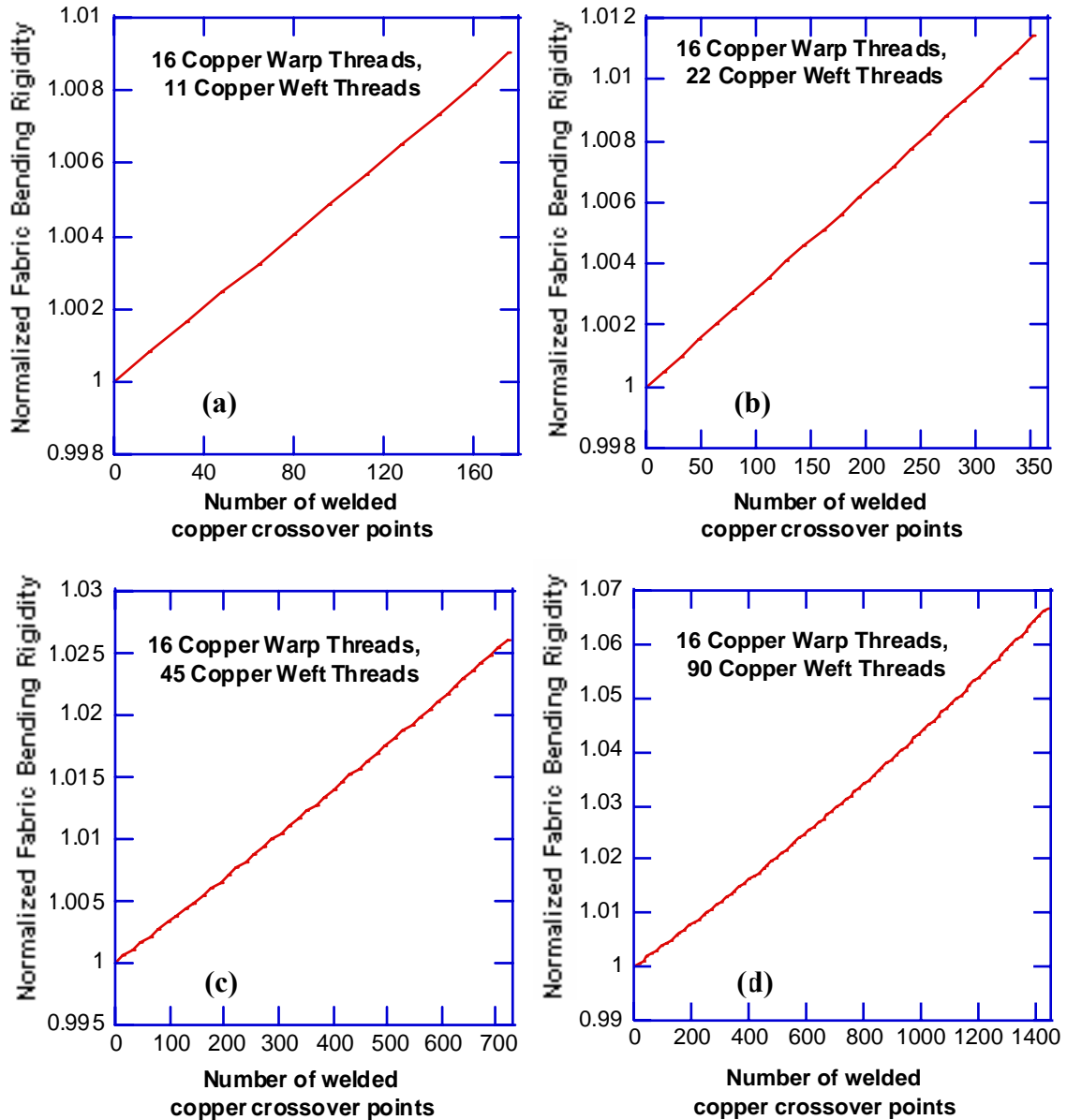


Figure 7. Theoretical values of normalized bending rigidity as the number of bonded crossover points, of orthogonal copper threads in a woven fabric circuit, is increased. All fabric samples that were evaluated had 16 copper yarns in the warp direction, the total number of warp threads in the fabric samples being 96. The normalization was carried out by dividing the theoretical value of bending rigidity of fabric samples containing bonded crossover point interconnects by the theoretical bending rigidity value of fabric circuit samples with no bonded crossover points

The value of the overall bending rigidity (A_F) of a woven fabric circuit was obtained by employing equation 13 to a set of fabric samples having 180 total threads in weft direction and 96 total threads in the warp direction. The proportion of conductive copper threads, in warp and weft directions, was varied as values of the overall bending rigidity (A_F) of the conductive fabric were obtained. Moreover, proportion of the constrained crossover points of orthogonal copper threads was also varied and value of the overall fabric bending rigidity (A_F) calculated by employing equations 12 and 13.

Results of varying the number of constrained crossover points, for fabrics with different proportions of copper threads in the warp and weft directions, are given in Figures 6, 7, 8, and 9. It can be seen in all the four Figures that as the number of constrained (via welding, soldering, or bonding) crossover points is increased, the bending rigidity of the fabric increases. The increase, relative to a fabric with all the crossover points being unconstrained, is only by ~ 0.3 percent for a fabric having 8 copper warp threads and 11 copper weft threads and all its copper crossover points being constrained. This is because there are a maximum of 88 constrained crossover points and the presence of such a small number of rigid crossover point interconnects, out of a total of 17280 crossover points in a fabric sample having 180 weft threads and 96 warp threads, does not increase the fabric bending rigidity substantially. The effect of constraining the crossover points is more pronounced in fabrics with a greater number of points of intersection of orthogonal conductive threads, as can be seen from Figures 8 and 9. In case of Figure 9d, one can observe that when all the threads of the fabric are copper threads and when all the 17280 copper yarn crossover points are constrained, the increase in fabric bending rigidity relative to a fabric, with all the crossover points being unconstrained, is around 116 percent. This is the maximum possible increase in bending rigidity of a conductive fabric sample, having 180 weft threads and 96 warp threads, due to constraining of the crossover points of conductive threads in the fabric. One can observe a non-linear relationship between the normalized bending rigidity and the proportion of constrained copper crossover points in Figures 7d, 8d, and 9c. This could be explained by the presence of a very high density of copper crossover points that are constrained. The relationship between A_F and the proportion of constrained copper crossover points, given by equations 12 and 13, is not linear and the high density of

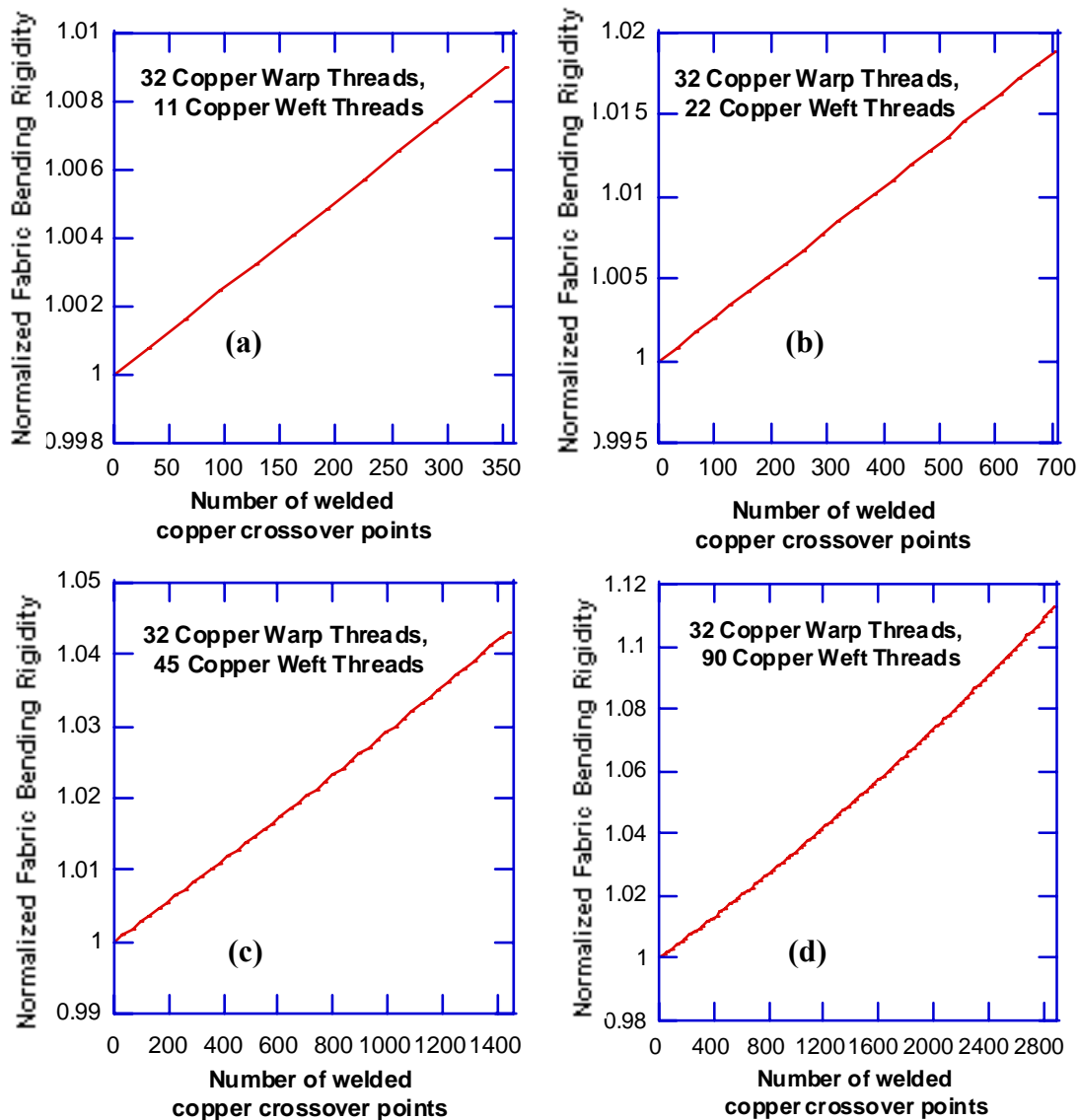


Figure 8. Theoretical values of normalized bending rigidity as the number of bonded crossover points, of orthogonal copper threads in a woven fabric circuit, is increased. All fabric samples that were evaluated had 32 copper yarns in the warp direction, the total number of warp threads in the fabric samples being 96. The normalization was carried out by dividing the theoretical value of bending rigidity of fabric samples containing bonded crossover point interconnects by the theoretical bending rigidity value of fabric circuit samples with no bonded crossover points

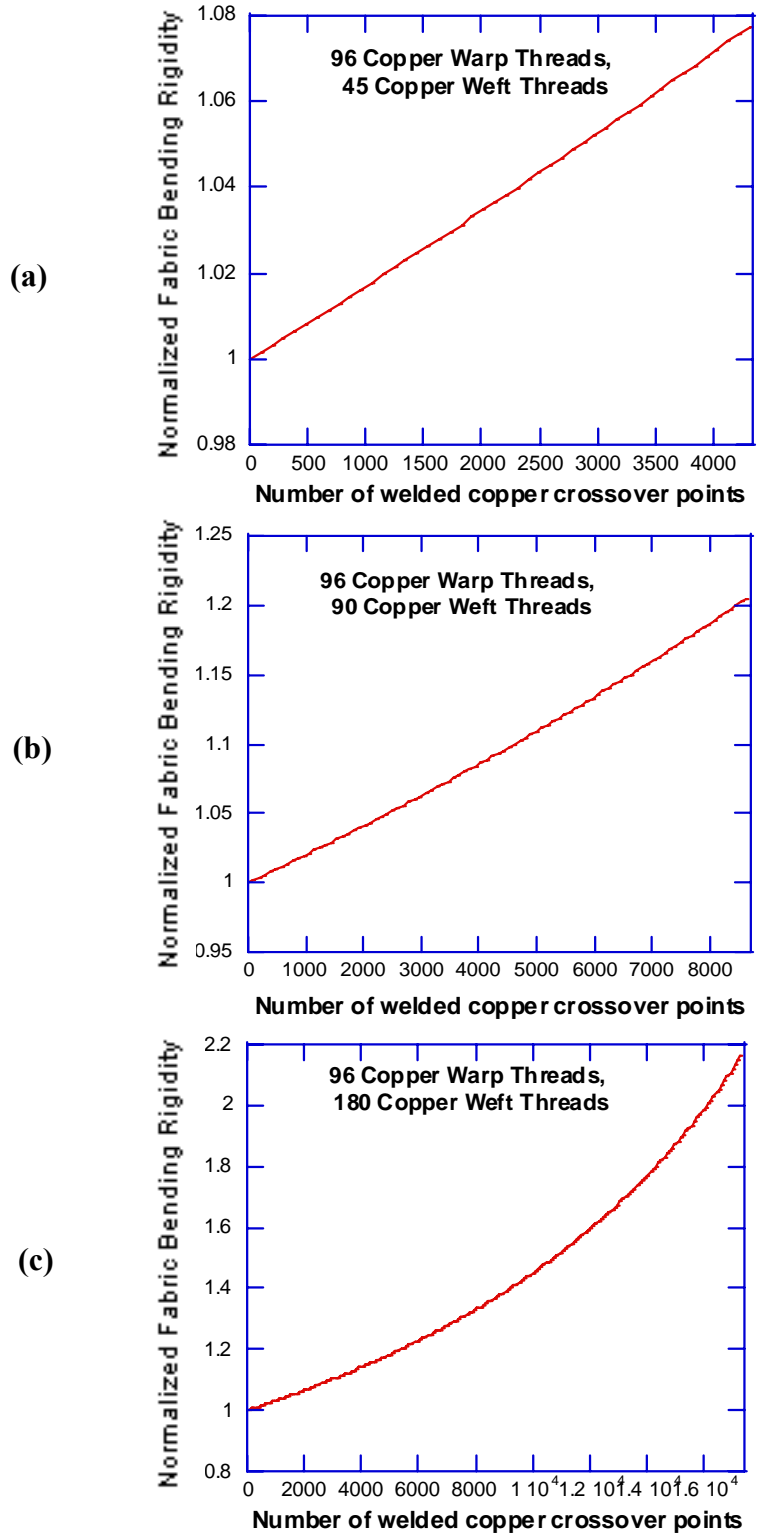


Figure 9. Theoretical values of normalized bending rigidity as a function of the number of constrained (welded, bonded, or fused) crossover points. All fabric samples that were evaluated had 96 copper yarns in the warp direction, the total number of warp threads in the fabric samples being 96

constrained copper crossover points leads to a more pronounced non-linearity.

In order to experimentally determine the bending rigidity of the fabric circuit structures, the Cantilever bending test was employed. The results of these evaluations are provided in Figures 10a and b. In Figure 10a one observes that the increase in bending rigidity of fabric circuit samples is around 14.3 percent, when all 77 copper crossover points are bonded. At the same time one has to note that there is an increase in fabric weight by around 13.1 percent when all 77 copper crossover points in a fabric circuit sample are bonded. In order to consider the effect of restriction of the axial yarn rotation only, upon forming a bond at the crossover point of orthogonal copper threads, we divide the values of the fabric bending rigidity by the weight of the fabric sample such that effect of weight loading by the conductive adhesive is eliminated. The result after eliminating the effect of weight loading is shown in Figure 10b. One can observe that there is ~ 1.5 percent increase in the fabric bending rigidity, relative to a fabric with all the crossover points being unconstrained, by considering only the effect of restriction of yarn rotation at the crossover point when it is bonded.

Figure 11 provides a comparison of the experimental and theoretical values of the normalized bending rigidity as the proportion of the number of bonded crossover points, of orthogonal copper threads in a woven fabric circuit developed from copper and polyester threads, is increased. The normalization was carried out by dividing all bending rigidity values, experimental and theoretical, by the experimental value of bending rigidity of fabric circuit samples with no bonded crossover points. One can observe in Figure 11 that the normalized bending rigidity values obtained theoretically are higher than the values determined experimentally, for all values of the proportion of the bonded copper crossover points. But at the same time one also observes that the percentage increase in the normalized bending rigidity, upon constraining or bonding the crossover points of copper yarns, is higher in the experimental samples (even after eliminating the effect of weight loading due to the conductive adhesive applied to form the bonds at the crossover points). This could be attributed to a possibility of bonding of neighboring crossover points around the crossover point of orthogonal copper yarns being bonded, thereby leading to higher measured bending rigidity values. One has to

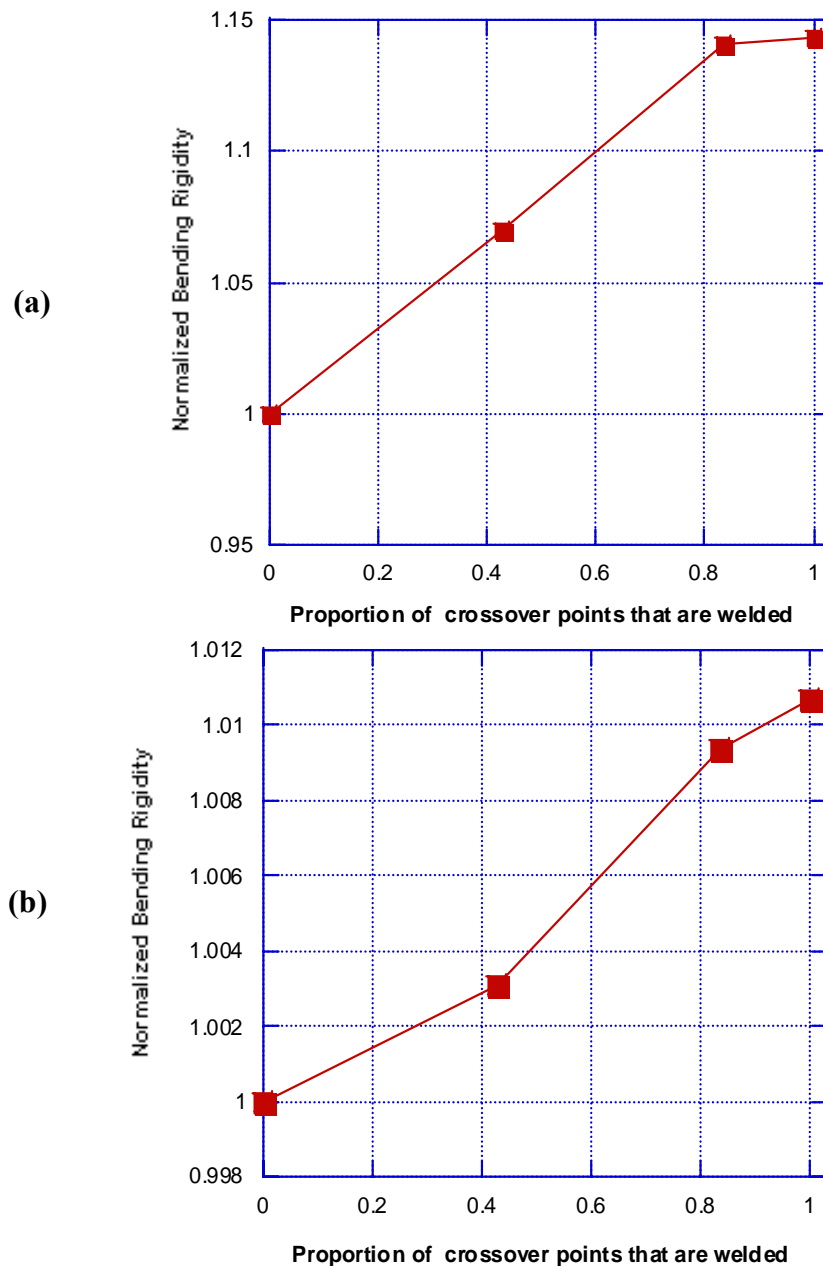


Figure 10. (a) Experimental value the normalized bending rigidity as the proportion of the number of bonded crossover points, of orthogonal copper threads in a woven fabric circuit developed from copper and polyester threads is increased. The normalization was carried out by dividing bending rigidity of fabric samples containing bonded crossover point interconnects by the bending rigidity value of fabric circuit samples with no bonded crossover points. (b) The effect of weight in the bending rigidity values is divided to obtain only the effect of constraining the crossover points on the bending rigidity of the fabric

mention that although precautions were taken to ensure dispensing of a similar amount of conductive adhesive at all the crossover points, this process was carried out manually and had the scope of human experimental error. It is recommended that in future work, other processes for the formation of crossover point interconnects - such as resistive welding should be employed - as in that case the problems of weight loading and non-uniformity of the crossover point bonds are less pronounced.

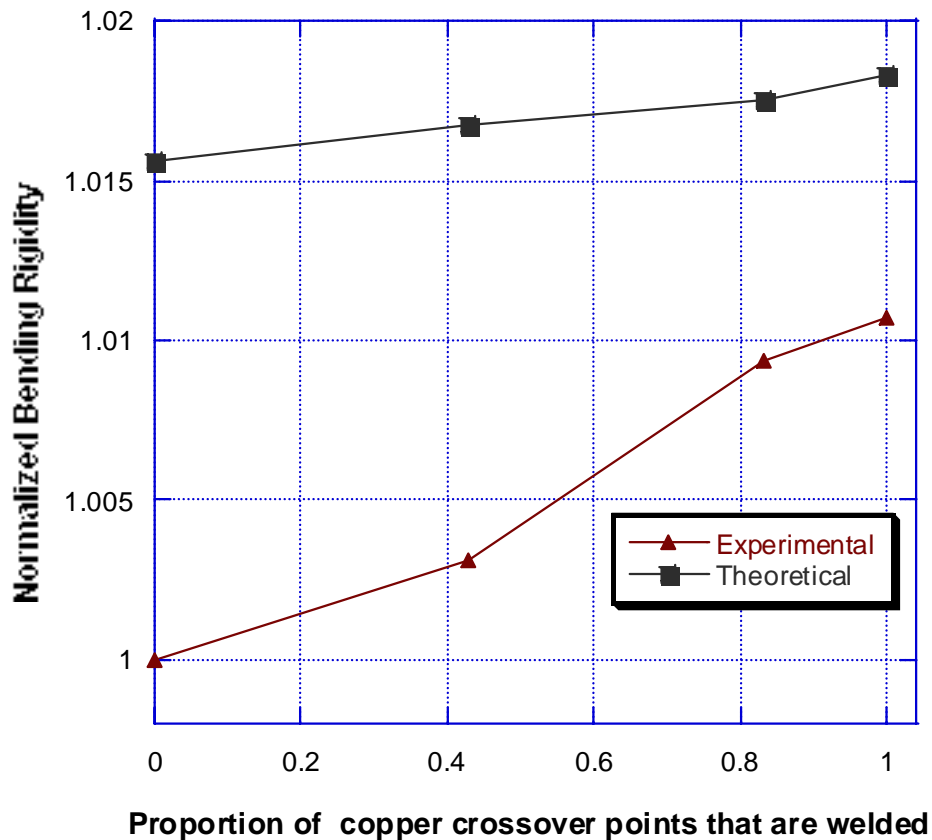


Figure 11. Comparison of experimental and theoretical values of increase in the normalized bending rigidity as the proportion of the number of bonded crossover points, of orthogonal copper threads in a woven fabric circuit developed from copper and polyester threads, is increased. The normalization was carried out by dividing all bending rigidity values, experimental and theoretical, by the experimental value of bending rigidity of fabric circuit samples with no bonded crossover points

5.5 References

1. A. Dhawan, T. K. Ghosh, A. M. Seyam, and J. F. Muth, "Woven Fabric-based Electrical Circuits Part I: Evaluation of Interconnect Methods," *Textile Research Journal*, October, 2004.
2. A. Dhawan, T. K. Ghosh, A. M. Seyam, and J. F. Muth, "Woven Fabric-based Electrical Circuits Part II: Yarn and fabric structures to reduce crosstalk noise in woven fabric-based circuits," *Textile Research Journal*, In Press, to be published in November, 2004.
3. A. Dhawan, T. K. Ghosh, A. M. Seyam, and J. F. Muth, "Woven Fabric-based Electrical Circuits," *Proc. of Textile Technology Forum, IFAI and the Textile Institute*, Charlotte, NC, 2002.
4. A. Dhawan, "Woven fabric-based electrical circuits," *Masters Thesis*, North Carolina State University, 2001.
5. A. Dhawan, T. K. Ghosh, A. M. Seyam, and J. F. Muth, "Development of Woven fabric-based electrical circuits," *Proc. of the Materials Research Society Conference Symposium D*, Boston, 2002.
6. A. Dhawan, T. K. Ghosh, A. M. Seyam, and J. F. Muth, "Formation of Electrical Circuits in Woven Structures," *Proc. of the International Interactive Textiles for the Warrior Conference organized by the Soldier and Biological Chemical Command, NASA, & DARPA*, Cambridge, MA, July 9-11, 2002.
7. D. Cottet, J. Grzyb, T. Kirstein, and G. Tröster, "Electrical Characterization of Textile Transmission Lines," *IEEE Transactions on Advanced Packaging*, Vol. 26, No. 2, May 2003, pages 182-190.
8. T. K. Ghosh, R. L. Barker, and S. K. Batra, "On the Bending Behavior of Plain Woven Fabrics, Part I: A Critical Review," *Textile Institute Journal*, 81, 255-271, 1990.
9. T. K. Ghosh, R. L. Barker, and S. K. Batra, "On the Bending Behavior of Plain Woven Fabrics, Part II: The Case of Linear Yarn Bending Behavior," *Textile Institute Journal*, 81, 272-287, 1990.
10. T. K. Ghosh, R. L. Barker, and S. K. Batra, "On the Bending Behavior of Plain Woven Fabrics, Part III: The Case of Bi-Linear Yarn Bending Behavior and the Effect of Fabric set," *Textile Institute Journal*, 81, 288-299, 1990.